Plio-Pleistocene Sediment Provenance and Erosion Rates Along the East African Rift System

by

Emily Elizabeth Zawacki

A Dissertation Presented in Partial Fulfillment
of the Requirements for the Degree
Doctor of Philosophy

Approved July 2021 by the
Graduate Supervisory Committee:

J Ramón Arrowsmith, Co-Chair
Christopher Campisano, Co-Chair
Arjun Heimsath
Kip Hodges
Kelin Whipple

ARIZONA STATE UNIVERSITY

August 2021

ABSTRACT

The tectonism, volcanism, and sedimentation along the East African Rift System (EARS) produced a series of rift basins with a rich paleoanthropological record, including a Late Miocene–present record of hominin evolution. To better understand the relationship between Earth system history and human evolution within the EARS, the Hominin Sites and Paleolakes Drilling Project (HSPDP) collected paleolake sediments near key paleoanthropological sites in Ethiopia and Kenya, compiling a multi-proxy, high-resolution geological and environmental record.

As part of the HSPDP, I studied the detrital mineral record of the basins and evaluated tectonic and climatic controls on East African landscapes during the Plio-Pleistocene using samples from three of the drill sites, Chew Bahir: (CHB, ~620–present; Ethiopia), Northern Awash (NA, ~3.3–2.9 Ma; Ethiopia,), and West Turkana (WTK, ~1.9–1.4 Ma; Kenya). I employed laser ablation U/Pb and (U-Th)/He double dating (LADD) of detrital zircons, which yields paired U/Pb and (U-Th)/He dates, and (U-Th)/He dating of detrital apatites to evaluate sediment provenance and the cooling history of the source rocks. In addition, I used *in situ* ^{10}Be cosmogenic radionuclide analyses to determine paleoerosion rates.

Two chapters of this dissertation focus on results from the NA and WTK drill sites. Source units for the NA and WTK drill sites are largely Cenozoic volcanic rocks, and the detrital zircon record yields an extensive record of the timing of various phases of volcanism within the EARS. Exceptionally young zircon (U-Th)/He dates reflect partial resetting associated with late mafic volcanism and/or hydrothermal activity. Erosion rates

are consistent and relatively low across the Plio-Pleistocene, despite significant tectonic and geomorphic shifts in the landscape.

Two other chapters of this dissertation cover results from the CHB drill site. The Chew Bahir basin has significant exposures of Neoproterozoic and Early Paleozoic crystalline basement units, and the detrital zircon record yields one singular phase of volcanism in the EARS. The CHB erosion rates show an overall decreasing trend over time, consistent with an aridifying climate, and increased environmental variability after ~200 ka.

ACKNOWLEDGEMENTS

I owe a huge debt of thanks to my advisors, Ramon Arrowsmith and Christopher Campisano, for taking me on as a student and providing me guidance and support over these last six years. I would also like to thank my committee members, Kip Hodges, Arjun Heimsath, and Kelin Whipple, for always providing helpful discussion and advice along the way.

Thank you to the Group 18 Laboratories and the WOMBAT cosmogenic nuclide laboratory for allowing me to process and analyze my samples in your facilities. Thank you especially to Michelle Aigner and Matthijs van Soest for all the laboratory training and analytical help.

I would like to thank the entire Hominin Sites and Paleolakes Drilling Project (HSPDP) team for the great yearly group meetings, as well as the Ledi-Geraru Research Project (LGRP) team for helpful discussions as I put together these dissertation chapters.

I would also like to thank and acknowledge the funding that made this dissertation research possible, including the National Science Foundation and the Graduate Completion Fellowship from Arizona State University.

I would not be where I am today if it were not for my undergraduate advisor, Marcia Bjørnerud, whose incredible passion for teaching sparked my love of geology. I am sure Marcia is very happy I decided to go to graduate school in geology instead of doing the Disney College Program. (I am pretty pleased with the decision too!)

Thank you to my parents and family for supporting me on this geological journey (or genealogical as my grandpa would always mistakenly say). A final loving thank you to those who were with me every day, Stefan (human), Selex (cat), and Mica (cat).

TABLE OF CONTENTS

CHAPTER Page

CHAPTER Page

APPENDIX Page

LIST OF TABLES

LIST OF FIGURES

Figure Page

Figure Page

CHAPTER 1

INTRODUCTION

1.1 The East African Rift System

The volcanically and tectonically active East African Rift System (EARS) extends for ~3,500 km through the eastern African continent and contains a series of structurally and magmatically controlled extensional basins (Chorowicz, 2005). The EARS is geographically divided into a western branch and an eastern branch (Figure 1.1). The western branch of the EARS has only isolated instances of volcanism that are typically restricted to the footwalls of border faults and structurally complex transfer faults (Ebinger et al., 1989; Pasteels et al., 1989). The eastern branch of the EARS features widespread, voluminous volcanism (Rooney, 2017). Pre-rift volcanism initiated at ~45 Ma in the eastern branch and has continued to the present (Ebinger et al., 2000).

Rift basins began to form over the late Oligocene and early Miocene, with sedimentation triggered by volcanic and tectonic activity (Chernet et al., 1998; Ebinger et al., 1993; WoldeGabriel et al., 1990, 2000). The rift basins of the EARS thus provide an archive of Neogene and Quaternary volcanism, tectonism, paleoclimate, and paleoenvironments, which include fossiliferous strata key to understanding faunal evolution, including that of humans and their fossil ancestors (e.g., deMenocal, 2004; WoldeGabriel et al., 2000).

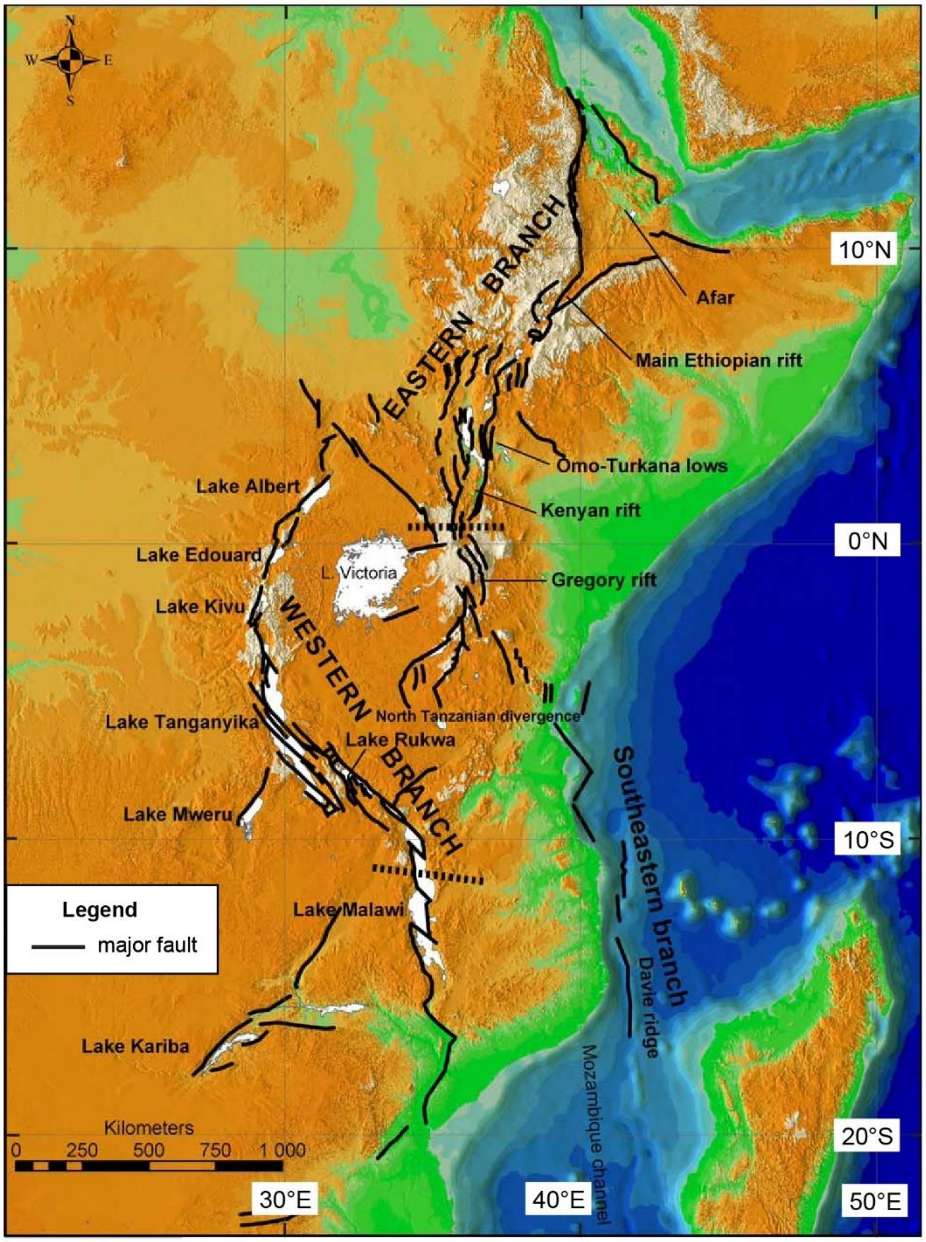

Figure 1.1 Map of the East African Rift System (EARS) showing primary geographic distinctions, main faults, rift segments, and rift lakes. Modified from Chorowicz (2005).

1.2 The Hominin Sites and Paleolakes Drilling Project

Understanding the relationship between Earth system history and human evolution has long been at the forefront of scientific inquiry. Numerous hypotheses have proposed links between climate-induced environmental changes and the evolution of mammalian fauna—including the origin and diversification of hominin lineages—over the last 6–7 My in East Africa (e.g., Dart, 1925; deMenocal, 2004; Potts, 1998; Vrba, 1995). While there has been significant research on Cenozoic African climate and environmental dynamics from marine sediment cores and outcrop sediments, marine records are not proximal to the sites that hominins occupied and outcrop sediments are often weathered and discontinuous.

To remedy the shortcomings inherent with marine and outcrop records, the Hominin Sites and Paleolakes Drilling Project (HSPDP) collected ~2,000 m of drill core sediments from six lacustrine depocenters near key paleoanthropological sites in Ethiopia and Kenya (Figure 1.2). With near-continuous sedimentary records covering the last ~3.5 My, HSPDP aims to compile high-resolution paleoenvironmental data that can be used to assess hypotheses that posit a relationship between Earth system history and human evolution (Campisano et al., 2017; Cohen et al., 2016).

My primary research focus with the HSPDP is to understand the basin-scale response to changes in climate and tectonics during the Plio-Pleistocene. Understanding the basin-scale response to regional tectonics and climate is a crucial component for linking global climate changes, and their subsequent environmental response, to patterns in human evolution.

I use the detrital mineral record of the drill cores (apatite, zircon, and quartz) to extrapolate out geomorphic information about the watersheds. I determine the provenance of the sediments from U/Pb dating of zircons to evaluate changes in sediment source region over time and paleowatershed configurations. The abundance of volcanic zircons within watersheds of the EARS also provided insight into the volcano-tectonic evolution of the EARS. (U-Th)/He dates of detrital apatites and zircons provide information about the cooling history of the samples and timing of rifting/heating processes. I also determine millennial-scale paleoerosion rates from *in situ* ^{10}Be cosmogenic radionuclide analyses, which helps to discern the relative importance of climatic and tectonic controls on landscape evolution.

This dissertation as part of the HSPDP focuses on three of the six drilling sites: Chew Bahir (CHB, ~620–present; Ethiopia), Northern Awash (NA, ~3.3–2.9 Ma; Ethiopia,), and West Turkana (WTK, ~1.9–1.4 Ma; Kenya) (Campisano et al., 2017; Cohen et al., 2016). I also collected and processed five samples from the Baringo/Tugen Hills drill core (BTB, ~3.29–2.56 Ma; Kenya) (Deino et al, 2019), but the samples did not yield sufficient heavy minerals for thermochronology analyses, and cosmogenic radionuclide analyses were unsuccessful.

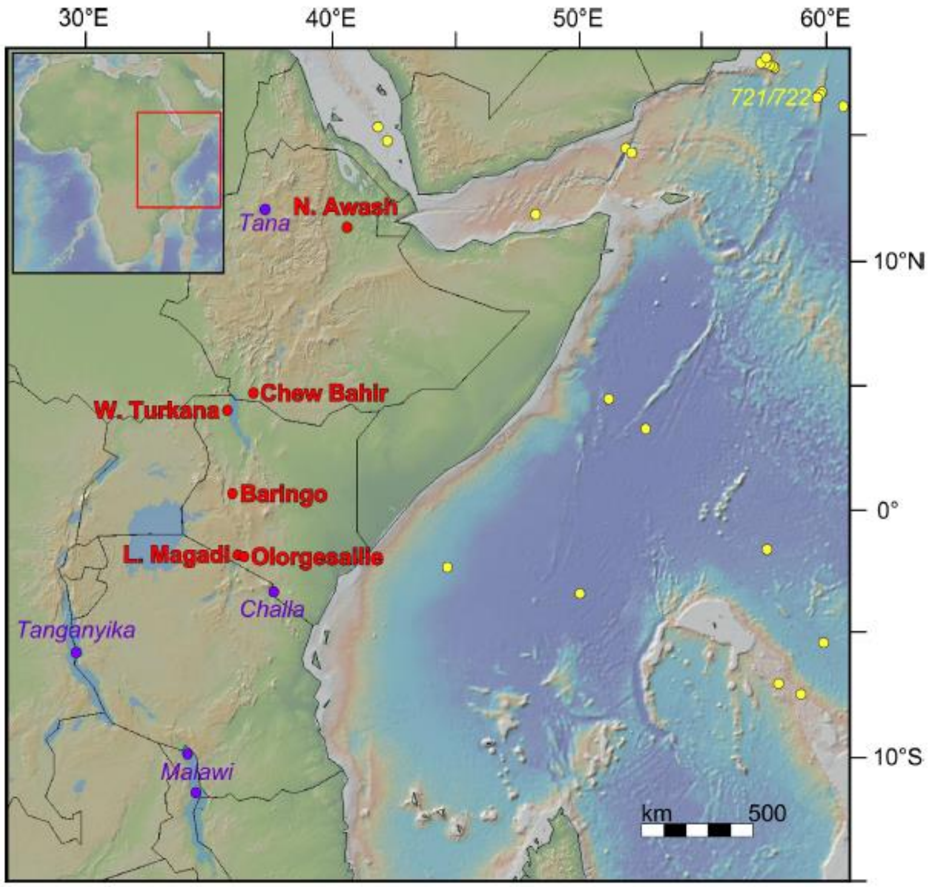

Figure 1.2 Map of eastern Africa showing the locations of the HSPDP drilling areas (red), modern lakes with long core records (purple), and ODP/DSDP drilling locations (yellow). Base map generated form GeoMapApp. Figure from Campisano et al. (2017).

1.3 Dissertation outline

This dissertation is divided into four primary chapters (2, 3, 4, and 5) with a final concluding synthesis chapter (6). Chapters 2 and 3 involve analyses performed on the same set of five samples from the NA and WTK drill cores. Chapters 4 and 5 involve analyses performed on the same set of ten samples from the CHB drill core. Chapters 2 and 5 include detrital zircon laser ablation double dating (LADD) techniques to yield paired U/Pb and (U-Th)/He dates for a single grain. Chapter 5 additionally includes conventional (U-Th)/He dating of detrital apatites. Chapters 3 and 4 utilize *in situ* ^{10}Be cosmogenic radionuclide analyses for paleoerosion rate determinations.

Chapter 2 discusses the detrital zircon record of the NA and WTK drill sites. By using the LADD method, I determine the provenance of the sediments based on the U/Pb dates and evaluate the cooling history of the samples based on the (U-Th)/He dates. The NA and WTK detrital zircon records are dominated by Cenozoic zircons (< 45 Ma) derived from silicic volcanic units associated with volcanism in the EARS, and they track the established timing of major volcanic phases in the EARS. Few detrital zircon (U-Th)/He dates are reflective of eruption ages, and the large spread in dates reflects partial resetting from volcanic heating and/or hydrothermal alteration. (U-Th)/He dates younger than the depositional ages of the samples are likely a result of post-depositional sub-lacustrine hydrothermal alteration. This chapter is co-authored by Matthijs C. van Soest, Kip V. Hodges, Jennifer J. Scott, Mélanie Barboni, Manfred R. Strecker, Craig S. Feibel, Christopher J. Campisano, and J Ramón Arrowsmith and is currently in review at *Earth and Planetary Science Letters*.

Chapter 3 examines Plio-Pleistocene paleoerosion rates from the NA and WTK drill sites derived from ^{10}Be analyses. I am able to take advantage of the high-resolution record and age-depth model of the drill cores to constrain uncertainties in paleoerosion rates that many other studies working with terrace samples do not address. The lack of identifiable sources of quartz for the NA sands complicates interpretations of paleoerosion rates as catchment mean rates, and quartz may be source from vein quartz or phenocrystic quartz within the rift-related magmatic and hydrothermal systems. The similarity of erosion rates across the Plio-Pleistocene transition, which features a notable tectonic and geomorphic reorganization, suggests that climate may play a stronger control on erosion of source regions than does tectonics.

Chapter 4 provides a record of Pleistocene paleoerosion rates from the CHB basin derived from ^{10}Be analyses. The abundant exposures of quartz-bearing crystalline basement rocks combined with the high-resolution record of the HSPDP drill cores, makes the Chew Bahir basin an excellent locale for studying changes in erosion rates over time. Data of modern erosion rates from subcatchments within the basin provide a useful comparison for which to interpret the paleoerosion rates. The paleoerosion rates are relatively consistent over time with a broad decreasing trend, consistent with an aridifying climate. In this significantly smaller, closed basin, erosion rates appear most linked to local tectonics.

Chapter 5 provides a Precambrian to Pleistocene overview of the CHB basin using low- and high-temperature thermochronology. LADD of detrital zircons provides abundant dates for Neoproterozoic and Early Paleozoic bedrock units within the basin, which helps to better understand the timing of events related to the East African Orogen in southern Ethiopia. The CHB detrital zircon record shows a stark contrast compared to the NA and WTK drill cores (Chapter 2), as there is only one pulse of Cenozoic volcanism recorded at ~19.5 Ma. Detrital apatite (U-Th)/He dates provide a comparison and refinement for the timing of Cenozoic rift initiation in the Broadly Rifted Zone (BRZ). During the Pleistocene, sediment input from the basin rift margin appears variable over time, likely related to pulses of tectonic activity and wet/dry climate conditions.

Chapter 6 is a final synthesis chapter that discusses the contributions made in Chapters 2–5 and presents potential avenues for future work.

1.4 References

Campisano, C. J., A.S. Cohen, J.R. Arrowsmith, A. Asrat, A.K. Behrensmeyer, E.T. Brown, A.L. Deino, D.M. Deocampo, C.S. Feibel, J.D. Kingston, H.F. Lamb, T.K. Lowenstein, A. Noren, D.O. Olago, R.B. Owen, J.D. Pelletier, R. Potts, K.E. Reed, R.W. Renaut, J.M. Russell, J.L. Russell, F. Schabitz, J.R. Stone, M.H. Trauth, and J.G. Wynn (2017). The Hominin Sites and Paleolakes Drilling Project: High-resolution paleoclimate records from the East African rift system and their implications for understanding the environmental context of hominin evolution. *PaleoAnthropology*, p. 1–43. https://doi:10.4207/PA.2017.ART104

Chernet, Tadiwos, William K. Hart, James L. Aronson, and Robert C. Walter (1998). New age constraints on the timing of volcanism and tectonism in the northern Main Ethiopian Rift–southern Afar transition zone (Ethiopia). *Journal of Volcanology and Geothermal Research*, 80, 3-4, p. 267–280. https://doi.org/10.1016/S0377-0273(97)00035-8

Chorowicz, Jean (2005). The East African Rift System. *Journal of African Earth Sciences*, 43, 1-3, p. 379–410. https://doi.org/10.1016/j.jafrearsci.2005.07.019

Cohen, A., C. Campisano, R. Arrowsmith, A. Asrat, A.K. Behrensmeyer, A. Deino, C. Feibel, A. Hill, R. Johnson, J. Kingston, H. Lamb, T. Lowenstein, A. Noren, D. Olago, R.B. Owen, R. Potts, K. Reed, R. Renaut, F. Schäbitz, J.-J. Tiercelin, M.H. Trauth, J. Wynn, S. Ivory, K. Brady, R. ÓGrady, J. Rodysill, J. Githiri, J. Russell, V. Foerster, R. Dommain, S. Rucina, D. Deocampo, J. Russell, A. Billingsley, C. Beck, G. Dorenbeck, L. Dullo, D. Feary, D. Garello, R. Gromig, T. Johnson, A. Junginger, M. Karanja, E. Kimburi, A. Mbuthia, T. McCartney, E. McNulty, V. Muiruri, E. Nambiro, E.W. Negash, D. Njagi, J.N. Wilson, N. Rabideaux, T. Raub, M.J. Sier, P. Smith, J. Urban, M. Warren, M. Yadeta, C. Yost, and B. Zinaye (2016). The Hominin Sites and Paleolakes Drilling Project: inferring the environmental context of human evolution from eastern African rift lake deposits, Sci. Dril., 21, p. 1–16. https://doi.org/10.5194/sd-21-1-2016

Dart, Raymond A., 1925. *Australopithecus africanus:* The Man-Ape of South Africa. *Science*, 115, p. 195–199. https://doi.org/10.1038/115195a0

Deino, Alan L., Mark J. Sier, Dominique I. Garello, C. Brenhin Keller, John D. Kingston, Jennifer J. Scott, Guillaume Dupont-Nivet, and Andrew S. Cohen (2019). Chronostratigraphy of the Baringo-Tugen Hills-Barsemoi (HSPDP-BTB13-1A) core–$^{40}Ar/^{39}Ar$ dating, magnetostratigraphy, tephrostratigraphy, sequence stratigraphy and Bayesian age modeling. *Palaeogeography*, *Palaeoclimatology*, *Palaeoecology*, 570, 109519, p. 1–15. https://doi.org/10.1016/j.palaeo.2019.109519 deMenocal, Peter B., 2004. African climate change and faunal evolution during the Pliocene-Pleistocene. *Earth and Planetary Science Letters*, 220, p. 3–24. https://doi.org/10.1016/S0012-821X(04)00003-2

Ebinger, C. J., Tilahun Yemane, D. J. Harding, Samson Tesfaye, S. Kelley, and D. C. Rex (2000). Rift deflection, migration, and propagation: Linkage of the Ethiopian and Eastern rifts, Africa. *Geological Society of America Bulletin*, 112, 2, p. 163–176. https://doi.org/10.1130/0016-7606(2000)112<163:RDMAPL>2.0.CO;2

Ebinger, C. J., Tesfaye Yemane, Giday Woldegabriel, J. L. Aronson, and R. C. Walter (1993). Late Eocene–Recent volcanism and faulting in the southern main Ethiopian rift. *Journal of the Geological Society*, 150, 1, p. 99–108. https://doi.org/10.1144/gsjgs.150.1.0099

Ebinger, Cindy J., Alan L. Deino, R. E. Drake, and A. L. Tesha (1989). Chronology of volcanism and rift basin propagation: Rungwe volcanic province, East Africa. *Journal of Geophysical Research: Solid Earth*, 94, B11, p. 15785–15803. https://doi.org/10.1029/JB094iB11p15785

Pasteels, P., M. Villeneuve, P. De Paepe, and J. Klerkx (1989). Timing of the volcanism of the southern Kivu province: implications for the evolution of the western branch of the East African Rift system. *Earth and Planetary Science Letters*, 94, 3-4, p. 353–363. https://doi.org/10.1016/0012-821X(89)90152-0

Potts, Richard, 1998. Variability selection in hominid evolution. *Evolutionary Anthropology*, 7, p. 81–96. https://doi.org/10.1002/(SICI)1520-6505(1998)7:3<81::AID-EVAN3>3.0.CO;2-A

Rooney, Tyrone O. (2017). The Cenozoic magmatism of East-Africa: Part I — Flood basalts and pulsed magmatism. *Lithos*, 286-287, p. 264–301. https://doi.org/10.1016/j.lithos.2017.05.014

Vrba, E., (1995). The fossil record of African antelopes (Mammalia, Bovidae) in relation to human evolution and paleoclimate. In E. Vrba et al. (eds.): *Paleoclimate and Evolution, With Emphasis on Human Origins*. New Haven: Yale University Press, p. 385–424.

WoldeGabriel, Giday, Grant Heiken, Tim D. White, Berhane Asfaw, William K. Hart, and Paul R. Renne (2000). Volcanism, tectonism, sedimentation, and the paleoanthropological record in the Ethiopian Rift System. *Geological Society of America*, Special Paper 345, p. 83–99. https://doi.org/10.1130/0-8137-2345-0.83

Woldegabriel, Giday, James L. Aronson, and Robert C. Walter (1990). Geology, geochronology, and rift basin development in the central sector of the Main

Ethiopia Rift. *Geological Society of America Bulletin*, 102, 4, p. 439–458.
https://doi.org/10.1130/0016-7606(1990)102<0439:GGARBD>2.3.CO;2

CHAPTER 2

SEDIMENT PROVENANCE AND VOLCANO-TECTONIC EVOLUTION OF THE EAST AFRICAN RIFT SYSTEM FROM U/PB AND (U-TH)/HE LASER ABLATION DOUBLE DATING OF DETRITAL ZIRCONS

Emily E. Zawacki[1], Matthijs C. van Soest[1], Kip V. Hodges[1], Jennifer J. Scott[2], Mélanie Barboni[1], Manfred R. Strecker[3], Craig S. Feibel[4], Christopher J. Campisano[5], J Ramón Arrowsmith[1]

[1] School of Earth and Space Exploration, Arizona State University, Tempe, AZ, USA

[2] Department of Earth and Environmental Sciences, Mount Royal University, Calgary, Canada

[3] Institut für Erd- und Umweltwissenschaften, Universität Potsdam, Potsdam, Germany

[4] Department of Earth and Planetary Sciences, Rutgers University, Piscataway, NJ, USA

[5] Institute of Human Origins, School of Human Evolution and Social Change, Arizona State University, Tempe, AZ, USA

This chapter is currently in review. It was submitted in April 2021 to *Earth and Planetary Science Letters.* This chapter appears in its submitted form.

2.1 Abstract

Detrital zircons from major rift basins within the East African Rift System (EARS) provide a means to evaluate not only sediment provenance and landscape dynamics in sedimentary basins, but also the timing of the volcano-tectonic evolution of

the rift system. I sampled from drill cores collected by the Hominin Sites and Paleolakes Drilling Project (HSPDP) in Ethiopia and Kenya to study the detrital mineral records of the Northern Awash (NA; 3.3–2.9 Ma) and West Turkana (WTK; 1.9–1.4 Ma) drill cores. We performed (U-Th)/He and U/Pb analyses on detrital zircons using single crystal laser ablation double dating (LADD) techniques. Analyses of four NA samples yielded zircon $^{206}Pb/^{238}U$ dates younger than ~45 Ma–consistent with derivation from silicic volcanic rocks associated with EARS activity. Samples lack zircon $^{206}Pb/^{238}U$ dates from ~22–13 Ma, due to a partial cessation in silicic volcanism and a watershed configuration prohibiting delivery of silicic source materials to the sample site. NA zircon $^{206}Pb/^{238}U$ dates imply a sedimentary source from the western Afar margin, with a transition to more localized sediment reworking within the Afar Depression after a major regional tectonic reorganization and disconformity at ~2.9 Ma. The WTK sample yielded many zircons with Cenozoic $^{206}Pb/^{238}U$ dates similar to those from the NA core, but the WTK sample also sources a small population of Neoproterozoic zircons associated with the Mozambique Belt. Despite being recorders of predominantly silicic activity, the detrital zircon U/Pb dates from both drill sites track the established timing of major volcanic phases in the EARS. A subset of zircons from both sites have concordant $^{206}Pb/^{238}U$ and (U-Th)/He dates, indicating a short duration between zircon crystallization and eruption of the host volcanic rock, but the majority of zircon (U-Th)/He dates are significantly younger than the $^{206}Pb/^{238}U$ dates for the same zircon. Some (U-Th)/He dates are even younger than the depositional age of the sedimentary sample from which it was collected. The observed spread in zircon (U-Th)/He dates likely reflects partial resetting associated with late mafic volcanism and/or hydrothermal activity within this dynamic rift environment.

2.2 Introduction

The East African Rift System (EARS) contains a series of structurally and magmatically controlled extensional basins spanning ~3,500 km from the Afar Triple Junction to Mozambique (Chorowicz, 2005). The EARS is divided into a western branch, where volcanism is isolated and often restricted to the footwalls of border faults and structurally complex transfer faults (Ebinger et al., 1989; Pasteels et al., 1989), and an eastern branch, where volcanism is widespread (Rooney, 2017). In the eastern branch, pre-rift volcanism initiated ~45 Ma and has continued to the present (Ebinger et al., 2000). As rift basins began to form over the late Oligocene and early Miocene, sedimentation triggered by volcanic and tectonic activity resulted in predominantly volcaniclastic deposits within the basins (WoldeGabriel et al., 1990, 2000). These basins also preserve an extraordinary record of Neogene and Quaternary paleoclimate, paleoenvironments, and faunal evolution, including that of humans and their fossil ancestors (e.g., deMenocal, 2004; WoldeGabriel et al., 2000).

Given the protracted volcanic activity in the eastern branch of the EARS and the predominantly volcaniclastic nature of the rift-basin deposits, the detrital zircon record within major watersheds of the EARS should be dominated by Cenozoic volcanic zircons. Although rare in mafic magmas, zircons are a common accessory mineral in silicic volcanic rocks. Volcanic zircons will crystallize when the phase becomes saturated in the magma, potentially well before the time of eruption (Boehnke et al., 2013, 2016).

The U/Pb date of a volcanic zircon is often used to infer its crystallization age, while its (U-Th)/He date is often interpreted as an eruption age (e.g., Farley et al., 2002). U/Pb dates of detrital zircons can be used to evaluate the evolution of source areas and sediment routing during deposition (e.g., Gehrels et al., 1995; Romans et al., 2016). The detrital zircon record of the EARS provides a way to examine sediment provenance and paleowatershed configurations in addition to characterizing the timing of the volcano-tectonic evolution of the EARS.

In this study, we employ laser ablation double dating (LADD) of detrital zircons (Horne et al., 2016) for samples collected from Hominin Sites and Paleolakes Drilling Project (HSPDP) drill cores (Campisano et al., 2017; Cohen et al., 2016). LADD integrates laser ablation gas-source mass spectrometry (LA-GMS) and laser ablation inductively coupled mass spectrometry techniques (LA-ICPMS) to determine both the formation U/Pb date of the zircon and the (U-Th)/He timing of its passage through the ~140–200^{o}C range, depending on the degree of diffusive anisotropy and radiation damage during post-crystallization cooling (Anderson et al., 2020). Sampling from the HSPDP drill cores provides novel access to a high-resolution sedimentary record that is constrained by an age-depth model—a record that is otherwise unexposed at the present-day surface. Targeting two of the HSPDP drill sites allows for a comparison between the Afar region in Ethiopia to the Omo-Turkana region in northern Kenya.

We use the detrital zircon record to determine the provenance of the sediments from the HSPDP drill cores and to evaluate changes in sediment source region over time. We also assess how well the detrital zircon record from within major watersheds of the

EARS captures the timing of established volcanic phases in the East African Rift. Finally, we examine the thermal history of the zircons, including an assessment of sedimentary features that indicate post-depositional hydrothermal alteration and sediment injection.

2.3 Geological Setting

Zircon-bearing source units within the EARS are divided between Precambrian basement rocks and Cenozoic silicic volcanic rocks. The Precambrian Mozambique Belt consists of gneisses and migmatites that are dated between ~885 and 540 Ma (Asrat et al., 2001; Shackleton, 1986). There are exposures of the Mozambique Belt in southern Ethiopia, including the Hammar Range bounding the Chew Bahir basin (Davidson, 1983), and a few exposures in northern Kenya.

The Turkana Volcanics in northern Kenya are some of the oldest volcanic rocks in Kenya. The base of the Turkana Volcanics comprises a >1000-m-thick sequence of basaltic flows, which were emplaced between ~37–35 Ma (McDougall and Brown, 2009; Tiercelin et al., 2012). Although this sequence is dominated by basaltic lavas, there are isolated coeval rhyolite flows (McDougall and Brown, 2009).

In southern Ethiopia, the oldest volcanic rocks associated with the EARS are part of the Amaro/Gamo unit (Rooney, 2017), previously called the Jimma volcanics (Tefera et al., 1996). Up to 45 Ma, they are composed of transitional to tholeiitic basalts and associated silicic rocks (Davidson, 1983). On the western Ethiopian Plateau, extensive basaltic trap volcanism was largely concentrated over a one-million-year period with a peak at ~30 Ma, while the majority of rhyolitic volcanism occurred shortly after flood basalt eruptions (Ayalew et al., 2002; Hofman et al., 1997).

Volcanic activity in the Turkana Depression during the Early and late Oligocene was focused west of Lake Turkana, with significant silicic units dated between ~32–31 Ma and ~26–25 Ma (McDougall and Brown, 2009). Between 27 and 22 Ma, volcanic activity shifted to the Afar margins and around the Turkana area. Silicic units from the western Afar rift margin during this period represent more localized eruptions accompanied by small basalt flows (Rooney, 2017). Similar activity also occurred along the western Afar margin during the Late Miocene (Stab et al., 2016).

Between 3.9 and 1.6 Ma, there was widespread volcanism within the Afar region producing the Stratoid Series (Rooney, 2020c). They are predominantly basaltic but contain rhyolitic intercalations throughout the Afar Depression (Barberi and Santacroce, 1980; Rooney, 2020c). The Lower Stratoid Series is contemporaneous with the base of the sedimentary Hadar Formation at ~3.8 Ma (Wynn et al., 2008). A regional disconformity at ~2.9–2.7 Ma, the result of a major tectonic and geomorphic reorganization in the region, marks the transition from the Hadar to Busidima Formation (Quade et al., 2004, 2008).

2.4 Sampling and Methods

2.4.1 Drill core sampling

We sampled from two Hominin Sites and Paleolakes Drilling Project (HSPDP) cores: Northern Awash (NA) and West Turkana (WTK) (Figure 2.1). The Northern Awash site in the Afar region of Ethiopia is situated within the modern Awash River basin, which encompasses an area of 119,890 km^2. Three drill cores from two sites ~3 km apart cover a composite stratigraphic interval of ~270 m. The cores include stratigraphic levels representing the age interval of ~3.3–2.9 Ma and targeted the lacustrine depocenter of the Hadar Formation (~3.6–2.9 Ma) in the Ledi-Geraru area (Campisano et al., 2017; Noren, 2020a).

The NA cores are predominantly composed of silty clays, with occasional sandy units and massive basalts (Cohen et al., 2016). We collected four samples from the sandy units, two samples from core HSPDP-NAO14-1D and two samples from core HSPDP-NAW14-1A (Table 2.1) (Figure 2.2). Samples were collected from across multiple core drives and are named after the top-most drive. Individual core drives collected up to ~3 m in length of material. Sampled material was predominantly planar bedded, unlithified, medium-grained sand. The sands are litharenites, dominated by basaltic rock fragments and minerals such as clinopyroxene, olivine, and weathered plagioclase.

The West Turkana drill site is located in northern Kenya on the western side of Lake Turkana within the modern Omo-Turkana basin, which encompasses an area of 149,362 km^2. The drill site targeted the lacustrine strata of Kaitio and Natoo Members of the Nachukui Formation (Campisano et al., 2017; Noren, 2020b). The single core taken, HSPDP-WTK13-1A (Table 2.1), represents a stratigraphic interval of ~1.9–1.4 Ma (Feibel et al., 2015; Lupien et al., 2018). The lower two thirds of the core consist of laminated to massive clays, while the upper third of the core records a pronounced lithologic transition with more frequent sandy intervals (Cohen et al., 2016). We collected one sample from an unlithified, volcanic-rich, fine- to medium-grained sand. The sand contains a fluvially-deposited tephra, which was $^{40}Ar/^{39}Ar$ dated to 1.497 ± 0.020 Ma (Lupien et al. 2018).

Table 2.1 HSPDP drill core samples. They are referred to by the top-most sampled core drive.

HSPDP Core	Latitude	Longitude	Sampled Core Drives
HSPDP-NAO14-1D	11.3152°	40.7370°	39Q-2, 40Q-1, 40Q-2
HSPDP-NAO14-1D	11.3152°	40.7370°	48Q-1, 48Q-2
HSPDP-NAW14-1A	11.3254°	40.7649°	8Q-1, 8Q-2, 8Q-3
HSPDP-NAW14-1A	11.3254°	40.7649°	36Q-1, 36Q-2
HSPDP-WTK13-1A	4.1097°	35.8718°	20Q-2, 20Q-3

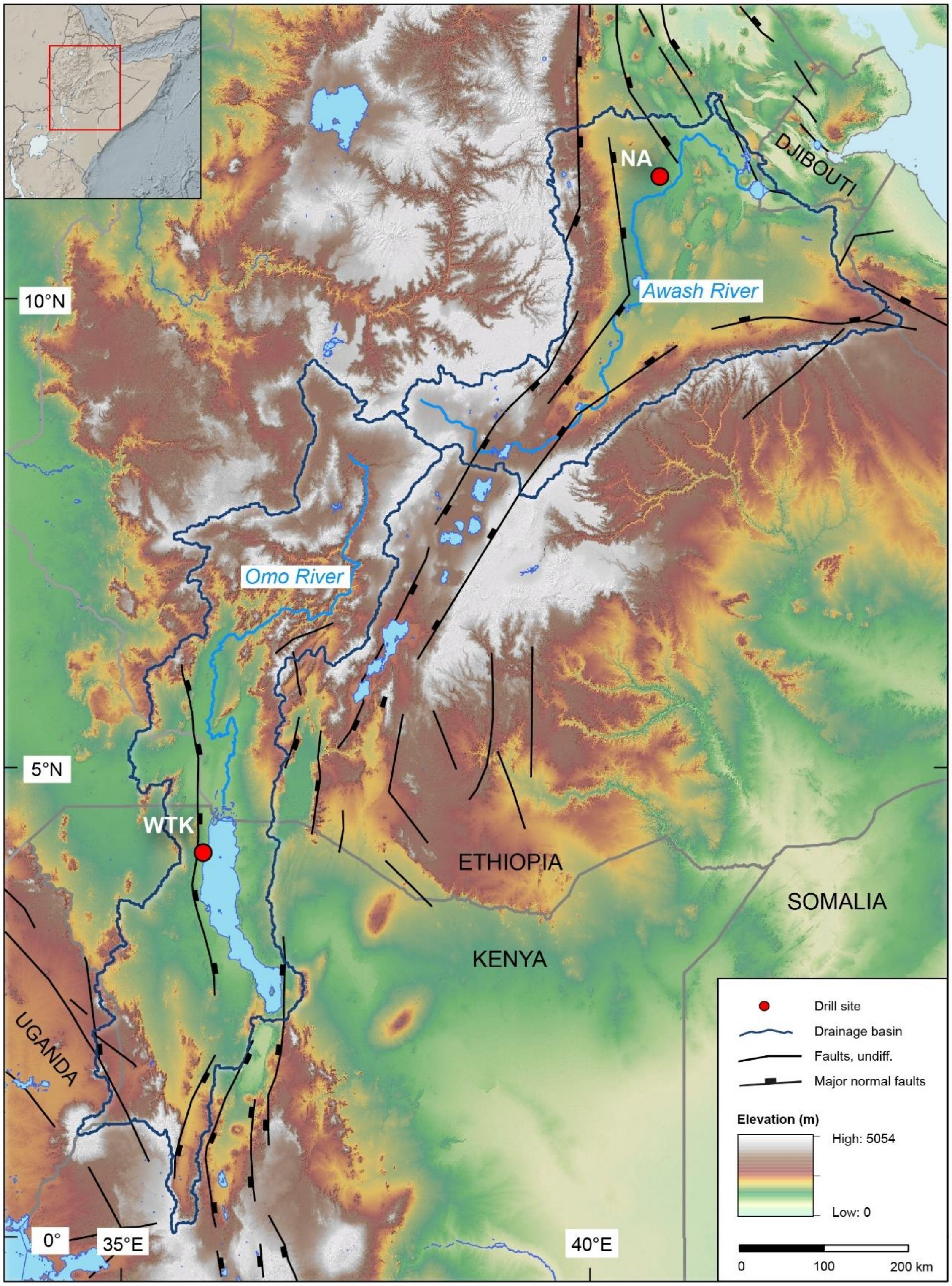

Figure 2.1 Geographic overview of the HSPDP drill sites in this study. Red dots mark drill site locations: Northern Awash (NA) and West Turkana (WTK). Present-day

watersheds are delineated in blue, and major modern rivers (Awash River and Omo River) and lakes are shown. Faults in black indicate major tectonic boundaries. Background is SRTM DEM (https://doi.org/10.5069/G9445JDF).

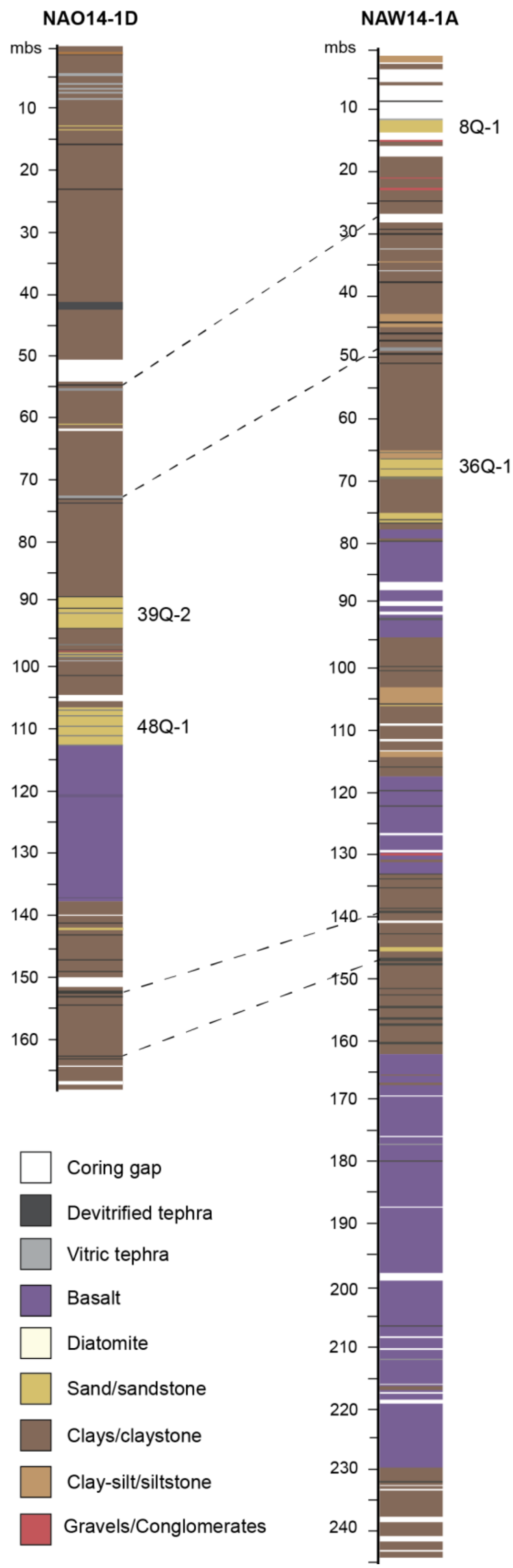
NAO14-1D
NAW14-1A
mbs
10
20
30
40
50
60
70
80
90
100
110
120
130
140
150
160
170
180
190
200
210
220
230
240
8Q-1
36Q-1
39Q-2
48Q-1
Coring gap
Devitrified tephra
Vitric tephra
Basalt
Diatomite
Sand/sandstone
Clays/claystone
Clay-silt/siltstone
Gravels/Conglomerates

Figure 2.2. Stratigraphic columns of the HSPDP-NAO14-1D and HSPDP-NAW14-1A drill cores shown in meters below surface (mbs). Sampled sand units are labeled. Dashed lines indicate stratigraphic correlations. Modified from Garello (2019).

2.4.2 Zircons – Laser ablation double dating (LADD)

Sand samples were sieved to isolate the 250–125 μm size fraction and were separated by Frantz magnetic separation and LST heavy liquid density separation to isolate the zircons. One hundred and ten zircon grains $\geq$ 80 μm in width from each sample were picked and mounted. The torr seal puck was polished to remove the outer 20–30 μm of the crystals to eliminate the need for (U-Th)/He alpha ejection correction and to ensure a smooth surface for analysis (Tripathy-Lang et al., 2013).

Analyses were conducted at the Group 18 Laboratories at Arizona State University generally following the methods outlined in Horne et al. (2016). Given the expected young (U-Th)/He dates for most of the samples, helium analyses were carried out on a Nu Instruments *Noblesse* magnetic sector noble gas mass spectrometer, as opposed to a quadrupole mass spectrometer described in Horne et al. (2016). The *Noblesse* system—which is fitted with an ATP discrete dynode secondary ion multiplier as the main detector—typically has better detection limits and better precision on small signals compared to the quadrupole system. We converted the helium signals measured on the *Noblesse* to abundances based on instrument sensitivity values determined using a helium standard.

Zircon LADD analytical protocols used a Teledyne Photon Machine *Analyte G2* excimer laser to ablate a shallow pit in the core region of a crystal under ultrahigh vacuum. These pits typically had 25 μm footprint diameters on the polished zircon surface. The material ablated from each of these pits *in vaccuo* was purified using metal alloy getters, and the nonreactive gas component was admitted to the *Noblesse* for ^{4}He analysis. Subsequently, the sample puck was removed from the vacuum line and remounted in a *HelEx2* two-volume cell for LA–ICPMS U+Th+Pb analysis. A second pit was ablated directly on top of the initial ^{4}He pit but with a considerably larger footprint to account for intracrystalline alpha redistribution effects when calculating (U-Th)/He dates (Tripathy-Lang et al., 2013). When using a 25 μm diameter laser ablation footprint for the LA-GMS analysis, we used a 65 μm footprint for the LA–ICPMS analysis. For some smaller crystals, we conducted the analytical sequence using 15 µm and 50 µm ablation footprints, and for a few larger crystals, we used 40 µm and 85 µm ablation footprints. U, Th, and Pb measurements were done on the material ablated from the larger pit using a Thermo Scientific *iCAP Q* ICPMS instrument. Primary isotopic standards used for data reduction in anticipation of U/Pb apparent age calculations were 91500 and Plešovice zircon (Sláma et al., 2018; Wiedenbeck et al., 1995). For U+Th concentrations, we used an in-house zircon syn-rock material that is more homogeneous for U and Th distribution than natural zircon crystals. In addition to these standards and the unknowns, we also analyzed in-house Sri Lankan zircon standards for U, Th, and He as an independent check on our laser ablation (U-Th)/He protocols. Additional procedural details may be found in Horne et al. (2016).

Data reduction for (U-Th)/He dates followed Horne et al. (2016), and U/Pb analyses were carried out using *Iolite 3.65* software (Paton et al., 2011). Specifically, we used the *VizualAge* data reduction scheme (Petrus and Kamber, 2012), which permits

Live Concordia-aided data reduction. As necessary, we made common Pb corrections using ^{204}Pb. For the rest of this paper, interpret the $^{206}Pb/^{238}U$ dates as zircon crystallization ages, but we also report $^{207}Pb/^{235}U$ dates calculated from measured ^{238}U and an assumed $^{238}U/^{235}U$ ratio of 137.818. All data are reported in Appendix A. Throughout this paper, all dates uncertainties are reported at the 2σ level. Zircon age peaks are defined based on probability density function (PDF) plots that sum a Gaussian distribution of each measurement based on the date and analytical precision (Sircombe, 2000).

2.4.3 Zircon characterization

Zircons separated from the NA samples were plentiful, relatively small ($\leq$ 120 μm wide), and typically euhedral to subhedral. The WTK sample yielded fewer, primarily subhedral zircons of similar size. Although we did not characterize all of the zircons mounted for LADD work prior to analysis, we obtained backscattered electron (BSE) and cathodoluminescence (CL) images for a subset of zircons from each major age population in samples NAO14-1D-39Q-2, NAW14-1A-8Q-1, and WTK13-1A-20Q-2. The CL images are shown in Appendix A. Nearly all of the imaged zircons showed some level of zoning. The most common types were patchy or oscillatory growth zoning, but a few of the zircons contained distinctive cores with younger zircon overgrowths. Unfortunately, the anticipated U/Pb and (U-Th)/He ages of these complex zircons were so young and the crystal sizes were so small that we were unable to analyze core and rim zircon components separately using the LADD technique. For such crystals, the dates probably represent only the core material for zircons such as WTK13-1A-20Q-2 z044 (Figure A4), only the overgrowth material in others such as NAO14-1D-39Q-2 z042 (Figure A2), or composite ages when the analytical footprint overlaps core and rim domains.

2.5. Results

2.5.1 Northern Awash LADD

For all NA samples, zircons yielded $^{206}Pb/^{238}U$ dates that define three distinctive clusters: one at ~7–8 Ma, a somewhat broader sub-distribution < 5 Ma, and a more diffuse cluster ranging from late Eocene to early Miocene (Figure 2.3). No dates were older than 44 Ma. Zircons of middle Miocene age are absent from three samples, and only one was found in NAO14-1A-48Q-1. The concentrations of zircons < 5 Ma increase stratigraphically up-section, and NAW14-1A-8Q-1contains a high concentration of ~3.7 Ma crystals. The youngest zircon dates for each sample place maximum constraints on the sample's depositional age. For the three stratigraphically lowest samples, these $^{206}Pb/^{238}U$ dates range from 2.81 ± 0.19 to 3.038 ± 0.048 Ma, consistent with the Kada Hadar Member of the Hadar Formation (Campisano and Feibel, 2008). In contrast, the stratigraphically highest sample (NAW14-1A-8Q-1) contains one detrital zircon with a $^{206}Pb/^{238}U$ date of 1.687 ± 0.099 Ma and additional zircons dated < 2.7 Ma. This maximum depositional age implies that NAW14-1A-8Q-1 was collected from the Busidima Formation (2.7–0.15 Ma), which is separated from the underlying Hadar Formation by a major regional disconformity (Campisano, 2012 and references therein).

NA zircons yielded (U-Th)/He PDFs with fewer distinctive clusters than the $^{206}Pb/^{238}U$ data for the same zircons. This observation in part reflects the higher analytical precision of the $^{206}Pb/^{238}U$ dates. Not all zircons belonging to a particular $^{206}Pb/^{238}U$

cluster had the same post-crystallization thermal histories. Zircons with statistically indistinguishable $^{206}Pb/^{238}U$ and (U-Th)/He dates should plot along the 1:1 reference line in Figure 2.4. Such crystals experienced simple, post-crystallization rapid cooling to ~200–170˚C (Reiners et al., 2005). Several of the NA zircons with a wide range of $^{206}Pb/^{238}U$ dates fall into this category. For these crystals, the simplest interpretation is that these zircons are sourced from volcanic rocks and the dates represent source eruption ages. However, many Eocene to Pliocene NA zircons have (U-Th)/He closure dates substantially younger than their corresponding $^{206}Pb/^{238}U$ dates implying: 1) long zircon residence times prior to eruption if the zircons are volcanic; 2) protracted cooling of their source regions if particular zircons are from metamorphic or plutonic sources; and/or 3) complete or partial resetting of the (U-Th)/He dates by later igneous or hydrothermal activity. Some of the zircons, those with $^{206}Pb/^{238}U$ dates less than 10 Ma, yielded (U-Th)/He dates younger than the notional depositional ages of the sediments in which they are found. This observation is most easily explained by post-depositional thermal resetting as a consequence of local volcanic or hydrothermal activity.

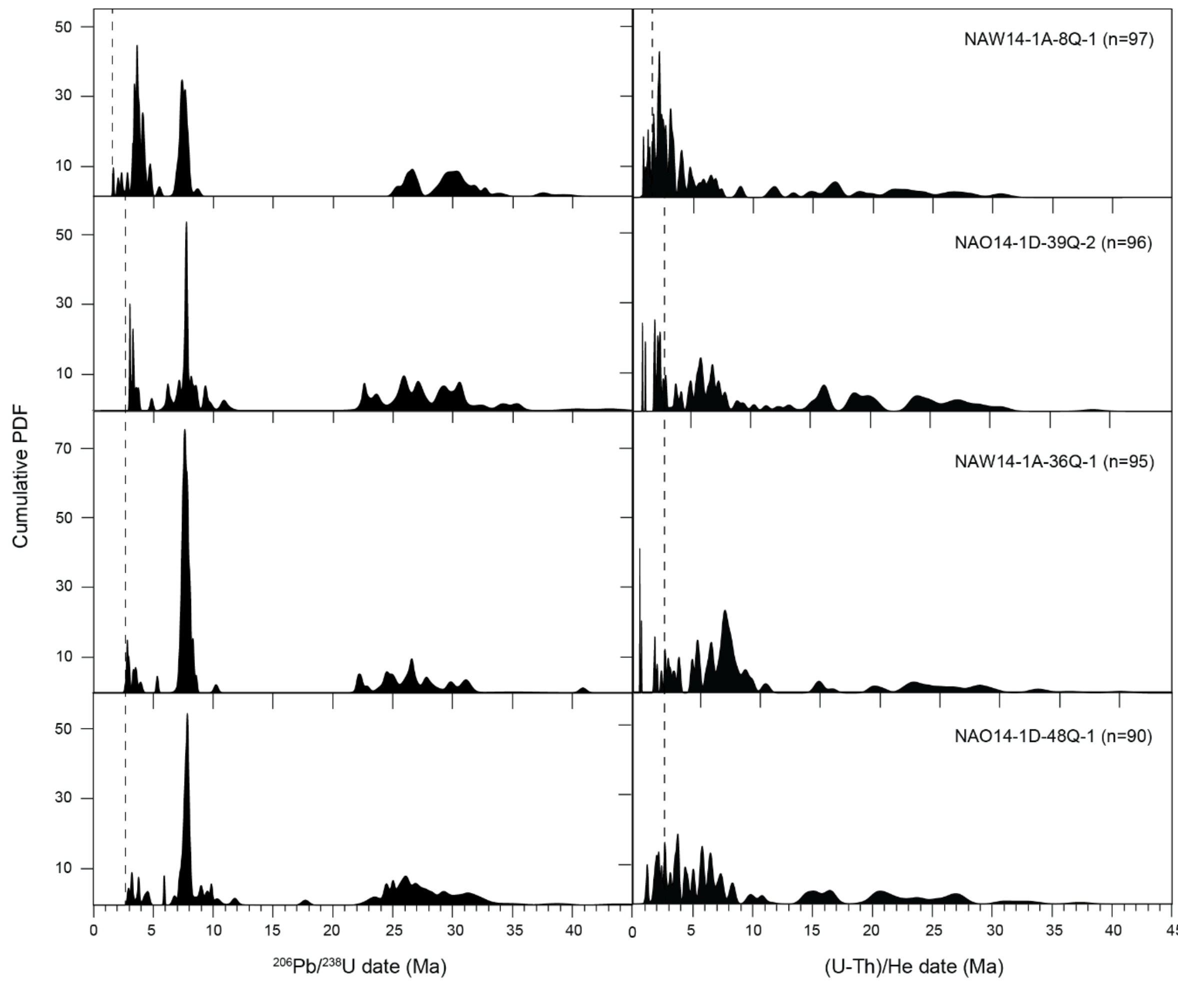

Figure 2.3 Cumulative probability density function (PDF) plots of detrital zircon $^{206}Pb/^{238}U$ and (U-Th)/He dates from the NA samples. Dashed lines indicate presumptive depositional age of the sample.

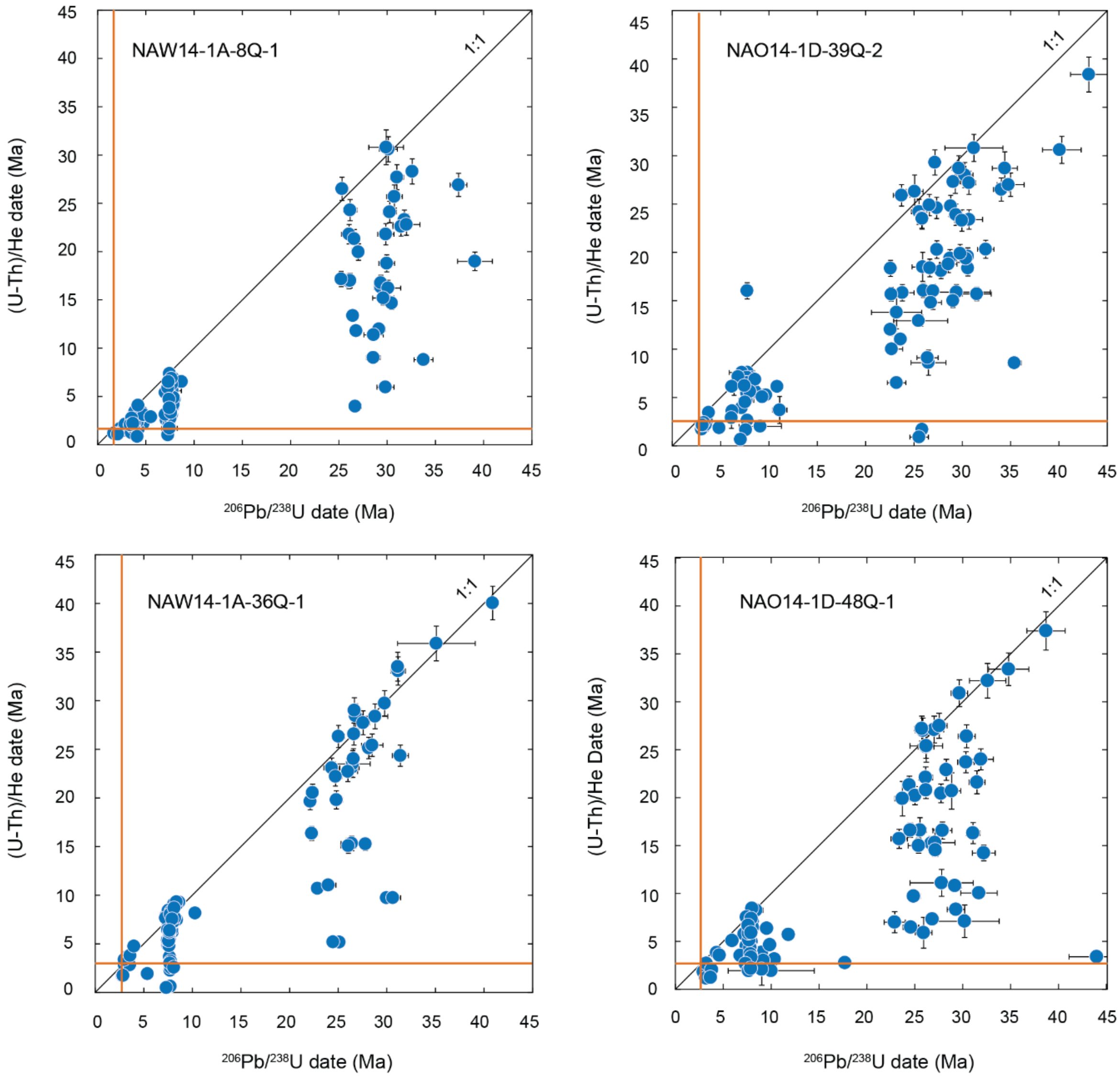

Figure 2.4 Double dating plots of (U-Th)/He vs. $^{206}Pb/^{238}U$ date of detrital zircons from the NA samples. Orange lines indicate approximate depositional age. The 1:1 line represents a short duration between zircon crystallization and eruption of the host volcanic rock. (U-Th)/He dates show a large spread for a given U/Pb age.

2.5.2 West Turkana LADD

The single WTK sample yielded many zircon $^{206}Pb/^{238}U$ dates of < 45 Ma, a smaller number of Proterozoic dates (877.7 ± 9.1 to 581.2 ± 7.1 Ma), two Cambrian dates (530.8 ± 8.1 and 421 ± 14 Ma), and a single Archean date of 2366 ± 26 Ma (Figure 2.5).

Of the Cenozoic zircons, $^{206}Pb/^{238}U$ dates define a sharp peak at ~1.6 Ma, with diffuse clusters between the late Oligocene and early Miocene and the Late Miocene and Early Pleistocene. The youngest $^{206}Pb/^{238}U$ date was 1.410 ± 0.086 Ma, which could be interpreted as a maximum depositional age. This date is within uncertainty of the 1.497 ± 0.020 Ma $^{40}Ar/^{39}Ar$ age for an interstratified fluvially-deposited tuff found at the same stratigraphic horizon in the core (Lupien et al., 2018), implying rapid transport of at least some of the zircons found in WTK13-1A-20Q-2.

The WTK sample shows more similarity between $^{206}Pb/^{238}U$ and (U-Th)/He dates than do the NA samples (Figure 2.5). (U-Th)/He dates range widely from the Late Devonian to Early Holocene, with the most prominent clusters around ~1.4 Ma. Zircons with U/Pb dates of ~32 Ma, ~22 Ma, and < 8 Ma show the greatest deviation from a 1:1 line (Figure 2.6). Some Proterozoic and Cenozoic zircons yield (U-Th)/He dates younger than the depositional age (Figure 2.6), indicating partial resetting.

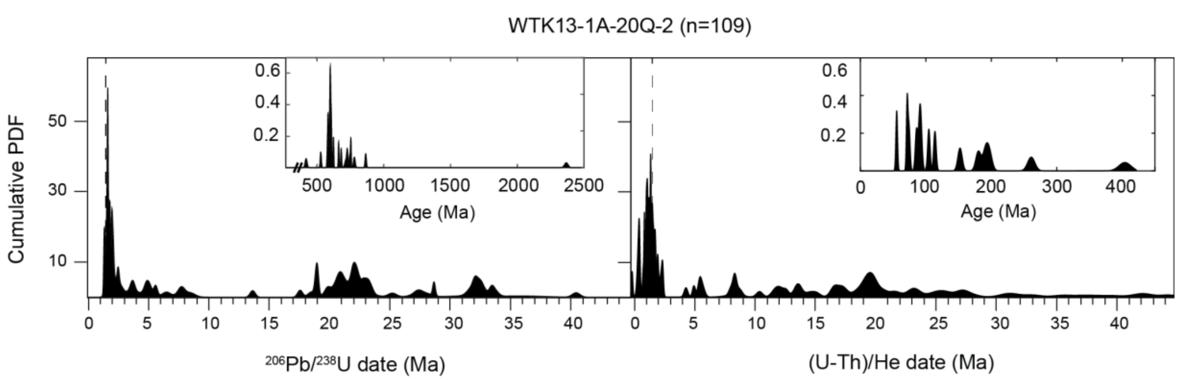

Figure 2.5 Cumulative probability density function (PDF) plot of WTK detrital zircon $^{206}Pb/^{238}U$ and (U-Th)/He apparent ages.

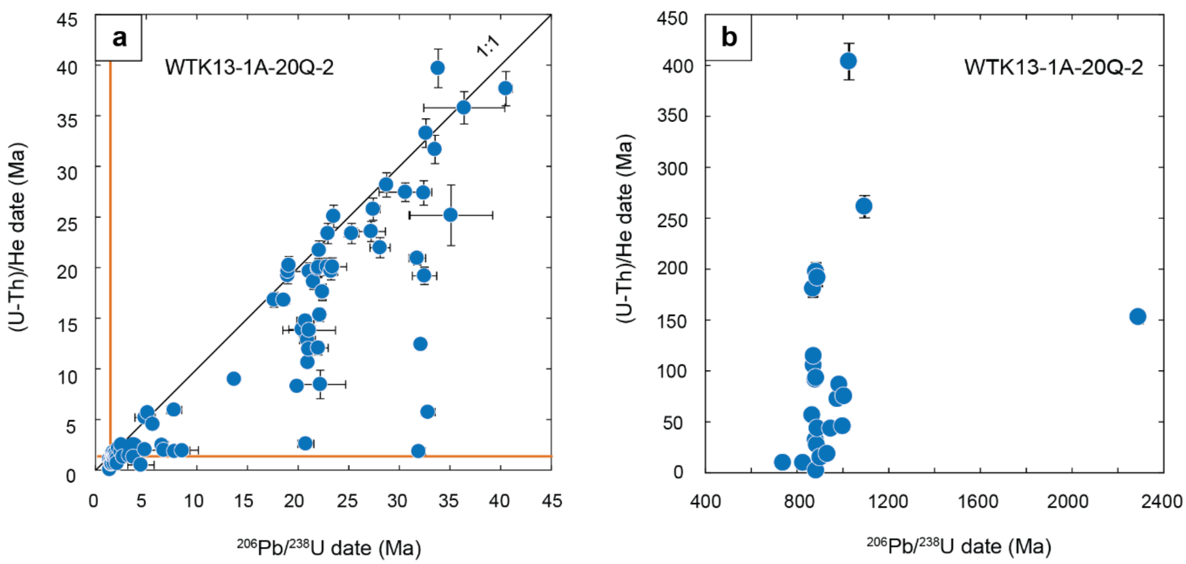

Figure 2.6 Double dating plots of (U-Th)/He vs. $^{206}Pb/^{238}U$ date of detrital zircons from the WTK sample for **a)** zircons < 45 Ma and **b)** zircons > 400 Ma. Orange lines indicate the approximate depositional age. Both populations yield (U-Th)/He ages younger than the depositional age.

2.6 Discussion

2.6.1 Sediment provenance and volcanism

We compare our detrital zircon $^{206}Pb/^{238}U$ dates to previously determined apparent ages of bedrock and volcanic units within the EARS to determine the most probable sediment sources and to gain information about changes in paleohydrology.

The Proterozoic zircons from the WTK sample match in age with rocks associated with the Mozambique Belt (Abbate et al., 2015). The single Paleoproterozoic grain dated at 2366 ± 26 Ma temporally correlates with deformation of volcanosedimentary basins in western Kenya between 2550 and 2300 Ma (Cahen and Snelling, 1966; Dodson et al., 1975), although more zircons of this age population would be needed to properly constrain provenance.

The Lapur Range located ~30 km north of the WTK drill site is the closest potential source of the WTK Proterozoic zircons (Figure 2.7). Lapur Range is composed of Mozambique Belt gneisses, amphibolites, granulites, and other metamorphic rocks and is overlain by the Upper Cretaceous–Lower Paleogene Lapur Sandstone (Arambourg and Wolff, 1969; Begg et al., 2009; Tiercelin et al., 2012). The Proterozoic detrital zircon $^{206}Pb/^{238}U$ dates for the WTK sample are consistent with zircon U/Pb dates from the Lapur Sandstone (Owusu Agyemang et al., 2019). Comparable Mozambique Belt exposures of the Hammar Range in southern Ethiopia might also be a potential source of Proterozoic zircons. Additionally, the Turkana Volcanics overlie the Lapur Range and temporally correlate with $^{206}Pb/^{238}U$ dates from the WTK sample. Thus, core material reflects local sediment sources.

With a few exceptions, the analyzed detrital zircons are derived from Cenozoic volcanic rocks related to silicic volcanism within the EARS. All samples yielded a small number of Eocene zircons dated between 45–34 Ma, which are derived from the earliest plume activity related to the EARS in southern Ethiopia and northern Kenya. Exposures of the Amaro/Gamo units are located ~100 km southeast of the southernmost boundary of the modern Awash watershed, but they lie within the present-day Omo River basin (Figure 2.7). Despite the slightly more proximal location of the Amaro/Gamo units to the WTK site and significant exposures within the modern Omo watershed, there is a proportionally equivalent amount of Middle Eocene zircons in both the NA and WTK samples. Given the fact that these source units lie outside of the modern Awash watershed, the presence of Eocene zircons in the NA samples indicates that there was a more widespread fluvial connectivity that allowed for delivery of these sediments to the Awash Basin, implying that the southern end of the basin has shifted northward over time.

Oligocene detrital zircons from the NA samples correlate with the period of extensive flood basalt activity across the Western Ethiopian Plateau at ~30 Ma and are likely derived from associated silicic units (Figures 2.3 and 2.7). Sample NAW14-1A-8Q-1 shows the most significant concentration of $^{206}Pb/^{238}U$ dates around ~30 Ma, but the zircon dates overall are dispersed through much of the Oligocene. This observation may reflect a greater diversity in source areas along the plateau. Ayalew et al. (2002) estimates that the total original volume of Oligocene rhyolitic ignimbrites was at least 6.3×10^4 km^3, which amounts to 20% of the entire volcanic sequence. Therefore, a significant proportion of basaltic source units is not reflected in the detrital zircon record, which only records the lesser silicic phases from the plateau. The less prominent zircon peaks from this interval are consistent with the subordinate volume of silicic source material.

Additional probable sediment sources of the NA samples from the western Afar margin and plateau include the Dessie Series (~30–24 Ma) (Stab et al., 2016; Ukstins et al., 2002) and the Chifra Formation (7.45 ± 0.74 Ma, (U-Th)/He) (Stab et al., 2016) (Figure 2.7). The sharp zircon peak at ~7.7 Ma in the NA samples suggests a uniform volcanic source, apart from NAW14-1A-8Q-1, which has a slightly broader peak between ~7.7–7.5 Ma (Figure 2.3). However, this ‘dual’ peak in NAW14-1A-8Q-1 is difficult to resolve within the uncertainty of analyses. The abundance of zircons of this age reflects the importance of the western Afar margin as a sedimentary source, particularly for the samples deposited at ~2.95 Ma.

Notably, the silicic products of the Boina volcanic center (12.7°N, 40.5°E) are temporally equivalent to the Dessie Series, although the Boina volcanic center is located ~70 km north of the northern extent of the modern Awash drainage basin (Figure 2.7). Based on the detrital zircon dates alone, it is not possible to determine whether the watershed extended further north to include this volcanic center as a sedimentary source at that time, or whether the basin boundary was similar to the modern.

The southeast Afar margin appears to only be a minor sedimentary source for the NA samples represented by low abundance zircons dated between ~12 to 9 Ma that are likely sourced from rhyolitic ignimbrites correlated with the "Main Silicic Phase" dated between 13.3–11.05 Ma (Juch, 1978; Kunz et al., 1975). Zircons of this age and others derived from the Amaro/Gamo unit to the south suggest limited transport from the southernmost extent of the basin, with the majority of sedimentary input from the west.

Zircons dated between 3.9–1.6 Ma in the NA samples are associated with the Stratoid Series (Rooney, 2020c) and thus represent localized active volcanism within the Afar Depression prior to the deposition of sediments retrieved from the cores. The youngest NA sample (NAW14-1A-8Q-1) was deposited at ~1.7 Ma and records the Busidima Formation (Quade et al., 2004, 2008). Sample NAW14-1A-8Q-1 lies above an unconformable contact to coarse-grained sediments (pebbles, cobbles), which suggests that there may have been a change in the drainage system prior to depositional of this sample. While the three older NA samples deposited at ~2.95 Ma indicate the western

Afar margin and western Ethiopian Plateau as the predominant sedimentary source, the youngest sample deposited at ~1.7 Ma has a primary modal zircon peak at ~3.7 Ma, which temporally correlates to the Stratoid Series. This significant increase in Pliocene zircons suggests more localized sediment sources and reworking from within the Afar Depression, which is most likely the result of a tectonic reorganization and basin compartmentalization associated with closely spaced normal faulting beginning at ~2.9 Ma (Campisano, 2012).

The single WTK sample is dominated by a detrital zircon major modal peak at ~1.6 Ma, representative of active volcanism prior to the deposition of cored sediments. The sand sample itself is dominated by a fluvially deposited tephra, which was previously unknown and not correlated to an existing outcrop.

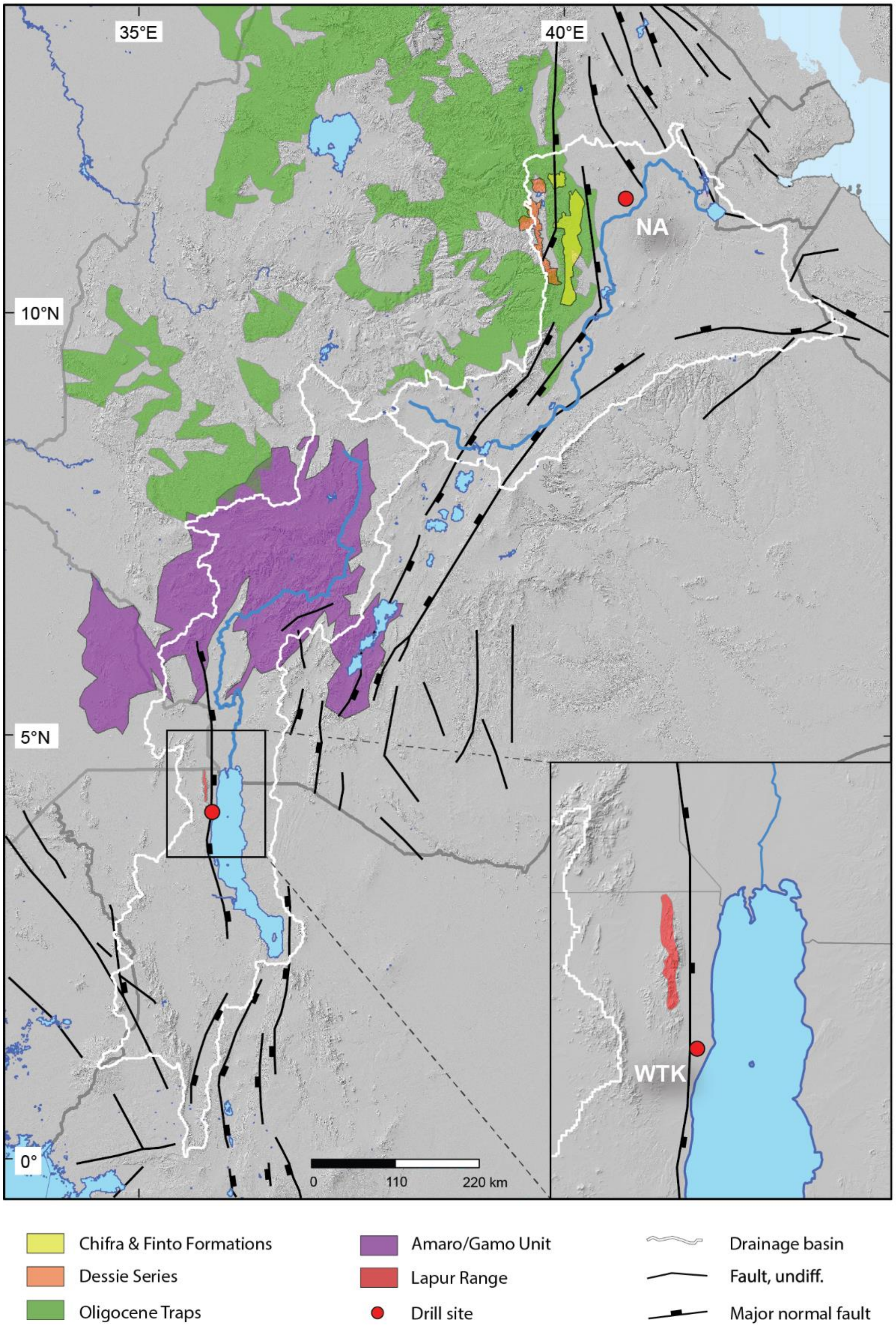

35°E
40°E
10°N
5°N
0°
NA
WTK
0
110
220 km
Chifra & Finto Formations
Dessie Series
Oligocene Traps
Amaro/Gamo Unit
Lapur Range
Drill site
Drainage basin
Fault, undiff.
Major normal fault

Figure 2.7 Probable zircon source units for the NA and WTK samples. The Lapur Range comprises Precambrian Mozambique Belt units that are overlain by an Upper Cretaceous-Lower Paleogene sandstone. Eocene Turkana Volcanics overlie the Lapur Range. The Amaro/Gamo unit is the oldest volcanic units associated with the EARS that began to be emplaced at ~45 Ma (Rooney, 2017). Oligocene Trap volcanism was predominantly focused at ~30 Ma and generated major basaltic units with subordinate rhyolitic units (Rooney, 2017). The Dessie Series represents units related to more localized silicic eruptions dated between ~30–24 Ma (Stab et al., 2016; Ukstins et al., 2002). The rhyolites of the Chifra Formation are dated to 7.45 ± 0.37 Ma by zircon (U-Th)/He (Stab et al., 2016) and account for the major modal apparent age peak in the NA samples.

2.6.2 Rift volcanism and the sedimentary record

Fractional crystallization is regarded as the primary process facilitating magmatic evolution within the EARS (Rooney, 2020d). Silicic lavas in which the zircons crystallize are typically derived from shallow and compositionally zoned magma chambers fed by the evolving mafic system, with minor interaction with the crust (Peccerillo et al., 2003, 2007). Silicic volcanic episodes within the EARS generally occurred after large basaltic episodes (Rooney, 2017; 2020c).

We use the detrital zircon record from the HSPDP cores as a metric to track the timing of volcanic phases within the EARS (Purcell, 2018; Rooney, 2017, 2020a, 2020b, 2020c). Despite the single sample from the WTK core, our data enables a comparison of the detrital zircon record of the Afar and northern Turkana regions. Figure 2.8 shows PDFs of the detrital zircon $^{206}Pb/^{238}U$ dates with superposed volcanic phases documented in the EARS.

The oldest Cenozoic zircons found in all samples are consistent with the timing of earliest plume activity in southern Ethiopia termed the “Eocene Initial Phase,” constrained to between 45 and 34 Ma (Rooney, 2017). The second episode was the

“Oligocene Traps Phase” between 34 to 27 Ma, a period of dominantly basaltic activity along the western Ethiopian Plateau (Rooney, 2017). Despite the largely basaltic nature of this phase, all samples yielded zircons recording the full duration of this time interval.

Rooney (2017) initially defined an “Early Miocene Resurgence Phase” of volcanic activity concentrated along the Afar margins and the Turkana area to between 27 and 22 Ma but later revised and extended the end of this phase to include continued activity in southern Ethiopia and Turkana between ~24–17 Ma (Rooney, 2020a). Purcell (2018) describes the time period between 22 and 17 Ma as Turkana being a “seed point” from where the EARS begins to expand both north and south. This timing is consistent with Rooney’s (2020a) extension of the Early Miocene Resurgence Phase in this region. All NA samples yielded zircons from the originally defined 27 to 22 Ma period, but only one zircon was dated between ~22 and 17 Ma (17.71 ± 0.59 Ma). The single WTK sample, however, yielded zircons with dates that correlate to the entirety of the Early Miocene Resurgence Phase. The absence of zircons dated between 22–17 Ma in the NA samples but their presence in the WTK sample is consistent with a southward shift in the locus of volcanic activity during this phase.

Rooney (2020a) defined 16 to 12 Ma as the “Flood Phonolites and Silicic Eruptive Phase,” which was characterized by rhyolitic volcanism with relative quiescence of basaltic eruptions. Within the Afar region, the Mablas Series (15.4–11.8 Ma) was the primary manifestation of this silicic activity and was located in Djibouti near the Gulf of Aden (Rooney, 2020c; Zumbo et al., 1995). In the Turkana region and southern Ethiopia, the Plateau Phonolites constituted a narrow belt of more silicic deposits during this phase

(Rooney, 2020a). Equivalent eruptive products were more volumetrically significant in the nascent Kenyan and Main Ethiopian rifts (Rooney, 2020a).

Despite a shift to predominantly silicic volcanism during this period, there is a notable paucity of coeval zircons in both the NA and WTK samples. The NA samples lack any zircons temporally associated with the Mablas Series and the Silicic Eruptive Phase. The WTK sample contained only one zircon dated at 13.71 ± 0.43 Ma. Because volcanism was occurring regionally over this interval, the gap in the zircon record is likely a result of either watershed boundaries restricting the delivery of these volcanic components to the basins occupied by the drill sites, or of restricted transport within the watershed. Flood Phonolite products in Kenya are found to the east of modern Lake Turkana and farther south in the Kenya Rift within the modern day Omo-Turkana watershed (Rooney, 2020a). The WTK sample therefore appears to reflect more localized sediment sourcing predominantly from the north and west. The NA samples reflect a northern watershed boundary similar to the present such that material from the Djibouti region near the Gulf of Aden does not enter the Awash watershed.

Rooney (2020a) defined 12 to 9 Ma as the “Mid-Miocene Resurgence Phase,” which marks a return to widespread basaltic volcanism. Although this time period is characterized by basaltic volcanism, the reappearance of zircons of this age in the NA samples reflects sourcing from rhyolitic ignimbrites of the “Main Silicic Phase” along the southeast Afar Margin (Juch, 1978; Kunz et al., 1975). Zircons of this age exist in small numbers in the NA samples but are absent from the younger NAW14-1A-8Q-1 sample. They likely reflect the lower input from the eastern Afar margin and less voluminous nature of these eruptive products. The WTK sample lacks any zircons of this age range due to the more southern and restricted aerial extent of Mid-Miocene Resurgence Phase volcanic rocks within the Omo-Turkana watershed (Rooney, 2020a).

Rooney (2020a) defined 9 to 4 Ma as the "Early Rift Development Phase" marked by bimodal volcanic activity. There was no significant magmatism in the Turkana Basin or southern Ethiopia during this interval, but magmatic activity within the northern Ethiopia rift was recorded as pyroclastic deposits (Rooney, 2020a). There was also a transition in the western Ethiopian Plateau from fissural basalt flows to more trachytic and rhyolitic central volcanoes (Rooney, 2020a). The dominant $^{206}Pb/^{238}U$ age peak at ~7.75 Ma in the NA samples correlates with the Early Rift Development Phase and captures this basin-ward migration of volcanic activity. This phase is strongly represented in the NA samples due to a combination of increased silicic activity and more proximal shift in volcanism to rift basins (Rooney, 2020c). Zircons dated between ~7 and 5 Ma in the NA samples are lacking, however. The WTK sample yields zircons younger than 8 Ma, but in low abundance, reflecting the lack of significant magmatism in the Turkana Basin and southern Ethiopia during this phase.

Extensive pyroclastics and flows along the Main Ethiopian Rift and the Afar Stratoid Series—including the Hadar and Busidima formations—are assigned to the "Stratoid Phase" from 4 to 0.5 Ma (Rooney, 2020a). This phase is best represented by zircons from NAW14-1A-8Q-1, reflecting a shift to more localized sediment sources and reworking of Stratoid Phase pyroclastics in the fluvial system. The single WTK sample records active volcanism prior to and approximately coeval with the deposition of cored sediments.

Overall, the detrital zircon dates track well with established phases in EARS volcanic activity, even when volcanism was predominantly basaltic. The significant gap in detrital zircon dates in the NA samples occurs during a period of dominantly silicic volcanism, and the lack of zircons of this age is most likely reflective of a watershed configuration that restricted the delivery of silicic volcanics of this age to the Awash basin. The distribution of apparent ages in the NA and WTK samples are similar despite their different locations within the EARS, and differences in their record reflect shifts in loci of volcanic activity.

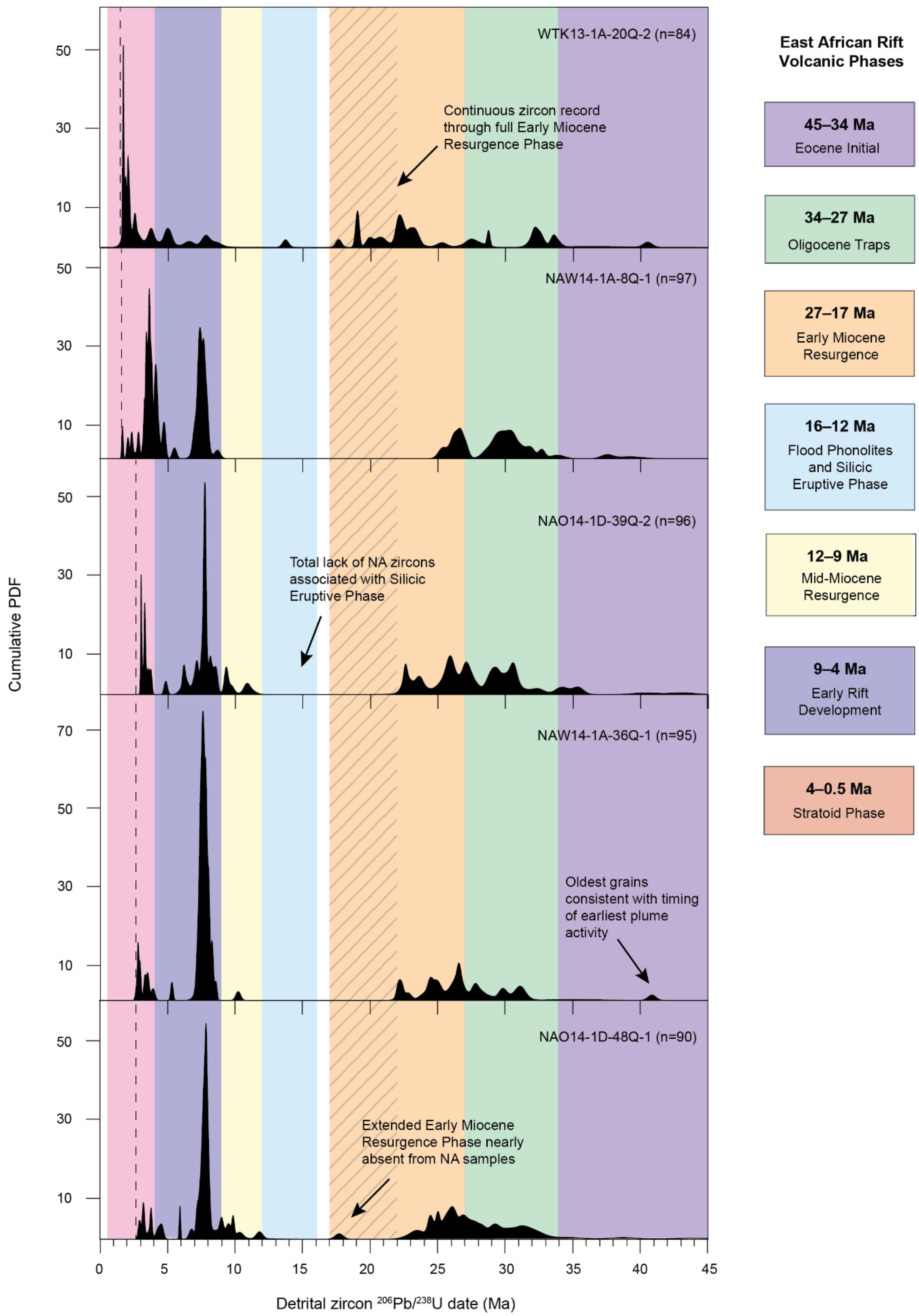

WTK13-1A-20Q-2 (n=84)
Continuous zircon record through full Early Miocene Resurgence Phase
NAW14-1A-8Q-1 (n=97)
NAO14-1D-39Q-2 (n=96)
Total lack of NA zircons associated with Silicic Eruptive Phase
NAW14-1A-36Q-1 (n=95)
Oldest grains consistent with timing of earliest plume activity
NAO14-1D-48Q-1 (n=90)
Extended Early Miocene Resurgence Phase nearly absent from NA samples
Cumulative PDF
Detrital zircon 206Pb/238U date (Ma)
East African Rift Volcanic Phases
45–34 Ma
Eocene Initial
34–27 Ma
Oligocene Traps
27–17 Ma
Early Miocene Resurgence
16–12 Ma
Flood Phonolites and Silicic Eruptive Phase
12–9 Ma
Mid-Miocene Resurgence
9–4 Ma
Early Rift Development
4–0.5 Ma
Stratoid Phase

Figure 2.8 Cumulative probability density function (PDF) plots of detrital zircon U/Pb ages in the context of East African Rift volcanic phases according to Rooney (2017, 2020a, 2020c). The zircon record covaries well with timing of established phases, with the exception of a gap during the Flood Phonolites and Silicic Eruptive Phase.

2.6.3 (U-Th)/He dates and volcanic heating/hydrothermal alteration

Because the majority of the detrital zircons are derived from Cenozoic volcanic rocks, only the Proterozoic zircons derived from the Lapur Range yield (U-Th)/He dates representative of "conventional" thermochronometic bedrock cooling ages. One ~400 Ma (U-Th)/He date from the WTK sample is consistent with (U-Th)/He zircon cooling ages from the Lapur Sandstone, and (U-Th)/He dates between ~100–200 Ma are consistent with zircon cooling ages from the Lapur Precambrian basement (Boone et al., 2018). However, Boone et al. (2018) found a negative correlation between single-grain dates and eU (effective uranium) for zircon basement samples, suggesting that intermediate Permian-Triassic (U-Th)/He zircons ages may have resulted from radiation damage effects and are not representative of a distinct tectonothermal event. Wide dispersion in zircon (U-Th)/He dates can be a result of radiation damage (Anderson et al., 2017), but our samples do not appear to show any significant age-eU correlation (Figure A5). The range in detrital zircon (U-Th)/He dates from the WTK sample between 400–1 Ma suggests a combination of exhumation-related cooling ages and later reheating and resetting from volcano-tectonic and/or hydrothermal processes.

Cenozoic zircons from both the NA and WTK samples yielded proportionally fewer (U-Th)/He dates that would be representative of eruption age, although the WTK sample yielded more zircons that fall along the 1:1 line than do any of the NA samples

(Figures 2.4 and 2.6). The lack of clustering in (U-Th)/He dates precludes a full resetting event. Zircon (U-Th)/He dates for a given $^{206}Pb/^{238}U$ date population show a spread from the presumptive eruption age to an age often younger than the depositional age of the sediments. Figure 2.9 shows a schematic path of zircons within the EARS with the potential locations and mechanisms causing partial resetting of (U-Th)/He dates.

Detrital zircon (U-Th)/He dates can be partially or fully reset by the emplacement of an overlying lava flow (Cooper et al., 2011). Whereas a zircon would need to be within ~7 cm of a 7-m-thick 1150°C lava flow for a day to be fully reset, zircons within ~50 cm of a flow can experience partial resetting (Cooper et al., 2011). The majority of zircons in the NA samples were derived from the western Ethiopian plateau and Afar margin where massive sequences of basalt flows with lesser rhyolitic units exist, which could have provided a protracted heating source. Sample NAO14-1D-48Q-1 also directly overlies a ~25 m thick basalt flow in the core. If the flow were still hot when the sediments were deposited, that basalt could provide another means of heat for partial resetting. However, this scenario is considered unlikely due to the lack of evidence for baking of the sediments.

Additionally, hydrothermal alteration could provide a mechanism for partial resetting of (U-Th)/He dates. Hydrothermal systems may develop in volcanic edifices where descending meteoric water encounters magmatic fluids (e.g., Aizawa et al., 2009), and stratovolcanoes within the rift may provide a source of incipient heating. Faulting and fault zones also provide a more widespread source of potential hydrothermal alteration within the rift, as they play an important role in the localization and evolution of hydrothermal flow (Curewitz and Karson, 1997 and references therein). There is evidence for hydrothermal alteration of some source units for the HSPDP sands, including the base of the Turkana Volcanics, which likely experienced loss of radiogenic argon due to hydrothermal alteration (McDougall and Brown, 2009; Tiercelin et al., 2012).

Hydrothermal heating of zircons on their path from crystallization to sampling (Figure 2.9) would provide the most likely mechanism to produce detrital zircon (U-Th)/He dates that are substantially younger than the depositional ages of the sediments. There is documented sub-lacustrine hydrothermal activity associated with modern East African lakes including Lake Tanganyika (e.g. Tiercelin et al., 1993), Lake Malawi (e.g., Branchu et al., 2005), Lake Bogoria (Renaut et al., 2013), Lake Baringo (Renaut et al., 2002; Tarits et al., 2006), and Lake Abhé (Dekov et al., 2014). Modern hot springs and fumeroles at Lake Turkana are known from Central Island, South Island, and Loiyangalani (Dunkley et al., 1993). Today, the geothermal field at Tendaho, just north of the NA drill sites, is fed by water heated at depth to up to ~270°C (Gianelli et al., 1998), potentially by a large and long-term magma reservoir at ~10–35 km depth (Desissa et al., 2013), and which flows through fractures in the Stratoid Series basalts (Didana et al., 2015).

Sedimentary evidence from both the NA and WTK cores indicates that post-depositional hydrothermal alteration of the sediments is a likely explanation for zircon resetting and the (U-Th)/He results (see Supplementary Material for full description of sedimentary features). Although the injectites (sedimentary dikes, sedimentary flows and sills) and brecciated zones observed in other units from the core provide evidence of pressurized fluid/sediment slurries, rather than a direct indication of hydrothermal fluids, they are associated with a suite of other features that together signify high-temperature alteration of the sediments. In particular, iron- and manganese-staining, alteration halos around injectites and discoloration (probably due to leaching or clay alteration) of non-pedogenic zones, non-pedogenic calcite deposits (i.e., veining), and silicification of diatomaceous sediments, are common throughout the NA cores (Figure A6). Similar features are observed in the WTK core.

In the WTK core, the presence of authigenic albite additionally suggests high-temperature hydrothermal alteration, as albitization of primary feldspars requires temperatures $\geq 100^{o}C$ (Chaudhary et al., 2016). Mixed-layered illite-smectite (I/S) was also identified in the basal section of the WTK core and has been interpreted to indicate hydrothermal alteration associated with tectonic activity (Rabideaux et al., 2014). X-ray diffraction of the upper portion of the core where sample WTK13-1A-20Q-2 was collected from provides evidence for a low degree of illitization, consistent with a complex alteration history (Rabideaux et al., 2016).

Based on cross-cutting relationships and stratigraphic positions of the sedimentary features observed in the NA cores, it appears that high-temperature and pressurized fluids influenced the sediments in multiple events. Some of the features observed (e.g., crystalline injectites and mud-flows) may have been syn-depositional or very early post-depositional, whereas other features (e.g., large dikes) could have occurred much later (Figure A6). Based on the discrete fill types of injectites (i.e., red-brown clay, basaltic sand, or brecciated mudclasts), there were likely several injection events. Direct observation of non-pedogenic slickensides on brittle fractures within the NA cores, as well as the intercalation of basalt flows within the sedimentary succession, indicate that both volcanism and earthquake activity are likely mechanisms for the pressure release and injection of heated fluid-sediment flows that contributed to the alteration of the zircons after burial at the core sites.

Within the two NA cores, laminated diatomaceous mudstones interbedded with red-brown clay slurries and small crystal-filled (e.g., gypsum) dikes indicate that there may also have been direct hydrothermal input into the Pliocene lake, which could have led to the local alteration of zircons prior to burial. The range of dates given by the (U-Th)/He results, along with the sedimentary evidence for cross-cutting relationships and stratigraphic position of some features, together indicate that zircons were likely partially reset at multiple periods prior to, during, and after the core interval (Figure 2.9).

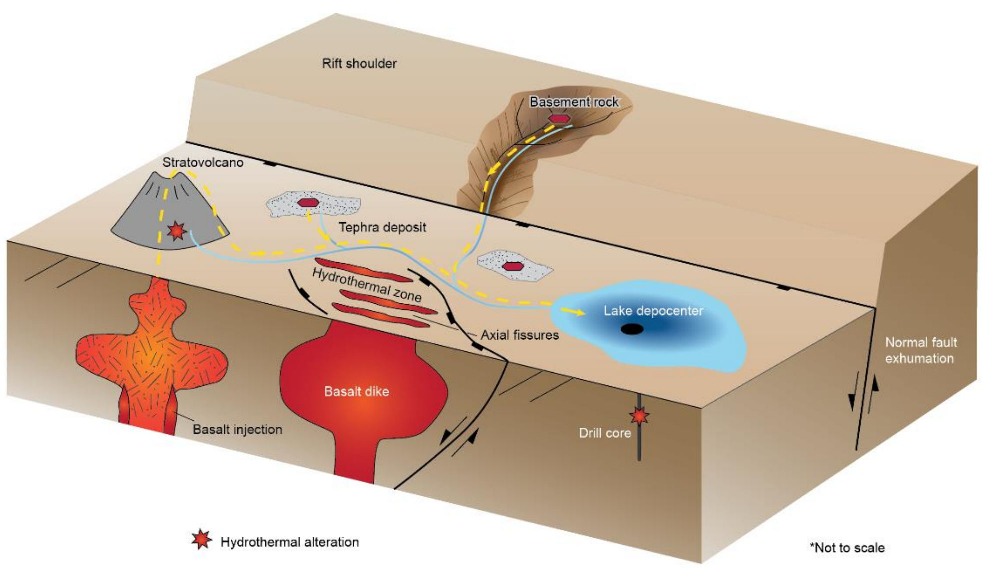

Figure 2.9 Schematic pathways of zircon distribution within the EARS. Volcanic zircons are dominantly formed from fractional crystallization in compositionally zoned shallow magma chambers. Zircons are derived from silicic volcanic eruptions and the associated deposits. Plutonic zircons are derived from crystalline bedrock where present. Zircons are eroded and are transported in the fluvial system where they may experience hydrothermal alteration directly in the immediate vicinity of a volcanic edifice, hydrothermal zones, or heating from basalt flows. After deposition and burial, zircons may experience sub-lacustrine hydrothermal alteration.

2.7 Conclusions

The detrital zircon record of the major watersheds within the EARS in Ethiopia and northern Kenya is dominated by volcanic zircons produced by silicic volcanism associated with rift system development. Only the single WTK sample yielded Proterozoic zircons derived from small exposures of the Mozambique Belt. The oldest Cenozoic detrital zircons dated at ~45 Ma are consistent with the timing of earliest plume activity related to the EARS in southern Ethiopia. Overall, the detrital zircon record tracks well with established EARS volcanic phases defined by Purcell (2018) and Rooney (2017, 2020a, 2020b, 2020c). Occasional gaps in the detrital zircon record reflect a cessation of silicic volcanism in the source area and/or a watershed configuration where volcanic zircons of a certain age are not transported within the fluvial network.

The western Afar margin provided the dominant sediment source for the NA samples, consistent with the vast amounts of material estimated to have been eroded from the plateau. After the tectonic reorganization in the Afar at ~2.9–2.7 Ma, there was increased localized sediment reworking and delivery. The WTK sample reflects relatively localized sediment sourcing, dominated by tephra produced by an eruption prior to the deposition of sediments.

Few detrital zircon (U-Th)/He dates are reflective of eruption ages in this study, as the majority indicate partial resetting. The large spread in (U-Th)/He dates reflects the dynamic nature of heating within the rift environment. Many (U-Th)/He dates are younger than the depositional ages of the sediments that host them, suggesting partial resetting by post-depositional heating. Possible causes of this are the emplacement of overlying lava flows or, more likely, hydrothermal alteration. As demonstrated by these detrital zircon results, LADD proves a powerful tool for understanding both the provenance and thermal histories of sediments.

2.8 Acknowledgements

We thank Mark Shapley, Emma Burnett, Pawel Kuczaj, and Tara Berglund for their contributions to the identification and interpretation of sedimentary injectites and other sedimentary indicators of hydrothermal activity. We thank the Ledi-Geraru Research Project team for helpful discussions. Initial core processing and sampling were conducted at the US National Lacustrine Core Facility (LacCore) at the University of Minnesota. We thank HSPDP PI Andy Cohen and the numerous members of the NA and WTK initial core sampling team and field team, including the people of the Nariokotome and Mille regions. Funding for the HSPDP NA and WTK sites was provided by the International Continental Drilling Program (ICDP), and the NSF (Grants EAR-1123942, BCS-1241859, and EAR-1338553).

2.9 References

Abbate, Ernesto, Pietro Bruni, and Mario Sagri (2015). Geology of Ethiopia: A Review and Geomorphological Perspectives. In *Landscapes and Landforms of Ethiopia*. P. Billi (ed.) https://doi.org/10.1007/978-94-017-8026-1_2

Aizawa, Koki, Yasuo Ogawa, and Tsuneo Ishido (2009). Groundwater flow and hydrothermal systems within volcanic edifices: Delineation by electric self-potential and magnetotellurics. *Journal of Geophysical Research: Solid Earth*, 224, B01208, p. 1–12. https://doi.org/10.1029/2008JB005910

Anderson, A. J., M. C. van Soest, K. V. Hodges, and J. M. Hanchar (2020). Helium diffusion in zircon: Effects of anisotropy and radiation damage revealed by laser depth profiling. *Geochimica et Cosmochimica Acta*, 274, p. 45– 62. https://doi.org/10.1016/j.gca.2020.01.049

Arambourg, C., and R. G. Wolff (1969). Nouvelles données paléontologique sur l'âge des "Gres du Lubur" (Turkana Grits) al'ouest du lac Rodolphe. *Comptes Rendus Société Géologique de France*, 9, 190–202.

Asrat, Asfawossen, P. Barbey, and G. Gleizes (2001). The Precambrian geology of Ethiopia: a review. *Africa Geoscience Review*, 8.3/4, p. 271–288.

Ayalew, Dereje, Pierre Barbey, Bernard Marty, Laurie Reisberg, Gezahegn Yirgu, and Raphael Pik (2002). Source, genesis, and timing of giant ignimbrite deposits associated with Ethiopian continental flood basalts. *Geochimica et Cosmochimica Acta*, 66, 8, p. 1429–1448. https://doi.org/10.1016/S0016-7037(01)00834-1

Barberi, F., and Rosenro Santacroce (1980). The Afar Stratoid Series and the magmatic evolution of East African rift system. *Bulletin de la Société Géologique de France*, 7, 6, p. 891–899.

Barberi, Franco, Giorgio Ferrara, R. Santacroce, M. Treuil, and J. Varet (1975). A transitional basalt-pantellerite sequence of fractional crystallization, the Boina Centre (Afar Rift, Ethiopia). *Journal of Petrology*, 16, 1, p. 22–56. https://doi.org/10.1093/petrology/16.1.22

Begg, G. C., W.L. Griffin, L. M. Natapov, S. Y. O'Reilly, S. P. Grand, C. J. O'Neill, and P. Bowden (2009). The lithospheric architecture of Africa: Seismic tomography, mantle petrology, and tectonic evolution. *Geosphere*, 5(1), p. 23–50. https://doi.org/10.1130/GES00179.1

Boehnke, P., Mélanie Barboni, and E. A. Bell (2016). Zircon U/Th model ages in the presence of melt heterogeneity. *Quaternary Geochronology*, 34, p. 69–74. https://doi.org/10.1016/j.quageo.2016.03.005

Boehnke, Patrick, E. Bruce Watson, Dustin Trail, T. Mark Harrison, and Axel K. Schmitt (2013). Zircon saturation re-revisited. *Chemical Geology*, 351, p. 324–334. https://doi.org/10.1016/j.chemgeo.2013.05.028

Boone, S. C., C. Seiler, B. P. Kohn, A. J. W. Gleadow, D. A. Foster, and L. Chung (2018). Influence of rift superposition on lithospheric response to East African Rift System extension: Lapur Range, Turkana, Kenya. *Tectonics*, 37, p. 182–207. https://doi.org/10.1002/2017TC004575

Branchu, Philippe, Laurent Bergonzini, Damien Delvaux, Marc De Batist, Vladimir Golubev, Marc Benedetti, and Jean Klerkx (2005). Tectonic, climatic and hydrothermal control on sedimentation and water chemistry of northern Lake Malawi (Nyasa), Tanzania. *Journal of African Earth Sciences*, 43, 4, p. 433–446. https://doi.org/10.1016/j.jafrearsci.2005.09.004

Brown, Francis H., and Ian Mcdougall (2011). Geochronology of the Turkana depression of northern Kenya and southern Ethiopia." *Evolutionary Anthropology: Issues, News, and Reviews*, 20, 6, p. 217–227. https://doi.org/10.1002/evan.20318

Cahen, L. and N. J. Snelling (1966). The geochronology of equatorial Africa. North-Holland Publishing Company, Amsterdam, The Netherlands.

Campisano, C. J., A.S. Cohen, J.R. Arrowsmith, A. Asrat, A.K. Behrensmeyer, E.T. Brown, A.L. Deino, D.M. Deocampo, C.S. Feibel, J.D. Kingston, H.F. Lamb, T.K. Lowenstein, A. Noren, D.O. Olago, R.B. Owen, J.D. Pelletier, R. Potts, K.E. Reed, R.W. Renaut, J.M. Russell, J.L. Russell, F. Schabitz, J.R. Stone, M.H. Trauth, and J.G. Wynn (2017). The Hominin Sites and Paleolakes Drilling Project: High-resolution paleoclimate records from the East African rift system and their implications for understanding the environmental context of hominin evolution. *PaleoAnthropology*, p. 1–43. https://doi:10.4207/PA.2017.ART104

Campisano, Christopher J., and Craig S. Feibel (2008). Tephrostratigraphy of the Hadar and Busidima Formations at Hadar, Afar Depression, Ethiopia. The Geology of Early Humans in the Horn of Africa. *Geological Society of America Special Paper* 446, p. 135–162. https://doi.org/10.1130/2008.2446(06)

Campisano, Christopher J. (2012). Geological summary of the Busidima formation (Plio-Pleistocene) at the Hadar paleoanthropological site, Afar Depression, Ethiopia. *Journal of Human Evolution*, 62, 3, p. 338–352. https://doi.org/10.1016/j.jhevol.2011.05.002

Chaudhary, Mamta Sanam, Nathan M. Rabideaux, Daniel M. Deocampo, Craig Feibel, and Andrew S. Cohen (2016). Reconstructing paleoenvironmental conditions from hydrothermally altered lacustrine sediments from HSPDP West Turkana-Kaitio core material via coupled mineralogical and geochemical analysis. Geological Society of America *Abstracts with Programs*, 48, 3. https://doi.org/10.1130/abs/2016SE-273372

Chorowicz, Jean (2005). The East African Rift System. *Journal of African Earth Sciences*, 43, 1-3, p. 379–410. https://doi.org/10.1016/j.jafrearsci.2005.07.019

Cohen, A., C. Campisano, R. Arrowsmith, A. Asrat, A.K. Behrensmeyer, A. Deino, C. Feibel, A. Hill, R. Johnson, J. Kingston, H. Lamb, T. Lowenstein, A. Noren, D. Olago, R.B. Owen, R. Potts, K. Reed, R. Renaut, F. Schäbitz, J.-J. Tiercelin, M.H. Trauth, J. Wynn, S. Ivory, K. Brady, R. ÓGrady, J. Rodysill, J. Githiri, J. Russell, V. Foerster, R. Dommain, S. Rucina, D. Deocampo, J. Russell, A. Billingsley, C. Beck, G. Dorenbeck, L. Dullo, D. Feary, D. Garello, R. Gromig, T. Johnson, A. Junginger, M. Karanja, E. Kimburi, A. Mbuthia, T. McCartney, E. McNulty, V. Muiruri, E. Nambiro, E.W. Negash, D. Njagi, J.N. Wilson, N. Rabideaux, T. Raub, M.J. Sier, P. Smith, J. Urban, M. Warren, M. Yadeta, C. Yost, and B. Zinaye (2016). The Hominin Sites and Paleolakes Drilling Project: inferring the environmental context of human evolution from eastern African rift lake deposits, Sci. Dril., 21, p. 1–16. https://doi.org/10.5194/sd-21-1-2016

Cooper, Frances J., Matthijs C. van Soest, and Kip V. Hodges (2011). Detrital zircon and apatite (U-Th)/He geochronology of intercalated baked sediments: A new approach to dating young basalt flows. *Geochemistry, Geophysics*, Geosystems, 12, 7, p. 1–8. https://doi.org/10.1029/2011GC003650

Davidson, Anthony (1983). The Omo river project, reconnaissance geology and geochemistry of parts of Ilubabor, Kefa, Gemu Gofa and Sidamo, *Ethiopian Institute of Geological Surveys Bulletin*, 2, p. 1–89.

Dekov, V. M., N. M. Egueh, G. D. Kamenov, G. Bayon, Stefan V. Lalonde, Mark Schmidt, Volker Liebetrau, F. Munnik, Y. Fouquet, M. Tanimizu, M. O. Awaleh, I. Guirreh, and B. Le Gall (2014). Hydrothermal carbonate chimneys from a continental rift (Afar Rift): Mineralogy, geochemistry, and mode of formation. *Chemical Geology*, 387, p. 87–100. https://doi.org/10.1016/j.chemgeo.2014.08.019

deMenocal, Peter, B. (2004). African climate change and faunal evolution during the Pliocene–Pleistocene. *Earth and Planetary Science Letters*, 220, 1-2, p. 3–24. https://doi.org/10.1016/S0012-821X(04)00003-2

Desissa, M., Johnson, N.E., Whaler, K.A., Hautot, S., Fisseha, S., Dawes, G.J.K. (2013). A mantle magma reservoir beneath an incipient mid-ocean ridge in Afar, Ethiopia. *Nature Geoscience*, 6, 861–865. https://dx.doi.org/10.1038/ngeo1925

Didana, Y.L., Thiel, S., Heinson, G. (2015). Three dimensional conductivity model of the Tendaho High Enthalpy Geothermal Field, NE Ethiopia. *Journal of Volcanology and Geothermal Research*, 290, p. 53–62. https://dx.doi.org/10.1016/j.jvolgeores.2014.11.013

Dodd, Thomas J.H., McCarthy, Dave J., Clarke, Stuart M. (2020). Clastic injectites, internal structures and flow regime during injection: The Sea Lion Injectite System, North Falkland Basin. *Sedimentology*, 67, p. 1014–1044. https://doi.org/10.1111/sed.12672

Dodson, M. H., A. R. Gledhill, R. M. Shackleton, and K. Bell (1975). Age differences between Archaean cratons of eastern and southern Africa. *Nature*. 254, 5498, p. 315–318. https://doi.org/10.1038/254315a0

Dunkley, R.N., Smith, M., Allen, D.J., Darling, W.G. (1993). The geothermal activity and geology of the northern sector of the Kenya Rift Valley. *British Geological Survey, Research Report*, SC/93/1, 185 p.

Ebinger, C. J., Tilahun Yemane, D. J. Harding, Samson Tesfaye, S. Kelley, and D. C. Rex (2000). Rift deflection, migration, and propagation: Linkage of the Ethiopian and Eastern rifts, Africa. *Geological Society of America Bulletin*, 112, 2, p. 163–176. https://doi.org/10.1130/0016-7606(2000)112<163:RDMAPL>2.0.CO;2

Ebinger, Cindy J., Alan L. Deino, R. E. Drake, and A. L. Tesha (1989). Chronology of volcanism and rift basin propagation: Rungwe volcanic province, East Africa. *Journal of Geophysical Research: Solid Earth*, 94, B11, p. 15785–15803. https://doi.org/10.1029/JB094iB11p15785

Farley, K. A., B. P. Kohn, and Bradley Pillans (2002). The effects of secular disequilibrium on (U–Th)/He systematics and dating of Quaternary volcanic zircon and apatite. *Earth and Planetary Science Letters*, 201, 1, p. 117–125. https://doi.org/10.1016/S0012-821X(02)00659-3

Feibel, C.S., Beck, C.C., Stockhecke, M., Gravina, A., Ortiz, K., Campisano, C.J., and Cohen, A.S. (2015). Seeing deeper into the mud: Insights from the WTK13 core, West Turkana, Kenya. *Geological Society of America Abstracts with Programs*, 47(7), 287. https://gsa.confex.com/gsa/2015AM/webprogram/Paper266297.html

Garello, Dominique Ines (2019). Tephrostratigraphy of Pliocene drill cores from Kenya and Ethiopia, and Pleistocene exposures in the Ledi-Geraru Research Project

Area, Ethiopia: geological context for the evolution of *Australopithecus* and *Homo*. PhD diss., Arizona State University.

Gehrels, George E., William R. Dickinson, Gerald M. Ross, John H. Stewart, and David G. Howell (1995). Detrital zircon reference for Cambrian to Triassic miogeoclinal strata of western North America. *Geology*, 23, 9, p. 831–834. https://doi.org/10.1130/0091-7613(1995)023<0831:DZRFCT>2.3.CO;2

Gianelli, G., Mekuria, N., Battaglia, S., Chersicla, A., Garofalo, P., Ruggieri, G., Manganelli, M., Gebregziabher, Z. (1998). Water-rock interaction and hydrothermal mineral equilibria in the Tendaho geothermal system. *Journal of Volcanology and Geothermal Research*, 86, p. 253–276.

Hofmann, C., V. Courtillot, G. Feraud, P. Rochette, G. Yirgu, E. Ketefo, and R. Pik (1997). Timing of the Ethiopian flood basalt event and implications for plume birth and global change. *Nature*, 389, 6653, p. 838–841. https://doi.org/10.1038/39853

Horne, Alexandra M., Matthijs C. van Soest, Kip V. Hodges, Alka Tripathy-Lang, and Jeremy K. Hourigan (2016). Integrated single crystal laser ablation U/Pb and (U–Th)/He dating of detrital accessory minerals–Proof-of-concept studies of titanites and zircons from the Fish Canyon tuff. *Geochimica et Cosmochimica Acta*, 178, p. 106–123. https://doi.org/10.1016/j.gca.2015.11.044

Juch, D., (1978). Geologic des Athiopischen Sudost-Escarpments 39° und 42° ostlicher Lange. *Clausthaler Geo. Abh*., 29, p. 1–139.

Kunz, K., H. Kreuzer, and P. Müller (1975). Potassium-Argon age determinations of the Trap basalt of the south-eastern part of the Afar Rift. Afar depression of Ethiopia, 1, 370–374 International Symposium on the Afar Region and Related Rift Problems (Bad Bergzabern, Germany).

Lupien, R. L., J. M. Russell, Craig Feibel, C. Beck, I. Castañeda, A. Deino, and A. S. Cohen (2018). A leaf wax biomarker record of early Pleistocene hydroclimate from West Turkana, Kenya. *Quaternary Science Reviews*, 186, p. 225–235. https://doi.org/10.1016/j.quascirev.2018.03.012

McDougall, I. A. N., and Francis H. Brown (2009). Timing of volcanism and evolution of the northern Kenya Rift. *Geological Magazine*, 146, 1, p. 34–47. https://doi.org/10.1017/S0016756808005347

Noren, Anders (2020a). HSPDP-NAO_NAW_public. OSF. https://doi.org/10.17605/OSF.IO/PBDT4

Noren, Anders (2020b). HSPDP-WTK_public. OSF. https://doi.org/10.17605/OSF.IO/B8QF2

Owusu Agyemang, Prince C., Eric M. Roberts, Bob Downie, and Joseph JW Sertich (2019). Sedimentary provenance and maximum depositional age analysis of the Cretaceous? Lapur and Muruanachok sandstones (Turkana Grits), Turkana Basin, Kenya. *Geological Magazine*, 156, 8, p. 1334–1356. https://doi.org/10.1017/S0016756818000663

Pasteels, P., M. Villeneuve, P. De Paepe, and J. Klerkx (1989). Timing of the volcanism of the southern Kivu province: implications for the evolution of the western branch of the East African Rift system. *Earth and Planetary Science Letters*, 94, 3-4, p. 353–363. https://doi.org/10.1016/0012-821X(89)90152-0

Paton, Chad, John Hellstrom, Bence Paul, Jon Woodhead, and Janet Hergt (2011). Iolite: Freeware for the visualisation and processing of mass spectrometric data. *Journal of Analytical Atomic Spectrometry*, 26, 12, p. 2508–2518. https://doi.org/10.1039/C1JA10172B

Peccerillo, A., C. Donati, A. P. Santo, A. Orlando, G. Yirgu, and D. Ayalew (2007). Petrogenesis of silicic peralkaline rocks in the Ethiopian rift: geochemical evidence and volcanological implications. *Journal of African Earth Sciences*, 48, 2-3, p. 161–173. https://doi.org/10.1016/j.jafrearsci.2006.06.010

Peccerillo, A., M. R. Barberio, G. Yirgu, D. Ayalew, M. W. U. T. W. Barbieri, and T. W. Wu (2003). Relationships between mafic and peralkaline silicic magmatism in continental rift settings: a petrological, geochemical and isotopic study of the Gedemsa volcano, central Ethiopian rift. *Journal of Petrology*, 44, 11, p. 2003–2032. https://doi.org/10.1093/petrology/egg068

Petrus, Joseph A., and Balz S. Kamber (2012). VizualAge: A novel approach to laser ablation ICP-MS U-Pb geochronology data reduction. *Geostandards and Geoanalytical Research*, 36, 3, p. 247–270. https://doi.org/10.1111/j.1751-908X.2012.00158.x

Purcell, P.G. (2018). Re-imagining and re-imaging the development of the East African Rift. *Petroleum Geoscience*, 24, p. 21–40. https://doi.org/10.1144/petgeo2017-036

Quade, Jay, Naomi E. Levin, Scott W. Simpson, Robert Butler, William C. McIntosh, Sileshi Semaw, Lynnette Kleinsasser, Guillaume Dupont-Nivet, Paul Renne, and Nelia Dunbar (2008). The geology of Gona, Afar, Ethiopia, in Quade, J., and Wynn, J.G., eds., The Geology of Early Humans in the Horn of Africa:

Geological Society of America Special Paper 446, p. 1–31. https://doi.org/10.1130/2008.2446(01)

Quade, Jay, Naomi Levin, Sileshi Semaw, Dietrich Stout, Paul Renne, Michael Rogers, and Scott Simpson (2004). Paleoenvironments of the earliest stone toolmakers, Gona, Ethiopia. *Geological Society of America Bulletin*, 116, 11-12, p. 1529–1544. https://doi.org/10.1130/B25358.1

Rabideaux, Nathan M., M. Sanam Chaudhary, Daniel Deocampo, Craig S. Feibel, and Andrew S. Cohen (2016). Unravelling the paleoenvironmental and diagenetic history of fluviolacustrine sediments from a Northern Kenya rift basin through analysis of HSPDP West Turkana-Kaitio Core material. *AGU Fall Meeting Abstracts*, p. PP23A-2312.

Rabideaux, Nathan M., Daniel M. Deocampo, Craig S. Feibel, Catherine C. Beck, and Dennis L. Nielson (2014). Illitization of smectite due to fault related hydrothermal alteration in HSPDP West Turkana core as revealed by clay mineralogy: implications for core interpretation. Geological Society of America *Abstracts with Programs*, 46, 6, p. 711.

Reiners, Peter W., I. H. Campbell, Stefan Nicolescu, Charlotte M. Allen, J. K. Hourigan, J. I. Garver, J. M. Mattinson, and D. S. Cowan (2005). (U-Th)/(He-Pb) double dating of detrital zircons. *American Journal of Science*, 305, 4, p. 259–311. https://doi.org/10.2475/ajs.305.4.259

Renaut, Robin W., Jones, Brian, Tierclin, Jean-Jaques, Tarits, Corinne (2002). Sublacustrine precipitation of hydrothermal silica in rift lakes: evidence from Lake Baringo, central Kenya Rift Valley. *Sedimentary Geology*, 148, p. 235–257.

Renaut, Robin W., R. Bernhart Owen, Brian Jones, Jean-Jacques Tiercelin, Corinne Tarits, John K. Ego, and Kurt O. Konhauser (2013). Impact of lake-level changes on the formation of thermogene travertine in continental rifts: evidence from Lake Bogoria, Kenya Rift Valley. *Sedimentology*, 60, 2, p. 428–468. https://doi.org/10.1111/j.1365-3091.2012.01347.x

Riedl, Simon, Daniel Melnick, Geoffrey K. Mibei, Lucy Njue, and Manfred R. Strecker (2020). Continental rifting at magmatic centres: structural implications from the Late Quaternary Menengai Caldera, central Kenya Rift. *Journal of the Geological Society*, 177, 1, p. 153–169. https://doi.org/10.1144/jgs2019-021

Romans, Brian W., Sébastien Castelltort, Jacob A. Covault, Andrea Fildani, and J. P. Walsh (2016). Environmental signal propagation in sedimentary systems across timescales. *Earth-Science Reviews*, 153, p. 7–29. https://doi.org/10.1016/j.earscirev.2015.07.012

Rooney, Tyrone O. (2017). The Cenozoic magmatism of East-Africa: Part I — Flood basalts and pulsed magmatism. *Lithos*, 286-287, p. 264–301. https://doi.org/10.1016/j.lithos.2017.05.014

Rooney, Tyrone O. (2020a). The Cenozoic magmatism of East Africa: Part II – Rifting of the mobile belt. *Lithos*, 360-361, 105291, p. 1–44. https://doi.org/10.1016/j.lithos.2019.105291

Rooney, Tyrone O. (2020b). The Cenozoic magmatism of East Africa: Part III – Rifting of the craton. *Lithos*, 360-361, 105390, p. 1–44. https://doi.org/10.1016/j.lithos.2020.105390

Rooney, Tyrone O. (2020c). The Cenozoic magmatism of East Africa: Part IV – The terminal stages of rifting preserved in the Northern East African Rift System. *Lithos*, 360-361, 105381, p. 1–29. https://doi.org/10.1016/j.lithos.2020.105381

Rooney, Tyrone O. (2020d). The Cenozoic magmatism of East Africa: Part V – Magma sources and processes in the East African Rift. *Lithos*, 360-361, 105296, p. 1–33. https://doi.org/10.1016/j.lithos.2019.105296

Shackleton, R. M. (1986). Precambrian collision tectonics in Africa. *Geological Society*, London, Special Publications 19, 1, p. 329–349. https://doi.org/10.1144/GSL.SP.1986.019.01.19

Sircombe, Keith N. (2000). Quantitative comparison of large sets of geochronological data using multivariate analysis: a provenance study example from Australia. *Geochimica et Cosmochimica Acta*, 64, 9, p. 1593–1616. https://doi.org/10.1016/S0016-7037(99)00388-9

Sláma, Jiří, Jan Košler, Daniel J. Condon, James L. Crowley, Axel Gerdes, John M. Hanchar, Matthew SA Horstwood, George A. Morris, Lutz Nasdala, Nicholas Norberg, Urs Schaltegger, Blair Shoene, Michael N. Tubrett, and Martin J. Whitehouse (2008). Plešovice zircon—a new natural reference material for U–Pb and Hf isotopic microanalysis. *Chemical Geology*, 249, 1-2, p. 1–35. https://doi.org/10.1016/j.chemgeo.2007.11.005

Stab, Martin, Nicolas Bellahsen, Raphaël Pik, Xavier Quidelleur, Dereje Ayalew, and Sylvie Leroy (2016). Modes of rifting in magma-rich settings: Tectonomagmatic evolution of Central Afar. *Tectonics*, 35, p. 2–38. https://doi.org/10.1002/2015TC003893

Tarits, Corinne, Renaut, Robin W., Tiercelin, Jean-Jaques, Le Hérisseé, Alain, Cotton, Jo, Cabon, Jean-Yves (2006). Geochemical evidence of hydrothermal recharge in

Lake Baringo, central Kenya Rift Valley. *Hydrological Processes*, 20, 2027–2055. https://doi.org/10.1002/hyp.6046

Tefera, M., T. Chernet, W. Haro, N. Teshome, and K. Woldie (1996). Geological map of Ethiopia. Geological Survey of Ethiopia.

Tiercelin, Jean-Jacques, Jean-Luc Potdevin, Peter Kinyua Thuo, Yassine Abdelfettah, Mathieu Schuster, Sylvie Bourquin, Hervé Bellon, Jean-Philippe Clément, Hervé Guillou, Thierry Nalpas, and Gilles Ruffet (2012). Stratigraphy, sedimentology and diagenetic evolution of the Lapur Sandstone in northern Kenya: Implications for oil exploration of the Meso-Cenozoic Turkana depression. *Journal of African Earth Sciences*, 71, p. 43–79. https://doi.org/10.1016/j.jafrearsci.2012.06.007

Tiercelin, Jean-Jacques, Catherine Pflumio, Maryse Castrec, Jacques Boulégue, Pascal Gente, Joël Rolet, Christophe Coussement, Karl O. Stetter, Robert Huber, Sony Buku, and Wafulu Mifundu (1993). Hydrothermal vents in Lake Tanganyika, East African, Rift system. *Geology*, 21, 6, p. 499–502. https://doi.org/10.1130/0091-7613(1993)021<0499:HVILTE>2.3.CO;2

Tripathy-Lang, Alka, Kip V. Hodges, Brian D. Monteleone, and Matthijs C. van Soest (2013). Laser (U-Th)/He thermochronology of detrital zircons as a tool for studying surface processes in modern catchments. *Journal of Geophysical Research: Earth Surface*, 118, 3, p. 1333–1341. https://doi.org/10.1002/jgrf.20091

Ukstins, Ingrid A., Paul R. Renne, Ellen Wolfenden, Joel Baker, Dereje Ayalew, and Martin Menzies (2002). Matching conjugate volcanic rifted margins: ^{40}Ar/^{39}Ar chrono-stratigraphy of pre-and syn-rift bimodal flood volcanism in Ethiopia and Yemen. *Earth and Planetary Science Letters*, 198, 3-4, p. 289–306. https://doi.org/10.1016/S0012-821X(02)00525-3

Wiedenbeck, M. A. P. C., P. Alle, Fy Corfu, W. L. Griffin, M. Meier, F. V. Oberli, A. von Quadt, J. C. Roddick, and W. Spiegel (1995). Three natural zircon standards for U-Th-Pb, Lu-Hf, trace element and REE analyses. *Geostandards Newsletter*, 19, 1, p. 1–23. https://doi.org/10.1111/j.1751-908X.1995.tb00147.x

WoldeGabriel, Giday, Grant Heiken, Tim D. White, Berhane Asfaw, William K. Hart, and Paul R. Renne (2000). Volcanism, tectonism, sedimentation, and the paleoanthropological record in the Ethiopian Rift System. *Geological Society of America*, Special Paper 345, p. 83–99. https://doi.org/10.1130/0-8137-2345-0.83

Woldegabriel, Giday, James L. Aronson, and Robert C. Walter (1990). Geology, geochronology, and rift basin development in the central sector of the Main

Ethiopia Rift. *Geological Society of America Bulletin*, 102, 4, p. 439–458. https://doi.org/10.1130/0016-7606(1990)102<0439:GGARBD>2.3.CO;2

Wynn, J.G., D.C. Roman, Z. Alemseged, D. Reed, D. Geraads, and S. Munro (2008). Stratigraphy, depositional environments, and basin structure of the Hadar and Busidima Formations at Dikika, Ethiopia, in Quade, J., and Wynn, J.G., eds., The Geology of Early Humans in the Horn of Africa: *Geological Society of America* Special Paper 446, p. 87–118. https://doi.org/10.1130/2008.2446(04)

Wynn, Jonathan G., Zeresenay Alemseged, René Bobe, Denis Geraads, Denné Reed, and Diana C. Roman (2006). Geological and palaeontological context of a Pliocene juvenile hominin at Dikika, Ethiopia. *Nature,* 443, 7109, p. 332–3336. https://doi.org/10.1038/nature05048

Zumbo, Vilma, Gilbert Féraud, Pierre Vellutin, Patrick Piguet, and Joëlle Vincent (1995). First ^{40}Ar/^{39}Ar dating on early pliocene to plio-pleistocene magmatic events of the Afar—Republic of Djibouti. *Journal of Volcanology and Geothermal Research*, 65, 3–4, p. 281–295. https://doi.org/10.1016/0377-0273(94)00107-R

CHAPTER 3

PLIO-PLEISTOCENE ^{10}BE-DERIVED PALEOEROSION RATES FOR THE NORTHERN EAST AFRICAN RIFT FROM SCIENTIFIC DRILL CORES

3.1 Abstract

Drill cores collected by the Hominin Sites and Paleolakes Drilling Project (HSPDP) in Ethiopia and Kenya provide an unusual opportunity to determine paleoerosion rates and basin-scale landscape dynamics during key intervals in Plio-Pleistocene hominin evolution. We collected four sand samples from the Northern Awash (NA; Afar, Ethiopia) drill cores, and one sample from the West Turkana (WTK; Kenya) core for *in situ* cosmogenic radionuclide ^{10}Be analyses. Core age models constrained largely by ^{40}Ar/^{39}Ar dating, tephrostratigraphy, and detrital zircon U/Pb geochronology indicate deposition at ~2.9–3.0 Ma for three of the NA samples, deposition at ~1.69 Ma for the fourth, and deposition at ~1.5 Ma for the WTK sample. We used these ages to determine the amount of ^{10}Be lost to radioactive decay, and we used sedimentation rates derived from age models of the cores to constrain post-depositional nuclide accumulation. Paleoerosion rates from the NA samples at ~2.9–3.0 Ma were consistent between 0.018 to 0.019 mm/yr. Deposition of these samples was relatively contemporaneous, and the narrow range of erosion rates indicates the uniform conditions under which samples were eroded. The NA sample deposited at ~1.69 Ma yielded a higher erosion rate of 0.021 mm/yr. Despite a significant tectonic reorganization within the Afar Depression at ~2.9–2.7 Ma, erosion rates were relatively consistent across the Pliocene to Pleistocene transition. Interestingly, all detrital zircons from the NA samples

are < 45 Ma and derived from silicic volcanic activity, thus not providing an identifiable quartz-bearing basement source. The NA erosion rates may therefore reflect erosion of vein quartz within the rift-related magmatic and hydrothermal systems, or local reworking of the limited clastic sedimentary units and may not be representative of large-scale catchment-mean erosion rates. The single WTK sample deposited at ~1.5 Ma yielded an erosion rate of 0.028 mm/yr, higher than the NA erosion rate during a similar interval. This rate is consistent with modern and Holocene erosion rates measured within the Kenya Rift. The WTK erosion rate is consistent with a wetter climate and stable, denser vegetation cover of the source region. While sampling from drill cores for ^{10}Be analyses provides significant benefits over traditional means, the lack of quartz-bearing source terranes complicates interpretations of erosion rates.

3.2 Introduction

Analyses of terrestrial cosmogenic nuclides (TCNs) such as ^{10}Be have become an essential tool for determining millennial-scale catchment mean erosion rates and evaluate tectonic and climate controls on landscape evolution (e.g., Bierman and Steig, 1996; Brown et al., 1995; Granger et al., 1996, 2013 and references therein). The ^{10}Be concentration in quartz accumulates while the material is actively being eroded and transported within the hillslope and fluvial system and decays at a fixed rate over time upon burial and shielding, thus providing a proxy for the rates at which a landscape erodes (von Blanckenburg, 2005).

In addition to being a powerful tool to quantify modern catchment mean erosion rates, ^{10}Be analyses can be used to determine paleoerosion rates over at least the last ~10

Myr (Madella et al., 2018). Quantifying erosion rates over the geologic past is an important component in understanding the interactions between climate, tectonics, and surface processes across time. Fluvial terrace samples are often used to determine ^{10}Be-derived paleoerosion rates (e.g., Bekaddour et al., 2014; Charreau et al., 2011; Schaller et al., 2002, 2004, 2016; Scherler et al., 2015), but there may be limited information on the post-depositional burial history of terrace samples, and specific care has to be taken to ensure the sampled material has been sufficiently shielded during exhumation and erosion. Therefore, the uncertainties associated with terrace samples may potentially lead to significant underestimations in erosion rates. On the other hand, sampling from drill cores for ^{10}Be analyses remedies these shortcomings and provides the necessary depositional history and age constraints based on independently determined core age models. Paleoerosion rates have previously been analyzed from Holocene sediment cores, which have negligible loss of ^{10}Be to radioactive decay (Grischott et al., 2016, 2017), but analyzing older samples takes advantage of the full benefits drill cores provide.

In this study, we sample from two drill core sites collected by the Hominin Sites and Paleolakes Drilling Project (HSPDP) for *in situ* ^{10}Be analyses to quantify Plio-Pleistocene paleoerosion rates (Figure 3.1). HSPDP seeks to understand the relationship between Earth system history and human evolution through collection and analysis of high-resolution paleoenvironmental records from paleolake drill cores near key paleoanthropological sites in East Africa (Cohen et al., 2016; Campisano et al., 2017). Understanding the basin-scale response to regional tectonics and climate through erosional response is a crucial component for linking global climate changes (and their subsequent environmental response) to patterns in human evolution. In addition, there is a special opportunity to tie the inferred paleoerosion rates to the rich paleoenvironmental proxy record determined by the HSPDP.

The HSPDP drill sites within the East African Rift provide an interesting study locale with a complex overlay of drainage networks on a tectonic template with climate-modulated surface processes. By evaluating paleoerosion rates, we can assess the relative impacts of tectonic activity and climatic fluctuations on erosion rates. We determine Plio-Pleistocene paleoerosion rates from the Northern Awash (Ethiopia) and West Turkana (Kenya) HSPDP drill cores. Erosion rates from the Northern Awash samples are relatively consistent across the Plio-Pleistocene and are similar to the Pleistocene erosion rate from West Turkana, albeit slightly lower. We compare the ^{10}Be-derived paleoerosion rates to modern, Holocene, and long-term erosion rates in East Africa, which show significant spatial variability. We also use the paleoenvironmental record from the HSPDP cores and paleoenvironmental reconstructions from adjacent outcrops to assess the climatic conditions under which the samples were eroded.

3.3 Geologic Setting: East African Rift

The East African Rift System (EARS) is expressed as a series of extensional graben basins that extends for ~3,500 km from the Afar Triple Junction to Mozambique (Chorowicz, 2005) (Figure 3.1). The EARS is split into eastern and western branches, with the eastern branch experiencing voluminous volcanism and the western branch experiencing only isolated volcanism. Rift volcanism initiated ~45 Ma and has continued into the present, creating complex relief and highly variable drainage conditions over time (Ebinger et al., 2000). This tectonism, volcanism, and subsequent sedimentation produced a series of rift basins with a rich paleontological record, including a notable Late Miocene to present record of hominin evolution (e.g., deMenocal, 2004; WoldeGabriel et al., 2000).

The geologic complexity of the EARS is further compounded by shifting climatic conditions over time. East African landscapes have overall shown a drying trend with an increase in open environments and an expansion of C_4 grasses over the late Cenozoic (Cerling et al., 2011), but regional basins show variable responses and less unidirectional trends. For example, records from marine drill cores off the coast of East Africa mark a shift in African climate at 2.8 Ma, coincident with a change in dominant orbital forcing and the intensification of Northern Hemisphere Glaciations (deMenocal, 1995, 2004). However, regional studies from the Awash and Omo-Turkana basins do not provide clear evidence for coherent environmental shifts at 2.8 Ma (e.g., Bobe and Behrensmeyer, 2004; DiMaggio et al., 2015; Levin et al., 2011, among others). Thus, local environmental signals display more heterogeneity in their response when subject to the same change in global climate conditions.

Regional basins have different tectonic histories that can have equally dramatic environmental implications as climatic events. For example, there is a regional disconformity at ~2.9–2.7 Ma in the Afar Depression that resulted from a major tectonic and geomorphic reorganization in the region. This tectonic reorganization marks the transition from the fluviolacustrine Hadar Formation (~3.8–2.9 Ma) to the high-energy fluvial Busidima Formation (2.7–0.15 Ma) (Campisano, 2012; Quade et al., 2004, 2008).

In addition, the Turkana region was impacted by a major tectonic event at ~2.4 Ma that involved the development of the Hammar/Hamar Uplift in southern Ethiopia and the shield volcano Mt. Kulal in northern Kenya (Feibel, 2011). This tectonic event impacted the paleogeography of the Turkana Basin at ~2.0 Ma, shifting from closed, lacustrine conditions to more open, fluvial conditions (Quinn et al., 2007).

Due to the extensive volcano-tectonic history of the EARS, surface exposures in the Awash and Turkana basins are largely dominated by Cenozoic volcanic rocks and volcaniclastic sedimentary rocks (WoldeGabriel et al., 2000). The Afar Depression is covered by the Stratoid Series (3.9–1.6 Ma), which contains basalts with rhyolitic intercalations (Barberi and Santacroce, 1980; Rooney, 2020), along with Quaternary alluvium. Late Eocene to Miocene volcanic rocks and Cretaceous to Quaternary sedimentary strata and alluvium cover large portions of the Turkana Basin (Feibel, 2011). There are exposures of Precambrian Mozambique Belt basement units (~885–540 Ma) in southern Ethiopia, including the Hammar Range that bounds the Chew Bahir basin (Davidson, 1983), and a few exposures in northern Kenya, with more significant exposures in the southern Turkana Basin (Asrat et al., 2001; Davidson, 1983; Shackleton, 1986). The extensive volcanic cover contributes to generally quartz-poor volcaniclastic sedimentary deposits.

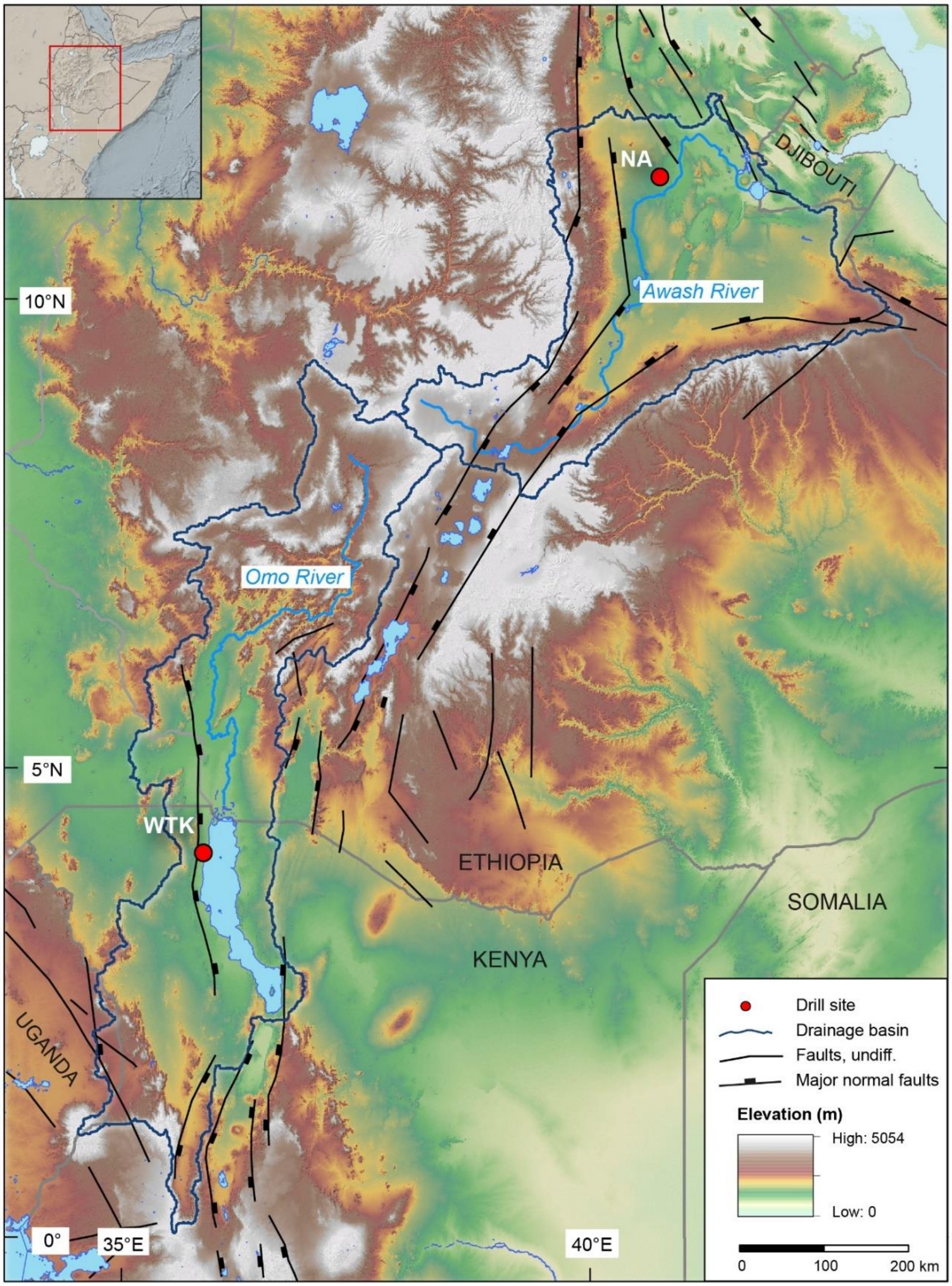

Figure 3.1 Geographic overview of the HSPDP drill sites in this study. Red dots mark drill site locations: Northern Awash (NA) and West Turkana (WTK). Present-day watersheds are delineated in dark blue, and major modern rivers (Awash River and Omo

River) and lakes are shown. Data source is a 30 m SRTM DEM projected over a hillshade model.

3.4 Quartz provenance

A critical assumption in inferring catchment mean erosion rates from *in situ* ^{10}Be measurements is that quartz is uniformly distributed throughout the catchment (Bierman and Steig, 1996; Brown et al., 1995). The ^{10}Be concentration will only reflect the portion of the landscape from which the quartz is eroding. We used U/Pb dating of detrital zircons from the same HSPDP sand samples analyzed here to provide constraints on sediment provenance and quartz availability within the basins (Zawacki et al., *in review*).

The detrital zircon record of the NA cores exclusively yielded zircons dated < 45 Ma derived from silicic volcanic rocks related to EARS volcanism (Zawacki et al., *in review*). The lack of zircons from crystalline basement sources in the NA samples thus implies that there are no quartz-bearing basement sources from which the sands were eroded. The detrital zircon record implies the western Afar margin and western Ethiopian Plateau as the predominant sedimentary source during the Plio-Pleistocene, and the eroding material is uniformly volcaniclastic (Zawacki et al., *in review*). The erosional signature recorded in the quartz grains may therefore reflect erosion of vein quartz or phenocrystic quartz within the rift-related magmatic and hydrothermal systems. Given the apparent limited availability of quartz within the Awash basin and the inability to precisely determine from where it is eroded, the ^{10}Be-derived erosion rates may not be representative of mean catchment-wide erosion rates.

In addition to many detrital zircons dated < 45 Ma in the WTK sample, the WTK sample also yielded a population of Proterozoic zircons (Zawacki et al., *in review*). The Proterozoic zircons from the WTK sample match in age with rocks associated with the Mozambique Belt (Abbate et al., 2015). Zawacki et al. (*in review*) suggested the likely sedimentary source of these zircons to be the Lapur Range, located ~30 km north of the WTK drill site. The Lapur Range is composed of Mozambique Belt gneisses, amphibolites, granulites, and other metamorphic assemblages, which are overlain by the Upper Cretaceous-Lower Paleogene Lapur Sandstone (Arambourg and Wolff, 1969; Begg et al., 2009; Boone et al., 2018; Tiercelin et al., 2012). The detrital zircon dates from the WTK sample are consistent with zircon U/Pb dates from the Lapur Sandstone (Owusu Agyemang et al. 2019). These units provide an identifiable, uniform source for quartz. Inferred erosion rates are thus interpreted to reflect erosion of the Lapur Range (see Figure 2.7).

3.5 Sampling and Methods

3.5.1 Drill core sampling

We sampled from two drill cores collected by the HSPDP: Northern Awash (NA) and West Turkana (WTK) (Figure 3.1). The Northern Awash site is situated within the modern Awash River basin in the Afar region of Ethiopia. Three drill cores were collected from 2 sites ~3 km apart for a composite stratigraphic interval of ~270 m. The cores target the lacustrine depocenter of the Hadar Formation (~3.6–2.9 Ma) in the Ledi-Geraru area and span in age from ~3.3–2.9 Ma (Campisano et al., 2017; Noren, 2020a). The NA cores are predominantly composed of silty clays, with occasional sandy units and massive basalts (Cohen et al., 2016). We collected four samples from the sandy units, two samples from core HSPDP-NAO14-1D and two samples from core HSPDP-NAW14-1A for *in situ* ^{10}Be analyses (Figure 3.2) (Table 3.1). The sands were quartz-poor and were dominated by basaltic rock fragments and minerals such as clinopyroxene, olivine, and weathered plagioclase (Figure 3.3). The depositional age of three of the samples is ~2.9–3.0 Ma, while the fourth sample has a depositional age of ~1.69 Ma (Table 3.1) (Zawacki et al., *in review*). A major regional disconformity exists in the Northern Awash stratigraphy at ~2.9–2.7 Ma, separating the Hadar Formation from the overlying Busidima Formation (2.7–0.15 Ma) (Campisano, 2012; Quade et al., 2004, 2008; Wynn et al., 2006, 2008). Therefore, the older three sands sample the Hadar Formation, the target formation of the drill cores, and the younger sand samples the Busidima Formation.

The West Turkana drill site is located on the western side of modern Lake Turkana in northern Kenya within the Omo-Turkana Basin (Figure 3.1). The drill core targets the lacustrine strata of the Kaitio and Natoo Members of the Nachukui Formation (Campisano et al., 2017), and the single core collected spans in age from ~1.9–1.4 Ma (Feibel et al., 2015; Lupien et al., 2018; Noren, 2020b). The upper third of the core has more frequent sandy intervals, while the lower two thirds of the core consist of laminated to massive clays (Cohen et al., 2016). We collected one sample from a sandy unit in HSPDP-WTK13-1A for *in situ* ^{10}Be analyses (Table 3.1). This sample was a volcaniclastic fine- to medium-grained sand. The sand contains a fluvially-deposited tephra, which was dated at 1.50 ± 0.02 Ma by ^{40}Ar/^{39}Ar single-crystal sanidine (Lupien et al. 2018), consistent with the youngest detrital zircon ages of this sample (Zawacki et al., *in review*).

Sampling potential from both drill sites was limited due to the modest amounts of massive fluvial sandy intervals within the cores. We first collected small ~50–140 g samples from each sandy interval to assess the grain size and quartz content of each sample. We only targeted sand units for full sampling that were sufficiently coarse (500–125 μm) and had enough volume to yield enough quartz (target ~50–100 g). We collected ~4–5 kg of bulk material per sample from across multiple continuous core drives.

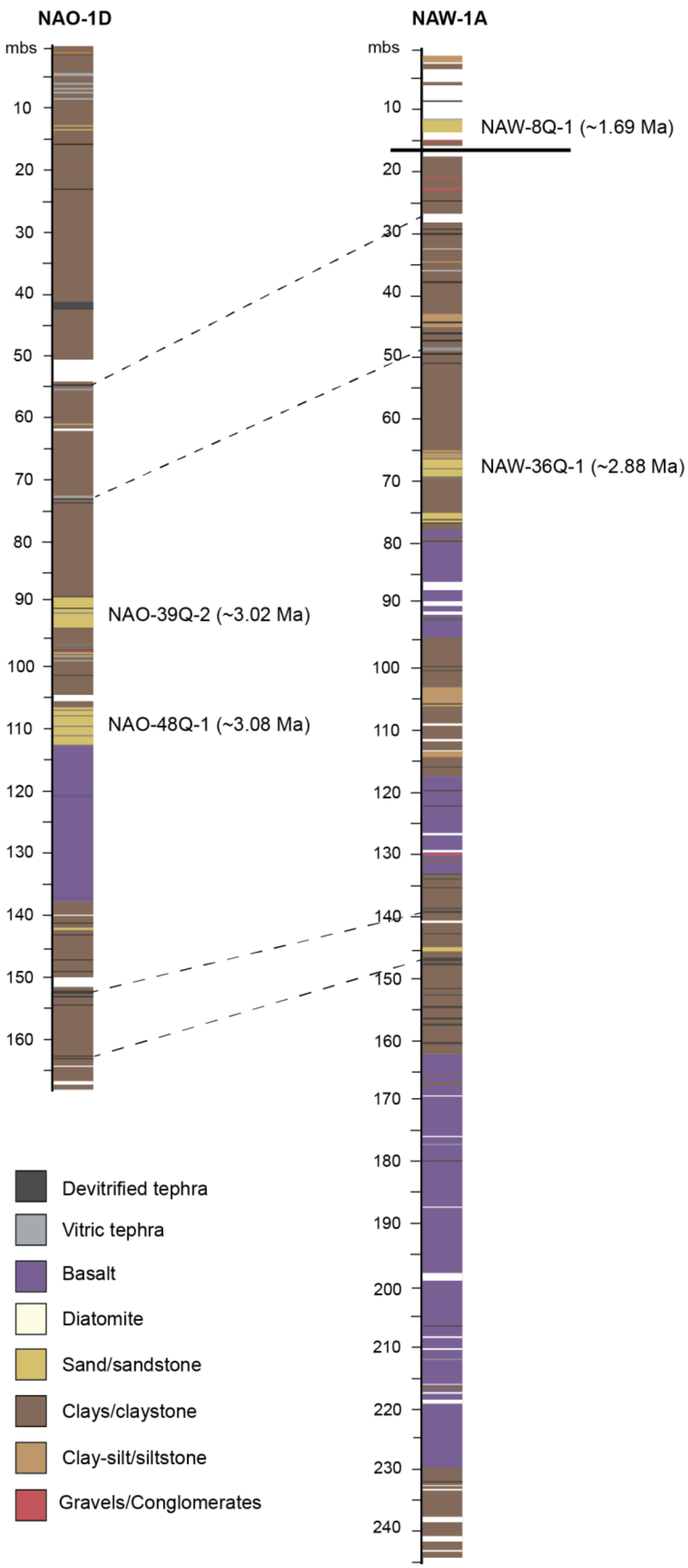
NAO-1D
NAW-1A
mbs
NAW-8Q-1 (~1.69 Ma)
NAW-36Q-1 (~2.88 Ma)
NAO-39Q-2 (~3.02 Ma)
NAO-48Q-1 (~3.08 Ma)
Devitrified tephra
Vitric tephra
Basalt
Diatomite
Sand/sandstone
Clays/claystone
Clay-silt/siltstone
Gravels/Conglomerates

Figure 3.2 Stratigraphic columns of the HSPDP-NAO14-1D and HSPDP-NAW14-1A drill cores shown in meters below surface (mbs). Sampled sand units are labeled. Dashed lines indicate stratigraphic correlations between cores. Solid black line indicates unconformity between the Hadar and Busidima Formations. Modified from Garello (2019).

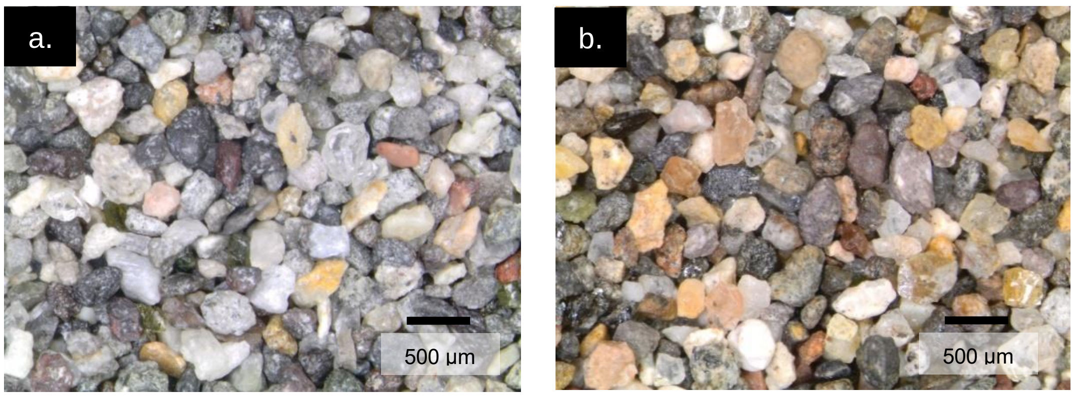

Figure 3.3 Photomicrographs of the 500–250 µm size fraction from **a.)** NAO14-1D-48Q-1 and **b.)** NAW14-1A-8Q-1. Sands are visibly quartz poor and heavily dominated by volcaniclastic material.

Table 3.1 Names and locations of sampled HSPDP drill cores, along with sampled core drives. Samples are referred to by the top-most drive. Individual core drives collected up to ~3 m in length of material. See text for discussion of depositional age estimate. Age uncertainties are expressed as 1σ.

HSPDP Core	Lat.	Long.	Site Elevation (m)	Sampled Core Drives	Upper Sample Depth (mbs)	Depositional Age (Ma)	Age Uncertainty (Myr)
Northern Awash							
HSPDP-NAW14-1A	11.3254	40.7649	493	8Q-1, 8Q-2, 8Q-3	11.5	1.69	0.049
HSPDP-NAW14-1A	11.3254	40.7649	493	36Q-1, 36Q-2	67	2.88	0.043
HSPDP-NAO14-1D	11.3152	40.7370	520	39Q-2, 40Q-1, 40Q-2	91	3.02	0.062
HSPDP-NAO14-1D	11.3152	40.7370	520	48Q-1, 48Q-2	109	3.08	0.049
West Turkana							
HSPDP-WTK13-1A	4.1097	35.8718	404	20Q-2, 20Q-3	58	1.50	0.010

3.5.2 Sample preparation

Samples were sieved to isolate the 500–250 and 250–125 μm size fractions and were processed through Frantz magnetic separation and LST heavy liquids density separations to remove abundant unwanted materials, such as basalt fragments. The limited sample availability and low quartz content necessitated a focus on physical separations to preserve as much quartz as possible. The quartz-bearing fraction was then cleaned in a 2:1 hydrochloric acid and nitric acid solution for 12 hours. Samples were leached at least seven times in 1% hydrofluoric acid solution on heated rollers following standard techniques outlined in Kohl and Nishiizumi (1992). To ensure the purity and cleanliness of the quartz, samples sat in 0.25% hydrofluoric acid solution for three to seven days. Between 25.3 and 78.9 g of clean quartz was yielded per sample. Samples were then dissolved in hydrofluoric acid with the addition of a 1074 ± 8 ppm low-background ^{9}Be carrier. Be was isolated through ion-exchange chromatography, oxidized, mixed with niobium powder, and packed in targets. Chemical separations and isolation procedures were carried out in the Cosmogenic and Short-Lived Isotopes Laboratory at Arizona State University. The Purdue Rare Isotope Measurement Laboratory (PRIME Lab) performed the ^{10}Be measurements based on revised ICN standards (Nishiizumi et al., 2007) (Table 3.2).

3.5.3 Paleoerosion rate calculations

In order to calculate paleoerosion rates from cosmogenic isotopes in older sedimentary sequences, it is necessary to know: (i) the depositional age of the sedimentary sequence, (ii) the cosmogenic paleoproduction rate in the basin at time of deposition, and (iii) the post-depositional cosmogenic nuclide accumulation between sediment deposition and sample collection (Charreau et al., 2011). We use the age models of the cores to independently constrain the depositional age of each sample (Table 3.1), and to derive sedimentation rates above each sample to constrain post-depositional nuclide accumulation (Table 3.2) (Campisano et al., *In prep* and A. Deino, pers. comm.).

We calculated ^{10}Be production rates using the time-dependent Lal (1991) and Stone (2000) scaling scheme ('Lm', Balco et al., 2008) based on reference production rates from Borchers et al. (2016) using CRONUScalc version 2.0 (Marrero et al., 2016). For samples older than 2 Ma, we used the PINT database to determine paleomagnetic intensity (Biggin et al, 2009) for production rate scaling. Muogenic production was calculated with fast muons being 0.65% and slow muon capture being 1.2% of the total surface production (Braucher et al., 2003). For hillslope production rates (P_{hill}), we assume that the mean elevation of the WTK source area was similar to that of the modern. Based on the modern topography, we use an elevation of 700 m for P_{hill} of the NA samples, as an intermediary between the elevation of the western Ethiopian Plateau and the Afar Depression, given that research suggests that the topography of the Afar (height of escarpments and elevation of the Depression) was similar to the present by the latest Miocene (Redfield et al., 2003). For burial production rates (P_{burial}), we take the modern depocenter elevation and subtract the sample depth below surface (Table 3.1) for the elevation at time of sample deposition. Calculated production rates are shown in Table 3.2.

Unless a sample is instantaneously buried, the material will continue to accumulate nuclide concentration after deposition until it is sufficiently shielded with ~3–5 m overlying material. The high-resolution record of the cores allows us to quantify the post-depositional accumulation of ^{10}Be (N_{post}), which can be described by the following equation (Braucher et al., 2000):

$$N_{post} = \sum_j \left[\frac{P_j}{(\lambda - \frac{S_r\rho}{\Lambda_j}} \left(e^{-t\frac{A_r\rho}{\Lambda_j}} - e^{-\lambda t} \right) \right] \qquad [1]$$

where P_j is the burial surface production rates by spallation, fast muon, and slow muon capture (atom g^{-1} yr^{-1}), λ is the radioactive decay constant (4.997×10^{-7} yr^{-1}) (Chmeleff et al., 2010), ρ is the overlying sediment density (1.9 g cm^{-3}, determined from Multi-Sensor Core Logger (MSCL-S) analyses; Cohen et al., 2016), A_r is the sedimentation accumulation rate (cm yr^{-1}), Λ_j is the attenuation length (g cm^{-2}), and t (yr) is the time during which the sediment is buried. We calculate average sedimentation rates above each sample based on the age models of the cores (Table 3.2) (Campisano et al., *In prep* and A. Deino, pers. comm.; Lupien et al., 2018), which will allow us to account for accumulation due to the long period of production from fast muons and slow muon capture. Due to the small amount of Busidima Formation material sampled by the NAW core, we use an accumulation rate for sample NAW14-1A-8Q-1 based on outcrop studies of the Busidima Formation (Quade et al., 2008).

^{10}Be atoms radioactively decay upon burial, and the loss of ^{10}Be atoms (N_{dec}) can be estimated:

$$N_{dec} = \frac{N_{mes} - N_{post}}{e^{-\lambda t}} - \left(N_{mes} - N_{post}\right) \qquad [2]$$

where N_{mes} (atoms g^{-1} qtz) is the measured nuclide concentration. Having determined the amount of ^{10}Be accumulated after deposition and the amount of ^{10}Be lost to decay since burial, the initial ^{10}Be concentration at the time of deposition (N_0, atoms g^{-1} qtz) can be calculated:

$$N_0 = N_{mes} + N_{dec} - N_{post} \qquad [3]$$

The initial nuclide concentration is inversely related to the catchment-wide erosion rate (Brown et al., 1995):

$$N_0 = \frac{P_0}{\lambda + \frac{\rho\varepsilon}{\Lambda}}\left(1 - e^{\left(-\lambda + \frac{\rho\varepsilon}{\Lambda}\right)t}\right) \qquad [4]$$

This equation can be simplified and solved for erosion rate:

$$\varepsilon = \frac{\Lambda}{\rho}\left(\frac{P_0}{N_0} - \lambda\right) \qquad [5]$$

where Λ is the mean attenuation length of the target material (ca. 165 g cm^{-2}), P_0 is the hillslope nuclide production rate at the surface (atoms $g^{-1}a^{-1}$), ρ is the material density (2.65 g cm^{-3}) and λ is the nuclide decay constant (4.997×10^{-7} yr^{-1}; Chmeleff et al., 2010). Estimated production rates are shown in Table 3.2.

To take advantage of the high-resolution record of the drill cores, we perform an assessment of erosion rate error using a Monte Carlo simulation. The Monte Carlo simulation uses repeated random sampling of all input variables to aggregate the individual uncertainties into a final probability distribution function (PDF) of the paleoerosion rates. We assume all variables have normally distributed uncertainties for our sampling. In addition to the uncertainty of the [^{10}Be] measurement, we account for the 1σ error of constant variables from the literature such as the ^{10}Be decay constant (Chmeleff et al., 2010) and attenuation lengths (Braucher et al., 2003). For the density of the eroding material and the buried sediment, we assume an uncertainty of 5%, based on MSCL-S gamma density log data of the drill cores (Cohen et al., 2016). ^{10}Be hillslope and burial production rate uncertainties are determined based on variances in the geomagnetic field strength over the 1σ age of the samples. We do not account for variation in elevation for production rate uncertainties, due to the likely relative similarity of basin topography over the observed time intervals. The 1σ age of the samples is used to constrain the uncertainty in ^{10}Be lost to radioactive decay, and we assume a 5% uncertainty in sediment accumulation rates for post-depositional ^{10}Be accumulation based on the average uncertainty of the core age model. The uncertainty in production rates constitutes the majority of the assessed uncertainty. Simulation results and PDFs from all samples and the resulting MATLAB codes are shown in the Appendix C. This assessment allows for a more objective evaluation of changes in erosion rates over time.

3.6 Results

^{10}Be analyses of the three NA samples deposited at ~2.9–3.0 Ma yielded erosion rates of 0.018 to 0.019 mm/yr (Table 3.2). Based on the core age model, deposition of these samples was relatively contemporaneous, and the narrow range of estimated paleoerosion rates indicates the uniform conditions under which the material was eroded and transported. Sample NAW14-1A-8Q-1 deposited at ~1.69 Ma yielded a similar erosion rate of 0.21 mm/yr, which is within our modeled error of the older NA erosion rates (Table 3.2). The significantly lower sediment accumulation rate associated with this sample yielded a post-depositional ^{10}Be concentration that was an order of magnitude greater than the post-depositional accumulation of the older three NA samples and contributed to significantly larger and more asymmetric error distribution based on Monte Carlo error analyses (Table 3.2). Not accounting for the ^{10}Be concentration accumulated after deposition in this sample would lead to a significant underestimation in the erosion rate.

The WTK sample deposited at ~1.5 Ma yielded an erosion rate of 0.028 mm/yr (Table 3.2). This rate is ~1.5 times higher than the erosion rates at ~2.9–3.0 Ma from the NA core and is also higher than the NA erosion rate at ~1.69 Ma within 1 sigma error. The amount of post-depositional accumulation in the WTK sample is similar to that accumulated in the Pliocene NA samples based on the similar sediment accumulation rate (Table 3.2).

Table 3.2 Cosmogenic nuclide analytical data for the NA and WTK samples. All uncertainties are expressed as 1σ except where noted. P_{hill} = hillslope production rate, P_{burial} = post-depositional burial production rate, A_r = accumulation rate, N_{post} = post-depositional nuclide accumulation. Erosion rate uncertainties show a slight asymmetric distribution from the Monte Carlo-based aggregation. All corresponding uncertainties of variables are shown and explored in Appendix C.

Sample	Sample Weight (g)	^{10}Be atoms x10^3 (atoms g^{-1} qtz)	^{10}Be Uncertainty x10^3 (atoms g^{-1} qtz)	P_{hill} Spallation (atoms g^{-1} yr^{-1})	P_{hill} Muons (atoms g^{-1} yr^{-1})	Depositional Age (ka)	Depositional Age Uncertainty (kyr)
Northern Awash							
NAW14-1A-8Q-1	46.723	108.9	4.4	4.87	0.09	1.69	0.049
NAW14-1A--36Q-1	31.561	50.2	3.2	5.53	0.10	2.88	0.043
NAO14-1D-39Q-2	25.339	45.5	2.1	5.53	0.10	3.02	0.062
NAO14-1D-48Q-1	43.372	43.4	2.6	5.53	0.10	3.08	0.049
West Turkana							
WTK13-1A-20Q-2	61.410	58.2	3.6	4.69	0.090	1.50	0.010

Sample	A_r (cm/yr)	P_{burial} Spallation (atoms g^{-1} yr^{-1})	P_{burial} Slow Muon Capture (atoms g^{-1} yr^{-1})	P_{burial} Fast Muons (atoms g^{-1} yr^{-1})	N_{post} x10^3 (atoms g-^{1} qtz)	Paleoerosion Rate (mm/yr)	Paleoerosion Rate Uncertainty (mm/yr) [2σ]
Northern Awash							
NAW14-1A-8Q-1	0.005	4.22	0.05	0.03	48.96	0.021	+0.0092 / -0.0058
NAW14-1A--36Q-1	0.030	4.56	0.06	0.03	4.62	0.018	+0.0022 / -0.0018
NAO14-1D-39Q-2	0.030	4.56	0.06	0.03	4.32	0.019	+0.0030 / -0.0026
NAO14-1D-48Q-1	0.030	4.56	0.06	0.03	4.18	0.019	+0.0026 / - 0.0022
West Turkana							
WTK13-1A-20Q-2	0.045	3.71	0.04	0.02	5.24	0.028	+0.0016 / -0.0012

3.7 Discussion

3.7.1 East African erosion rate comparisons

We compare the inferred ^{10}Be-derived paleoerosion rates from the HSPDP sands to modern, Holocene, and long-term denudation rates in East Africa to contextualize rates of landscape change (Figure 3.4). The paleoerosion rates from the HSPDP drill cores provide the first millennial-scale ^{10}Be-derived erosion rate data for the Plio-Pleistocene in East Africa. The most apt comparisons for these erosion rates are thus million-year time scale erosion rates from thermochronometry data that cover the Plio-Pleistocene and Holocene–modern millennial-scale erosion rates derived from ^{10}Be analyses.

Although the low quartz content of sands within the Awash basin complicates interpretations of ^{10}Be-derived erosion rates, other cosmogenic isotopes and thermochronometers provide comparisons for erosion rates in Ethiopia. Puchol et al. (2017) used cosmogenic ^{3}He in detrital pyroxenes from Ethiopian river sands to determine denudation rates of the Mille and Tekeze rivers. The Mille river is a tributary of the Awash proximal to the NA drill sites and flows eastward from the western Afar margin toward the Afar depression, while the Tekeze river is a tributary of the Nile River and flows northwest across the northwestern Ethiopian plateau. The Mille river thus provides a modern erosional equivalent source for the NA sands. The average denudation rates of 0.07 ± 0.02 and 0.057 ±0.005 mm/yr obtained for the Mille and Tekeze rivers, respectively, are higher than any of the paleoerosion rates from the NA cores (Figure 3.4) (Puchol et al., 2017). The ^{3}He-derived rates are consistent with denudation rates along the western Ethiopian escarpment determined from low-temperature (U-Th)/He thermochronology, which yield rates between 0.09–0.18 mm/yr over the last 5–10 Myr (Pik et al., 2003). However, the large Blue Nile basin yielded a lower, longer-term denudation rate of 0.03 mm/yr over the last 25–29 Myr (Figure 3.4) (Pik et al., 2003). The paleoerosion rates from the NA cores are most consistent with the long-term average erosion rates from the large basins that drain the internal upland plateau.

The low paleoerosion rates inferred from the NA sample are in contrast with the high sediment accumulation rates in the Ledi-Gararu area during the late Pliocene. Sediment accumulation rates at ~3.4–2.9 Ma in the Ledi-Geraru area were ~0.9 mm/yr (Dupont-Nivet et al., 2008), and sediment accumulation rates farther west at the Hadar and Gona areas during this time were ~0.2–0.3 mm/yr (Campisano and Feibel, 2007; Quade et al., 2008). The accumulation rates of the NA core ranges from ~0.3–0.9 mm/yr (Deino and Campisano, pers. comm.), which are consistent with rates determined from outcrop studies. The sediment accumulation rates are an order of magnitude higher than the estimated paleoerosion rates (Figure 3.5). However, the accumulation of the Hadar Formation may not have been primarily controlled by faulting along the rift escarpment to the west, but rather by increased subsidence toward the Afar Depression (Dupont-Nivet et al., 2009). The high sediment accumulation rates likely suggest a close proximity to the depositional center of the Hadar Basin (Garello, 2019).

We note little change in the inferred paleoerosion rates from the ~2.9–3.0 Ma to the ~1.69 Ma samples in the NA core despite a stark transition in depositional settings and drastic reduction in sediment accumulation rates from the Hadar to Busidima formations. The Busidima Formation represents high-energy fluvial settings with highly erosional channel conglomerates and silt-dominated paleosols, while the fluviolacustrine Hadar Formation is dominated by fluvial sands, mudstone paleosols, and lacustrine clays (Campisano, 2012; Campisano and Feibel, 2008). The Busidima Formation represented at Gona yielded a sediment accumulation rate of 0.05 mm/yr (Quade et al., 2008), which is fully consistent with the modern ^{3}He-derived erosion rates of the Mille and Tekeze rivers (Puchol et al., 2017). The accumulation rates of the Busidima Formation are of approximately the same order of magnitude as the paleoerosion rate from the NA core Busidima equivalent, reflecting a shift to more uniform rather than localized deposition within the basin. Despite the significant tectonic and geomorphic shift at the Plio-Pleistocene, the consistency in ^{10}Be-derived erosion rates over time may suggest that the source of the eroded quartz within the Awash basin may be less influenced by tectonic evolution. Tectonic activity may have led to a reworking of material within the basin but did not actually change source erosion.

Given the more significant exposures of the Mozambique Belt within central and southern Kenya, there have been more studies evaluating ^{10}Be-derived erosion rates within the Kenya Rift. Garcin et al. (2017) determined paleo- and modern erosion rates in the Suguta Valley of the northern Kenya Rift, which is located to just south of the Turkana Basin. ^{10}Be-derived paleoerosion rates during the African Humid Period at ~11.8 cal. kyr BP ranged from 0.035 to 0.086 mm/yr, and were 0.024 mm/yr at ~8.7 cal. kyr BP. These paleoerosion rates were all higher than the modern catchment-mean erosion rate of 0.013 mm/yr (Garcin et al., 2017). The 0.028 mm/yr erosion rate at ~1.5 Ma from the WTK sample is consistent with erosion rates during the Holocene in this region of the northern Kenya Rift, although they lie within different catchments (Figure 3.4).

However, there is a significant amount of variability in modern erosion rates throughout the Kenya Rift. ^{10}Be-derived erosion rates for additional catchments within the northern Kenya Rift range from 0.0052 to 0.0962 mm/yr, and erosion rates from the central and southern Kenya Rift range from 0.001 to 0.132 mm/yr (Figure 3.4) (Torres Acosta et al., 2015). By comparison, modern erosion rates in the Rwenzori Mountains of the Albertine Rift range from 0.0077 to 0.077 mm/yr (Figure 3.4) (Roller et al., 2012). While the erosion rates from the Kenya and Albertine Rift vary, they show a trend where denser vegetation cover yields lower erosion rates for a given hillslope gradient (Torres Acosta et al., 2015). This observed modern relationship between erosion rate, vegetation cover, and hillslope gradient provides interesting context in which to interpret paleolandscapes based on erosion rates. Sediment accumulation rates within the WTK core ranged from 0.33 to 0.71 mm/yr (Lupien et al., 2018), similar to the relatively high Pliocene accumulation rates in the NA core (Figure 3.5).

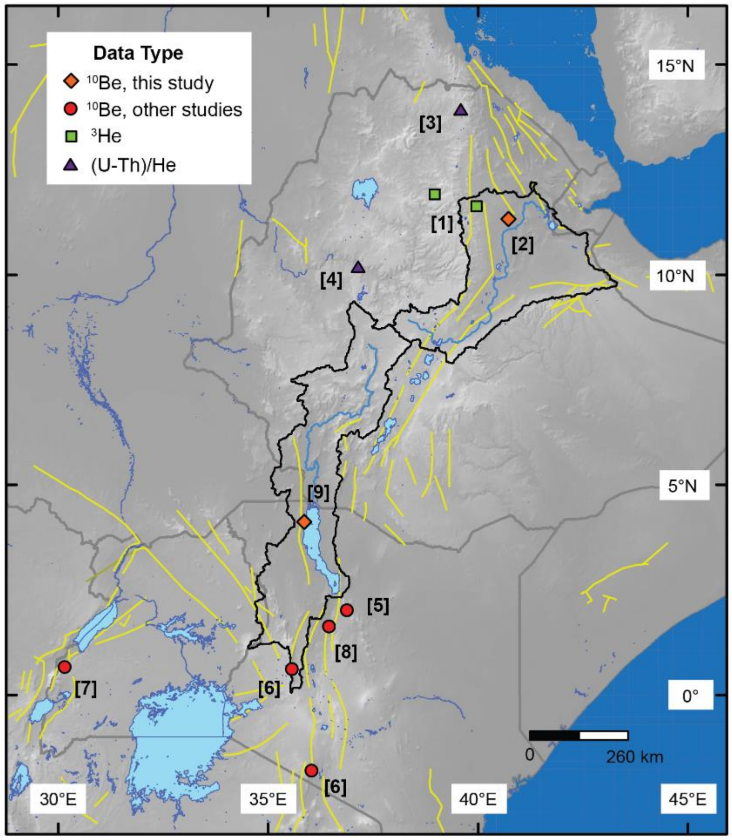
Data Type
¹⁰Be, this study
¹⁰Be, other studies
³He
(U-Th)/He
15°N
10°N
5°N
0°
[1]
[2]
[3]
[4]
[5]
[6]
[7]
[8]
[9]
0
260 km
30°E
35°E
40°E
45°E

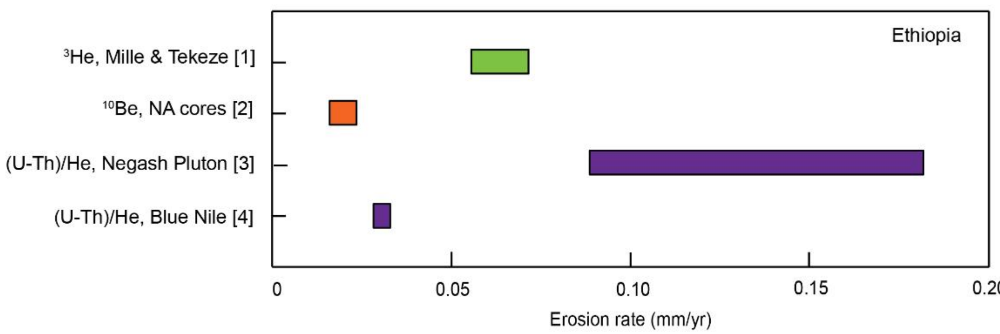
Ethiopia
³He, Mille & Tekeze [1]
¹⁰Be, NA cores [2]
(U-Th)/He, Negash Pluton [3]
(U-Th)/He, Blue Nile [4]
0
0.05
0.10
0.15
0.20
Erosion rate (mm/yr)

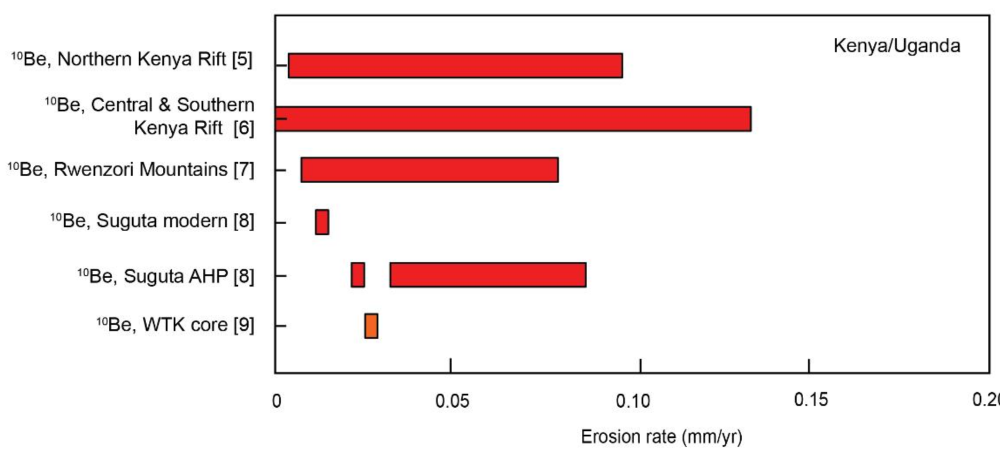
Kenya/Uganda
¹⁰Be, Northern Kenya Rift [5]
¹⁰Be, Central & Southern Kenya Rift [6]
¹⁰Be, Rwenzori Mountains [7]
¹⁰Be, Suguta modern [8]
¹⁰Be, Suguta AHP [8]
¹⁰Be, WTK core [9]
0
0.05
0.10
0.15
0.20
Erosion rate (mm/yr)

Figure 3.4 Comparison of modern and paleoerosion rates across East Africa derived from ^{10}Be (orange=this study, red=other studies), ^{3}He (green), and (U-Th)/He (purple) analyses. [1] Mille and Tekeze rivers, modern (Puchol et al., 2017); [2] NA drill cores, ~2.9–3.0 and ~1.69 Ma, this study; [3] Negash pluton, last 5–10 Myr (Pik et al., 2003); [4] Blue Nile basin, last 25–29 Myr (Pik et al., 2003); [5] northern Kenya Rift, modern (Torres Acosta et al., 2015); [6] central and southern Kenya Rift, modern (Torres Acosta et al., 2015); [7] Albertine Rift, modern (Roller et al., 2012); [8] Suguta valley, modern and African Humid Period (AHP) ~8.7 and ~11.8 cal. kyr BP (Garcin et al., 2017); [9] WTK drill core, ~1.5 Ma, this study.

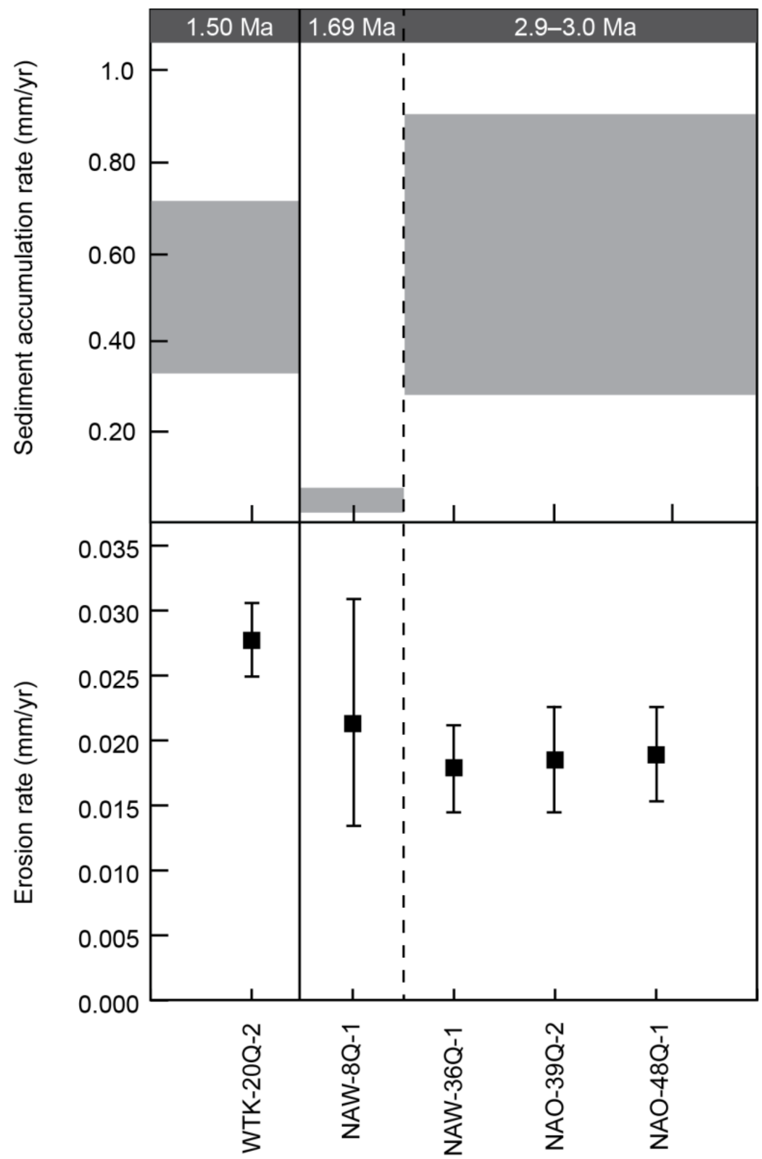

Figure 3.5 Range of sediment accumulation rates in the NA and WTK drill cores (outcrop rate for NAW-8Q-1; Quade et al., 2004, 2008) and ^{10}Be-derived erosion rates for each of the samples. Erosion rates from the NA samples stay consistent over time, despite the sharp reduction of associated sediment accumulation rates.

3.7.2 Paleoenvironmental context

A significant benefit of the HSPDP drill cores is the additional paleoenvironmental context they provide from other paleo-proxy records throughout the cores. This additional context allows for a fuller understanding of the environmental conditions under which the sands were eroding and aids in interpretation of what the erosion rates signify, as erosion rates are influenced both by climate and tectonics.

Mineralogical analyses of the NA cores show that the region was significantly more humid during the Pliocene than it is today (Davis et al., 2017). The leaf wax hydrogen isotope record of rainfall (δD_{precip}) in the NA cores shows no long-term trend during the Pliocene, indicating relative stabilityin East African rainfall during this period (Lupien, 2019). Paleoenvironmental reconstructions based on paleoecology of the Hadar Formation suggest that the environment during the late Pliocene was mainly bushland, open woodlands, and shrubland, with varying regions of wetlands or edaphic grasslands through time (Reed, 2008). At ~3.1 Ma, there was a distinct faunal turnover and influx of more arid-adapted mammalian taxa, indicating a significant ecological change (Reed, 2008). The paleorainfall at Hadar was likely highly seasonal and twice that of modern amounts, based on $\delta^{18}O$ of carbonates and paleosol character (Aronson et al., 2008). Climatic parameters reconstructed from pollen also indicate that the Pliocene was significantly wetter, cooler, and with greater vegetation compared to present times (Bonnefille et al., 2004).

Although there was a significant tectonic and geomorphic regime change between the Hadar and Busidima Formations at ~2.9–2.7 Ma (Quade et al., 2004, 2008), erosion rates from the NA cores changed little over the Plio-Pleistocene. The change of tectonics within the basin is thus not represented in the paleoerosion rates, and tectonic activity may not have perturbed the erosional source area. Ethiopia’s climate did not shift to the present, mostly arid, regime from the pluvial climate regime until ~1 Ma (Aronson et al., 2008), significantly after the deposition of the youngest NA sample at ~1.69 Ma. A comparison to modern ^{10}Be-derived erosion rates from the Awash watershed would be helpful to see if erosion rates show a shift related to a new climatic regime.

The WTK core (~1.9–1.4 Ma) captures a sedimentary record of paleo-Lake Lorenyang, which initially formed at ~2.14 Ma, temporally correlated with the eruption of basalts blocking the southeast outlet of the Turkana Basin (Lepre, 2014). The formation of this lacustrine basin via volcano-tectonic impounding resulted in a major topographic and hydrologic reorganization of the Omo-Turkana Basin (Lepre, 2014; Levin et al., 2011). Shifts in δ^{13}C of paleosol carbonates also suggests that regionally there was decreased monsoon intensity and higher aridity after ~2.0 Ma (Levin et al., 2011). The WTK sample is therefore representative of an environment ~500 kyr after a major reorganization of the Omo-Turkana basin and slight climatic shift.

Within the ~1.9–1.4 Ma record of the WTK core, there is no observed long-term shift in δ^{13}C of leaf wax, implying that there was little change in mean vegetation composition and mean precipitation during this interval in the Turkana Basin (Lupien et al., 2018). When the WTK sample was deposited, there appears to have been a relatively stable vegetation and climatic regime within the basin. However, the lack of additional substantive sand units in the WTK precludes comparisons of erosion rates over time to investigate if they also remained uniform. The average δD_{wax} of the WTK core record is ~25% more depleted than late Holocene sediments from modern Lake Turkana, which indicates that the Turkana Basin was wetter during the early Pleistocene than the present (Lupien et al., 2018; Morrissey, 2014). Therefore, despite a shift to higher aridity at ~2.0

Ma, conditions during ~1.9–1.4 Ma were apparently wetter and more vegetated than the present.

Given the modern erosion rates from the Kenya and Albertine Rifts that show a trend where denser vegetation cover yields lower erosion rates for a given hillslope gradient (Torres Acosta et al., 2015), we can assess if the lower erosion rate from the WTK core is consistent with this trend. The Lapur Range has relief up to ~900 m and an average hillslope gradient of ~0.2. Assuming that the modern topography of the Lapur Range is relatively similar to that of ~1.5 Ma, the WTK sample would fit on a trend of lower erosion rate for a given hillslope gradient where the enhanced vegetation index (EVI) > 0.35 (see Figure 4.4B). EVI provides a satellite-based measure of modern vegetation cover and is reflective of variations in canopy structures (Huete et al., 2002). An EVI > 0.35 would reflect little to no exposed bare rock or soil and significant coverings of trees and herbaceous cover (Torres Acosta et al., 2015). This degree of vegetation would appear to be consistent with the wetter climate and stable vegetation regime of the Omo-Turkana Basin at the time of the WTK sample deposition.

3.8 Conclusions

In determining ^{10}Be-derived paleoerosion rates, the HSPDP drill cores provide the exceptional benefit of an age model to independently constrain the depositional age of material and the post-depositional nuclide accumulation, as well as a rich paleoenvironmental proxy record. However, cosmogenic analyses required sampling significant volumes of core material due to the very low quartz content of the sands and thus precluded more substantive examinations of changes in erosion rates over time.

Due to the low abundance of quartz-bearing units and extremely high proportion of volcanic units within the Awash watershed, NA paleoerosion rates are likely not representative of catchment mean erosion rates. The NA samples yielded consistently low erosion rates across the Plio-Pleistocene boundary, lower than erosion rates determined through additional nuclides and chronometers. The quartz may be sourced from vein quartz or phenocrystic quartz within the rift-related magmatic and hydrothermal systems, thus being spatially limited and representing a slowly eroding portion of the landscape less influenced by regional tectonics. Primary tectonic activity along the active Afar rift margin likely occurred farther downstream (Wolfenden et al., 2005).

The erosion rate from the single WTK sample is consistent with, but on the lower end of, modern and Holocene erosion rates in Kenya determined from ^{10}Be analyses. The quartz is likely derived from the Lapur Range to the north of the drill site during a period of relative tectonic and climatic stability within the Omo-Turkana basin. Based on the correlation between modern erosion rates, hillslope gradient and vegetation, the low erosion rate from the WTK sample would be consistent with denser vegetation cover on a higher hillslope gradient. Analyses of modern erosion rates at the drill sites would provide an interesting direct comparison for controls on erosional processes.

3.9 References

Abbate, Ernesto, Pietro Bruni, and Mario Sagri (2015). Geology of Ethiopia: A Review and Geomorphological Perspectives. In *Landscapes and Landforms of Ethiopia*. P. Billi (ed.) https://doi.org/10.1007/978-94-017-8026-1_2

Arambourg, C., and R. G. Wolff (1969). Nouvelles données paléontologique sur l'âge des "Gres du Lubur" (Turkana Grits) al'ouest du lac Rodolphe. *Comptes Rendus Société*

Aronson, James L., Million Hailemichael, and Samuel M. Savin (2008). Hominid environments at Hadar from paleosol studies in a framework of Ethiopian climate change. *Journal of Human Evolution*, 55, 4, p. 532–550. https://doi.org/10.1016/j.jhevol.2008.04.004

Asrat, Asfawossen, P. Barbey, and G. Gleizes (2001). The Precambrian geology of Ethiopia: a review. *Africa Geoscience Review*, 8.3/4, p. 271–288.

Balco, Greg, John O. Stone, Nathaniel A. Lifton, and Tibor J. Dunai (2008). A complete and easily accessible means of calculating surface exposure ages or erosion rates from ^{10}Be and ^{26}Al measurements. *Quaternary Geochronology*, 3, 3, p. 174–195. https://doi.org/10.1016/j.quageo.2007.12.001

Barberi, F., and Rosenro Santacroce (1980). The Afar Stratoid Series and the magmatic evolution of East African rift system. *Bulletin de la Société Géologique de France*, 7, 6, p. 891–899.

Begg, G. C., W.L. Griffin, L. M. Natapov, S. Y. O'Reilly, S. P. Grand, C. J. O'Neill, and P. Bowden (2009). The lithospheric architecture of Africa: Seismic tomography, mantle petrology, and tectonic evolution. *Geosphere*, 5(1), p. 23–50. https://doi.org/10.1130/GES00179.1

Bekaddour, Toufik, Fritz Schlunegger, Hendrik Vogel, Romain Delunel, Kevin P. Norton, Naki Akçar and Peter Kubik (2014). Paleo erosion rates and climate shifts recorded by Quaternary cut-and-fill sequences in the Pisco valley, central Peru. *Earth and Planetary Science Letters*, 390, p. 103–115. https://doi.org/10.1016/j.epsl.2013.12.048

Bierman, Paul, and Eric J. Steig (1996). Estimating rates of denudation using cosmogenic isotope abundances in sediment. *Earth Surface Processes and Landforms*, 21, 2, p. 125–139. https://doi.org/10.1002/(SICI)1096-9837(199602)21:2<125::AID-ESP511>3.0.CO;2-8

Biggin, Andrew J., Geert HMA Strik, and Cor G. Langereis (2009). The intensity of the geomagnetic field in the late-Archaean: new measurements and an analysis of the updated IAGA palaeointensity database. *Earth, Planets and Space*, 61, 1, 9–22. https://doi.org/10.1186/BF03352881

Bobe, René and Anna K. Behrensmeyer (2004). The expansion of grassland ecosystems in Africa in relation to mammalian expansion and the origin of the genus *Homo*. *Palaeogeography, Palaeoclimatology, Palaeoecology*, 207, p. 399–420. https://doi.org/10.1016/j.palaeo.2003.09.033

Bonnefille, Raymonde, Richard Potts, Françoise Chalié, Dominique Jolly, and Odile Peyron (2004). High-resolution vegetation and climate change associated with Pliocene Australopithecus afarensis. *Proceedings of the National Academy of Sciences*, 101, 33, p. 12125–12129. https://doi.org/10.1073/pnas.0401709101

Borchers, Brian, Shasta Marrero, Greg Balco, Marc Caffee, Brent Goehring, Nathaniel Lifton, Kunihiko Nishiizumi, Fred Phillips, Joerg Schaefer, and John Stone (2016). Geological calibration of spallation production rates in the CRONUS-Earth project. *Quaternary Geochronology*, 31, p. 188–198. https://doi.org/10.1016/j.quageo.2015.01.009

Boone, S. C., C. Seiler, B. P. Kohn, A. J. W. Gleadow, D. A. Foster, and L. Chung (2018). Influence of rift superposition on lithospheric response to East African Rift System extension: Lapur Range, Turkana, Kenya. *Tectonics*, 37, p. 182–207. https://doi.org/10.1002/2017TC004575

Braucher, R., Brown, E.T., Bourlès, D.L., Colin, F. (2003). *In situ* produced ^{10}Be measurements at great depths: implications for production rates by fast muons. *Earth and Planetary Science Letters*, 211, p. 251–258. https://doi.org/10.1016/S0012-821X(03)00205-X

Braucher, R., Bourlès, D.L., Brown, E.T., Colin, F., Muller, J.-P., Braun, J.-J., Delaune, M., Minko, A.E., Lescouet, C., Raisbeck, G.M., Yiou, F. (2000). Application of *in situ* produced cosmogenic ^{10}Be and ^{26}Al to the study of lateritic soil development in tropical forest: theory and examples from Cameroon and Gabon. *Chemical Geology*, 170, p. 95–111. https://doi.org/10.1016/S0009-2541(99)00243-0

Brown, Erik Thorson, Robert F. Stallard, Matthew C. Larsen, Grant M. Raisbeck, and Françoise Yiou (1995). Denudation rates determined from the accumulation of in situ-produced ^{10}Be in the Luquillo Experimental Forest, Puerto Rico. *Earth and*

Planetary Science Letters, 129, 1-4, p.193–202. https://doi.org/10.1016/0012-821X(94)00249-X

Campisano, Christopher J. (2012). Geological summary of the Busidima formation (Plio-Pleistocene) at the Hadar paleoanthropological site, Afar Depression, Ethiopia. *Journal of Human Evolution*, 62, 3, p. 338–352. https://doi.org/10.1016/j.jhevol.2011.05.002

Campisano, C. J., A.S. Cohen, J.R. Arrowsmith, A. Asrat, A.K. Behrensmeyer, E.T. Brown, A.L. Deino, D.M. Deocampo, C.S. Feibel, J.D. Kingston, H.F. Lamb, T.K. Lowenstein, A. Noren, D.O. Olago, R.B. Owen, J.D. Pelletier, R. Potts, K.E. Reed, R.W. Renaut, J.M. Russell, J.L. Russell, F. Schabitz, J.R. Stone, M.H. Trauth, and J.G. Wynn (2017). The Hominin Sites and Paleolakes Drilling Project: High-resolution paleoclimate records from the East African rift system and their implications for understanding the environmental context of hominin evolution. *PaleoAnthropology*, p. 1–43. https://doi:10.4207/PA.2017.ART104

Campisano, Christopher J., and Craig S. Feibel (2008). Depositional environments and stratigraphic summary of the Pliocene Hadar formation at Hadar, Afar depression, Ethiopia. *Geological Society of America Special Paper* 446, p. 179–201. https://doi.org/10.1130/2008.2446(08)

Campisano, Christopher J., and Craig S. Feibel (2007). Connecting local environmental sequences to global climate patterns: evidence from the hominin-bearing Hadar Formation, Ethiopia. *Journal of Human Evolution*, 53, 5, p. 515–527. https://doi.org/10.1016/j.jhevol.2007.05.015

Cerling, Thure E., Jonathan G. Wynn, Samuel A. Andanje, Michael I. Bird, David Kimutai Korir, Naomi E. Levin, William Mace, Anthony N. Macharia, Jay Quade, and Christopher H. Remien (2011). Woody cover and hominin environments in the past 6 million years. *Nature*, 476, 7358, p. 51–56. https://doi.org/10.1038/nature10306

Charreau, Julien, P-H. Blard, N. Puchol, J-P. Avouac, Elisabeth Lallier-Vergès, D. Bourlès, Regis Braucher, A. Gallaud, R. Finkel, M. Jolivet, Y. Chen, and P. Roy (2011). Paleo-erosion rates in Central Asia since 9 Ma: A transient increase at the onset of Quaternary glaciations? *Earth and Planetary Science Letters*, 304, 1-2, p. 85–92. https://doi.org/10.1016/j.epsl.2011.01.018

Chmeleff, Jérôme, Friedhelm von Blanckenburg, Karsten Kossert, and Dieter Jakob (2010). Determination of the ^{10}Be half-life by multicollector ICP-MS and liquid scintillation counting. *Nuclear Instruments and Methods in Physics Research Section B: Beam Interactions with Materials and Atoms*, 268, 2, p. 192–199. https://doi.org/10.1016/j.nimb.2009.09.012

Chorowicz, Jean (2005). The East African rift system. *Journal of African Earth Sciences*, 43, 1-3 p. 379–410. https://doi.org/10.1016/j.jafrearsci.2005.07.019

Cohen, A., C. Campisano, R. Arrowsmith, A. Asrat, A.K. Behrensmeyer, A. Deino, C. Feibel, A. Hill, R. Johnson, J. Kingston, H. Lamb, T. Lowenstein, A. Noren, D. Olago, R.B. Owen, R. Potts, K. Reed, R. Renaut, F. Schäbitz, J.-J. Tiercelin, M.H. Trauth, J. Wynn, S. Ivory, K. Brady, R. ÓGrady, J. Rodysill, J. Githiri, J. Russell, V. Foerster, R. Dommain, S. Rucina, D. Deocampo, J. Russell, A. Billingsley, C. Beck, G. Dorenbeck, L. Dullo, D. Feary, D. Garello, R. Gromig, T. Johnson, A. Junginger, M. Karanja, E. Kimburi, A. Mbuthia, T. McCartney, E. McNulty, V. Muiruri, E. Nambiro, E.W. Negash, D. Njagi, J.N. Wilson, N. Rabideaux, T. Raub, M.J. Sier, P. Smith, J. Urban, M. Warren, M. Yadeta, C. Yost, and B. Zinaye (2016). The Hominin Sites and Paleolakes Drilling Project: inferring the environmental context of human evolution from eastern African rift lake deposits, Sci. Dril., 21, p. 1–16. https://doi.org/10.5194/sd-21-1-2016

Davidson, Anthony (1983). The Omo river project, reconnaissance geology and geochemistry of parts of Ilubabor, Kefa, Gemu Gofa and Sidamo, *Ethiopian Institute of Geological Surveys Bulletin*, 2, p. 1–89.

Davis, David Michael, Daniel Deocampo, Nathan Michael Rabideaux, and Christopher J. Campisano (2017). A Mineralogical analysis of HSPDP core samples from the Northern Awash Pliocene Hadar Formation, Ethiopia: the tale of an East African paleolake." *AGUFM*, PP13B-1081.

deMenocal, Peter, B. (2004). African climate change and faunal evolution during the Pliocene–Pleistocene. *Earth and Planetary Science Letters*, 220, 1-2, p. 3–24. https://doi.org/10.1016/S0012-821X(04)00003-2

deMenocal, Peter B. (1995). Plio-Pleistocene African climate. *Science*, 270, 5233, p. 53–59. https://doi.org/10.1126/science.270.5233.53

DiMaggio, Erin N., Christopher J. Campisano, John Rowan, Guillaume Dupont-Nivet, Alan L. Deino, Faysal Bibi, Margaret E. Lewis, Antoine Souron, Dominique Garello, Lars Werdelin, Kaye E. Reed, J Ramón Arrowsmith (2015). Late Pliocene fossiliferous sedimentary record and the environmental context of early

Homo from Afar, Ethiopia. *Science*, 347, 6228, p. 1355–1359. https://doi.org/10.1126/science.aaa1415

Dupont-Nivet, Guillaume, Mark Sier, Christopher J. Campisano, J. Ramón Arrowsmith, Erin DiMaggio, Kaye Reed, Charles Lockwood, Christine Franke, and Silja Hüsing (2008). Magnetostratigraphy of the eastern Hadar Basin (Ledi-Geraru research area, Ethiopia) and implications for hominin paleoenvironments. *The Geology of Early Humans in the Horn of Africa: Geological Society of America Special Paper 446*, p. 67–85. https://doi.org/10.1130/2008.2446(03)

Ebinger, C. J., Tilahun Yemane, D. J. Harding, Samson Tesfaye, S. Kelley, and D. C. Rex (2000). Rift deflection, migration, and propagation: Linkage of the Ethiopian and Eastern rifts, Africa. *Geological Society of America Bulletin*, 112, 2, p. 163–176. https://doi.org/10.1130/0016-7606(2000)112<163:RDMAPL>2.0.CO;2

Feibel, Craig S. (2011). A geological history of the Turkana Basin. *Evolutionary Anthropology: Issues, News, and Reviews*, 20, 6, p. 2065–216. https://doi.org/10.1002/evan.20331

Garcin, Yannick, Taylor F. Schildgen, Verónica Torres Acosta, Daniel Melnick, Julien Guillemoteau, Jane Willenbring, and Manfred R. Strecker (2017). Short-lived increase in erosion during the African Humid Period: evidence from the northern Kenya Rift. *Earth and Planetary Science Letters*, 459, p. 58–69. https://doi.org/10.1016/j.epsl.2016.11.017

Garello, Dominique Ines (2019). Tephrostratigraphy of Pliocene drill cores from Kenya and Ethiopia, and Pleistocene exposures in the Ledi-Geraru Research Project Area, Ethiopia: geological context for the evolution of *Australopithecus* and *Homo*. PhD diss., Arizona State University.

Granger, Darryl E., Nathaniel A. Lifton, and Jane K. Willenbring (2013). A cosmic trip: 25 years of cosmogenic nuclides in geology. *GSA Bulletin*, 125, 9-10, p. 1379–1402. https://doi.org/10.1130/B30774.1

Granger, Darryl E., James W. Kirchner, and Robert Finkel (1996). Spatially averaged long-term erosion rates measured from in situ-produced cosmogenic nuclides in alluvial sediment. *The Journal of Geology*, 104, 3, p. 249–257. https://doi.org/10.1086/629823

Grischott, Reto, Florian Kober, Maarten Lupker, Juergen M. Reitner, Ruth Drescher-Schneider, Irka Hajdas, Marcus Christl, and Sean D. Willett (2017). Millennial scale variability of denudation rates for the last 15 kyr inferred from the detrital ^{10}Be record of Lake Stappitz in the Hohe Tauern massif, Austrian Alps. *The Holocene*, 27, 12, p. 19149–1927. https://doi.org/10.1177/0959683617708451

Grischott, Reto, Florian Kober, Maarten Lupker, Kristina Hippe, Susan Ivy-Ochs, Irka Hajdas, Bernhard Salcher, and Marcus Christl (2016). Constant denudation rates in a high alpine catchment for the last 6 kyrs. *Earth Surface Processes and Landforms*, 42, 7, p. 1065-1077. https://doi.org/10.1002/esp.4070

Huete, Alfredo, Kamel Didan, Tomoaki Miura, E. Patricia Rodriguez, Xiang Gao, and Laerte G. Ferreira (2002). Overview of the radiometric and biophysical performance of the MODIS vegetation indices. *Remote Sensing of Environment*, 83, 1-2, p. 195–213. https://doi.org/10.1016/S0034-4257(02)00096-2

Kohl, C. P., and Kunihiko Nishiizumi (1992). Chemical isolation of quartz for measurement of in-situ-produced cosmogenic nuclides. *Geochimica et Cosmochimica Acta*, 56, 9, p. 3583–3587. https://doi.org/10.1016/0016-7037(92)90401-4

Lal, Devendra (1991). Cosmic ray labeling of erosion surfaces: *in situ* nuclide production rates and erosion models. *Earth and Planetary Science Letters*, 104, 2-4, p. 424–439. https://doi.org/10.1016/0012-821X(91)90220-C

Lepre, Christopher J. (2014). Early Pleistocene lake formation and hominin origins in the Turkana–Omo rift. *Quaternary Science Reviews*, 102, p. 181–191. https://doi.org/10.1016/j.quascirev.2014.08.012

Levin, Naomi E., Francis H. Brown, Anna K. Behrensmeyer, René Bobe, and Thure E. Cerling (2011). Paleosol carbonates from the Omo Group: Isotopic records of local and regional environmental change in East Africa. *Palaeogeography, Palaeoclimatology, Palaeoecology*, 307, 1-4, p. 75–89. https://doi.org/10.1016/j.palaeo.2011.04.026

Lupien, Rachel L. (2019). The Plio-Pleistocene climate history of East Africa and the role of environmental change on human evolution: studies of leaf wax isotopes from paleolake sediment. Dissertation, Brown University. https://doi.org/10.26300/h7yg-fe45

Lupien, R. L., J. M. Russell, Craig Feibel, C. Beck, I. Castañeda, A. Deino, and A. S. Cohen (2018). A leaf wax biomarker record of early Pleistocene hydroclimate from West Turkana, Kenya. *Quaternary Science Reviews*, 186, p. 225–235. https://doi.org/10.1016/j.quascirev.2018.03.012

Madella, Andrea, Romain Delunel, Naki Akçar, Fritz Schlunegger, and Marcus Christl (2018). ^{10}Be-inferred paleo-denudation rates imply that the mid-Miocene western central Andes eroded as slowly as today. Scientific Reports, 8, 1, p. 1–9. https://doi.org/10.1038/s41598-018-20681-x

Morrissey, Amy (2014). Stratigraphic Framework and Quaternary Paleolimnology of the Lake Turkana Rift, Kenya. PhD Thesis. Syracuse University, Syracuse, NY. https://surface.syr.edu/etd/62

Nishiizumi, Kunihiko, Mineo Imamura, Marc W. Caffee, John R. Southon, Robert C. Finkel, and Jeffrey McAninch (2007). Absolute calibration of 10Be AMS standards." *Nuclear Instruments and Methods in Physics Research Section B: Beam Interactions with Materials and Atoms*, 258, 2, p. 403–413. https://doi.org/10.1016/j.nimb.2007.01.297

Noren, Anders (2020a). HSPDP-NAO_NAW_public. OSF. https://doi.org/10.17605/OSF.IO/PBDT4

Noren, Anders (2020b). HSPDP-WTK_public. OSF. https://doi.org/10.17605/OSF.IO/B8QF2

Owusu Agyemang, Prince C., Eric M. Roberts, Bob Downie, and Joseph JW Sertich (2019). Sedimentary provenance and maximum depositional age analysis of the Cretaceous? Lapur and Muruanachok sandstones (Turkana Grits), Turkana Basin, Kenya. Geological Magazine, 156, 8, p. 1334–1356. https://doi.org/10.1017/S0016756818000663

Pik, Raphaël, Bernar Marty, Jean Carignan, and Jérôme Lavé (2003). Stability of the Upper Nile drainage network (Ethiopia) deduced from (U-Th)/He thermochronometry: implications for uplift and erosion of the Afar plume dome. *Earth and Planetary Science Letters*, 215, p. 73–88. https://doi.org/10.1016/S0012-821X(03)00457-6

Puchol, Nicolas, Pierre-Henri Blard, Raphaël Pik, Bouchaïb Tibari, and Jérôme Lavé (2019). Variability of magmatic and cosmogenic ^{3}He in Ethiopian river sands of detrital pyroxenes: Impact on denudation rate determinations. *Chemical Geology*, 448, p. 13–25. https://doi.org/10.1016/j.chemgeo.2016.10.033

Quade, Jay, Naomi E. Levin, Scott W. Simpson, Robert Butler, William C. McIntosh, Sileshi Semaw, Lynnette Kleinsasser, Guillaume Dupont-Nivet, Paul Renne, and Nelia Dunbar (2008). The geology of Gona, Afar, Ethiopia, in Quade, J., and Wynn, J.G., eds., The Geology of Early Humans in the Horn of Africa: Geological Society of America Special Paper 446, p. 1–31. https://doi.org/10.1130/2008.2446(01)

Quade, Jay, Naomi Levin, Sileshi Semaw, Dietrich Stout, Paul Renne, Michael Rogers, and Scott Simpson (2004). Paleoenvironments of the earliest stone toolmakers, Gona, Ethiopia. *Geological Society of America Bulletin*, 116, 11-12, p. 1529–1544. https://doi.org/10.1130/B25358.1

Quinn, Rhonda L., Christopher J. Lepre, James D. Wright, and Craig S. Feibel (2007). Paleogeographic variations of pedogenic carbonate $\delta^{13}C$ values from Koobi Fora, Kenya: implications for floral compositions of Plio-Pleistocene hominin environments." Journal of Human Evolution 53, 5, p. 560–573. https://doi.org/10.1016/j.jhevol.2007.01.013

Redfield, T. F., W. H. Wheeler, and M. Often (2003). A kinematic model for the development of the Afar Depression and its paleogeographic implications. *Earth and Planetary Science Letters*, 216, 3, 383–398. https://doi.org/10.1016/S0012-821X(03)00488-6

Reed, Kaye E. (2008). Paleoecological patterns at the Hadar hominin site, Afar regional state, Ethiopia. *Journal of Human Evolution*, 54, 6, p. 743–768. https://doi.org/10.1016/j.jhevol.2007.08.013

Roller, S., H. Wittmann, M. Kastowski, and M. Hinderer (2012). Erosion of the Rwenzori Mountains, East African Rift, from in situ-produced cosmogenic ^{10}Be. *Journal of Geophysical Research: Earth Surface*, 117, F3. https://doi.org/10.1029/2011JF002117

Rooney, Tyrone O. (2020). The Cenozoic magmatism of East Africa: Part IV – The terminal stages of rifting preserved in the Northern East African Rift System. *Lithos*, 360-361, 105381, p. 1–29. https://doi.org/10.1016/j.lithos.2020.105381

Schaller, M., T. A. Ehlers, T. Stor, J. Torrent, L. Lobato, Marcus Christl, and Christof Vockenhuber (2016). Spatial and temporal variations in denudation rates derived from cosmogenic nuclides in four European fluvial terrace sequences. *Geomorphology*, 274, p. 180–192. https://doi.org/10.1016/j.geomorph.2016.08.018

Schaller, M., F. von Blanckenburg, Niels Hovius, A. Veldkamp, Meindert W. van den Berg, and P. W. Kubik (2004). Paleoerosion rates from cosmogenic 10Be in a 1.3

Ma terrace sequence: response of the River Meuse to changes in climate and rock uplift. *The Journal of Geology*, 112, 2, p. 127–144. https://doi.org/10.1086/381654

Schaller, M., Friedhelm von Blanckenburg, A. Veldkamp, L. A. Tebbens, N. Hovius, and P. W. Kubik (2002). " 30 000 yr record of erosion rates from cosmogenic ^{10}Be in Middle European river terraces. *Earth and Planetary Science Letters*, 204, 1-2, p. 307–320. https://doi.org/10.1016/S0012-821X(02)00951-2

Scherler, Dirk, Bodo Bookhagen, Hendrik Wulf, Frank Preusser, and Manfred R. Strecker (2015). Increased late Pleistocene erosion rates during fluvial aggradation in the Garhwal Himalaya, northern India. *Earth and Planetary Science Letters*, 428, p. 255–266. https://doi.org/10.1016/j.epsl.2015.06.034

Shackleton, R. M. (1986). Precambrian collision tectonics in Africa. *Geological Society*, London, Special Publications 19, 1, p. 329–349. https://doi.org/10.1144/GSL.SP.1986.019.01.19

Stone, John O (2000). Air pressure and cosmogenic isotope production. *Journal of Geophysical Research: Solid Earth*, 105, B10, p. 23753–23759. https://doi.org/10.1029/2000JB900181

Tiercelin, Jean-Jacques, Jean-Luc Potdevin, Peter Kinyua Thuo, Yassine Abdelfettah, Mathieu Schuster, Sylvie Bourquin, Hervé Bellon, Jean-Philippe Clément, Hervé Guillou, Thierry Nalpas, and Gilles Ruffet (2012). Stratigraphy, sedimentology and diagenetic evolution of the Lapur Sandstone in northern Kenya: Implications for oil exploration of the Meso-Cenozoic Turkana depression. *Journal of African Earth Sciences*, 71, p. 43–79. https://doi.org/10.1016/j.jafrearsci.2012.06.007

Torres Acosta, Verónica, Taylor F. Schildgen, Brian A. Clarke, Dirk Scherler, Bodo Bookhagen, Hella Wittmann, Friedhelm von Blanckenburg, and Manfred R. Strecker (2015). Effect of vegetation cover on millennial-scale landscape denudation rates in East Africa." *Lithosphere*, 7, 4, p. 408–420. https://doi.org/10.1130/L402.1

Von Blanckenburg, Friedhelm (2005). The control mechanisms of erosion and weathering at basin scale from cosmogenic nuclides in river sediment. *Earth and Planetary Science Letters*, 237, 3-4, p. 462–479. https://doi.org/10.1016/j.epsl.2005.06.030

WoldeGabriel, Giday, Grant Heiken, Tim D. White, Berhane Asfaw, William K. Hart, and Paul R. Renne (2000). Volcanism, tectonism, sedimentation, and the paleoanthropological record in the Ethiopian Rift System. *Geological Society of America*, Special Paper 345, p. 83–99. https://doi.org/10.1130/0-8137-2345-0.83

Wolfenden, Ellen, Cynthia Ebinger, Gezahegn Yirgu, Paul R. Renne, and Simon P. Kelley (2005). Evolution of a volcanic rifted margin: Southern Red Sea, Ethiopia. *Geological Society of America Bulletin*, 117, 7-8, p. 846–864. https://doi.org/10.1130/B25516.1

Wynn, J.G., D.C. Roman, Z. Alemseged, D. Reed, D. Geraads, and S. Munro (2008). Stratigraphy, depositional environments, and basin structure of the Hadar and Busidima Formations at Dikika, Ethiopia, in Quade, J., and Wynn, J.G., eds., The Geology of Early Humans in the Horn of Africa: *Geological Society of America* Special Paper 446, p. 87–118. https://doi.org/10.1130/2008.2446(04)

Wynn, Jonathan G., Zeresenay Alemseged, René Bobe, Denis Geraads, Denné Reed, and Diana C. Roman (2006). Geological and palaeontological context of a Pliocene juvenile hominin at Dikika, Ethiopia. *Nature*, 443, 7109, p. 332–3336. https://doi.org/10.1038/nature05048

Zawacki, Emily E., Matthijs C. van Soest, Kip V. Hodges, Jennifer J. Scott, Manfred R. Strecker, Mélanie Barboni, Craig S. Feibel, Christopher J. Campisano, J Rámon Arrowsmith (2021). Sediment provenance and volcano-tectonic evolution of the East African Rift System from (U-Th)/He and U/Pb laser ablation double dating of detrital zircons. *Earth and Planetary Science Letters*, In review.

CHAPTER 4

^{10}BE-DERIVED PALEOEROSION RATES FROM THE CHEW BAHIR BASIN, SOUTHERN ETHIOPIA OVER THE LAST ~620 KYR

4.1 Abstract

Understanding regional manifestations of tectonic activity and climatic fluctuations during the Plio-Pleistocene in East Africa is of significant interest for studies of East African paleoenvironments and faunal evolution. Analyzing changes in erosion rates over time provides valuable insights into tectonic and climatic driven changes controlling landscape evolution. We analyzed ten sand samples from the Chew Bahir (CHB), Ethiopia Hominin Sites and Paleolakes Drilling Project drill cores for *in situ* cosmogenic ^{10}Be to investigate changes in paleoerosion rates over time and the relative tectonic and climatic controls on the landscape. The CHB cores yield a ~620 ka to present sedimentary record of a small, hydrologically closed basin in the Southern Ethiopian rift. We used the core age model to determine the depositional age of the samples and to derive sedimentation rates to constrain the amount of post-depositional ^{10}Be accumulation. The ten samples yielded erosion rates ranging from 0.045 to 0.060 mm/yr, with the two youngest samples yielding the lowest erosion rates. Erosion rates show a general decreasing trend over time with minor excursions. Modern erosion rates from subcatchments within the Chew Bahir basin range from 0.020 to 0.16 mm/yr, with a weighted average based on drainage area of 0.079 mm/yr. Modern erosion rates show significantly greater variability than the paleoerosion rates do, but the average of the paleoerosion rates is of a similar scale to the weighted average of the modern erosion

rates. The modern erosion rates show a positive correlation with hillslope gradient, but they do not show a similar scaling relationship with enhanced vegetation index (EVI) that other catchments within the East African Rift do. The spatial variability of erosion rates within the Chew Bahir basin therefore appears predominantly controlled by local tectonic forcing. The proxy record of the CHB cores can be divided into three phases that suggest a humid to arid transition over time. The high erosion rates at the base of the core are consistent with a more humid environment with greater moisture availability for erosional efficacy and fluvial transport. The paleoerosion rates overall show a decrease over time and are broadly consistent with a shift to more arid conditions over the record of the core. The paleoerosion rates do not appear to capture millennial-scale climatic variability within the different phases, and excursions in erosion rates are likely a result of increased tectonic activity. Steady paleoerosion rates over time are consistent with a dominant tectonic signature with a long-term decreasing trend driven by a drying climate.

4.2 Introduction

Within the East African Rift System (EARS), understanding the local environmental response to changes in climate and tectonic activity is of significant interest in studies of Plio-Pleistocene paleoenvironments and faunal evolution (e.g., deMenocal, 2004 and references therein). Understanding the basin-scale response to regional tectonics and climate is a crucial component in being able to link global climate changes—and their subsequent environmental response—to patterns in faunal and hominin evolution. Although East African landscapes have overall shown a drying trend with increased open environments and an expansion of C_4 grasses over the late Cenozoic

(Cerling et al., 2011), regional basins do not necessarily display uniform environmental responses under the same global climate conditions (e.g., Bobe and Behrensmeyer, 2004; DiMaggio et al., 2015; Levin et al., 2011, among others).

The effects of a shifting climate are further compounded by the geologic complexity of the EARS. The EARS contains a series of structurally and magmatically controlled extensional basins that extend for ~3,500 km from the Afar Triple Junction to Mozambique (Chorowicz, 2005). Pre-rift volcanism was initiated at ~45 Ma and has continued into the Holocene, creating complex relief and highly variable drainage conditions over time (Ebinger et al., 2000). Regional basins have variable tectonic histories, and major tectonic events can have just as dramatic implications as climate shifts (Campisano, 2012; Feibel, 2011; Quade et al., 2008; Quinn et al., 2007).

Evaluating changes in erosion rates over time provides useful insight into the relative importance of climatic and tectonic controls on landscape evolution. Analyses of terrestrial cosmogenic radionuclides, such as *in situ* ^{10}Be, have become an essential tool for determining millennial-scale catchment mean erosion rates (e.g., Bierman and Steig, 1996; Brown et al., 1995; Granger et al., 1996, 2013 and references therein). In addition to assessing modern erosion rates, ^{10}Be analyses can be used to determine paleoerosion rates over at least the last ~10 Myr (Madella et al., 2018).

Traditionally, fluvial terrace samples are used to determine ^{10}Be-derived paleoerosion rates (e.g., Bekaddour et al., 2014; Charreau et al., 2011; Schaller et al., 2002, 2004, 2016; Scherler et al., 2015). However, terrace samples may have a complex post-depositional history that is difficult to constrain, which could result in a significant underestimation of erosion rates. Alternatively, samples collected from drill cores remedy many shortcomings of traditional paleoerosion rate analyses but providing an age-depth model to constrain the dspositional age of the sample and loss of ^{10}Be to radioactive decay, in addition to the post-depositional ^{10}Be accumulation (Grischott et al., 2016, 2017).

To quantify paleoerosion rates during the Pleistocene in East Africa and evaluate regional tectonic and climatic effects on the landscape, we sampled from the Chew Bahir (CHB), Ethiopia drill cores collected by the Hominin Sites and Paleolakes Drilling Project (HSPDP) for *in situ* ^{10}Be analyses. (Figure 4.1). The drill cores yield a ~620 kyr to present sedimentary record from a tectonically active basin within the EARS. We compare the paleoerosion rates from the drill cores to modern erosion rates from subcatchments within the Chew Bahir basin and evaluate relative tectonic vs. vegetation/climatic controls on erosion rates. Paleoerosion rates overall show a decreasing trend over time and are relatively similar to the weighted average of modern erosion rates from subcatchments within the Chew Bahir basin. Additionally, we compare the paleoerosion rates to the hydroclimate paleoenvironmental proxy record from the CHB drill core to assess if the paleoerosion rates correspond with observed climate shifts and trends.

4.3 Geologic Setting

The Chew Bahir basin is a small (22,000 km^2) hydrologically closed basin located in the southern Ethiopian Rift (Figure 4.1). The basin is bounded to the west by the Hammar Range, which consists of Precambrian basement with mainly undivided gneisses

(Davidson, 1983; Foerster et al., 2012), and lies adjacent to the Omo-Turkana basin. The escarpment of the Teltele–Konso range bounds the basin to the east and exposes Miocene basalt flows with subordinate rhyolitic intercalations (Davidson and Rex, 1980; Ebinger et al., 2000). Alluvial fans draining the Hammar Range and the Teltele Plateau provide a large portion of the sediment influx to the basin (Foerster et al., 2012). Precambrian basement units in the northern, northwestern, and northeastern parts of the basin are partly overlain by Oligocene basalt flows with subordinate rhyolitic units (Moore and Davidson, 1978; Davidson, 1983). The northern portions of the basin are drained by the perennial Weyto and Segen rivers, which form a delta and provide another major sedimentary influx (Foerster et al., 2012).

Rifting of the Chew Bahir basin has been continuous since initiation of extension in the early Miocene (~20 Ma) with denudation rates of 110 m/Myr based on apatite (U-Th)/He thermochronometry of the Hammar Range (Pik et al., 2008). Thermochronology data from the adjacent Beto and Galana basins to the north similarly suggest early Miocene (~20–17 Ma) initial basin formation in the region (Boone et al., 2019). Of note, there does not appear to have been a significant increase in rates of rifting and rock uplift during the Plio-Pleistocene (Pik et al., 2008), differing from earlier hypotheses that suggested that Plio-Pleistocene rifting and uplift triggered climatic and environmental changes (e.g., Sepulcre et al., 2006; Spiegel et al., 2007). Geomorphological analysis suggests recent fault activity along the western margin of the Chew Bahir basin (Philippon et al., 2014). Therefore, there appears to have been steady, continuous tectonic activity in the Chew Bahir basin since the early Miocene.

Present day Chew Bahir is a playa/saline mudflat that episodically fills to a shallow lake during the rainy season. Rainfall is strongly seasonal, causing highly episodic sediment and water influx (Foerster et al., 2012). Pilot studies of ~20 m deep short cores from Chew Bahir indicate fluctuating moisture availability on millennial to centennial timescales, in addition to precessional timescales over the last ~60 kyr, thus suggesting that the basin responded to both regional and global climate changes (Foerster et al., 2012, 2015).

Modern ^{10}Be-derived erosion rates from subcatchments within the Chew Bahir basin range from 0.0202 to 0.16 mm/yr (Dorgerloh, 2016). While the erosion rates do not show a correlation with enhanced vegetation index (EVI) as they do in other catchments in East Africa (Torres Acosta et al., 2015), the erosion rates show a positive correlation with mean gradient and mean annual precipitation and suggest that local tectonics has the strongest control on erosion rates with respect to regional climatic patterns (Dorgerloh, 2016).

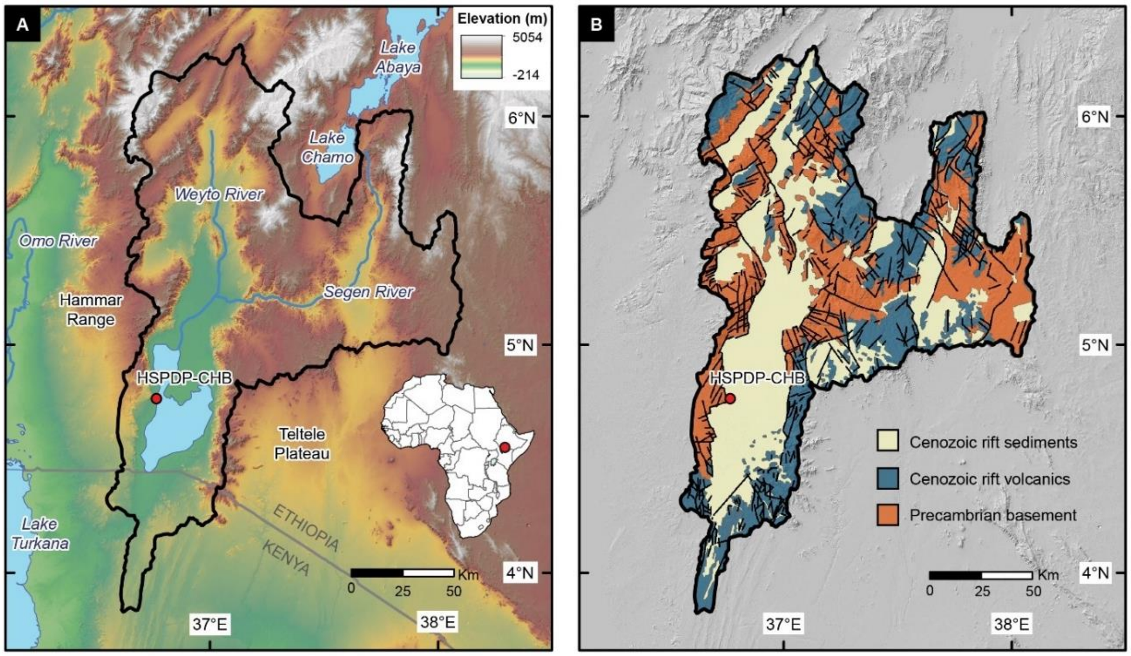

Figure 4.1 A) Geographic overview of Chew Bahir basin near the Ethiopia-Kenya border. HSPDP-CHB drill site is marked in red, and the basin watershed is delineated in black. Data source is a 30 m SRTM DEM projected over a hillshade. **B)** Geologic map of the Chew Bahir basin grouped into generalized rock types over a hillshade. The Precambrian basement consists of Proterozoic granite, gabbro, diorite, pegmatite, gneiss, schist, phyllite, amphibolite, dunite, and metasediments. Cenozoic rift volcanics include basalt, rhyolite, trachyte, phonolite, ignimbrite, and tuff. Cenozoic rift sediments consist of lacustrine silt and clay, fluvial silt and sand, and alluvium. Geologic map is based following Foerster et al. (2018) and Trauth et al. (2018, 2019).

4.4 Sampling and Methods

4.4.1 Drill core sampling

Two parallel drill cores with a maximum depth of ~280 m were collected in November–December 2014 near the southwestern border of the basin. Cored sediments were predominantly silty and sandy clays with occasional coarser calcareous sand beds, primarily in the upper ~100 m (Campisano et al., 2017; Cohen et al., 2016). The sediments represent a ~620 ka to present record of paleolake Chew Bahir (Roberts et al., *in review*). We collected 10 samples from the two correlated cores, HSPDP-CHB14-2A and HSPDP-CHB14-2B (Table 4.1) (Figure 4.2). Samples ranged in depositional age from ~79 to 617 ka. Sands were quartz-rich with a high mica content, often mixed with drilling fluid mud. We collected ~1500 g of bulk material per sample, usually from across multiple drives. Individual core drives sample up to ~1.5–3 m in length of material.

Table 4.1 HSPDP Chew Bahir drill core samples. They are referred to by the top-most sampled core drive.

Core	Latitude	Longitude	Drives	Upper Sample Depth (mbs)	Age (ka)	Age Uncertainty [1σ)] (kyr)
HSPDP-CHB14-2B	4.7613	36.7670	20H-1, 20H-2, 21H-1, 21H-2	41	78.9	3.7
HSPDP-CHB14-2B	4.7613	36.7670	23E-1	46	87.7	5.4
HSPDP-CHB14-2A	4.7612	36.7668	28A-1, 28A-2	54	112.1	10.6
HSPDP-CHB14-2A	4.7612	36.7668	29Q-1, 29Q-2	58	121.9	10.8
HSPDP-CHB14-2B	4.7613	36.7670	35E-1	66	149.5	9.5
HSPDP-CHB14-2A	4.7612	36.7668	51Q-1	104	212.6	14.4
HSPDP-CHB14-2B	4.7613	36.7670	72Q-1	140	278.7	17.3
HSPDP-CHB14-2B	4.7613	36.7670	75Q-1, 75Q-2	146	289.2	17.4
HSPDP-CHB14-2A	4.7612	36.7668	90Q-1, 90Q-2	202	397.7	12.8
HSPDP-CHB14-2A	4.7612	36.7668	117Q-2, 117Q-3	277	616.8	10.5

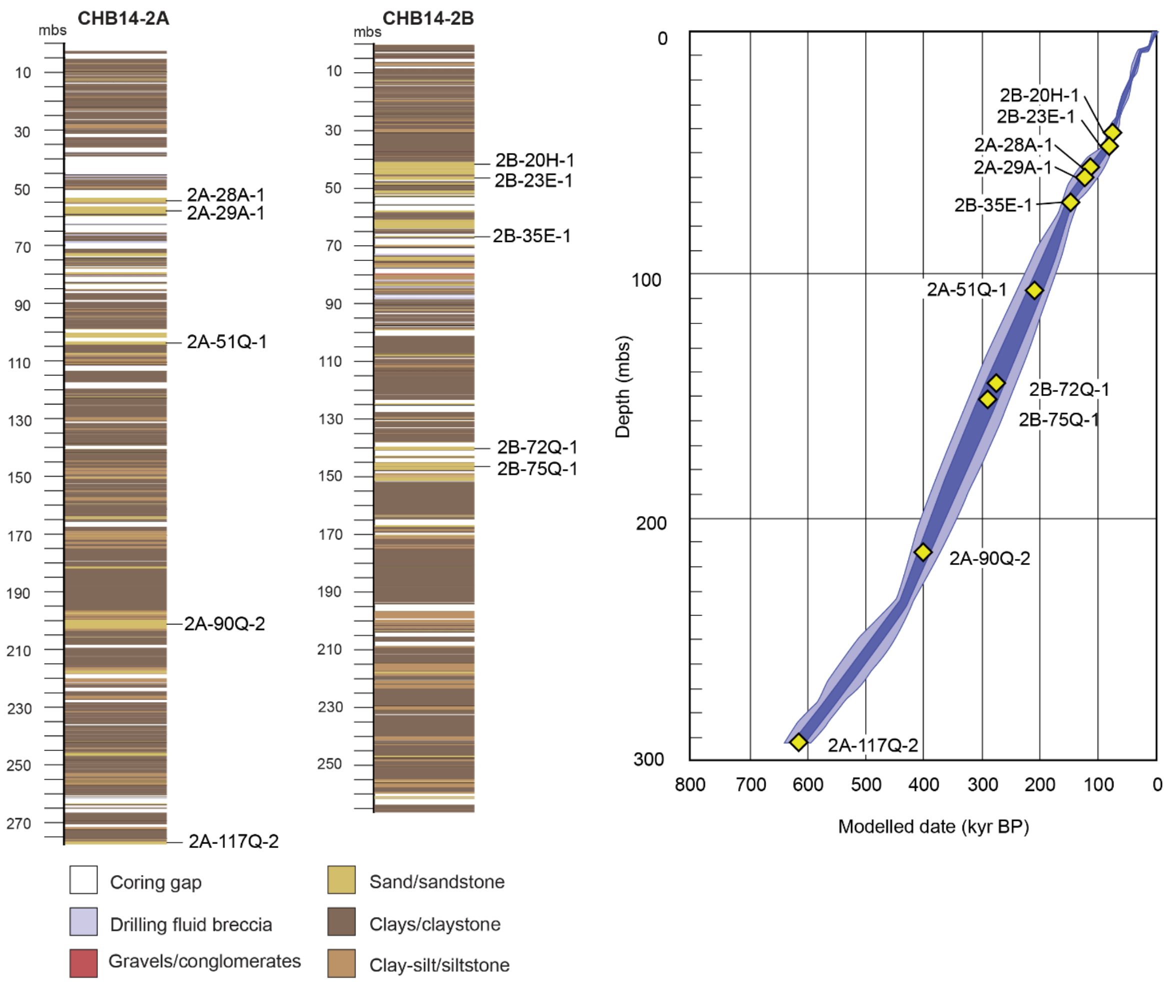

Figure 4.2 Stratigraphic columns of the HSPDP-CHB14-2A and HSPDP-CHB14-2B drill cores shown in meters below surface (mbs). Sampled sand units are labeled. Sampled units are also indicated on the model for the cores (Roberts et al., *in review*).

4.4.2 Sample preparation

Samples were sieved to isolate the 500–250 μm size fraction and processed through Frantz magnetic separation and LST heavy liquid density separations to remove micaceous material. The quartz-bearing fraction was cleaned in a 2:1 hydrochloric acid and nitric acid solution for 12 hours to remove unwanted carbonate and organic material. Samples were leached a minimum of seven times in a 1% hydrofluoric acid solution on heated rollers following standard techniques outlined in Kohl and Nishiizumi (1992). Samples sat in a 0.25% hydrofluoric acid solution for seven days to ensure the purity and cleanliness of the quartz and yielded between 40.0g and 87.2 g of clean quartz. Samples were dissolved in hydrofluoric acid with the addition of a 1074 ± 8 ppm low-background ^{9}Be carrier. Be was then isolated through ion-exchange chromatography, oxidized, mixed with niobium powder, and packed in targets. Chemical separations and isolation procedures were carried out in the Cosmogenic and Short-Lived Isotopes Laboratory at Arizona State University. The Purdue Rare Isotope Measurement Laboratory (PRIME Lab) performed the ^{10}Be measurements based on revised ICN standards (Nishiizumi et al., 2007) (Table 4.2).

4.4.3 Paleoerosion rate calculations

Given variances in the geomagnetic field over time, it is necessary to determine the cosmogenic paleoproduction rate in the basin at the time of deposition. As well, it is necessary to independently determine the depositional age of the sample and the amount of post-depositional nuclide accumulation to calculate paleoerosion rates (Charreau et al., 2011). We use the age model of the core (Figure 4.2) to constrain the depositional age of the samples and to derive sedimentation rates above each sample to constrain post-depositional nuclide accumulation (Table 4.2). The age model of the CHB core is based on ^{14}C dating of ostracods, optically stimulated luminescence (OSL) dating, $^{40}Ar/^{39}Ar$ of feldspars from microtephra layers, and geochemical correlation to tephra in outcrop (Roberts et al., *in review).*

We calculated ^{10}Be production rates using the time-dependent Lal (1991) and Stone (2000) scaling scheme (‘Lm’, Balco et al., 2008) based on reference production rates from Borchers et al. (2016) using CRONUScalc version 2.0 (Marrero et al., 2016). Muogenic production was calculated with fast muons being 0.65% and slow muon capture being 1.2% of the total surface production (Braucher et al., 2003). For hillslope production rates (P_{hill}), we assumed that the mean basin elevation was similar to that of the modern and assumed an average paleoproduction rate over the age of the sample (± 1σ). For burial production rates (P_{burial}), we took the modern depocenter elevation (500 m) and subtracted the sample depth below surface for the elevation at time of sample deposition. Due to the relative similarity of basin topography over the observed time intervals, we do not account for variations and uncertainty in elevation for production rates. Calculated production rates are shown in Table 4.2. Calculations for paleoerosion rates are the same as in the previous chapter, and equations and procedures are detailed in Chapter 3. We additionally employ the same Monte Carlo simulation for error assessment as detailed in Chapter 3 section 3.5.3. Simulation results and PDFs from all samples are shown in Appendix D, and the resulting MATLAB codes are shown in Appendix C.

4.5 Results

^{10}Be-derived paleoerosion rates from the ten samples were in a relatively consistent range from 0.045 to 0.060 mm/yr (Table 4.2). Sample CHB-2B-75Q-1 deposited at ~289 ka yielded the highest erosion rate of 0.060 mm/yr, similar to the 0.058 mm/yr erosion rate from the oldest sample deposited at ~617 ka. Between ~279 to ~149 ka, erosion rates decreased to between 0.048 to 0.052 mm/yr. Samples deposited at ~122 and ~112 ka yielded higher erosion rates of 0.056 and 0.058 mm/yr, respectively. The two youngest samples deposited ~87 and ~79 ka yielded the lowest erosion rates of 0.045 mm/yr each.

Sediment accumulation rates above samples in the core ranged from 0.29 to 0.74 mm/yr, resulting in post-depositional ^{10}Be accumulation between 5.65 x 10^3 and 15.03 x 10^3 atoms g^{-1} qtz^{-1} (Table 4.2). The ^{10}Be production rate at the depocenter drill site is approximately half that of the hillslope production rate due to the significantly lower elevation. The post-depositional ^{10}Be accumulation is greater than the uncertainty in the ^{10}Be AMS measurement for over half of the samples and thus proves an important consideration that otherwise unaccounted for would result in lower erosion rates. The uncertainty in the erosion rates based on Monte Carlo modeling shows a slight positive skew due to the consideration of and uncertainty related to post-depositional ^{10}Be accumulation (Table 4.2).

Table 4.2 Cosmogenic nuclide analytical data for Chew Bahir samples. All uncertainties are expressed as 1σ except where noted. P_{hill} = hillslope production rate, P_{burial} = post-depositional burial production rate, A_r = accumulation rate, N_{post} = post-depositional nuclide accumulation. Erosion rate uncertainties show a slight asymmetric distribution from the Monte Carlo-based aggregation. All corresponding uncertainties of variables are shown and explored in Appendix D.

Sample	Sample Weight (g)	^{10}Be atoms x10^3 (atoms g^{-1} qtz)	^{10}Be Uncertainty x10^3 (atoms g^{-1} qtz)	P_{hill} Spallation (atoms g^{-1} yr^{-1})	P_{hill} Muons (atoms g^{-1} yr^{-1})	Depositional Age (ka)	Depositional Age Uncertainty (kyr)
CHB-2B-20H-1	54.4725	100.63	5.95	7.05	0.13	78.8	3.7
CHB-2B-23E-1	39.7617	111.71	3.02	7.48	0.14	87.7	5.4
CHB-2A-28A-1	63.1899	108.58	2.77	9.03	0.17	112.1	10.6
CHB-2A-29A-1	62.2264	104.06	5.69	8.55	0.16	121.9	10.8
CHB-2B-35E-1	60.6995	96.85	4.70	7.02	0.13	149.5	9.5
CHB-2A-51Q-1	57.9746	98.89	2.60	7.77	0.15	212.6	14.4
CHB-2B-72Q-1	62.0676	98.39	2.12	8.62	0.16	278.7	17.3
CHB-2B-75Q-1	62.0144	86.26	2.86	8.61	0.16	289.2	17.4
CHB-2A-90Q-1	61.2635	80.05	7.10	8.00	0.15	397.7	12.8
CHB-2A-117Q-2	44.4336	70.65	3.06	7.51	0.14	616.8	10.5

Sample	A_r (cm/yr)	P_{burial} Spallation (atoms g^{-1} yr^{-1})	P_{burial} Slow Muon Capture (atoms g^{-1} yr^{-1})	P_{burial} Fast Muons (atoms g^{-1} yr^{-1})	N_{post} x10^3 (atoms g-^{1} qtz)	Paleoerosion Rate (mm/yr)	Paleoerosion Rate Uncertainty (mm/yr) [2σ]
CHB-2B-20H-1	0.074	3.55	0.4	0.2	5.65	0.045	+0.0010 / -0.0008
CHB-2B-23E-1	0.035	3.55	0.4	0.2	11.21	0.045	+0.0016 / -0.0014
CHB-2A-28A-1	0.034	4.57	0.6	0.3	15.03	0.058	+0.0034 / -0.0028
CHB-2A-29A-1	0.034	4.30	0.5	0.3	14.17	0.056	+0.0032 / -0.0026
CHB-2B-35E-1	0.034	3.48	0.4	0.2	11.55	0.048	+0.0024 / -0.0020
CHB-2A-51Q-1	0.057	3.74	0.5	0.2	7.46	0.048	+0.0022 / -0.0016
CHB-2B-72Q-1	0.058	4.09	0.5	0.3	7.78	0.052	+0.0026 / -0.0022
CHB-2B-75Q-1	0.058	4.06	0.5	0.3	7.70	0.060	+0.0032 / -0.0028
CHB-2A-90Q-1	0.057	3.60	0.4	0.2	6.58	0.056	+0.0026 / -0.0020
CHB-2A-117Q-2	0.029	3.19	0.4	0.2	10.34	0.058	+0.0042 / -0.0036

4.6 Discussion

4.6.1 Comparison to modern erosion rates

Modern ^{10}Be-derived erosion rates from subcatchments within the Chew Bahir basin provide a useful comparison and context for which to interpret the paleoerosion rates from the CHB cores. Over the ~620 kyr core record, the paleoerosion rates span a range of 0.045 to 0.060 mm/yr, while the modern erosion rates from subcatchments span from 0.020 to 0.16 mm/yr (Figure 4.3) (Table 4.3) (Dorgerloh, 2016). The paleoerosion rates are therefore consistent within the range of modern erosion rates, though they show significantly less variability. The weighted average of the modern erosion rates normalized to drainage area is 0.079 mm/yr, slightly higher than the 0.053 mm/yr average paleoerosion rate over the ~620 kyr record. The average paleoerosion rate is more similar to the 0.047 mm/yr modern erosion rate from the largest subcatchment SEGA (Figure 4.3) (Table 4.3). We therefore generally interpret the paleoerosion rates as a whole catchment average, with the possibility of temporal fluctuations and certain source areas being more represented than others.

The three smallest subcatchments (11–31 km^2) that drain the steep flanks of the Hammar Range on the western edge of the basin yielded some of the highest modern erosion rates, between 0.104 and 0.183 mm/yr (Figure 4.3) (Table 4.3). These high rates are consistent with the denudation rate of 110 m/Ma (0.110 mm/yr) based on thermochronometry of the Hammar Range (Pik et al., 2008). This correspondence would suggest that the ^{10}Be-derived erosion rates from these small subcatchments with steep hillslope gradients are strongly controlled by and reflective of local tectonics. The high erosion rates additionally support the geomorphological analyses that suggest recent fault activity along the western margin of the basin (Philippon et al., 2014). The significantly lower paleoerosion rates and analysis of sediment provenance (Chapter 5) suggests that the sediment in the cores in not fully dominated by the adjacent alluvial fans drainaing the Hammar Range, although contributions from other portions of the basin is variable over time.

The subcatchments within the Chew Bahir basin overall show a positive correlation between mean hillslope gradient and erosion rate (Figure 4.3), where hillslope gradient and erosion rate are also positively correlated with mean annual precipitation due to orographic effects (Dorgerloh, 2016). However, the modern erosion rates from the Chew Bahir basin do not show a similar correspondence to enhanced vegetation index (EVI) as compared to basins within the Kenya Rift and the Rwenzori Mountains of the Albertine Rift (Figure 4.4) (Torres Acosta et al., 2015). Catchments in the Kenya Rift and the Rwenzori Mountains show two different scaling relationships between erosion rate and hillslope gradient, depending on whether the EVI of the catchment is less than or greater than 0.35. Catchments with an EVI <0.35 yield a higher erosion rate for a given hillslope gradient and fall on a steeper scaling relationship. In the Chew Bahir basin, there is significant variability in vegetation type related to elevation and steepness that may result in a mean subcatchment EVI that lacks a correlation with erosion rate due to local effects that strongly impact erosion rate (Dorgerloh, 2016).

Based upon the contextual understanding of the modern erosion rates within the Chew Bahir basin, the paleoerosion rates from the CHB cores therefore primarily appear reflective of long-term tectonic activity setting topographic relief, with variation likely overprinted by shorter-term climatic and vegetation changes within the basin.

Table 4.3 Modern ^{10}Be-derived erosion rates and subcatchments characteristics within the Chew Bahir basin from Dorgerloh (2016).

Basin name	Drainage area (km^2)	Mean gradient (m/m)	Relief (m)	Erosion rate (mm/yr)	Erosion rate uncertainty (mm/yr)
BAKO	91	0.19	974	0.051	0.0038
BAME	320	0.23	2020	0.070	0.0054
BETO	319	0.40	2307	0.066	0.0051
DALF	1,383	0.29	2512	0.072	0.0058
DUDO	1,366	0.36	2345	0.123	0.0099
HAMN	12	0.58	1423	0.183	0.0155
HAMS	11	0.44	1304	0.160	0.0126
SART	1,150	0.16	1458	0.020	0.0016
SCHI	31	0.34	1536	0.104	0.0083
SEGA	6,824	0.18	2656	0.047	0.0036
TEPS	92	0.34	1458	0.081	0.0060
WEYT	4,505	0.23	2345	0.132	0.0150

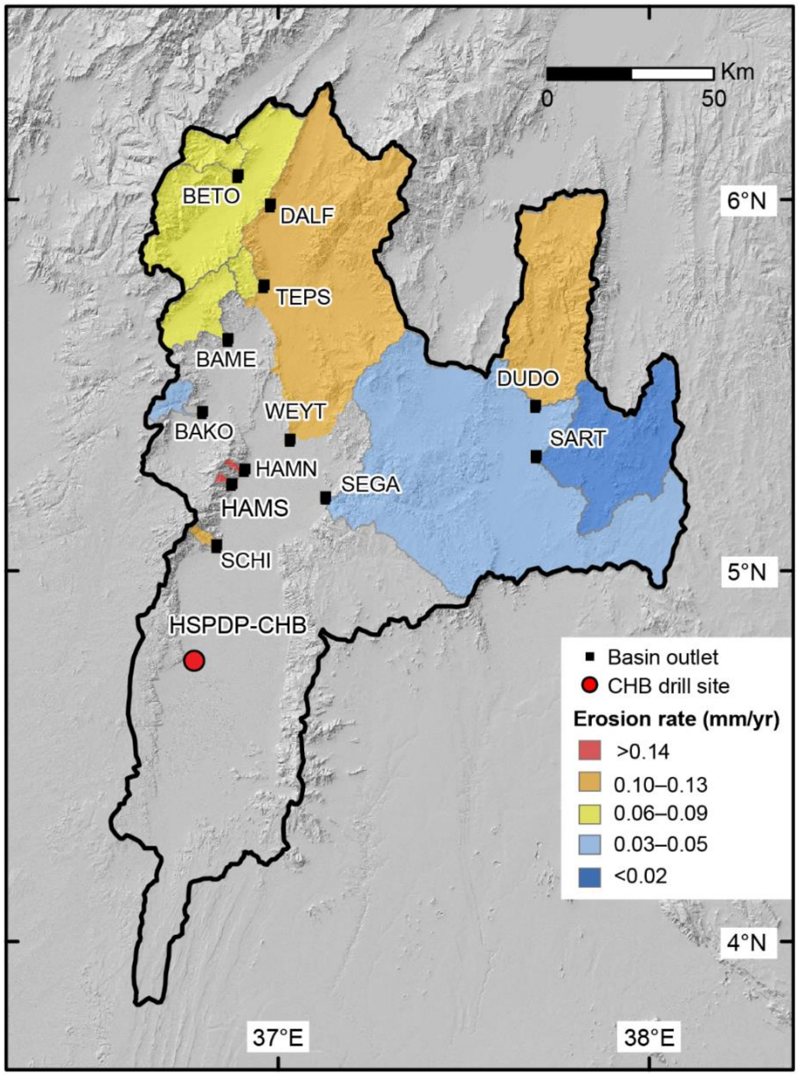

Figure 4.3 Modern paleoerosion rates measured within the Chew Bahir basin. The smallest basins HAMS and HAMN draining the Hammar Range yield the highest erosion rates. Erosion rates show a positive correlation with mean catchment gradient. Data from Dorgerloh (2016).

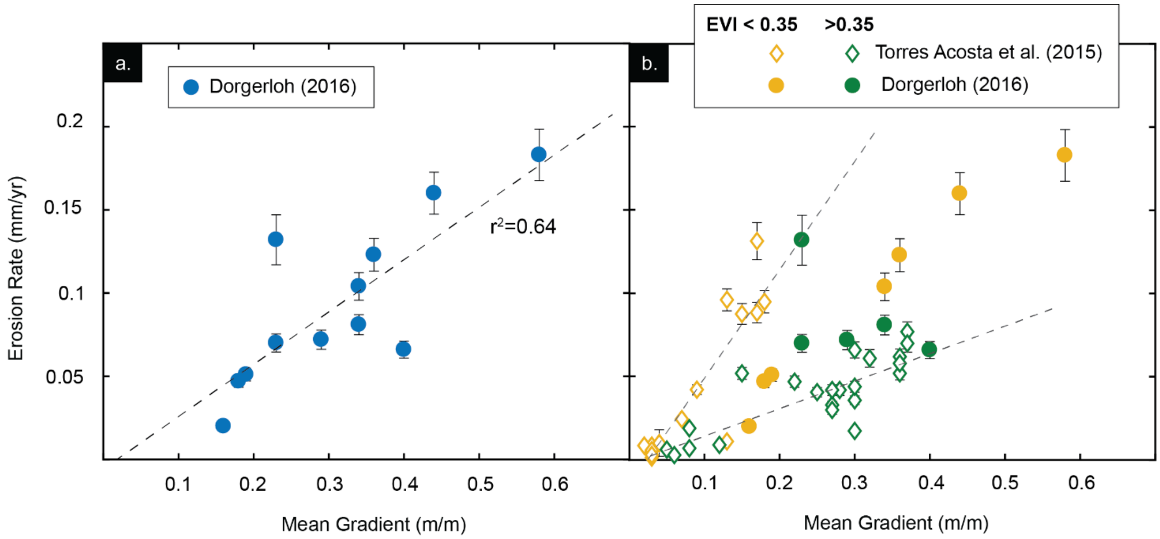

Figure 4.4 A) Plot of erosion rate vs. mean hillslope gradient for the modern Chew Bahir subcatchments from Dorgerloh (2016). Erosion rates show a positive correlation hillslope gradient. **B)** Erosion rate vs. mean hillslope gradient for subcatchments in the Chew Bahir basin (Dorgerloh, 2016), the Kenya Rift and Rwenzori Mountains in the Albertine Rift (Torres Acosta et al., 2015), based on enhanced vegetation index (EVI) values less than and greater than 0.35. The data from Torres Acosta et al. (2015) show a trend where an EVI <0.35 yields a higher erosion rate for a given hillslope gradient. Dashed regression lines from Torres Acosta et al. (2015) are shown.

4.6.2 Paleoenvironmental context

Given the apparent long-term tectonic control on erosion rates within the Chew Bahir basin, variations in erosion rates over time are likely due to moisture availability and changes in vegetation driven by climatic shifts and/or excursions in tectonic activity (Foerster et al., 2012, *in review*). The high-resolution record of the CHB cores provide a paleoenvironmental proxy record detailing changes in climate in the Chew Bahir basin over the last ~620 ka.

Geophysical and geochemical indicators such as potassium (K) aridity proxy, sediment color, and authigenic minerals provide a record of climatic and environmental changes throughout the core (Foerster et al., *in review*). Based on these indicators, the proxy record of the cores can be divided into three phases (Figure 4.5): Phase I occurs from ~620 to ~410 ka, where there is a long-term shift from humid to arid conditions, with slightly increasing variability over time. Phase II begins at ~410 ka and continues to ~210 ka with a pronounced millennial-scale humidity increase and shift to more humid conditions. Phase III from ~210 ka onward shows a long-term aridification trend, with a distinct increase in variability and amplitude (Foerster et al., *in review*).

Additionally, in comparing wetness indices to determine episodes with high correlation between the CHB core and ocean drill core ODP 967 from the eastern Mediterranean Sea, the period between ~570 and ~350 ka is dominated by a correlation that corresponds with orbital precession, whereas the period after ~350 ka reflects a strong influence of atmospheric CO_2 (Duesing et al., 2019, 2021).

Only one sample analyzed for ^{10}Be was deposited during the Phase I period and yielded one of the higher erosion rates of 0.058 mm/yr (Figure 4.5). The deposition at ~617 ka should correspond to a period of higher humidity with greater moisture availability. The end of Phase I and beginning of Phase II is marked by a shift to greater humidity, and the first two samples deposited during Phase II continued to yield relatively high erosion rates of 0.056 to 0.060 mm/yr, consistent with the beginning of Phase I (Figure 4.5). As the end of Phase II represents continued humid conditions, erosion rates in turn decreased to 0.052 and 0.048 mm/yr. Erosion rates remained consistently low at 0.048 mm/yr during the beginning of Phase III. The oscillating climatic changes may not be directly reflected in the CRN-derived erosion rates due to the longer timescale that lower erosion rates record and the higher amplitude and variability of these climate shifts (Schaller and Ehlers, 2006).

There notably is a large increase in erosion rates at ~115 ka during Phase III, similar to the higher rates from Phase I and the beginning of Phase II (Figure 4.5). Given that Phase III represents a long-term aridification trend with an increase in amplitude and variability, these higher erosion rates may in turn be reflective of higher sediment input from the Hammar Range to the west, which yields the highest modern erosion rates (Figure 4.3). This sharp increase in erosion rates may thus be reflective of a tectonic or geomorphic shift providing more sediment from the adjacent Hammar Range, rather than from the more slowly eroding northern parts of the basin (see exploration of sediment provenance in Chapter 5).

The two youngest samples deposited at ~80 ka in Phase III yielded the lowest erosion rates (0.045 mm/yr), consistent with the aridification trend and reduced moisture availability of Phase III (Figure 4.5). The paleoerosion rates from the Chew Bahir basin overall support a shift to more arid conditions over time, although they do not appear to capture and record the millennial-scale climatic shifts within the different phases. Significant excursions in erosion rates within short time frames are likely reflective of enhanced tectonic activity or greater sediment input from the steep Hammar Range.

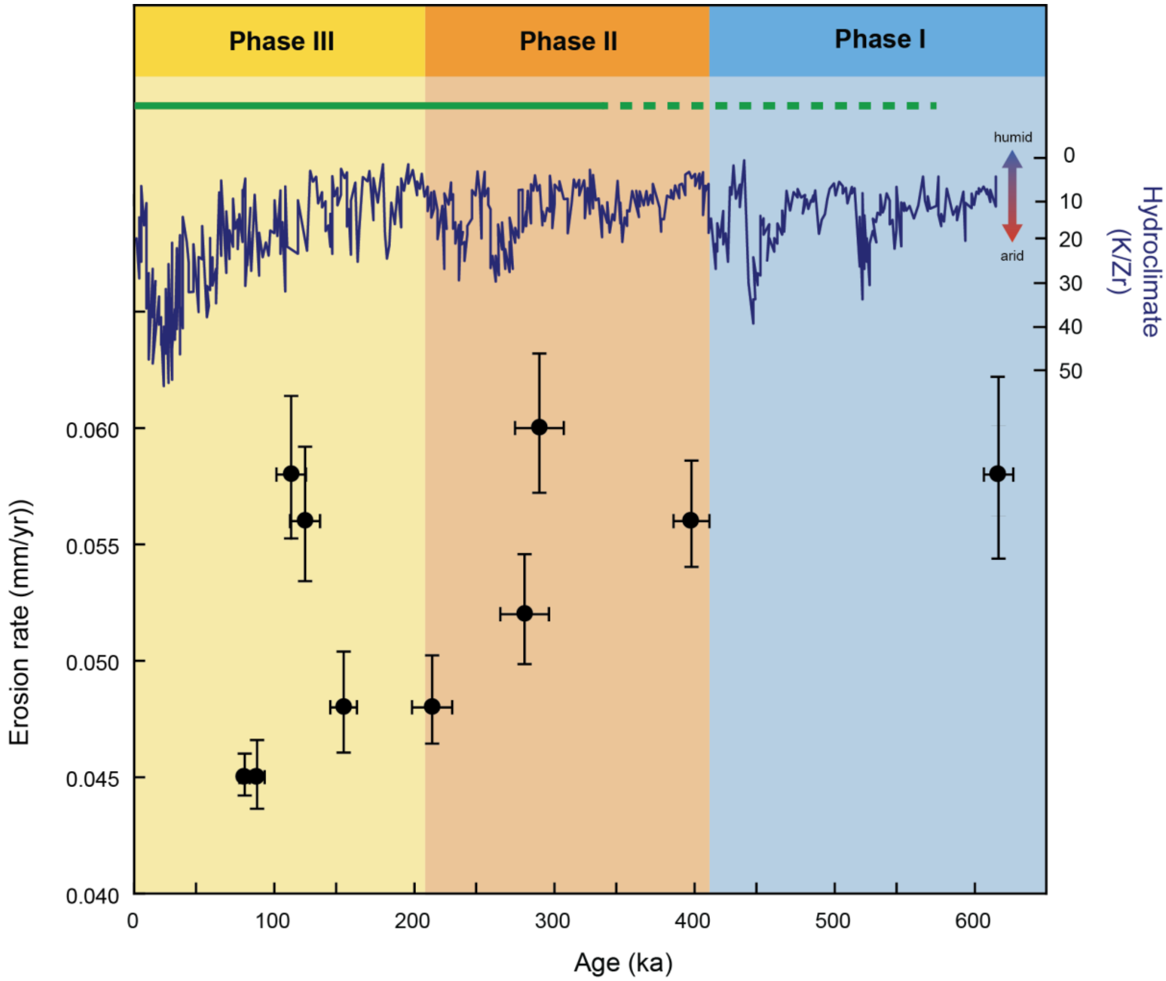

Figure 4.5 Paleoerosion rates from the HSPDP-CHB drill cores with corresponding Phase I-III time periods and K/Zr hydroclimate proxy data from (Foerster et al., *in review*). Solid green line indicates period dominated by orbital precession and green dashed line indicates period reflecting strong influence of atmospheric CO_2 (Duesing et al., 2019, 2021).

4.7 Conclusion

Paleoerosion rates derived from the ~620 kyr record of the CHB core range from 0.045 to 0.060 mm/yr. The erosion rates show a general decreasing trend over time and are largely consistent with a weighted average of modern erosion rates from subcatchments within the Chew Bahir basin (Dorgerloh, 2016). Unlike other catchments within the EARS that show a strong correspondence between erosion rate and a combination of EVI and hillslope gradient (Torres Acosta et al., 2015), modern erosion rates within the Chew Bahir basin only show a relationship with hillslope gradient, not EVI. This contrast in behavior is most likely the result the significant changes in vegetation type due to elevation and steepness within the Chew Bahir basin, where the mean EVI of a subcatchment does not reflect the local effects that strongly control the erosion rate. Variances in erosion rates over time are thus likely due to overprinting of climate-modulated vegetation changes and moisture availability on the base tectonic signature and/or enhanced tectonic/geomorphic activity shifting sediment sources.

The three phases based on the proxy record of the CHB core suggest shifts between humid and more arid conditions, with increasing variability over time (Foerster et al., *in review*). The paleoerosion rates are consistent with the most humid environment represented at the base of the core and a general aridification trend and decrease of moisture availability and erosion rates over time. However, most of the decline in erosion rates is accomplished before any systematic shift to more arid conditions begins based on the hydroclimate record. The relative consistency in paleoerosion rates over time likely reflects the dominant control of tectonics on erosion rates within the Chew Bahir basin, and the brief higher excursions in erosion rates tectonic-modulated geomorphic shifts impacting sediment source and transport capacity.

4.8 References

Bekaddour, Toufik, Fritz Schlunegger, Hendrik Vogel, Romain Delunel, Kevin P. Norton, Naki Akçar and Peter Kubik (2014). Paleo erosion rates and climate shifts recorded by Quaternary cut-and-fill sequences in the Pisco valley, central Peru. *Earth and Planetary Science Letters*, 390, p. 103–115. https://doi.org/10.1016/j.epsl.2013.12.048

Bierman, Paul, and Eric J. Steig (1996). Estimating rates of denudation using cosmogenic isotope abundances in sediment. *Earth Surface Processes and Landforms*, 21, 2, p. 125–139. https://doi.org/10.1002/(SICI)1096-9837(199602)21:2<125::AID-ESP511>3.0.CO;2-8

Bobe, René and Anna K. Behrensmeyer (2004). The expansion of grassland ecosystems in Africa in relation to mammalian expansion and the origin of the genus *Homo*. *Palaeogeography, Palaeoclimatology, Palaeoecology*, 207, p. 399–420. https://doi.org/10.1016/j.palaeo.2003.09.033

Boone, S. C., M-L. Balestrieri, B. P. Kohn, G. Corti, A. J. W. Gleadow, and C. Seiler (2019). Tectonothermal evolution of the Broadly Rifted Zone, Ethiopian Rift. *Tectonics*, 38, 3, p. 1070–1100. https://doi.org/10.1029/2018TC005210

Borchers, Brian, Shasta Marrero, Greg Balco, Marc Caffee, Brent Goehring, Nathaniel Lifton, Kunihiko Nishiizumi, Fred Phillips, Joerg Schaefer, and John Stone (2016). Geological calibration of spallation production rates in the CRONUS-Earth project. *Quaternary Geochronology*, 31, p. 188–198. https://doi.org/10.1016/j.quageo.2015.01.009

Braucher, R., Brown, E.T., Bourlès, D.L., Colin, F. (2003). *In situ* produced ^{10}Be measurements at great depths: implications for production rates by fast muons. *Earth and Planetary Science Letters*, 211, p. 251–258. https://doi.org/10.1016/S0012-821X(03)00205-X

Braucher, R., Bourlès, D.L., Brown, E.T., Colin, F., Muller, J.-P., Braun, J.-J., Delaune, M., Minko, A.E., Lescouet, C., Raisbeck, G.M., Yiou, F. (2000). Application of *in situ* produced cosmogenic ^{10}Be and ^{26}Al to the study of lateritic soil development in tropical forest: theory and examples from Cameroon and Gabon. *Chemical Geology*, 170, p. 95–111. https://doi.org/10.1016/S0009-2541(99)00243-0

Brown, Erik Thorson, Robert F. Stallard, Matthew C. Larsen, Grant M. Raisbeck, and Françoise Yiou (1995). Denudation rates determined from the accumulation of in situ-produced ^{10}Be in the Luquillo Experimental Forest, Puerto Rico. *Earth and Planetary Science Letters*, 129, 1-4, p.193–202. https://doi.org/10.1016/0012-821X(94)00249-X

Campisano, C. J., A.S. Cohen, J.R. Arrowsmith, A. Asrat, A.K. Behrensmeyer, E.T. Brown, A.L. Deino, D.M. Deocampo, C.S. Feibel, J.D. Kingston, H.F. Lamb, T.K. Lowenstein, A. Noren, D.O. Olago, R.B. Owen, J.D. Pelletier, R. Potts, K.E. Reed, R.W. Renaut, J.M. Russell, J.L. Russell, F. Schabitz, J.R. Stone, M.H. Trauth, and J.G. Wynn (2017). The Hominin Sites and Paleolakes Drilling Project: High-resolution paleoclimate records from the East African rift system and their implications for understanding the environmental context of hominin evolution. *PaleoAnthropology*, p. 1–43. https://doi:10.4207/PA.2017.ART104

Campisano, Christopher J. (2012). Geological summary of the Busidima formation (Plio-Pleistocene) at the Hadar paleoanthropological site, Afar Depression, Ethiopia. *Journal of Human Evolution*, 62, 3, p. 338–352. https://doi.org/10.1016/j.jhevol.2011.05.002

Cerling, Thure E., Jonathan G. Wynn, Samuel A. Andanje, Michael I. Bird, David Kimutai Korir, Naomi E. Levin, William Mace, Anthony N. Macharia, Jay Quade, and Christopher H. Remien (2011). Woody cover and hominin environments in the past 6 million years. *Nature*, 476, 7358, p. 51–56. https://doi.org/10.1038/nature10306

Charreau, Julien, P-H. Blard, N. Puchol, J-P. Avouac, Elisabeth Lallier-Vergès, D. Bourlès, Regis Braucher, A. Gallaud, R. Finkel, M. Jolivet, Y. Chen, and P. Roy (2011). Paleo-erosion rates in Central Asia since 9 Ma: A transient increase at the onset of Quaternary glaciations? *Earth and Planetary Science Letters*, 304, 1-2, p. 85–92. https://doi.org/10.1016/j.epsl.2011.01.018

Chorowicz, Jean (2005). The East African rift system. *Journal of African Earth Sciences*, 43, 1-3 p. 379–410. https://doi.org/10.1016/j.jafrearsci.2005.07.019

Cohen, A., C. Campisano, R. Arrowsmith, A. Asrat, A.K. Behrensmeyer, A. Deino, C. Feibel, A. Hill, R. Johnson, J. Kingston, H. Lamb, T. Lowenstein, A. Noren, D. Olago, R.B. Owen, R. Potts, K. Reed, R. Renaut, F. Schäbitz, J.-J. Tiercelin, M.H. Trauth, J. Wynn, S. Ivory, K. Brady, R. ÓGrady, J. Rodysill, J. Githiri, J. Russell, V. Foerster, R. Dommain, S. Rucina, D. Deocampo, J. Russell, A. Billingsley, C. Beck, G. Dorenbeck, L. Dullo, D. Feary, D. Garello, R. Gromig, T. Johnson, A. Junginger, M. Karanja, E. Kimburi, A. Mbuthia, T. McCartney, E. McNulty, V. Muiruri, E. Nambiro, E.W. Negash, D. Njagi, J.N. Wilson, N. Rabideaux, T. Raub, M.J. Sier, P. Smith, J. Urban, M. Warren, M. Yadeta, C. Yost, and B. Zinaye (2016). The Hominin Sites and Paleolakes Drilling Project: inferring the environmental context of human evolution from eastern African rift lake deposits, Sci. Dril., 21, p. 1–16. https://doi.org/10.5194/sd-21-1-2016

Davidson, A., and D. C. Rex (1980). Age of volcanism and rifting in southwestern Ethiopia. *Nature*, 283, 5748, p. 657–658. https://doi.org/10.1038/283657a0

Davidson, A. (1983). The Omo River project: reconnaissance geology and geochemistry of parts of Ilubabor, Kefa, Gemu Gofa and Sidamo. *Ethiopian Institute of Geological Surveys Bulletin*, 2, p. 1–89.

deMenocal, Peter, B. (2004). African climate change and faunal evolution during the Pliocene–Pleistocene. *Earth and Planetary Science Letters*, 220, 1-2, p. 3–24. https://doi.org/10.1016/S0012-821X(04)00003-2

DiMaggio, Erin N., Christopher J. Campisano, John Rowan, Guillaume Dupont-Nivet, Alan L. Deino, Faysal Bibi, Margaret E. Lewis, Antoine Souron, Dominique Garello, Lars Werdelin, Kaye E. Reed, J Ramón Arrowsmith (2015). Late Pliocene fossiliferous sedimentary record and the environmental context of early *Homo* from Afar, Ethiopia. *Science*, 347, 6228, p. 1355–1359. https://doi.org/10.1126/science.aaa1415

Duesing, Walter, Nadine Berner, Alan L. Deino, Verena Foerster, K. Hauke Kraemer, Norbert Marwan, and Martin H. Trauth (2021). Multiband wavelet age modeling for a ∼293 m (∼600 kyr) sediment core from Chew Bahir Basin, Southern Ethiopian Rift. *Frontiers in Earth Science*, 9, 35. https://doi.org/10.3389/feart.2021.594047

Duesing, Walter, Hauke Kraeme, Asfawossen Asrat, Melissa Chapot, Andrew Cohen, Alan Deino, Verena Foerster, Henry Lamb, Norbert Marwan, Christine Lane, Mark Maslin, Christopher Ramsey, Helen Roberts, Frank Schaebitz, Martin Trauth, and Céline Vidal (2019). Differentiating local from regional climate signals using the 600 ka Chew Bahir paleoclimate record from South Ethiopia. *In EGU General Assembly Conference Abstracts*, 21, p. 14836.

Dorgerloh, Florian (2016). Basin-wide erosion rates from in-situ ^{10}Be in the Chew Bahir basin, southern Ethiopia. Bachelor thesis, Universität Potsdam.

Ebinger, C. J., Tilahun Yemane, D. J. Harding, Samson Tesfaye, S. Kelley, and D. C. Rex (2000). Rift deflection, migration, and propagation: Linkage of the Ethiopian and Eastern rifts, Africa. *Geological Society of America Bulletin*, 112, 2, p. 163–176. https://doi.org/10.1130/0016-7606(2000)112<163:RDMAPL>2.0.CO;2

Feibel, Craig S. (2011). A geological history of the Turkana Basin. *Evolutionary Anthropology: Issues, News, and Reviews*, 20, 6, p. 2065–216. https://doi.org/10.1002/evan.20331

Foerster, Verena, Asfawossen Asrat, Christopher Bronk Ramsey, Erik T. Brown, Melissa S. Chapot, Alan Deino, Daniel M. Deocampo, Walter Duesing, Annette Hahn, Annett Junginger, Stefanie Kaboth-Bahr, Christine S. Lane, Stephan Opitz, Anders Noren, Helen M. Roberts, Mona Stockhecke, Ralph Tiedemann, Céline Vidal, Ralf Vogelsang, Andrew S. Cohen, Henry F. Lamb, Frank Schaebitz, and Martin H. Trauth. 620,000 years of eastern Africa climate variability and hominin evolution. *Nature Geoscience* (In review).

Foerster, Verena, Daniel M. Deocampo, Asfawossen Asrat, Christina Günter, Annett Junginger, Kai Hauke Krämer, Nicole A. Stroncik, and Martin H. Trauth (2018). Towards an understanding of climate proxy formation in the Chew Bahir basin, southern Ethiopian Rift. *Palaeogeography, Palaeoclimatology, Palaeoecology*, 501, p. 111–123. https://doi.org/10.1016/j.palaeo.2018.04.009

Foerster, Verena, Ralf Vogelsang, Annett Junginger, Asfawossen Asrat, Henry F. Lamb, Frank Schaebitz, and Martin H. Trauth (2015). Environmental change and human occupation of southern Ethiopia and northern Kenya during the last 20,000 years. *Quaternary Science Reviews*, 129, p. 333–340. https://doi.org/10.1016/j.quascirev.2015.10.026

Foerster, Verena, Annett Junginger, Oliver Langkamp, Tsige Gebru, Asfawossen Asrat, Mohammed Umer, Henry F. Lamb, Volker Wenrich, Janet Rethemeyer, Norbert Nowaczyk, Martin H. Trauth, and Frak Schaebitz (2012). Climatic change recorded in the sediments of the Chew Bahir basin, southern Ethiopia, during the last 45,000 years. *Quaternary International*, 274, p. 25–37. https://doi.org/10.1016/j.quaint.2012.06.028

Granger, Darryl E., Nathaniel A. Lifton, and Jane K. Willenbring (2013). A cosmic trip: 25 years of cosmogenic nuclides in geology. *GSA Bulletin*, 125, 9-10, p. 1379–1402. https://doi.org/10.1130/B30774.1

Granger, Darryl E., James W. Kirchner, and Robert Finkel (1996). Spatially averaged long-term erosion rates measured from in situ-produced cosmogenic nuclides in alluvial sediment. *The Journal of Geology*, 104, 3, p. 249–257. https://doi.org/10.1086/629823

Grischott, Reto, Florian Kober, Maarten Lupker, Juergen M. Reitner, Ruth Drescher-Schneider, Irka Hajdas, Marcus Christl, and Sean D. Willett (2017). Millennial scale variability of denudation rates for the last 15 kyr inferred from the detrital ^{10}Be record of Lake Stappitz in the Hohe Tauern massif, Austrian Alps. *The Holocene*, 27, 12, p. 19149–1927. https://doi.org/10.1177/0959683617708451

Grischott, Reto, Florian Kober, Maarten Lupker, Kristina Hippe, Susan Ivy-Ochs, Irka Hajdas, Bernhard Salcher, and Marcus Christl (2016). Constant denudation rates in a high alpine catchment for the last 6 kyrs. *Earth Surface Processes and Landforms*, 42, 7, p. 1065-1077. https://doi.org/10.1002/esp.4070

Kohl, C. P., and Kunihiko Nishiizumi (1992). Chemical isolation of quartz for measurement of in-situ-produced cosmogenic nuclides. *Geochimica et Cosmochimica Acta*, 56, 9, p. 3583–3587. https://doi.org/10.1016/0016-7037(92)90401-4

Lal, Devendra (1991). Cosmic ray labeling of erosion surfaces: *in situ* nuclide production rates and erosion models. *Earth and Planetary Science Letters*, 104, 2-4, p. 424–439. https://doi.org/10.1016/0012-821X(91)90220-C

Levin, Naomi E., Francis H. Brown, Anna K. Behrensmeyer, René Bobe, and Thure E. Cerling (2011). Paleosol carbonates from the Omo Group: Isotopic records of local and regional environmental change in East Africa. *Palaeogeography, Palaeoclimatology, Palaeoecology*, 307, 1-4, p. 75–89. https://doi.org/10.1016/j.palaeo.2011.04.026

Madella, Andrea, Romain Delunel, Naki Akçar, Fritz Schlunegger, and Marcus Christl (2018). ^{10}Be-inferred paleo-denudation rates imply that the mid-Miocene western central Andes eroded as slowly as today. Scientific Reports, 8, 1, p. 1–9. https://doi.org/10.1038/s41598-018-20681-x

Marrero, Shasta M., Fred M. Phillips, Brian Borchers, Nathaniel Lifton, Robert Aumer, and Greg Balco (2016). Cosmogenic nuclide systematics and the CRONUScalc program. *Quaternary Geochronology*, 31, p. 160–187. https://doi.org/10.1016/j.quageo.2015.09.005

Moore, J.M., Davidson, A. (1978). Rift structure in southern Ethiopia. *Tectonophysics*, 46, p. 159–173. https://doi.org/10.1016/0040-1951(78)90111-7

Nishiizumi, Kunihiko, Mineo Imamura, Marc W. Caffee, John R. Southon, Robert C. Finkel, and Jeffrey McAninch (2007). Absolute calibration of 10Be AMS standards." *Nuclear Instruments and Methods in Physics Research Section B: Beam Interactions with Materials and Atoms*, 258, 2, p. 403–413. https://doi.org/10.1016/j.nimb.2007.01.297

Philippon, Melody, Giacomo Corti, Federico Sani, Marco Bonini, Maria-Laura Balestrieri, Paola Molin, Ernst Willingshofer, Dimitrios Sokoutis, and Sierd Cloetingh (2014). Evolution, distribution, and characteristics of rifting in southern Ethiopia. *Tectonics*, 33, 4, p. 485–508. https://doi.org/10.1002/2013TC003430

Pik, Raphaël, Bernard Marty, Jean Carignan, Gezahegn Yirgu, and Teklewold Ayalew (2008). Timing of East African Rift development in southern Ethiopia:

Implication for mantle plume activity and evolution of topography. *Geology*, 36, 2, p. 167–170. https://doi.org/10.1130/G24233A.1

Quade, Jay, Naomi E. Levin, Scott W. Simpson, Robert Butler, William C. McIntosh, Sileshi Semaw, Lynnette Kleinsasser, Guillaume Dupont-Nivet, Paul Renne, and Nelia Dunbar (2008). The geology of Gona, Afar, Ethiopia. *Geological Society of America Special Paper 446*, p. 1–31. https://doi.org/10.1130/2008.2446(01)

Roberts, Helen M., Christopher Bronk Ramsey, Melissa S. Chapot, Alan L. Deino, Christine S. Lane, Céline Vidal, Asfawossen Asrat, Andrew Cohen, Verena Foerster, Henry F. Lamb, Frank Schaebitz, Martin H. Trauth. Using multiple chronometers to establish a long, directly dated lacustrine record: constraining >600,000 years of environmental change at Chew Bahir, Ethiopia. *Quaternary Science Reviews* (In review).

Roller, S., H. Wittmann, M. Kastowski, and M. Hinderer (2012). Erosion of the Rwenzori Mountains, East African Rift, from in situ-produced cosmogenic ^{10}Be. *Journal of Geophysical Research: Earth Surface*, 117, F03003, p. 1–20. https://doi.org/10.1029/2011JF002117

Schaller, M., T. A. Ehlers, T. Stor, J. Torrent, L. Lobato, Marcus Christl, and Christof Vockenhuber (2016). Spatial and temporal variations in denudation rates derived from cosmogenic nuclides in four European fluvial terrace sequences. *Geomorphology*, 274, p. 180–192. https://doi.org/10.1016/j.geomorph.2016.08.018

Schaller, M., and T.A. Ehlers (2006). Limits to quantifying climate driven changes in denudation rates with cosmogenic radionuclides. *Earth and Planetary Science Letters*, 248, p. 153–167. https://doi.org/10.1016/j.epsl.2006.05.027

Schaller, M., F. von Blanckenburg, Niels Hovius, A. Veldkamp, Meindert W. van den Berg, and P. W. Kubik (2004). Paleoerosion rates from cosmogenic 10Be in a 1.3 Ma terrace sequence: response of the River Meuse to changes in climate and rock uplift. *The Journal of Geology*, 112, 2, p. 127–144. https://doi.org/10.1086/381654

Schaller, M., Friedhelm von Blanckenburg, A. Veldkamp, L. A. Tebbens, N. Hovius, and P. W. Kubik (2002). " 30 000 yr record of erosion rates from cosmogenic ^{10}Be in Middle European river terraces. *Earth and Planetary Science Letters*, 204, 1-2, p. 307–320. https://doi.org/10.1016/S0012-821X(02)00951-2

Scherler, Dirk, Bodo Bookhagen, Hendrik Wulf, Frank Preusser, and Manfred R. Strecker (2015). Increased late Pleistocene erosion rates during fluvial aggradation in the Garhwal Himalaya, northern India. *Earth and Planetary Science Letters*, 428, p. 255–266. https://doi.org/10.1016/j.epsl.2015.06.034

Sepulchre, Pierre, Gilles Ramstein, Frédéric Fluteau, Mathieu Schuster, Jean-Jacques Tiercelin, and Michel Brunet (2009). Tectonic uplift and Eastern Africa aridification. Science, 313, 5792, p. 1419–1423. https://doi.org/10.1126/science.1129158

Spiegel, Cornelia, Barry P. Kohn, David X. Belton, and Andrew JW Gleadow (2007). Morphotectonic evolution of the central Kenya rift flanks: Implications for late Cenozoic environmental change in East Africa. Geology, 35, 5 p. 427–430. https://doi.org/10.1130/G23108A.1

Stone, John O (2000). Air pressure and cosmogenic isotope production. *Journal of Geophysical Research: Solid Earth*, 105, B10, p. 23753–23759. https://doi.org/10.1029/2000JB900181

Torres Acosta, Verónica, Taylor F. Schildgen, Brian A. Clarke, Dirk Scherler, Bodo Bookhagen, Hella Wittmann, Friedhelm von Blanckenburg, and Manfred R. Strecker (2015). Effect of vegetation cover on millennial-scale landscape denudation rates in East Africa." *Lithosphere*, 7, 4, p. 408–420. https://doi.org/10.1130/L402.1

Trauth, Martin H., Asfawossen Asrat, Walter Duesing, Verena Foerster, K. Hauke Kraemer, Norbert Marwan, Mark A. Maslin, and Frank Schaebitz (2019). Classifying past climate change in the Chew Bahir basin, southern Ethiopia, using recurrence quantification analysis. *Climate Dynamics*, 53, 5, p. 2557–2572. https://doi.org/10.1007/s00382-019-04641-3

Trauth, Martin, Verena Foerster, Annett Junginger, Asfawossen Asrat, Henry Lamb, and Frank Schaebitz (2018). Abrupt or Gradual? Change Point Analysis of the Late Pleistocene-Holocene Chew Bahir Record from Southern Ethiopia. *Quaternary Research*, 90, 2, p. 321–330. https://doi.org/10.1017/qua.2018.30

Quinn, Rhonda L., Christopher J. Lepre, James D. Wright, and Craig S. Feibel (2007). Paleogeographic variations of pedogenic carbonate $\delta^{13}C$ values from Koobi Fora, Kenya: implications for floral compositions of Plio-Pleistocene hominin environments." Journal of Human Evolution 53, 5, p. 560–573. https://doi.org/10.1016/j.jhevol.2007.01.013

CHAPTER 5

PRECAMBRIAN TECTONOTHERMAL HISTORY, CENOZOIC RIFTING AND VOLCANISM, AND PLEISTOCENE BASIN DYNAMICS OF THE CHEW BAHIR BASIN, SOUTHERN ETHIOPIA

5.1 Abstract

Given the exposures of both Precambrian crystalline bedrock and Cenozoic volcanic units in southern Ethiopia, the detrital mineral record of basins in southern Ethiopia holds significant potential to investigate various tectonic, magmatic, and geomorphic processes over multiple time scales. We sampled from the Chew Bahir (CHB) drill core (~620 kyr–present) collected by the Hominin Sites and Paleolakes Drilling Project (HSPDP) to evaluate the Precambrian tectonothermal history, the timing of Cenozoic rifting and volcanism, and Pleistocene basin dynamics of the Chew Bahir basin, Ethiopia. We performed (U-Th)/He and U/Pb analyses on detrital zircons using single crystal laser ablation double dating (LADD) techniques, in addition to conventional (U-Th)/He analyses on detrital apatites. The crystalline bedrock sourced from the CHB core is predominantly associated with the Berguda (550–500 Ma) tectonothermal event, which was a period of extensive granitic magmatism in southern Ethiopia related to the end of the East African Orogen (EAO). Crystalline bedrock units are also related to the Megado (770–720 Ma) and Moyale (700–550 Ma) tectonothermal events, associated with orogenic closures of oceanic basins. Since magmatic emplacement in the Late Neoproterozoic to Early Cambrian, zircon (U-Th)/He dates show subsequent crustal uplift and protracted cooling of these terranes. Detrital apatite

cooling (U-Th)/He dates are consistent with bedrock apatite exhumation dates that suggest Cenozoic rift initiation at ~20 Ma and continual rift development since initiation. Extensive ~20 Ma volcanic products suggests that major volcanism was coeval with rift initiation in the region. Cenozoic volcanic zircons are restricted to a population at ~19.5 Ma, derived from silicic units of the Teltele basalts on the Teltele Plateau that bounds the basin to the east. Sediment input from the basin rift margin appears variable over time, likely related to pulses of tectonic activity and wet/dry climate conditions. Based on the detrital zircon record alone, it is difficult to temporally resolve episodes of basin connectivity and overflow that have been identified during the Quaternary, although zircons with exceptionally young (U-Th)/He dates may be derived from adjacent basins with greater sources of volcanic and/or hydrothermal heating. The sedimentary record examined here supports additional proxy research from the CHB core that suggests increased climate variability and amplitude after ~200 ka in the Chew Bahir basin.

5.2 Introduction

The geologic record of southern Ethiopia provides a near billion-year history of continental accretion and incipient continental rifting with the exposures of Precambrian crystalline basement and Cenozoic volcanic rocks and rift sediments. The Neoproterozoic–Early Paleozoic rocks of the basement in southern Ethiopia were formed/deformed during the East African Orogeny (EAO), which lasted from ~850–550 Ma and was associated with the collision of East and West Gondwana following the closure of the Mozambique Ocean (Fritz et al., 2013; Stern, 1994). The EAO forms the largest continuous Neoproterozoic–Cambrian orogen on Earth (6000 km N–S) and is categorized into a northern segment, the Arabian Nubian Shield (ANS), and a southern segment, the Mozambique Belt (MB) (Fritz et al., 2013 and references therein). Southern Ethiopia occupies a unique position within the EAO with occurrences of both medium- to high-grade metamorphic rocks associated with the Mozambique Belt, and low- to medium-grade volcano-sedimentary rocks of the Arabian Nubian Shield (e.g. Fritz et al., 2003; Hargrove et al., 2006; Sommer et al., 2003).

The Precambrian basement in southern Ethiopia is often directly overlain by Cenozoic volcanic rocks associated with the East African Rift System (EARS). The EARS contains a series of structurally and magmatically controlled extensional basins that reach for ~3,500 km from the Afar Triple Junction to Mozambique and is a textbook example for incipient continental rifting (Chorowicz, 2005). Pre-rift volcanism was initiated at ~45 Ma in southern Ethiopia and continues to the present (Ebinger et al., 2000). Rift basins began to form along the future EARS from the late Oligocene to early Miocene, with volcanic and tectonic activity triggering sedimentation (Chernet et al., 1998; Ebinger et al., 1993; WoldeGabriel et al., 1990, 2000). These rift basins preserve an exceptional record of Neogene and Quaternary paleoclimate, paleoenvironments, and faunal evolution, including that of humans and their fossil ancestors (e.g., deMenocal, 2004; WoldeGabriel et al., 2000).

In this study, we analyze the detrital mineral record of the Chew Bahir basin in southern Ethiopia to provide insight into the regional Precambrian EAO magmatic and tectonothermal history, the timing of Cenozoic EARS rifting and volcanism, and Pleistocene watershed and sedimentary basin dynamics. We sample from the Chew Bahir

(CHB) drill core collected by the Hominin Sites and Paleolakes Drilling Project (Campisano et al., 2017; Cohen et al., 2016), which yields a ~620 ka to present sedimentary record of the Chew Bahir basin (Foerster et al., *in review*; Roberts et al., *in review*). Studying the detrital mineral record allows for an integrated evaluation of multiple processes across diverse timescales, and sampling from the HSPDP drill core allows for access to a well-dated sedimentary record that is otherwise unexposed at the modern surface.

We employ laser ablation double dating of detrital zircons (LADD) (Horne et al., 2016), which integrates laser ablation gas-source mass spectrometry (LA-GMS) with laser ablation inductively coupled mass spectrometry (LA-ICPMS) techniques to determine both the crystallization U/Pb date of the zircon and the (U-Th)/He timing of its passage through the ~140–200ºC range, depending on the degree of diffusive anisotropy and radiation damage during post-crystallization cooling (Anderson et al., 2020). U/Pb dates of detrital zircons can be used to evaluate the evolution of source areas and sediment routing during deposition (e.g., Gehrels et al., 1995; Romans et al., 2016), and (U-Th)/He dates provide information on the thermal history of the source rock (Reiners, 2005) (Zawacki et al., *in review*). We also perform conventional (U-Th)/He dating on detrital apatites. The lower closure temperature (∼70°C) of the apatite (U-Th)/He system quantifies the cooling history of the source rock as it passes through the upper 1–3 km of the crust (Ehlers and Farley, 2003).

Through our analyses, we determine the ages of the Precambrian source units within the Chew Bahir basin and relate them to tectonothermal episodes of the EAO. We also evaluate the cooling history of the source rocks and assess any additional notable thermal events. This LADD approach provides an abundance of new dates to better understand the Precambrian and Early Paleozoic evolution in southern Ethiopia. Detrital apatite (U-Th)/He dates provide a useful way to evaluate and refine the timing of Cenozoic rift initiation in the Chew Bahir basin related to the evolution of the EARS. By identifying the provenance of the sediments, we evaluate the geomorphic basin dynamics during the Pleistocene, which show variability based on pulses of tectonic activity combined with wet phases. The detrital mineral record of the Chew Bahir basin thus provides an excellent lens through which to view Precambrian tectonothermal events, Cenozoic rifting and volcanism, and Pleistocene basin dynamics.

5.3 Geologic Setting

The Chew Bahir basin is a small (22,000 km^2) hydrologically closed basin that forms the southernmost part of the Broadly Rifted Zone (BRZ) in southern Ethiopia (Figure 5.1). The BRZ is a wide (~300 km), diffuse region of basins and ranges that extend from the southern Main Ethiopian Rift to the Turkana Depression in northern Kenya (Baker et al., 1972; Davidson and Rex, 1980). The Chew Bahir basin is largely symmetric, unlike basins farther north in the Gofa Province, and is defined by large normal faults that dominantly strike N-S (Philippon et al., 2014).

The basin is bounded to the west by the Hammar Range (alternatively Hamer/Hamar), which consists of Precambrian basement with mainly undivided gneisses and granitoids (Davidson, 1983) (Figure 5.2). The Precambrian basement of southern Ethiopia is associated with the five tectonothermal events during the evolution of the

EAO: the Adola (1157 ± 2 to 1030 ± 40 Ma), Bulbul–Awata (~876 ± 5 Ma), Megado (770–720 Ma), Moyale (700–550 Ma), and Berguda (550–500 Ma) events (Yibas et al., 2002). Based on $^{207}Pb/^{206}Pb$ dating of zircons, episodes of magmatism within southern Ethiopia were largely constrained to ~850, ~750–700 and ~650–550 Ma (Teklay et al., 1998). U/Pb analyses of zircons from plutonic and high-grade metamorphic rocks of the Hammar Domain exposed in the northern-central portion of the Chew Bahir basin yielded dates of ~785 to ~702 Ma and ~630 Ma (Verner et al., 2021). The emplacement of the Konso pluton, also in the northern-central portion of the basin, is constrained to 449 ± 2 Ma (Asrat and Barbey, 2003). (All specific dates in this contribution are reported with 2σ uncertainties.)

The escarpment of Teltele–Konso range exposing Miocene basalt flows and subordinate rhyolitic intercalations bounds the Chew Bahr basin to the east (Foerster et al., 2012) (Figure 5.2). The Teltele basalts have been dated to ~20 Ma (Ebinger et al., 2000), with a tuff layer dated to 18.7 ± 0.8 Ma (Davidson and Rex, 1980). The Teltele basalts are conformably overlain by the Kumbi rhyolitic tuff and lavas volcanic succession, which have been dated to ~14.5 Ma (Ebinger et al., 2000). Precambrian basement units in the northern portion of the basin are partly overlain by limited exposures of the Amaro/Gamo units, which are the oldest volcanic rocks associated with the EARS (Figure 5.2). The Amaro/Gamo units are composed of transitional to tholeiitic basalts and associated silicic rocks dated between ~45–35 Ma (Davidson, 1983; Ebinger et al., 1993, 2000). More significant exposures of the Amaro/Gamo unit are found in the Chamo and Galana basins to the north. Within the southernmost extent of the Chew Bahir basin, there are localized basalts dated to 3.2 ± 0.6 Ma (Ebinger et al., 2000). Alluvial fans draining the Hammar Range and the Teltele Plateau provide a large portion of the sediment influx in the basin, in addition to the perennial Weyto and Segen rivers that drain the northern portions of the basin (Foerster et al., 2012).

Rifting within the Chew Bahir basin is proposed to have commenced at ~20 Ma, based on apatite (U/Th)/He thermochronometry of samples from the Hammar Range (Pik et al., 2008). Previous studies placed a minimum age constraint on the onset of rifting in the Gofa Province basins to the north at ~12 Ma (Balestrieri et al., 2016; Philippon et al., 2014), but the timing was later refined to ~20–17 Ma (Boone et al., 2019). Therefore, as opposed to a northward propagation of rifting through the BRZ, rifting initiation in the region appears to have been largely synchronous at ~20 Ma. The synchronous, widespread extension of the BRZ is supported by Moho depth and seismic tomography imaging (Emishaw et al., 2017). Geomorphological analysis suggests recent fault activity along the western margin of the Chew Bahir basin (Philippon et al., 2014), which supports long-term thermochronology data indicating that rift development has been continuous since initiation in the Miocene (Pik et al., 2008).

The Chew Bahir basin today holds a saline mudflat that episodically fills to a shallow lake during the rainy season. Rainfall is highly seasonal, making sediment influx from drainage networks at the border faults episodic (Foerster et al., 2012). Basin overflow connecting Lakes Abaya and Chamo to Lake Turkana via the Chew Bahir basin during wet periods in the Pleistocene and early Holocene has been suggested based on migration of fish faunas (Grove et al., 1975). The lake basins were most recently hydrologically linked during high stands of the African Humid Period (AHP, ~15–5 ka) (Fischer et al., 2020).

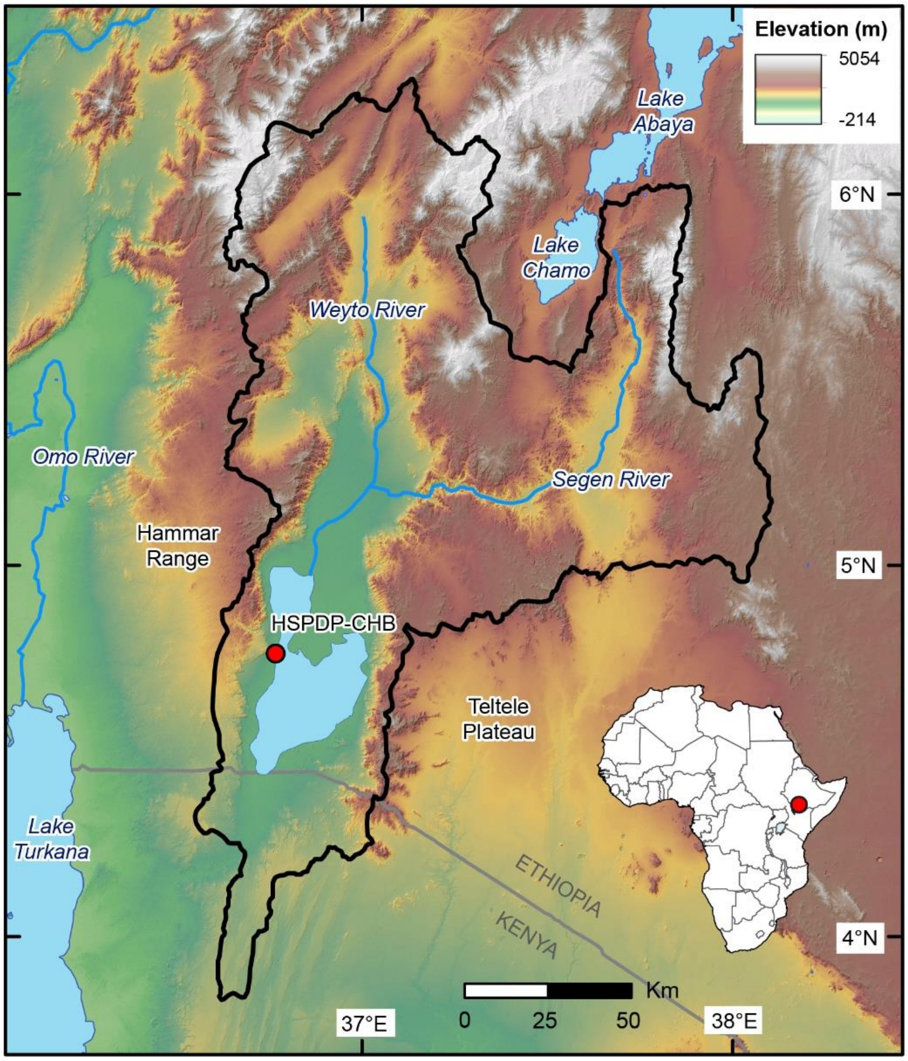

Figure 5.1 Geographic overview of Chew Bahir basin near the Ethiopia-Kenya border. HSPDP-CHB drill site is marked in red, and the basin watershed is delineated in black. Data source is a 30 m SRTM DEM projected over a hillshade.

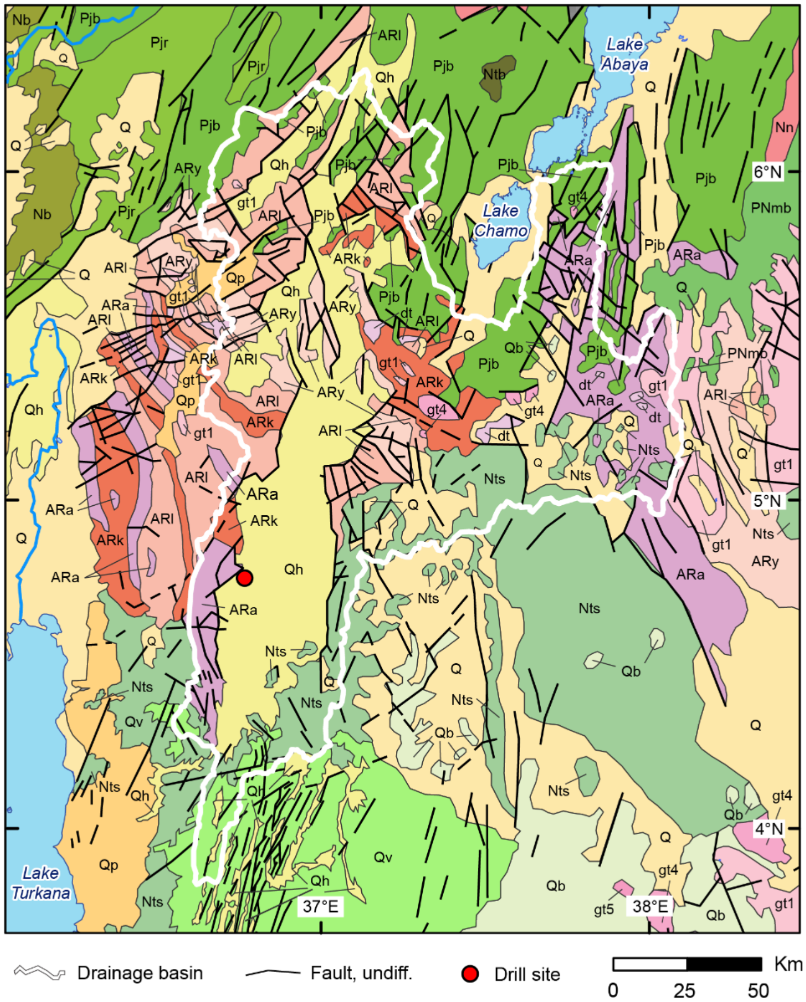

Quaternary Undifferentiated

- **Q** — Alluvial and lacustrine deposits, diatomite, limestone, and beach sand
- **Qb** — Plateau basalt: Alkaline basalt and trachyte

Holocene

- **Qh** — Undifferentiated alluvial, lacustrine, and beach sediments

Plio-Pleistocene

- **Qp** — Alluvial, colluvial, lacustrine, and marine sediments
- **Qv** — Trachytes, basalts, and pyroclastics
- **Nb** — Mursi and Bofa Basalts: Alkaline basalt

Miocene-Pliocene

- **Nn** — Nazaret Series: Ignimbrites, unwelded tuffs, ash flows, rhyolitic flows, domes, and trachyte

Middle Miocene

- **Ntb** — Tarmaber Megezez Formation: Transitional and alkaline basalt
- **Nts** — Teltele and Surma Basalt: Flood basalts (Ethiopia); Phonolites, trachytes, and basalts (Kenya)

Oligocene-Miocene

- **PNmb** — Makonnen Basalts: Flood basalts, commonly directly overlaying crystalline basement

Late Eocene-Late Oligocene

- **Pjr** — Amaro/Gamo (Upper part): Rhyolite and trachyte flows and tuff with minor basalt
- **Pjb** — Amaro/Gamo (Lower part): Flood basalt with minor salic flows [Formerly Jimma Volcanics]

Precambrian-Early Phanerozoic

- **ARy** — Yavello Group: Quartzo-feldspathic gneiss and granulite
- **ARa** — Awata Group: Biotite, hornblende, sillimanite-garnet, calc-silicate and quartzo-feldspathic gneisses, marble, and granite
- **ARl** — Alghe Group: Biotite and hornblende gneisses, granulite, and migmatite with minor metasedimentary gneisses
- **ARk** — Konso Group: Hornblende, pyroxene, garnet-pyroxene gneisses, and amphibolite with minor metasedimentary gneiss

Precambrian and Phanerozoic instrusive rocks

- **gt5** — Alkali granite and syenite
- **gt4** — Post-tectonic granite and syenite
- **gt1** — Pre-tectonic and syn-tectonic granite
- **dt** — Diorite

Figure 5.2 Full geologic map of the Chew Bahir basin and surrounding region. Exposed rock units include Precambrian basement, Cenozoic rift volcanics, and Cenozoic rift sediments. Geologic map is a compilation of the Geological Map of Ethiopia (Ethiopian Ministry of Mines and Geological Survey of Ethiopia, 2nd Ed. 1996) and the Geological Map of Kenya (Ministry of Energy and Regional Development of Kenya, Ed. 1987).

5.4 Sampling & Methods

5.4.1 Drill core sampling

Two parallel duplicative drill cores were collected near the southwestern border of the Chew Bahir basin in November–December 2014. The two cores combined yield a ~293 m long composite sedimentary core record that covers the last ~617 ka (Foerster et al., *in review*; Roberts et al., *in review*). The cored sediments were predominantly silty and sandy clays, with occasional coarser calcareous beds predominantly in the upper ~100 m (Campisano et al., 2017; Cohen et al., 2016). 10 samples from sandy units in the two correlated cores, HSPDP-CHB14-2A and HSPDP-CHB14-2B, were collected (Figure 5.3) (Table 5.1). Individual core drives sampled up to ~3 m in length of material. The depositional ages of the samples ranged from ~79 to ~617 ka (Table 5.1). Sands were quartz-rich with a high mica content, often mixed with drilling fluid mud.

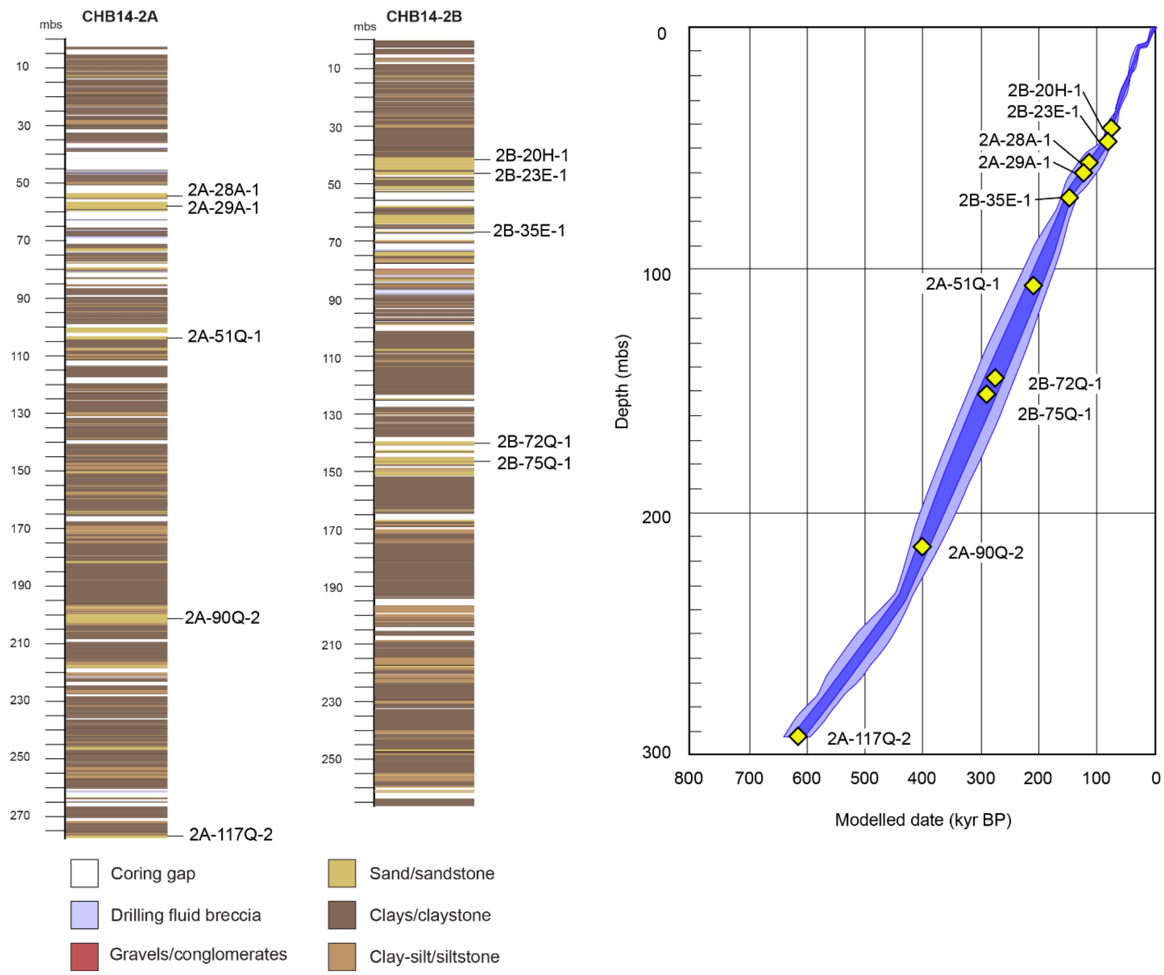

Figure 5.3 Stratigraphic columns of the HSPDP-CHB14-2A and HSPDP-CHB14-2B drill cores shown in meters below surface (mbs). Sampled sand units are labeled (Table 1). Sampled units are also indicated on the age model for the composite core (Roberts et al., *in review*).

Table 5.1 HSPDP Chew Bahir drill core samples. They are referred to by the top-most sampled core drive.

Drill Core	Lat.	Long.	Drives	Upper Sample Depth (mbs)	Age (ka)	Age Uncertainty [2σ] (kyr)
HSPDP-CHB14-2B	4.7613	36.7670	20H-1, 20H-2, 21H-1, 21H-2	41	78.9	7.4
HSPDP-CHB14-2B	4.7613	36.7670	23E-1	46	87.7	10.8
HSPDP-CHB14-2A	4.7612	36.7668	28A-1, 28A-2	54	112.1	21.1
HSPDP-CHB14-2A	4.7612	36.7668	29Q-1, 29Q-2	58	121.9	21.5
HSPDP-CHB14-2B	4.7613	36.7670	35E-1	66	149.5	19.0
HSPDP-CHB14-2A	4.7612	36.7668	51Q-1	104	212.6	28.7
HSPDP-CHB14-2B	4.7613	36.7670	72Q-1	140	278.7	34.6
HSPDP-CHB14-2B	4.7613	36.7670	75Q-1, 75Q-2	146	289.2	34.8
HSPDP-CHB14-2A	4.7612	36.7668	90Q-1, 90Q-2	202	397.7	25.7
HSPDP-CHB14-2A	4.7612	36.7668	117Q-2, 117Q-3	277	616.8	20.9

5.4.2 Zircons – Laser ablation double dating (LADD)

Sand samples were sieved to isolate the 250–125 μm size fraction and were separated by Frantz magnetic separation and LST heavy liquid density separation to isolate the zircons. Zircon abundance was variable between samples. The crystals were primarily subhedral and $\leq$ 120 μm wide, although there were a few significantly larger crystals. One hundred and ten zircon grains ≥ 80 μm in width from each sample were picked and mounted. The torr seal puck was polished to remove the outer 20–30 μm of the crystals to eliminate the need for (U-Th)/He alpha ejection correction and to ensure a smooth surface for analysis (Tripathy-Lang et al., 2013).

Analyses were conducted at the Group 18 Laboratories at Arizona State University following the methods outlined in Horne et al. (2016). Zircon LADD analytical protocols use a Teledyne Photon Machine *Analyte G2* excimer laser to ablate a shallow pit in the core region of a crystal under ultrahigh vacuum. These pits had either a 15 μm or 25 μm footprint diameter on the polished zircon surface, depending on the crystal width. The material ablated from each of these pits *in vaccuo* was purified using metal alloy getters, and the nonreactive gas component was admitted to an ASI *Alphachron* analytical system for ^{4}He analysis.

The sample puck was then remounted in a *HelEx2* two-volume cell for LA–ICPMS U+Th+Pb analysis. A second pit was ablated directly on top of the initial ^{4}He pit but with a considerably larger footprint to account for intracrystalline alpha redistribution effects when calculating (U-Th)/He dates (Tripathy-Lang et al., 2013). For 15 μm and 25 μm diameter laser ablation footprints for the LA-GMS analysis, 50 μm and 65 μm footprints were used for the LA-ICPMS analysis, respectively. U, Th, and Pb measurements were conducted on the material ablated from the larger pit using a Thermo Scientific *iCAP Q* ICPMS instrument.

Primary isotopic standards used for data reduction included the 91500 and Plešovice zircons (Sláma et al., 2018; Wiedenbeck et al., 1995). For U+Th concentrations, an in-house zircon syn-rock material that is more homogeneous for U and Th distribution than natural zircon crystals was used. In addition to these standards and the unknowns, in-house Sri Lankan zircon standards for U, Th, and He were also analyzed as an independent check on the laser ablation (U-Th)/He protocols. Full procedural details can be found in Horne et al. (2016).

Data reduction for (U-Th)/He dates followed Horne et al. (2016), and U/Pb analyses were carried out using *Iolite 3.65* software (Paton et al., 2011), specifically using the *VizualAge* data reduction scheme (Petrus and Kamber, 2012), which permits *Live Concordia*-aided data reduction. As necessary, common Pb corrections using ^{204}Pb were made. Here, the ^{206}Pb/^{238}U dates are interpreted as zircon crystallization ages, but ^{207}Pb/^{235}U dates calculated from measured ^{238}U and an assumed ^{238}U/^{235}U ratio of 137.818 are also reported. All data are reported in Appendix E. All date uncertainties are reported at the 2σ level. Zircon age peaks are defined based on probability density function (PDF) plots that sum a Gaussian distribution of each measurement based on the date and analytical precision (Sircombe, 2000). Of note, the large spot sizes for U-Th-Pb measurements with the LADD technique precludes separate analyses of core and rim zircon components, and dates may represent only the core material, overgrowth material, or composite ages when the analytical footprint overlaps the core and rim domains.

5.4.3 Apatite (U-Th)/He dating

Apatites were physically separated using the same procedures as the zircons. 10 grains per sample were picked and mounted in niobium tubes. Grains were chosen to be $\geq$ 100 μm in diameter, euhedral in shape, and free of any visible inclusions. The dimensions of the apatite crystals were measured prior to analysis to allow for alpha ejection corrections (Farley et al., 1996; Hourigan et al., 2005).

Analyses were conducted at the Group 18 Laboratories at Arizona State University. A full description of conventional (U-Th)/He methodology in the Group 18 laboratories can be found in van Soest et al. (2011). Helium measurements were made using an ASI *Alphachron* analytical system. The *Alphachron* system uses a 980 nm (IR) diode laser for gas extraction and a Balzers Prisma QMS 200 quadrupole mass spectrometer for isotopic analyses. Apatite grains were heated for five minutes at 9 A, and extracted gases were mixed with a ^{3}He spike and cleaned of any reactive gases before quadrupole analyses. Empty niobium tubes were also included in each run to allow for system blank corrections, and shards of Durango apatite (32.2 ± 0.51 Ma; Chew et al., 2014) were analyzed as age standards.

After ^{4}He analysis, the samples were removed from the laser chamber and dissolved for U and Th analysis following dissolution procedures outlined in Evans et al. (2005). U and Th analyses were conducted by solution ICPMS using the *iCAP Q* instrument. Apatite dates were corrected for alpha ejection following Hourigan et al. (2005) assuming a uniform U-Th distribution. All reported date uncertainties of individual grains are reported at the 2σ level. All data are reported in Appendix E.

5.5 Results

5.5.1 Detrital apatite (U-Th)/He dates

Sixty-five apatites yielded (U-Th)/He dates that ranged from 4.58 ± 0.50 to 209.1 ± 5.4 Ma (Figure 5.4). Only one sample, CHB14-2B-35E-1, yielded apatite (U-Th)/He dates older than 80 Ma, with three dates ranging from ~115 to ~210 Ma. Across the other samples, apatite (U-Th)/He dates were primarily concentrated < 40 Ma, with age peaks at ~18 Ma, ~14 Ma, and ~9 Ma.

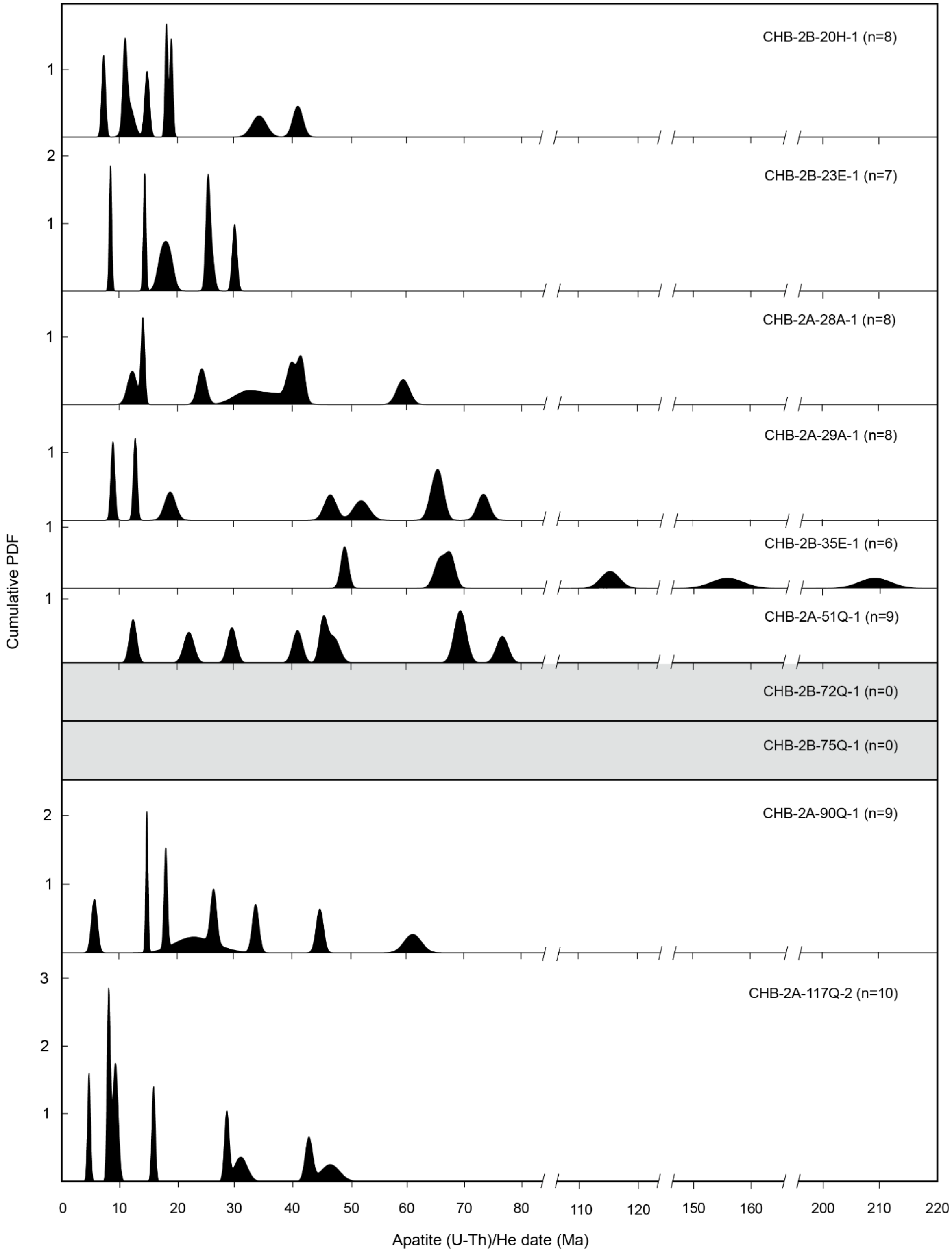

Figure 5.4 Cumulative probability density function (PDF) plots of detrital apatite (U-Th)/He dates. All dates are < 80 Ma, aside from three grains dated > 100 Ma.

5.5.2 Detrital zircon LADD

Zircons yielded $^{206}Pb/^{238}U$ dates with a distinct cluster at ~19.5 Ma, a somewhat broader distribution at ~550 and ~500 Ma, and small clusters ranging across the Neoproterozoic (Figure 5.5). Concentrations of zircons dated at ~19.5 Ma varied considerably among the samples, with CHB14-2A-51Q-1 yielding the highest abundance of ~19.5 Ma grains (n=15), and CHB14-2A-117Q-2 yielding the lowest abundance (n=1). Only four zircons yielded Cenozoic $^{206}Pb/^{238}U$ dates outside of the ~19.5 Ma age peak. Sample CHB14-2B-72Q-1 yielded the youngest date of 3.49 ± 0.55 Ma. Sample CHB14-2A-29A-1 yielded one date of 24.8 ± 1.4 Ma, and samples CHB14-2B-23E-1 and CHB14-2B-35E-1 each yielded a date of ~28 Ma. Many samples yielded individual zircons with Paleozoic to Early Mesozoic $^{206}Pb/^{238}U$ dates. All samples yielded high abundances of Early Cambrian and Precambrian zircon dates, with the oldest date of 945 ± 22 Ma from sample CHB14-2B-75Q-1.

Zircons yielded (U-Th)/He PDFs with fewer distinctive clusters than the $^{206}Pb/^{238}U$ data for the same zircons (Figure 5.5). This observation is in part reflective of the higher analytical precision of the $^{206}Pb/^{238}U$ dates, as well as the protracted cooling history of most of the source rocks. Zircons with statistically indistinguishable $^{206}Pb/^{238}U$ and (U-Th)/He dates plot along the 1:1 reference line in Figure 5.6. Such crystals experienced simple, post-crystallization rapid cooling to ~200–170˚C (Reiners et al., 2005). Zircons with Cenozoic $^{206}Pb/^{238}U$ dates largely fall along the 1:1 line, but many corresponding (U-Th)/He dates are younger, which in this case may either indicate a long zircon residence time prior to eruption/exhumation or a complete/partial resetting of the (U-Th)/He dates by later igneous or hydrothermal activity.

Precambrian and Early Cambrian zircons show a large spread of (U-Th)/He dates, with the majority of dates ranging from crystallization age to ~200 Ma (Figure 5.6). There are minor clusters of (U-Th)/He dates at ~350 Ma, particularly seen in samples CHB14-2B-23E-1 and CHB14-2B-75Q-1. As well, there are small clusters of (U-Th)/He dates at ~100 Ma in samples CHB14-2B-20H-1, 2A-20H-1, 2A-90Q-2, and 2A-117Q-2. Some Paleozoic and Early Mesozoic zircons yielded exceptionally young (U-Th)/He dates, with the youngest date of 1.081 ± 0.057 Ma. There is no observed age-eU correlation amongst (U-Th)/He dates (Appendix E).

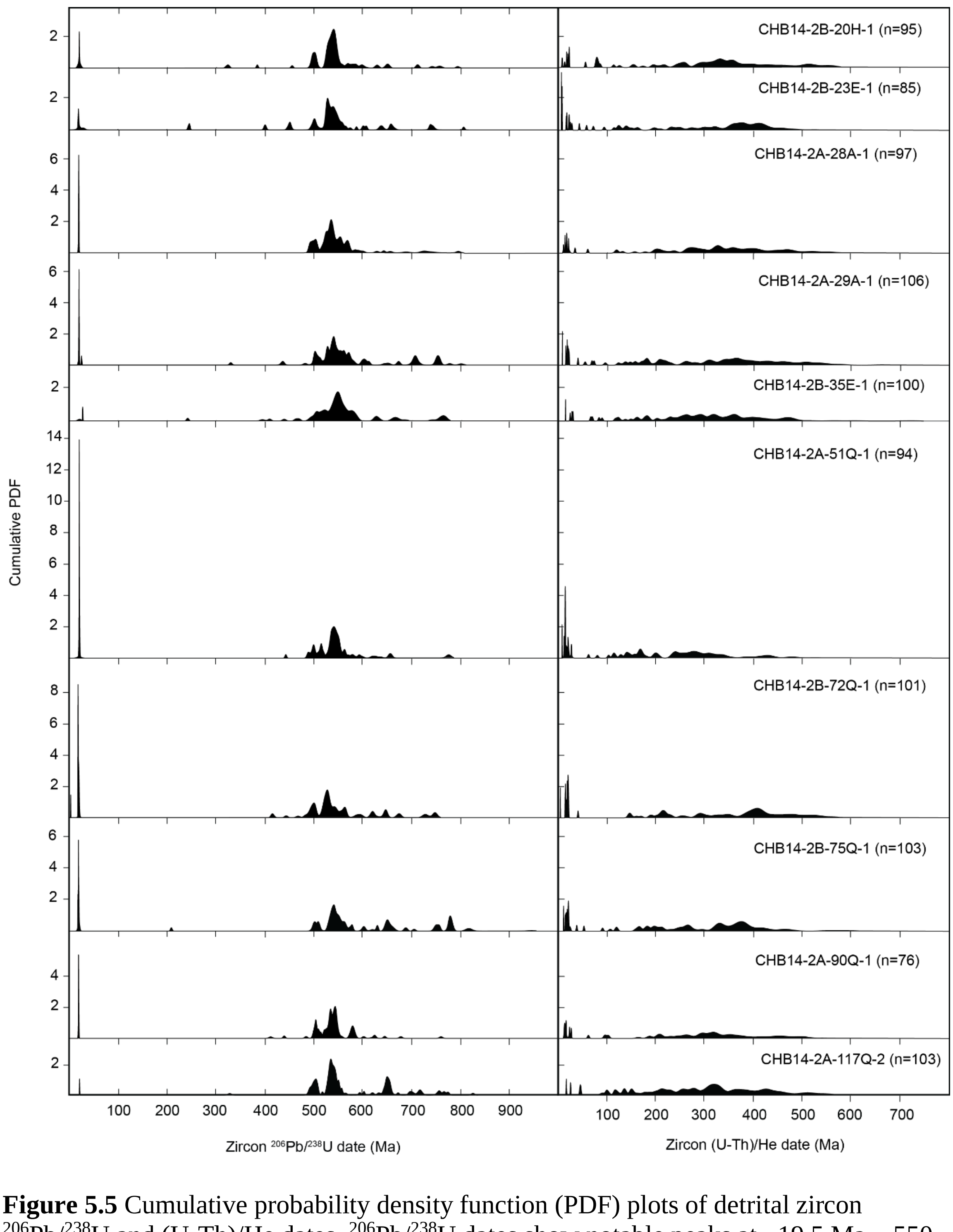

Figure 5.5 Cumulative probability density function (PDF) plots of detrital zircon $^{206}Pb/^{238}U$ and (U-Th)/He dates. $^{206}Pb/^{238}U$ dates show notable peaks at ~19.5 Ma, ~550 Ma, and ~500 Ma. (U-Th)/He dates show significantly more diffuse date peaks.

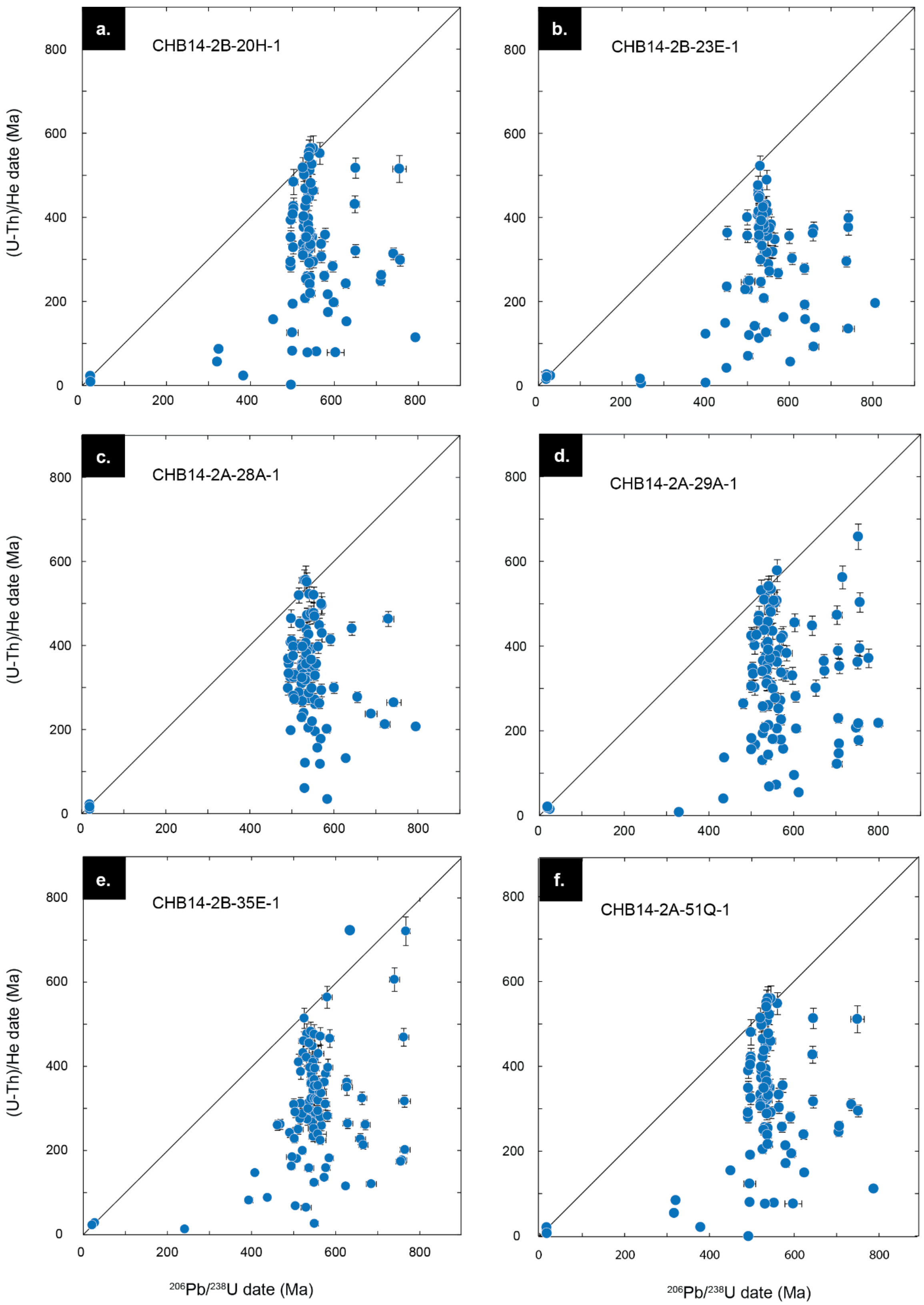
a.
CHB14-2B-20H-1
b.
CHB14-2B-23E-1
c.
CHB14-2A-28A-1
d.
CHB14-2A-29A-1
e.
CHB14-2B-35E-1
f.
CHB14-2A-51Q-1
(U-Th)/He date (Ma)
206Pb/238U date (Ma)
0
200
400
600
800

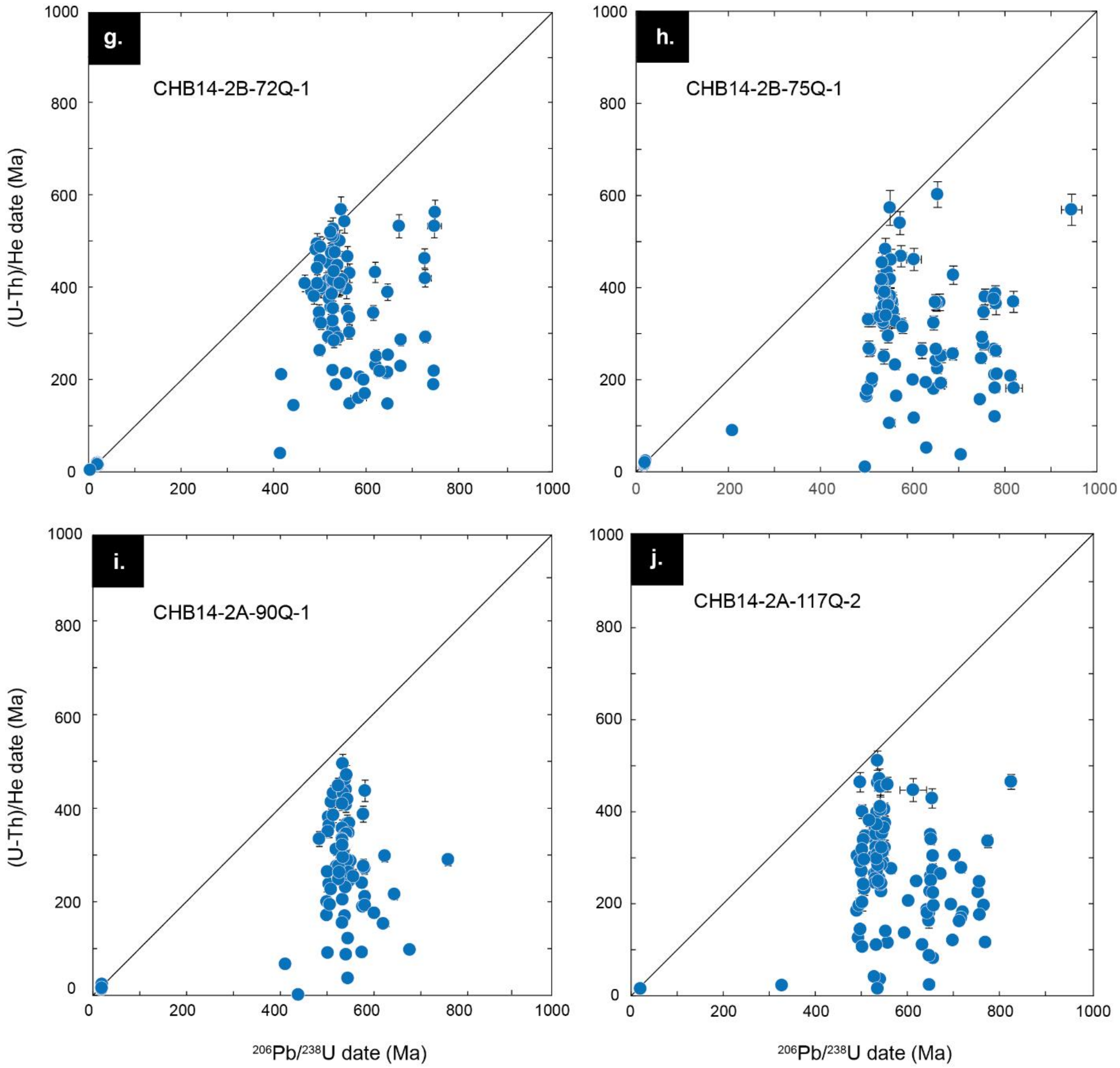

Figure 5.6 Double dating plots of (U-Th)/He vs. $^{206}Pb/^{238}U$ date of detrital zircons. The 1:1 line represents a short duration between zircon crystallization and cooling/eruption of the host volcanic rock. (U-Th)/He dates show a large spread for a given U/Pb age.

5.6 Discussion

5.6.1 Tectonothermal history of the Chew Bahir basin

The abundance of detrital zircons analyzed with the LADD method provides insight into tectonothermal events in southern Ethiopia during the Precambrian and beyond. There are no zircons that correspond with either the Adola tectonothermal event

(1157 ± 2 to 1030 ± 40 Ma) or the Bulbul–Awata tectonothermal event (~876 ± 5 Ma) (Figure 5.7) (Yibas et al., 2002). The oldest cluster of zircon $^{206}Pb/^{238}U$ dates are related to the Megado tectonothermal event 770–720 Ma (Figure 5.7) (Yibas et al., 2002). This event included emplacement of granitoids either in attenuated continental crust or in a subduction-related setting that was associated with the closure of the Megado oceanic basin (Yibas, 2000).

The detrital zircons also record the Moyale tectonothermal event (700–550 Ma), which is concentrated at ~660 Ma (Figure 5.7) (Stern et al., 2012; Yibas et al., 2002). The Moyale tectonothermal event is related to the closure of the Moyale oceanic basin with protracted subduction-related granitic magmatism (Yibas, 2000).

The majority of the detrital zircons from the Chew Bahir basin temporally correlate with the Berguda tectonothermal event (~550–500 Ma) (Figure 5.7) and are derived from late- to post-tectonic, post-orogenic granitoids that are associated with uplift and final cooling that marks the end of the East African Orogen (Yibas et al., 2002). The most intense period of granitic magmatism occurred between 580 to 540 Ma (Ayalew and Gichile 1990), with granitoid intrusion continuing until ~470 Ma (Küster and Harms 1998). Based on the crystallization ages of the detrital zircons, the Chew Bahir region experienced significant magmatism and/or deformation until ~500 Ma.

(U-Th)/He dates of Precambrian and Early Cambrian zircons show a protracted spread over time (Figure 5.7). Some zircons experienced rapid cooling and exhumation during emplacement, where they fall along a 1:1: line of $^{206}Pb/^{238}U$ and (U-Th)/He dates.

The continuous spread in dates over time reflects the long, sustained ature of cooling and uplift after the East African Orogen.

Although it is difficult to discern individual populations of (U-Th)/He dates amongst all the Precambrian and Early Cambrian zircons (Figure 5.7), individual samples potentially record other younger resetting episodes (Figures 5.5a, f, i, and j). For example, the clusters of (U-Th)/He dates at ~100 Ma observed in a number of samples are similar to the ~97–95 Ma emplacement ages of basaltic dike intrusions in the region (Ebinger et al., 2000), and may thus regionally provide restricted heating of some zircon source rocks.

Interestingly, some Paleozoic-aged zircons yielded exceptionally young (U-Th)/He dates, even younger than the (U-Th)/He dates of any of the Cenozoic volcanic zircons (Figure 5.7 and 5.8). Detrital zircons from the Awash and Omo-Turkana basins show extensive evidence of partial resetting of (U-Th)/He dates due to volcanic heating and/or hydrothermal activity, including post-depositional resetting from hydrothermal heating (Zawacki et al., *in review*). These young (U-Th)/He dates suggest partial or full resetting due to volcanic/hydrothermal processes related to recent EARS activity and/or heating from faulting. The small proportion of young zircon (U-Th)/He dates would suggest that volcanic/hydrothermal heating is a less pervasive prolific process within the Chew Bahir basin than Afar or Omo-Turkana apparently.

The Cenozoic volcanic zircons also show a degree of variability in their (U-Th)/He dates (Figure 5.8) that may be related to subsequent volcanic heating after eruption. The ~19.5 Ma volcanic zircons yielded (U-Th)/He dates as young 8.20 ± 1.4

Ma, with a small peak at ~14 Ma. The ~14.5 Ma Kumbi rhyolitic tuffs and lavas overlie the Teltele basalts on the Teltele Plateau and could provide a heat source to cause resetting of (U-Th)/He dates (Cooper et al., 2011).

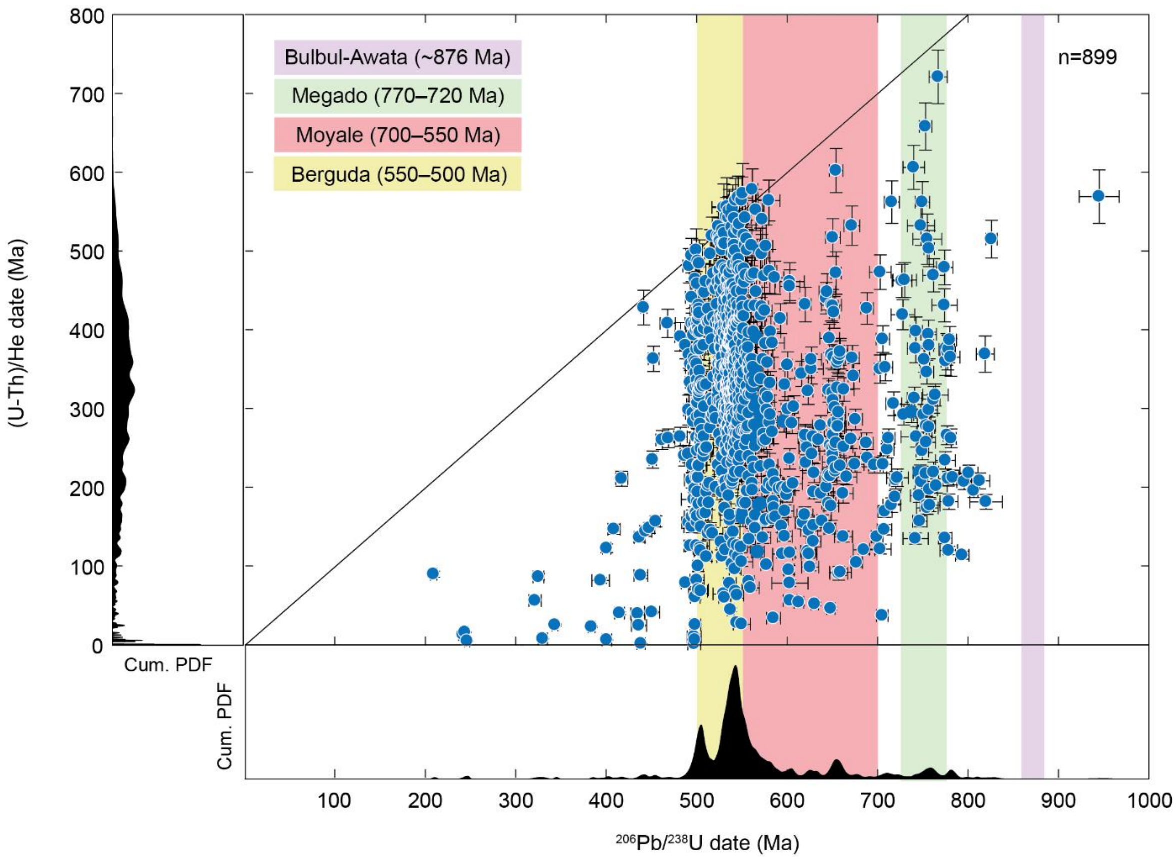

Figure 5.7 Double dating plots of (U-Th)/He vs. $^{206}Pb/^{238}U$ date of CHB detrital zircons with corresponding cumulative PDF plots excluding Cenozoic age zircons and associated tectonothermal events observed in the Precambrian of southern Ethiopia (Yibas et al., 2002). The majority of zircons are associated with the Berguda event and the end of the Moyale event.

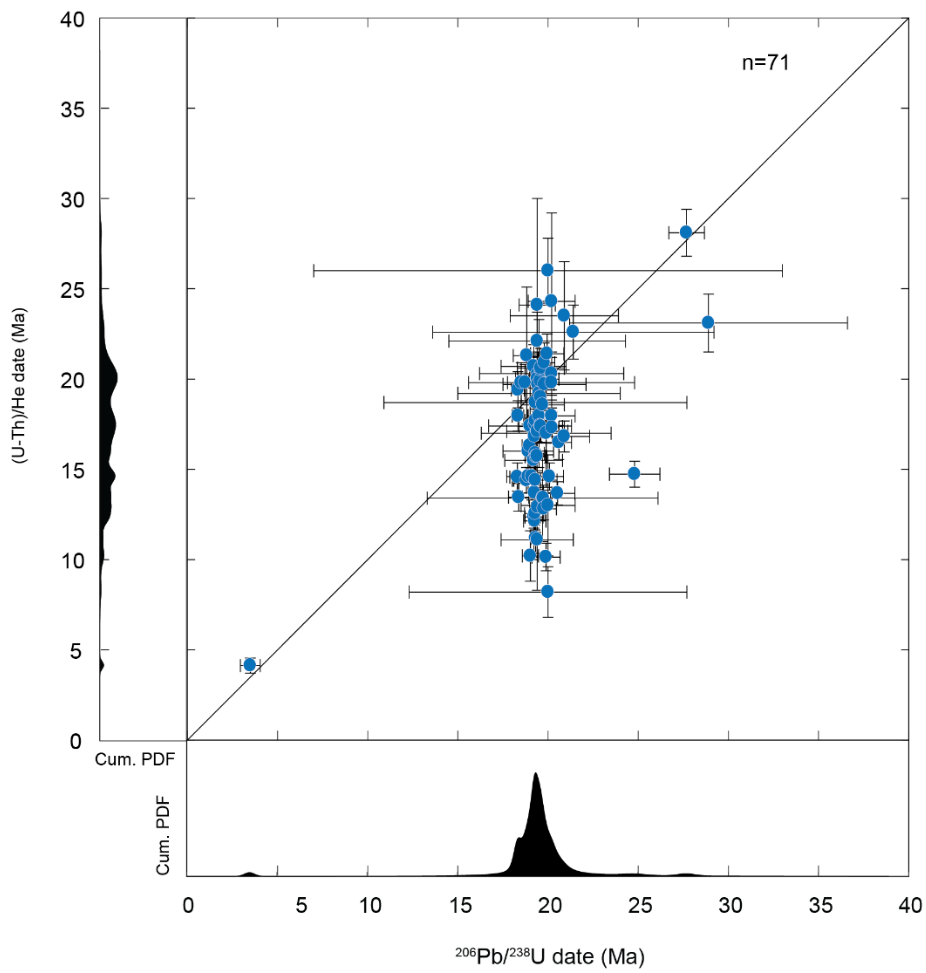

Figure 5.8 Double dating plots of (U-Th)/He vs. $^{206}Pb/^{238}U$ date of CHB Cenozoic volcanic detrital zircons with corresponding cumulative PDF plots. (U-Th)/He dates show a minor degree of spread away from the 1:1 line, which represents a short duration between zircon crystallization eruption of the host volcanic rock.

5.6.2 Evaluating timing of Cenozoic rift initiation

Understanding the degree of (U-Th)/He resetting from volcanic/hydrothermal heating in the double dated zircons is important in interpreting detrital apatite (U-Th)/He dates, due to the significantly lower (~70°C) closure temperature of the apatite (U-Th)/He system (Ehlers and Farley, 2003). The zircon LADD data overall suggest that there is minimal volcanic and/or hydrothermal resetting of (U-Th)/He dates and that (U-Th)/He dates are largely representative of bedrock cooling ages related to exhumation.

The detrital apatite (U-Th)/He dates provide additional constraints on the timing of rift initiation related to the modern EARS in the Chew Bahir basin. We compare our detrital apatite (U-Th)/He data to bedrock apatite (U-Th)/He dates from the Hammar Range published in Pik et al. (2008) (Figure 5.9). Pik et al. (2008) determined rifting initiated at ~20 Ma, which is consistent with the ~20–17 Ma timing determined for rift initiation of the Gofa Province basins to the north (Boone et al., 2019).

The detrital apatite data captures the predominant age peaks in the bedrock data from Pik et al. (2008), although the detrital apatites examined here yield additional (U-Th)/He age peaks not observed in the bedrock samples (Figure 5.9). The detrital apatite (U-Th)/He dates show notable age peaks < 20 Ma. The age peak at ~18–19 Ma may be artificially inflated if any of the apatites are volcanic and related to the ~19.5 Ma episode of volcanism along the Teltele Plateau, the but the pattern of age distributions of detrital apatites largely matches the ages from bedrock. The greater diversity in detrital apatite (U-Th)/He dates is likely a result of the detrital record sourcing from bedrock throughout the basin with more variable cooling histories than were sampled explicitly by Pik et al. (2008).

The correspondence of detrital apatite (U-Th)/He dates with bedrock apatite (U-Th)/He dates and significant increase in age peaks after ~20 Ma supports control by initiation of rifting in the Chew Bahir basin ~20 Ma on their ages. The continued abundance and peaks in detrital apatite (U-Th)/He dates after ~20 Ma also supports that rift development and erosion along the footwalls has been continuous since the Miocene. The volcanism at ~20 Ma along the Teltele Plateau thus suggest that major volcanism in the region was coeval with the initiation of rifting.

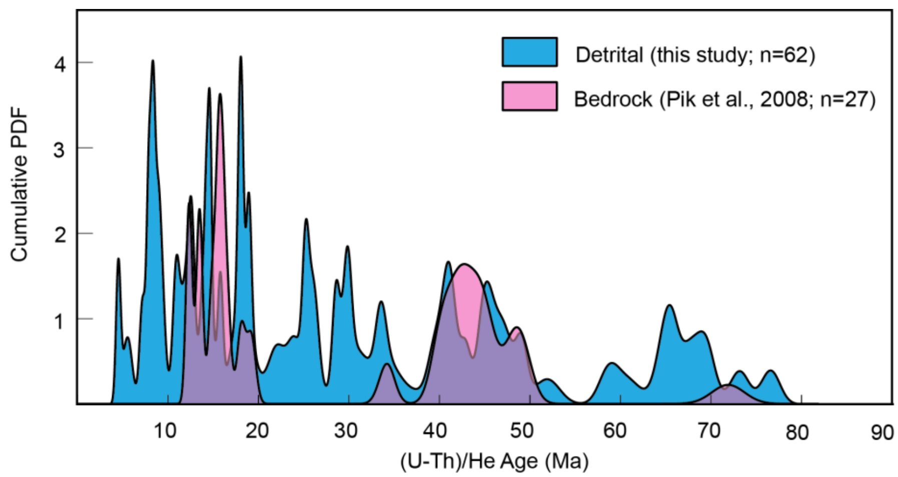

Figure 5.9 Cumulative PDF plots of detrital apatite (U-Th)/He dates excluding three dates > 100 Ma, compared to bedrock apatite (U-Th)/He dates from Pik et al. (2008).

5.6.3 Sediment provenance and Pleistocene basin dynamics

Unlike the detrital zircon records of the Awash and Omo-Turkana basins that are dominated by Cenozoic volcanic zircons that record most phases of East African Rift-related volcanism (Zawacki et al., *in review*), the detrital zircons from the Chew Bahir basin record a limited phase of Cenozoic volcanism and contain a high abundance of zircons derived from crystalline bedrock of the watershed. The distinct ~19.5 Ma peak in zircon $^{206}Pb/^{238}U$ dates temporally correlates with the Teltele basalts from the Teltele Plateau bounding the basin to the east (Ebinger et al., 2000), recording an associated silicic phase of volcanism (Figure 5.2). The variable concentration of ~19.5 Ma zircons across samples likely reflects tectonically controlled sediment pulses from the Teltele Plateau. The concentration of ~19.5 Ma zircons shows an increase in samples deposited from ~617 to ~213 ka (Figure 5.5), indicating a continued increase in sedimentary input from the eastern basin margin over time. After ~213 ka, the number of ~19.5 Ma gains per sample shows significant variability, which may indicate a combination of enhanced climate-modulated variability and/or episodes of faulting impacting sedimentation from the eastern margin. The hydroclimate proxy record of the CHB core indicates a shift at ~210 ka onward that shows a long-term aridification trend, with a distinct increase in variability and amplitude (Foerster et al., *in review*). This shift to greater environmental variability is consistent with the greater variability in sediment input after ~213 ka.

Although the ~14.5 Ma Kumbi rhyolitic tuff and lavas overlie the Teltele basalts and a rhyolitic tuff from a landslide deposit in the southern portion of the basin was dated at 14.0 ± 1.0 Ma (Ebinger et al., 2000), the CHB samples did not yield any zircons of this age. This observation is interesting due to the silicic nature of the volcanic products. Either zircons are not present in these particular units, or they represent a small to negligible sedimentary contribution in the basin.

Exposures of the Amaro/Gamo unit overlie basement units in the northern portion of the basin, but the exposures are predominantly basaltic, and no zircons corresponding to the ages of Amaro/Gamo unit were not found in any samples. Exposures of more extensive rhyolitic sections of the Amaro/Gamo unit are found farther north and west of the Chew Bahir basin, indicating no evidence of inter-basin transport of silicic Amaro/Gamo products related to basin spillover events. However, the two zircons with $^{206}Pb/^{238}U$ dates of ~28 Ma do not correlate to any known units found within the Chew Bahir basin. These dates do temporally correlate with the Makonnen basalt found just outside the northeast extent of the basin. The Makonnen basalts have been dated from 28.8 to 34.8 Ma (Davidson, 1983), although there is a notable absence of silicic volcanism within the Makonnen basalts sequence (Rooney, 2017). The ~28 Ma and ~24 Ma zircons may record limited amounts of silicic activity outside of the basin that then entered the watershed, they may be related to small previously unmapped units within the basin, or the resulting dates may be a hybrid of core-rim ages from the LADD technique.

The single 3.49 ± 0.55 Ma zircon temporally correlates with basalts found in the southernmost extent of the Chew Bahir basin and may be derived from associated silicic volcanism. The lack of additional zircons of this age either indicates a lack of zircon-bearing volcanic units in the south and/or limited to no transport of materials from the southern portion of the basin northwards.

Crystalline basement composes the majority of the source units for the Chew Bahir basin (Figure 5.5), and detrital zircon $^{206}Pb/^{238}U$ dates constrain the ages of the source terranes primarily between ~800 to ~500 Ma, which are consistent with dates of basement units from southern Ethiopia (Asrat et al., 2001; Teklay et al., 1998; Yibas et al., 2000). The majority of zircons dated to ~550 Ma are likely derived from the Alghe Group (559.9 ± 0.9 Ma; Teklay et al., 1998) and associated granites, which are exposed along the western and eastern portions of the Chew Bahir basin (Figure 5.2). The abundance of these zircons reflects the high sedimentary influx from alluvial fans draining the Hammar Range.

Samples also yielded zircons with dates correlated to the ~450 Ma Konso pluton (Asrat and Barbey, 2003), and ~785–702 and ~630 Ma plutonic and high-grade metamorphic rocks (Verner et al., 2021) exposed within the northern-central portion of the basin. Detrital zircons derived from these units would be related to transport from the Weyto and Segen rivers that drain the northern portions of the basin.

Over the ~620 kyr record of the CHB core, the detrital zircon record reflects variable pulses of sediment input from the eastern margin, likely due to episodes of fault activity combined with wet phases, with somewhat more consistent sedimentary input from the western margin. Sedimentary input from the northern portions of the basin via the Weyto and Segen rivers appear to be more limited, as transport is dependent on climate conditions that support river flow. Increased variability in sediment sourcing occurs after ~200 ka, with a consistent with the timing of increased climatic variability and amplitude observed in the CHB proxy record (Foerster et al., *in review*).

Based on the detrital zircon record alone, it is difficult to identify distinct episodes of basin spillover events. However, the Paleozoic zircons with exceptionally young (U-Th)/He dates may be derived from adjacent basins where there is more notable volcanic and/or hydrothermal sources of heating, like the Omo-Turkana (Zawacki et al., *in review).* The mineralogical record of the CHB core reflects an authigenic mineral assemblage consistent with environments of enhanced evaporative concentration (Gebregiorgis et al., 2021). This record differs from that of the Northern Awash (Ethiopia) and West Turkana (Kenya) HSPDP drill cores that have mineral assemblages and additional features consistent with high-temperature hydrothermal alteration (Zawacki et al., *in review*). Considering the paucity of evidence for hydrothermal alteration within the Chew Bahir basin, the zircons with exceptionally young (U-Th)/He dates provide the strongest evidence for inter-basin transport.

5.7 Conclusions

The detrital mineral record from the HSPDP-CHB drill cores provides a Neoproterozoic to Pleistocene record of the thermo-magmatic, tectonic, volcanic, and geomorphic evolution of southern Ethiopia. The zircon LADD dataset provides abundant new dates to better understand the timing of Neoproterozoic and Early Phanerozoic of magmatism and tectonothermal events in southern Ethiopia. The crystalline bedrock exposed within the Chew Bahir basin is associated with the Megado (770–720 Ma), Moyale (700–550 Ma), and Berguda (550–500 Ma) tectonothermal events that impacted southern Ethiopia (Yibas et al., 2002). The majority of zircons dated at ~550–500 Ma are derived from late- to post-tectonic, post-orogenic granitoids that mark the end of the East African Orogen. Since magmatic emplacement in the Late Neoproterozoic to Early Cambrian, zircon (U-Th)/He dates show subsequent uplift and long, protracted cooling of these terranes.

Detrital apatite (U-Th)/He dates are consistent with bedrock apatite dates from the Hammar Range that suggest rift initiation at ~20 Ma. The detrital apatite record is also consistent continual rift development since initiation in the Miocene. The abundance of ~19.5 Ma volcanic zircons and ~20 Ma age of basalts from the Teltele Plateau suggests that major volcanism was coeval with rift initiation in the region at ~20 Ma.

Unlike the extensive record of Cenozoic volcanic zircons related to EARS volcanic activity found in large basins like the Awash and Omo-Turkana, Cenozoic volcanic zircons in the Chew Bahir basin are restricted to ~19.5 Ma silicic units from the Teltele basalts on the Teltele Plateau bounding the basin to the east. Sediment input from the eastern basin margin is variable over time, likely related to input from pulses of tectonic activity combined with wet phases. Crystalline basement units of the Hammar Range dated between ~550–500 Ma constitute the majority of the sediment influx in the basin, with lesser contribution from Neoproterozoic units exposed in the north transported by the Weyto and Segen rivers, which are more controlled by climatic conditions than tectonic. The detrital zircon record alone cannot definitively distinguish episodes of basin spillover from adjacent basins into the Chew Bahir basin, but Paleozoic zircons with young (U-Th)/He dates may be derived from other basins with more substantial sources of volcanic and/or hydrothermal heating.

5.8 References

Anderson, A. J., M. C. van Soest, K. V. Hodges, and J. M. Hanchar (2020). Helium diffusion in zircon: Effects of anisotropy and radiation damage revealed by laser depth profiling. *Geochimica et Cosmochimica Acta*, 274, p. 45– 62. https://doi.org/10.1016/j.gca.2020.01.049

Asrat, Asfawossen, and Pierre Barbey (2003). Petrology, geochronology and Sr–Nd isotopic geochemistry of the Konso pluton, south-western Ethiopia: implications for transition from convergence to extension in the Mozambique Belt. *International Journal of Earth Sciences*, 92, 6, p. 873–890. https://doi.org/10.1007/s00531-003-0360-9

Asrat, Asfawossen, P. Barbey, and G. Gleizes (2001). The Precambrian geology of Ethiopia: a review. *Africa Geoscience Review*, 8, 3/4, p. 271–288.

Ayalew, Teklewold, and Samuel Gichile (1990). Preliminary U-Pb ages from southern Ethiopia. Publication occasionnelle-Centre international pour la formation et les échanges géologiques, 22, p. 127–130.

Baker, Brian Howard, Paul A. Mohr, and Laurence Albert Joseph Williams (1972). Geology of the eastern rift system of Africa. *Geological Society of America Special Papers*, 136, p. 1–68. https://doi.org/10.1130/SPE136-p1

Balestrieri, Maria Laura, Marco Bonini, Giacomo Corti, Federico Sani, and Melody Philippon (2016). A refinement of the chronology of rift-related faulting in the Broadly Rifted Zone, southern Ethiopia, through apatite fission-track analysis. *Tectonophysics*, 671, p. 42–55. https://doi.org/10.1016/j.tecto.2016.01.012

Boone, S. C., M-L. Balestrieri, B. P. Kohn, G. Corti, A. J. W. Gleadow, and C. Seiler (2019). Tectonothermal evolution of the Broadly Rifted Zone, Ethiopian Rift. *Tectonics*, 38, p. 1070–1100. https://doi.org/10.1029/2018TC005210

Campisano, C. J., A.S. Cohen, J.R. Arrowsmith, A. Asrat, A.K. Behrensmeyer, E.T. Brown, A.L. Deino, D.M. Deocampo, C.S. Feibel, J.D. Kingston, H.F. Lamb, T.K. Lowenstein, A. Noren, D.O. Olago, R.B. Owen, J.D. Pelletier, R. Potts, K.E. Reed, R.W. Renaut, J.M. Russell, J.L. Russell, F. Schabitz, J.R. Stone, M.H. Trauth, and J.G. Wynn (2017). The Hominin Sites and Paleolakes Drilling Project: High-resolution paleoclimate records from the East African rift system and their implications for understanding the environmental context of hominin evolution. *PaleoAnthropology*, p. 1–43. https://doi:10.4207/PA.2017.ART104

Chernet, Tadiwos, William K. Hart, James L. Aronson, and Robert C. Walter (1998). New age constraints on the timing of volcanism and tectonism in the northern

Main Ethiopian Rift–southern Afar transition zone (Ethiopia). *Journal of Volcanology and Geothermal Research*, 80, 3-4, p. 267–280. https://doi.org/10.1016/S0377-0273(97)00035-8

Chew, D.M., Petrus, J.A. and Kamber, B.S. (2014). U–Pb LA–ICPMS dating using accessory mineral standards with variable common Pb. *Chemical Geology*, 363, p. 185–199. https://doi.org/10.1016/j.chemgeo.2013.11.006

Chorowicz, Jean (2005). The East African Rift System. *Journal of African Earth Sciences*, 43, 1-3, p. 379–410. https://doi.org/10.1016/j.jafrearsci.2005.07.019

Cohen, A., C. Campisano, R. Arrowsmith, A. Asrat, A.K. Behrensmeyer, A. Deino, C. Feibel, A. Hill, R. Johnson, J. Kingston, H. Lamb, T. Lowenstein, A. Noren, D. Olago, R.B. Owen, R. Potts, K. Reed, R. Renaut, F. Schäbitz, J.-J. Tiercelin, M.H. Trauth, J. Wynn, S. Ivory, K. Brady, R. ÓGrady, J. Rodysill, J. Githiri, J. Russell, V. Foerster, R. Dommain, S. Rucina, D. Deocampo, J. Russell, A. Billingsley, C. Beck, G. Dorenbeck, L. Dullo, D. Feary, D. Garello, R. Gromig, T. Johnson, A. Junginger, M. Karanja, E. Kimburi, A. Mbuthia, T. McCartney, E. McNulty, V. Muiruri, E. Nambiro, E.W. Negash, D. Njagi, J.N. Wilson, N. Rabideaux, T. Raub, M.J. Sier, P. Smith, J. Urban, M. Warren, M. Yadeta, C. Yost, and B. Zinaye (2016). The Hominin Sites and Paleolakes Drilling Project: inferring the environmental context of human evolution from eastern African rift lake deposits, Sci. Dril., 21, p. 1–16. https://doi.org/10.5194/sd-21-1-2016

Cooper, Frances J., Matthijs C. van Soest, and Kip V. Hodges (2011). Detrital zircon and apatite (U-Th)/He geochronology of intercalated baked sediments: A new approach to dating young basalt flows. *Geochemistry, Geophysics*, Geosystems, 12, 7, p. 1–8. https://doi.org/10.1029/2011GC003650

Davidson, Anthony (1983). The Omo river project, reconnaissance geology and geochemistry of parts of Ilubabor, Kefa, Gemu Gofa and Sidamo, *Ethiopian Institute of Geological Surveys Bulletin*, 2, p. 1–89.

Davidson, A., and D. C. Rex (1980). Age of volcanism and rifting in southwestern Ethiopia. *Nature*, 283, 5748, p. 657–658. https://doi.org/10.1038/283657a0

deMenocal, Peter, B. (2004). African climate change and faunal evolution during the Pliocene–Pleistocene. *Earth and Planetary Science Letters*, 220, 1-2, p. 3–24. https://doi.org/10.1016/S0012-821X(04)00003-2

Ebinger, C. J., Tilahun Yemane, D. J. Harding, Samson Tesfaye, S. Kelley, and D. C. Rex (2000). Rift deflection, migration, and propagation: Linkage of the Ethiopian and Eastern rifts, Africa. *Geological Society of America Bulletin*, 112, 2, p. 163–176. https://doi.org/10.1130/0016-7606(2000)112<163:RDMAPL>2.0.CO;2

Ebinger, C. J., Tesfaye Yemane, Giday Woldegabriel, J. L. Aronson, and R. C. Walter (1993). Late Eocene–Recent volcanism and faulting in the southern main Ethiopian rift. *Journal of the Geological Society*, 150, 1, p. 99–108. https://doi.org/10.1144/gsjgs.150.1.0099

Ehlers, Todd A., and Kenneth A. Farley (2003). Apatite (U–Th)/He thermochronometry: methods and applications to problems in tectonic and surface processes. *Earth and Planetary Science Letters*, 206, 1-2, p. 1–14. https://doi.org/10.1016/S0012-821X(02)01069-5

Emishaw, Luelseged, Daniel A. Laó-Dávila, Mohamed G. Abdelsalam, Estella A. Atekwana, and Stephen S. Gao (2017). Evolution of the broadly rifted zone in southern Ethiopia through gravitational collapse and extension of dynamic topography. *Tectonophysics*, 699, p. 213–226. https://doi.org/10.1016/j.tecto.2016.12.009

Evans, N. J., J. P. Byrne, J. T. Keegan, and L. E. Dotter (2005). Determination of uranium and thorium in zircon, apatite, and fluorite: Application to laser (U-Th)/He thermochronology. *Journal of Analytical Chemistry*, 60, 12, p. 1159-1165. https://doi.org/10.1007/s10809-005-0260-1

Farley, Kenneth A. (2002). (U-Th)/He dating: Techniques, calibrations, and applications. *Reviews in Mineralogy and Geochemistry*, 47, 1, p. 819-844. https://doi.org/10.2138/rmg.2002.47.18

Farley, K. A., R. A. Wolf, and L. T. Silver (1996). The effects of long alpha-stopping distances on (U-Th)/He ages. *Geochimica et Cosmochimica Acta*, 60, 21, p. 4223–4229. https://doi.org/10.1016/S0016-7037(96)00193-7

Fischer, Markus, Monika Markowska, Felix Bachofer, Verena Foerster, Asrat Asfawossen, Christoph Zielhofer, Martin Trauth, and Annett Junginger (2020). Determining the Pace and Magnitude of Lake Level Changes in Southern Ethiopia Over the Last 20,000 Years Using Lake Balance Modeling and SEBAL. *Frontiers in Earth Science*, 8, 197, p. 1–21. https://doi.org/10.3389/feart.2020.00197

Foerster, Verena, Asfawossen Asrat, Christopher Bronk Ramsey, Erik T. Brown, Melissa S. Chapot, Alan Deino, Daniel M. Deocampo, Walter Duesing, Annette Hahn, Annett Junginger, Stefanie Kaboth-Bahr, Christine S. Lane, Stephan Opitz, Anders Noren, Helen M. Roberts, Mona Stockhecke, Ralph Tiedemann, Céline Vidal, Ralf Vogelsang, Andrew S. Cohen, Henry F. Lamb, Frank Schaebitz, and Martin H. Trauth. 620,000 years of eastern Africa climate variability and hominin evolution. *Nature Geoscience* (In review).

Foerster, Verena, Annett Junginger, Oliver Langkamp, Tsige Gebru, Asfawossen Asrat, Mohammed Umer, Henry F. Lamb, Volker Wenrich, Janet Rethemeyer, Norbert Nowaczyk, Martin H. Trauth, and Frak Schaebitz (2012). Climatic change recorded in the sediments of the Chew Bahir basin, southern Ethiopia, during the last 45,000 years. *Quaternary International*, 274, p. 25–37. https://doi.org/10.1016/j.quaint.2012.06.028

Fritz, H., M. Abdelsalam, K. A. Ali, B. Bingen, A. S. Collins, A. R. Fowler, W. Ghebreab, C.A. Hauzenberger, P.R. Johnson, T.M. Kusky, P. Macey, S. Muhongo, R.J. Stern, and G. Viola (2013). Orogen styles in the East African Orogen: A review of the Neoproterozoic to Cambrian tectonic evolution. *Journal of African Earth Sciences*, 86, p. 65–106. https://doi.org/10.1016/j.jafrearsci.2013.06.004

Gebregiorgis, Daniel, Daniel M. Deocampo, Verena Foerster, Fred J. Longstaffe, Jeremy S. Delaney, Frank Schaebitz, Annett Junginger, Monika Markowska, Stephan Opitz, Martin H. Trauth, Henry F. Lamb, and Asfawossen Asrat (2021). Modern sedimentation and authigenic mineral formation in the Chew Bahir Basin, southern Ethiopia: implications for interpretation of Late Quaternary paleoclimate records. *Frontiers in Earth Science*, 9 (2021): 244. https://doi.org/10.3389/feart.2021.607695

Gehrels, George E., William R. Dickinson, Gerald M. Ross, John H. Stewart, and David G. Howell (1995). Detrital zircon reference for Cambrian to Triassic miogeoclinal strata of western North America. *Geology*, 23, 9, p. 831–834. https://doi.org/10.1130/0091-7613(1995)023<0831:DZRFCT>2.3.CO;2

Grove, Alan T., F. Alayne Street, and A. S. Goudie (1975). Former lake levels and climatic change in the Rift Valley of southern Ethiopia. *Geographical Journal*, p. 177–194. https://doi.org/10.2307/1797205

Hargrove, U. S., R. J. Stern, J-I. Kimura, W. I. Manton, and P. R. Johnson (2006). How juvenile is the Arabian–Nubian Shield? Evidence from Nd isotopes and pre-Neoproterozoic inherited zircon in the Bi'r Umq suture zone, Saudi Arabia. *Earth and Planetary Science Letters*, 252, 3-4, p. 308–326. https://doi.org/10.1016/j.epsl.2006.10.002

Horne, Alexandra M., Matthijs C. van Soest, Kip V. Hodges, Alka Tripathy-Lang, and Jeremy K. Hourigan (2016). Integrated single crystal laser ablation U/Pb and (U–Th)/He dating of detrital accessory minerals–Proof-of-concept studies of titanites and zircons from the Fish Canyon tuff. *Geochimica et Cosmochimica Acta*, 178, p. 106–123. https://doi.org/10.1016/j.gca.2015.11.044

Hourigan, J. K., P. W. Reiners, and M. T. Brandon (2005). U-Th zonation-dependent alpha-ejection in (U-Th)/He chronometry. *Geochimica et Cosmochimica Acta*, 69, 13, p. 3349–3365. https://doi.org/10.1016/j.gca.2005.01.024

Küster, Dirk, and Ulrich Harms (1998). Post-collisional potassic granitoids from the southern and northwestern parts of the Late Neoproterozoic East African Orogen: a review. *Lithos*, 45, 1-4, p. 177–195. https://doi.org/10.1016/S0024-4937(98)00031-0

Moore, J.M., Davidson, A. (1978). Rift structure in southern Ethiopia. *Tectonophysics*, 46, p. 159–173. https://doi.org/10.1016/0040-1951(78)90111-7

Paton, Chad, John Hellstrom, Bence Paul, Jon Woodhead, and Janet Hergt (2011). Iolite: Freeware for the visualisation and processing of mass spectrometric data. *Journal of Analytical Atomic Spectrometry*, 26, 12, p. 2508–2518. https://doi.org/10.1039/C1JA10172B

Petrus, Joseph A., and Balz S. Kamber (2012). VizualAge: A novel approach to laser ablation ICP-MS U-Pb geochronology data reduction. *Geostandards and Geoanalytical Research*, 36, 3, p. 247–270. https://doi.org/10.1111/j.1751-908X.2012.00158.x

Philippon, Melody, Giacomo Corti, Federico Sani, Marco Bonini, Maria-Laura Balestrieri, Paola Molin, Ernst Willingshofer, Dimitrios Sokoutis, and Sierd Cloetingh (2014). Evolution, distribution, and characteristics of rifting in southern Ethiopia. *Tectonics*, 33, 4, p. 485–508. https://doi.org/10.1002/2013TC003430

Pik, Raphaël, Bernard Marty, Jean Carignan, Gezahegn Yirgu, and Teklewold Ayalew (2008). Timing of East African Rift development in southern Ethiopia: Implication for mantle plume activity and evolution of topography. *Geology*, 36, 2, p. 167–170. https://doi.org/10.1130/G24233A.1

Sircombe, Keith N. (2000). Quantitative comparison of large sets of geochronological data using multivariate analysis: a provenance study example from Australia. *Geochimica et Cosmochimica Acta*, 64, 9, p. 1593–1616. https://doi.org/10.1016/S0016-7037(99)00388-9

Sommer, H., A. Kröner, C. Hauzenberger, S. Muhongo, and M. T. D. Wingate (2003). Metamorphic petrology and zircon geochronology of high-grade rocks from the central Mozambique Belt of Tanzania: crustal recycling of Archean and Palaeoproterozoic material during the Pan-African orogeny. *Journal of Metamorphic Geology*, 21, 9, p. 915–934. https://10.1046/j.1525-1314.2003.00491.x

Stern, Robert James, Kamal A. Ali, Mohamed G. Abdelsalam, Simon A. Wilde, and Qin Zhou (2012). U–Pb zircon geochronology of the eastern part of the Southern Ethiopian Shield. *Precambrian Research*, 206, p. 159–167. https://doi.org/10.1016/j.precamres.2012.02.008

Stern, Robert J. (1994). Arc assembly and continental collision in the Neoproterozoic East African Orogen: implications for the consolidation of Gondwanaland. *Annual Review of Earth and Planetary Sciences*, 22, 1, p. 319–351. https://doi.org/10.1146/annurev.ea.22.050194.001535

Teklay, M., A. Kröner, Klaus Mezger, and R. Oberhänsli (1998). Geochemistry, Pb-Pb single zircon ages and Nd-Sr isotope composition of Precambrian rocks from southern and eastern Ethiopia: implications for crustal evolution in East Africa. *Journal of African Earth Sciences*, 26, 2, p. 207–227. https://doi.org/10.1016/S0899-5362(98)00006-2

Tripathy-Lang, Alka, Kip V. Hodges, Brian D. Monteleone, and Matthijs C. van Soest (2013). Laser (U-Th)/He thermochronology of detrital zircons as a tool for studying surface processes in modern catchments. *Journal of Geophysical Research: Earth Surface*, 118, 3, p. 1333–1341. https://doi.org/10.1002/jgrf.20091

Reiners, Peter W. (2005). Zircon (U-Th)/He thermochronometry." Reviews in Mineralogy and Geochemistry 58, no. 1 (2005): 151-179. https://doi.org/10.2138/rmg.2005.58.6

Reiners, Peter W., I. H. Campbell, Stefan Nicolescu, Charlotte M. Allen, J. K. Hourigan, J. I. Garver, J. M. Mattinson, and D. S. Cowan (2005). (U-Th)/(He-Pb) double dating of detrital zircons. *American Journal of Science*, 305, 4, p. 259–311. https://doi.org/10.2475/ajs.305.4.259

Roberts, Helen M., Christopher Bronk Ramsey, Melissa S. Chapot, Alan L. Deino, Christine S. Lane, Céline Vidal, Asfawossen Asrat, Andrew Cohen, Verena Foerster, Henry F. Lamb, Frank Schaebitz, Martin H. Trauth. Using multiple chronometers to establish a long, directly dated lacustrine record: constraining >600,000 years of environmental change at Chew Bahir, Ethiopia. *Quaternary Science Reviews* (In review).

Rooney, Tyrone O. (2017). The Cenozoic magmatism of East-Africa: Part I — Flood basalts and pulsed magmatism. *Lithos*, 286-287, p. 264–301. https://doi.org/10.1016/j.lithos.2017.05.014

Romans, Brian W., Sébastien Castelltort, Jacob A. Covault, Andrea Fildani, and J. P. Walsh (2016). Environmental signal propagation in sedimentary systems across timescales. *Earth-Science Reviews*, 153, p. 7–29. https://doi.org/10.1016/j.earscirev.2015.07.012

Sláma, Jiří, Jan Košler, Daniel J. Condon, James L. Crowley, Axel Gerdes, John M. Hanchar, Matthew SA Horstwood, George A. Morris, Lutz Nasdala, Nicholas Norberg, Urs Schaltegger, Blair Shoene, Michael N. Tubrett, and Martin J. Whitehouse (2008). Plešovice zircon—a new natural reference material for U–Pb and Hf isotopic microanalysis. *Chemical Geology*, 249, 1-2, p. 1–35. https://doi.org/10.1016/j.chemgeo.2007.11.005

van Soest, Matthijs C., Kip V. Hodges, Jo-Anne Wartho, Marc B. Biren, Brian D. Monteleone, Jahandar Ramezani, John G. Spray, and Lucy M. Thompson (2011). (U-Th)/He dating of terrestrial impact structures: The Manicouagan example. *Geochemistry, Geophysics, Geosystems*, 12, 5, p. 4–8. https://doi.org/10.1029/2010GC003465

Verner, Kryštof, David Buriánek, Martin Svojtka, Vít Peřestý, Leta Megerssa, Tarekegn Tadesse, Aspiron Kussita, Diriba Alemayehu, and Tomáš Hroch (2021). Tectonometamorphic evolution and U–Pb dating of the high-grade Hammar Domain (Southern Ethiopian Shield); implications for the East-African Orogeny. *Precambrian Research*, 361, 106270. https://doi.org/10.1016/j.precamres.2021.106270

Wiedenbeck, M. A. P. C., P. Alle, Fy Corfu, W. L. Griffin, M. Meier, F. V. Oberli, A. von Quadt, J. C. Roddick, and W. Spiegel (1995). Three natural zircon standards for U-Th-Pb, Lu-Hf, trace element and REE analyses. *Geostandards Newsletter*, 19, 1, p. 1–23. https://doi.org/10.1111/j.1751-908X.1995.tb00147.x

WoldeGabriel, Giday, Grant Heiken, Tim D. White, Berhane Asfaw, William K. Hart, and Paul R. Renne (2000). Volcanism, tectonism, sedimentation, and the paleoanthropological record in the Ethiopian Rift System. *Geological Society of America*, Special Paper 345, p. 83–99. https://doi.org/10.1130/0-8137-2345-0.83

Woldegabriel, Giday, James L. Aronson, and Robert C. Walter (1990). Geology, geochronology, and rift basin development in the central sector of the Main Ethiopia Rift. *Geological Society of America Bulletin*, 102, 4, p. 439–458. https://doi.org/10.1130/0016-7606(1990)102<0439:GGARBD>2.3.CO;2

Yibas, B., W. U. Reimold, Richard Armstrong, Christian Koeberl, C. R. Anhaeusser, and David Phillips (2002). The tectonostratigraphy, granitoid geochronology and geological evolution of the Precambrian of southern Ethiopia. *Journal of African Earth Sciences*, 34, 1-2, 57–84. https://doi.org/10.1016/S0899-5362(01)00099-9

Yibas, B. (2000). The Precambrian geology, tectonic evolution, and controls of gold mineralisations in southern Ethiopia. Ph.D. Thesis, University of the Witwatersrand, Johannesburg, South Africa, 448 pp.

Zawacki, Emily E., Matthijs C. van Soest, Kip V. Hodges, Jennifer J. Scott, Mélanie Barboni, Manfred R. Strecker, Craig S. Feibel, Christopher J. Campisano, and J Ramón Arrowsmith. Sediment provenance and volcano-tectonic evolution of the East African Rift System from U/Pb and (U-Th)/He laser ablation double dating of detrital zircons. *Earth and Planetary Science Letters*. In review.

CHAPTER 6

SYNTHESIS

6.1 Research contribution

These five chapters combined provide new insight into the climatic and tectonic influences on Plio-Pleistocene landscapes in East Africa, as related to sediment provenance and erosion rates. My research evaluates the geomorphic and volcano-tectonic evolution of the EARS within different sedimentary basins, providing a multi-disciplinary view of landscape evolution to serve as a background for studies of Neogene and Quaternary paleoenvironments and faunal evolution.

The research presented in Chapters 2 and 5 is one of the first applications of the LADD method to understand both the provenance and thermal evolution of zircons in sedimentary rock samples. LADD proves an extremely powerful analytical tool, and these chapters have provided an extensive new dataset of zircon U/Pb and (U-Th)/He dates for Ethiopia and Kenya. The abundance of volcanic zircons in major basins of the EARS allows for a way to simultaneously study geomorphic processes related to traditional studies of sediment provenance as well as the unique volcano-tectonic history of the EARS.

In Chapter 2, I demonstrate the ubiquity of hydrothermal alteration in rift basin lacustrine settings, based on the exceptionally young (U-Th)/He dates. The young (U-Th)/He dates observed in the NA and WTK samples reflect the dynamic and multi-stage nature of volcanic and/or hydrothermal heating within the rift environment. Conversely, the Chew Bahir basin in Chapter 5 demonstrates a lack of these processes, reflecting a variability in magmatic heating along different portions of the EARS.

The paleoerosion rates determined in Chapters 3 and 4 are the oldest ^{10}Be-derived erosion rates from drill core samples and are the oldest millennial-scale erosion rates for Eastern Africa. These data significantly expand on the quantification of African erosion rates over time, which aids in comparative understanding of relative tectonic and climatic controls on erosion rates. I was able to take advantage of the rich paleoenvironmental proxy record from the HSPDP drill cores to assess the climatic/environmental conditions under which the samples were eroded. While the NA and WTK samples from large basins perhaps suggest a stronger climatic control on erosion rates, the smaller, hydrologically closed Chew Bahir basin appears to reflect a stronger tectonic control, with long-term climatic overprinting.

The Monte Carlo assessment of erosion rate error from ^{10}Be analyses in Chapters 3 and 4 fills a gap of uncertainty propagation that often exists in cosmogenic nuclide studies. Not correctly accounting for post-depositional ^{10}Be accumulation, uncertainties in depositional age, and uncertainties in sediment accumulation rate can cause a significant underestimation of paleoerosion rates, and a 'true' quantification of error is necessary when attempting to identify trends in erosion rates over time.

6.2 Future research

There is significant potential to expand on and continue the research presented in this dissertation. Sampling of the HSPDP drill cores for this dissertation work was restricted to medium-grained sandy intervals that would provide sufficient material needed for cosmogenic ^{10}Be analyses. However, there are significantly more small sandy units and fine-grained sandy units within the cores that would be suitable for detrital zircon analyses. Expanding the dataset of U/Pb detrital zircon dates would help to better understand the evolution of sediment source units and paleowatersheds over time, particularly for the WTK core for which there was only one sample analyzed. LADD dating of these zircons would likely be unnecessary given the ubiquity of volcanic heating and/or hydrothermal alteration partially resetting (U-Th)/He dates, which has already been evaluated in this dissertation. Targeting the detrital zircon record is ideal because it provides an amalgamation of material that would be much more difficult and tedious to sample from *in situ*.

From the HSPDP drill core material that has already been sampled, there is significant potential for future geochemical research done on the Cenozoic volcanic zircons. Understanding the major and trace element geochemistry of the detrital volcanic zircons would provide further insight into the magmatic processes and evolution of volcanism within the EARS. Existing sampled material could also benefit from refined zircon U/Pb dating of individual core and rim domains to better understand the magmatic chronology recorded in the zircons.

While the high-resolution sedimentary record and age-depth model of the drill cores was extremely beneficial in assessing and quantifying paleoerosion rates and the associated error, the small volume of material that the drill core samples is less than ideal for cosmogenic analyses in quartz-poor terranes. The paleoerosion rates from the cores would significantly benefit from comparisons to ^{10}Be-derived erosion rates from sandstone outcrops, where available material is more abundant, and from modern sand samples. However, to make this research more useful, it would be pertinent to further explore and identify the source of the eroding quartz.

Beyond the target sites of the HSPDP, other basins within the EARS offer rich potential for investigations of the detrital mineral record. It would be particularly interesting to see how the detrital mineral record of other basins in the Broadly Rifted Zone (BRZ) compares to that of the Chew Bahir basin. What is the relationship between tectonic and climatic controls on landscape evolution observed there? As well, targeting the southern or eastern portion of the Awash watershed would provide a fuller overview of evolution of the Awash River and basin as related to the development of the EARS.

REFERENCES

Abbate, Ernesto, Pietro Bruni, and Mario Sagri (2015). Geology of Ethiopia: A Review and Geomorphological Perspectives. In *Landscapes and Landforms of Ethiopia*. P. Billi (ed.) https://doi.org/10.1007/978-94-017-8026-1_2

Aizawa, Koki, Yasuo Ogawa, and Tsuneo Ishido (2009). Groundwater flow and hydrothermal systems within volcanic edifices: Delineation by electric self-potential and magnetotellurics. *Journal of Geophysical Research: Solid Earth*, 224, B01208, p. 1–12. https://doi.org/10.1029/2008JB005910

Anderson, A. J., M. C. van Soest, K. V. Hodges, and J. M. Hanchar (2020). Helium diffusion in zircon: Effects of anisotropy and radiation damage revealed by laser depth profiling. *Geochimica et Cosmochimica Acta*, 274, p. 45– 62. https://doi.org/10.1016/j.gca.2020.01.049

Arambourg, C., and R. G. Wolff (1969). Nouvelles données paléontologique sur l'âge des "Gres du Lubur" (Turkana Grits) al'ouest du lac Rodolphe. *Comptes Rendus Société Géologique de France*, 9, 190–202.

Aronson, James L., Million Hailemichael, and Samuel M. Savin (2008). Hominid environments at Hadar from paleosol studies in a framework of Ethiopian climate change. *Journal of Human Evolution*, 55, 4, p. 532–550. https://doi.org/10.1016/j.jhevol.2008.04.004

Asrat, Asfawossen, and Pierre Barbey (2003). Petrology, geochronology and Sr–Nd isotopic geochemistry of the Konso pluton, south-western Ethiopia: implications for transition from convergence to extension in the Mozambique Belt. *International Journal of Earth Sciences*, 92, 6, p. 873–890. https://doi.org/10.1007/s00531-003-0360-9

Asrat, Asfawossen, P. Barbey, and G. Gleizes (2001). The Precambrian geology of Ethiopia: a review. *Africa Geoscience Review*, 8.3/4, p. 271–288.

Ayalew, Dereje, Pierre Barbey, Bernard Marty, Laurie Reisberg, Gezahegn Yirgu, and Raphael Pik (2002). Source, genesis, and timing of giant ignimbrite deposits associated with Ethiopian continental flood basalts. *Geochimica et Cosmochimica Acta*, 66, 8, p. 1429–1448. https://doi.org/10.1016/S0016-7037(01)00834-1

Ayalew, Teklewold, and Samuel Gichile (1990). Preliminary U-Pb ages from southern Ethiopia. Publication occasionnelle-Centre international pour la formation et les échanges géologiques, 22, p. 127–130.

Baker, Brian Howard, Paul A. Mohr, and Laurence Albert Joseph Williams (1972). Geology of the eastern rift system of Africa. *Geological Society of America Special Papers*, 136, p. 1–68. https://doi.org/10.1130/SPE136-p1

Balco, Greg, John O. Stone, Nathaniel A. Lifton, and Tibor J. Dunai (2008). A complete and easily accessible means of calculating surface exposure ages or erosion rates from ^{10}Be and ^{26}Al measurements. *Quaternary Geochronology*, 3, 3, p. 174–195. https://doi.org/10.1016/j.quageo.2007.12.001

Balestrieri, Maria Laura, Marco Bonini, Giacomo Corti, Federico Sani, and Melody Philippon (2016). A refinement of the chronology of rift-related faulting in the Broadly Rifted Zone, southern Ethiopia, through apatite fission-track analysis. *Tectonophysics*, 671, p. 42–55. https://doi.org/10.1016/j.tecto.2016.01.012

Barberi, F., and Rosenro Santacroce (1980). The Afar Stratoid Series and the magmatic evolution of East African rift system. *Bulletin de la Société Géologique de France*, 7, 6, p. 891–899.

Barberi, Franco, Giorgio Ferrara, R. Santacroce, M. Treuil, and J. Varet (1975). A transitional basalt-pantellerite sequence of fractional crystallization, the Boina Centre (Afar Rift, Ethiopia). *Journal of Petrology*, 16, 1, p. 22–56. https://doi.org/10.1093/petrology/16.1.22

Begg, G. C., W.L. Griffin, L. M. Natapov, S. Y. O'Reilly, S. P. Grand, C. J. O'Neill, and P. Bowden (2009). The lithospheric architecture of Africa: Seismic tomography, mantle petrology, and tectonic evolution. *Geosphere*, 5(1), p. 23–50. https://doi.org/10.1130/GES00179.1

Bekaddour, Toufik, Fritz Schlunegger, Hendrik Vogel, Romain Delunel, Kevin P. Norton, Naki Akçar and Peter Kubik (2014). Paleo erosion rates and climate shifts recorded by Quaternary cut-and-fill sequences in the Pisco valley, central Peru. *Earth and Planetary Science Letters*, 390, p. 103–115. https://doi.org/10.1016/j.epsl.2013.12.048

Bierman, Paul, and Eric J. Steig (1996). Estimating rates of denudation using cosmogenic isotope abundances in sediment. *Earth Surface Processes and Landforms*, 21, 2, p. 125–139. https://doi.org/10.1002/(SICI)1096-9837(199602)21:2<125::AID-ESP511>3.0.CO;2-8

Biggin, Andrew J., Geert HMA Strik, and Cor G. Langereis (2009). The intensity of the geomagnetic field in the late-Archaean: new measurements and an analysis of the updated IAGA palaeointensity database. *Earth, Planets and Space*, 61, 1, 9–22. https://doi.org/10.1186/BF03352881

Bobe, René and Anna K. Behrensmeyer (2004). The expansion of grassland ecosystems in Africa in relation to mammalian expansion and the origin of the genus *Homo*. *Palaeogeography, Palaeoclimatology, Palaeoecology*, 207, p. 399–420. https://doi.org/10.1016/j.palaeo.2003.09.033

Boehnke, P., Mélanie Barboni, and E. A. Bell (2016). Zircon U/Th model ages in the presence of melt heterogeneity. *Quaternary Geochronology*, 34, p. 69–74. https://doi.org/10.1016/j.quageo.2016.03.005

Boehnke, Patrick, E. Bruce Watson, Dustin Trail, T. Mark Harrison, and Axel K. Schmitt (2013). Zircon saturation re-revisited. *Chemical Geology*, 351, p. 324–334. https://doi.org/10.1016/j.chemgeo.2013.05.028

Bonnefille, Raymonde, Richard Potts, Françoise Chalié, Dominique Jolly, and Odile Peyron (2004). High-resolution vegetation and climate change associated with Pliocene Australopithecus afarensis. *Proceedings of the National Academy of Sciences*, 101, 33, p. 12125–12129. https://doi.org/10.1073/pnas.0401709101

Boone, S. C., M-L. Balestrieri, B. P. Kohn, G. Corti, A. J. W. Gleadow, and C. Seiler (2019). Tectonothermal evolution of the Broadly Rifted Zone, Ethiopian Rift. *Tectonics*, 38, p. 1070–1100. https://doi.org/10.1029/2018TC005210

Boone, S. C., C. Seiler, B. P. Kohn, A. J. W. Gleadow, D. A. Foster, and L. Chung (2018). Influence of rift superposition on lithospheric response to East African Rift System extension: Lapur Range, Turkana, Kenya. *Tectonics*, 37, p. 182–207. https://doi.org/10.1002/2017TC004575

Borchers, Brian, Shasta Marrero, Greg Balco, Marc Caffee, Brent Goehring, Nathaniel Lifton, Kunihiko Nishiizumi, Fred Phillips, Joerg Schaefer, and John Stone (2016). Geological calibration of spallation production rates in the CRONUS-Earth project. *Quaternary Geochronology*, 31, p. 188–198. https://doi.org/10.1016/j.quageo.2015.01.009

Branchu, Philippe, Laurent Bergonzini, Damien Delvaux, Marc De Batist, Vladimir Golubev, Marc Benedetti, and Jean Klerkx (2005). Tectonic, climatic and hydrothermal control on sedimentation and water chemistry of northern Lake Malawi (Nyasa), Tanzania. *Journal of African Earth Sciences*, 43, 4, p. 433–446. https://doi.org/10.1016/j.jafrearsci.2005.09.004

Braucher, R., Brown, E.T., Bourlès, D.L., Colin, F. (2003). *In situ* produced ^{10}Be measurements at great depths: implications for production rates by fast muons. *Earth and Planetary Science Letters*, 211, p. 251–258. https://doi.org/10.1016/S0012-821X(03)00205-X

Braucher, R., Bourlès, D.L., Brown, E.T., Colin, F., Muller, J.-P., Braun, J.-J., Delaune, M., Minko, A.E., Lescouet, C., Raisbeck, G.M., Yiou, F. (2000). Application of *in situ* produced cosmogenic ^{10}Be and ^{26}Al to the study of lateritic soil development in tropical forest: theory and examples from Cameroon and Gabon. *Chemical Geology*, 170, p. 95–111. https://doi.org/10.1016/S0009-2541(99)00243-0

Brown, Erik Thorson, Robert F. Stallard, Matthew C. Larsen, Grant M. Raisbeck, and Françoise Yiou (1995). Denudation rates determined from the accumulation of in situ-produced ^{10}Be in the Luquillo Experimental Forest, Puerto Rico. *Earth and Planetary Science Letters*, 129, 1-4, p.193–202. https://doi.org/10.1016/0012-821X(94)00249-X

Brown, Francis H., and Ian Mcdougall (2011). Geochronology of the Turkana depression of northern Kenya and southern Ethiopia." *Evolutionary Anthropology: Issues, News, and Reviews*, 20, 6, p. 217–227. https://doi.org/10.1002/evan.20318

Cahen, L. and N. J. Snelling (1966). The geochronology of equatorial Africa. North-Holland Publishing Company, Amsterdam, The Netherlands.

Campisano, C. J., A.S. Cohen, J.R. Arrowsmith, A. Asrat, A.K. Behrensmeyer, E.T. Brown, A.L. Deino, D.M. Deocampo, C.S. Feibel, J.D. Kingston, H.F. Lamb, T.K. Lowenstein, A. Noren, D.O. Olago, R.B. Owen, J.D. Pelletier, R. Potts, K.E. Reed, R.W. Renaut, J.M. Russell, J.L. Russell, F. Schabitz, J.R. Stone, M.H. Trauth, and J.G. Wynn (2017). The Hominin Sites and Paleolakes Drilling Project: High-resolution paleoclimate records from the East African rift system and their implications for understanding the environmental context of hominin evolution. *PaleoAnthropology*, p. 1–43. https://doi:10.4207/PA.2017.ART104

Campisano, Christopher J. (2012). Geological summary of the Busidima formation (Plio-Pleistocene) at the Hadar paleoanthropological site, Afar Depression, Ethiopia. *Journal of Human Evolution*, 62, 3, p. 338–352. https://doi.org/10.1016/j.jhevol.2011.05.002

Campisano, Christopher J., and Craig S. Feibel (2008). Tephrostratigraphy of the Hadar and Busidima Formations at Hadar, Afar Depression, Ethiopia. The Geology of Early Humans in the Horn of Africa. *Geological Society of America Special Paper* 446, p. 135–162. https://doi.org/10.1130/2008.2446(06)

Campisano, Christopher J., and Craig S. Feibel (2007). Connecting local environmental sequences to global climate patterns: evidence from the hominin-bearing Hadar Formation, Ethiopia. *Journal of Human Evolution*, 53, 5, p. 515–527. https://doi.org/10.1016/j.jhevol.2007.05.015

Cerling, Thure E., Jonathan G. Wynn, Samuel A. Andanje, Michael I. Bird, David Kimutai Korir, Naomi E. Levin, William Mace, Anthony N. Macharia, Jay Quade, and Christopher H. Remien (2011). Woody cover and hominin environments in the past 6 million years. *Nature*, 476, 7358, p. 51–56. https://doi.org/10.1038/nature10306

Charreau, Julien, P-H. Blard, N. Puchol, J-P. Avouac, Elisabeth Lallier-Vergès, D. Bourlès, Regis Braucher, A. Gallaud, R. Finkel, M. Jolivet, Y. Chen, and P. Roy (2011). Paleo-erosion rates in Central Asia since 9 Ma: A transient increase at the onset of Quaternary glaciations? *Earth and Planetary Science Letters*, 304, 1-2, p. 85–92. https://doi.org/10.1016/j.epsl.2011.01.018

Chaudhary, Mamta Sanam, Nathan M. Rabideaux, Daniel M. Deocampo, Craig Feibel, and Andrew S. Cohen (2016). Reconstructing paleoenvironmental conditions from hydrothermally altered lacustrine sediments from HSPDP West Turkana-Kaitio core material via coupled mineralogical and geochemical analysis. Geological Society of America *Abstracts with Programs*, 48, 3. https://doi.org/10.1130/abs/2016SE-273372

Chernet, Tadiwos, William K. Hart, James L. Aronson, and Robert C. Walter (1998). New age constraints on the timing of volcanism and tectonism in the northern Main Ethiopian Rift–southern Afar transition zone (Ethiopia). *Journal of Volcanology and Geothermal Research*, 80, 3-4, p. 267–280. https://doi.org/10.1016/S0377-0273(97)00035-8

Chew, D.M., Petrus, J.A. and Kamber, B.S. (2014). U–Pb LA–ICPMS dating using accessory mineral standards with variable common Pb. *Chemical Geology*, 363, p. 185–199. https://doi.org/10.1016/j.chemgeo.2013.11.006

Chmeleff, Jérôme, Friedhelm von Blanckenburg, Karsten Kossert, and Dieter Jakob (2010). Determination of the ^{10}Be half-life by multicollector ICP-MS and liquid scintillation counting. *Nuclear Instruments and Methods in Physics Research Section B: Beam Interactions with Materials and Atoms*, 268, 2, p. 192–199. https://doi.org/10.1016/j.nimb.2009.09.012

Chorowicz, Jean (2005). The East African rift system. *Journal of African Earth Sciences*, 43, 1-3 p. 379–410. https://doi.org/10.1016/j.jafrearsci.2005.07.019

Cohen, A., C. Campisano, R. Arrowsmith, A. Asrat, A.K. Behrensmeyer, A. Deino, C. Feibel, A. Hill, R. Johnson, J. Kingston, H. Lamb, T. Lowenstein, A. Noren, D. Olago, R.B. Owen, R. Potts, K. Reed, R. Renaut, F. Schäbitz, J.-J. Tiercelin, M.H. Trauth, J. Wynn, S. Ivory, K. Brady, R. ÓGrady, J. Rodysill, J. Githiri, J. Russell, V. Foerster, R. Dommain, S. Rucina, D. Deocampo, J. Russell, A. Billingsley, C. Beck, G. Dorenbeck, L. Dullo, D. Feary, D. Garello, R. Gromig, T. Johnson, A.

Junginger, M. Karanja, E. Kimburi, A. Mbuthia, T. McCartney, E. McNulty, V. Muiruri, E. Nambiro, E.W. Negash, D. Njagi, J.N. Wilson, N. Rabideaux, T. Raub, M.J. Sier, P. Smith, J. Urban, M. Warren, M. Yadeta, C. Yost, and B. Zinaye (2016). The Hominin Sites and Paleolakes Drilling Project: inferring the environmental context of human evolution from eastern African rift lake deposits, Sci. Dril., 21, p. 1–16. https://doi.org/10.5194/sd-21-1-2016

Cooper, Frances J., Matthijs C. van Soest, and Kip V. Hodges (2011). Detrital zircon and apatite (U-Th)/He geochronology of intercalated baked sediments: A new approach to dating young basalt flows. *Geochemistry*, *Geophysics*, Geosystems, 12, 7, p. 1–8. https://doi.org/10.1029/2011GC003650

Dart, Raymond A., 1925. *Australopithecus africanus:* The Man-Ape of South Africa. *Science*, 115, p. 195–199. https://doi.org/10.1038/115195a0

Davidson, Anthony. (1983). The Omo River project: reconnaissance geology and geochemistry of parts of Ilubabor, Kefa, Gemu Gofa and Sidamo. *Ethiopian Institute of Geological Surveys Bulletin*, 2, p. 1–89.

Davidson, A., and D. C. Rex (1980). Age of volcanism and rifting in southwestern Ethiopia. *Nature*, 283, 5748, p. 657–658. https://doi.org/10.1038/283657a0

Davis, David Michael, Daniel Deocampo, Nathan Michael Rabideaux, and Christopher J. Campisano (2017). A Mineralogical analysis of HSPDP core samples from the Northern Awash Pliocene Hadar Formation, Ethiopia: the tale of an East African paleolake." *AGUFM*, PP13B-1081.

Deino, Alan L., Mark J. Sier, Dominique I. Garello, C. Brenhin Keller, John D. Kingston, Jennifer J. Scott, Guillaume Dupont-Nivet, and Andrew S. Cohen (2019). Chronostratigraphy of the Baringo-Tugen Hills-Barsemoi (HSPDP-BTB13-1A) core–^{40}Ar/^{39}Ar dating, magnetostratigraphy, tephrostratigraphy, sequence stratigraphy and Bayesian age modeling. *Palaeogeography*, *Palaeoclimatology*, *Palaeoecology*, 570, 109519, p. 1–15. https://doi.org/10.1016/j.palaeo.2019.109519

Dekov, V. M., N. M. Egueh, G. D. Kamenov, G. Bayon, Stefan V. Lalonde, Mark Schmidt, Volker Liebetrau, F. Munnik, Y. Fouquet, M. Tanimizu, M. O. Awaleh, I. Guirreh, and B. Le Gall (2014). Hydrothermal carbonate chimneys from a continental rift (Afar Rift): Mineralogy, geochemistry, and mode of formation. *Chemical Geology*, 387, p. 87–100. https://doi.org/10.1016/j.chemgeo.2014.08.019

deMenocal, Peter, B. (2004). African climate change and faunal evolution during the Pliocene–Pleistocene. *Earth and Planetary Science Letters*, 220, 1-2, p. 3–24. https://doi.org/10.1016/S0012-821X(04)00003-2

deMenocal, Peter B. (1995). Plio-Pleistocene African climate. *Science*, 270, 5233, p. 53–59. https://doi.org/10.1126/science.270.5233.53

Desissa, M., Johnson, N.E., Whaler, K.A., Hautot, S., Fisseha, S., Dawes, G.J.K. (2013). A mantle magma reservoir beneath an incipient mid-ocean ridge in Afar, Ethiopia. *Nature Geoscience*, 6, 861–865. https://dx.doi.org/10.1038/ngeo1925

Didana, Y.L., Thiel, S., Heinson, G. (2015). Three dimensional conductivity model of the Tendaho High Enthalpy Geothermal Field, NE Ethiopia. *Journal of Volcanology and Geothermal Research*, 290, p. 53–62. https://dx.doi.org/10.1016/j.jvolgeores.2014.11.013

DiMaggio, Erin N., Christopher J. Campisano, John Rowan, Guillaume Dupont-Nivet, Alan L. Deino, Faysal Bibi, Margaret E. Lewis, Antoine Souron, Dominique Garello, Lars Werdelin, Kaye E. Reed, J Ramón Arrowsmith (2015). Late Pliocene fossiliferous sedimentary record and the environmental context of early *Homo* from Afar, Ethiopia. *Science*, 347, 6228, p. 1355–1359. https://doi.org/10.1126/science.aaa1415

Dodd, Thomas J.H., McCarthy, Dave J., Clarke, Stuart M. (2020). Clastic injectites, internal structures and flow regime during injection: The Sea Lion Injectite System, North Falkland Basin. *Sedimentology*, 67, p. 1014–1044. https://doi.org/10.1111/sed.12672

Dodson, M. H., A. R. Gledhill, R. M. Shackleton, and K. Bell (1975). Age differences between Archaean cratons of eastern and southern Africa. *Nature*. 254, 5498, p. 315–318. https://doi.org/10.1038/254315a0

Dorgerloh, Florian (2016). Basin-wide erosion rates from in-situ ^{10}Be in the Chew Bahir basin, southern Ethiopia. Bachelor thesis, Universität Potsdam.

Duesing, Walter, Nadine Berner, Alan L. Deino, Verena Foerster, K. Hauke Kraemer, Norbert Marwan, and Martin H. Trauth (2021). Multiband wavelet age modeling for a ~293 m (~600 kyr) sediment core from Chew Bahir Basin, Southern Ethiopian Rift. *Frontiers in Earth Science*, 9, 35. https://doi.org/10.3389/feart.2021.594047

Duesing, Walter, Hauke Kraeme, Asfawossen Asrat, Melissa Chapot, Andrew Cohen, Alan Deino, Verena Foerster, Henry Lamb, Norbert Marwan, Christine Lane, Mark Maslin, Christopher Ramsey, Helen Roberts, Frank Schaebitz, Martin Trauth, and Céline Vidal (2019). Differentiating local from regional climate signals using the 600 ka Chew Bahir paleoclimate record from South Ethiopia. *In EGU General Assembly Conference Abstracts*, 21, p. 14836.

Dunkley, R.N., Smith, M., Allen, D.J., Darling, W.G. (1993). The geothermal activity and geology of the northern sector of the Kenya Rift Valley. *British Geological Survey, Research Report*, SC/93/1, 185 p.

Dupont-Nivet, Guillaume, Mark Sier, Christopher J. Campisano, J. Ramón Arrowsmith, Erin DiMaggio, Kaye Reed, Charles Lockwood, Christine Franke, and Silja Hüsing (2008). Magnetostratigraphy of the eastern Hadar Basin (Ledi-Geraru research area, Ethiopia) and implications for hominin paleoenvironments. *The Geology of Early Humans in the Horn of Africa: Geological Society of America Special Paper 446*, p. 67–85. https://doi.org/10.1130/2008.2446(03)

Ebinger, C. J., Tilahun Yemane, D. J. Harding, Samson Tesfaye, S. Kelley, and D. C. Rex (2000). Rift deflection, migration, and propagation: Linkage of the Ethiopian and Eastern rifts, Africa. *Geological Society of America Bulletin*, 112, 2, p. 163–176. https://doi.org/10.1130/0016-7606(2000)112<163:RDMAPL>2.0.CO;2

Ebinger, C. J., Tesfaye Yemane, Giday Woldegabriel, J. L. Aronson, and R. C. Walter (1993). Late Eocene–Recent volcanism and faulting in the southern main Ethiopian rift. *Journal of the Geological Society*, 150, 1, p. 99–108. https://doi.org/10.1144/gsjgs.150.1.0099

Ebinger, Cindy J., Alan L. Deino, R. E. Drake, and A. L. Tesha (1989). Chronology of volcanism and rift basin propagation: Rungwe volcanic province, East Africa. *Journal of Geophysical Research: Solid Earth*, 94, B11, p. 15785–15803. https://doi.org/10.1029/JB094iB11p15785

Ehlers, Todd A., and Kenneth A. Farley (2003). Apatite (U–Th)/He thermochronometry: methods and applications to problems in tectonic and surface processes. *Earth and Planetary Science Letters*, 206, 1-2, p. 1–14. https://doi.org/10.1016/S0012-821X(02)01069-5

Emishaw, Luelseged, Daniel A. Laó-Dávila, Mohamed G. Abdelsalam, Estella A. Atekwana, and Stephen S. Gao (2017). Evolution of the broadly rifted zone in southern Ethiopia through gravitational collapse and extension of dynamic topography. *Tectonophysics*, 699, p. 213–226. https://doi.org/10.1016/j.tecto.2016.12.009

Evans, N. J., J. P. Byrne, J. T. Keegan, and L. E. Dotter (2005). Determination of uranium and thorium in zircon, apatite, and fluorite: Application to laser (U-Th)/He thermochronology. *Journal of Analytical Chemistry*, 60, 12, p. 1159-1165. https://doi.org/10.1007/s10809-005-0260-1

Farley, K. A., B. P. Kohn, and Bradley Pillans (2002). The effects of secular disequilibrium on (U–Th)/He systematics and dating of Quaternary volcanic zircon and apatite. *Earth and Planetary Science Letters*, 201, 1, p. 117–125. https://doi.org/10.1016/S0012-821X(02)00659-3

Farley, K. A., R. A. Wolf, and L. T. Silver (1996). The effects of long alpha-stopping distances on (U-Th)/He ages. *Geochimica et Cosmochimica Acta*, 60, 21, p. 4223–4229. https://doi.org/10.1016/S0016-7037(96)00193-7

Feibel, C.S., Beck, C.C., Stockhecke, M., Gravina, A., Ortiz, K., Campisano, C.J., and Cohen, A.S. (2015). Seeing deeper into the mud: Insights from the WTK13 core, West Turkana, Kenya. *Geological Society of America Abstracts with Programs*, 47(7), 287. https://gsa.confex.com/gsa/2015AM/webprogram/Paper266297.html

Feibel, Craig S. (2011). A geological history of the Turkana Basin. *Evolutionary Anthropology: Issues, News, and Reviews*, 20, 6, p. 2065–216. https://doi.org/10.1002/evan.20331

Fischer, Markus, Monika Markowska, Felix Bachofer, Verena Foerster, Asrat Asfawossen, Christoph Zielhofer, Martin Trauth, and Annett Junginger (2020). Determining the Pace and Magnitude of Lake Level Changes in Southern Ethiopia Over the Last 20,000 Years Using Lake Balance Modeling and SEBAL. *Frontiers in Earth Science*, 8, 197, p. 1–21. https://doi.org/10.3389/feart.2020.00197

Foerster, Verena, Asfawossen Asrat, Christopher Bronk Ramsey, Erik T. Brown, Melissa S. Chapot, Alan Deino, Daniel M. Deocampo, Walter Duesing, Annette Hahn, Annett Junginger, Stefanie Kaboth-Bahr, Christine S. Lane, Stephan Opitz, Anders Noren, Helen M. Roberts, Mona Stockhecke, Ralph Tiedemann, Céline Vidal, Ralf Vogelsang, Andrew S. Cohen, Henry F. Lamb, Frank Schaebitz, and Martin H. Trauth. 620,000 years of eastern Africa climate variability and hominin evolution. *Nature Geoscience* (In review).

Foerster, Verena, Daniel M. Deocampo, Asfawossen Asrat, Christina Günter, Annett Junginger, Kai Hauke Krämer, Nicole A. Stroncik, and Martin H. Trauth (2018). Towards an understanding of climate proxy formation in the Chew Bahir basin, southern Ethiopian Rift. *Palaeogeography, Palaeoclimatology, Palaeoecology*, 501, p. 111–123. https://doi.org/10.1016/j.palaeo.2018.04.009

Foerster, Verena, Ralf Vogelsang, Annett Junginger, Asfawossen Asrat, Henry F. Lamb, Frank Schaebitz, and Martin H. Trauth (2015). Environmental change and human occupation of southern Ethiopia and northern Kenya during the last 20,000 years. *Quaternary Science Reviews*, 129, p. 333–340. https://doi.org/10.1016/j.quascirev.2015.10.026

Foerster, Verena, Annett Junginger, Oliver Langkamp, Tsige Gebru, Asfawossen Asrat, Mohammed Umer, Henry F. Lamb, Volker Wenrich, Janet Rethemeyer, Norbert Nowaczyk, Martin H. Trauth, and Frak Schaebitz (2012). Climatic change recorded in the sediments of the Chew Bahir basin, southern Ethiopia, during the last 45,000 years. *Quaternary International*, 274, p. 25–37. https://doi.org/10.1016/j.quaint.2012.06.028

Fritz, H., M. Abdelsalam, K. A. Ali, B. Bingen, A. S. Collins, A. R. Fowler, W. Ghebreab, C.A. Hauzenberger, P.R. Johnson, T.M. Kusky, P. Macey, S. Muhongo, R.J. Stern, and G. Viola (2013). Orogen styles in the East African Orogen: A review of the Neoproterozoic to Cambrian tectonic evolution. *Journal of African Earth Sciences*, 86, p. 65–106. https://doi.org/10.1016/j.jafrearsci.2013.06.004

Garcin, Yannick, Taylor F. Schildgen, Verónica Torres Acosta, Daniel Melnick, Julien Guillemoteau, Jane Willenbring, and Manfred R. Strecker (2017). Short-lived increase in erosion during the African Humid Period: evidence from the northern Kenya Rift. *Earth and Planetary Science Letters*, 459, p. 58–69. https://doi.org/10.1016/j.epsl.2016.11.017

Garello, Dominique Ines (2019). Tephrostratigraphy of Pliocene drill cores from Kenya and Ethiopia, and Pleistocene exposures in the Ledi-Geraru Research Project Area, Ethiopia: geological context for the evolution of *Australopithecus* and *Homo*. PhD diss., Arizona State University.

Gebregiorgis, Daniel, Daniel M. Deocampo, Verena Foerster, Fred J. Longstaffe, Jeremy S. Delaney, Frank Schaebitz, Annett Junginger, Monika Markowska, Stephan Opitz, Martin H. Trauth, Henry F. Lamb, and Asfawossen Asrat (2021). Modern sedimentation and authigenic mineral formation in the Chew Bahir Basin, southern Ethiopia: implications for interpretation of Late Quaternary paleoclimate records. *Frontiers in Earth Science*, 9 (2021): 244. https://doi.org/10.3389/feart.2021.607695

Gehrels, George E., William R. Dickinson, Gerald M. Ross, John H. Stewart, and David G. Howell (1995). Detrital zircon reference for Cambrian to Triassic miogeoclinal strata of western North America. *Geology*, 23, 9, p. 831–834. https://doi.org/10.1130/0091-7613(1995)023<0831:DZRFCT>2.3.CO;2

Gianelli, G., Mekuria, N., Battaglia, S., Chersicla, A., Garofalo, P., Ruggieri, G., Manganelli, M., Gebregziabher, Z. (1998). Water-rock interaction and hydrothermal mineral equilibria in the Tendaho geothermal system. *Journal of Volcanology and Geothermal Research*, 86, p. 253–276.

Granger, Darryl E., Nathaniel A. Lifton, and Jane K. Willenbring (2013). A cosmic trip: 25 years of cosmogenic nuclides in geology. *GSA Bulletin*, 125, 9-10, p. 1379–1402. https://doi.org/10.1130/B30774.1

Granger, Darryl E., James W. Kirchner, and Robert Finkel (1996). Spatially averaged long-term erosion rates measured from in situ-produced cosmogenic nuclides in alluvial sediment. *The Journal of Geology*, 104, 3, p. 249–257. https://doi.org/10.1086/629823

Grischott, Reto, Florian Kober, Maarten Lupker, Juergen M. Reitner, Ruth Drescher-Schneider, Irka Hajdas, Marcus Christl, and Sean D. Willett (2017). Millennial scale variability of denudation rates for the last 15 kyr inferred from the detrital ^{10}Be record of Lake Stappitz in the Hohe Tauern massif, Austrian Alps. *The Holocene*, 27, 12, p. 19149–1927. https://doi.org/10.1177/0959683617708451

Grischott, Reto, Florian Kober, Maarten Lupker, Kristina Hippe, Susan Ivy-Ochs, Irka Hajdas, Bernhard Salcher, and Marcus Christl (2016). Constant denudation rates in a high alpine catchment for the last 6 kyrs. *Earth Surface Processes and Landforms*, 42, 7, p. 1065-1077. https://doi.org/10.1002/esp.4070

Grove, Alan T., F. Alayne Street, and A. S. Goudie (1975). Former lake levels and climatic change in the Rift Valley of southern Ethiopia. *Geographical Journal*, p. 177–194. https://doi.org/10.2307/1797205

Hargrove, U. S., R. J. Stern, J-I. Kimura, W. I. Manton, and P. R. Johnson (2006). How juvenile is the Arabian–Nubian Shield? Evidence from Nd isotopes and pre-Neoproterozoic inherited zircon in the Bi'r Umq suture zone, Saudi Arabia. *Earth and Planetary Science Letters*, 252, 3-4, p. 308–326. https://doi.org/10.1016/j.epsl.2006.10.002

Hofmann, C., V. Courtillot, G. Feraud, P. Rochette, G. Yirgu, E. Ketefo, and R. Pik (1997). Timing of the Ethiopian flood basalt event and implications for plume birth and global change. *Nature*, 389, 6653, p. 838–841. https://doi.org/10.1038/39853

Horne, Alexandra M., Matthijs C. van Soest, Kip V. Hodges, Alka Tripathy-Lang, and Jeremy K. Hourigan (2016). Integrated single crystal laser ablation U/Pb and (U–Th)/He dating of detrital accessory minerals–Proof-of-concept studies of titanites and zircons from the Fish Canyon tuff. *Geochimica et Cosmochimica Acta*, 178, p. 106–123. https://doi.org/10.1016/j.gca.2015.11.044

Hourigan, J. K., P. W. Reiners, and M. T. Brandon (2005). U-Th zonation-dependent alpha-ejection in (U-Th)/He chronometry. *Geochimica et Cosmochimica Acta*, 69, 13, p. 3349–3365. https://doi.org/10.1016/j.gca.2005.01.024

Huete, Alfredo, Kamel Didan, Tomoaki Miura, E. Patricia Rodriguez, Xiang Gao, and Laerte G. Ferreira (2002). Overview of the radiometric and biophysical performance of the MODIS vegetation indices. *Remote Sensing of Environment*, 83, 1-2, p. 195–213. https://doi.org/10.1016/S0034-4257(02)00096-2

Juch, D., (1978). Geologic des Athiopischen Sudost-Escarpments 39° und 42° ostlicher Lange. *Clausthaler Geo. Abh*., 29, p. 1–139.

Kohl, C. P., and Kunihiko Nishiizumi (1992). Chemical isolation of quartz for measurement of in-situ-produced cosmogenic nuclides. *Geochimica et Cosmochimica Acta*, 56, 9, p. 3583–3587. https://doi.org/10.1016/0016-7037(92)90401-4

Kunz, K., H. Kreuzer, and P. Müller (1975). Potassium-Argon age determinations of the Trap basalt of the south-eastern part of the Afar Rift. Afar depression of Ethiopia, 1, 370–374 International Symposium on the Afar Region and Related Rift Problems (Bad Bergzabern, Germany).

Küster, Dirk, and Ulrich Harms (1998). Post-collisional potassic granitoids from the southern and northwestern parts of the Late Neoproterozoic East African Orogen: a review. *Lithos*, 45, 1-4, p. 177–195. https://doi.org/10.1016/S0024-4937(98)00031-0

Lal, Devendra (1991). Cosmic ray labeling of erosion surfaces: *in situ* nuclide production rates and erosion models. *Earth and Planetary Science Letters*, 104, 2-4, p. 424–439. https://doi.org/10.1016/0012-821X(91)90220-C

Lepre, Christopher J. (2014). Early Pleistocene lake formation and hominin origins in the Turkana–Omo rift. *Quaternary Science Reviews*, 102, p. 181–191. https://doi.org/10.1016/j.quascirev.2014.08.012

Levin, Naomi E., Francis H. Brown, Anna K. Behrensmeyer, René Bobe, and Thure E. Cerling (2011). Paleosol carbonates from the Omo Group: Isotopic records of local and regional environmental change in East Africa. *Palaeogeography, Palaeoclimatology, Palaeoecology*, 307, 1-4, p. 75–89. https://doi.org/10.1016/j.palaeo.2011.04.026

Lupien, Rachel L. (2019). The Plio-Pleistocene climate history of East Africa and the role of environmental change on human evolution: studies of leaf wax isotopes from paleolake sediment. PhD Diss., Brown University. https://doi.org/10.26300/h7yg-fe45

Lupien, R. L., J. M. Russell, Craig Feibel, C. Beck, I. Castañeda, A. Deino, and A. S. Cohen (2018). A leaf wax biomarker record of early Pleistocene hydroclimate from West Turkana, Kenya. *Quaternary Science Reviews*, 186, p. 225–235. https://doi.org/10.1016/j.quascirev.2018.03.012

Madella, Andrea, Romain Delunel, Naki Akçar, Fritz Schlunegger, and Marcus Christl (2018). ^{10}Be-inferred paleo-denudation rates imply that the mid-Miocene western central Andes eroded as slowly as today. Scientific Reports, 8, 1, p. 1–9. https://doi.org/10.1038/s41598-018-20681-x

Marrero, Shasta M., Fred M. Phillips, Brian Borchers, Nathaniel Lifton, Robert Aumer, and Greg Balco (2016). Cosmogenic nuclide systematics and the CRONUScalc program. *Quaternary Geochronology*, 31, p. 160–187. https://doi.org/10.1016/j.quageo.2015.09.005

McDougall, I. A. N., and Francis H. Brown (2009). Timing of volcanism and evolution of the northern Kenya Rift. *Geological Magazine*, 146, 1, p. 34–47. https://doi.org/10.1017/S0016756808005347

Moore, J.M., Davidson, A. (1978). Rift structure in southern Ethiopia. *Tectonophysics*, 46, p. 159–173. https://doi.org/10.1016/0040-1951(78)90111-7

Morrissey, Amy (2014). Stratigraphic Framework and Quaternary Paleolimnology of the Lake Turkana Rift, Kenya. PhD Thesis. Syracuse University, Syracuse, NY. https://surface.syr.edu/etd/62

Nishiizumi, Kunihiko, Mineo Imamura, Marc W. Caffee, John R. Southon, Robert C. Finkel, and Jeffrey McAninch (2007). Absolute calibration of 10Be AMS standards." *Nuclear Instruments and Methods in Physics Research Section B: Beam Interactions with Materials and Atoms*, 258, 2, p. 403–413. https://doi.org/10.1016/j.nimb.2007.01.297

Noren, Anders (2020a). HSPDP-NAO_NAW_public. OSF. https://doi.org/10.17605/OSF.IO/PBDT4

Noren, Anders (2020b). HSPDP-WTK_public. OSF. https://doi.org/10.17605/OSF.IO/B8QF2

Owusu Agyemang, Prince C., Eric M. Roberts, Bob Downie, and Joseph JW Sertich (2019). Sedimentary provenance and maximum depositional age analysis of the Cretaceous? Lapur and Muruanachok sandstones (Turkana Grits), Turkana Basin, Kenya. Geological Magazine, 156, 8, p. 1334–1356. https://doi.org/10.1017/S0016756818000663

Pasteels, P., M. Villeneuve, P. De Paepe, and J. Klerkx (1989). Timing of the volcanism of the southern Kivu province: implications for the evolution of the western branch of the East African Rift system. *Earth and Planetary Science Letters*, 94, 3-4, p. 353–363. https://doi.org/10.1016/0012-821X(89)90152-0

Paton, Chad, John Hellstrom, Bence Paul, Jon Woodhead, and Janet Hergt (2011). Iolite: Freeware for the visualisation and processing of mass spectrometric data. *Journal of Analytical Atomic Spectrometry*, 26, 12, p. 2508–2518. https://doi.org/10.1039/C1JA10172B

Peccerillo, A., C. Donati, A. P. Santo, A. Orlando, G. Yirgu, and D. Ayalew (2007). Petrogenesis of silicic peralkaline rocks in the Ethiopian rift: geochemical evidence and volcanological implications. *Journal of African Earth Sciences*, 48, 2-3, p. 161–173. https://doi.org/10.1016/j.jafrearsci.2006.06.010

Peccerillo, A., M. R. Barberio, G. Yirgu, D. Ayalew, M. W. U. T. W. Barbieri, and T. W. Wu (2003). Relationships between mafic and peralkaline silicic magmatism in continental rift settings: a petrological, geochemical and isotopic study of the Gedemsa volcano, central Ethiopian rift. *Journal of Petrology*, 44, 11, p. 2003–2032. https://doi.org/10.1093/petrology/egg068

Petrus, Joseph A., and Balz S. Kamber (2012). VizualAge: A novel approach to laser ablation ICP-MS U-Pb geochronology data reduction. *Geostandards and Geoanalytical Research*, 36, 3, p. 247–270. https://doi.org/10.1111/j.1751-908X.2012.00158.x

Philippon, Melody, Giacomo Corti, Federico Sani, Marco Bonini, Maria-Laura Balestrieri, Paola Molin, Ernst Willingshofer, Dimitrios Sokoutis, and Sierd Cloetingh (2014). Evolution, distribution, and characteristics of rifting in southern Ethiopia. *Tectonics*, 33, 4, p. 485–508. https://doi.org/10.1002/2013TC003430

Pik, Raphaël, Bernard Marty, Jean Carignan, Gezahegn Yirgu, and Teklewold Ayalew (2008). Timing of East African Rift development in southern Ethiopia: Implication for mantle plume activity and evolution of topography. *Geology*, 36, 2, p. 167–170. https://doi.org/10.1130/G24233A.1

Pik, Raphaël, Bernar Marty, Jean Carignan, and Jérôme Lavé (2003). Stability of the Upper Nile drainage network (Ethiopia) deduced from (U-Th)/He thermochronometry: implications for uplift and erosion of the Afar plume dome. *Earth and Planetary Science Letters*, 215, p. 73–88. https://doi.org/10.1016/S0012-821X(03)00457-6

Potts, Richard, 1998. Variability selection in hominid evolution. *Evolutionary Anthropology*, 7, p. 81–96. https://doi.org/10.1002/(SICI)1520-6505(1998)7:3<81::AID-EVAN3>3.0.CO;2-A

Puchol, Nicolas, Pierre-Henri Blard, Raphaël Pik, Bouchaïb Tibari, and Jérôme Lavé (2019). Variability of magmatic and cosmogenic ^{3}He in Ethiopian river sands of detrital pyroxenes: Impact on denudation rate determinations. *Chemical Geology*, 448, p. 13–25. https://doi.org/10.1016/j.chemgeo.2016.10.033

Purcell, P.G. (2018). Re-imagining and re-imaging the development of the East African Rift. *Petroleum Geoscience*, 24, p. 21–40. https://doi.org/10.1144/petgeo2017-036

Quade, Jay, Naomi E. Levin, Scott W. Simpson, Robert Butler, William C. McIntosh, Sileshi Semaw, Lynnette Kleinsasser, Guillaume Dupont-Nivet, Paul Renne, and Nelia Dunbar (2008). The geology of Gona, Afar, Ethiopia. *Geological Society of America Special Paper 446*, p. 1–31. https://doi.org/10.1130/2008.2446(01)

Quade, Jay, Naomi Levin, Sileshi Semaw, Dietrich Stout, Paul Renne, Michael Rogers, and Scott Simpson (2004). Paleoenvironments of the earliest stone toolmakers, Gona, Ethiopia. *Geological Society of America Bulletin*, 116, 11-12, p. 1529–1544. https://doi.org/10.1130/B25358.1

Quinn, Rhonda L., Christopher J. Lepre, James D. Wright, and Craig S. Feibel (2007). Paleogeographic variations of pedogenic carbonate δ^{13}C values from Koobi Fora, Kenya: implications for floral compositions of Plio-Pleistocene hominin environments." Journal of Human Evolution 53, 5, p. 560–573. https://doi.org/10.1016/j.jhevol.2007.01.013

Rabideaux, Nathan M., M. Sanam Chaudhary, Daniel Deocampo, Craig S. Feibel, and Andrew S. Cohen (2016). Unravelling the paleoenvironmental and diagenetic history of fluviolacustrine sediments from a Northern Kenya rift basin through analysis of HSPDP West Turkana-Kaitio Core material. *AGU Fall Meeting Abstracts*, p. PP23A-2312.

Rabideaux, Nathan M., Daniel M. Deocampo, Craig S. Feibel, Catherine C. Beck, and Dennis L. Nielson (2014). Illitization of smectite due to fault related hydrothermal alteration in HSPDP West Turkana core as revealed by clay mineralogy:

implications for core interpretation. Geological Society of America *Abstracts with Programs*, 46, 6, p. 711.

Redfield, T. F., W. H. Wheeler, and M. Often (2003). A kinematic model for the development of the Afar Depression and its paleogeographic implications. *Earth and Planetary Science Letters*, 216, 3, 383–398. https://doi.org/10.1016/S0012-821X(03)00488-6

Reed, Kaye E. (2008). Paleoecological patterns at the Hadar hominin site, Afar regional state, Ethiopia. *Journal of Human Evolution*, 54, 6, p. 743–768. https://doi.org/10.1016/j.jhevol.2007.08.013

Reiners, Peter W. (2005). Zircon (U-Th)/He thermochronometry." Reviews in Mineralogy and Geochemistry 58, no. 1 (2005): 151-179. https://doi.org/10.2138/rmg.2005.58.6

Reiners, Peter W., I. H. Campbell, Stefan Nicolescu, Charlotte M. Allen, J. K. Hourigan, J. I. Garver, J. M. Mattinson, and D. S. Cowan (2005). (U-Th)/(He-Pb) double dating of detrital zircons. *American Journal of Science*, 305, 4, p. 259–311. https://doi.org/10.2475/ajs.305.4.259

Renaut, Robin W., R. Bernhart Owen, Brian Jones, Jean-Jacques Tiercelin, Corinne Tarits, John K. Ego, and Kurt O. Konhauser (2013). Impact of lake-level changes on the formation of thermogene travertine in continental rifts: evidence from Lake Bogoria, Kenya Rift Valley. *Sedimentology*, 60, 2, p. 428–468. https://doi.org/10.1111/j.1365-3091.2012.01347.x

Renaut, Robin W., Jones, Brian, Tierclin, Jean-Jaques, Tarits, Corinne (2002). Sublacustrine precipitation of hydrothermal silica in rift lakes: evidence from Lake Baringo, central Kenya Rift Valley. *Sedimentary Geology*, 148, p. 235–257.

Riedl, Simon, Daniel Melnick, Geoffrey K. Mibei, Lucy Njue, and Manfred R. Strecker (2020). Continental rifting at magmatic centres: structural implications from the Late Quaternary Menengai Caldera, central Kenya Rift. *Journal of the Geological Society*, 177, 1, p. 153–169. https://doi.org/10.1144/jgs2019-021

Roberts, Helen M., Christopher Bronk Ramsey, Melissa S. Chapot, Alan L. Deino, Christine S. Lane, Céline Vidal, Asfawossen Asrat, Andrew Cohen, Verena Foerster, Henry F. Lamb, Frank Schaebitz, Martin H. Trauth. Using multiple chronometers to establish a long, directly dated lacustrine record: constraining >600,000 years of environmental change at Chew Bahir, Ethiopia. *Quaternary Science Reviews* (In review).

Roller, S., H. Wittmann, M. Kastowski, and M. Hinderer (2012). Erosion of the Rwenzori Mountains, East African Rift, from in situ-produced cosmogenic ^{10}Be. *Journal of Geophysical Research: Earth Surface*, 117, F03003, p. 1–20. https://doi.org/10.1029/2011JF002117

Romans, Brian W., Sébastien Castelltort, Jacob A. Covault, Andrea Fildani, and J. P. Walsh (2016). Environmental signal propagation in sedimentary systems across timescales. *Earth-Science Reviews*, 153, p. 7–29. https://doi.org/10.1016/j.earscirev.2015.07.012

Rooney, Tyrone O. (2017). The Cenozoic magmatism of East-Africa: Part I — Flood basalts and pulsed magmatism. *Lithos*, 286-287, p. 264–301. https://doi.org/10.1016/j.lithos.2017.05.014

Rooney, Tyrone O. (2020). The Cenozoic magmatism of East Africa: Part IV – The terminal stages of rifting preserved in the Northern East African Rift System. *Lithos*, 360-361, 105381, p. 1–29. https://doi.org/10.1016/j.lithos.2020.105381

Rooney, Tyrone O. (2020a). The Cenozoic magmatism of East Africa: Part II – Rifting of the mobile belt. *Lithos*, 360-361, 105291, p. 1–44. https://doi.org/10.1016/j.lithos.2019.105291

Rooney, Tyrone O. (2020b). The Cenozoic magmatism of East Africa: Part III – Rifting of the craton. *Lithos*, 360-361, 105390, p. 1–44. https://doi.org/10.1016/j.lithos.2020.105390

Rooney, Tyrone O. (2020c). The Cenozoic magmatism of East Africa: Part IV – The terminal stages of rifting preserved in the Northern East African Rift System. *Lithos*, 360-361, 105381, p. 1–29. https://doi.org/10.1016/j.lithos.2020.105381

Rooney, Tyrone O. (2020d). The Cenozoic magmatism of East Africa: Part V – Magma sources and processes in the East African Rift. *Lithos*, 360-361, 105296, p. 1–33. https://doi.org/10.1016/j.lithos.2019.105296

Schaller, M., T. A. Ehlers, T. Stor, J. Torrent, L. Lobato, Marcus Christl, and Christof Vockenhuber (2016). Spatial and temporal variations in denudation rates derived from cosmogenic nuclides in four European fluvial terrace sequences. *Geomorphology*, 274, p. 180–192. https://doi.org/10.1016/j.geomorph.2016.08.018

Schaller, M., and T.A. Ehlers (2006). Limits to quantifying climate driven changes in denudation rates with cosmogenic radionuclides. *Earth and Planetary Science Letters*, 248, p. 153–167. https://doi.org/10.1016/j.epsl.2006.05.027

Schaller, M., F. von Blanckenburg, Niels Hovius, A. Veldkamp, Meindert W. van den Berg, and P. W. Kubik (2004). Paleoerosion rates from cosmogenic 10Be in a 1.3 Ma terrace sequence: response of the River Meuse to changes in climate and rock uplift. *The Journal of Geology*, 112, 2, p. 127–144. https://doi.org/10.1086/381654

Schaller, M., Friedhelm von Blanckenburg, A. Veldkamp, L. A. Tebbens, N. Hovius, and P. W. Kubik (2002). " 30 000 yr record of erosion rates from cosmogenic ^{10}Be in Middle European river terraces. *Earth and Planetary Science Letters*, 204, 1-2, p. 307–320. https://doi.org/10.1016/S0012-821X(02)00951-2

Scherler, Dirk, Bodo Bookhagen, Hendrik Wulf, Frank Preusser, and Manfred R. Strecker (2015). Increased late Pleistocene erosion rates during fluvial aggradation in the Garhwal Himalaya, northern India. *Earth and Planetary Science Letters*, 428, p. 255–266. https://doi.org/10.1016/j.epsl.2015.06.034

Sepulchre, Pierre, Gilles Ramstein, Frédéric Fluteau, Mathieu Schuster, Jean-Jacques Tiercelin, and Michel Brunet (2009). Tectonic uplift and Eastern Africa aridification. Science, 313, 5792, p. 1419–1423. https://doi.org/10.1126/science.1129158

Shackleton, R. M. (1986). Precambrian collision tectonics in Africa. *Geological Society*, London, Special Publications 19, 1, p. 329–349. https://doi.org/10.1144/GSL.SP.1986.019.01.19

Sircombe, Keith N. (2000). Quantitative comparison of large sets of geochronological data using multivariate analysis: a provenance study example from Australia. *Geochimica et Cosmochimica Acta*, 64, 9, p. 1593–1616. https://doi.org/10.1016/S0016-7037(99)00388-9

Sláma, Jiří, Jan Košler, Daniel J. Condon, James L. Crowley, Axel Gerdes, John M. Hanchar, Matthew SA Horstwood, George A. Morris, Lutz Nasdala, Nicholas Norberg, Urs Schaltegger, Blair Shoene, Michael N. Tubrett, and Martin J. Whitehouse (2008). Plešovice zircon—a new natural reference material for U–Pb and Hf isotopic microanalysis. *Chemical Geology*, 249, 1-2, p. 1–35. https://doi.org/10.1016/j.chemgeo.2007.11.005

Sommer, H., A. Kröner, C. Hauzenberger, S. Muhongo, and M. T. D. Wingate (2003). Metamorphic petrology and zircon geochronology of high-grade rocks from the central Mozambique Belt of Tanzania: crustal recycling of Archean and Palaeoproterozoic material during the Pan-African orogeny. *Journal of Metamorphic Geology*, 21, 9, p. 915–934. https://10.1046/j.1525-1314.2003.00491.x

Spiegel, Cornelia, Barry P. Kohn, David X. Belton, and Andrew JW Gleadow (2007). Morphotectonic evolution of the central Kenya rift flanks: Implications for late Cenozoic environmental change in East Africa. Geology, 35, 5 p. 427–430. https://doi.org/10.1130/G23108A.1

Stab, Martin, Nicolas Bellahsen, Raphaël Pik, Xavier Quidelleur, Dereje Ayalew, and Sylvie Leroy (2016). Modes of rifting in magma-rich settings: Tectonomagmatic evolution of Central Afar. *Tectonics*, 35, p. 2–38. https://doi.org/10.1002/2015TC003893

Stern, Robert James, Kamal A. Ali, Mohamed G. Abdelsalam, Simon A. Wilde, and Qin Zhou (2012). U–Pb zircon geochronology of the eastern part of the Southern Ethiopian Shield. *Precambrian Research*, 206, p. 159–167. https://doi.org/10.1016/j.precamres.2012.02.008

Stern, Robert J. (1994). Arc assembly and continental collision in the Neoproterozoic East African Orogen: implications for the consolidation of Gondwanaland. *Annual Review of Earth and Planetary Sciences*, 22, 1, p. 319–351. https://doi.org/10.1146/annurev.ea.22.050194.001535

Stone, John O (2000). Air pressure and cosmogenic isotope production. *Journal of Geophysical Research: Solid Earth*, 105, B10, p. 23753–23759. https://doi.org/10.1029/2000JB900181

Tarits, Corinne, Renaut, Robin W., Tiercelin, Jean-Jaques, Le Hérisseé, Alain, Cotton, Jo, Cabon, Jean-Yves (2006). Geochemical evidence of hydrothermal recharge in Lake Baringo, central Kenya Rift Valley. *Hydrological Processes*, 20, 2027–2055. https://doi.org/10.1002/hyp.6046

Tefera, M., T. Chernet, W. Haro, N. Teshome, and K. Woldie (1996). Geological map of Ethiopia. Geological Survey of Ethiopia.

Teklay, M., A. Kröner, Klaus Mezger, and R. Oberhänsli (1998). Geochemistry, Pb-Pb single zircon ages and Nd-Sr isotope composition of Precambrian rocks from southern and eastern Ethiopia: implications for crustal evolution in East Africa. *Journal of African Earth Sciences*, 26, 2, p. 207–227. https://doi.org/10.1016/S0899-5362(98)00006-2

Tiercelin, Jean-Jacques, Jean-Luc Potdevin, Peter Kinyua Thuo, Yassine Abdelfettah, Mathieu Schuster, Sylvie Bourquin, Hervé Bellon, Jean-Philippe Clément, Hervé Guillou, Thierry Nalpas, and Gilles Ruffet (2012). Stratigraphy, sedimentology and diagenetic evolution of the Lapur Sandstone in northern Kenya: Implications for oil exploration of the Meso-Cenozoic Turkana depression. *Journal of African Earth Sciences*, 71, p. 43–79. https://doi.org/10.1016/j.jafrearsci.2012.06.007

Tiercelin, Jean-Jacques, Catherine Pflumio, Maryse Castrec, Jacques Boulégue, Pascal Gente, Joël Rolet, Christophe Coussement, Karl O. Stetter, Robert Huber, Sony Buku, and Wafulu Mifundu (1993). Hydrothermal vents in Lake Tanganyika, East African, Rift system. *Geology*, 21, 6, p. 499–502. https://doi.org/10.1130/0091-7613(1993)021<0499:HVILTE>2.3.CO;2

Torres Acosta, Verónica, Taylor F. Schildgen, Brian A. Clarke, Dirk Scherler, Bodo Bookhagen, Hella Wittmann, Friedhelm von Blanckenburg, and Manfred R. Strecker (2015). Effect of vegetation cover on millennial-scale landscape denudation rates in East Africa." *Lithosphere*, 7, 4, p. 408–420. https://doi.org/10.1130/L402.1

Trauth, Martin H., Asfawossen Asrat, Walter Duesing, Verena Foerster, K. Hauke Kraemer, Norbert Marwan, Mark A. Maslin, and Frank Schaebitz (2019). Classifying past climate change in the Chew Bahir basin, southern Ethiopia, using recurrence quantification analysis. *Climate Dynamics*, 53, 5, p. 2557–2572. https://doi.org/10.1007/s00382-019-04641-3

Trauth, Martin, Verena Foerster, Annett Junginger, Asfawossen Asrat, Henry Lamb, and Frank Schaebitz (2018). Abrupt or Gradual? Change Point Analysis of the Late Pleistocene-Holocene Chew Bahir Record from Southern Ethiopia. *Quaternary Research*, 90, 2, p. 321–330. https://doi.org/10.1017/qua.2018.30

Tripathy-Lang, Alka, Kip V. Hodges, Brian D. Monteleone, and Matthijs C. van Soest (2013). Laser (U-Th)/He thermochronology of detrital zircons as a tool for studying surface processes in modern catchments. *Journal of Geophysical Research: Earth Surface*, 118, 3, p. 1333–1341. https://doi.org/10.1002/jgrf.20091

Ukstins, Ingrid A., Paul R. Renne, Ellen Wolfenden, Joel Baker, Dereje Ayalew, and Martin Menzies (2002). Matching conjugate volcanic rifted margins: $^{40}Ar/^{39}Ar$ chrono-stratigraphy of pre-and syn-rift bimodal flood volcanism in Ethiopia and Yemen. *Earth and Planetary Science Letters*, 198, 3-4, p. 289–306. https://doi.org/10.1016/S0012-821X(02)00525-3

van Soest, Matthijs C., Kip V. Hodges, Jo-Anne Wartho, Marc B. Biren, Brian D. Monteleone, Jahandar Ramezani, John G. Spray, and Lucy M. Thompson (2011). (U-Th)/He dating of terrestrial impact structures: The Manicouagan example. *Geochemistry, Geophysics, Geosystems*, 12, 5, p. 4–8. https://doi.org/10.1029/2010GC003465

Verner, Kryštof, David Buriánek, Martin Svojtka, Vít Peřestý, Leta Megerssa, Tarekegn Tadesse, Aspiron Kussita, Diriba Alemayehu, and Tomáš Hroch (2021). Tectonometamorphic evolution and U–Pb dating of the high-grade Hammar Domain (Southern Ethiopian Shield); implications for the East-African Orogeny. *Precambrian Research*, 361, 106270. https://doi.org/10.1016/j.precamres.2021.106270

Von Blanckenburg, Friedhelm (2005). The control mechanisms of erosion and weathering at basin scale from cosmogenic nuclides in river sediment. *Earth and Planetary Science Letters*, 237, 3-4, p. 462–479. https://doi.org/10.1016/j.epsl.2005.06.030

Vrba, E., (1995). The fossil record of African antelopes (Mammalia, Bovidae) in relation to human evolution and paleoclimate. In E. Vrba et al. (eds.): *Paleoclimate and Evolution, With Emphasis on Human Origins*. New Haven: Yale University Press, p. 385–424.

Wiedenbeck, M. A. P. C., P. Alle, Fy Corfu, W. L. Griffin, M. Meier, F. V. Oberli, A. von Quadt, J. C. Roddick, and W. Spiegel (1995). Three natural zircon standards for U-Th-Pb, Lu-Hf, trace element and REE analyses. *Geostandards Newsletter*, 19, 1, p. 1–23. https://doi.org/10.1111/j.1751-908X.1995.tb00147.x

WoldeGabriel, Giday, Grant Heiken, Tim D. White, Berhane Asfaw, William K. Hart, and Paul R. Renne (2000). Volcanism, tectonism, sedimentation, and the paleoanthropological record in the Ethiopian Rift System. *Geological Society of America*, Special Paper 345, p. 83–99. https://doi.org/10.1130/0-8137-2345-0.83

Woldegabriel, Giday, James L. Aronson, and Robert C. Walter (1990). Geology, geochronology, and rift basin development in the central sector of the Main Ethiopia Rift. *Geological Society of America Bulletin*, 102, 4, p. 439–458. https://doi.org/10.1130/0016-7606(1990)102<0439:GGARBD>2.3.CO;2

Wolfenden, Ellen, Cynthia Ebinger, Gezahegn Yirgu, Paul R. Renne, and Simon P. Kelley (2005). Evolution of a volcanic rifted margin: Southern Red Sea, Ethiopia. *Geological Society of America Bulletin*, 117, 7-8, p. 846–864. https://doi.org/10.1130/B25516.1

Wynn, J.G., D.C. Roman, Z. Alemseged, D. Reed, D. Geraads, and S. Munro (2008). Stratigraphy, depositional environments, and basin structure of the Hadar and Busidima Formations at Dikika, Ethiopia, in Quade, J., and Wynn, J.G., eds., The Geology of Early Humans in the Horn of Africa: *Geological Society of America* Special Paper 446, p. 87–118. https://doi.org/10.1130/2008.2446(04)

Wynn, Jonathan G., Zeresenay Alemseged, René Bobe, Denis Geraads, Denné Reed, and Diana C. Roman (2006). Geological and palaeontological context of a Pliocene juvenile hominin at Dikika, Ethiopia. *Nature*, 443, 7109, p. 332–3336. https://doi.org/10.1038/nature05048

Yibas, B., W. U. Reimold, Richard Armstrong, Christian Koeberl, C. R. Anhaeusser, and David Phillips (2002). The tectonostratigraphy, granitoid geochronology and geological evolution of the Precambrian of southern Ethiopia. *Journal of African Earth Sciences*, 34, 1-2, 57–84. https://doi.org/10.1016/S0899-5362(01)00099-9

Yibas, B. (2000). The Precambrian geology, tectonic evolution, and controls of gold mineralisations in southern Ethiopia. Ph.D. Thesis, University of the Witwatersrand, Johannesburg, South Africa, 448 pp.

Zawacki, Emily E., Matthijs C. van Soest, Kip V. Hodges, Jennifer J. Scott, Manfred R. Strecker, Mélanie Barboni, Craig S. Feibel, Christopher J. Campisano, J Rámon Arrowsmith (2021). Sediment provenance and volcano-tectonic evolution of the East African Rift System from (U-Th)/He and U/Pb laser ablation double dating of detrital zircons. *Earth and Planetary Science Letters*, In review.

Zumbo, Vilma, Gilbert Féraud, Pierre Vellutin, Patrick Piguet, and Joëlle Vincent (1995). First $^{40}Ar/^{39}Ar$ dating on early pliocene to plio-pleistocene magmatic events of the Afar—Republic of Djibouti. *Journal of Volcanology and Geothermal Research*, 65, 3–4, p. 281–295. https://doi.org/10.1016/0377-0273(94)00107-R

APPENDIX A

CHAPTER 2 SUPPLEMENTARY MATERIALS

1 Cathodoluminescence Imagery

We obtained representative, post-analytical cathodoluminescence (CL) images of zircons of each major age population from NAO14-1D-39Q-2, NAW14-1A-8Q-1, and WTK13-1A-20Q-2. Images were acquired using a JEOL JXA-8530F electron microprobe with an acquisition time of 2 ms/pixel for a resolution of 0.26 μm/pixel.

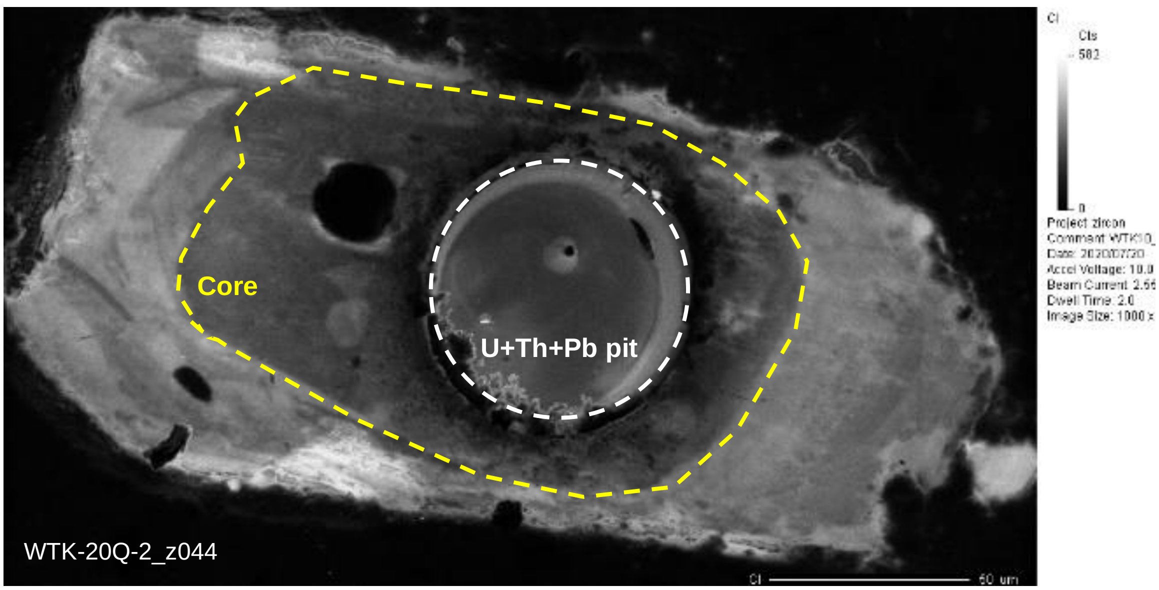

Figure A1. Example of CL imagery depicting distinct rim and core relationship (WTK13-1A-20Q-2_z044). Grains typically display zonation. The large pit size required for LADD analyses precludes measurements of both rim and core. U-Pb date of zircon is 22.02 Ma.

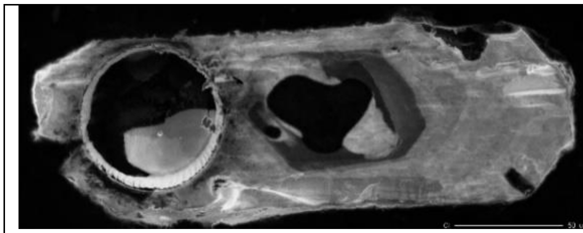

43.1 Ma (NAO14-1D-39Q-2_z042)

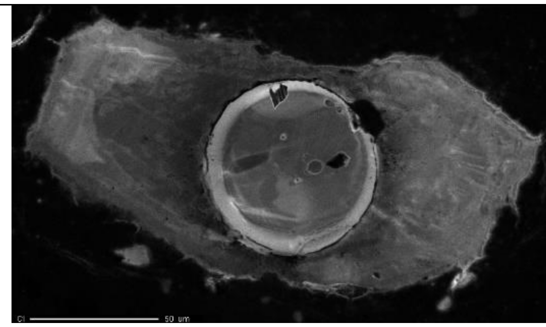

40.3 Ma (NAO14-1D-39Q-2_z108)

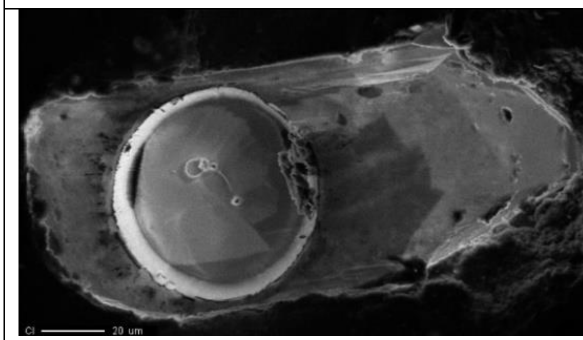

29.96 Ma (NAO14-1D-39Q-2_z078)

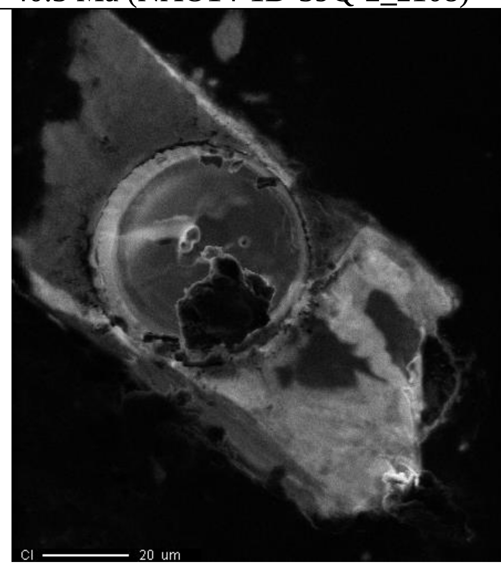

29.04 Ma (NAO14-1D-39Q-2_z085)

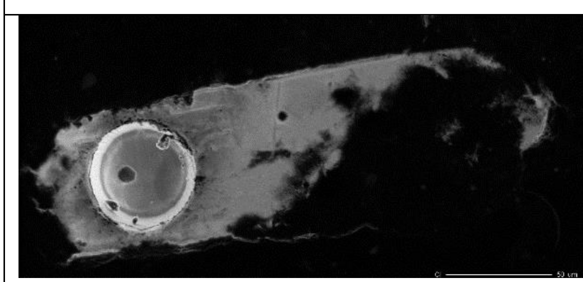

23.20 Ma (NAO14-1D-39Q-2_z088)

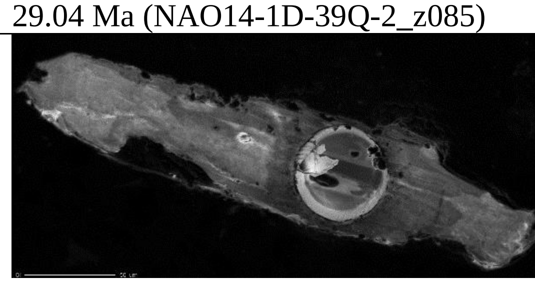

22.25 Ma (NAO14-1D-39Q-2_z069)

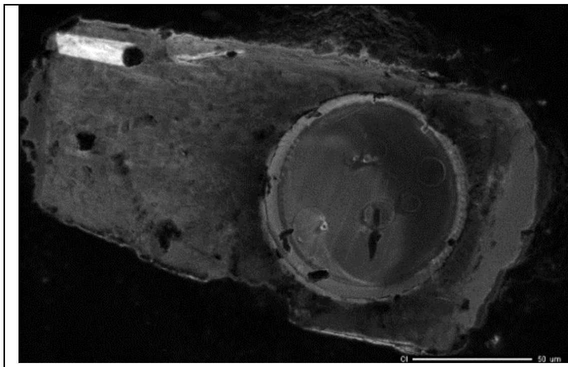

7.81 Ma (NAO14-1D-39Q-2_z065)

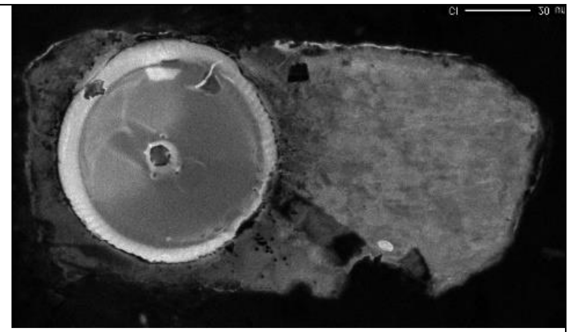

7.66 Ma (NAO14-1D-39Q-2_z054)

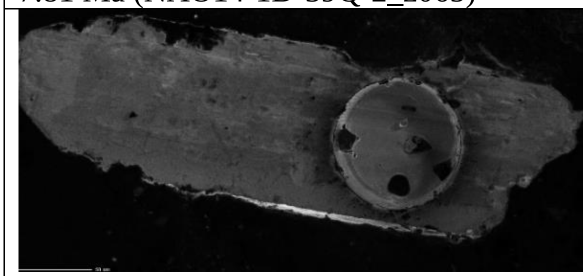

3.45 Ma (NAO14-1D-39Q-2_z070)

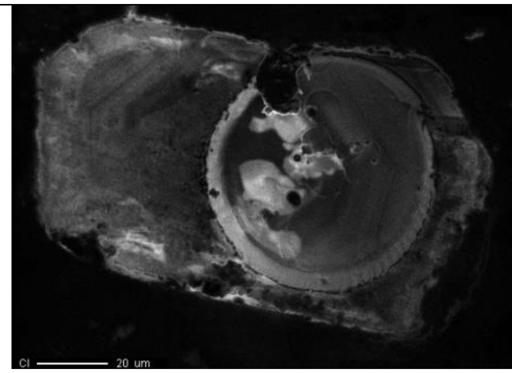

3.038 Ma (NAO14-1D-39Q-2_z046)

Figure A2. CL images from selected detrital zircon age populations from sample NAO14-1D-39Q-2. Denoted age is U-Pb age.

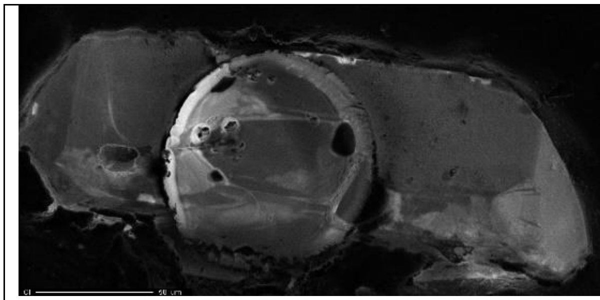	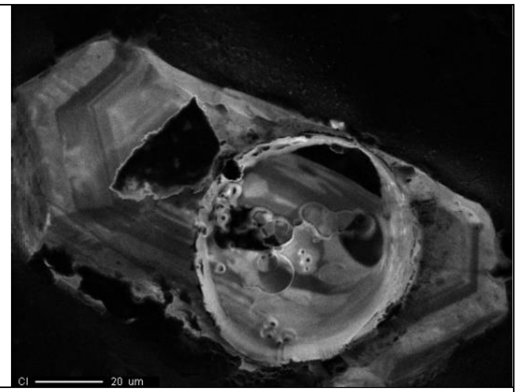
39.1 Ma (NAW14-1A-8Q-1_z101)	37.40 Ma (NAW14-1A-8Q-1_z102)
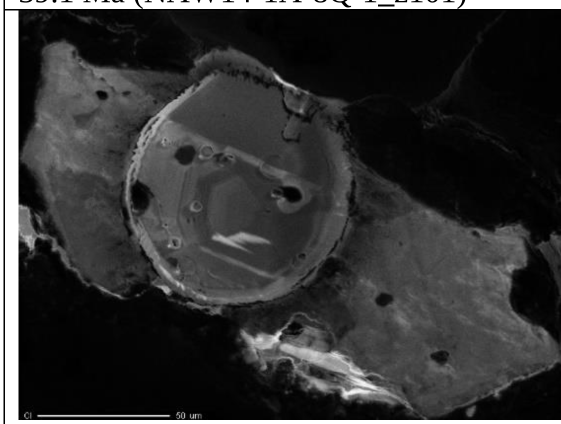	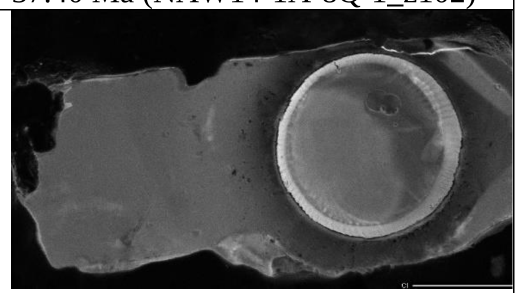
31.01 Ma (NAW14-1A-8Q-1_z109)	29.36 Ma (NAW14-1A-8Q-1_z003)
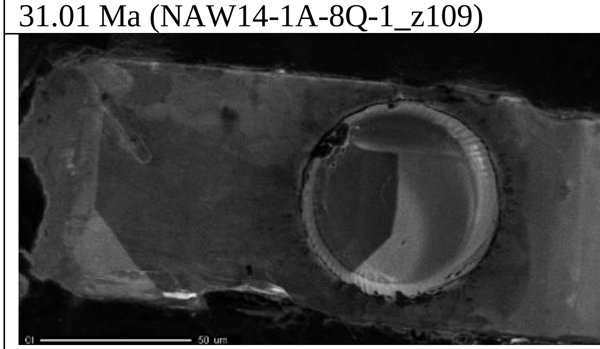	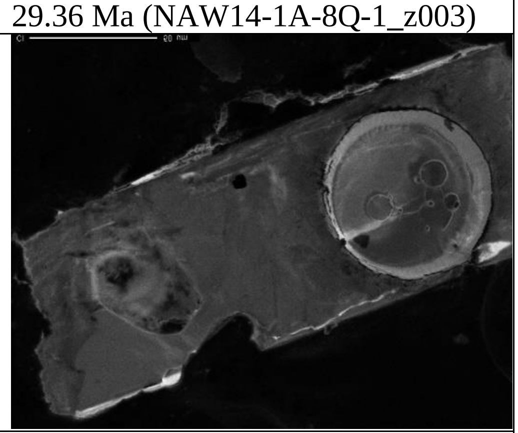
26.79 Ma (NAW14-1A-8Q-1_z050)	26.05 Ma (NAW14-1A-8Q-1_z002)

	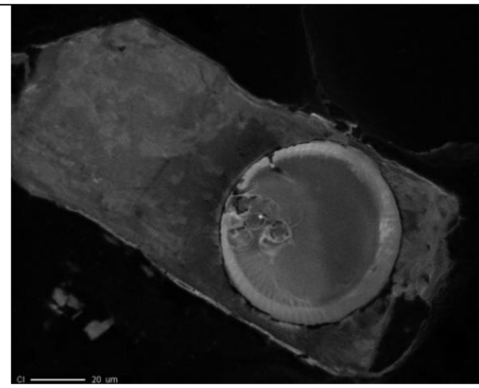
7.74 Ma (NAW14-1A-8Q-1_z067)	7.36 Ma (NAW14-1A-8Q-1_z028)
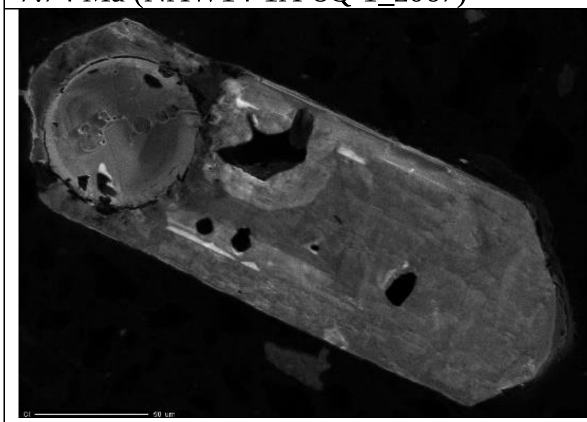	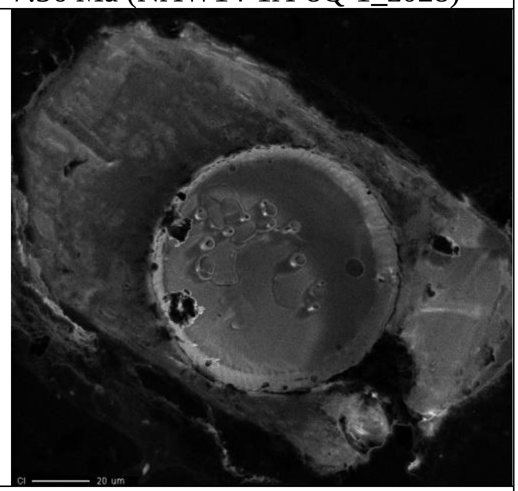
3.80 Ma (NAW14-1A-8Q-1_z001)	3.43 Ma (NAW14-1A-8Q-1_z033)
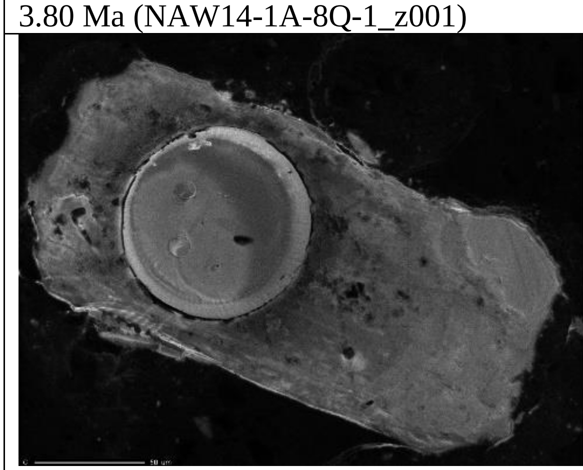	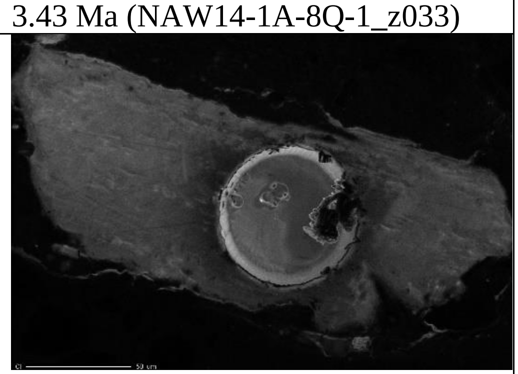
2.37 Ma (NAW14-1A-8Q-1_z019)	1.687 Ma (NAW14-1A-8Q-1_z063)

Figure A3. CL images from selected detrital zircon age populations from sample NAW14-1A-8Q-1. Grains z109 and z067 appear to show distinct rim-core relationships. Denoted age is U-Pb age.

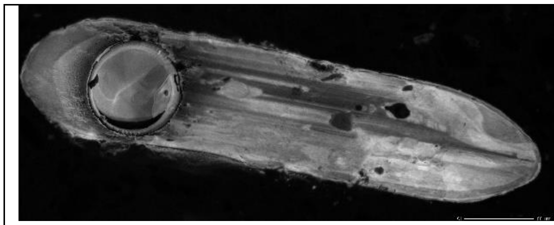

683.1 Ma (WTK13-1A-20Q-2_z080)

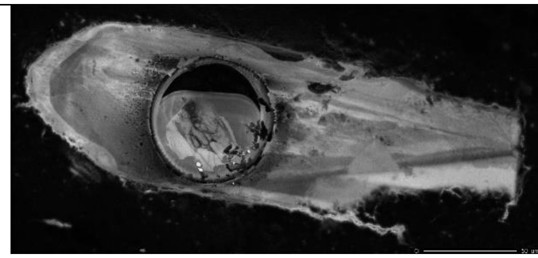

585.0 Ma (WTK13-1A-20Q-2_z024)

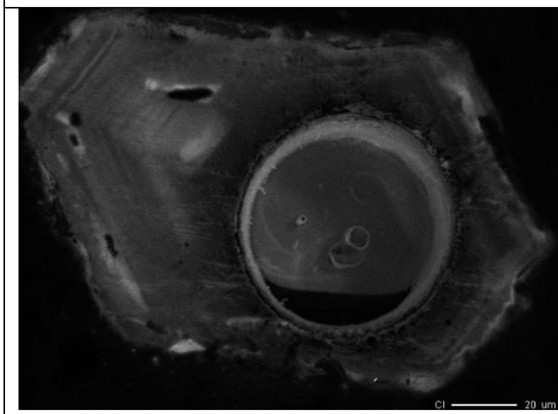

40.54 Ma (WTK13-1A-20Q-2_z069)

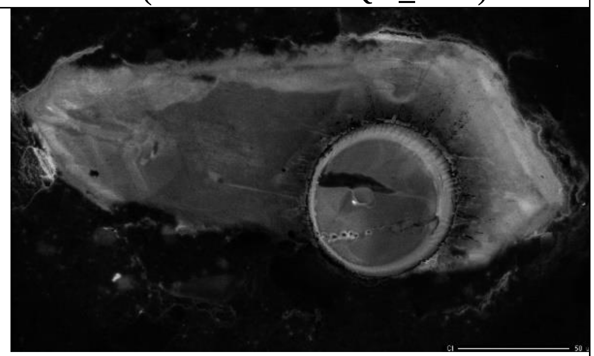

36.4 Ma (WTK13-1A-20Q-2_z040)

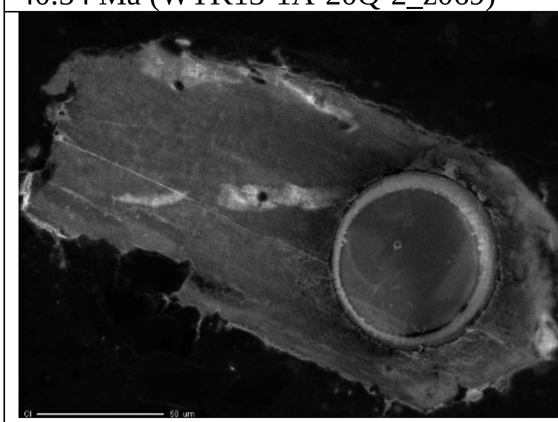

33.52 Ma (WTK13-1A-20Q-2_z093)

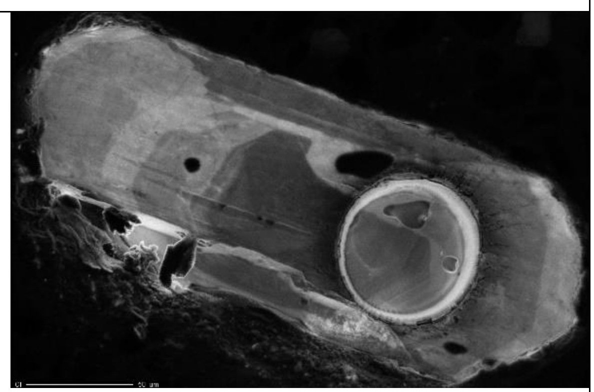

32.48 (WTK13-1A-20Q-2_z087)

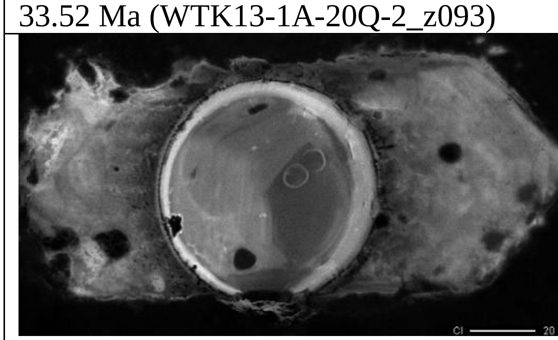

28.1 Ma (WTK13-1A-20Q-2_z062)

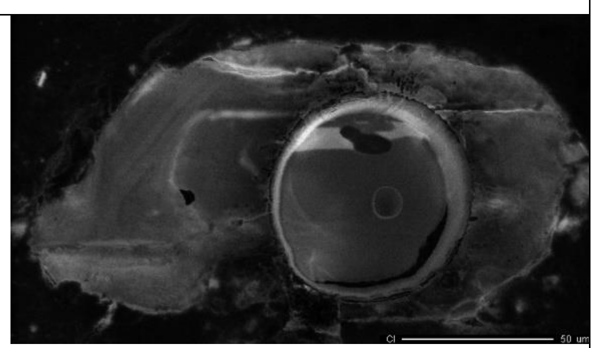

27.22 Ma (WTK13-1A-20Q-2_z002)

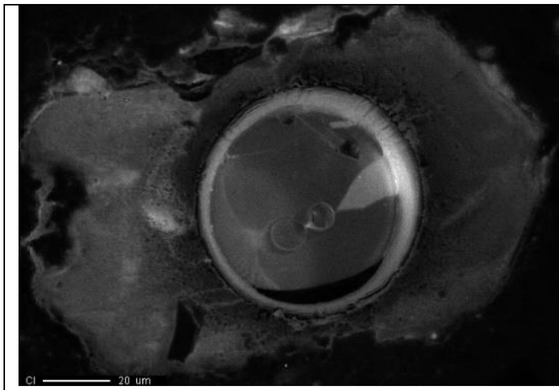

22.88 Ma (WTK13-1A-20Q-2_z106)

22.02 Ma (WTK13-1A-20Q-2_z044)

19.00 Ma (WTK13-1A-20Q-2_z032)

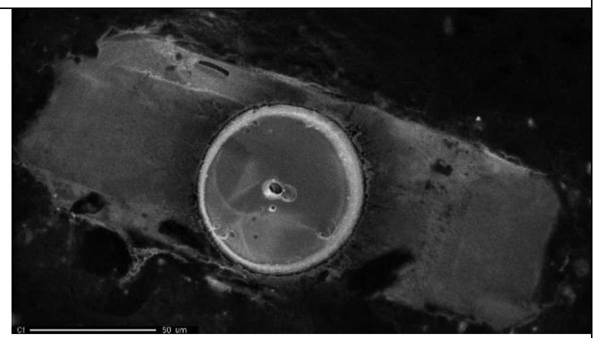

17.64 Ma (WTK13-1A-20Q-2_z086)

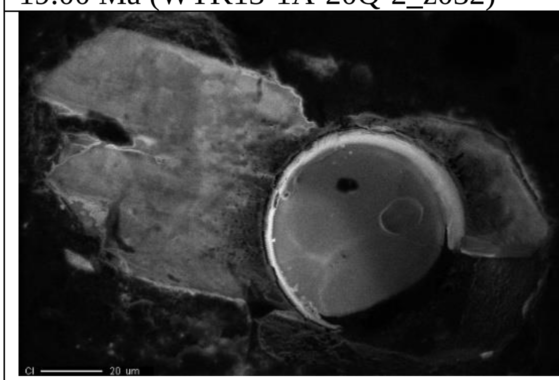

1.75 Ma (WTK13-1A-20Q-2_z099)

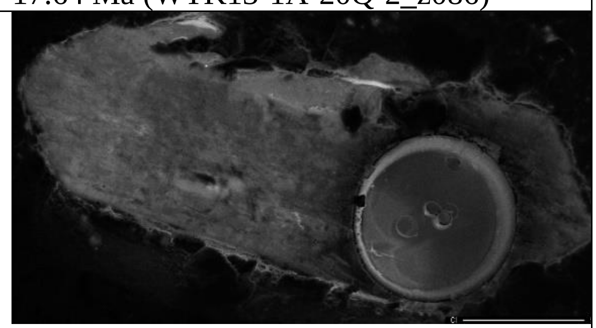

1.707 Ma (WTK13-1A-20Q-2_z065)

Figure A4. CL images from selected detrital zircon age populations from sample WTK13-1A-20Q-2. Grains z002 and z044 appear to show distinct rim-core relationships. Denoted age is U-Pb age.

2 (U-Th)/He Thermochronology

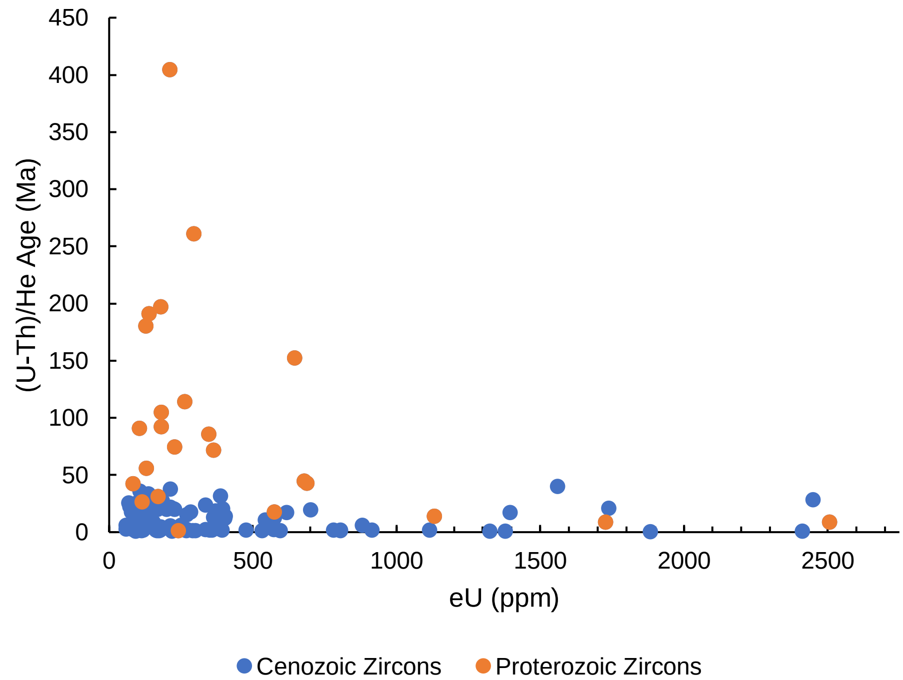

Figure A5. Effective uranium (eU) concentration vs. (U-Th)/He age of detrital zircons from the WTK13-1A-20Q-2 sample. There is no observed eU-age correlation amongst either the population of Cenozoic or Proterozoic zircons.

3 Sedimentary evidence for injection

Sedimentary evidence for high-pressure injected material and potential high-temperature fluids was recorded from visual and tactile observations of core and high-resolution images of the two Afar cores (HSPDP-NAO14-1D and HSPDP NAW14-1A) and the Turkana core (HSPDP-WTK13-1A). Sedimentary features including sedimentary dikes and sills, or injectites, were recognized with comparison to published examples (e.g., Dodd et al., 2020; Hurst et al., 2011). Several types of sedimentary features that indicate post-depositional hydrothermal alteration and sediment injection were observed in the NA cores. Sedimentary dikes, although less abundant, are also present in the WTK core.

3.1 Sedimentary injectites and flows

Sedimentary injection features observed in the NA cores comprise vertically oriented to oblique dikes that cross-cut original bedding at a high angle and sills (Figure A6a, b, c). The boundaries of the dikes range from straight to lobate and cuspate and may contain angular clasts ripped from the side walls within the fill of the structure. Most dikes are ~3–6 cm in diameter. Dike fill material mainly includes lithic (basaltic) sandstone, brecciated mudstone clasts, and red-brown clay. Vague, roughly horizontal bedding is observed in some examples with brecciated mudstone fill (Figure A6b), sandstone fill is mainly structureless (Figure A6), and the red-brown clay may be laminated or structureless. Sedimentary sills are also composed of these materials, but are oriented at a low angle to original bedding—some display stepped margins. These features are interpreted to have formed in the early to late post-depositional burial environment.

Some examples of fine-grained slurry flows and/or sills are filled mainly by red-brown clay and crystalline material (e.g., euhedral gypsum), and appear interbedded with diatomaceous laminated mudstones in the syn-depositional to early post-depositional setting (Figure A6d, e). They may be associated with small-sized dikes (~2–3 cm diameter) filled with the same material, as well as brecciated and silicified diatomaceous mudstone.

3.2 Cemented, stained, altered, and brecciated zones

Small-scale fracture networks that cross-cut laminated diatomaceous and non-diatomaceous mudstone as well as pedogenically modified mudstones are typically associated with white to yellowish orange carbonate and possibly iron-carbonate cement, as well as black and orange-red zones of amorphous mineralization and subhedral to euhedral black and red-black crystals (not yet identified; Figure A6e). Fracture networks that cross-cut laminated lacustrine mudstones may be filled with euhedral gypsum. Orange-red, yellow, and black stained zones are sometimes associated with carbonate cement and distinct fracture networks. Discolored alteration zones in non-pedogenic and pedogenic brown mudstones (both outside of and within dikes) are a dull brownish grey or bluish grey (Figure A6c).

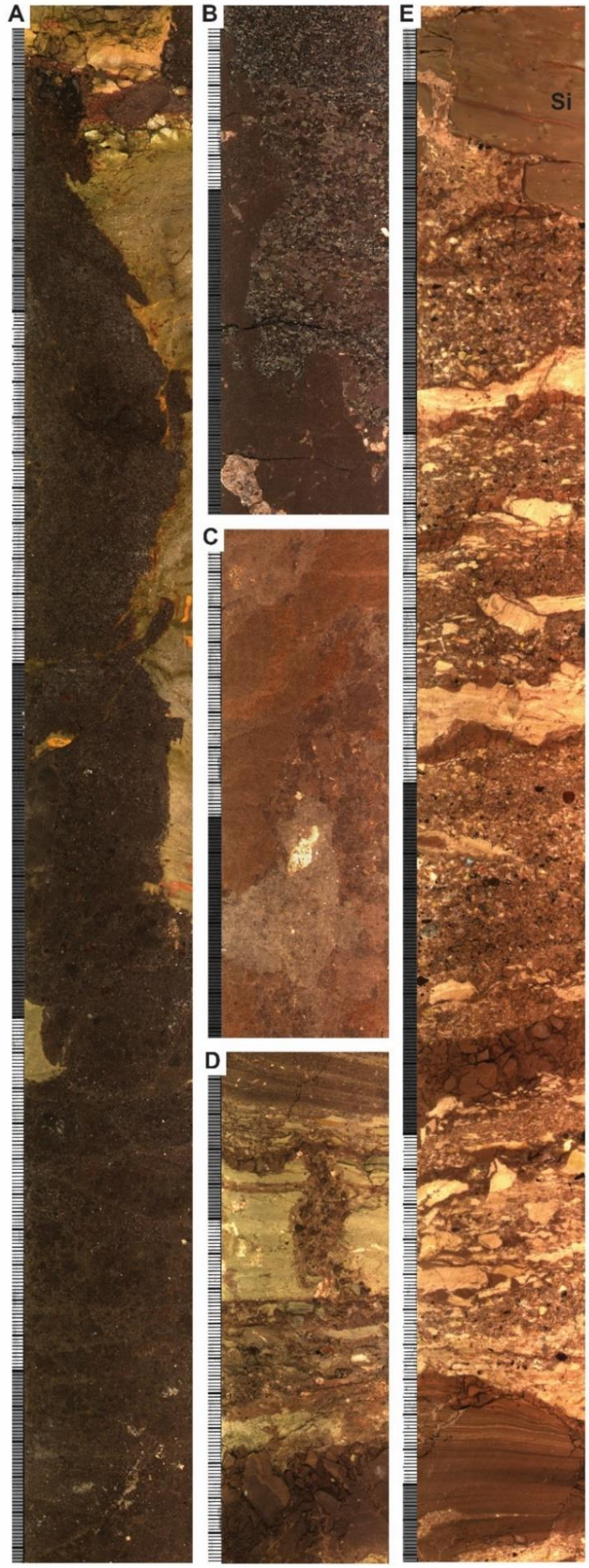
A
B
C
D
E
Si

Figure A6. Scanned core images from Afar (NAO14-1D; NAW14-1A). Scales are in mm with 10 cm intervals alternating between white and grey. (a) Lithic sandstone fill in vertical dike cross-cutting laminated green mudstones. Note orange mineralization at dike boundaries and in adjacent lacustrine mudstones (HSPDP-NAO14-1D-31Q-2-A). (b) Mudstone clast-filled dike with sharp, lobate, and cuspate boundaries cross-cutting pedogenically modified sandy mudstone with carbonate nodules and rhizoliths. Note alignment of mudstone clasts within dike fill (HSPDP-NAO14-1D-41Q-2-A). (c) Structureless and discolored zone of grey clay and brecciated material within dike that cross-cuts pedogenically modified siltstone (HSPDP-NAW14-1A-27Q-1-A). (d) Small vertical dike with brecciated mudstone fill associated with brecciated lacustrine mudstone and laminated flow above. Lower part of images shows dark brown clay band (?sill). Injectite features cross-cut and are interbedded with lake beds (HSPDP-NAO14-1D-23Q-2-A). (e) Thick disrupted zone with laminated red-brown clay; brecciated diatomaceous mudstones; and mafic crystalline material and gypsum. Injected material cross-cuts silicified laminated lacustrine mudstones (top) (HSPDP-NAW14-1A-14Q-2-A).

References:

Dodd, Thomas J.H., McCarthy, Dave J., Clarke, Stuart M. (2020). Clastic injectites, internal structures and flow regime during injection: The Sea Lion Injectite System, North Falkland Basin. Sedimentology, 67, p. 1014–1044. https://doi.org/10.1111/sed.12672

Hurst, Andrew, Scott, Anthony, Vigorito, Mario (2011). Physical characteristics of sand injectites. Earth-Science Reviews, 106, p. 215–246. https://doi.org/10.1016/j.earscirev.2011.02.004

Explanation of variables for Supplementary Tables A1-5

- He pit vol. (μm^3) = The volume of the helium analysis determined by white light interferometry.
- err. (2σ) = Associated 2σ error for corresponding variable.
- U-Th Pit Vol. (μm^3) = The volume of the material ablated during U-Th-Pb LA-ICP-MS analysis, which is the measured void volume as determined by white light interferometry minus the pit.
- [^{4}He] (nmoles/g) = The ^{4}He concentration in nmoles/g calculated from the blank corrected measured He amount in moles and the helium laser pit volume converted to an ablated sample mass using a nominal zircon density of 4.65 g/cm^3.
- [^{238}U] (nmoles/g) = The U concentration in nmoles/g.
- [^{232}Th] (nmoles/g) = The Th concentration in nmoles/g.
- $^{232}Th/^{238}U$ = $^{232}Th/^{238}U$ ratio
- eU (ppm) = The effective uranium concentration calculated as follows: U + 0.235 x Th.
- (U-Th)/He date (Ma) = The (U-Th/He) date calculated using the He, U, and Th concentrations in the table using the iterative approach.
- $^{207}Pb/^{235}U$ date (Ma) and err. (2σ) = The $^{207}Pb/^{235}U$ date and 2σ error, which includes all analytical errors including those in the U/Pb standard and downhole fractionation correction, but not errors in the decay constants.
- $^{206}Pb/^{238}U$ = The $^{206}Pb/^{238}U$ ratio as exported from the Iolite Data Reduction software.

- $^{206}Pb/^{238}U$ date (Ma) and err. (2σ) = The $^{206}Pb/^{238}U$ date and 2σ error, which includes all analytical errors including those in the U/Pb standard and downhole fractionation correction, but not errors in the decay constants.

Supplementary Table A1
(U-Th)/He and U/Pb dates by LADD of detrital zircon for sample NAO14-1D-39Q-2

Grain	He Pit Vol. (μm^3)	err. (2σ)	U-Th Pit Vol. (μm^3)	err. (2σ)	[^{4}He] (nmol/g)	err. (2σ)	[^{238}U] (nmol/g)	err. (2σ)	[^{232}Th] (nmol/g)	err. (2σ)	^{232}Th/^{238}U	eU (ppm)	(U-Th)/He date (Ma)	err. (2σ)	^{207}Pb/^{235}U date (Ma)	err. (2σ)	^{206}Pb/^{238}U	err. (2σ)	^{206}Pb/^{238}U date (Ma)	err. (2σ)
3	7374.8	84.0	138024	1785	9.2	0.2	1053.4	41.6	1027.8	92.9	0.94	309	5.5	0.2	9.1	2.0	0.0013	0.0000	8.3	0.2
4	7253.2	86.9	138287	2209	13.4	0.4	975.7	39.9	1014.2	92.6	1.01	289	8.6	0.4	39.1	2.8	0.0055	0.0001	35.4	0.7
5	2631.0	27.3	85769	922	10.0	0.3	309.7	11.4	312.9	27.9	0.98	91	20.3	0.9	31.0	4.8	0.0050	0.0001	32.4	0.9
6	7582.3	85.3	144826	2018	13.1	0.3	543.2	21.6	380.9	34.5	0.68	151	16.1	0.7	29.0	0.6	0.0040	0.0001	26.0	0.5
8	7608.0	78.6	135809	1761	7.3	0.2	900.1	35.4	789.9	71.4	0.85	259	5.2	0.2	11.1	0.8	0.0014	0.0000	9.3	0.3
9	7119.0	78.7	137233	1643	13.5	0.4	1239.0	48.3	1592.5	144.4	1.24	384	6.5	0.3	7.7	2.0	0.0012	0.0000	7.9	0.3
10	7101.5	78.5	136134	2018	2.2	0.1	600.1	24.0	363.9	33.0	0.59	164	2.5	0.1	4.1	10.1	0.0006	0.0000	3.6	0.2
11	6860.4	78.4	120485	2084	3.8	0.1	639.8	26.5	507.7	46.3	0.77	181	3.9	0.2	7.6	0.5	0.0011	0.0000	7.2	0.2
12	2928.0	29.9	56097	610	8.3	0.3	1188.2	43.9	705.0	63.0	0.57	323	4.7	0.2	8.1	3.2	0.0012	0.0000	7.7	0.2
13	7309.4	78.4	136144	2038	118.6	3.0	4471.9	180.6	2288.9	207.9	0.50	1197	18.4	0.8	22.9	0.4	0.0035	0.0000	22.6	0.2
14	6881.8	76.2	133009	2258	6.1	0.2	769.0	31.7	597.7	54.5	0.75	217	5.2	0.2	12.0	1.9	0.0015	0.0001	9.7	0.4
15	2606.7	27.8	80473	910	22.6	0.6	623.7	23.1	353.3	31.5	0.55	169	24.8	1.1	35.4	2.4	0.0045	0.0001	28.8	0.5
16	6784.7	76.8	147687	2100	13.4	0.3	299.9	12.0	389.7	35.3	1.26	93	26.5	1.2	40.5	2.5	0.0053	0.0001	34.0	0.8
18	6774.3	75.9	135779	2314	7.7	0.2	1914.0	79.0	1556.8	141.9	0.79	544	2.6	0.1	9.8	1.9	0.0012	0.0000	7.8	0.1
19	6716.9	77.8	139577	2187	20.9	0.5	1762.6	71.6	1614.8	146.7	0.89	511	7.6	0.3	10.9	0.8	0.0012	0.0000	7.8	0.1
20	2728.7	28.2	80226	898	10.1	0.3	3420.5	126.5	2738.7	244.6	0.77	969	1.9	0.1	3.5	0.8	0.0005	0.0000	3.3	0.1
21	706.6	7.2	41178	417	10.8	0.5	233.3	8.5	242.9	21.6	1.01	69	28.7	1.7	45.9	2.4	0.0054	0.0002	34.4	1.3
22	2841.0	29.4	79301	887	4.1	0.2	1313.4	48.7	1177.5	105.2	0.87	379	2.0	0.1	3.1	0.2	0.0005	0.0000	3.1	0.1
23	2892.7	29.9	80000	898	137.9	3.4	3106.9	114.9	4409.6	393.8	1.37	903	25.9	1.1	24.8	0.6	0.0037	0.0001	23.7	0.9
25	2622.8	26.8	91897	1030	4.8	0.2	425.0	15.9	279.7	25.0	0.64	117	7.6	0.4	7.5	0.6	0.0011	0.0002	7.2	1.3
26	6859.4	77.3	133563	2132	3.4	0.1	653.0	26.7	454.9	41.4	0.67	181	3.4	0.2	5.9	2.3	0.0006	0.0000	3.8	0.2
27	730.9	7.7	42898	437	13.3	0.6	384.8	14.1	169.9	15.1	0.43	102	24.2	1.3	26.7	3.0	0.0040	0.0001	25.5	0.8
28	7079.7	84.7	134350	1760	18.3	0.5	506.9	19.8	301.8	27.2	0.58	136	24.6	1.1	29.0	0.5	0.0043	0.0001	27.4	0.5
29	7838.2	115.1	142850	2059	9.1	0.3	313.9	12.4	217.9	19.7	0.67	87	19.4	0.9	32.5	0.7	0.0045	0.0001	28.7	0.7
30	6509.1	74.9	147512	2457	20.3	0.5	2075.7	83.8	1458.5	132.4	0.68	577	6.5	0.3	10.5	0.6	0.0012	0.0000	7.8	0.1
31	2479.0	26.1	82362	934	3.0	0.1	1038.8	38.7	1471.6	131.5	1.37	329	1.7	0.1	26.0	1.6	0.0040	0.0001	25.9	0.6
32	2901.3	30.0	84023	934	15.3	0.4	340.2	12.6	195.4	17.4	0.56	92	30.8	1.4	38.8	13.7	0.0049	0.0005	31.2	3.0
33	2686.2	28.2	81753	874	5.8	0.2	240.9	8.9	186.1	16.6	0.75	68	15.9	0.8	38.3	4.0	0.0046	0.0005	29.4	3.5
34	805.0	8.3	46234	471	2.4	0.3	174.5	6.4	183.5	16.4	1.02	52	8.6	1.3	26.1	5.2	0.0041	0.0003	26.5	1.8
35	765.6	8.0	41967	426	5.5	0.4	195.7	7.2	153.2	13.7	0.76	55	18.5	1.5	28.9	1.2	0.0040	0.0002	25.9	1.1
36	743.5	7.8	53007	544	57.7	1.6	1349.3	49.6	747.3	66.6	0.54	364	29.3	1.3	28.6	0.8	0.0042	0.0001	27.2	0.5
37	2545.4	26.3	81680	927	8.1	0.3	835.5	31.0	803.6	71.8	0.93	244	6.1	0.3	12.0	1.1	0.0017	0.0001	10.9	0.4
40	2540.1	26.8	87363	957	7.8	0.3	192.3	7.1	99.7	8.9	0.50	52	28.0	1.3	33.0	8.8	0.0047	0.0001	30.3	0.9

Supplementary Table A1 Continued

Grain	He Pit Vol. (μm^3)	err. (2σ)	U-Th Pit Vol. (μm^3)	err. (2σ)	[^{4}He] (nmol/g)	err. (2σ)	[^{238}U] (nmol/g)	err. (2σ)	[^{232}Th] (nmol/g)	err. (2σ)	^{232}Th/^{238}U	eU (ppm)	(U-Th)/He date (Ma)	err. (2σ)	^{207}Pb/^{235}U date (Ma)	err. (2σ)	^{206}Pb/^{238}U	err. (2σ)	^{206}Pb/^{238}U date (Ma)	err. (2σ)
41	2641.3	27.4	74575	871	22.3	0.6	991.4	36.9	382.2	34.2	0.37	259	16.0	0.7	31.0	1.7	0.0042	0.0001	27.0	0.4
42	2669.7	28.7	103259	1135	7.1	0.2	120.5	4.5	101.2	9.0	0.81	34	38.4	1.8	49.4	3.5	0.0067	0.0003	43.1	1.9
43	5613.0	57.3	98127	1204	2.3	0.1	908.0	34.2	826.1	74.0	0.88	263	1.6	0.1	9.2	0.8	0.0012	0.0001	7.6	0.4
44	754.1	7.9	46995	474	8.7	0.5	221.9	8.3	148.2	13.3	0.65	61	26.3	1.7	31.6	4.2	0.0039	0.0001	25.1	0.9
45	2579.3	27.4	79921	851	13.6	0.4	1332.8	50.5	1249.2	112.2	0.91	388	6.5	0.3	24.2	1.7	0.0036	0.0002	23.2	1.0
46	2566.7	27.7	87356	1058	19.4	0.5	7793.1	290.8	4377.3	391.5	0.54	2107	1.7	0.1	3.1	0.3	0.0005	0.0000	3.0	0.0
48	3118.3	31.7	80448	857	3.9	0.1	1211.3	44.8	996.6	89.0	0.80	345	2.1	0.1	3.2	0.3	0.0005	0.0000	3.1	0.1
49	2496.4	25.9	83915	927	10.2	0.3	270.6	10.0	203.7	18.2	0.73	76	24.9	1.1	28.8	0.8	0.0041	0.0001	26.6	0.7
50	671.1	7.0	52460	536	1.0	0.4	181.4	6.7	165.7	14.8	0.88	53	3.7	1.4	13.3	1.9	0.0017	0.0001	11.1	0.8
51	6847.9	74.4	138395	2099	20.1	0.5	1757.4	69.9	1963.2	177.8	1.08	528	7.0	0.3	10.1	4.5	0.0013	0.0000	8.2	0.2
52	2859.9	29.9	79544	863	15.2	0.4	532.7	19.6	200.4	17.9	0.36	139	20.3	0.9	29.2	0.7	0.0043	0.0001	27.4	0.6
53	2545.3	27.0	81572	908	13.4	0.4	338.3	12.5	180.9	16.2	0.52	91	27.2	1.2	34.9	8.3	0.0048	0.0001	30.7	0.7
54	2495.6	25.9	83607	896	4.6	0.2	641.9	23.7	516.7	46.1	0.78	182	4.7	0.2	7.7	0.5	0.0012	0.0001	7.7	0.8
55	2609.0	26.9	82957	910	4.3	0.2	181.0	6.7	122.3	10.9	0.65	50	15.8	0.9	24.3	1.3	0.0037	0.0002	23.8	1.2
56	6583.6	72.4	138933	2143	5.2	0.1	527.1	21.1	928.0	84.1	1.70	177	5.4	0.3	7.3	0.7	0.0012	0.0001	7.7	0.3
57	2472.0	25.7	80685	883	23.0	0.6	2065.8	76.2	1950.7	174.1	0.91	602	7.1	0.3	7.7	0.3	0.0012	0.0000	7.7	0.1
58	2401.5	25.3	78991	878	9.2	0.3	381.9	14.2	305.5	27.3	0.77	108	15.7	0.7	25.2	2.2	0.0035	0.0001	22.7	0.5
59	737.2	7.6	45661	460	22.5	0.8	1221.6	44.7	1545.7	137.8	1.22	377	11.0	0.5	27.0	1.9	0.0037	0.0001	23.6	0.5
60	2707.5	27.9	79537	837	2.0	0.1	677.6	24.9	488.6	43.7	0.70	189	2.0	0.1	9.5	2.2	0.0014	0.0003	9.1	2.2
61	2457.0	25.5	84195	922	18.0	0.5	688.1	25.4	874.2	78.1	1.23	213	15.7	0.7	38.8	6.4	0.0049	0.0002	31.5	1.5
62	6719.8	74.4	121856	1626	29.0	0.7	791.1	30.9	637.5	57.5	0.78	224	23.9	1.1	39.1	2.9	0.0046	0.0001	29.3	0.4
63	7979.5	97.2	151094	2073	1.6	0.1	1860.8	73.0	275.3	24.8	0.14	461	0.7	0.0	9.5	3.3	0.0011	0.0001	7.1	0.6
64	659.7	6.9	42147	428	6.1	0.5	1059.4	38.9	1114.0	99.4	1.02	315	3.6	0.3	8.0	1.0	0.0010	0.0000	6.2	0.2
65	6461.5	71.8	134834	2392	13.9	0.4	1559.2	65.7	1340.1	122.7	0.83	447	5.8	0.3	9.8	0.6	0.0012	0.0000	7.8	0.2
66	2904.6	32.8	79835	865	9.6	0.3	1040.6	38.4	1213.9	108.4	1.13	316	5.6	0.3	9.1	1.0	0.0013	0.0000	8.6	0.3
69	661.1	6.7	43845	448	17.6	0.7	817.4	32.0	1370.5	124.8	1.62	271	12.0	0.6	26.4	3.5	0.0035	0.0001	22.6	0.6
70	6328.1	72.5	137222	1852	1.1	0.1	358.5	14.5	211.3	19.2	0.57	97	2.2	0.1	3.3	1.5	0.0005	0.0001	3.5	0.3
71	6772.2	74.1	141895	2203	6.1	0.2	1688.5	69.5	1305.5	118.9	0.75	476	2.4	0.1	3.4	2.4	0.0005	0.0000	3.3	0.1
72	2709.0	28.2	79513	891	14.2	0.4	552.8	20.4	231.5	20.7	0.41	145	18.1	0.8	29.1	0.8	0.0043	0.0001	27.8	0.6
73	719.9	7.6	46392	473	0.9	0.4	212.8	7.9	167.1	14.9	0.76	60	2.9	1.1	7.4	0.5	0.0010	0.0001	6.1	0.5
74	6419.4	71.2	138953	2526	15.4	0.4	1503.3	63.6	1421.0	130.2	0.91	438	6.5	0.3	7.8	0.6	0.0012	0.0000	7.7	0.1
75	2413.6	25.2	85503	935	15.6	0.4	440.5	16.2	320.9	28.6	0.71	123	23.4	1.0	30.0	1.6	0.0048	0.0002	30.7	1.4
76	694.2	7.2	41647	423	25.2	0.8	760.4	27.8	288.9	25.7	0.37	196	23.6	1.1	35.6	4.5	0.0040	0.0001	25.8	0.6

Supplementary Table A1 Continued

Grain	He Pit Vol. (μm^3)	err. (2σ)	U-Th Pit Vol. (μm^3)	err. (2σ)	[^{4}He] (nmol/g)	err. (2σ)	[^{238}U] (nmol/g)	err. (2σ)	[^{232}Th] (nmol/g)	err. (2σ)	$^{232}Th/^{238}U$	eU (ppm)	(U-Th)/He date (Ma)	err. (2σ)	$^{207}Pb/^{235}U$ date (Ma)	err. (2σ)	$^{206}Pb/^{238}U$	err. (2σ)	$^{206}Pb/^{238}U$ date (Ma)	err. (2σ)
77	2474.3	25.9	82715	955	2.0	0.1	697.3	25.9	589.6	52.7	0.82	199	1.9	0.1	4.9	0.7	0.0008	0.0000	4.9	0.2
78	2378.5	24.3	86451	925	10.6	0.3	311.0	11.5	172.7	15.4	0.54	84	23.3	1.1	41.0	5.0	0.0047	0.0001	30.0	0.7
79	2418.1	25.8	84377	927	15.4	0.4	527.4	19.4	345.9	30.9	0.63	145	19.6	0.9	32.0	4.1	0.0048	0.0001	30.6	0.5
81	2563.8	27.3	84090	933	29.3	0.8	1118.3	41.5	494.9	44.2	0.43	295	18.4	0.8	34.9	7.5	0.0048	0.0001	30.6	0.4
82	2543.3	26.7	81565	918	7.3	0.2	877.7	32.4	666.5	59.5	0.73	247	5.4	0.3	7.6	0.5	0.0012	0.0000	7.7	0.2
84	6689.1	72.6	135226	2117	13.1	0.3	444.8	18.4	336.6	30.7	0.73	125	19.4	0.9	43.0	6.1	0.0047	0.0001	30.4	0.6
85	685.9	7.0	46358	471	34.6	1.1	1370.5	50.6	1794.0	160.2	1.27	426	15.0	0.7	29.0	0.8	0.0045	0.0001	29.0	0.4
86	2373.1	24.7	84050	931	12.9	0.4	306.7	11.3	178.3	15.9	0.56	83	28.7	1.3	31.4	3.1	0.0046	0.0001	29.6	0.7
87	6378.0	70.0	144215	2147	11.9	0.3	353.7	14.5	164.1	14.9	0.45	94	23.5	1.1	25.8	3.6	0.0040	0.0001	25.9	0.5
88	655.6	6.7	42502	429	4.0	0.5	189.4	6.9	141.8	12.7	0.72	53	13.8	1.7	25.7	2.5	0.0036	0.0004	23.2	2.6
89	6424.6	72.9	132294	1865	2.1	0.1	156.6	6.4	102.1	9.3	0.63	43	9.1	0.5	27.9	3.2	0.0041	0.0002	26.4	1.1
91	6631.7	71.4	134530	2592	7.1	0.2	269.6	12.1	134.9	12.6	0.48	72	18.4	0.9	25.0	1.8	0.0041	0.0002	26.6	1.0
92	720.7	7.4	48985	499	11.2	0.5	1009.7	37.1	1114.8	99.4	1.07	303	6.9	0.4	8.4	1.1	0.0013	0.0000	8.6	0.3
93	6683.0	74.7	122500	2147	11.8	0.3	374.9	15.9	356.8	32.7	0.92	109	19.9	0.9	34.3	2.7	0.0046	0.0001	29.8	0.6
94	2461.5	25.4	79353	858	4.8	0.2	203.0	7.5	129.3	11.5	0.62	56	16.0	0.8	31.7	4.2	0.0040	0.0002	25.5	1.0
95	17082	189.1	151440	2161	1.5	0.0	1075.1	44.1	904.8	82.4	0.81	307	0.9	0.0	8.6	0.8	0.0012	0.0000	7.8	0.1
96	2545.4	27.1	78079	875	9.6	0.3	355.5	13.2	165.1	14.7	0.45	94	18.8	0.9	28.6	1.1	0.0044	0.0001	28.6	0.9
97	2492.6	25.8	86642	1170	10.8	0.3	1228.8	46.5	1121.3	100.5	0.88	356	5.6	0.3	8.7	0.7	0.0012	0.0001	8.0	0.5
98	652.5	6.6	45670	464	11.2	0.5	1425.5	52.0	1281.6	114.2	0.87	412	5.1	0.3	9.6	1.0	0.0014	0.0000	9.3	0.3
99	2430.4	25.6	83184	907	9.1	0.3	1321.7	48.7	1054.2	94.1	0.77	374	4.5	0.2	8.5	0.7	0.0012	0.0000	7.5	0.2
100	2821.0	29.6	82747	890	5.0	0.2	229.1	8.5	130.3	11.6	0.55	62	14.8	0.7	28.7	1.2	0.0042	0.0001	27.0	0.9
101	2659.3	27.8	85987	979	12.6	0.4	599.2	22.6	684.4	61.3	1.11	181	12.9	0.6	25.5	0.8	0.0040	0.0004	25.7	2.8
102	2578.8	27.0	85060	972	9.3	0.3	224.1	8.3	180.5	16.1	0.78	64	27.0	1.2	48.2	8.1	0.0055	0.0002	35.0	1.4
103	775.9	8.1	52973	542	6.8	0.4	612.1	22.7	546.8	48.9	0.86	177	7.1	0.5	7.6	0.4	0.0011	0.0001	7.0	0.3
104	683.0	7.2	45879	469	2.8	0.4	311.9	11.4	203.6	18.1	0.63	86	6.1	0.9	7.2	0.6	0.0010	0.0001	6.4	0.4
106	3264.4	34.6	75558	872	5.7	0.2	364.0	13.5	325.9	29.1	0.87	105	10.0	0.5	24.8	1.0	0.0036	0.0001	22.9	0.9
107	712.6	7.5	45211	455	45.9	1.3	1056.2	38.6	1070.3	95.5	0.98	312	27.3	1.2	36.6	2.1	0.0046	0.0001	29.3	0.5
108	2385.1	24.4	86069	938	12.7	0.4	254.7	9.4	282.0	25.2	1.07	76	30.6	1.4	47.9	5.6	0.0063	0.0003	40.3	2.0
109	6397.1	70.3	154981	2508	12.5	0.3	1301.7	53.6	1078.3	98.3	0.80	371	6.2	0.3	10.3	0.8	0.0012	0.0000	7.7	0.1
110	6359.3	72.3	138036	2204	5.5	0.2	1681.6	69.5	1315.7	120.0	0.76	475	2.1	0.1	4.0	0.6	0.0005	0.0000	3.3	0.1

Supplementary Table A3

(U-Th)/He and U/Pb dates by LADD of detrital zircon for sample NAW14-1A-8Q-1

Grain	He Pit Vol. (µm^3)	err. (2σ)	U-Th Pit Vol. (µm^3)	err. (2σ)	[^{4}He] (nmol/g)	err. (2σ)	[^{238}U] (nmol /g)	err. (2σ)	[^{232}Th] (nmol /g)	err. (2σ)	^{232}Th/ ^{238}U	eU (ppm)	(U-Th)/ He date (Ma)	err. (2σ)	^{207}Pb/ ^{235}U date (Ma)	err. (2σ)	^{206}Pb/ ^{238}U	err. (2σ)	^{206}Pb/ ^{238}U date (Ma)	err. (2σ)
1	2198.6	24.7	74625	831	5.3	0.2	1379.6	51.4	1279.4	114.4	0.90	400	2.4	0.1	4.7	1.6	0.0006	0.0000	3.8	0.2
2	2788.7	29.1	78492	850	16.6	0.5	692.1	25.9	291.4	26.0	0.41	182	16.9	0.8	28.0	1.9	0.0041	0.0001	26.1	0.6
3	4442.7	71.9	136096	1830	6.4	0.2	245.8	9.5	256.7	23.1	1.01	73	16.3	0.8	31.6	2.9	0.0046	0.0001	29.4	0.7
4	5571.8	60.8	128246	1658	7.7	0.2	1717.4	66.1	868.5	78.1	0.49	459	3.1	0.1	8.7	2.2	0.0012	0.0000	7.7	0.2
5	5714.0	60.5	129009	1966	15.6	0.4	711.2	28.2	482.5	43.7	0.66	197	14.7	0.7	31.0	7.3	0.0047	0.0001	30.5	0.5
6	2041.9	21.2	88249	967	4.0	0.2	665.3	24.6	270.1	24.1	0.39	174	4.3	0.3	10.1	1.1	0.0012	0.0001	7.7	0.5
7	1612.3	16.4	95934	1034	26.6	0.8	708.1	26.3	303.1	27.1	0.41	186	26.5	1.2	24.7	2.4	0.0039	0.0001	25.3	0.6
8	5587.9	60.9	151011	1917	2.0	0.1	158.1	6.1	73.5	6.6	0.45	42	8.8	0.5	47.7	4.6	0.0053	0.0002	33.8	1.0
9	1884.1	19.1	99875	1097	0.5	0.2	322.1	12.0	157.8	14.1	0.47	86	1.1	0.5	2.6	0.9	0.0003	0.0000	2.1	0.2
10	5659.2	61.6	131137	1923	1.5	0.1	348.9	13.7	170.5	15.4	0.47	93	3.0	0.2	3.9	0.5	0.0006	0.0000	3.7	0.3
11	5621.0	61.7	103317	1449	5.6	0.2	1806.4	70.3	1254.6	113.0	0.67	501	2.1	0.1	4.7	0.4	0.0007	0.0000	4.4	0.2
12	5602.6	66.7	121133	1639	17.8	0.5	528.5	20.4	276.1	24.8	0.51	142	23.3	1.0	43.2	4.9	0.0049	0.0001	31.8	0.5
13	5605.4	61.2	108335	1905	19.1	0.5	2783.0	112.7	1526.5	138.6	0.53	750	4.7	0.2	9.6	1.1	0.0012	0.0000	8.0	0.2
15	2160.2	21.6	64294	713	1.6	0.2	596.7	22.4	299.0	26.8	0.48	159	1.9	0.2	4.0	0.9	0.0005	0.0000	3.2	0.2
16	2243.8	23.5	78496	855	9.0	0.3	1556.7	57.8	819.6	73.2	0.51	418	4.0	0.2	9.4	0.7	0.0012	0.0000	7.9	0.2
17	7616.5	114.7	150514	2425	2.2	0.1	388.1	15.8	181.8	16.6	0.45	103	4.0	0.2	29.1	0.8	0.0041	0.0001	26.7	0.6
18	5447.7	63.2	106687	1904	8.1	0.2	304.6	12.4	310.8	28.3	0.99	90	16.8	0.8	32.0	3.1	0.0046	0.0001	29.4	0.7
19	5290.2	57.0	125879	1863	1.5	0.1	596.3	23.5	341.8	30.9	0.55	162	1.7	0.1	2.6	0.4	0.0004	0.0000	2.4	0.1
20	5193.8	59.2	130840	1596	2.0	0.1	508.2	19.7	446.4	40.2	0.85	146	2.6	0.1	7.2	0.6	0.0011	0.0001	7.1	0.6
21	2209.2	23.5	85053	1045	7.2	0.3	1901.4	71.4	1592.7	142.6	0.81	543	2.5	0.1	3.9	0.3	0.0006	0.0000	3.6	0.1
23	2116.4	22.2	76534	840	7.8	0.3	1913.7	71.1	1398.3	124.9	0.71	535	2.7	0.1	5.3	1.3	0.0006	0.0000	4.1	0.1
24	5454.0	64.2	127877	1899	3.3	0.1	933.9	36.8	688.7	62.2	0.71	261	2.3	0.1	4.0	0.4	0.0006	0.0000	3.7	0.1
25	2196.3	22.3	79086	871	3.9	0.2	1004.9	37.4	729.6	65.2	0.70	281	2.6	0.2	4.2	0.5	0.0006	0.0000	4.1	0.3
26	2187.6	22.1	79750	854	10.9	0.3	348.4	12.8	170.4	15.2	0.47	93	21.8	1.0	27.2	3.1	0.0041	0.0001	26.1	0.8
27	4023.7	41.1	88690	1028	11.8	0.3	884.0	34.6	557.5	50.4	0.61	242	9.0	0.4	39.6	3.8	0.0044	0.0001	28.6	0.7
28	2242.3	23.3	80748	916	5.6	0.2	778.5	28.8	388.8	34.7	0.48	208	5.0	0.3	7.4	0.3	0.0011	0.0000	7.4	0.3
29	5430.3	59.4	140941	1928	4.4	0.1	231.7	9.0	243.0	21.9	1.02	69	12.0	0.6	30.1	2.4	0.0045	0.0001	29.2	0.6
30	5468.7	60.2	131285	1562	2.4	0.1	739.9	28.4	684.1	61.5	0.89	215	2.1	0.1	7.3	0.2	0.0012	0.0001	7.4	0.3
31	2260.4	22.9	74890	800	11.8	0.4	345.5	12.7	131.4	11.7	0.37	90	24.3	1.1	28.0	3.1	0.0041	0.0001	26.2	0.7
32	5380.7	63.3	136306	1961	7.1	0.2	192.2	7.5	87.9	7.9	0.44	51	25.7	1.2	35.9	6.4	0.0048	0.0001	30.8	0.8
33	5476.5	62.6	119862	1833	5.6	0.2	1683.5	66.8	1289.8	116.6	0.74	474	2.2	0.1	3.6	0.1	0.0005	0.0000	3.4	0.1
34	2241.5	22.7	78541	875	20.2	0.6	1059.1	39.6	469.1	42.0	0.43	279	13.4	0.6	26.2	1.6	0.0041	0.0001	26.5	0.6

Supplementary Table A3 Continued

Grain	He Pit Vol. (µm³)	err. (2σ)	U-Th Pit Vol. (µm³)	err. (2σ)	[^{4}He] (nmol/g)	err. (2σ)	[^{238}U] (nmol /g)	err. (2σ)	[^{232}Th] (nmol /g)	err. (2σ)	^{232}Th/ ^{238}U	eU (ppm)	(U-Th)/ He date (Ma)	err. (2σ)	^{207}Pb/ ^{235}U date (Ma)	err. (2σ)	^{206}Pb/ ^{238}U	err. (2σ)	^{206}Pb/ ^{238}U date (Ma)	err. (2σ)
35	2079.3	20.8	83240	970	5.8	0.2	1244.1	46.2	841.2	75.2	0.65	344	3.1	0.2	7.5	1.1	0.0012	0.0001	7.6	0.4
36	2122.0	21.4	72912	808	3.8	0.2	1109.9	41.0	1043.3	93.2	0.91	323	2.2	0.1	6.2	0.5	0.0007	0.0000	4.7	0.2
37	2068.8	21.1	76749	866	17.5	0.5	1744.2	64.9	920.1	82.2	0.51	468	6.9	0.3	10.9	2.4	0.0012	0.0000	7.8	0.2
38	2070.9	20.9	75957	817	20.0	0.6	568.6	21.1	318.3	28.4	0.54	154	24.1	1.1	36.1	2.4	0.0047	0.0001	30.3	0.7
39	1997.2	20.0	77572	844	41.0	1.1	1658.4	62.2	906.9	81.4	0.53	447	17.0	0.7	27.4	1.2	0.0041	0.0001	26.2	0.5
40	2140.0	21.9	74390	816	3.1	0.2	630.1	23.5	453.9	40.6	0.70	176	3.3	0.2	4.9	0.8	0.0007	0.0000	4.7	0.3
41	5530.0	65.1	129164	1633	9.8	0.3	932.2	35.7	414.0	37.2	0.43	246	7.4	0.3	7.1	0.5	0.0012	0.0000	7.5	0.2
44	1975.6	20.0	69080	781	27.2	0.7	623.0	23.2	281.2	25.1	0.44	165	30.6	1.3	33.9	4.7	0.0047	0.0002	30.1	0.9
45	5940.1	65.9	131154	1911	6.1	0.2	1689.4	66.0	1486.6	134.1	0.85	486	2.3	0.1	3.8	0.2	0.0006	0.0000	3.8	0.1
46	5112.3	67.3	127104	1716	3.8	0.1	1594.1	61.8	1250.1	112.7	0.76	450	1.6	0.1	5.4	0.3	0.0007	0.0000	4.2	0.2
49	1990.4	20.3	65346	753	6.8	0.3	1116.6	41.8	651.4	58.5	0.56	303	4.1	0.2	10.8	3.2	0.0012	0.0000	7.8	0.3
50	1897.4	19.7	69480	780	23.5	0.7	1385.4	52.3	693.2	62.2	0.48	370	11.8	0.5	26.9	1.4	0.0042	0.0001	26.8	0.5
51	2231.2	22.7	79799	860	3.2	0.2	640.2	23.7	428.6	38.3	0.65	177	3.3	0.2	4.1	0.6	0.0006	0.0000	4.1	0.3
54	5477.1	80.0	127312	1777	5.2	0.2	1060.3	41.3	823.8	74.2	0.75	299	3.2	0.2	7.3	0.6	0.0011	0.0001	7.2	0.4
55	2003.0	20.5	64871	769	0.4	0.2	211.4	8.0	129.1	11.6	0.59	58	1.4	0.6	2.8	0.7	0.0004	0.0001	2.6	0.5
56	1945.5	19.9	76290	782	8.1	0.3	2488.1	91.9	1695.7	151.5	0.66	689	2.2	0.1	3.4	0.3	0.0005	0.0000	3.3	0.1
57	1954.7	19.9	75495	843	12.1	0.4	370.9	13.8	184.7	16.5	0.48	99	22.6	1.0	38.9	5.0	0.0049	0.0001	31.4	0.8
58	2032.9	20.9	50687	553	8.2	0.3	316.8	11.8	317.1	28.4	0.97	93	16.2	0.8	35.4	5.1	0.0047	0.0002	30.1	1.3
59	4392.2	52.8	137046	1874	7.7	0.2	2160.3	83.5	1580.1	142.3	0.71	604	2.4	0.1	4.2	0.3	0.0006	0.0000	4.2	0.2
60	5156.9	57.3	69451	931	5.5	0.2	1425.6	55.3	665.7	59.9	0.45	378	2.7	0.1	7.7	1.6	0.0012	0.0000	7.5	0.3
61	4461.6	62.2	155927	1670	32.8	0.9	1094.4	42.4	408.1	36.7	0.36	285	21.3	1.0	32.5	1.9	0.0041	0.0001	26.6	0.4
62	5264.3	63.5	122988	1884	9.5	0.3	1945.5	78.8	855.2	77.6	0.43	513	3.4	0.2	5.1	2.0	0.0006	0.0000	3.9	0.1
63	2041.4	21.0	74442	871	2.1	0.2	1209.7	45.1	711.0	63.6	0.57	329	1.2	0.1	2.1	0.2	0.0003	0.0000	1.7	0.1
64	1824.5	18.6	80212	870	1.7	0.2	1210.5	44.8	502.7	44.9	0.40	318	1.0	0.1	7.4	0.3	0.0011	0.0000	7.3	0.2
65	5256.5	58.3	144493	1780	4.0	0.1	1188.4	46.8	935.7	84.5	0.76	336	2.2	0.1	4.1	0.9	0.0006	0.0000	3.8	0.2
66	1750.1	17.8	68840	847	10.6	0.4	620.1	23.3	440.7	39.5	0.69	173	11.4	0.6	28.6	3.2	0.0045	0.0002	28.6	1.0
67	1890.0	19.4	78023	930	4.1	0.2	452.5	16.9	490.5	43.9	1.05	135	5.6	0.4	10.7	1.8	0.0012	0.0001	7.7	0.9
68	2118.1	21.5	77165	858	3.0	0.2	777.0	28.8	549.0	49.0	0.68	216	2.5	0.2	3.6	1.1	0.0006	0.0000	3.7	0.2
69	1914.5	19.6	72679	798	14.4	0.4	1510.8	55.9	881.1	78.7	0.56	410	6.5	0.3	9.7	1.4	0.0014	0.0001	8.7	0.4
70	5218.3	57.0	103880	1491	3.1	0.1	660.4	26.5	485.3	44.0	0.71	185	3.1	0.2	7.2	0.3	0.0011	0.0000	7.0	0.3
72	2020.6	20.4	74422	847	2.1	0.2	663.4	24.7	407.3	36.4	0.59	181	2.1	0.2	3.6	0.7	0.0004	0.0000	2.9	0.1
73	1851.2	18.7	69296	782	1.9	0.2	783.8	29.5	421.7	37.9	0.52	211	1.7	0.2	3.9	1.4	0.0006	0.0000	3.6	0.2
74	1996.9	20.3	69067	782	6.2	0.3	870.9	32.4	500.1	44.7	0.56	236	4.9	0.3	9.4	1.7	0.0012	0.0001	7.9	0.4
75	1950.5	20.0	70342	743	4.2	0.2	1419.5	52.5	1272.4	113.8	0.87	410	1.9	0.1	3.4	0.2	0.0006	0.0000	3.6	0.1

Supplementary Table A3 Continued

Grain	He Pit Vol. (µm³)	err. (2σ)	U-Th Pit Vol. (µm³)	err. (2σ)	[⁴He] (nmol/g)	err. (2σ)	[²³⁸U] (nmol /g)	err. (2σ)	[²³²Th] (nmol /g)	err. (2σ)	²³²Th/ ²³⁸U	eU (ppm)	(U-Th)/ He date (Ma)	err. (2σ)	²⁰⁷Pb/ ²³⁵U date (Ma)	err. (2σ)	²⁰⁶Pb/ ²³⁸U	err. (2σ)	²⁰⁶Pb/ ²³⁸U date (Ma)	err. (2σ)
76	1865.1	18.8	65967	761	17.0	0.5	1882.6	70.1	963.6	86.2	0.50	504	6.3	0.3	8.1	1.5	0.0012	0.0000	7.7	0.2
77	1907.8	19.2	49795	538	16.9	0.5	682.9	25.3	348.8	31.1	0.49	183	17.1	0.8	28.4	2.2	0.0039	0.0001	25.2	0.6
78	4767.6	60.6	118001	1594	6.2	0.2	3030.2	120.9	2005.8	181.7	0.64	836	1.4	0.1	4.2	0.4	0.0005	0.0000	3.4	0.1
79	4912.0	59.8	124680	1648	101.0	2.6	2231.5	88.5	2276.7	205.8	0.99	659	28.3	1.3	45.1	3.4	0.0051	0.0001	32.6	0.4
80	1817.7	18.9	71543	753	4.3	0.2	525.7	19.4	414.0	36.9	0.76	149	5.4	0.3	7.1	0.2	0.0011	0.0000	7.0	0.3
81	4990.3	55.9	127369	1590	4.1	0.1	867.8	34.1	404.7	36.6	0.45	230	3.3	0.2	10.4	1.0	0.0012	0.0000	7.6	0.2
82	5013.5	54.7	75761	1187	7.3	0.2	4121.1	167.9	1896.1	172.3	0.45	1091	1.2	0.1	3.5	0.1	0.0005	0.0000	3.5	0.1
83	2108.5	23.8	79175	892	3.6	0.2	1359.9	50.8	976.8	87.5	0.70	379	1.8	0.1	4.1	1.6	0.0006	0.0000	3.7	0.2
84	1833.2	18.4	63397	671	5.3	0.2	3785.0	142.1	4494.1	403.9	1.15	1152	0.8	0.0	4.4	0.7	0.0006	0.0000	4.1	0.3
85	2009.1	20.3	67523	707	84.9	2.1	2960.1	109.3	1422.3	127.1	0.47	787	20.0	0.9	35.6	1.6	0.0042	0.0001	27.0	0.4
86	1970.0	20.2	68028	733	9.5	0.3	307.3	11.4	134.4	12.0	0.42	81	21.8	1.1	30.0	1.8	0.0046	0.0001	29.9	0.8
87	1929.0	19.8	77728	1019	12.7	0.4	467.0	17.6	240.4	21.5	0.50	125	18.8	0.9	30.1	1.5	0.0047	0.0001	30.0	0.8
88	4794.0	52.3	62504	637	11.2	0.3	1132.8	42.0	570.6	51.0	0.49	303	6.9	0.3	9.1	2.0	0.0012	0.0000	7.7	0.3
89	2027.2	20.5	75954	866	8.7	0.3	1852.2	69.0	1453.8	129.9	0.76	523	3.1	0.2	5.2	0.3	0.0007	0.0000	4.8	0.2
90	1734.5	17.4	66107	711	6.8	0.3	1565.6	57.9	1504.4	134.4	0.93	457	2.7	0.2	3.6	1.1	0.0006	0.0000	3.5	0.1
92	1894.9	19.3	66471	733	15.5	0.5	1829.6	67.8	937.4	83.8	0.50	490	5.9	0.3	10.2	0.9	0.0011	0.0000	7.3	0.2
94	2019.6	20.3	62999	816	12.2	0.4	541.6	20.4	343.9	30.8	0.61	149	15.2	0.7	33.9	7.7	0.0046	0.0002	29.6	1.1
95	1870.8	18.9	56766	606	6.0	0.3	892.6	33.0	384.3	34.3	0.42	235	4.7	0.3	7.9	1.1	0.0012	0.0000	7.4	0.3
96	1546.6	16.3	77711	862	7.6	0.3	173.1	6.6	79.5	7.1	0.44	46	30.8	1.8	29.9	3.0	0.0047	0.0003	29.9	1.8
97	1785.9	18.0	69861	769	2.6	0.2	269.2	10.0	290.4	25.9	1.04	80	6.0	0.5	35.8	3.3	0.0046	0.0001	29.8	0.9
99	1769.9	18.0	65926	735	14.1	0.5	428.8	15.9	210.4	18.8	0.47	114	22.8	1.1	45.0	6.6	0.0050	0.0002	32.0	1.4
100	1856.1	18.9	71061	803	17.9	0.5	1902.2	70.6	1012.1	90.4	0.51	511	6.5	0.3	10.3	0.8	0.0011	0.0000	7.3	0.2
101	5007.0	59.0	167425	3102	4.9	0.2	179.1	7.4	80.5	7.3	0.43	47	19.0	1.0	46.0	7.9	0.0061	0.0003	39.1	1.8
102	2121.3	22.5	77121	896	32.5	0.9	786.1	29.4	636.1	56.9	0.78	223	26.9	1.2	51.9	3.0	0.0058	0.0001	37.4	0.9
103	4943.0	56.3	133203	1825	2.9	0.1	960.3	38.2	593.5	53.7	0.60	263	2.0	0.1	3.4	0.7	0.0005	0.0000	3.4	0.2
104	5125.7	56.0	120956	1491	7.4	0.2	1355.9	52.8	620.0	55.9	0.44	359	3.8	0.2	7.2	0.1	0.0012	0.0000	7.5	0.2
105	5251.8	61.8	114219	1246	6.4	0.2	1059.5	40.8	677.9	60.9	0.62	291	4.1	0.2	4.7	0.4	0.0007	0.0000	4.2	0.2
106	1857.6	18.9	65644	723	2.1	0.2	505.3	18.8	291.5	26.0	0.56	137	2.9	0.3	6.6	0.8	0.0009	0.0000	5.5	0.3
107	4769.5	53.4	118817	1756	7.9	0.2	2519.7	100.4	1188.4	107.6	0.46	669	2.2	0.1	4.0	0.3	0.0006	0.0000	3.7	0.1
109	2961.2	57.6	129545	2306	35.3	1.1	847.0	34.8	604.2	55.0	0.69	236	27.7	1.3	38.3	3.8	0.0048	0.0001	31.0	0.7
110	1554.6	15.6	74272	788	6.3	0.3	2413.9	90.2	1884.1	168.8	0.76	686	1.7	0.1	7.9	1.5	0.0012	0.0001	7.5	0.8

Supplementary Table A4
(U-Th)/He and U/Pb dates by LADD of detrital zircon for sample NAW14-1A-36Q-1

Grain	He Pit Vol. (μm^3)	err. (2σ)	U-Th Pit Vol. (μm^3)	err. (2σ)	[^4He] (nmol/g)	err. (2σ)	[^{238}U] (nmol /g)	err. (2σ)	[^{232}Th] (nmol /g)	err. (2σ)	$^{232}Th/^{238}U$	eU (ppm)	(U-Th)/ He date (Ma)	err. (2σ)	$^{207}Pb/^{235}U$ date (Ma)	err. (2σ)	$^{206}Pb/^{238}U$	err. (2σ)	$^{206}Pb/^{238}U$ date (Ma)	err. (2σ)
1	2543.0	25.5	101028	1124	8.0	0.2	2837.4	106.2	44.6	89.2	1.11	858	1.7	0.1	2.9	0.1	0.0004	0.0000	2.9	0.1
2	2318.2	23.3	100981	1121	8.6	0.3	2259.8	87.1	61.8	123.6	0.63	621	2.6	0.1	8.1	0.2	0.0013	0.0000	8.1	0.2
3	2340.4	23.4	98986	1039	22.5	0.6	2239.2	82.5	8.4	16.9	0.94	656	6.4	0.3	8.4	0.4	0.0012	0.0000	7.7	0.1
4	2242.3	22.6	103045	1171	18.1	0.5	334.2	12.4	12.0	24.0	1.06	100	33.5	1.5	30.8	0.6	0.0048	0.0001	31.1	0.6
5	2230.2	22.4	99341	1041	15.0	0.4	1556.4	57.3	17.7	35.5	0.85	448	6.2	0.3	9.8	0.9	0.0012	0.0000	7.7	0.2
6	3155.0	31.8	99753	1038	11.4	0.3	1342.1	49.5	92.6	185.1	1.02	399	5.3	0.2	9.3	1.7	0.0012	0.0001	7.6	0.4
7	2641.2	27.3	102716	1113	4.3	0.1	280.7	10.4	48.0	96.0	0.88	81	9.7	0.5	30.3	0.8	0.0048	0.0001	30.6	0.8
8	2295.2	23.1	102369	1103	18.6	0.5	1601.9	59.2	34.2	68.3	0.80	456	7.5	0.3	9.2	0.6	0.0012	0.0000	7.9	0.1
9	2252.7	22.7	102811	1069	59.9	1.5	2752.5	101.6	117.5	234.9	0.44	728	15.3	0.7	29.0	1.4	0.0043	0.0001	27.8	0.4
10	2253.9	22.7	102665	1107	12.9	0.4	1248.9	46.2	30.0	60.0	1.03	372	6.4	0.3	8.8	1.0	0.0012	0.0000	7.5	0.2
11	2328.0	23.5	101100	702	25.6	0.7	1830.0	65.8	43.1	86.3	1.06	548	8.7	0.4	8.1	0.1	0.0013	0.0000	8.1	0.1
12	2404.2	24.3	102827	1075	2.6	0.1	369.2	14.1	35.5	70.9	0.68	103	4.7	0.3	4.0	0.3	0.0006	0.0000	4.0	0.3
13	5105.6	53.9	117721	1268	4.4	0.1	302.4	11.2	13.6	27.1	0.67	84	9.7	0.4	29.6	0.5	0.0047	0.0001	30.0	0.6
14	17035.0	170.4	118967	1222	0.6	0.0	832.5	31.1	30.3	60.5	0.76	235	0.5	0.0	7.3	0.3	0.0011	0.0000	7.3	0.3
15	2297.0	23.2	100387	1052	17.3	0.5	1377.7	50.7	27.3	54.7	0.87	398	8.0	0.4	7.8	0.4	0.0012	0.0000	7.8	0.3
16	2245.5	22.7	101920	1093	7.5	0.2	589.3	21.7	76.0	152.0	1.19	181	7.7	0.4	10.0	1.0	0.0013	0.0000	8.2	0.2
17	2243.8	22.7	98703	1055	3.3	0.1	580.0	21.4	10.6	21.3	0.70	162	3.8	0.2	3.6	0.2	0.0006	0.0000	3.6	0.2
18	2180.8	21.8	99240	702	3.8	0.1	161.9	5.8	3.1	6.2	0.89	47	15.1	0.8	31.2	3.3	0.0041	0.0001	26.1	0.8
19	2256.0	22.8	98643	1062	7.6	0.2	634.8	23.7	58.5	117.0	1.18	194	7.2	0.3	8.0	0.3	0.0013	0.0000	8.1	0.3
20	2226.2	22.3	102075	1091	15.2	0.4	1241.1	45.7	28.2	56.4	1.01	368	7.7	0.3	8.0	1.1	0.0011	0.0001	7.3	0.6
21	2281.3	23.0	102431	1117	18.2	0.5	1634.4	60.3	21.3	42.7	0.98	482	7.0	0.3	8.3	0.5	0.0012	0.0000	7.9	0.1
22	2466.8	26.5	100987	1103	3.9	0.1	743.7	28.0	8.1	16.3	0.85	214	3.4	0.2	3.0	0.2	0.0005	0.0000	3.0	0.2
23	2584.3	26.1	105562	1148	12.5	0.3	386.6	14.5	39.8	79.7	0.52	104	22.2	1.0	24.5	0.6	0.0038	0.0001	24.7	0.7
24	4115.0	49.6	118070	1244	3.7	0.1	227.7	8.4	17.8	35.6	0.65	63	11.0	0.5	23.8	0.8	0.0037	0.0001	24.0	0.8
25	2231.9	22.3	97551	1130	17.5	0.5	1437.9	53.5	66.6	133.2	0.84	413	7.9	0.3	8.5	0.6	0.0012	0.0000	7.7	0.1
26	2217.2	22.2	102709	1113	16.8	0.5	342.4	12.6	54.1	108.1	0.62	94	33.0	1.4	30.8	0.8	0.0049	0.0001	31.2	0.7
27	2228.5	22.3	102490	1102	13.5	0.4	1356.0	50.0	7.1	14.2	0.83	388	6.4	0.3	10.1	1.1	0.0012	0.0000	7.9	0.2
28	2320.0	23.4	101188	1080	55.0	1.4	6162.1	228.2	13.7	27.4	0.73	1731	5.9	0.3	8.7	0.5	0.0012	0.0000	7.6	0.1
29	2260.5	22.6	99939	1086	15.5	0.4	1828.1	67.7	58.9	117.7	0.94	535	5.4	0.2	7.5	0.3	0.0012	0.0000	7.5	0.3
30	2266.2	22.7	100496	1048	19.0	0.5	1509.3	55.7	16.8	33.7	0.90	439	8.0	0.3	9.5	0.7	0.0012	0.0000	7.7	0.1
31	2398.0	24.2	99110	702	49.0	1.2	4125.7	148.4	115.5	230.9	1.84	1417	6.4	0.3	7.6	0.3	0.0012	0.0000	7.5	0.1
32	2404.4	24.1	102164	1119	8.7	0.3	653.4	24.1	49.1	98.3	1.09	197	8.2	0.4	10.5	0.4	0.0016	0.0001	10.3	0.4

Supplementary Table A4 Continued

Grain	He Pit Vol. (µm³)	err. (2σ)	U-Th Pit Vol. (µm³)	err. (2σ)	[⁴He] (nmol/g)	err. (2σ)	[²³⁸U] (nmol /g)	err. (2σ)	[²³²Th] (nmol /g)	err. (2σ)	²³²Th/ ²³⁸U	eU (ppm)	(U-Th)/ He date (Ma)	err. (2σ)	²⁰⁷Pb/ ²³⁵U date (Ma)	err. (2σ)	²⁰⁶Pb/ ²³⁸U	err. (2σ)	²⁰⁶Pb/ ²³⁸U date (Ma)	err. (2σ)
33	2336.2	23.4	101372	1077	28.0	0.7	2239.1	82.6	8.4	16.8	1.16	683	7.6	0.3	8.6	0.5	0.0012	0.0000	7.8	0.1
34	2192.2	22.2	103575	1098	6.7	0.2	1450.0	53.4	5.9	11.7	0.83	416	3.0	0.1	7.7	0.2	0.0012	0.0000	7.7	0.2
35	2276.6	23.2	103171	1097	9.6	0.3	234.3	8.6	4.2	8.4	1.03	70	25.4	1.1	28.1	1.0	0.0044	0.0002	28.5	1.1
36	2558.8	25.6	98159	1071	7.8	0.2	1076.9	39.7	18.6	37.3	0.72	302	4.8	0.2	10.1	1.0	0.0012	0.0000	7.6	0.3
38	2182.3	21.8	103263	1123	18.0	0.5	1571.1	58.0	21.9	43.8	0.91	457	7.3	0.3	8.8	0.5	0.0012	0.0000	7.9	0.1
39	2248.7	22.7	102051	1083	5.0	0.2	498.5	18.4	73.6	147.1	1.08	150	6.2	0.3	8.7	1.1	0.0012	0.0000	8.0	0.2
40	2220.4	22.2	105821	1108	15.9	0.4	1181.2	43.6	16.2	32.4	1.08	355	8.3	0.4	9.5	0.9	0.0012	0.0000	7.8	0.2
41	2521.8	25.3	103055	1113	7.8	0.2	655.7	24.2	69.6	139.2	0.83	188	7.7	0.3	11.0	2.3	0.0012	0.0000	7.8	0.2
42	2301.7	23.3	98205	1048	27.2	0.7	1845.2	68.2	50.1	100.2	0.95	541	9.3	0.4	9.3	0.7	0.0013	0.0000	8.4	0.2
43	2469.0	24.7	104257	1111	13.3	0.4	374.3	13.8	1.3	2.6	0.80	107	23.1	1.0	27.9	3.3	0.0038	0.0001	24.3	0.8
44	2309.1	23.2	100682	1074	21.8	0.6	1498.3	55.2	18.2	36.3	1.41	478	8.4	0.4	8.0	0.2	0.0013	0.0000	8.1	0.2
45	2770.0	27.9	105006	1144	2.0	0.1	517.2	19.3	44.3	88.6	0.68	144	2.5	0.1	9.0	0.9	0.0012	0.0000	7.8	0.2
46	2252.7	22.6	104391	1147	14.4	0.4	1302.8	48.1	21.3	42.5	0.89	378	7.0	0.3	9.7	0.9	0.0012	0.0000	7.9	0.2
47	2286.5	22.9	101100	702	10.1	0.3	1171.7	42.1	260.0	519.9	0.96	345	5.5	0.2	9.2	1.0	0.0012	0.0000	7.7	0.2
48	2445.2	24.7	104463	1115	21.5	0.6	1607.0	59.6	13.4	26.8	0.66	445	8.9	0.4	8.3	0.2	0.0013	0.0000	8.4	0.2
49	2212.2	22.1	99329	1114	3.0	0.1	231.3	8.6	102.6	205.1	0.81	66	8.4	0.5	6.6	5.1	0.0012	0.0001	7.5	0.6
50	2147.0	21.5	100038	1095	179.7	4.5	4699.0	173.7	8.6	17.2	0.47	1252	26.6	1.1	26.4	0.2	0.0041	0.0000	26.6	0.3
52	2320.0	23.4	99926	1095	12.2	0.3	307.2	11.4	48.7	97.5	0.95	90	25.1	1.1	36.0	6.0	0.0044	0.0001	28.1	0.6
53	2486.0	25.1	103094	1135	43.9	1.1	3342.2	123.9	51.9	103.8	1.68	1118	7.3	0.3	8.4	0.5	0.0012	0.0000	7.5	0.2
54	4075.8	44.1	104991	1123	1.8	0.1	504.7	18.6	53.7	107.5	0.91	147	2.3	0.1	10.0	2.2	0.0012	0.0000	7.7	0.3
56	2316.4	23.9	104008	1122	14.3	0.4	1252.9	46.3	16.2	32.3	0.77	354	7.4	0.3	8.4	0.2	0.0013	0.0000	8.4	0.2
57	2350.0	23.7	103668	1126	2.4	0.1	575.1	21.3	97.6	195.2	0.68	160	2.8	0.2	3.7	0.4	0.0006	0.0000	3.6	0.3
58	2314.5	23.2	109092	1155	4.0	0.1	78.7	2.9	13.7	27.4	0.36	20	35.9	1.8	39.8	5.9	0.0055	0.0006	35.1	4.0
59	2350.0	23.7	113475	1245	18.3	0.5	1272.4	47.2	81.1	162.3	0.85	366	9.3	0.4	8.6	0.2	0.0013	0.0000	8.6	0.2
60	2369.8	24.2	101943	1123	172.1	4.3	2963.3	111.6	25.2	50.3	0.50	795	40.0	1.7	41.9	5.5	0.0064	0.0001	40.9	0.6
63	2156.0	22.5	101526	1090	7.5	0.2	457.3	17.0	58.7	117.3	0.77	129	10.7	0.5	22.7	0.4	0.0036	0.0001	22.9	0.5
64	2421.8	24.8	101759	1085	20.2	0.5	1750.9	64.9	24.7	49.5	0.91	510	7.3	0.3	10.6	1.2	0.0012	0.0000	7.9	0.2
66	2395.9	24.2	105391	1169	3.8	0.1	695.4	26.1	65.7	131.5	0.68	193	3.7	0.2	3.4	0.2	0.0005	0.0000	3.4	0.2
67	2928.0	29.5	106706	1128	2.4	0.1	473.1	17.5	35.9	71.9	0.85	136	3.2	0.2	7.9	0.4	0.0012	0.0001	7.8	0.3
68	2980.0	30.1	103870	1131	7.3	0.2	226.9	8.5	11.1	22.3	0.40	59	22.7	1.0	25.8	1.0	0.0041	0.0002	26.0	1.0
69	2115.3	21.2	106452	1125	11.0	0.3	263.8	9.8	55.8	111.5	0.48	70	29.0	1.3	26.4	0.6	0.0042	0.0001	26.7	0.6
70	2033.3	20.4	103525	1156	7.3	0.2	240.5	8.9	119.3	238.7	0.76	68	19.8	0.9	24.6	0.6	0.0039	0.0001	24.8	0.6
71	2246.4	22.7	93890	1013	15.5	0.4	1339.5	49.5	32.7	65.4	0.80	381	7.5	0.3	9.2	0.6	0.0012	0.0000	7.9	0.2

Supplementary Table A4 Continued

Grain	He Pit Vol. (μm³)	err. (2σ)	U-Th Pit Vol. (μm³)	err. (2σ)	[⁴He] (nmol/g)	err. (2σ)	[²³⁸U] (nmol /g)	err. (2σ)	[²³²Th] (nmol /g)	err. (2σ)	²³²Th/ ²³⁸U	eU (ppm)	(U-Th)/ He date (Ma)	err. (2σ)	²⁰⁷Pb/ ²³⁵U date (Ma)	err. (2σ)	²⁰⁶Pb/ ²³⁸U	err. (2σ)	²⁰⁶Pb/ ²³⁸U date (Ma)	err. (2σ)
73	2148.6	21.5	103563	1121	88.7	2.2	2012.5	75.1	348.6	697.2	1.24	623	26.3	1.1	24.8	1.6	0.0039	0.0001	25.0	0.6
74	2163.0	21.8	102092	1085	24.7	0.6	706.7	26.0	62.9	125.8	0.52	190	24.0	1.0	30.1	3.1	0.0041	0.0001	26.6	0.6
75	2281.7	22.9	104774	1110	13.9	0.4	1069.9	39.5	79.6	159.2	1.19	328	7.8	0.4	7.3	0.2	0.0011	0.0000	7.3	0.2
76	2132.2	21.3	100473	1117	13.4	0.4	303.0	11.2	208.0	416.0	0.98	89	27.7	1.2	27.3	0.6	0.0043	0.0001	27.6	0.7
77	2079.0	21.0	115700	1249	4.8	0.2	203.9	7.6	51.6	103.2	0.75	58	15.3	0.7	26.2	1.1	0.0041	0.0002	26.4	1.1
80	4203.0	42.4	110621	1229	1.2	0.1	1166.2	43.2	9.8	19.6	1.00	346	0.6	0.0	7.7	0.2	0.0012	0.0000	7.7	0.2
81	2114.2	21.2	100425	1083	14.5	0.4	1296.2	47.9	55.9	111.8	1.11	392	6.9	0.3	9.1	0.8	0.0012	0.0000	7.5	0.2
82	2071.5	20.7	101400	1094	2.6	0.1	639.3	23.7	6.8	13.6	0.60	175	2.8	0.2	3.0	0.1	0.0005	0.0000	3.0	0.1
84	6069.7	60.7	121503	1255	7.7	0.2	953.1	36.8	9.3	18.6	0.90	277	5.2	0.2	25.4	1.1	0.0038	0.0001	24.5	0.3
85	2154.8	21.5	103096	1121	10.5	0.3	290.4	10.7	29.4	58.9	0.61	80	24.3	1.1	32.6	2.1	0.0049	0.0001	31.4	0.8
86	2086.7	21.1	102123	1079	1.5	0.1	596.9	22.0	73.9	147.7	0.77	169	1.7	0.1	2.8	0.2	0.0004	0.0000	2.8	0.2
88	2153.8	21.6	96475	1052	2.6	0.1	892.4	33.0	58.1	116.2	0.69	248	1.9	0.1	5.4	0.2	0.0008	0.0000	5.4	0.2
89	2125.0	21.3	100141	1080	17.2	0.5	1353.2	50.0	34.6	69.1	0.94	396	8.0	0.4	8.0	0.2	0.0012	0.0000	8.0	0.2
90	2110.5	21.2	98663	1110	2.5	0.1	65.2	2.4	6.6	13.2	1.02	19	23.5	1.4	25.9	2.0	0.0041	0.0003	26.5	1.8
91	2202.3	22.1	100965	1130	14.7	0.4	326.4	12.1	18.6	37.3	0.71	91	29.7	1.3	31.5	1.9	0.0046	0.0001	29.8	0.5
92	2134.8	21.5	99240	1071	18.3	0.5	2348.9	86.7	32.3	64.6	0.70	656	5.2	0.2	7.6	0.1	0.0012	0.0000	7.6	0.2
93	2166.0	21.7	102931	1097	6.7	0.2	560.8	20.7	55.2	110.5	1.06	168	7.4	0.3	7.5	0.2	0.0012	0.0000	7.5	0.3
95	2197.1	22.0	108251	1139	10.2	0.3	851.1	31.4	29.1	58.1	0.77	241	7.9	0.4	9.1	0.7	0.0012	0.0001	7.5	0.4
96	2069.0	20.7	105100	1134	12.4	0.4	266.9	9.9	9.4	18.8	1.10	81	28.4	1.3	28.4	1.2	0.0045	0.0002	28.8	1.3
97	2275.3	22.8	102239	1118	19.4	0.5	735.1	27.4	11.7	23.4	1.04	219	16.3	0.7	22.1	0.6	0.0035	0.0001	22.3	0.6
98	2344.0	23.6	99584	1045	21.7	0.6	1623.9	60.0	88.7	177.5	0.58	442	9.1	0.4	9.6	0.5	0.0013	0.0000	8.1	0.1
99	2213.4	22.1	99380	1038	4.5	0.2	513.8	19.1	59.6	119.2	1.26	160	5.2	0.3	27.0	2.3	0.0039	0.0001	25.1	0.5
101	2778.4	28.0	97457	1054	28.0	0.7	2302.4	85.8	55.7	111.4	1.10	695	7.5	0.3	8.8	0.7	0.0011	0.0000	7.4	0.2
102	2231.0	22.5	103158	1132	8.6	0.2	929.7	34.4	59.2	118.4	0.80	265	6.0	0.3	8.2	0.7	0.0012	0.0000	7.7	0.2
103	2101.6	21.1	102262	1130	12.4	0.4	1195.6	44.2	11.4	22.9	0.87	345	6.6	0.3	7.8	0.7	0.0012	0.0000	7.6	0.1
105	2231.4	23.1	100275	1115	79.4	2.0	2513.8	93.2	63.2	126.5	0.80	716	20.5	0.9	22.8	0.6	0.0035	0.0000	22.4	0.3
106	2241.6	22.7	102093	1099	25.7	0.7	766.7	28.3	61.2	122.4	0.50	205	23.1	1.0	26.2	0.7	0.0041	0.0001	26.4	0.7
107	2203.6	22.0	101843	1097	20.7	0.6	500.0	18.5	16.4	32.7	0.52	135	28.4	1.2	26.4	2.7	0.0042	0.0001	26.8	0.6
108	2571.7	25.7	99995	1105	1.3	0.1	237.5	8.8	97.4	194.8	0.77	67	3.6	0.3	7.9	0.5	0.0012	0.0001	7.7	0.4
109	2152.0	21.7	101000	1072	9.5	0.3	1190.0	43.9	65.7	131.4	1.13	361	4.9	0.2	9.6	1.2	0.0012	0.0000	7.5	0.2
110	2160.7	21.9	114391	1399	42.8	1.1	1457.2	56.0	146.8	293.5	0.66	403	19.6	0.9	22.0	0.3	0.0034	0.0000	22.1	0.3

Supplementary Table A5
(U-Th)/He and U/Pb dates by LADD of detrital zircon for sample WTK13-1A-20Q-2

Grain	He Pit Vol. (μm^3)	err. (2σ)	U-Th Pit Vol. (μm^3)	err. (2σ)	[^{4}He] (nmol/g)	err. (2σ)	[^{238}U] (nmol/g)	err. (2σ)	[^{232}Th] (nmol/g)	err. (2σ)	$^{232}Th/^{238}U$	eU (ppm)	(U-Th)/He date (Ma)	err. (2σ)	$^{207}Pb/^{235}U$ date (Ma)	err. (2σ)	$^{206}Pb/^{238}U$	err. (2σ)	$^{206}Pb/^{238}U$ date (Ma)	err. (2σ)
1	1987.0	20.1	98299	1085	537.0	13.3	2475.1	91.6	964.6	86.2	0.38	646	152.2	6.6	2515.9	8.6	0.4435	0.0059	2366.0	26.0
2	2047.0	20.7	96107	1029	42.8	1.1	1223.2	45.1	766.8	68.4	0.61	335	23.6	1.0	30.5	2.5	0.0042	0.0002	27.2	1.4
3	2149.6	21.5	100382	1138	6.6	0.2	2688.0	100.4	2949.1	264.1	1.06	805	1.5	0.1	2.2	0.6	0.0003	0.0000	1.7	0.0
4	2064.4	20.8	102501	1089	51.7	1.3	336.4	12.4	446.5	39.8	1.28	105	90.6	4.0	607.5	6.2	0.0972	0.0007	597.8	4.4
5	2037.5	20.4	98711	1035	18.0	0.5	621.2	22.8	371.2	33.1	0.58	169	19.7	0.9	26.7	2.0	0.0036	0.0001	23.3	0.4
6	2141.5	21.5	103621	1171	24.9	0.6	510.7	18.9	286.5	25.6	0.54	138	33.3	1.4	33.8	3.6	0.0051	0.0001	32.6	0.5
7	2280.2	23.0	99763	1102	1.0	0.1	430.0	15.9	290.2	25.9	0.65	119	1.5	0.1	2.7	0.8	0.0003	0.0001	2.0	0.6
8	2284.0	22.9	109597	1213	161.2	4.0	1314.4	49.3	574.6	51.4	0.42	346	85.7	3.7	726.3	4.8	0.1198	0.0014	729.2	8.1
9	2354.4	23.6	106063	1125	53.9	1.4	2256.5	83.9	636.1	56.8	0.27	576	17.4	0.8	676.9	4.3	0.1085	0.0009	664.2	5.0
11	2190.9	22.1	99428	1063	5.5	0.2	1309.3	48.4	1331.2	119.1	0.98	386	2.6	0.1	22.5	0.8	0.0032	0.0001	20.8	0.8
12	2354.4	23.6	102239	1083	1.9	0.1	770.8	28.6	947.3	84.7	1.19	236	1.5	0.1	4.4	1.1	0.0005	0.0001	3.3	0.9
13	2334.2	23.6	101439	1108	2.2	0.1	982.6	36.3	1015.0	90.7	1.00	291	1.4	0.1	1.8	0.2	0.0003	0.0000	1.7	0.1
14	2248.6	22.7	103142	1090	91.4	2.3	525.6	20.1	1029.7	93.1	1.90	182	92.3	4.3	607.5	6.2	0.0979	0.0008	602.3	4.8
15	2454.0	24.8	99746	1069	1.8	0.1	952.4	35.2	1343.3	120.0	1.37	302	1.1	0.1	2.3	1.2	0.0003	0.0000	2.1	0.1
16	2586.7	27.1	103501	1126	91.6	2.3	903.2	33.5	200.7	17.9	0.22	227	74.2	3.3	758.7	4.9	0.1244	0.0009	755.7	5.0
17	2209.6	22.1	99335	1050	3.0	0.1	893.7	33.2	1046.0	93.5	1.13	271	2.1	0.1	5.5	0.9	0.0008	0.0001	4.9	0.4
18	2495.8	25.0	106440	1128	39.0	1.0	400.9	14.9	609.9	54.6	1.47	129	55.5	2.5	592.9	9.1	0.0944	0.0012	581.2	7.1
19	2521.6	25.2	109411	1151	193.9	4.8	602.6	22.3	645.0	57.6	1.04	180	196.9	8.5	608.0	5.4	0.0979	0.0008	601.8	4.8
20	2252.0	22.6	93257	1011	14.1	0.4	387.8	14.3	145.4	13.0	0.36	101	25.8	1.1	29.2	4.7	0.0043	0.0001	27.4	0.7
21	2261.4	23.0	105025	1187	336.0	8.3	4211.6	156.0	10100.1	902.1	2.32	1560	39.7	1.9	39.0	3.1	0.0053	0.0001	33.8	0.6
22	2491.0	25.2	106070	1127	3.2	0.1	1291.1	47.5	909.4	81.1	0.68	359	1.6	0.1	1.9	0.6	0.0003	0.0001	2.0	0.8
23	2550.4	25.7	111351	1182	43.2	1.1	1390.5	51.3	1125.1	100.4	0.78	395	20.3	0.9	21.6	0.4	0.0030	0.0000	19.1	0.2
24	2256.7	22.6	77841	888	126.4	3.1	426.7	16.0	473.0	42.4	1.07	128	180.2	7.8	586.6	8.6	0.0950	0.0009	585.0	5.0
25	2409.1	25.0	141820	1502	0.8	0.1	212.1	8.0	140.1	12.5	0.64	58	2.5	0.2	7.7	1.1	0.0010	0.0001	6.6	0.7
27	2258.2	22.9	100798	1158	13.5	0.4	402.8	15.1	190.5	17.0	0.46	107	23.4	1.0	26.0	6.2	0.0039	0.0001	25.3	0.7
28	2297.5	23.2	101613	1114	16.4	0.4	371.0	13.8	489.0	43.8	1.28	116	26.2	1.2	610.3	7.8	0.0986	0.0008	606.1	4.7
29	2399.1	24.3	121359	1342	1.4	0.1	375.6	14.5	520.8	47.1	1.34	118	2.3	0.2	4.1	0.5	0.0006	0.0001	3.8	0.6
30	2441.4	24.7	107836	1159	28.7	0.7	549.1	20.4	716.5	64.2	1.26	171	31.1	1.4	630.7	9.9	0.0976	0.0009	600.3	5.0
31	2435.2	24.4	84764	898	25.5	0.7	1958.7	72.8	1817.4	162.5	0.90	569	8.3	0.4	21.9	0.6	0.0031	0.0001	19.9	0.5
32	2082.7	20.8	96712	1015	24.2	0.6	808.8	29.8	625.9	55.8	0.75	228	19.7	0.8	18.2	2.6	0.0030	0.0000	19.0	0.3
33	2433.1	25.3	104600	1144	423.8	10.5	1130.7	41.8	431.4	38.6	0.37	295	260.7	11.4	915.2	6.7	0.1439	0.0016	866.7	9.1
35	2299.4	23.1	98790	1044	1.2	0.1	325.3	12.0	158.4	14.1	0.47	87	2.5	0.2	3.6	1.1	0.0004	0.0000	2.6	0.2
36	2437.0	24.5	102595	1150	84.5	2.1	3329.2	123.5	6128.9	547.6	1.78	1132	13.8	0.6	631.7	4.1	0.1020	0.0007	625.8	4.1

Supplementary Table A5 Continued

Grain	He Pit Vol. (μm^3)	err. (2σ)	U-Th Pit Vol. (μm^3)	err. (2σ)	[^4He] (nmol/g)	err. (2σ)	[^{238}U] (nmol /g)	err. (2σ)	[^{232}Th] (nmol /g)	err. (2σ)	$^{232}Th/^{238}U$	eU (ppm)	(U-Th)/ He date (Ma)	err. (2σ)	$^{207}Pb/^{235}U$ date (Ma)	err. (2σ)	$^{206}Pb/^{238}U$	err. (2σ)	$^{206}Pb/^{238}U$ date (Ma)	err. (2σ)
37	2192.9	22.1	101279	1062	6.2	0.2	2008.3	74.3	1691.1	151.0	0.81	574	2.0	0.1	9.1	3.5	0.0010	0.0005	6.8	3.4
38	2361.2	23.8	122204	1276	1.8	0.1	643.2	24.0	448.6	40.1	0.67	179	1.8	0.1	3.4	0.9	0.0004	0.0001	2.5	0.8
39	2284.0	23.1	104037	1124	7.5	0.2	296.2	11.0	140.0	12.5	0.46	79	17.6	0.8	26.3	2.2	0.0035	0.0001	22.4	0.5
40	2619.5	26.4	101988	1110	20.7	0.5	381.7	14.1	280.5	25.0	0.71	107	35.8	1.6	42.0	5.7	0.0057	0.0006	36.4	4.0
41	2676.0	27.0	104977	1148	1.9	0.1	190.1	7.4	248.1	22.4	1.26	59	6.0	0.4	9.1	1.0	0.0012	0.0001	7.8	0.7
42	2234.5	22.5	95493	1010	10.0	0.3	460.1	17.0	278.1	24.8	0.59	125	14.8	0.7	22.2	1.1	0.0032	0.0001	20.7	0.8
43	2062.1	20.6	100424	1095	72.9	1.8	2391.5	88.7	2337.2	208.8	0.95	701	19.3	0.8	21.5	0.6	0.0029	0.0000	19.0	0.2
44	2100.3	21.7	97917	1019	18.0	0.5	617.8	22.8	325.9	29.1	0.51	166	20.0	0.9	27.4	2.0	0.0034	0.0001	22.0	0.4
45	2495.3	25.0	110600	1209	15.0	0.4	493.0	18.4	370.7	33.1	0.73	138	20.1	0.9	24.7	3.6	0.0036	0.0002	23.4	1.4
47	2213.0	22.3	109943	1190	145.9	3.6	470.0	17.4	489.6	43.7	1.01	139	191.0	8.2	611.9	5.6	0.0992	0.0008	609.8	4.9
48	2001.9	20.1	97946	1066	1.7	0.1	615.7	22.7	271.9	24.3	0.43	162	1.9	0.1	7.9	1.3	0.0012	0.0001	7.8	0.5
50	2091.1	21.1	109432	1226	27.5	0.7	632.3	23.7	622.9	55.9	0.95	186	27.4	1.2	41.6	2.6	0.0050	0.0001	32.4	0.5
51	1976.9	19.8	105691	1120	4.0	0.2	1229.6	45.8	750.2	67.1	0.59	336	2.2	0.1	2.6	0.8	0.0004	0.0001	2.3	0.6
52	2052.0	20.7	103402	1069	15.6	0.4	465.9	17.2	224.0	20.0	0.47	124	23.4	1.0	25.4	3.0	0.0036	0.0001	23.0	0.4
54	2136.7	22.1	99883	1098	3.7	0.1	1401.2	52.1	1041.6	93.3	0.72	393	1.8	0.1	2.2	0.5	0.0003	0.0000	2.0	0.1
58	2535.9	25.8	91002	1004	1.9	0.1	953.6	35.4	731.6	65.4	0.74	268	1.3	0.1	2.4	0.5	0.0003	0.0000	1.9	0.1
60	2145.0	22.0	93296	1100	373.8	9.3	8090.8	302.8	9344.4	836.3	1.12	2449	28.2	1.2	30.1	0.5	0.0045	0.0000	28.7	0.2
61	2155.6	22.1	92460	1011	478.8	11.9	816.6	30.8	295.0	26.3	0.35	212	404.3	18.1	787.1	7.1	0.1290	0.0022	781.8	12.0
62	2044.0	20.6	86204	951	8.6	0.3	267.0	9.9	147.8	13.2	0.54	72	22.0	1.0	30.9	3.3	0.0044	0.0002	28.1	1.0
64	2210.4	22.6	96117	1115	21.5	0.6	721.3	27.0	495.5	44.4	0.66	200	19.9	0.9	28.4	1.9	0.0034	0.0001	22.0	0.9
65	1973.8	19.8	94473	980	2.9	0.1	1241.8	45.8	959.6	85.7	0.75	350	1.6	0.1	1.7	0.1	0.0003	0.0000	1.7	0.1
66	1915.0	19.3	95286	1010	25.0	0.7	793.4	29.4	423.1	37.8	0.52	213	21.7	0.9	23.2	0.8	0.0034	0.0001	22.1	0.4
69	2260.8	22.6	93907	1103	43.4	1.1	669.0	25.2	959.9	86.1	1.39	213	37.7	1.7	44.2	3.2	0.0063	0.0001	40.5	0.6
78	2175.4	22.6	96267	1092	1.1	0.1	384.7	14.3	290.9	26.0	0.73	108	1.9	0.2	32.1	2.1	0.0050	0.0001	31.9	0.6
80	2034.2	20.3	91123	1016	19.1	0.5	326.1	12.2	98.5	8.8	0.29	84	42.3	1.9	683.8	8.3	0.1118	0.0012	683.1	6.7
82	2974.4	29.9	91670	1002	0.8	0.1	416.3	15.5	259.1	23.2	0.60	114	1.3	0.1	4.9	1.6	0.0006	0.0001	3.8	0.3
83	2386.0	24.1	90107	939	22.5	0.6	972.4	35.9	693.3	61.9	0.69	271	15.4	0.7	24.0	0.8	0.0034	0.0001	22.2	0.4
84	2148.0	21.7	94971	1011	1.3	0.1	604.3	22.6	551.1	49.3	0.88	175	1.4	0.1	2.0	0.8	0.0003	0.0000	2.1	0.1
86	1971.0	19.9	95226	1062	56.2	1.4	2055.2	76.3	2284.0	204.0	1.08	617	16.8	0.7	20.6	1.0	0.0027	0.0001	17.6	0.4
87	2001.0	20.0	89872	984	10.7	0.3	349.0	12.9	355.9	31.8	0.99	103	19.2	0.9	38.2	4.8	0.0051	0.0002	32.5	1.2
88	1974.1	19.9	89298	984	1.2	0.1	555.4	20.8	623.2	56.2	1.09	167	1.4	0.1	3.4	0.7	0.0004	0.0001	2.8	0.4
90	2133.0	21.5	129155	1488	6.0	0.2	717.8	28.0	761.5	68.7	1.03	214	5.2	0.3	6.0	1.3	0.0008	0.0002	4.9	1.0
91	1939.0	19.6	70115	721	0.3	0.1	316.1	11.8	308.6	27.7	0.94	93	0.6	0.2	5.3	2.1	0.0007	0.0002	4.5	1.3
93	2024.7	20.3	87364	930	66.7	1.7	1325.4	49.0	1301.2	116.3	0.95	389	31.7	1.4	37.4	1.7	0.0052	0.0001	33.5	0.4

Supplementary Table A5

Grain	He Pit Vol. (μm^3)	err. (2σ)	U-Th Pit Vol. (μm^3)	err. (2σ)	[^4He] (nmol/g)	err. (2σ)	[^{238}U] (nmol /g)	err. (2σ)	[^{232}Th] (nmol /g)	err. (2σ)	$^{232}Th/^{238}U$	eU (ppm)	(U-Th)/ He date (Ma)	err. (2σ)	$^{207}Pb/^{235}U$ date (Ma)	err. (2σ)	$^{206}Pb/^{238}U$	err. (2σ)	$^{206}Pb/^{238}U$ date (Ma)	err. (2σ)
94	2086.7	20.9	90338	972	4.3	0.2	1630.0	60.3	1566.7	139.9	0.93	476	1.7	0.1	1.7	0.3	0.0003	0.0000	1.7	0.1
95	2236.5	22.4	102787	1114	21.6	0.6	549.1	20.5	507.9	45.4	0.90	159	25.1	1.1	25.7	0.7	0.0037	0.0001	23.5	0.4
99	2108.2	21.1	88490	957	8.8	0.3	2964.6	110.4	3759.3	336.3	1.23	916	1.8	0.1	1.7	0.2	0.0003	0.0000	1.7	0.2
100	1920.0	19.4	89536	1049	6.9	0.2	2573.9	96.1	3022.5	270.4	1.14	782	1.6	0.1	1.8	0.6	0.0003	0.0001	1.8	0.5
101	1800.6	18.0	86483	926	38.7	1.0	2152.7	80.0	1091.7	97.6	0.49	576	12.5	0.5	36.3	1.3	0.0050	0.0001	32.1	0.4
102	2190.9	22.1	80755	839	4.1	0.2	2096.2	77.9	1716.1	153.3	0.79	596	1.3	0.1	1.7	0.2	0.0003	0.0000	1.8	0.2
104	2022.5	20.6	87376	1074	27.0	0.7	1022.4	38.2	700.3	62.6	0.66	283	17.6	0.8	30.7	1.6	0.0035	0.0001	22.4	0.4
105	2122.9	21.8	120843	1358	7.7	0.2	920.9	35.4	541.7	48.9	0.57	250	5.7	0.3	6.8	1.2	0.0008	0.0001	5.2	0.4
106	2081.1	20.9	91704	996	24.5	0.6	821.1	30.4	522.2	46.6	0.62	225	20.1	0.9	25.0	0.6	0.0036	0.0001	22.9	0.5
107	2028.2	20.3	76461	814	6.0	0.2	468.0	17.3	221.5	19.8	0.46	124	9.0	0.4	15.7	2.2	0.0021	0.0001	13.7	0.4
108	2119.0	21.4	96590	1056	0.9	0.1	252.6	9.7	421.1	38.1	1.61	84	2.0	0.2	10.4	2.0	0.0013	0.0001	8.6	0.8
110	2154.1	21.7	114348	1276	30.5	0.8	1406.3	54.0	1245.7	112.2	0.86	405	13.9	0.6	22.2	5.9	0.0032	0.0002	20.4	1.3
2_1	1899.2	19.5	64276	692	4.4	0.3	628.9	13.1	0.0	0.0	0.82	180	4.6	0.3	7.1	2.2	0.0009	0.0000	5.7	0.3
2_2	523.3	5.4	34611	360	37.3	1.3	1339.0	26.8	533.7	25.3	0.65	370	18.6	0.7	22.6	2.3	0.0033	0.0001	21.5	0.7
2_3	1929.4	20.0	63794	688	23.9	0.7	586.7	12.2	903.2	42.6	0.62	161	27.5	0.9	35.8	6.8	0.0048	0.0004	30.6	2.6
2_4	499.2	5.2	32999	338	4.6	1.0	4232.7	86.3	374.7	17.7	1.30	1326	0.6	0.1	1.7	0.2	0.0002	0.0000	1.6	0.1
2_5	2057.1	21.1	60915	688	163.9	4.1	2431.0	50.9	5702.3	270.3	0.70	678	44.6	1.4	755.3	6.8	0.1231	0.0017	748.3	9.6
2_6	1759.1	18.0	62072	707	4.9	0.3	2379.7	49.7	1752.9	83.5	1.75	805	1.1	0.1	1.6	0.2	0.0002	0.0000	1.4	0.1
2_7	1668.4	17.2	46947	525	116.2	2.9	9001.9	188.1	4296.0	203.6	0.69	2508	8.6	0.3	547.1	6.6	0.0858	0.0014	530.8	8.1
2_8	383.0	4.4	27937	306	9.2	1.3	7665.0	165.7	6420.7	304.1	1.33	2412	0.7	0.1	2.2	0.3	0.0003	0.0000	1.9	0.1
2_9	434.0	4.3	28151	286	31.3	1.4	1994.4	40.7	10543.5	507.6	0.58	544	10.7	0.5	25.1	2.2	0.0033	0.0001	21.0	0.5
2_10	519.5	5.8	42582	439	127.1	3.4	4213.1	85.8	1199.9	56.6	1.63	1396	16.8	0.6	17.6	8.0	0.0029	0.0001	18.6	0.6
2_11	508.6	5.3	34995	361	197.0	5.0	5773.5	117.3	7087.6	334.9	1.09	1738	21.0	0.7	31.6	8.0	0.0049	0.0001	31.8	0.8
2_12	1834.9	19.0	61404	666	0.8	0.3	782.6	16.1	6499.0	306.5	0.69	218	0.7	0.2	4.5	2.8	0.0003	0.0000	2.1	0.3
2_13	1210.1	14.0	46601	549	80.9	2.2	6587.1	138.7	559.9	26.5	0.40	1729	8.7	0.3	463.2	9.0	0.0674	0.0023	421.0	14.0
2_14	449.6	4.5	29625	300	26.0	1.3	1460.0	32.3	2740.5	130.3	0.64	402	12.0	0.6	28.0	3.2	0.0033	0.0001	21.1	0.6
2_16	386.9	4.0	33096	341	103.9	2.9	648.6	13.2	962.7	46.0	0.74	183	104.6	3.6	592.3	39.1	0.0956	0.0015	588.5	9.0
2_18	1545.0	16.4	59773	670	9.4	0.4	451.9	9.5	497.8	23.5	0.67	125	13.9	0.6	21.3	2.8	0.0033	0.0004	21.1	2.6
2_22	409.1	4.8	26542	273	163.9	4.4	810.9	16.5	313.5	14.8	1.53	264	113.9	3.8	574.0	52.5	0.0957	0.0019	589.0	11.0
2_23	436.0	4.4	25048	255	7.1	1.1	587.5	11.9	1282.6	60.4	0.42	155	8.5	1.4	24.1	8.3	0.0035	0.0004	22.2	2.5
2_24	456.6	4.6	23724	239	1.1	1.1	6125.2	123.7	257.0	12.1	1.20	1884	0.1	0.1	1.3	0.4	0.0002	0.0000	1.4	0.1
2_25	303.4	3.9	26120	269	27.4	1.8	2902.5	59.7	7622.0	358.9	1.13	881	5.8	0.4	37.5	3.4	0.0051	0.0001	32.8	0.7
2_26	421.4	4.2	27289	282	1.3	1.2	702.8	14.5	3393.7	160.7	1.86	242	1.0	0.9	613.6	61.0	0.0980	0.0017	602.4	9.9
2_27	1795.1	18.0	59685	678	5.8	0.3	317.3	6.7	1349.6	71.0	0.69	88	12.1	0.7	26.9	4.7	0.0034	0.0002	22.0	1.0

Supplementary Table A5

Grain	He Pit Vol. (μm^3)	err. (2σ)	U-Th Pit Vol. (μm^3)	err. (2σ)	[^4He] (nmol/g)	err. (2σ)	[^{238}U] (nmol /g)	err. (2σ)	[^{232}Th] (nmol /g)	err. (2σ)	$^{232}Th/^{238}U$	eU (ppm)	(U-Th)/He date (Ma)	err. (2σ)	$^{207}Pb/^{235}U$ date (Ma)	err. (2σ)	$^{206}Pb/^{238}U$	err. (2σ)	$^{206}Pb/^{238}U$ date (Ma)	err. (2σ)
2_28	493.7	5.2	31512	322	5.1	1.0	4535.7	100.0	226.5	10.8	1.14	1378	0.7	0.1	1.8	0.3	0.0003	0.0000	1.6	0.2
2_29	1757.4	18.2	57389	603	25.3	0.7	1307.7	26.5	5338.7	256.5	0.69	364	12.9	0.4	22.1	6.0	0.0033	0.0001	20.9	0.8
2_31	453.4	5.1	57114	575	9.5	1.1	226.5	5.6	929.7	44.0	1.18	69	25.2	3.0	39.2	5.7	0.0055	0.0006	35.1	4.1
2_32	479.8	5.3	30639	315	158.2	4.1	2260.4	50.1	276.1	14.4	1.15	688	42.5	1.4	614.7	12.8	0.0992	0.0017	610.0	9.8
2_33	1775.1	19.0	63199	685	10.0	0.4	3576.2	79.7	2677.0	131.4	1.29	1116	1.7	0.1	1.9	0.7	0.0003	0.0000	1.7	0.3
2_35	1708.7	18.1	71504	1060	10.3	0.4	364.8	8.7	4749.5	230.4	0.47	97	19.6	0.9	21.7	2.9	0.0033	0.0004	21.1	2.8
2_36	1858.3	19.1	71430	751	140.8	3.5	1364.1	29.3	176.6	8.6	0.48	364	71.4	2.3	727.9	9.0	0.1180	0.0029	719.0	16.0
2_38	1597.5	17.5	53163	585	3.0	0.3	1794.9	37.5	671.1	32.2	1.02	533	1.0	0.1	3.0	1.7	0.0002	0.0000	1.6	0.2

APPENDIX B

NORTHERN AWASH AND WEST TURKANA DETRITAL APATITE

(U-TH/HE) DATES

Detrital apatite (U-Th)/He analyses were also carried out on the NA and WTK samples discussed in Chapter 2 following procedures and methods outlined in Chapter 5. Results were not included in the main text due to the high degree of partial resetting observed in the zircon (U-Th)/He dates.

Supplementary tables B1-5

- R = half-width (μm)
- L= length (μm)
- Apatite F_T correction following Farley, Kenneth A. (2002). U-Th)/He dating: Techniques, calibrations, and applications. *Reviews in Mineralogy and Geochemistry*, 47, 1, p. 819–844.

Supplementary Table B1. (U-Th)/He detrital apatite data for sample NAO14-1D-39Q-2.

Grain	R (μm)	L (μm)	He (pmol)	[238U] (ppm)	[232Th] (ppm)	F_T	Raw Age (Ma)	Corr. Age (Ma)	err. (2σ)
1	37.0	227.1	0.0003	5.09	13.28	0.651	2.23	3.42	0.40
2	46.5	309.6	0.0007	4.39	19.54	0.714	2.39	3.35	0.22
3	38.0	239.6	0.0010	4.14	13.24	0.659	8.22	12.47	0.90
4	76.5	322.6	0.0082	3.14	18.60	0.807	11.40	14.12	0.48
5	45.2	248.2	0.0003	3.19	8.56	0.705	2.18	3.10	0.50
6	42.0	199.2	0.0002	3.52	9.21	0.679	2.20	3.25	0.66
7	51.5	174.7	0.0029	3.51	22.38	0.710	13.44	18.92	1.3
8	43.5	289.9	0.0005	2.05	6.65	0.699	5.03	7.19	0.79
9	51.2	152.1	0.0025	2.21	15.31	0.700	19.15	27.4	2.3
10	37.7	226.4	0.0004	5.29	24.88	0.650	2.52	3.87	0.32
11	57.9	226.4	0.0011	1.91	6.66	0.751	8.95	11.91	1.6
12	47.0	226.4	0.0005	1.12	5.74	0.704	8.35	11.85	1.5

Supplementary Table B2. (U-Th)/He detrital apatite data for sample NAO14-1D-48Q-1.

Grain	R (μm)	L (μm)	He (pmol)	[238U] (ppm)	[232Th] (ppm)	F_T	Raw Age (Ma)	Corr. Age (Ma)	err. (2σ)
1	47.3	206.7	0.0188	4.15	21.47	0.702	82.12	117.0	4.2
3	52.9	219.5	0.0021	2.25	13.42	0.728	10.60	14.56	0.82
4	39.9	227.1	0.0012	2.83	17.60	0.662	8.72	13.16	0.81
5	47.0	194.8	0.0008	1.82	9.21	0.698	10.05	14.40	1.2
6	39.5	131.2	0.0003	2.40	10.17	0.636	7.18	11.30	1.7
7	46.9	233.5	0.0013	2.45	14.35	0.704	7.90	11.22	0.70
8	53.4	168.6	0.0009	2.04	11.38	0.717	8.00	11.16	0.82
9	55.7	179.6	0.0015	2.47	14.74	0.728	7.81	10.73	0.62
10	46.9	225.5	0.0044	2.47	23.32	0.699	21.47	30.73	1.3

Supplementary Table B3. (U-Th)/He detrital apatite data for sample NAW14-1A-8Q-1.

Grain	R (μm)	L (μm)	He (pmol)	[^{238}U] (ppm)	[^{232}Th] (ppm)	F_T	Raw Age (Ma)	Corr. Age (Ma)	err. (2σ)
2	52.4	183.4	0.0044	7.57	30.12	0.720	13.03	18.08	0.84
3	71.5	290.7	0.0007	1.96	4.67	0.799	3.31	4.14	0.50
7	55.3	276.2	0.0012	2.87	9.09	0.750	5.59	7.45	0.83
9	50.3	182.9	0.0009	2.93	9.74	0.713	7.80	10.94	1.01
10	38.9	199.6	0.0008	5.42	13.52	0.660	6.33	9.59	0.75
11	60.5	204.5	0.0062	2.38	16.06	0.750	24.14	32.21	1.51
12	43.5	152.8	0.0001	0.78	2.06	0.673	5.38	7.99	3.30
13	46.4	189.5	0.0028	10.13	49.64	0.694	6.80	9.80	1.25
14	54.3	201.3	0.0041	0.81	4.69	0.729	58.34	80.01	4.39
16	49.6	178.3	0.0008	0.88	3.96	0.706	19.86	28.13	2.73
17	46.7	185.8	0.0013	5.84	23.61	0.696	5.89	8.47	0.78

Supplementary Table B4. (U-Th)/He detrital apatite data for sample NAW14-1A-36Q-1.

Grain	R (μm)	L (μm)	He (pmol)	[^{238}U] (ppm)	[^{232}Th] (ppm)	F_T	Raw Age (Ma)	Corr. Age (Ma)	err. (2σ)
1	56.6	216.1	0.0018	2.74	7.55	0.746	11.74	15.72	2.66
2	44.6	138.7	0.0007	2.96	9.89	0.671	10.40	15.50	1.77
3	41.7	193.5	0.0013	2.69	15.53	0.668	10.69	16.00	1.62
4	46.7	159.3	0.0009	5.63	13.88	0.693	5.83	8.42	0.77
5	46.3	124.1	0.0004	2.56	5.76	0.676	8.29	12.27	1.39
6	61.8	225.2	0.0031	2.50	18.16	0.757	9.58	12.65	1.20
7	45.2	143.6	0.0006	2.52	10.76	0.674	8.37	12.42	1.24
8	49.3	124.9	0.0012	5.25	25.19	0.682	7.54	11.05	1.42
9	43.6	201.4	0.0013	4.51	16.09	0.685	8.34	12.17	1.77
10	50.3	141.7	0.0006	0.62	3.34	0.694	23.12	33.29	3.58

Supplementary Table B5. (U-Th)/He detrital apatite data for sample WTK13-1A-20Q-2.

Grain	**R (μm)**	**L (μm)**	**He (pmol)**	**[^{238}U] (ppm)**	**[^{232}Th] (ppm)**	**F_T**	**Raw Age (Ma)**	**Corr. Age (Ma)**	**err. (2σ)**
1	57.3	245.5	0.0277	43.72	2.82	0.765	17.16	22.42	0.61
2	61.3	308.1	0.0060	12.64	21.40	0.777	6.40	8.23	0.34
3	65.4	329.3	0.0116	14.77	40.53	0.788	7.49	9.51	0.29
4	48.0	191.4	0.0003	1.79	6.08	0.705	4.61	6.53	0.91
6	40.0	186.9	0.0003	3.40	3.34	0.671	5.71	8.50	1.41
7	53.4	276.6	0.0026	6.38	24.40	0.742	5.89	7.94	0.88
8	51.6	142.4	0.0010	3.14	13.14	0.702	9.32	13.27	1.68
9	55.2	172.2	0.0115	28.37	4.56	0.742	16.38	22.07	0.74
10	56.6	167.5	0.0008	3.31	14.76	0.730	4.78	6.55	0.59

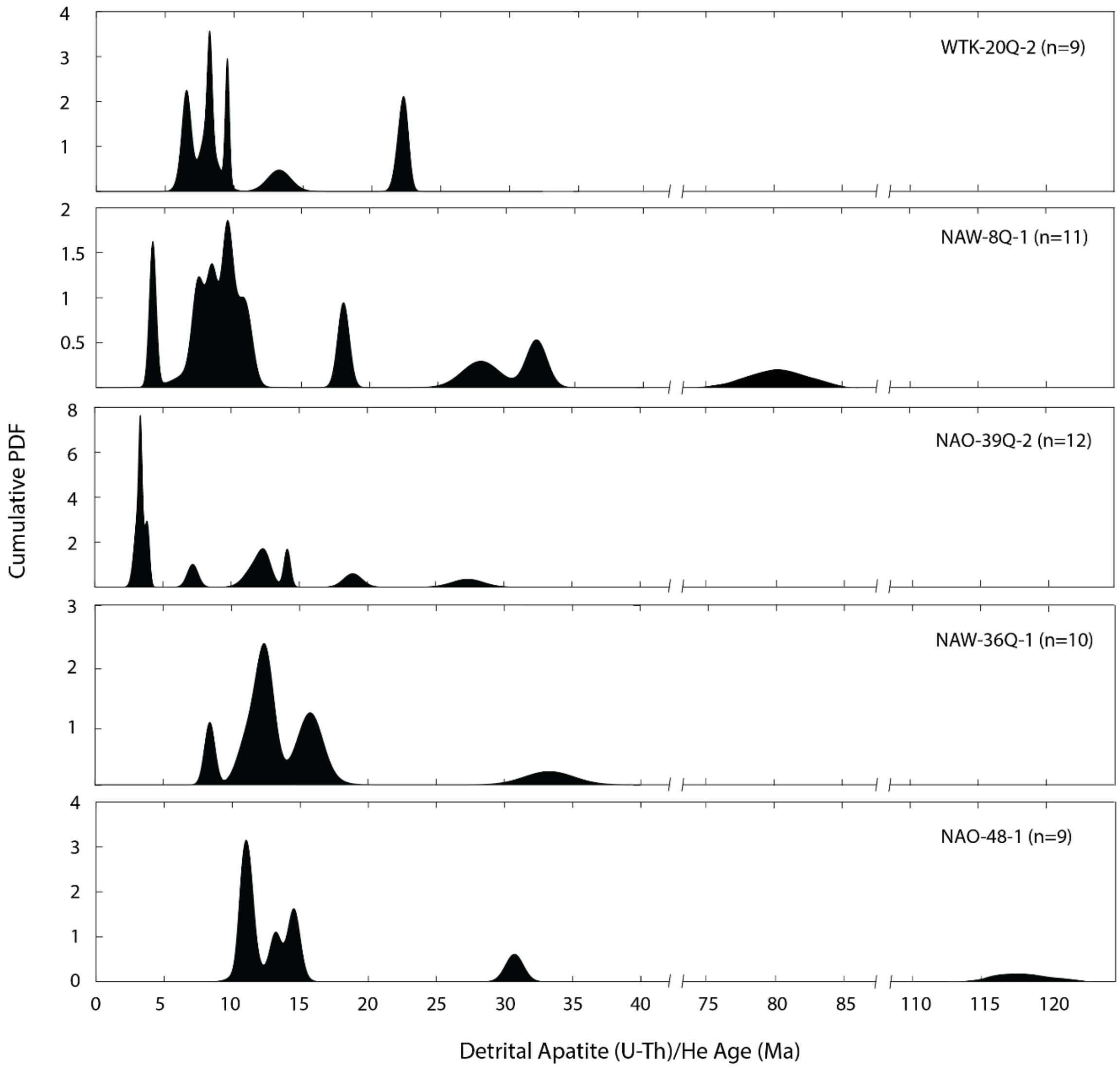

Figure B1. Cumulative probability density function (PDF) plots of NA and WTK detrital apatite (U-Th)/He dates.

APPENDIX C

CHAPTER 3 SUPPLEMENTARY MATERIALS

1. Overview

The Monte Carlo simulation uses repeated random sampling of all input variables to aggregate the individual uncertainties into a final probability distribution function (PDF) of the paleoerosion rates. Paleoerosion rate calculations are performed following Equations 1–5 in Chapter 3. We assume all variables have normally distributed uncertainties for our sampling. We account for the 1σ uncertainty of the [^{10}Be] measurement (Table 3.2) and for the 1σ error of constant variables from the literature such as the ^{10}Be decay constant (Chmeleff et al., 2010) and attenuation lengths (Braucher et al., 2003). For the density of the eroding material and the buried sediment, we assume an uncertainty of 5%, based on MSCL-S gamma density log data of the drill cores (Cohen et al., 2016). ^{10}Be hillslope and burial production rate uncertainties are determined based on variances in the geomagnetic field strength over the 1σ age of the samples. Production rates follow the time-dependent 'Lm' scaling scheme described in Balco et al. (2008). We do not account for variation in elevation for production rate uncertainties, due to the likely relative similarity of basin topography over the observed time intervals. The 1σ age of the samples is used to constrain the uncertainty in ^{10}Be lost to radioactive decay, and we assume a 5% uncertainty in sediment accumulation rates for post-depositional ^{10}Be accumulation based on the average uncertainty of the core age model. In Figure C7 we model the results using a 10% uncertainty on sediment accumulation and material density. A 10%

uncertainty yields a slightly higher maximum erosion rate and only minor decrease in minimum erosion rate. An example script follows this section.

2. Code explanation

    a. Monte Carlo implementation

        i. We take the calculation workflow and assign a normal error to each variable with an uncertainty that is known independently or a 5% (or more) default uncertainty. From that, we sample all of the parameters 1 million times (see intermediate histograms below) and then compute the final paleoerosion rates.

        ii. We use the *rand* MATLAB function to create a uniformly distributed random numbers https://www.mathworks.com/help/matlab/ref/rand.html

        iii. To determine the final resulting paleoerosion rate and propagated errors, we make a normalized PDF (area=1) from the final erosion rate histogram and trim the PDF from the bottom to the specified significance level (here we use 0.99). We then determine the modal and mean rates of the PDF, which are typically very similar. We finally find the extremes of the specified significance level (0.99) as the maximum and minimum value for the error range on the modal and mean rates.

References:

Balco, Greg, John O. Stone, Nathaniel A. Lifton, and Tibor J. Dunai (2008). A complete and easily accessible means of calculating surface exposure ages or erosion rates from ^{10}Be and ^{26}Al measurements. *Quaternary Geochronology*, 3, 3, p. 174–195. https://doi.org/10.1016/j.quageo.2007.12.001

Braucher, R., Brown, E.T., Bourlès, D.L., Colin, F. (2003). *In situ* produced ^{10}Be measurements at great depths: implications for production rates by fast muons. *Earth and Planetary Science Letters*, 211, p. 251–258. https://doi.org/10.1016/S0012-821X(03)00205-X

Chmeleff, Jérôme, Friedhelm von Blanckenburg, Karsten Kossert, and Dieter Jakob (2010). Determination of the ^{10}Be half-life by multicollector ICP-MS and liquid scintillation counting. *Nuclear Instruments and Methods in Physics Research Section B: Beam Interactions with Materials and Atoms*, 268, 2, p. 192–199. https://doi.org/10.1016/j.nimb.2009.09.012

Cohen, A., C. Campisano, R. Arrowsmith, A. Asrat, A.K. Behrensmeyer, A. Deino, C. Feibel, A. Hill, R. Johnson, J. Kingston, H. Lamb, T. Lowenstein, A. Noren, D. Olago, R.B. Owen, R. Potts, K. Reed, R. Renaut, F. Schäbitz, J.-J. Tiercelin, M.H. Trauth, J. Wynn, S. Ivory, K. Brady, R. ÓGrady, J. Rodysill, J. Githiri, J. Russell, V. Foerster, R. Dommain, S. Rucina, D. Deocampo, J. Russell, A. Billingsley, C. Beck, G. Dorenbeck, L. Dullo, D. Feary, D. Garello, R. Gromig, T. Johnson, A. Junginger, M. Karanja, E. Kimburi, A. Mbuthia, T. McCartney, E. McNulty, V. Muiruri, E. Nambiro, E.W. Negash, D. Njagi, J.N. Wilson, N. Rabideaux, T. Raub, M.J. Sier, P. Smith, J. Urban, M. Warren, M. Yadeta, C. Yost, and B. Zinaye (2016). The Hominin Sites and Paleolakes Drilling Project: inferring the environmental context of human evolution from eastern African rift lake deposits, Sci. Dril., 21, p. 1–16. https://doi.org/10.5194/sd-21-1-2016

```
clc
clear all
close all

%Script to calculate paleoerosion rates from [10Be] - EEZ
%modified by JRA to try Monte Carlo for error propagation
%______________________________________________________________________
_
%Set the MC values
n=1000000; %number of samples
num_std=4; %number of standard deviations to sample for the different
variables.
%We assume normal distributions in general
truncate = 1; %truncate = 1 yes cut the distribution at the num_std
sigma or no if = other
min_erosion_rate = 0.015; %just to help with plotting [mm/yr]
max_erosion_rate = 0.024; %just to help with plotting [mm/yr]
erosion_rate_step = 0.0001; %bin size for the final histogram [mm/y]
sigmas=0.99; %0.6827 is one sigma and 0.9545 is two sigma range to cut
pdf 1.0 takes all 0.99 cleans it
simple_error = 0.05; %simple error assumption for input values in the
absence of other information
sample_name='NAO14-1D-39Q-2';
calc_name=strcat(sample_name);

%______________________________________________________________________
%Set constant variables for erosion rate calculations
%(sd is standard deviation)
atten_spal = 165;                               %spallation attenuation
length [g/cm^2]
atten_spal_sd = atten_spal.*simple_error;       %spallation attenuation
length sd
atten_fast = 1500;                  %fast muons attenuation length [g/cm^2]
atten_fast_sd = 100;       %fast muons attenuation length sd
atten_slow = 5300;                  % slow muons atten length [g/cm^2]
atten_slow_sd = 950;       %slow muons atten length sd
lambda = 4.998e-7;                %10Be decay constant (yr^-1)
lambda_sd = 0.043e-7;           %10Be decay constant sd
rho_hill = 2.65;                  %density of hillslope material [g/cm^3]
rho_hill_sd = rho_hill.*simple_error;       %density of hillslope
material sd
rho_burial = 1.9;                 %density of burial overburden [g/cm^3]
rho_burial_sd = rho_burial.*simple_error;       %density of burial
overburden

%and sample for normal distribution for each
[atten_spal_range, atten_spal_samples, atten_spal_histogram] =
normal_sample_pdf(atten_spal, atten_spal_sd , num_std, n, truncate);
[atten_fast_range, atten_fast_samples, atten_fast_histogram] =
normal_sample_pdf(atten_fast, atten_fast_sd , num_std, n, truncate);
[atten_slow_range, atten_slow_samples, atten_slow_histogram] =
normal_sample_pdf(atten_slow, atten_slow_sd , num_std, n, truncate);
[lambda_range, lambda_samples, lambda_histogram] =
normal_sample_pdf(lambda, lambda_sd , num_std, n, truncate);
```

```
[rho_hill_range, rho_hill_samples, rho_hill_histogram] =
normal_sample_pdf(rho_hill, rho_hill_sd , num_std, n, truncate);
[rho_burial_range, rho_burial_samples, rho_burial_histogram] =
normal_sample_pdf(rho_burial, rho_burial_sd , num_std, n, truncate);

figure(1)
clf
ncols=2; nrows=3;
hold on
subplot(nrows, ncols, 1)
histogram(atten_spal_samples)
xlabel('atten\_spal [g/cm^2]')
subplot(nrows, ncols, 2)
histogram(atten_fast_samples)
xlabel('atten\_fast [g/cm^2]')
subplot(nrows, ncols, 3)
histogram(atten_slow_samples)
xlabel('atten\_slow [g/cm^2]')
subplot(nrows, ncols, 4)
histogram(lambda_samples)
xlabel('10Be decay constant \lambda (yr^-1)')
subplot(nrows, ncols, 5)
histogram(rho_hill_samples)
xlabel('\rho hill [g/cm^3]')
subplot(nrows, ncols, 6)
histogram(rho_burial_samples)
xlabel('\rho burial [g/cm^3]')


%Set sample-specific variables (Using NAW8 values
here)______________________

%Production rate values from time-dependent Lal-Stone ('Lm') -
different
%rates for each sample
%(sd is standard deviation)
P_hill = 5.64;                  %Total hillslope production rate
[atoms/g/yr]
P_hill_sd = 0.77;               %Total hillslope production rate sd
Pspal_burial = 4.56;            %Spallation production at burial site
[atoms/g/yr]
Pspal_burial_sd = 0.61;         %Spallation production sd
Pmf_burial = 0.03;              %Fast muons production at burial
[atoms/g/yr]
Pmf_burial_sd = 0.005;          %Fast muons production sd
Pms_burial  = 0.06;             %Slow muon production at burial
[atoms/g/yr]
Pms_burial_sd = 0.008;          %Slow muon production sd

N_mes = 45491.86;          %Measured [10Be] concentration
N_mes_E = 2076.49;         %Measured [10Be] uncertainty assume normal
dist'n
```

```
t = 3020000;              %Depositional age of sample [yr]
t_E = 62000;              %1 sigma depositional age uncertainty [yr]

AR = 0.03;                  %Sediment accumulation rate above sample
[cm/yr]
AR_E = AR.*simple_error;        %1 sigma sed accumulation uncertainty

%and sample for normal distribution for each (production rates)
[P_hill_range, P_hill_samples, P_hill_histogram] =
normal_sample_pdf(P_hill, P_hill_sd , num_std, n, truncate);
[Pspal_burial_range, Pspal_burial_samples, Pspal_burial_histogram] =
normal_sample_pdf(Pspal_burial, Pspal_burial_sd , num_std, n,
truncate);
[Pmf_burial_range, Pmf_burial_samples, Pmf_burial_histogram] =
normal_sample_pdf(Pmf_burial, Pmf_burial_sd , num_std, n, truncate);
[Pms_burial_range, Pms_burial_samples, Pms_burial_histogram] =
normal_sample_pdf(Pms_burial, Pms_burial_sd , num_std, n, truncate);


figure(2)
clf
ncols=2; nrows=2;
hold on
subplot(nrows, ncols, 1)
histogram(P_hill_samples)
xlabel('P\_hill [atoms/g/yr]')
title(calc_name)
subplot(nrows, ncols, 2)
histogram(Pspal_burial_samples)
xlabel('Pspal\_burial [atoms/g/yr]')
subplot(nrows, ncols, 3)
histogram(Pmf_burial_samples)
xlabel('Pmf\_burial [atoms/g/yr]')
subplot(nrows, ncols, 4)
histogram(Pms_burial_samples)
xlabel('Pms\_burial [atoms/g/yr]')

%and sample for normal distribution for each (other important
parameters)
[N_mes_range, N_mes_samples, N_mes_histogram] =
normal_sample_pdf(N_mes, N_mes_E , num_std, n, truncate);
[t_range, t_samples, t_histogram] = normal_sample_pdf(t, t_E , num_std,
n, truncate);
[AR_range, AR_samples, AR_histogram] = normal_sample_pdf(AR, AR_E ,
num_std, n, truncate);

figure(3)
clf
ncols=1; nrows=3;
hold on
subplot(nrows, ncols, 1)
histogram(N_mes_samples)
xlabel('Measured [10Be] concentration')
```

```
title(calc_name)
subplot(nrows, ncols, 2)
histogram(t_samples)
xlabel('Depositional age of sample [yr]')
subplot(nrows, ncols, 3)
histogram(AR_samples)
xlabel('Sediment accumulation rate [cm/yr]')


%Calculate post-depositional 10Be
accumulation___________________________

%Set grouped variables (accumulation rate * burial density /
attenuation length)
ADA_spal = AR_samples .* rho_burial_samples ./ atten_spal_samples;
ADA_fast = AR_samples .* rho_burial_samples ./ atten_fast_samples;
ADA_slow = AR_samples .* rho_burial_samples ./ atten_slow_samples;
%(decay constant * time [age])
LT = lambda_samples .* t_samples;

%Calculate for spallation
Post_spal = Pspal_burial ./ (lambda - ADA_spal) .* (exp(-t*ADA_spal) -
exp(-LT));
%Calculate for fast muons
Post_fast = Pmf_burial ./ (lambda - ADA_fast) .* (exp(-t*ADA_fast) -
exp(-LT));
%Calculate for slow muons
Post_slow = Pms_burial ./ (lambda - ADA_slow) .* (exp(-t*ADA_slow) -
exp(-LT));

%Total post-depositional accumulation
N_post = Post_spal + Post_fast + Post_slow;


%Calculate nuclide loss to radioactive
decay____________________________

N_dec = ((N_mes - N_post) ./ exp(-LT)) - (N_mes - N_post);


%Calculate initial nuclide concentration ______________________________
N_0 = N_mes + N_dec - N_post;

figure(4) %nuclides
clf
ncols=1; nrows=3;
hold on
subplot(nrows, ncols, 1)
histogram(N_post)
xlabel('Post depositional nuclides')
title(calc_name)
subplot(nrows, ncols, 2)
```

```
histogram(N_dec)
xlabel('Decayed nuclides')
subplot(nrows, ncols, 3)
histogram(N_0)
xlabel('Initial nuclides')


%Calculate erosion rate [cm/yr]___________________________________
E_cm = (atten_spal ./ rho_hill) * ((P_hill ./ N_0) - lambda);

%Convert to [mm/yr]
E_mm = E_cm .* 10;

edges = min_erosion_rate:erosion_rate_step:max_erosion_rate;


figure(5) %erosion rate
clf
%ncols=1; nrows=3;
hold on
%subplot(nrows, ncols, 1)
h=histogram(E_mm, edges);
xlabel('Hillslope erosion rate (mm/yr)')
title(calc_name)

figure(6)
clf
[most_common_rate, max_rate, min_rate] = clean_and_process_pdf(h,
sigmas, calc_name, 0.020)
title(calc_name)
xlabel('Hillslope erosion rate (mm/yr)')
```

```
function [a_range, a, a_histogram] = normal_sample_pdf(a_mean, a_std,
num_std, n, truncate)
%This function computes the normally distributed pdf
%It assumes that the parameter is a normal distribution centered on
a_mean
%with num_std standard deviations (elev_std) and samples it n times.
%JRA October 20, 2016
%Updated October 23, 2018 fot the truncation
%updated and generalized Oct. 14, 2020
%variables that are returned:
% a_range = range of sample values
% a = samples
% a_histogram = histogram output over the a_range
%truncate = 1 yes cut it at the 2 sigma or no if = other


[increment, a_range] = compute_increment_range(a_mean+num_std.*a_std,
a_mean-num_std.*a_std, n);
a = a_mean+a_std.*randn(length(a_range),1);
%here we are going to truncate the gaussian at 2*std
if truncate==1
locs_minus = find(a<a_mean+num_std.*a_std);
a=a(locs_minus);
locs = find(a>a_mean-num_std.*a_std);
a=a(locs);
end
%but that cuts out some that we actually need to have the same number
as we
%had initially input

nn=length(a); %Length of the concatenated list of rates
numsamples=n; %Sample it the same number of times as the first sampling
m=ceil(rand(numsamples,1).*nn); %Choose randomly and evenly across the
length of the concatenated list of rates
sampled_a=[];
for i = 1:numsamples
    sampled_a(i)=a(m(i)); %Sample the composite pdf; THIS IS WHAT WE
USE GOING FORWARD
end
a=sampled_a';
a_histogram = hist(a, length(a_range));
end
```

```
function [increment,range_of_values]= compute_increment_range(maxvalue,
minvalue, n)
%This function computes the increment for the sample range given the
min
%and max and the number of samples
%JRA October 20, 2016
increment=(maxvalue-minvalue)/(n-1);
range_of_values=[minvalue:increment:maxvalue];
end


function [most_common_rate, max_rate, min_rate] =
clean_and_process_pdf(h, sigmas, run_name, x)
%funcation taks input histogram of pdf of rates and normalizes it and
then
%clips it by the amount in sigmas
%J R Arrowsmith, January 2021
%x is just the x location of the text for the plot

MFC=[1,1,1];
bincenters =
h.BinEdges(1):h.BinWidth:(h.BinEdges(h.NumBins)+h.BinWidth);
a = size(bincenters);

wbc=h.BinCounts;
b= size(wbc);

%this is a little hack to fix why sometimes the lengths of these
vectors
%don't match
if a(2)~=b(2)
    bincenters = h.BinEdges(1):h.BinWidth:(h.BinEdges(h.NumBins));
end

area_of_each_bar=wbc.*h.BinWidth;
orginal_area_under_curve=sum(area_of_each_bar);
normalized_area_of_each_bar =
area_of_each_bar./orginal_area_under_curve;
plot(bincenters, normalized_area_of_each_bar,'k-')
na = sum(normalized_area_of_each_bar);

%adjust for significance
while na>sigmas
    tf=find(wbc>0);
    temp=wbc(tf)-1;
    wbc(tf)=temp;
    area_of_each_bar=wbc.*h.BinWidth;
    area_under_curve=sum(area_of_each_bar);
    normalized_area_of_each_bar =
area_of_each_bar./orginal_area_under_curve;
    na=sum(normalized_area_of_each_bar);
end

%find the mean
```

```
t=0; mean_pos=0;
while t<=sigmas/2
    mean_pos=mean_pos+1;
    t=t+normalized_area_of_each_bar(mean_pos);
end
mean_rate=bincenters(mean_pos);
t/sigmas;

hold on

fill(bincenters, normalized_area_of_each_bar,[192/255 192/255 192/255])
plot(mean_rate,normalized_area_of_each_bar(mean_pos),'d',...
    'MarkerSize',10,...
    'MarkerEdgeColor','b',...
    'MarkerFaceColor',MFC)
max_prob=max(normalized_area_of_each_bar);
loc=find(normalized_area_of_each_bar==max_prob);
most_common_rate=bincenters(loc);
plot(most_common_rate,max_prob, 'o',...
    'MarkerSize',10,...
    'MarkerEdgeColor','r',...
    'MarkerFaceColor',MFC)
tf=normalized_area_of_each_bar>0;
min_rate = min(bincenters(tf))

%loc=find(bincenters==min_rate)-1  %this is the first non-zero but we
want
%the last zero old way
loc=find(bincenters==min_rate);  %this is the first non-zero but we
want the last zero
min_rate = bincenters(loc);
plot(min_rate,normalized_area_of_each_bar(loc), 's',...
    'MarkerSize',10,...
    'MarkerEdgeColor','g',...
    'MarkerFaceColor',MFC)
max_rate=max(bincenters(tf));
loc=find(bincenters==max_rate)+1;%this is the las non-zero but we want
the first zero on the high side
if loc>length(bincenters)
    loc=length(bincenters);
end
max_rate=bincenters(loc);
plot(max_rate,normalized_area_of_each_bar(loc), 's',...
    'MarkerSize',10,...
    'MarkerEdgeColor','g',...
    'MarkerFaceColor',MFC)


atxt=[];
atxt = sprintf('Most common rate = %0.4f\nsig range = %0.4f\nmin =
%0.4f to max = %0.4f\nMean rate =
%0.4f',most_common_rate,sigmas,min_rate,max_rate,mean_rate);
%atxt=strcat({atxt},{run_name});
%[A]=gtext(atxt)
```

```
text(x,max_prob,atxt, 'VerticalAlignment','top')
ylabel('probability')

end
```

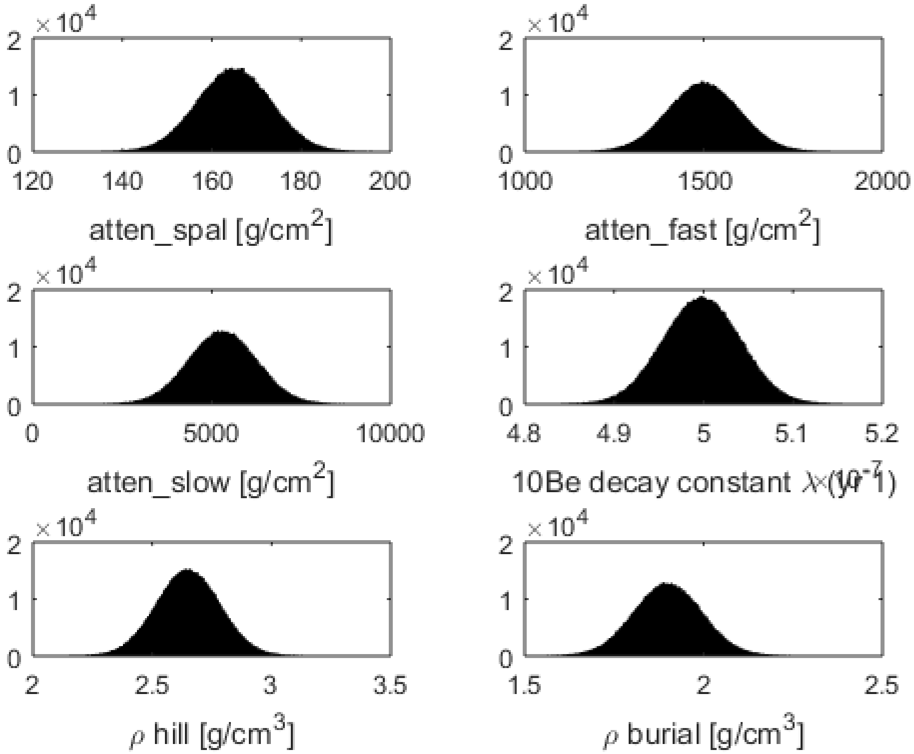

Figure C1. Normal distributions of constant variables used for all paleoerosion rate calculations. atten_spal = spallation attenuation length (g/cm^2), atten_fast = fast muons attenuation length (g/cm^2), atten_slow = slow muon capture attenuation length (g/cm^2), ^{10}Be decay constant (yr^{-1}), ρ hill = density of hillslope material (g/cm^3), ρ burial = density of burial overburden (g/cm^3).

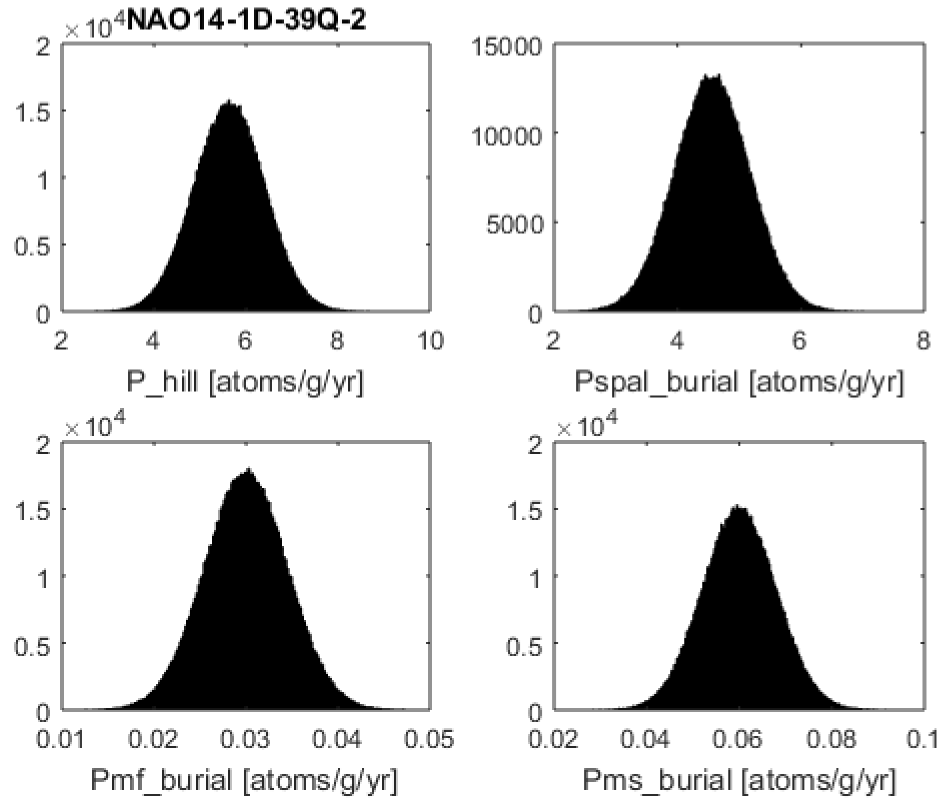

Figure C2. Normal distributions of production rate variables for sample NAO14-1D-39Q-2. P_hill = total hillslope production rate (atoms g^{-1} yr^{-1}), Pspal_burial = spallation production at burial site (atoms g^{-1} yr^{-1}), Pmf_burial = fast muons production at burial site (atoms g^{-1} yr^{-1}), and Pms_burial = slow muon capture production at burial site (atoms g^{-1} yr^{-1}).

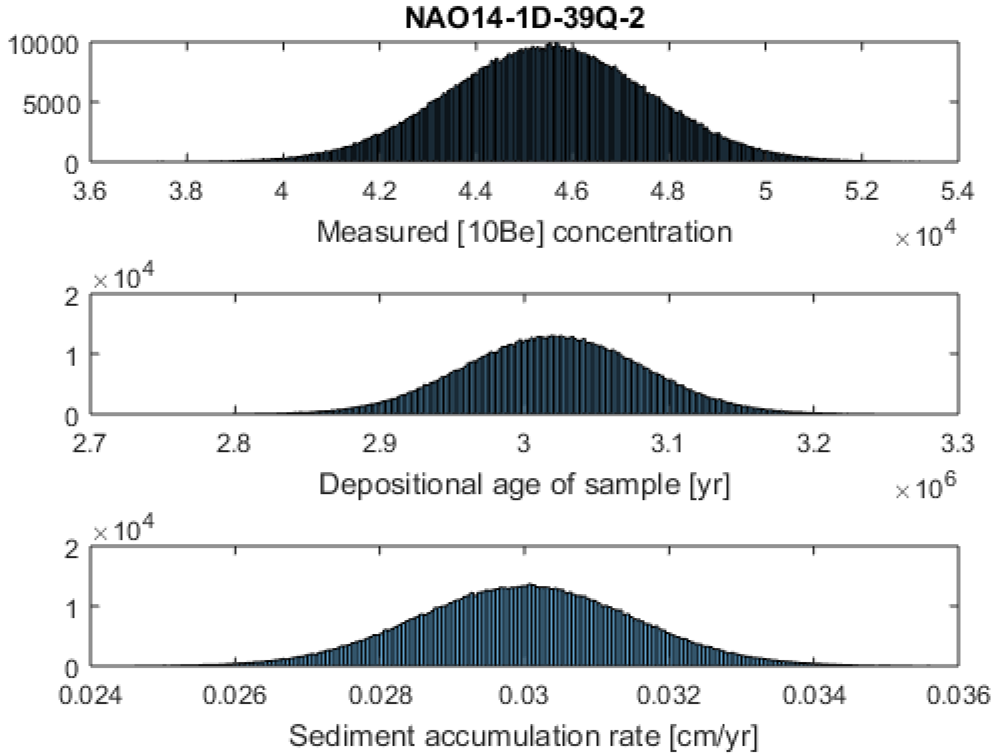

Figure C3. Normal histogram distribution of measured [^{10}Be] concentration, the depositional age of the sample, and sediment accumulation rate for sample NAO14-1D-39Q-2.

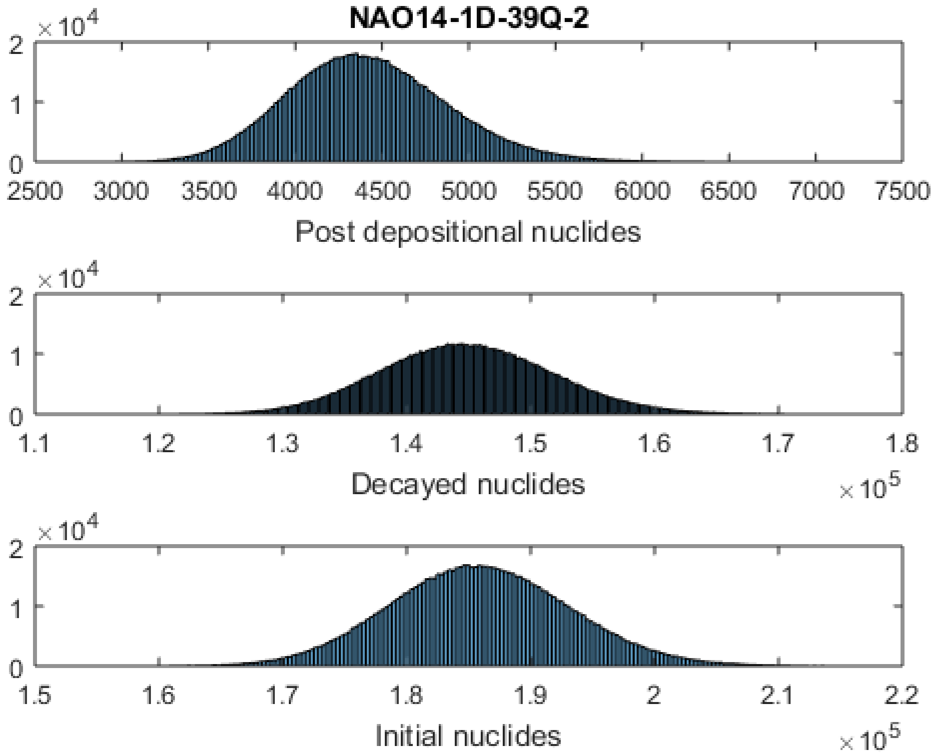

Figure C4. Calculated intermediate histogram distributions of total post-depositional nuclide accumulation, nuclide loss to radioactive decay, and the initial nuclide concentration for sample NAO14-1D-39Q-2.

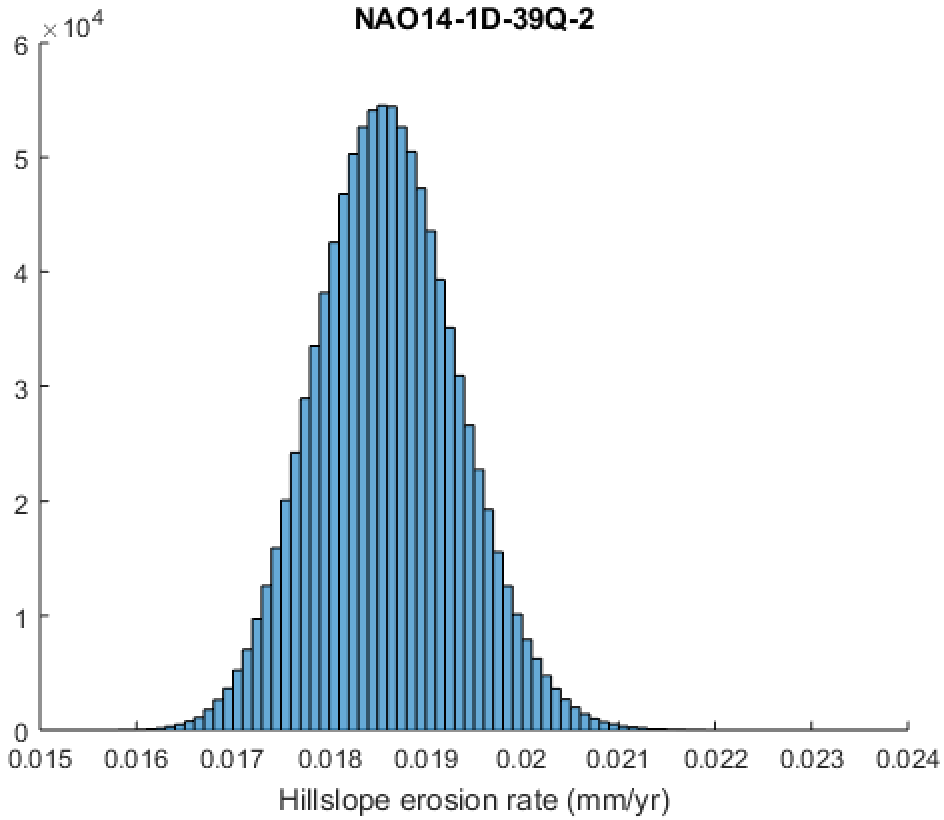

Figure C5. Calculated histogram distribution of paleoerosion rates for sample NAO14-1D-39Q-2.

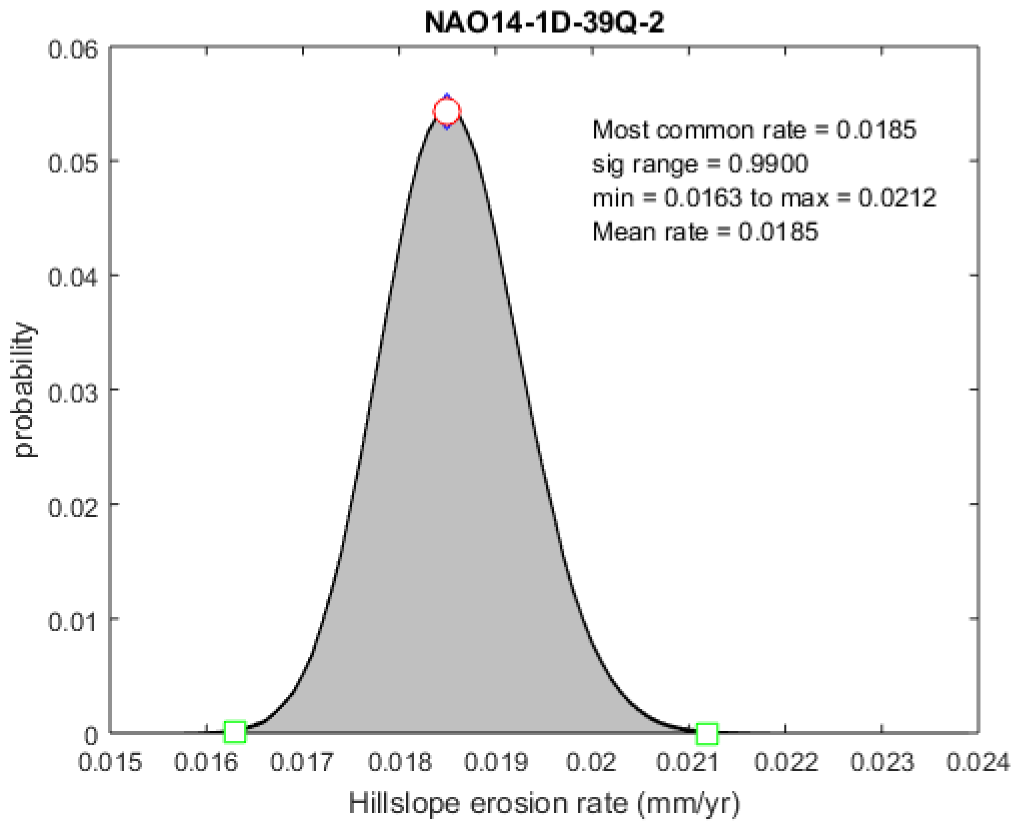

Figure C6. Normalized PDF of paleoerosion rate at 0.99 significance level with modal, mean, maximum, and minimum erosion rates for sample NAO14-1D-39Q-2.

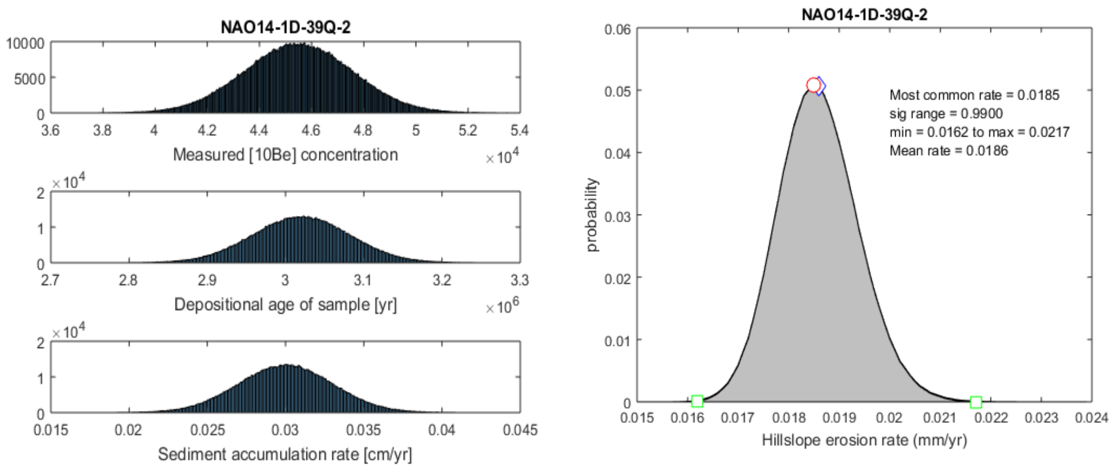

Figure C7. Normal histogram distribution of measured [^{10}Be] concentration, the depositional age of the sample, and sediment accumulation rate assuming a 10% uncertainty (rather than 5%) for sediment accumulation rate and material density, and normalized PDF for NAO14-1D-39Q-2. The increased uncertainty on sediment accumulation rate yields a 0.0005 mm/yr higher maximum erosion rate.

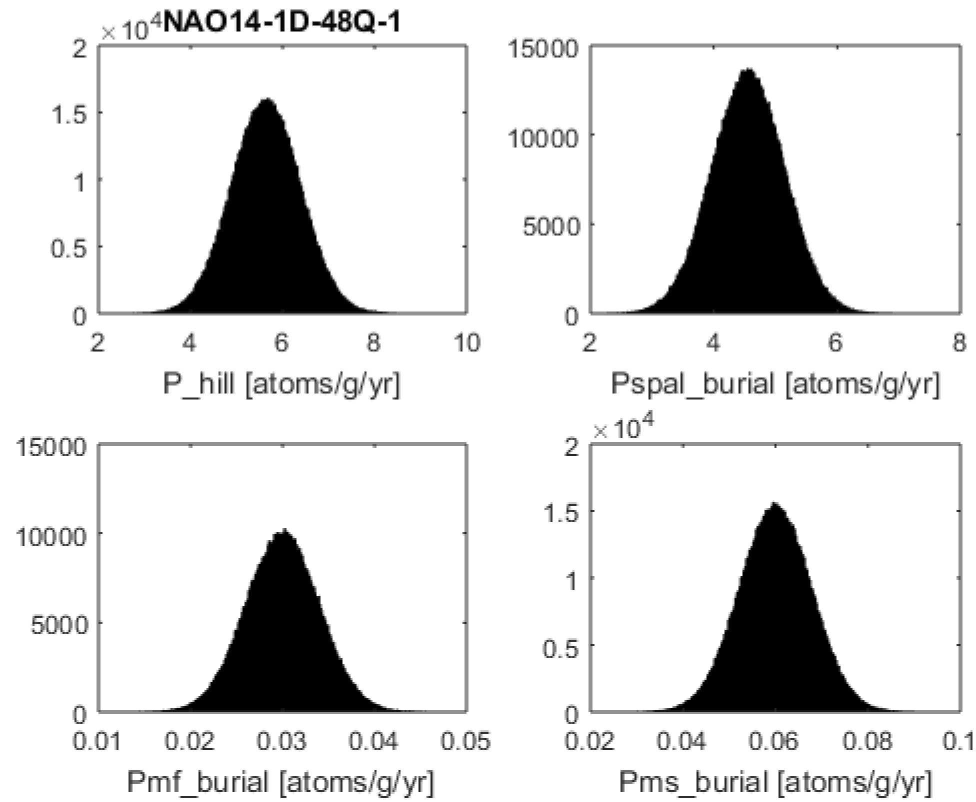

Figure C8. Normal distributions of production rate variables for sample NAO14-1D-48Q-1. P_hill = total hillslope production rate (atoms g^{-1} yr^{-1}), Pspal_burial = spallation production at burial site (atoms g^{-1} yr^{-1}), Pmf_burial = fast muons production at burial site (atoms g^{-1} yr^{-1}), and Pms_burial = slow muon capture production at burial site (atoms g^{-1} yr^{-1}).

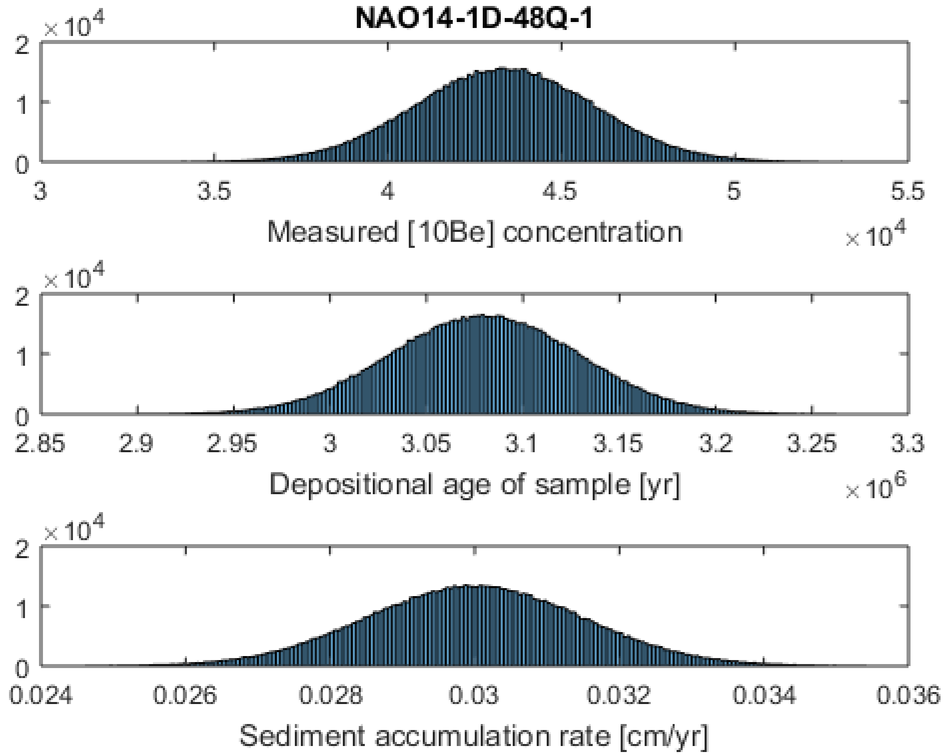

Figure C9. Normal histogram distribution of measured [^{10}Be] concentration, the depositional age of the sample, and sediment accumulation rate for sample NAO14-1D-48Q-1.

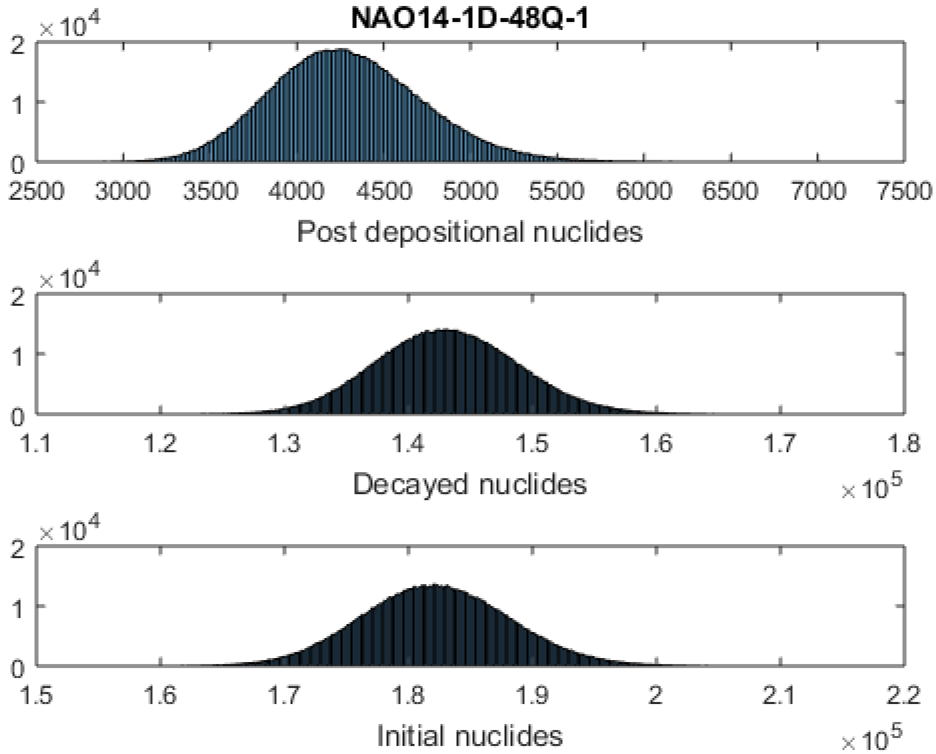

Figure C10. Calculated intermediate histogram distributions of total post-depositional nuclide accumulation, nuclide loss to radioactive decay, and the initial nuclide concentration for sample NAO14-1D-48Q-1.

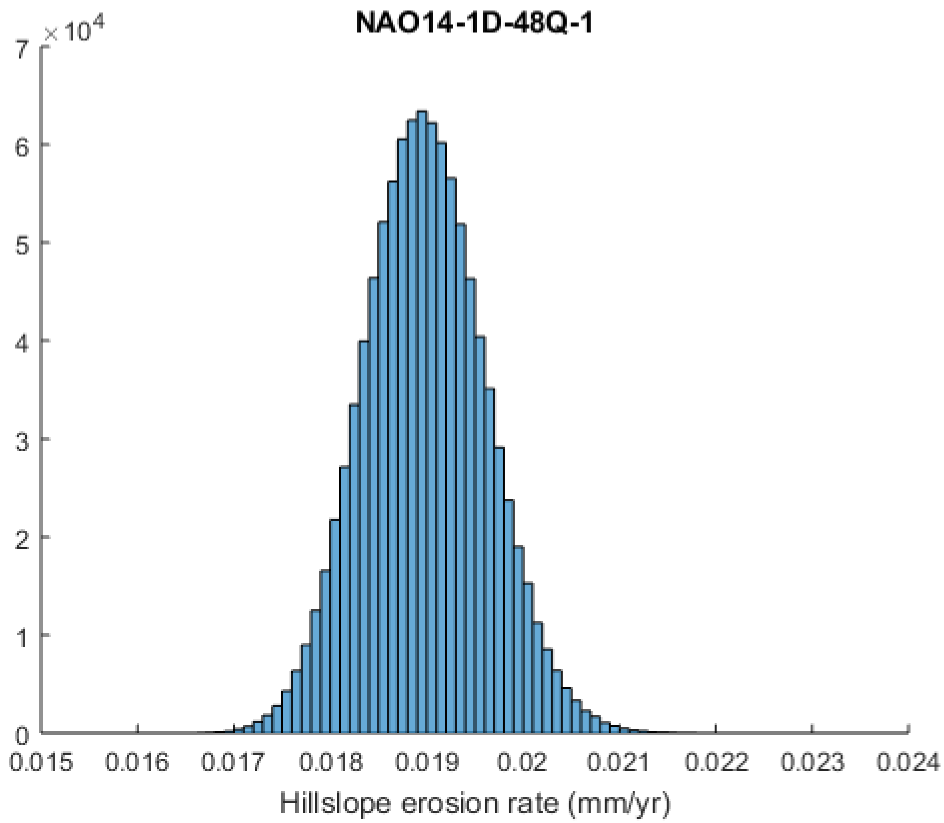

Figure C11. Calculated histogram distribution of paleoerosion rates for sample NAO14-1D-48Q-1.

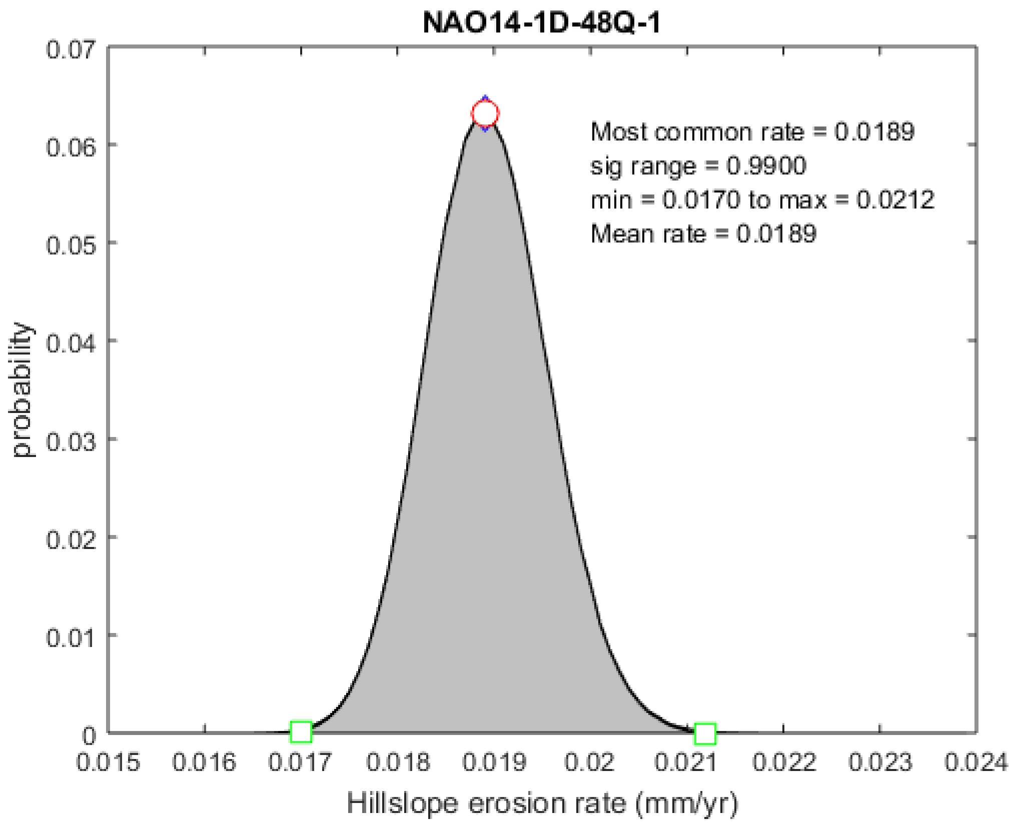

Figure C12. Normalized PDF of paleoerosion rate at 0.99 significance level with modal, mean, maximum, and minimum erosion rates for sample NAO14-1D-48Q-1.

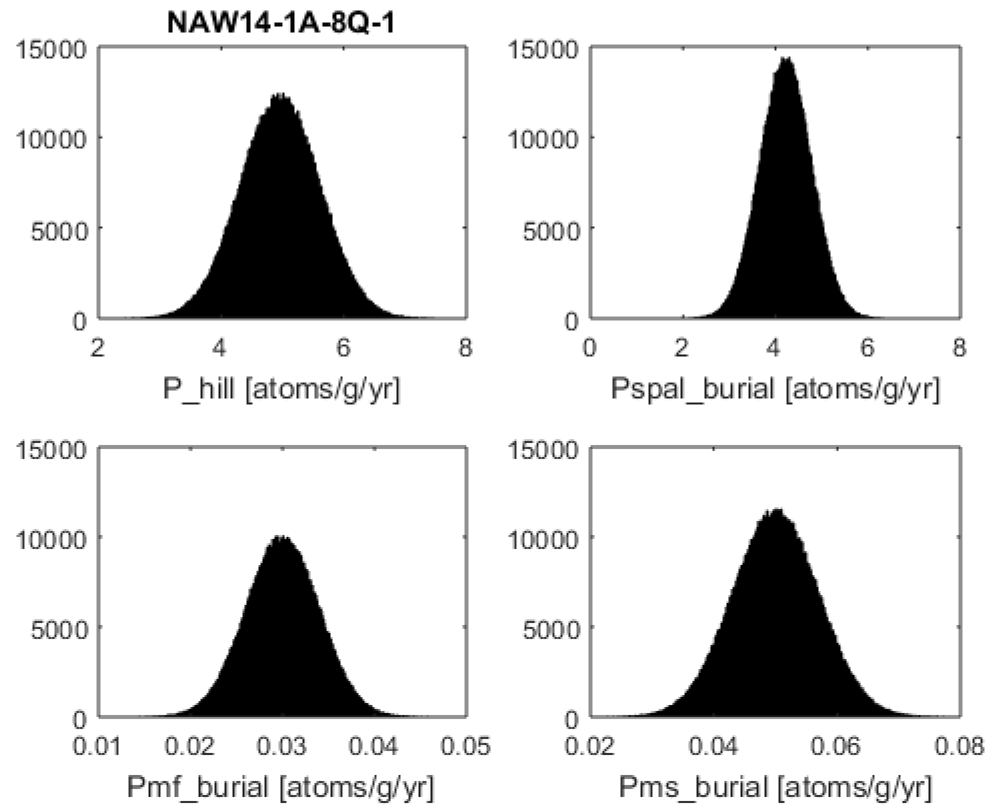

Figure C13. Normal distributions of production rate variables for sample NAW14-1A-8Q-1. P_hill = total hillslope production rate (atoms g^{-1} yr^{-1}), Pspal_burial = spallation production at burial site (atoms g^{-1} yr^{-1}), Pmf_burial = fast muons production at burial site (atoms g^{-1} yr^{-1}), and Pms_burial = slow muon capture production at burial site (atoms g^{-1} yr^{-1}).

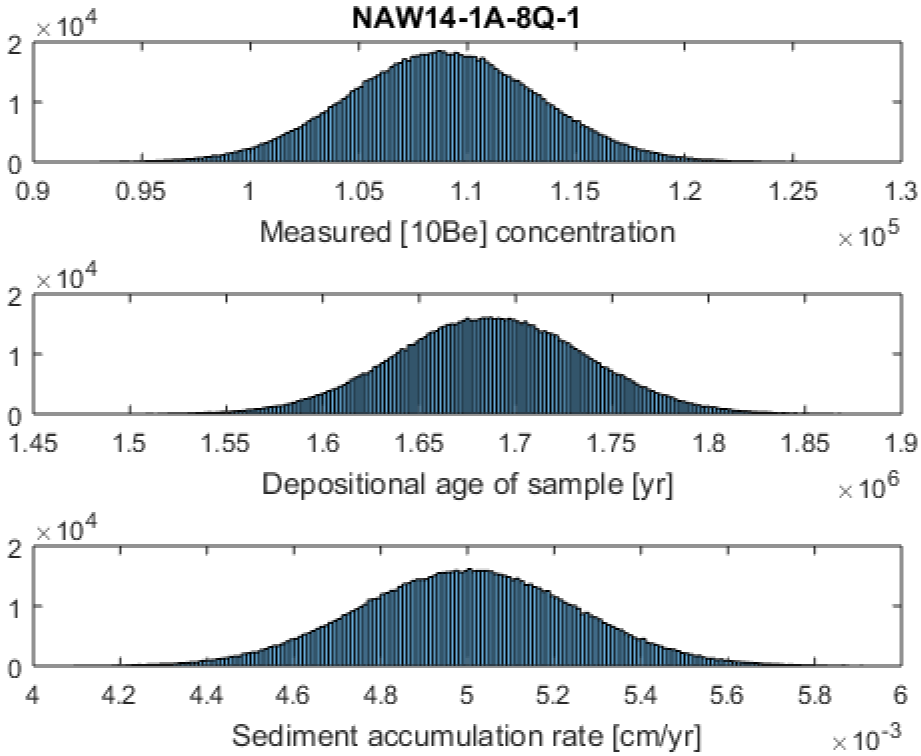

Figure C14. Normal histogram distribution of measured [^{10}Be] concentration, the depositional age of the sample, and sediment accumulation rate for sample NAW14-1A-8Q-1.

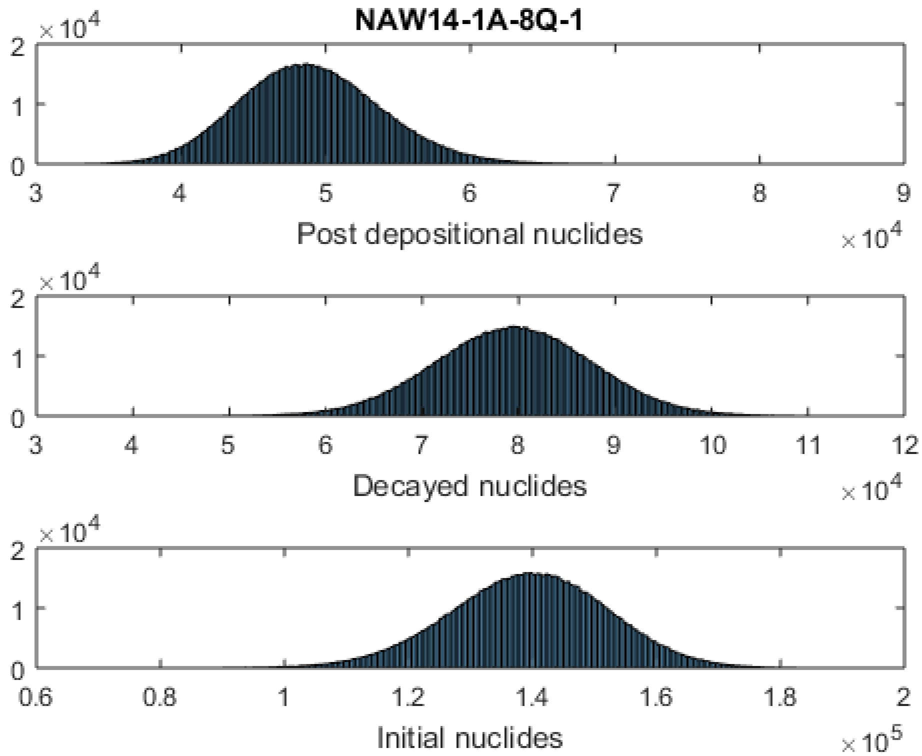

Figure C15. Calculated intermediate histogram distributions of total post-depositional nuclide accumulation, nuclide loss to radioactive decay, and the initial nuclide concentration for sample NAW14-1A-8Q-1.

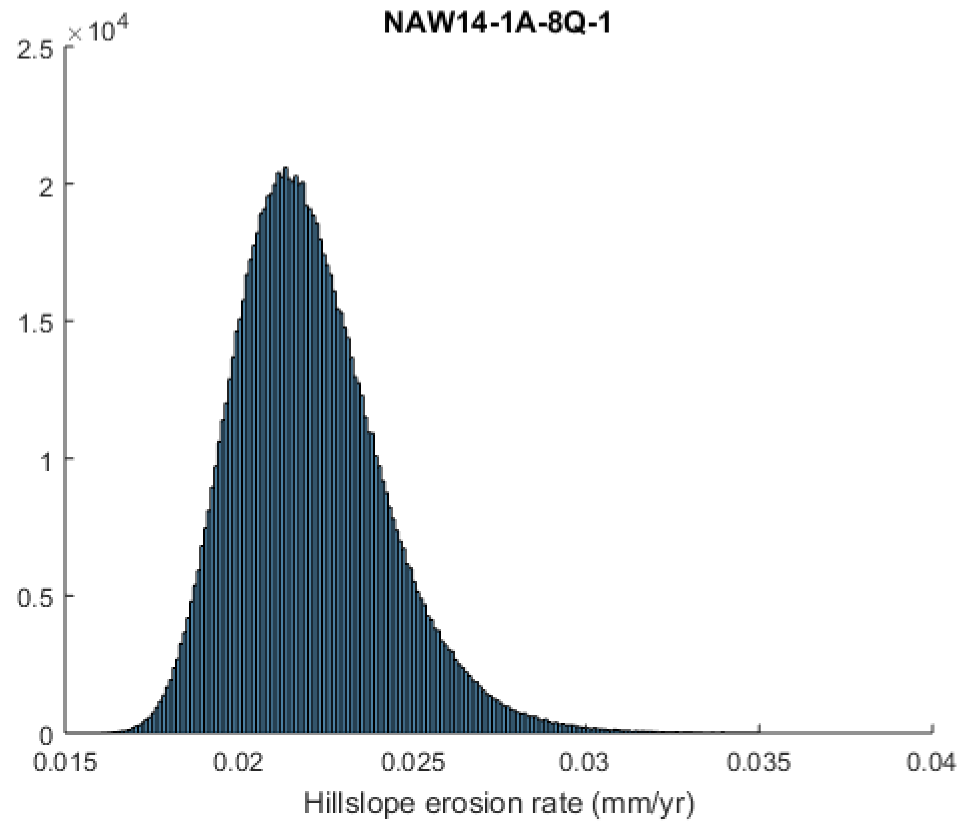

Figure C16. Calculated histogram distribution of paleoerosion rates for sample NAW14-1A-8Q-1.

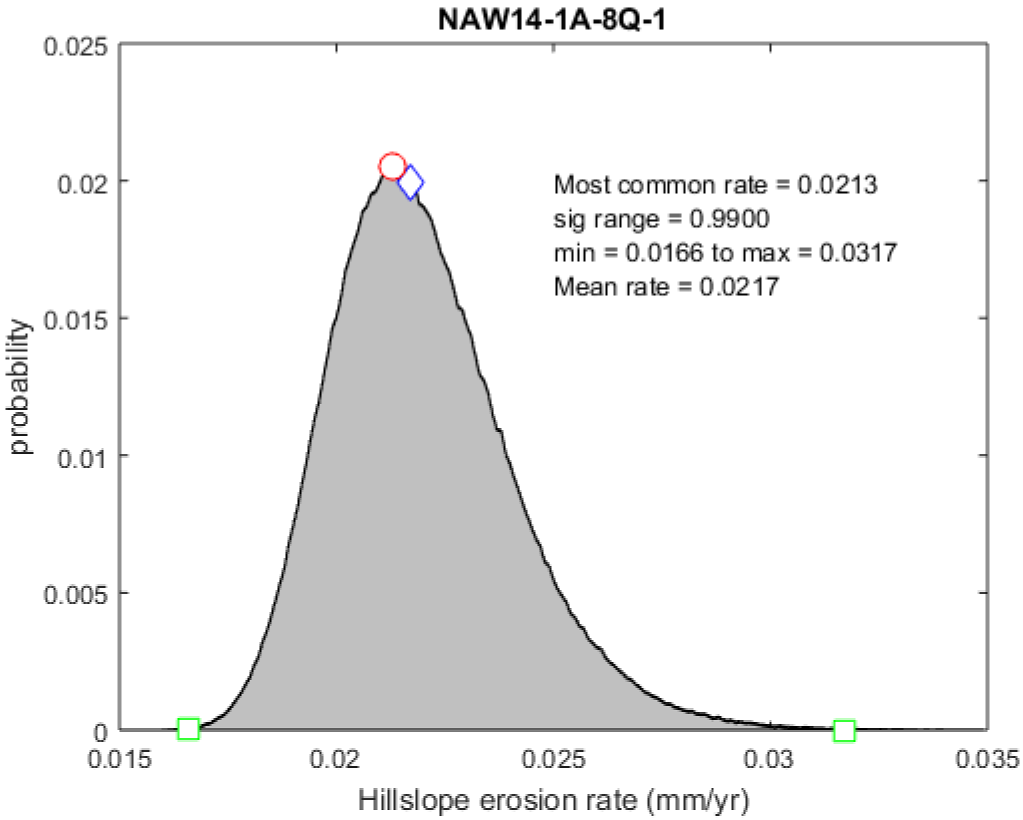

Figure C17. Normalized PDF of paleoerosion rate at 0.99 significance level with modal, mean, maximum, and minimum erosion rates for sample NAW14-1A-8Q-1.

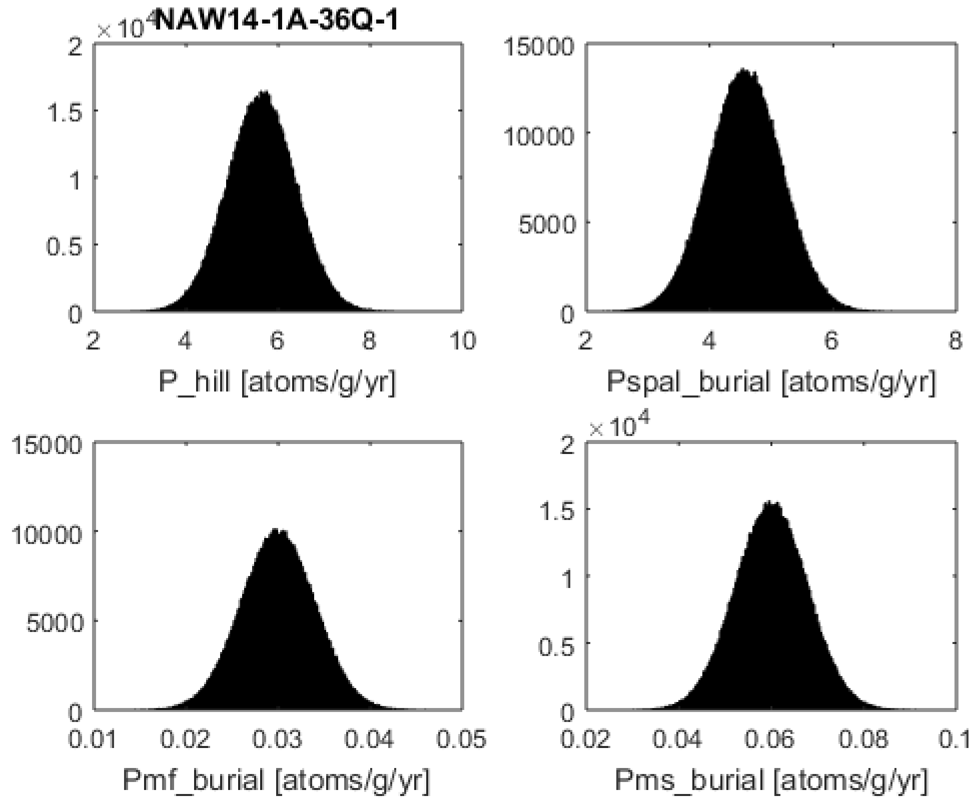

Figure C18. Normal distributions of production rate variables for sample NAW14-1A-36Q-1. P_hill = total hillslope production rate (atoms g^{-1} yr^{-1}), Pspal_burial = spallation production at burial site (atoms g^{-1} yr^{-1}), Pmf_burial = fast muons production at burial site (atoms g^{-1} yr^{-1}), and Pms_burial = slow muon capture production at burial site (atoms g^{-1} yr^{-1}).

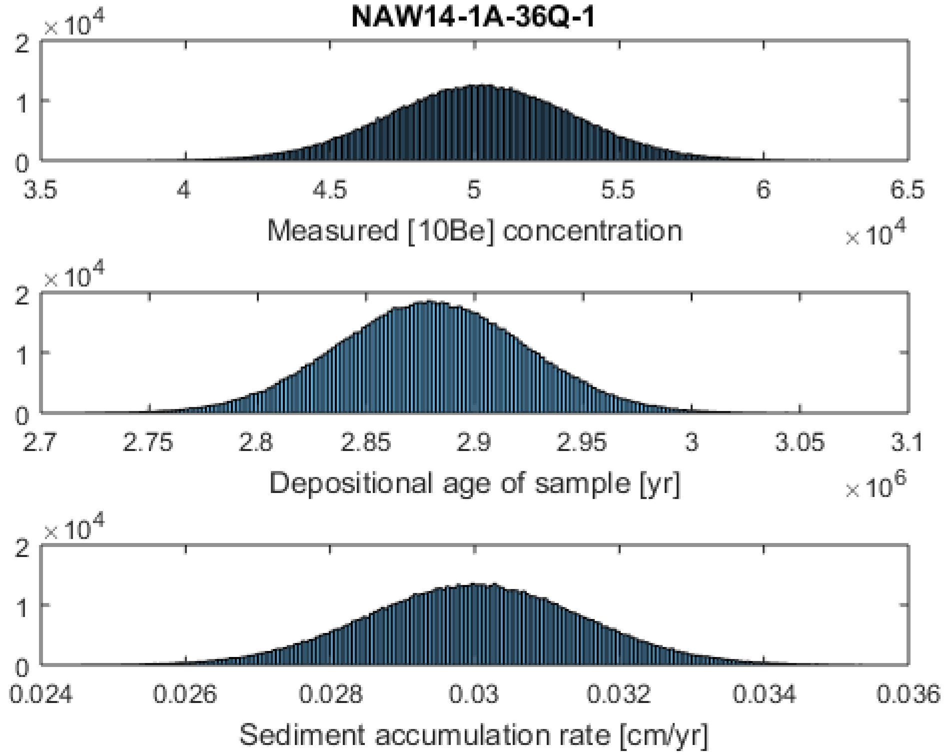

Figure C19. Normal histogram distribution of measured [^{10}Be] concentration, the depositional age of the sample, and sediment accumulation rate for sample NAW14-1A-36Q-1.

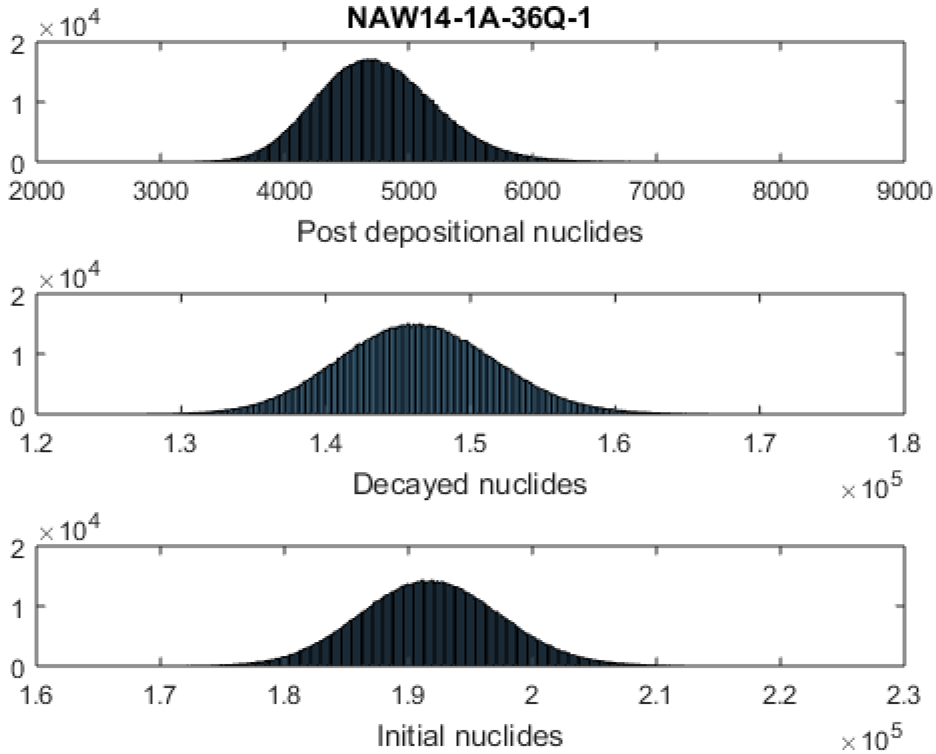

Figure C20. Calculated intermediate histogram distributions of total post-depositional nuclide accumulation, nuclide loss to radioactive decay, and the initial nuclide concentration for sample NAW14-1A-36Q-1.

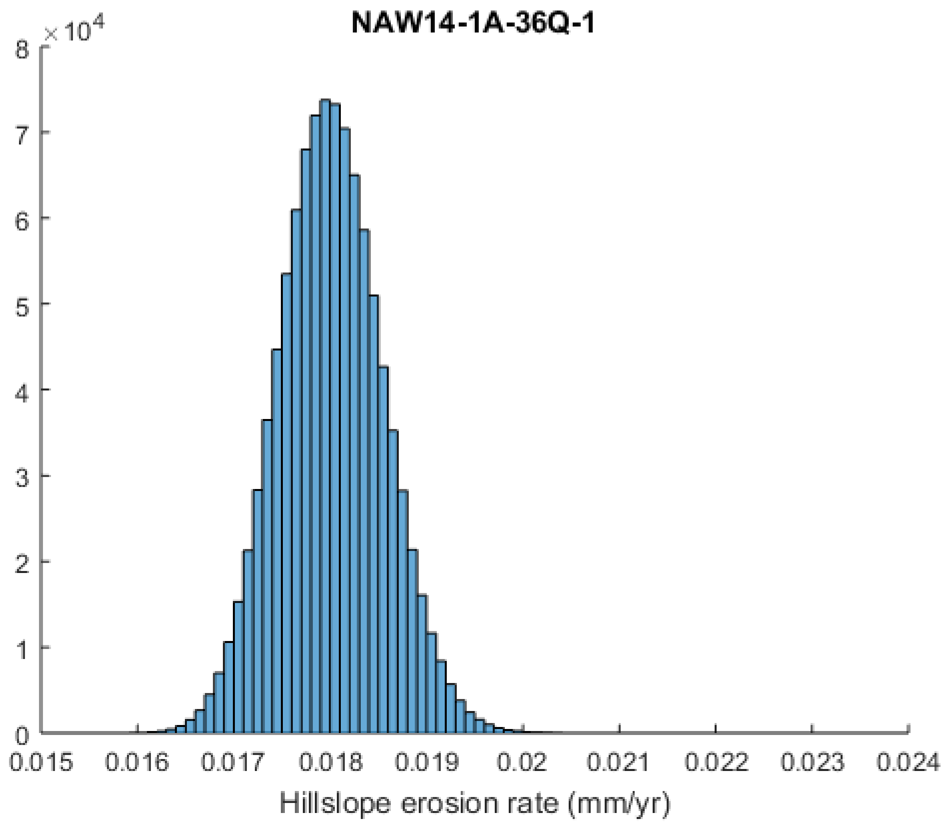

Figure C21. Calculated histogram distribution of paleoerosion rates for sample NAW14-1A-36Q-1.

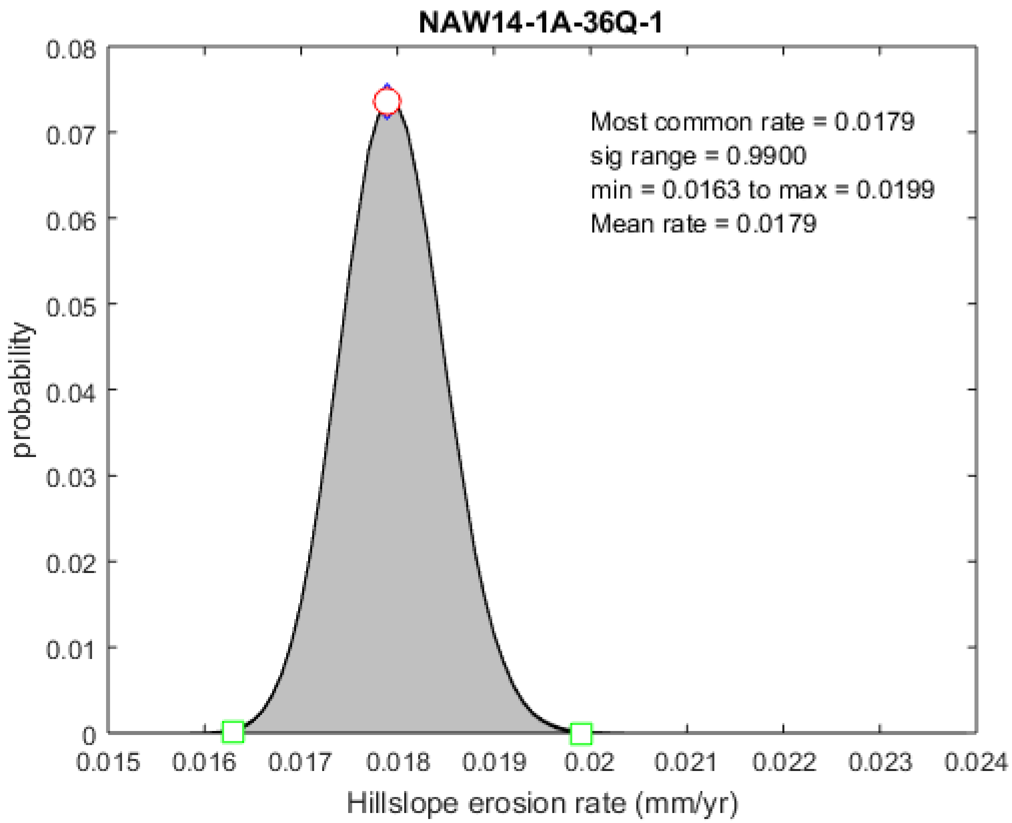

Figure C22. Normalized PDF of paleoerosion rate at 0.99 significance level with modal, mean, maximum, and minimum erosion rates for sample NAW14-1A-36Q-1.

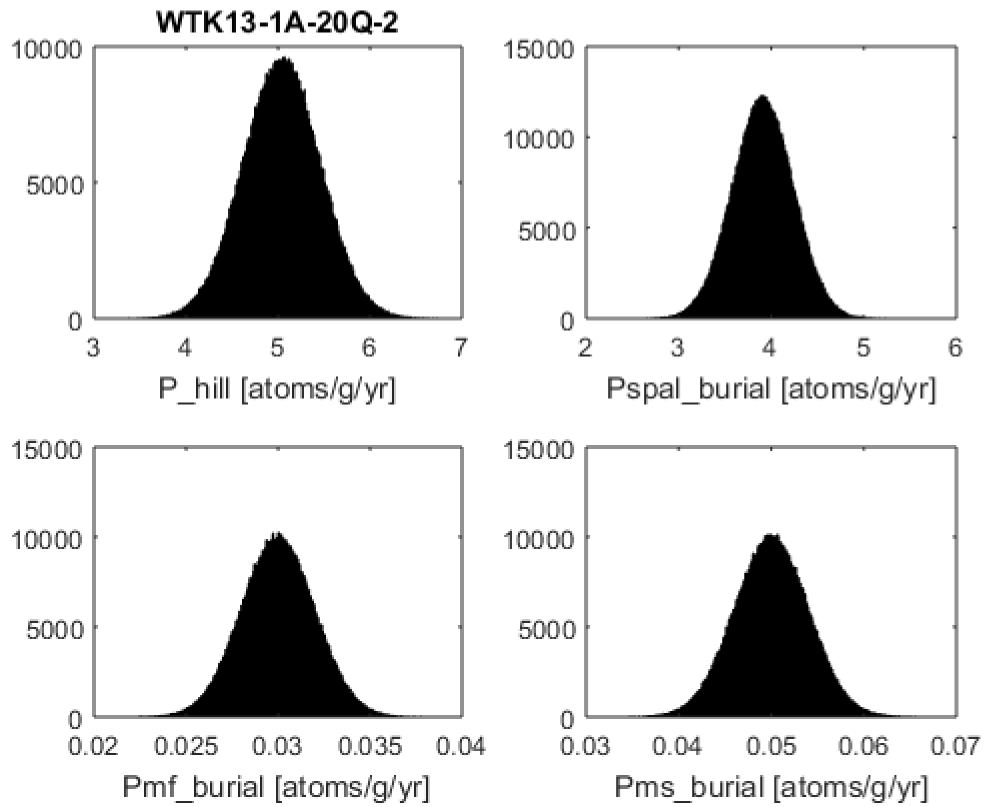

Figure C23. Normal distributions of production rate variables for sample WTK13-1A-20Q-2. P_hill = total hillslope production rate (atoms g^{-1} yr^{-1}), Pspal_burial = spallation production at burial site (atoms g^{-1} yr^{-1}), Pmf_burial = fast muons production at burial site (atoms g^{-1} yr^{-1}), and Pms_burial = slow muon capture production at burial site (atoms g^{-1} yr^{-1}).

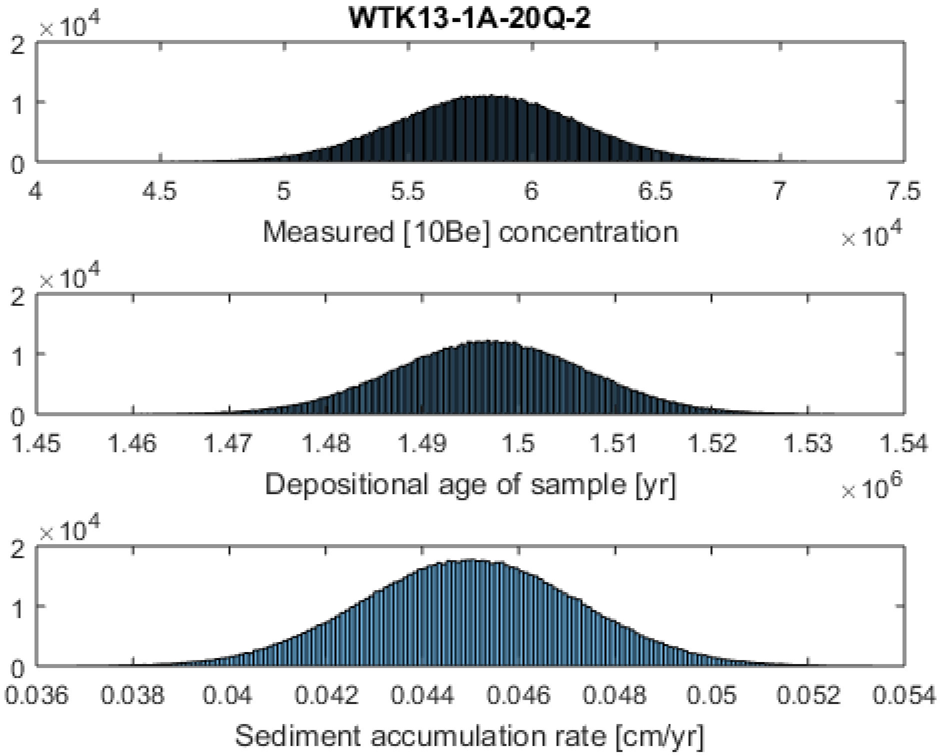

Figure C24. Normal histogram distribution of measured [^{10}Be] concentration, the depositional age of the sample, and sediment accumulation rate for sample WTK13-1A-20Q-2.

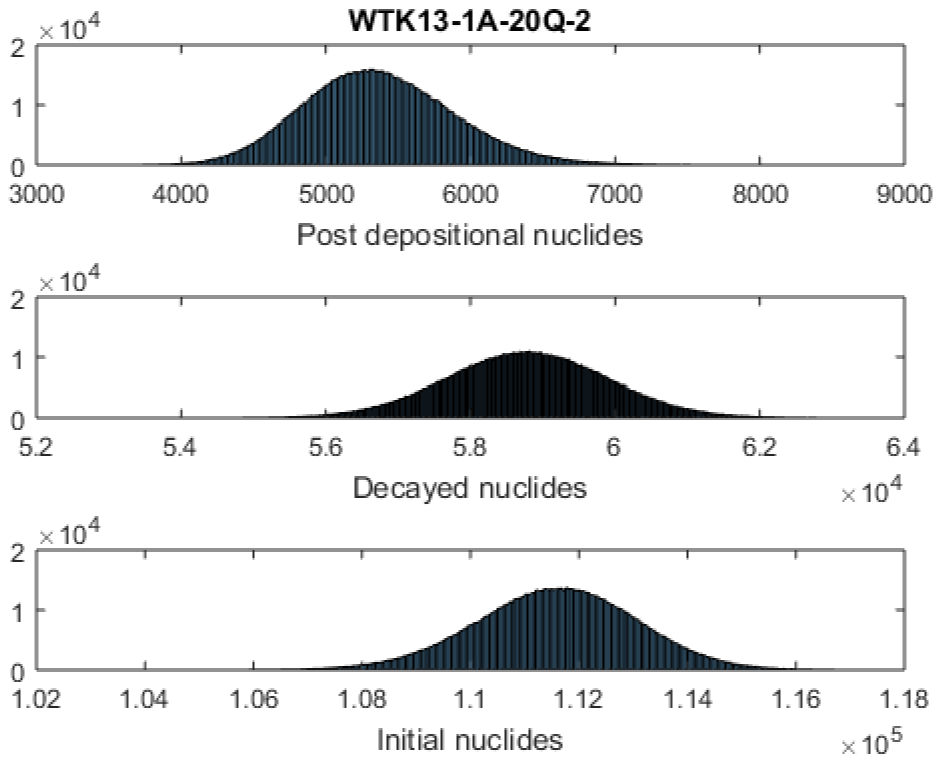

Figure C25. Calculated intermediate histogram distributions of total post-depositional nuclide accumulation, nuclide loss to radioactive decay, and the initial nuclide concentration for sample WTK13-1A-20Q-2.

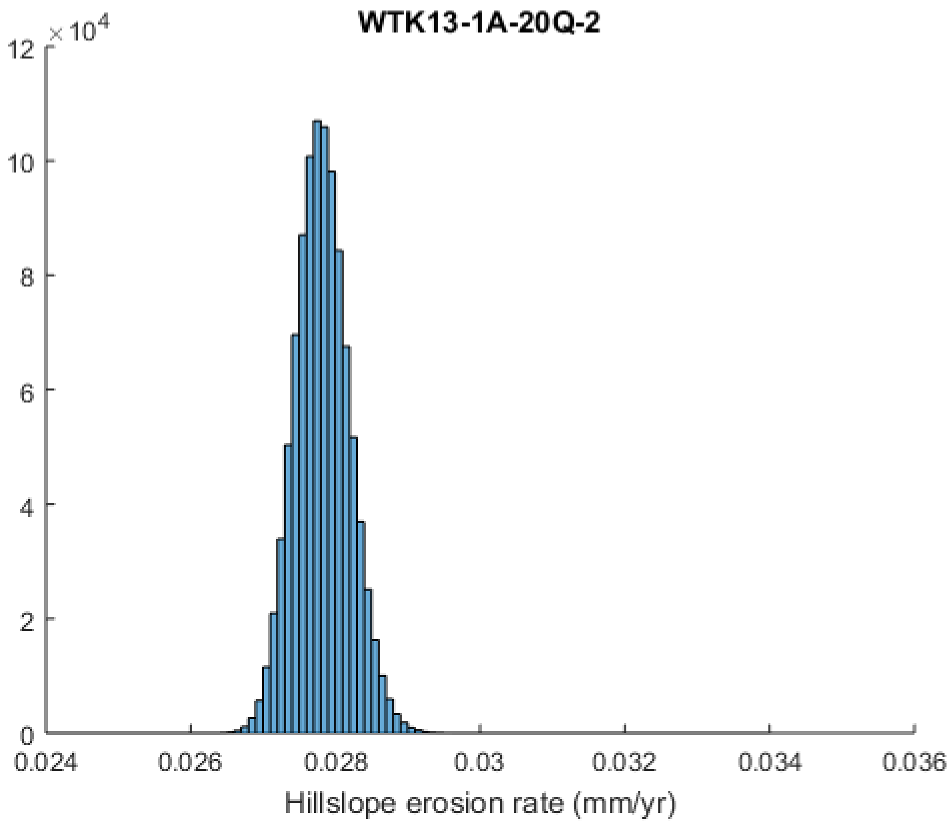

Figure C26. Calculated histogram distribution of paleoerosion rates for sample WTK13-1A-20Q-2.

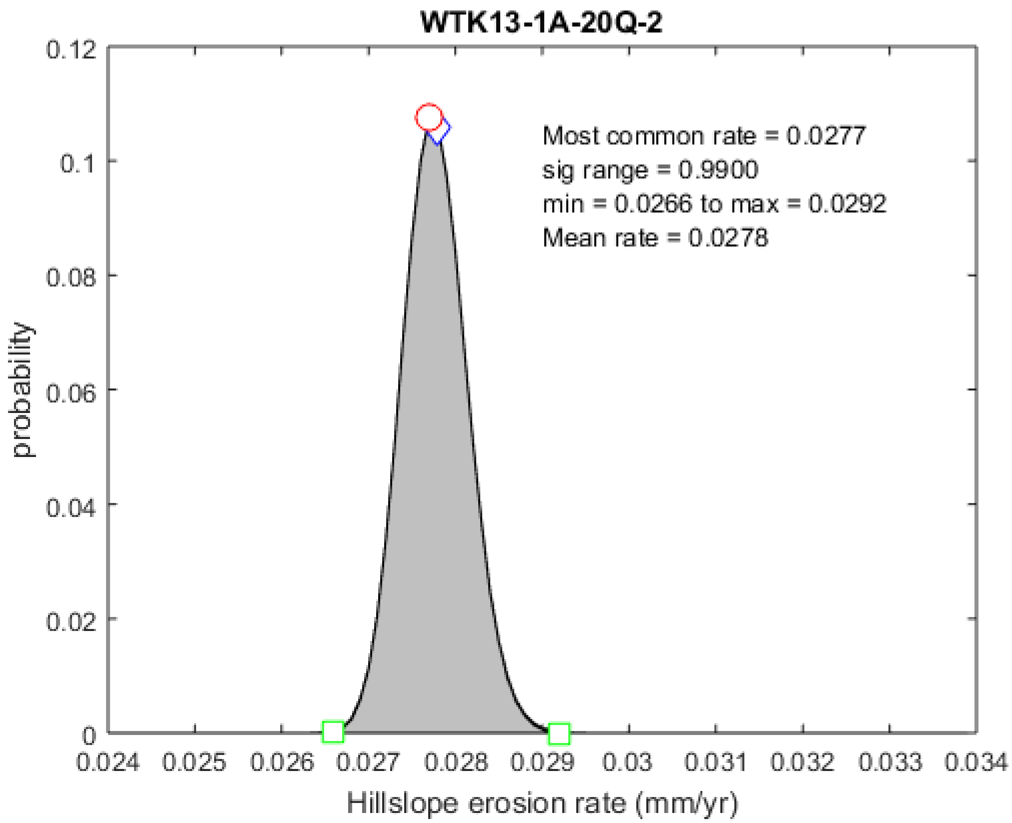

Figure C27. Normalized PDF of paleoerosion rate at 0.99 significance level with modal, mean, maximum, and minimum erosion rates for sample WTK13-1A-20Q-2.

APPENDIX D

CHAPTER 4 SUPPLEMENTARY MATERIALS

Paleoerosion rates for the CHB samples are calculated in the same manner as fully detailed in Appendix C.

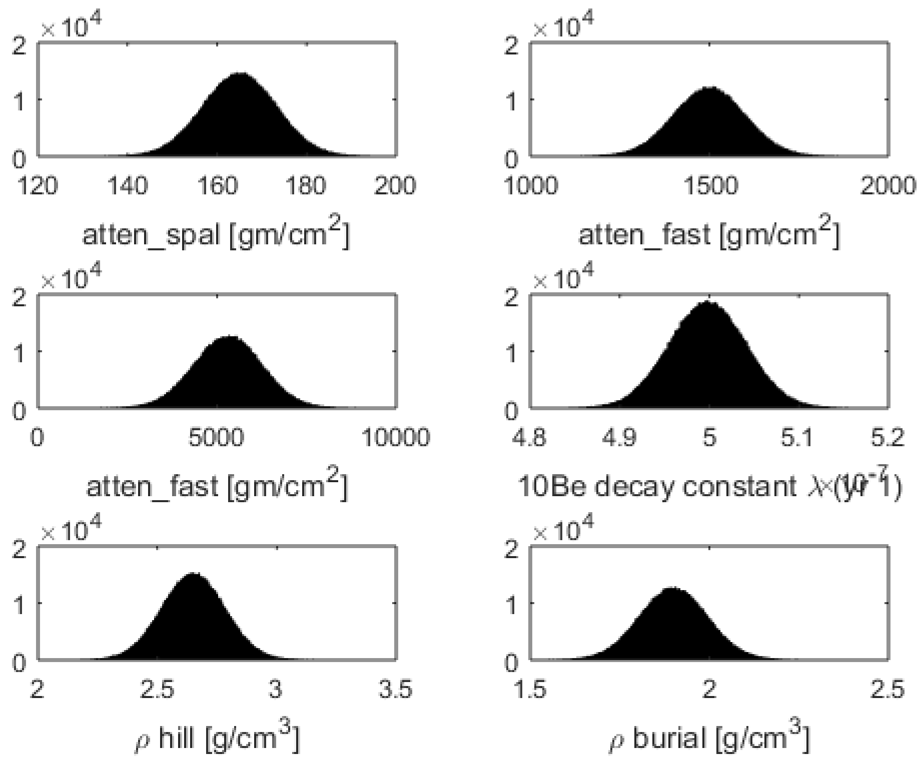

Figure D1. Normal distributions of constant variables used for all paleoerosion rate calculations. atten_spal = spallation attenuation length (g/cm^2), atten_fast = fast muons attenuation length (g/cm^2), atten_slow = slow muon capture attenuation length (g/cm^2), ^{10}Be decay constant (yr^{-1}), ρ hill = density of hillslope material (g/cm^3), ρ burial = density of burial overburden (g/cm^3).

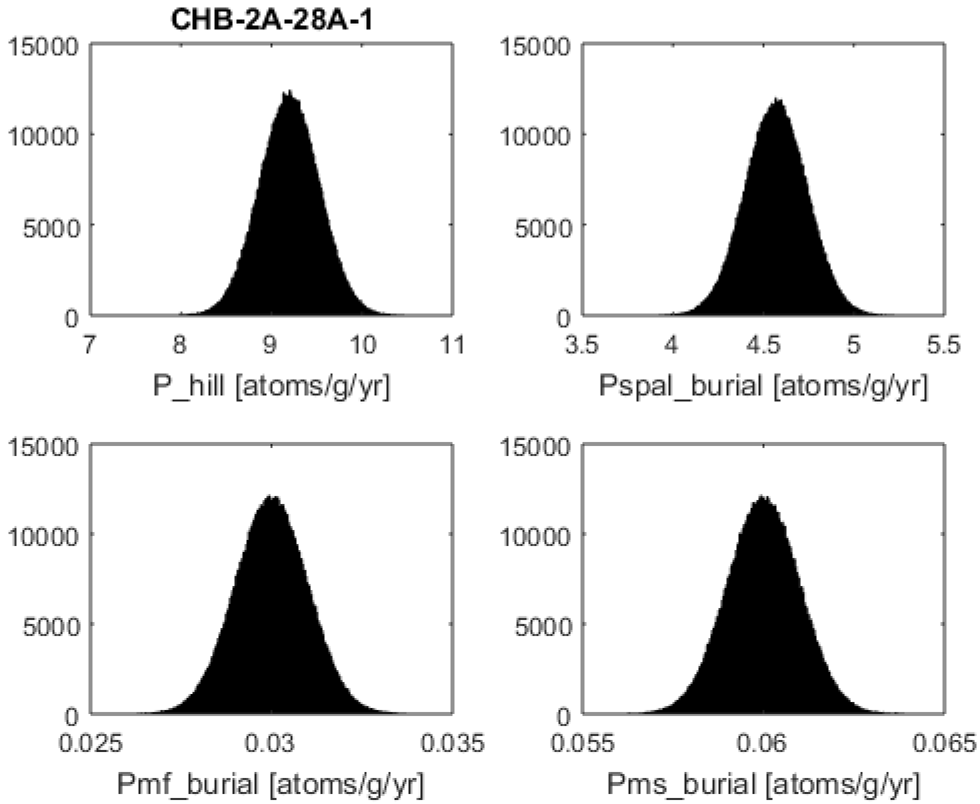

Figure D2. Normal distributions of production rate variables for sample CHB14-2A-28A-1. P_hill = total hillslope production rate (atoms g^{-1} yr^{-1}), Pspal_burial = spallation production at burial site (atoms g^{-1} yr^{-1}), Pmf_burial = fast muons production at burial site (atoms g^{-1} yr^{-1}), and Pms_burial = slow muon capture production at burial site (atoms g^{-1} yr^{-1}).

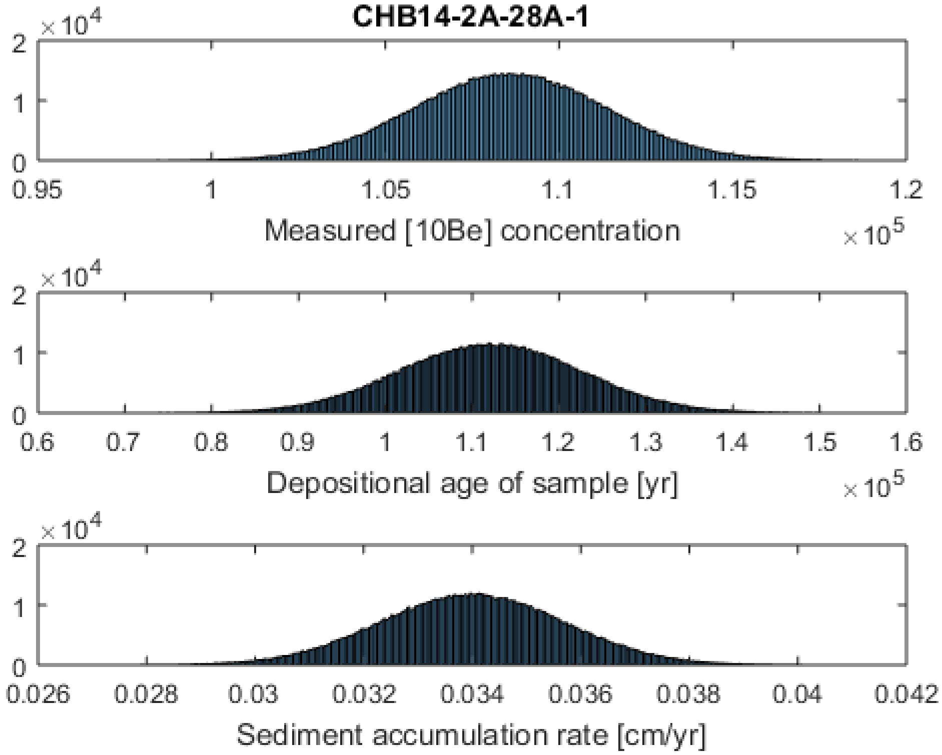

Figure D3. Normal histogram distribution of measured [^{10}Be] concentration, the depositional age of the sample, and sediment accumulation rate for sample CHB14-2A-28A-1.

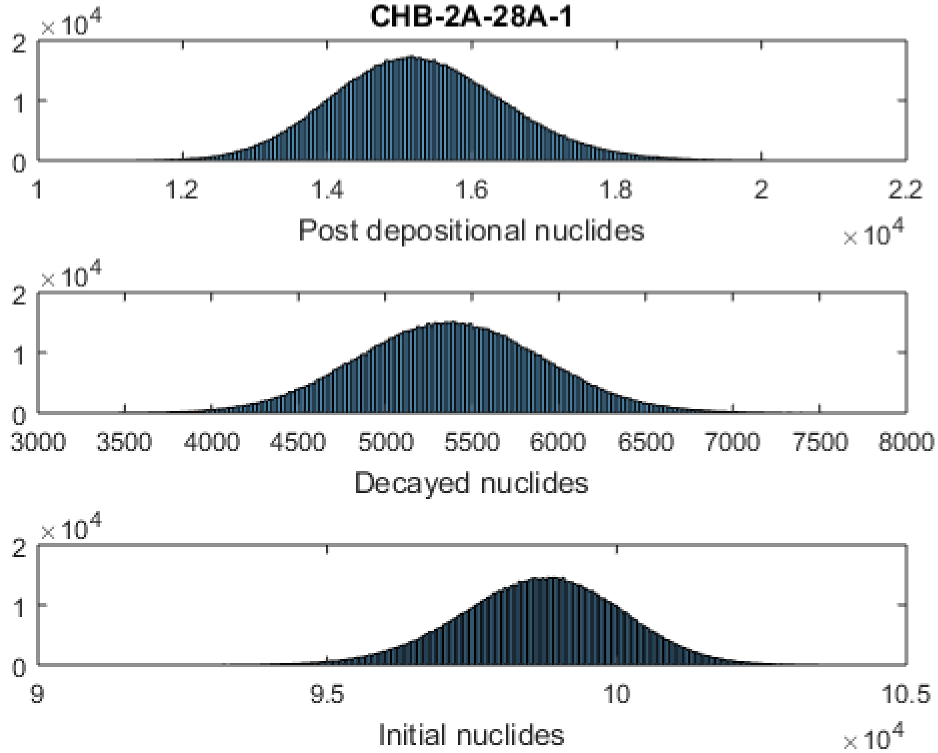

Figure D4. Calculated intermediate histogram distributions of total post-depositional nuclide accumulation, nuclide loss to radioactive decay, and the initial nuclide concentration for sample CHB14-2A-28A-1.

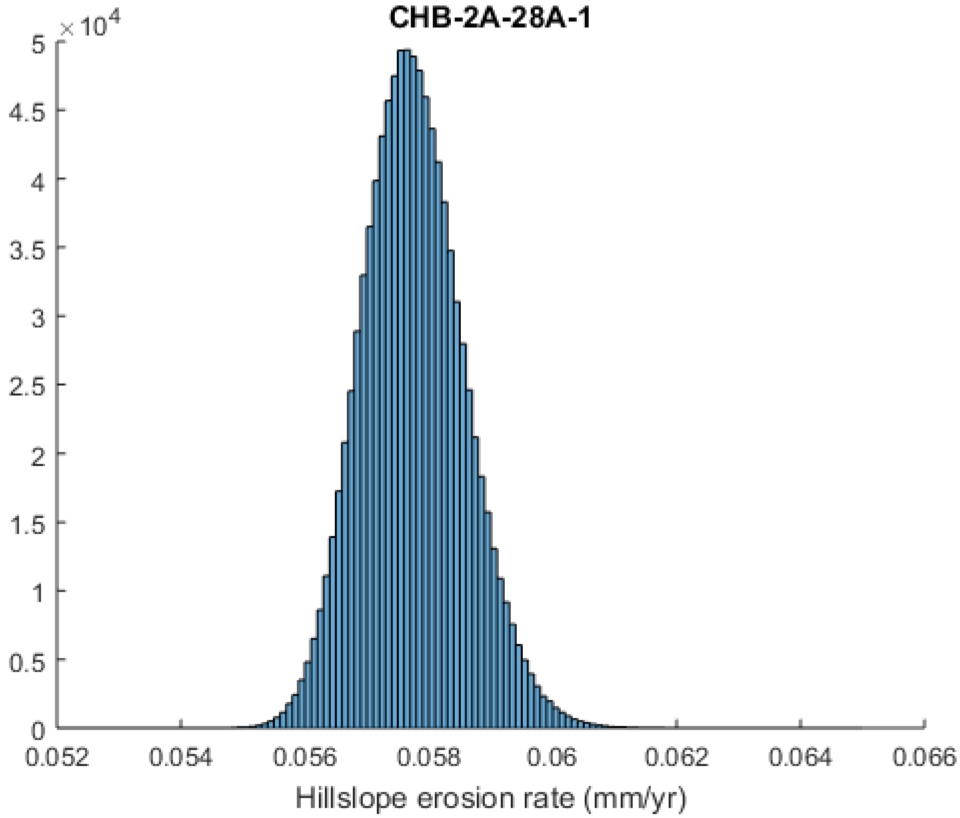

Figure D5. Calculated histogram distribution of paleoerosion rates for sample CHB14-2A-28A-1.

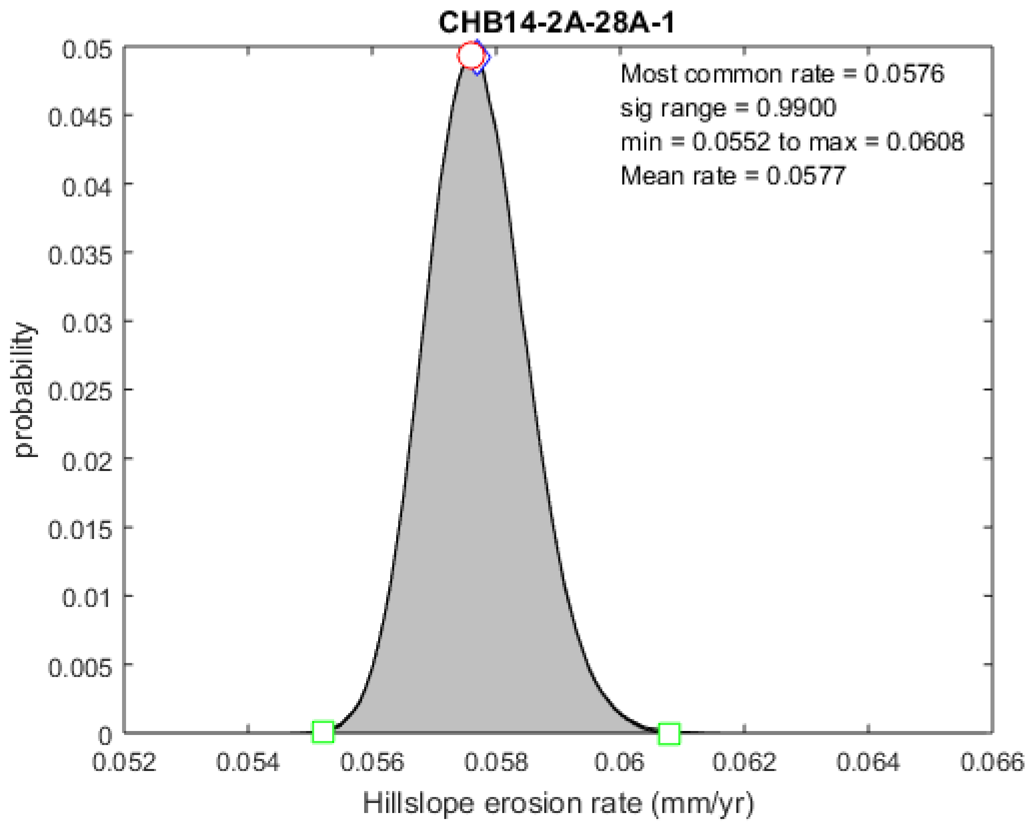

Figure D6. Normalized PDF of paleoerosion rate at 0.99 significance level with modal, mean, maximum, and minimum erosion rates for sample CHB14-2A-28A-1.

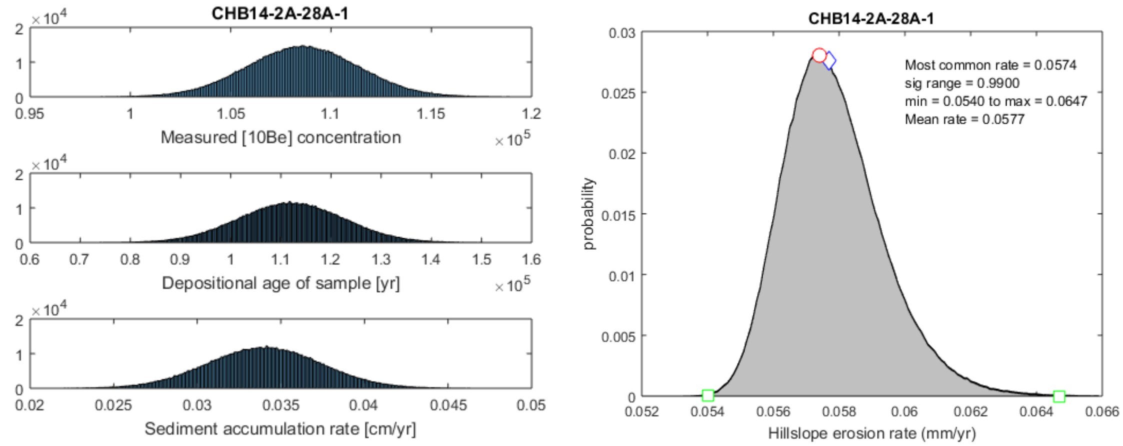

Figure D7. Normal histogram distribution of measured [^{10}Be] concentration, the depositional age of the sample, and sediment accumulation rate assuming a 10% uncertainty (rather than 5%) for sediment accumulation rate and material density, and normalized PDF for CHB14-2A-28A-1. The increased uncertainty on sediment accumulation rate yields a 0.0039 mm/yr higher maximum erosion rate and 0.0012 mm/yr lower minimum erosion rate.

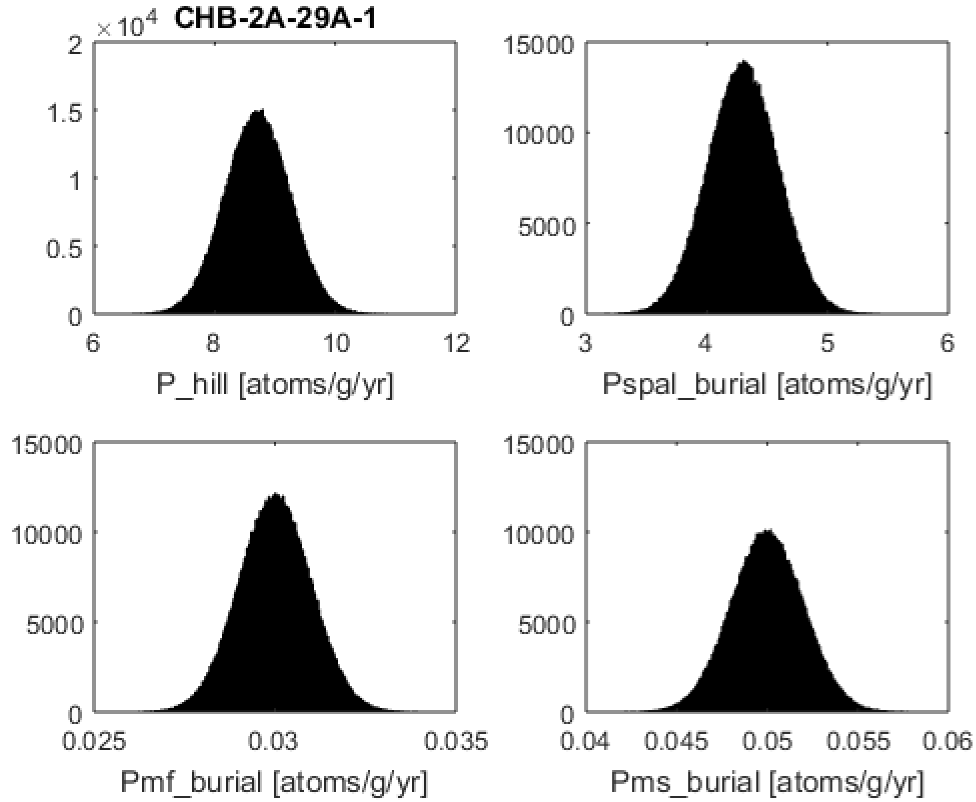

Figure D8. Normal distributions of production rate variables for sample CHB14-2A-29A-1. P_hill = total hillslope production rate (atoms g^{-1} yr^{-1}), Pspal_burial = spallation production at burial site (atoms g^{-1} yr^{-1}), Pmf_burial = fast muons production at burial site (atoms g^{-1} yr^{-1}), and Pms_burial = slow muon capture production at burial site (atoms g^{-1} yr^{-1}).

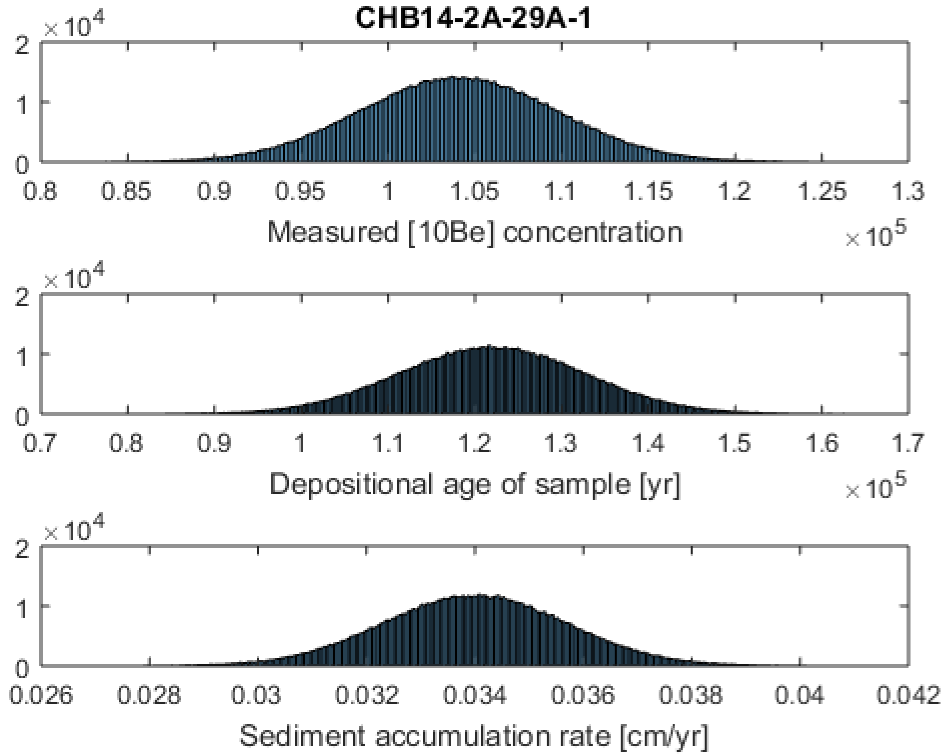

Figure D9. Normal histogram distribution of measured [^{10}Be] concentration, the depositional age of the sample, and sediment accumulation rate for sample CHB14-2A-29A-1.

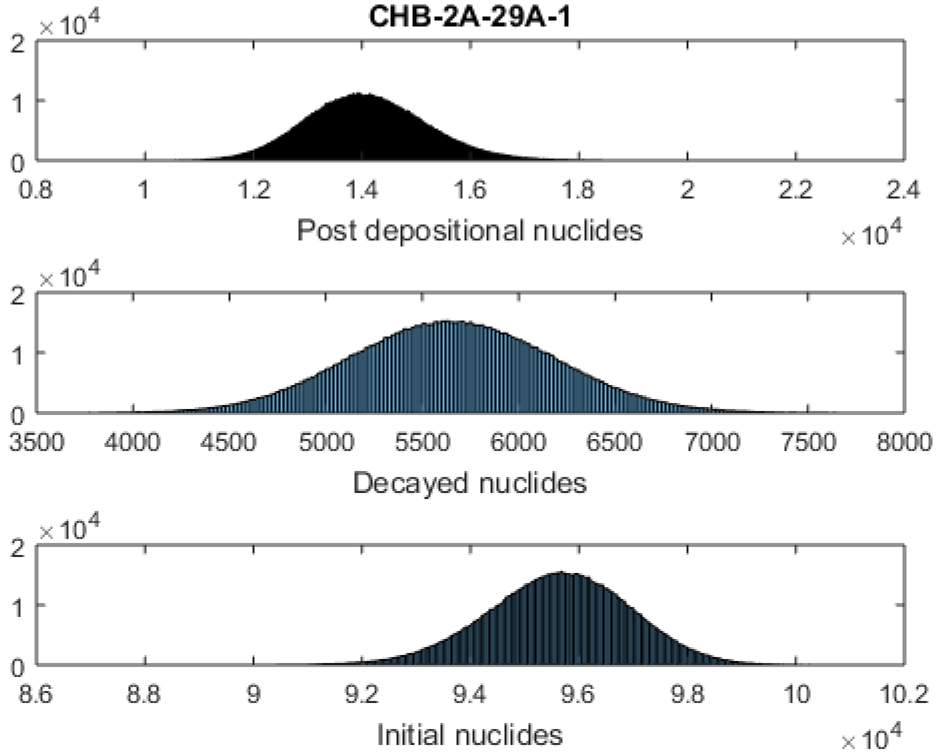

Figure D10. Calculated intermediate histogram distributions of total post-depositional nuclide accumulation, nuclide loss to radioactive decay, and the initial nuclide concentration for sample CHB14-2A-29A-1.

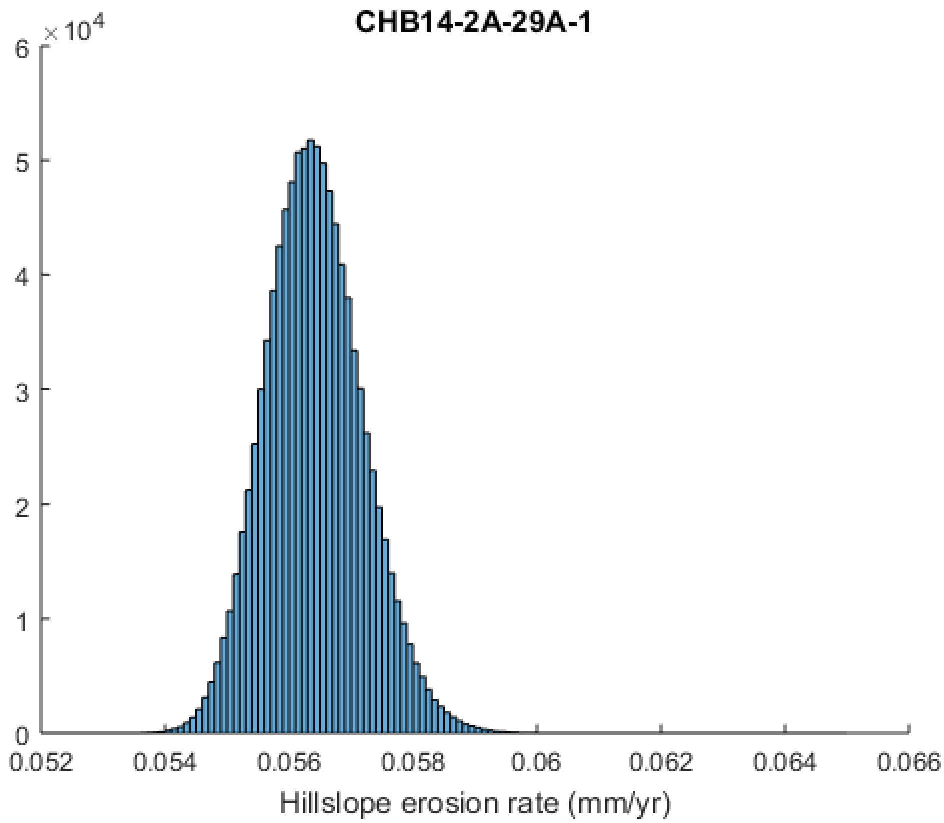

Figure D11. Calculated histogram distribution of paleoerosion rates for sample CHB14-2A-29A-1.

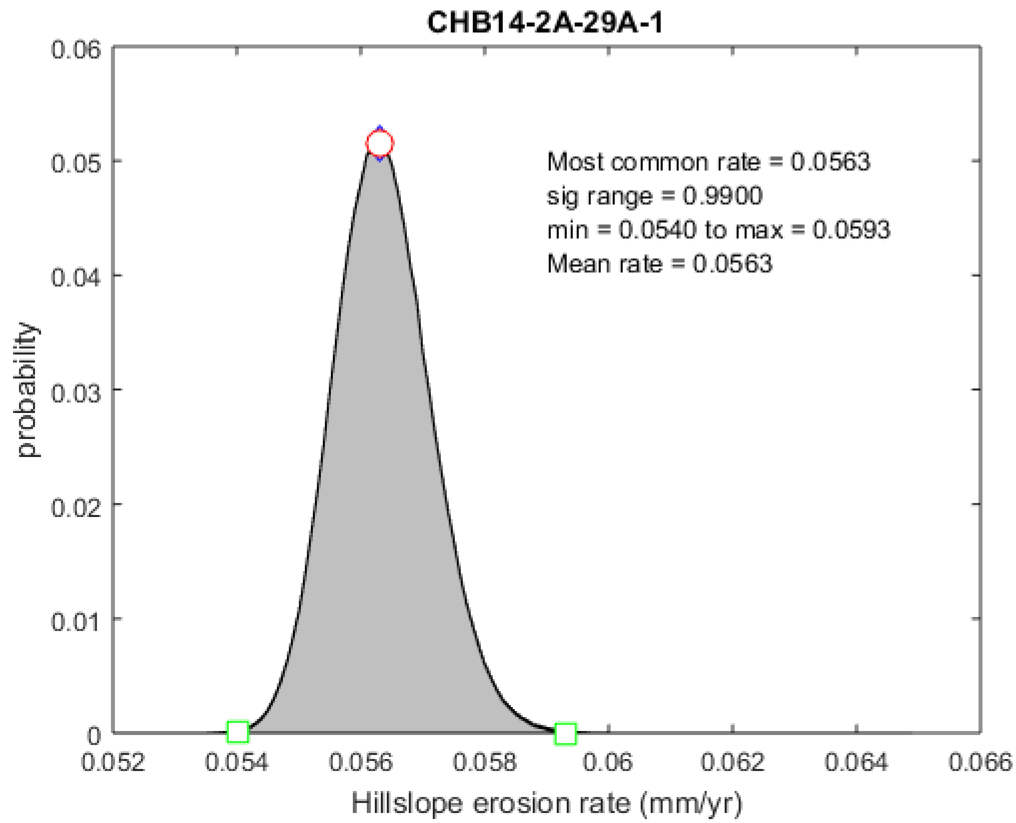

Figure D12. Normalized PDF of paleoerosion rate at 0.99 significance level with modal, mean, maximum, and minimum erosion rates for sample CHB14-2A-29A-1.

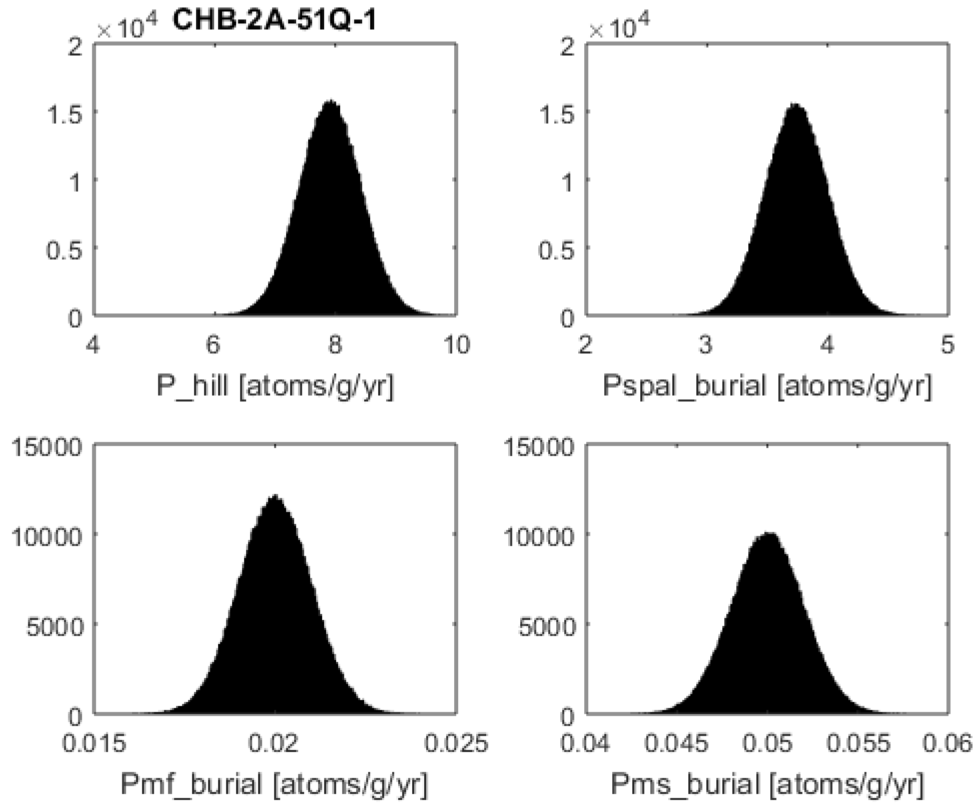

Figure D13. Normal distributions of production rate variables for sample CHB14-2A-51Q-1. P_hill = total hillslope production rate (atoms g^{-1} yr^{-1}), Pspal_burial = spallation production at burial site (atoms g^{-1} yr^{-1}), Pmf_burial = fast muons production at burial site (atoms g^{-1} yr^{-1}), and Pms_burial = slow muon capture production at burial site (atoms g^{-1} yr^{-1}).

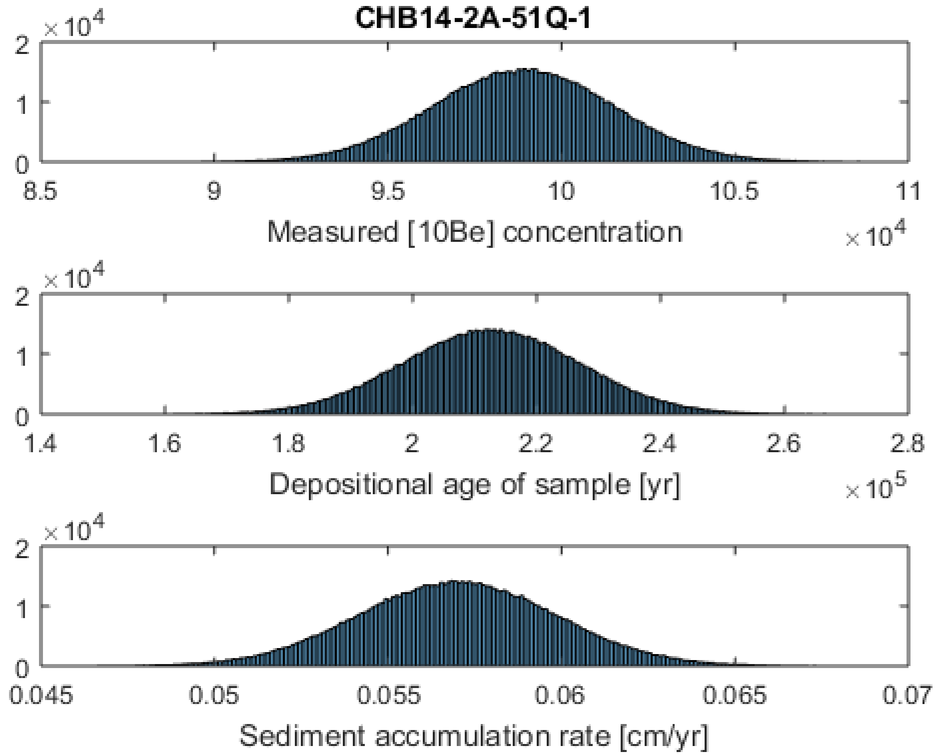

Figure D14. Normal histogram distribution of measured [^{10}Be] concentration, the depositional age of the sample, and sediment accumulation rate for sample CHB14-2A-51Q-1.

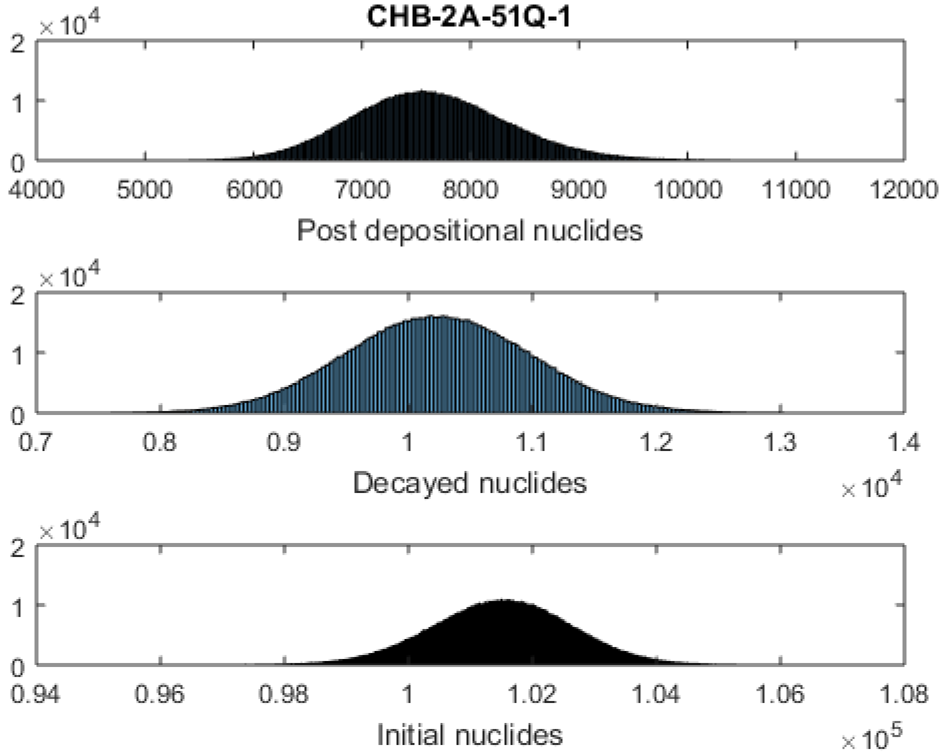

Figure D15. Calculated intermediate histogram distributions of total post-depositional nuclide accumulation, nuclide loss to radioactive decay, and the initial nuclide concentration for sample CHB14-2A-51Q-1.

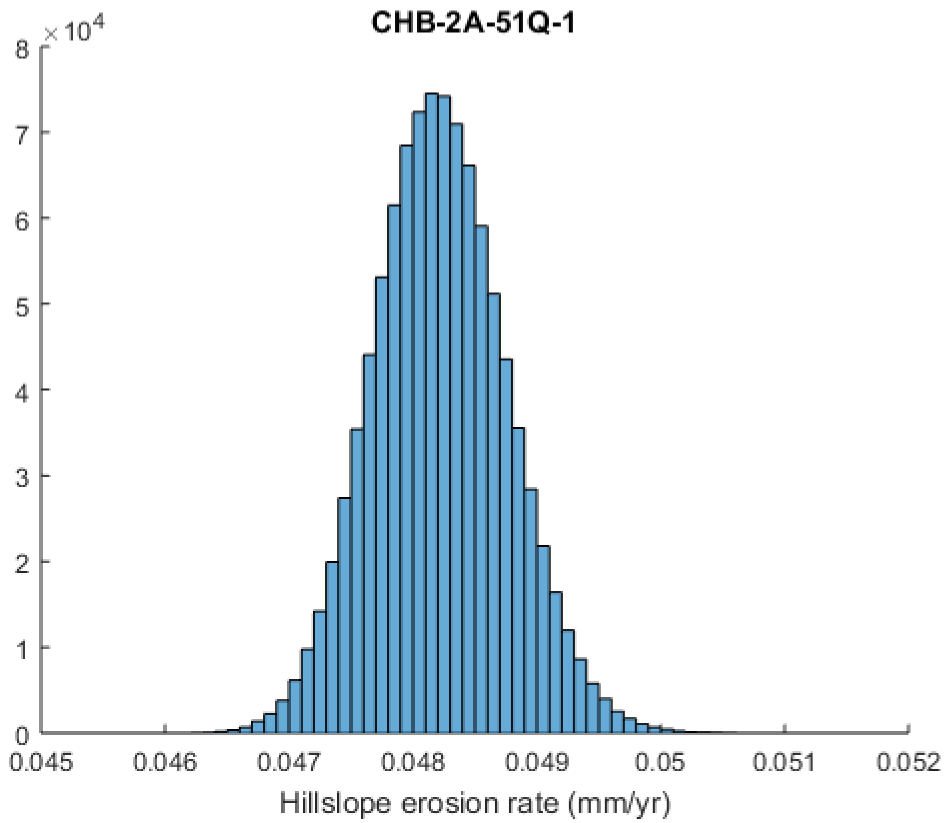

Figure D16. Calculated histogram distribution of paleoerosion rates for sample CHB14-2A-51Q-1.

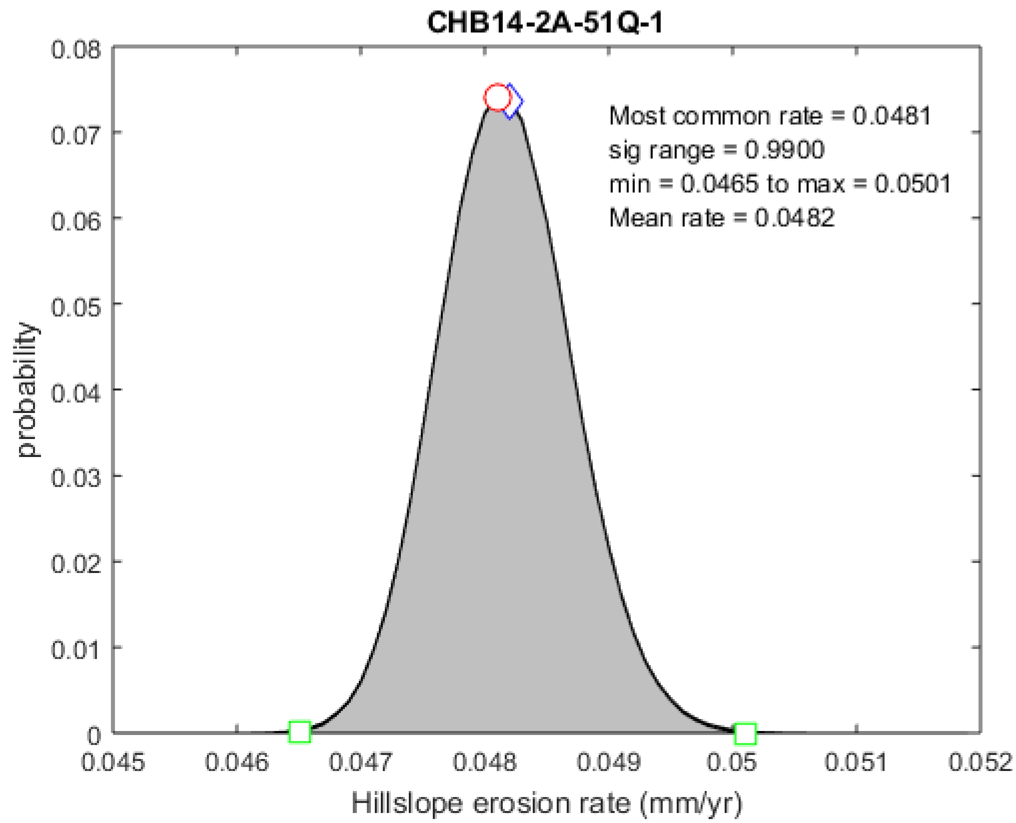

Figure D17. Normalized PDF of paleoerosion rate at 0.99 significance level with modal, mean, maximum, and minimum erosion rates for sample CHB14-2A-51Q-1.

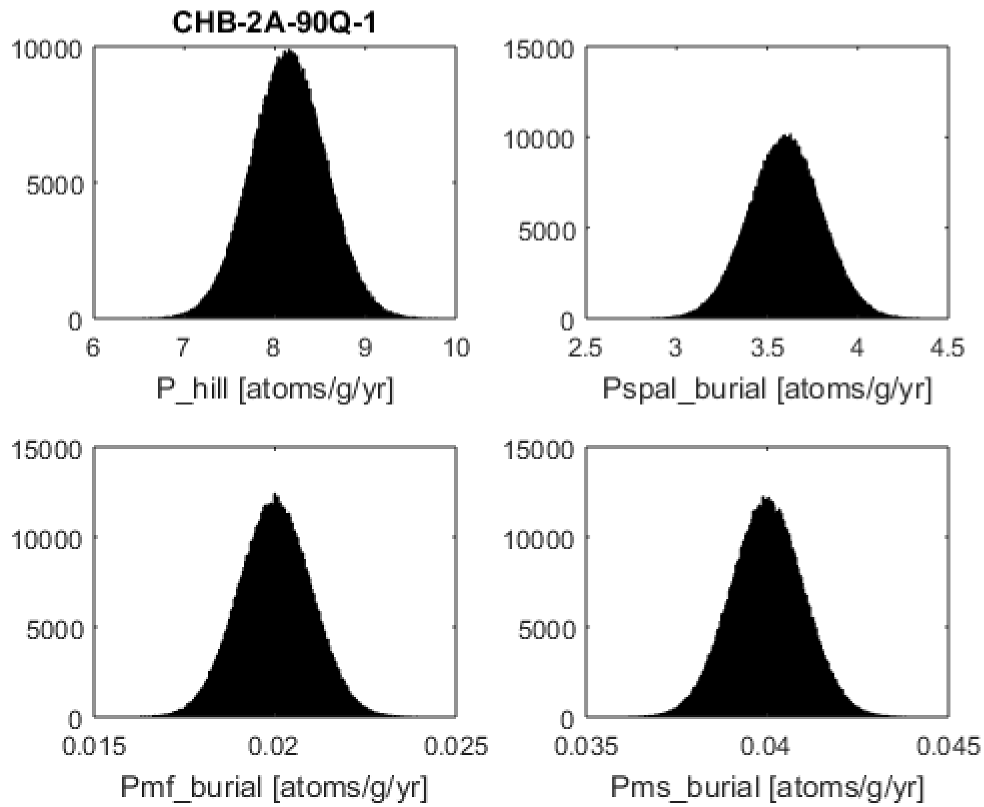

Figure D18. Normal distributions of production rate variables for sample CHB14-2A-90Q-1. P_hill = total hillslope production rate (atoms g^{-1} yr^{-1}), Pspal_burial = spallation production at burial site (atoms g^{-1} yr^{-1}), Pmf_burial = fast muons production at burial site (atoms g^{-1} yr^{-1}), and Pms_burial = slow muon capture production at burial site (atoms g^{-1} yr^{-1}).

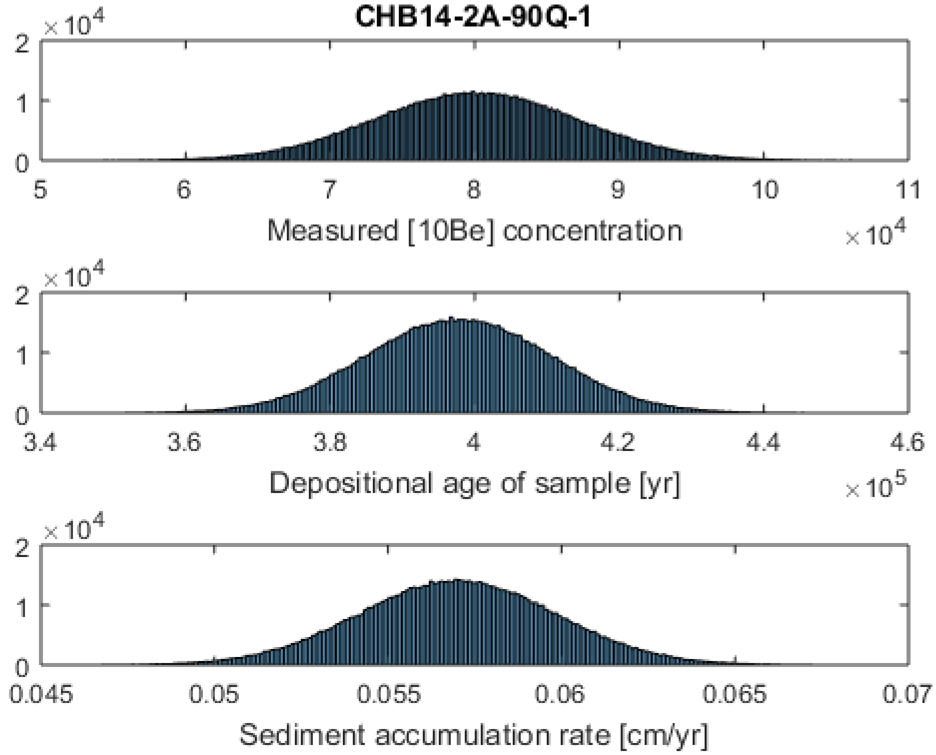

Figure D19. Normal histogram distribution of measured [^{10}Be] concentration, the depositional age of the sample, and sediment accumulation rate for sample CHB14-2A-90Q-1.

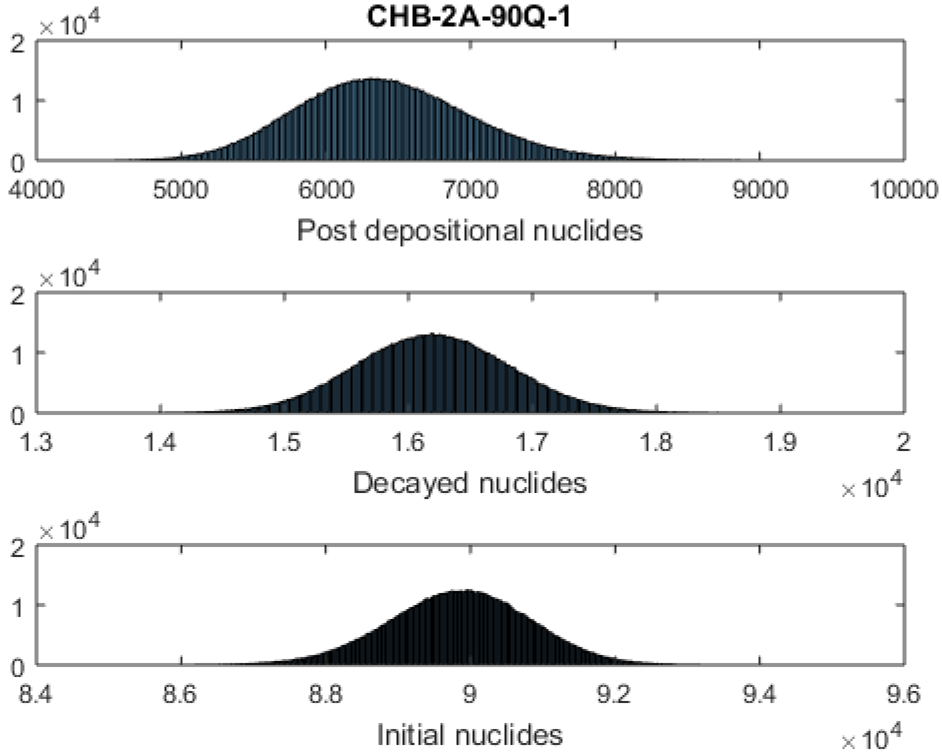

Figure D20. Calculated intermediate histogram distributions of total post-depositional nuclide accumulation, nuclide loss to radioactive decay, and the initial nuclide concentration for sample CHB14-2A-90Q-1.

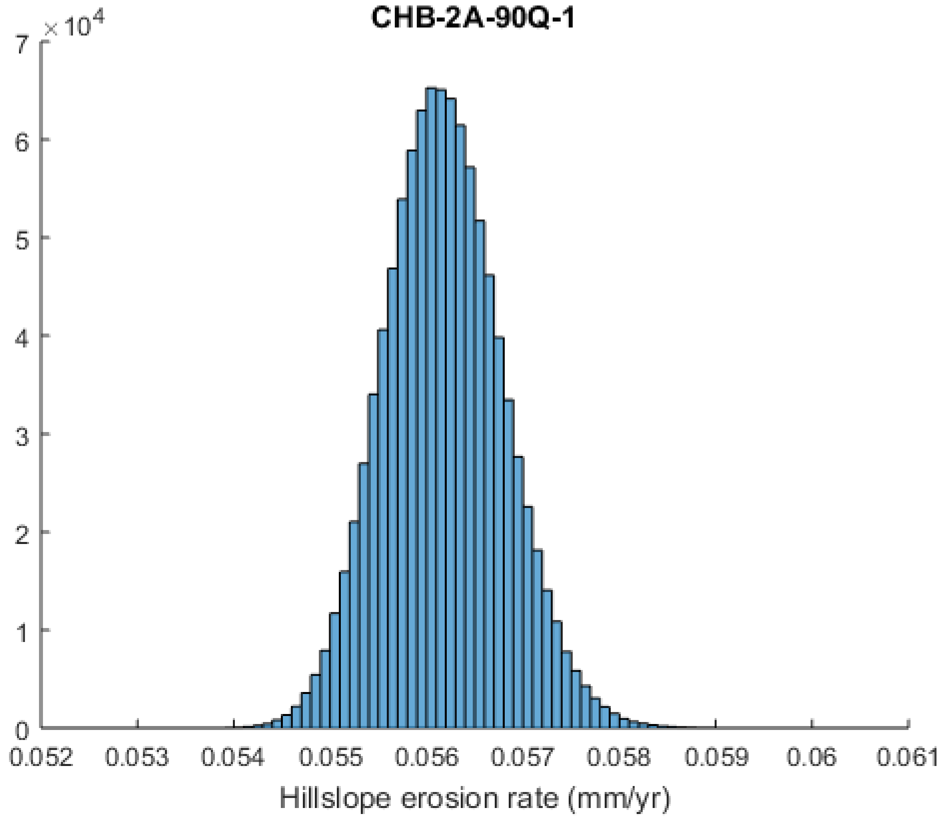

Figure D21. Calculated histogram distribution of paleoerosion rates for sample CHB14-2A-90Q-1.

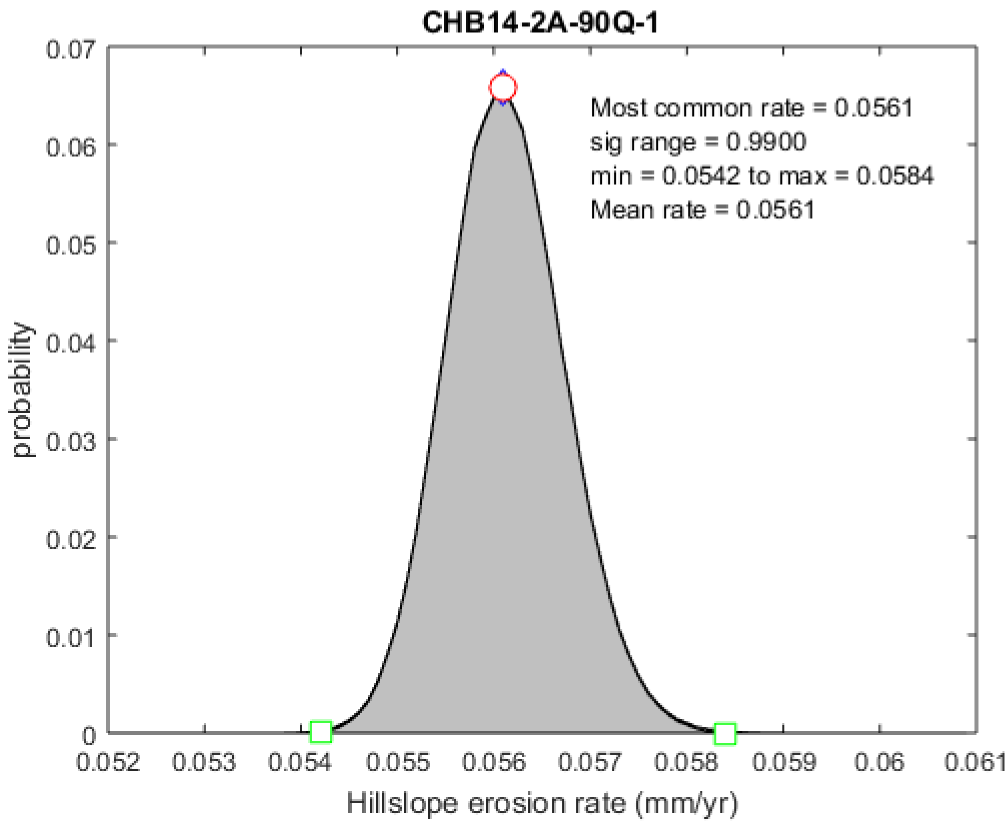

Figure D22. Normalized PDF of paleoerosion rate at 0.99 significance level with modal, mean, maximum, and minimum erosion rates for sample CHB14-2A-90Q-1.

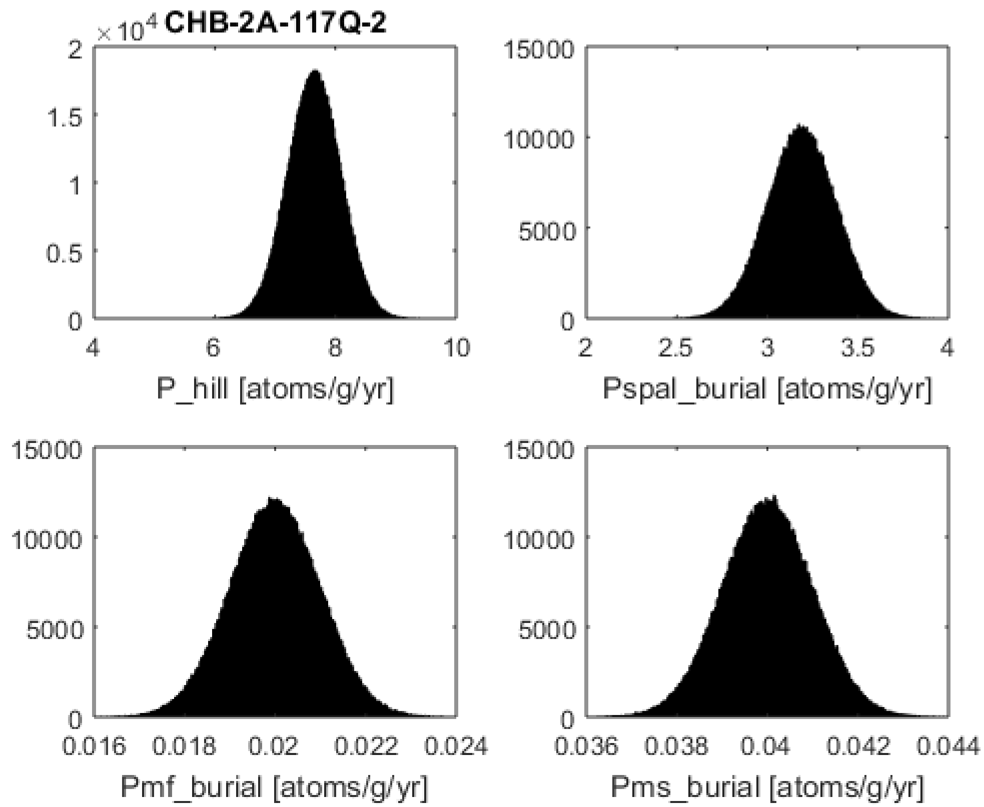

Figure D23. Normal distributions of production rate variables for sample CHB14-2A-117Q-2. P_hill = total hillslope production rate (atoms g^{-1} yr^{-1}), Pspal_burial = spallation production at burial site (atoms g^{-1} yr^{-1}), Pmf_burial = fast muons production at burial site (atoms g^{-1} yr^{-1}), and Pms_burial = slow muon capture production at burial site (atoms g^{-1} yr^{-1}).

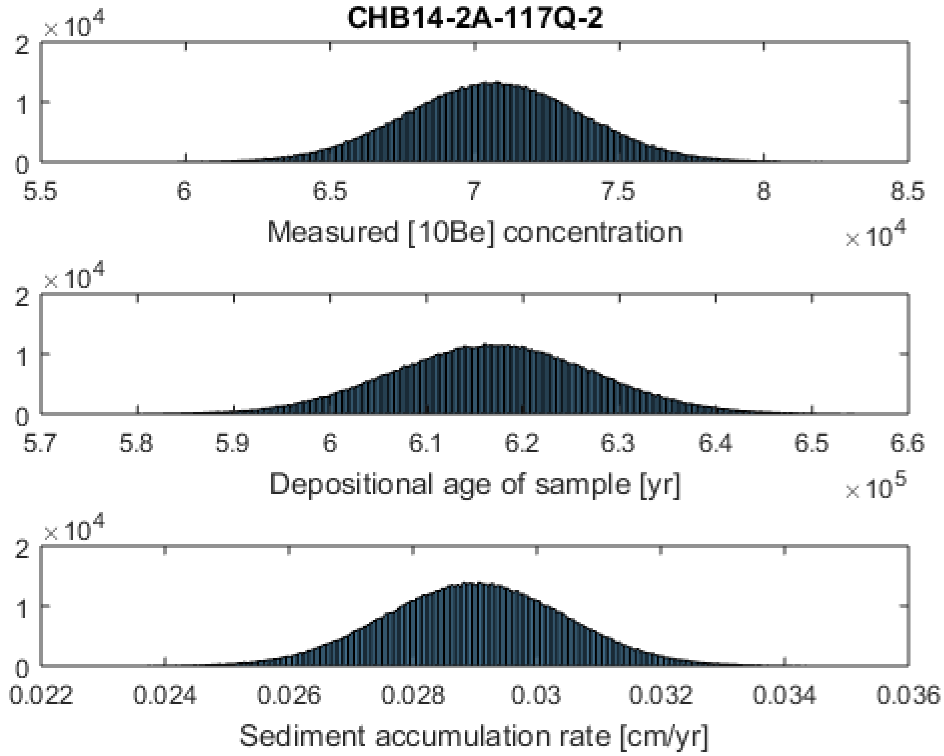

Figure D24. Normal histogram distribution of measured [^{10}Be] concentration, the depositional age of the sample, and sediment accumulation rate for sample CHB14-2A-117Q-2.

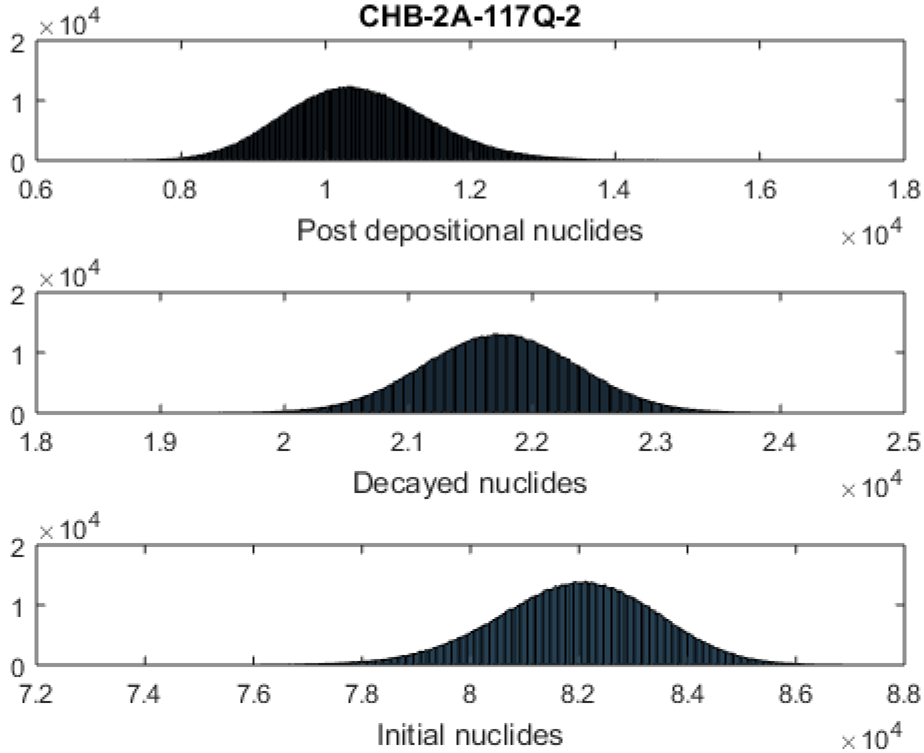

Figure D25. Calculated intermediate histogram distributions of total post-depositional nuclide accumulation, nuclide loss to radioactive decay, and the initial nuclide concentration for sample CHB14-2A-117Q-2.

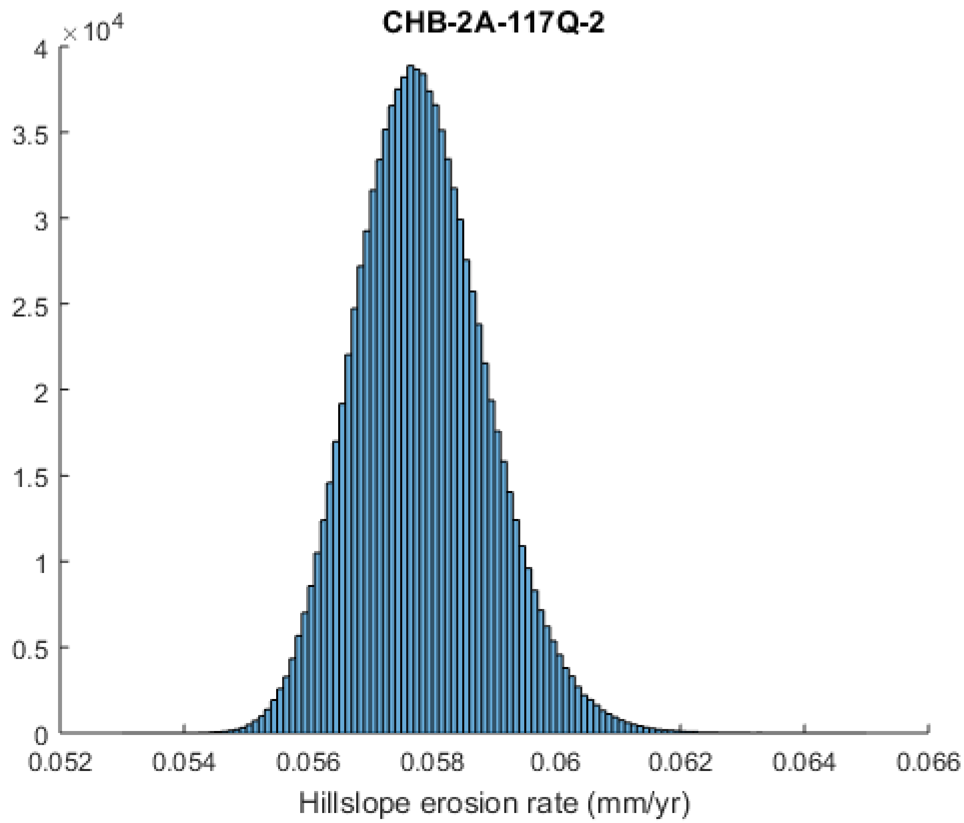

Figure D26. Calculated histogram distribution of paleoerosion rates for sample CHB14-2A-117Q-2.

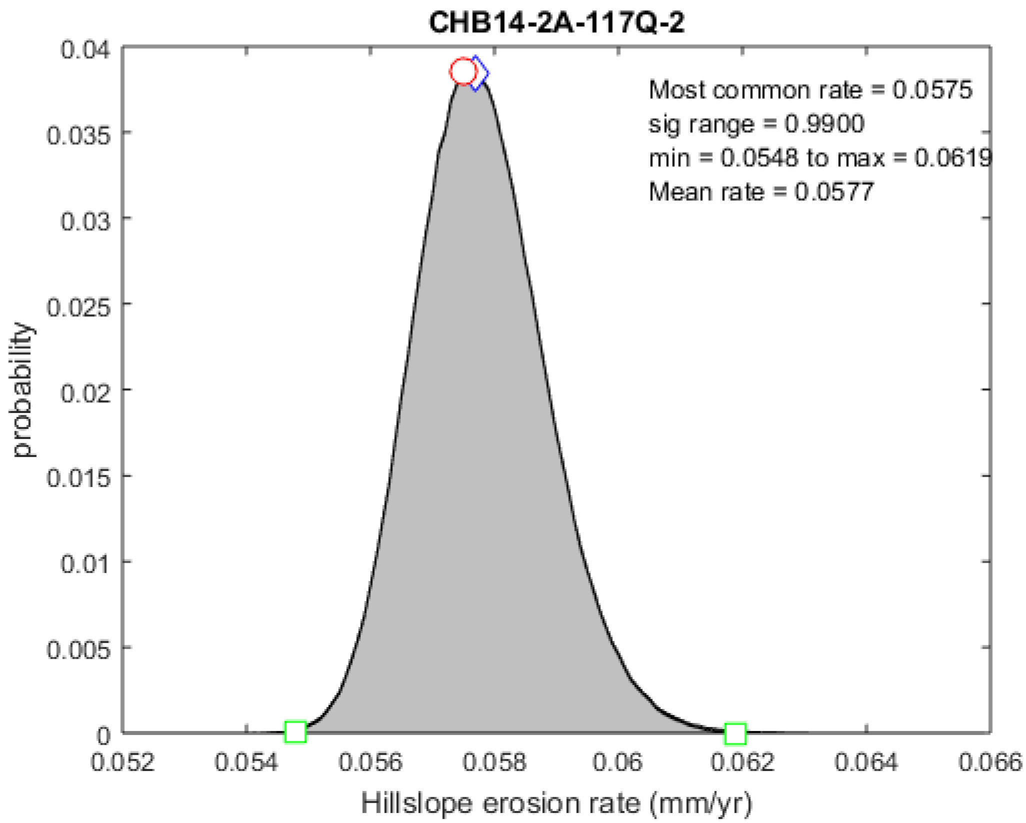

Figure D27. Normalized PDF of paleoerosion rate at 0.99 significance level with modal, mean, maximum, and minimum erosion rates for sample CHB14-2A-117Q-2.

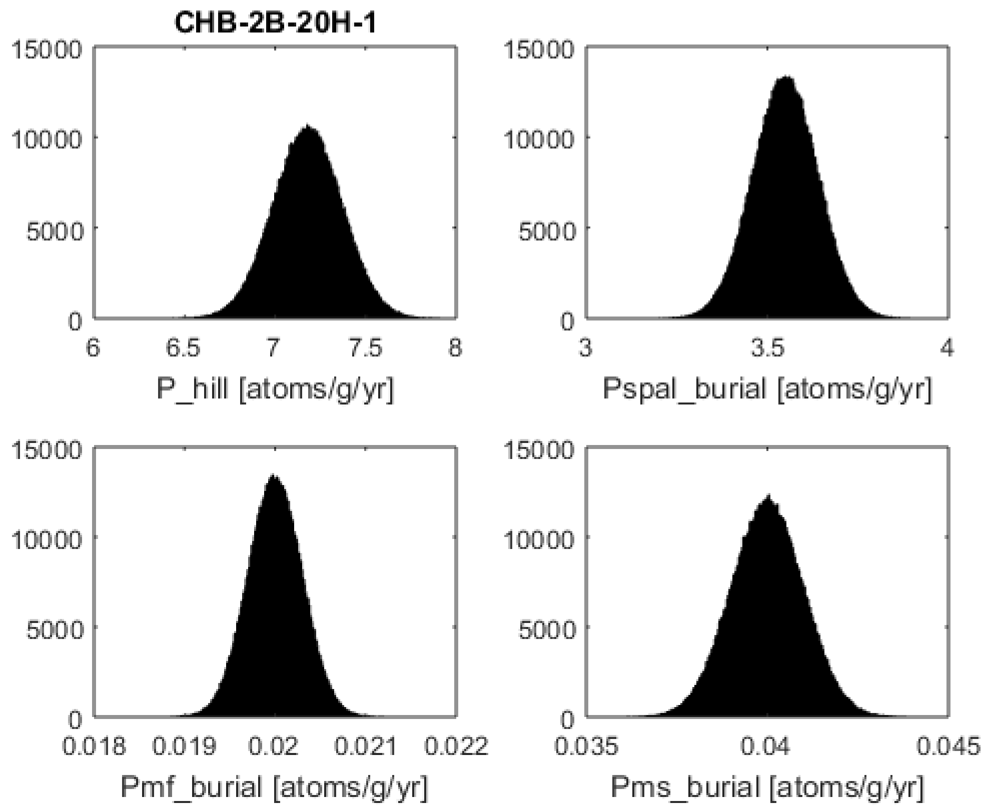

Figure D28. Normal distributions of production rate variables for sample CHB14-2B-20H-1. P_hill = total hillslope production rate (atoms g^{-1} yr^{-1}), Pspal_burial = spallation production at burial site (atoms g^{-1} yr^{-1}), Pmf_burial = fast muons production at burial site (atoms g^{-1} yr^{-1}), and Pms_burial = slow muon capture production at burial site (atoms g^{-1} yr^{-1}).

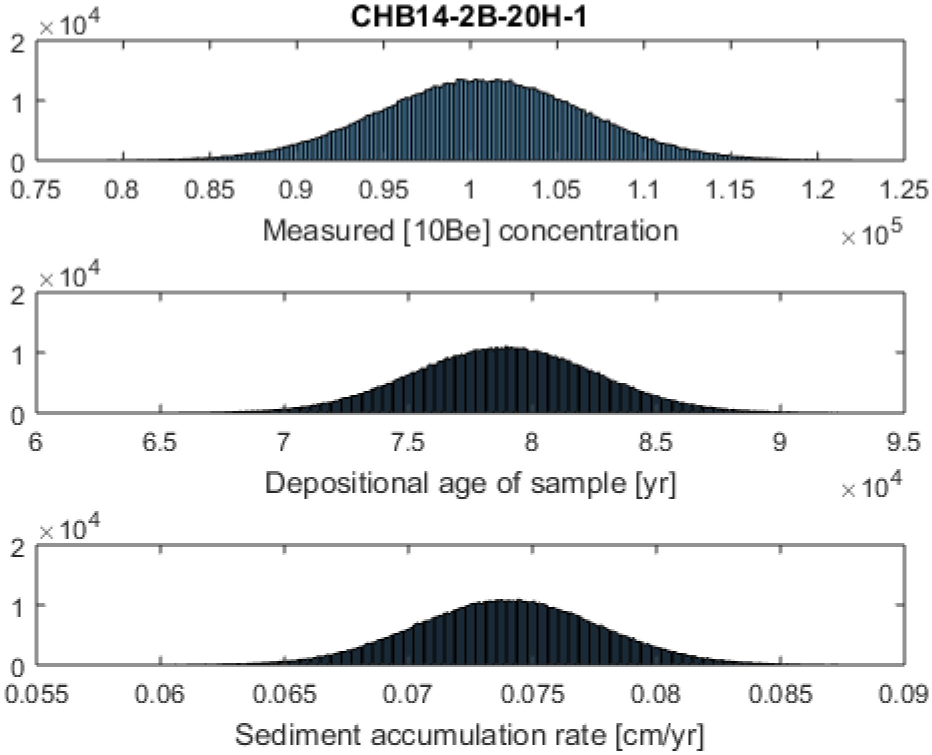

Figure D29. Normal histogram distribution of measured [^{10}Be] concentration, the depositional age of the sample, and sediment accumulation rate for sample CHB14-2B-20H-1.

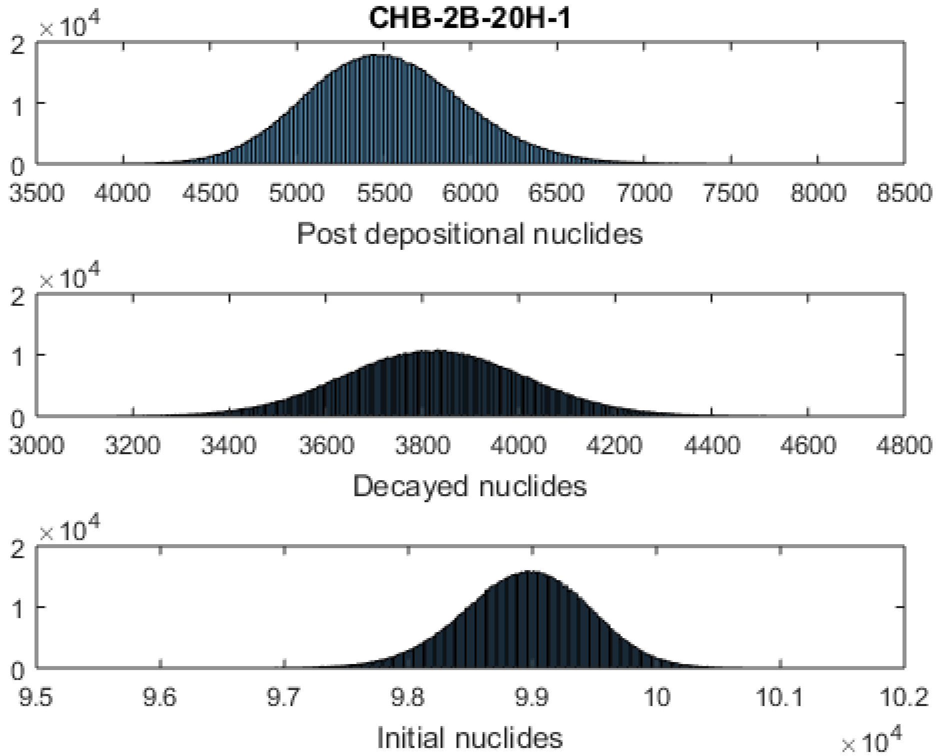

Figure D30. Calculated intermediate histogram distributions of total post-depositional nuclide accumulation, nuclide loss to radioactive decay, and the initial nuclide concentration for sample CHB14-2B-20H-1.

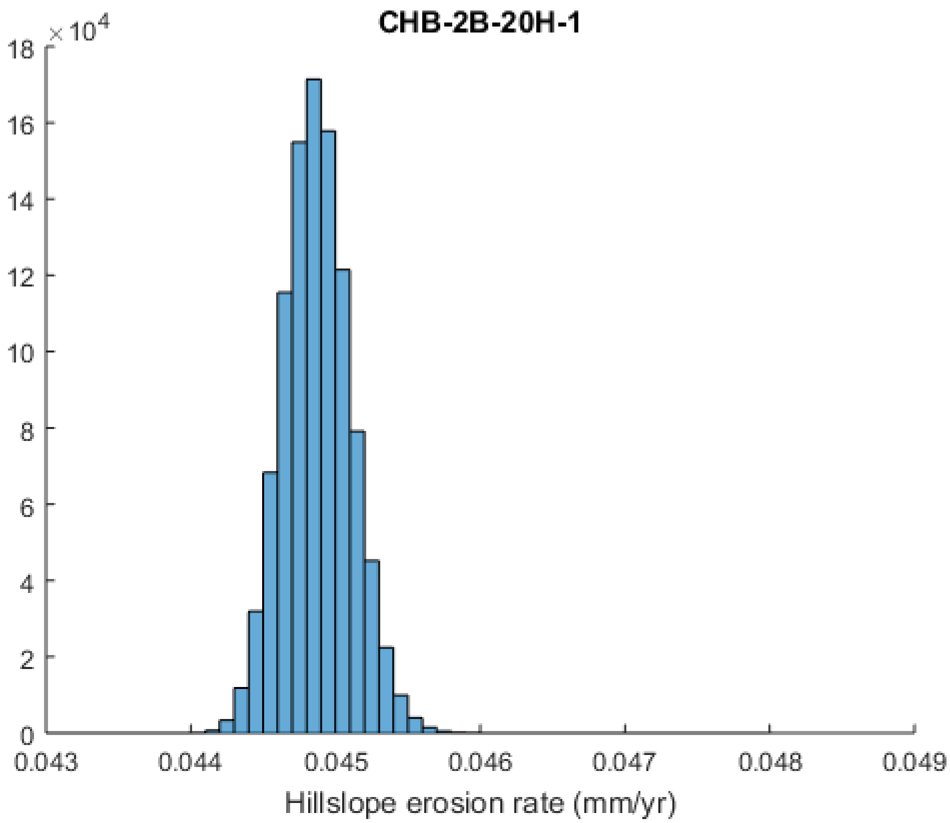

Figure D31. Calculated histogram distribution of paleoerosion rates for sample CHB14-2B-20H-1.

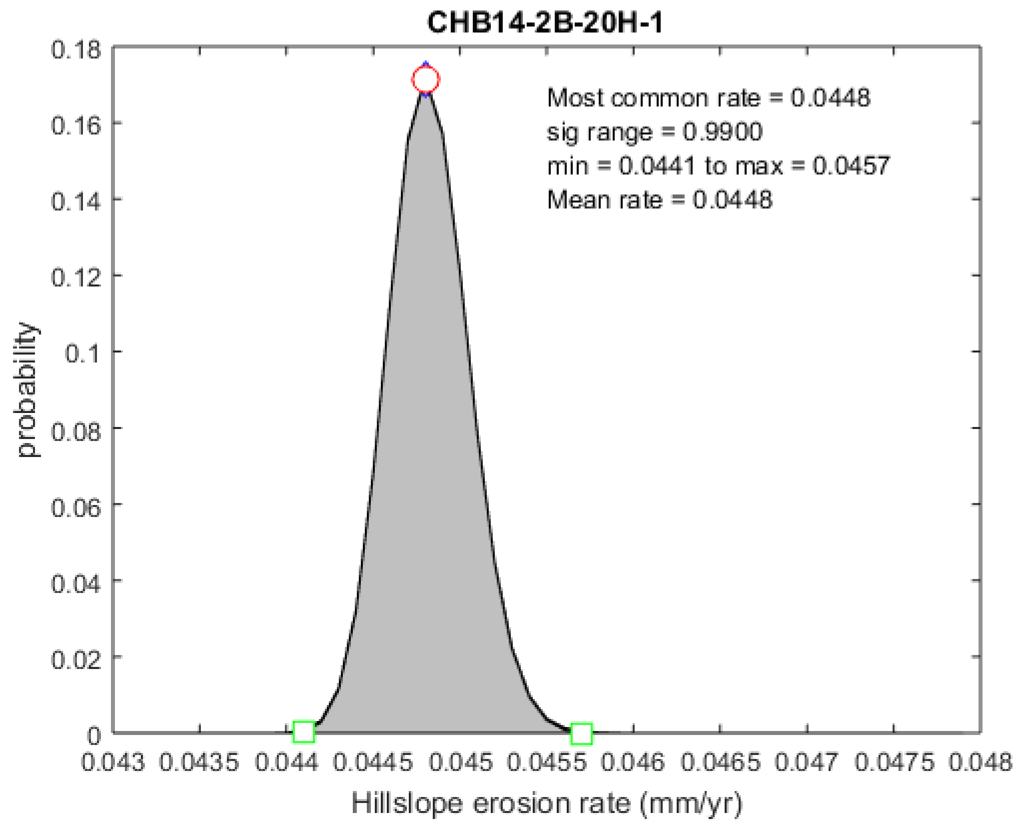

Figure D32. Normalized PDF of paleoerosion rate at 0.99 significance level with modal, mean, maximum, and minimum erosion rates for sample CHB14-2B-20H-1.

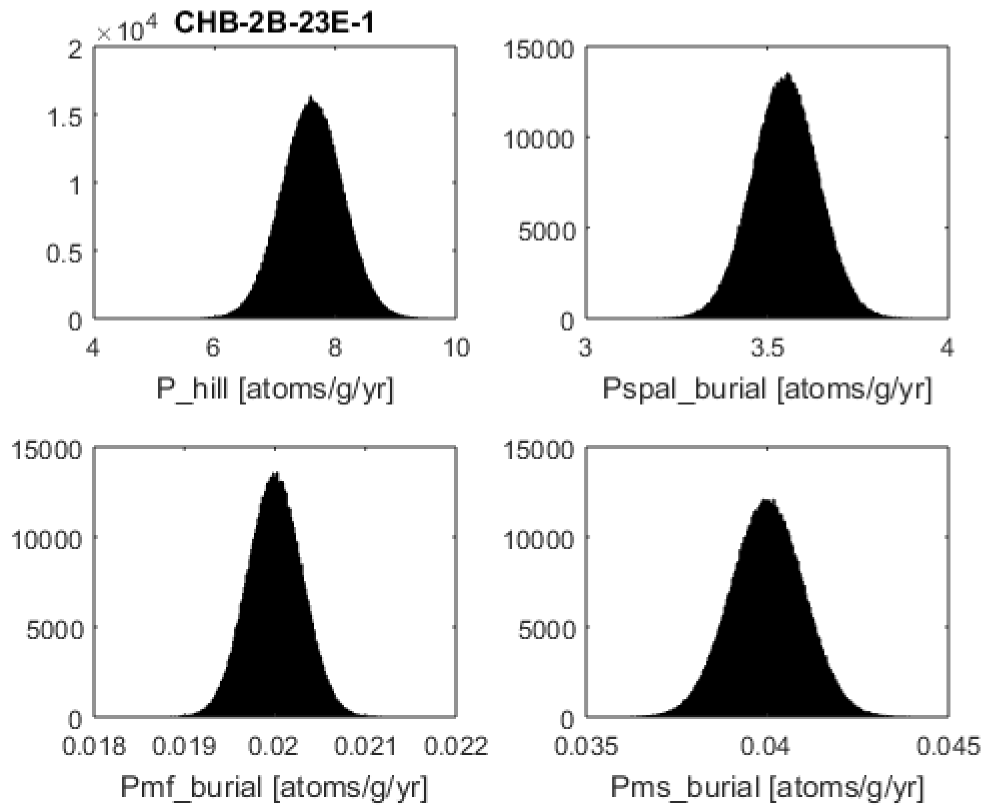

Figure D33. Normal distributions of production rate variables for sample CHB14-2B-23E-1 P_hill = total hillslope production rate (atoms g^{-1} yr^{-1}), Pspal_burial = spallation production at burial site (atoms g^{-1} yr^{-1}), Pmf_burial = fast muons production at burial site (atoms g^{-1} yr^{-1}), and Pms_burial = slow muon capture production at burial site (atoms g^{-1} yr^{-1}).

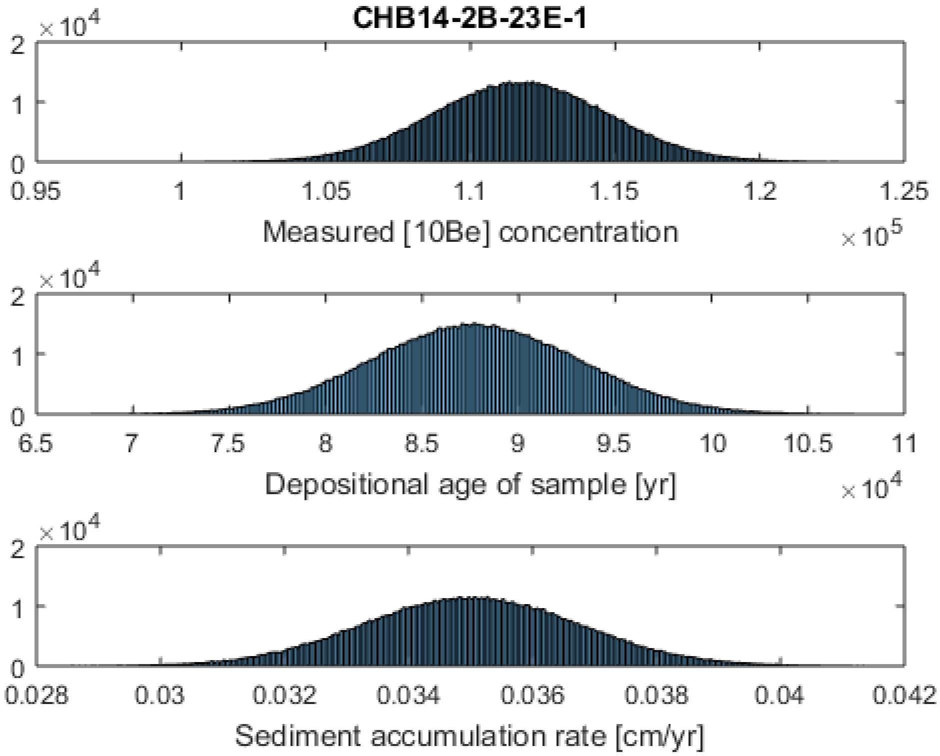

Figure D34. Normal histogram distribution of measured [^{10}Be] concentration, the depositional age of the sample, and sediment accumulation rate for sample CHB14-2B-23E-1

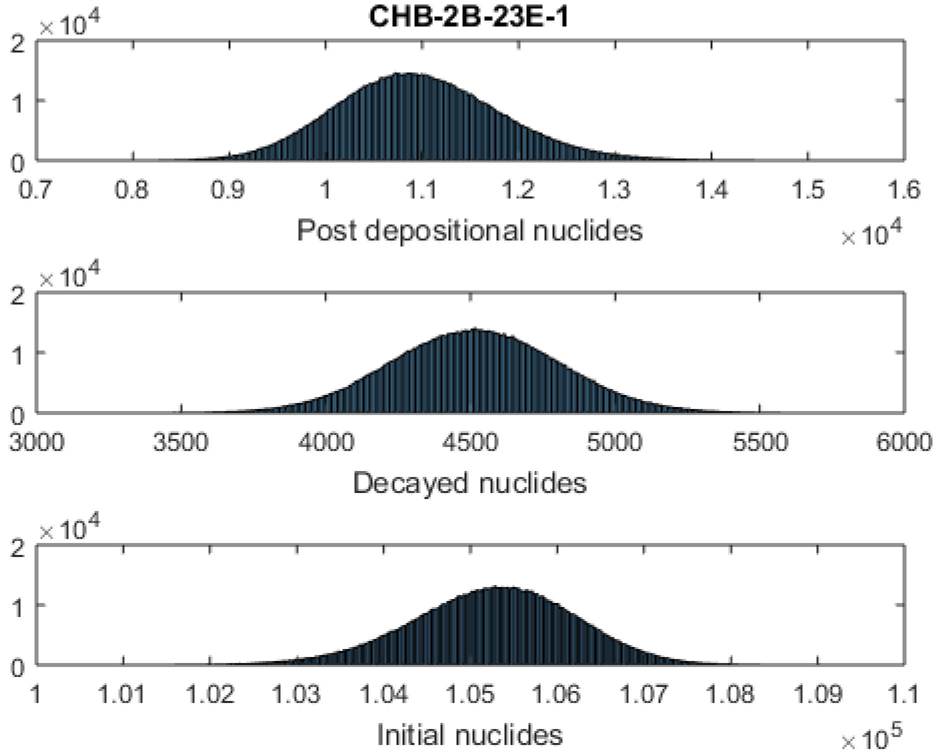

Figure D35. Calculated intermediate histogram distributions of total post-depositional nuclide accumulation, nuclide loss to radioactive decay, and the initial nuclide concentration for sample CHB14-2B-23E-1.

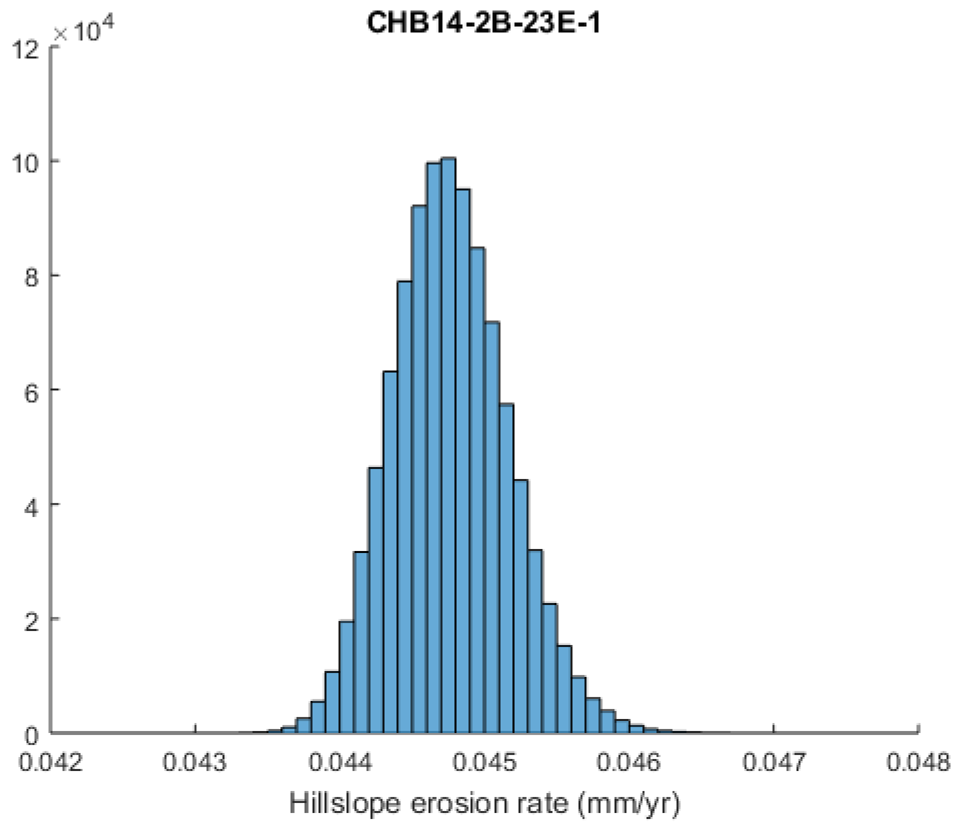

Figure D36. Calculated histogram distribution of paleoerosion rates for sample CHB14-2B-23E-1.

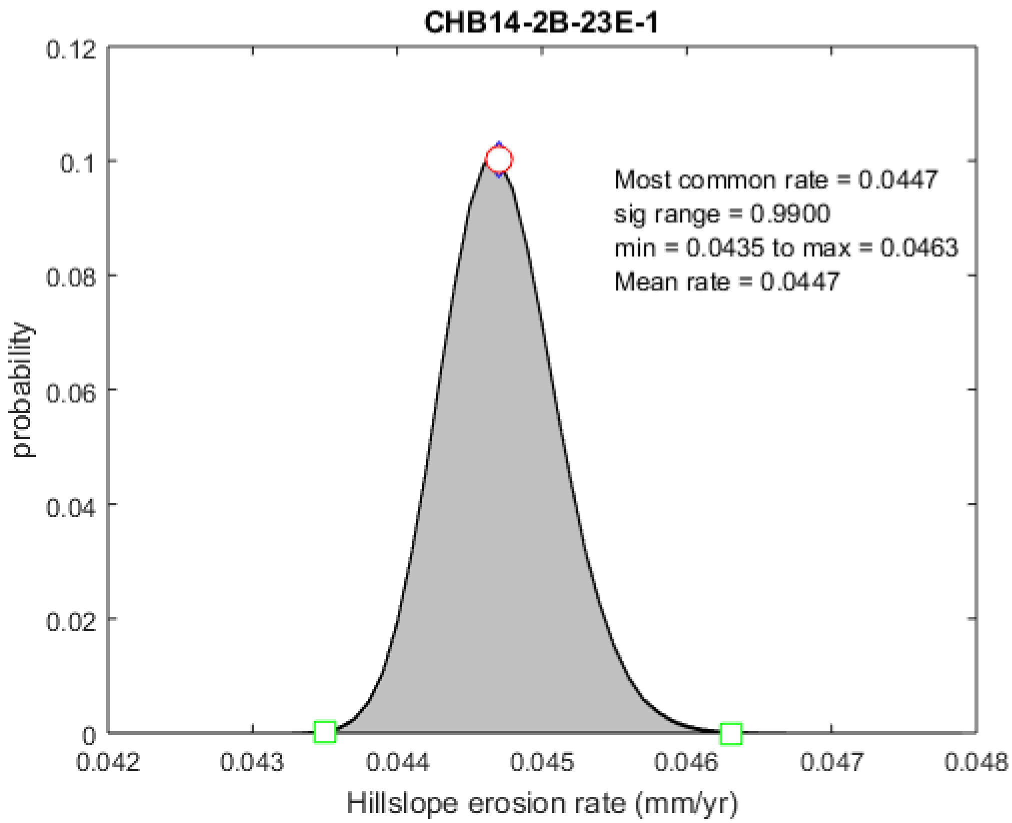

Figure D37. Normalized PDF of paleoerosion rate at 0.99 significance level with modal, mean, maximum, and minimum erosion rates for sample CHB14-2B-23E-1.

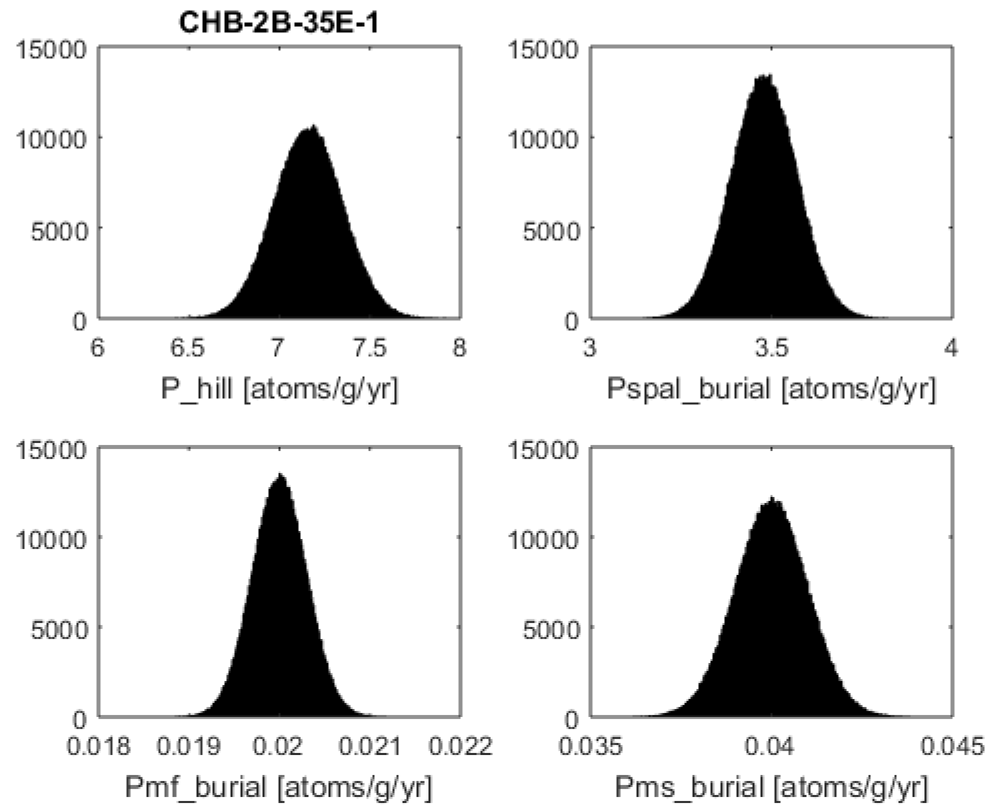

Figure D38. Normal distributions of production rate variables for sample CHB14-2B-35E-1 P_hill = total hillslope production rate (atoms g^{-1} yr^{-1}), Pspal_burial = spallation production at burial site (atoms g^{-1} yr^{-1}), Pmf_burial = fast muons production at burial site (atoms g^{-1} yr^{-1}), and Pms_burial = slow muon capture production at burial site (atoms g^{-1} yr^{-1}).

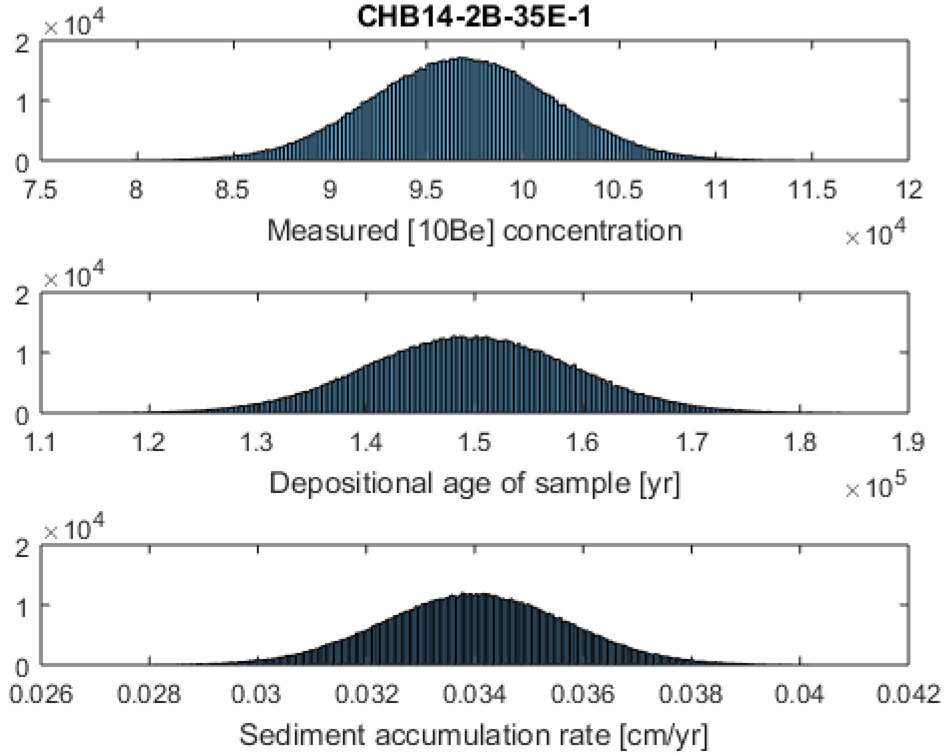

Figure D39. Normal histogram distribution of measured [^{10}Be] concentration, the depositional age of the sample, and sediment accumulation rate for sample CHB14-2B-35E-1.

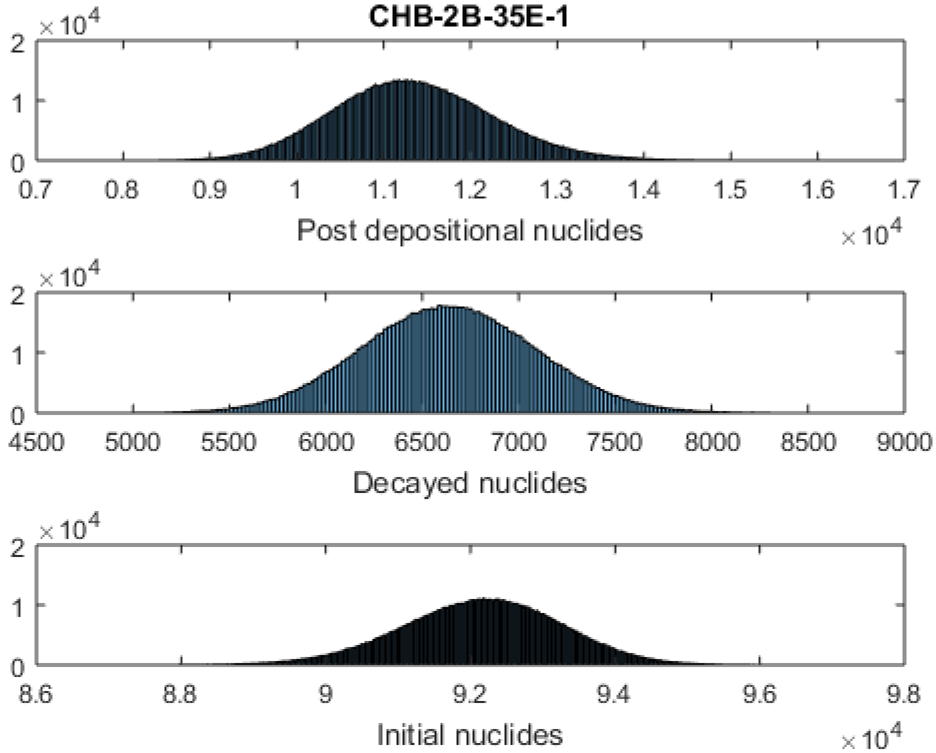

Figure D40. Calculated intermediate histogram distributions of total post-depositional nuclide accumulation, nuclide loss to radioactive decay, and the initial nuclide concentration for sample CHB14-2B-35E-1.

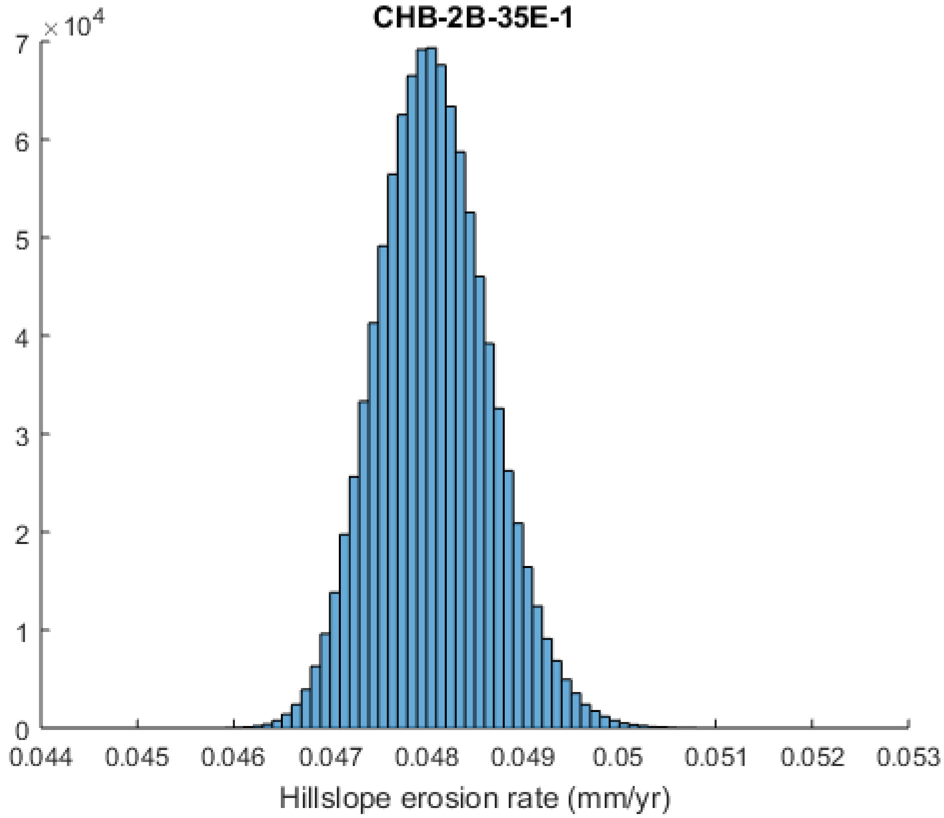

Figure D41. Calculated histogram distribution of paleoerosion rates for sample CHB14-2B-35E-1.

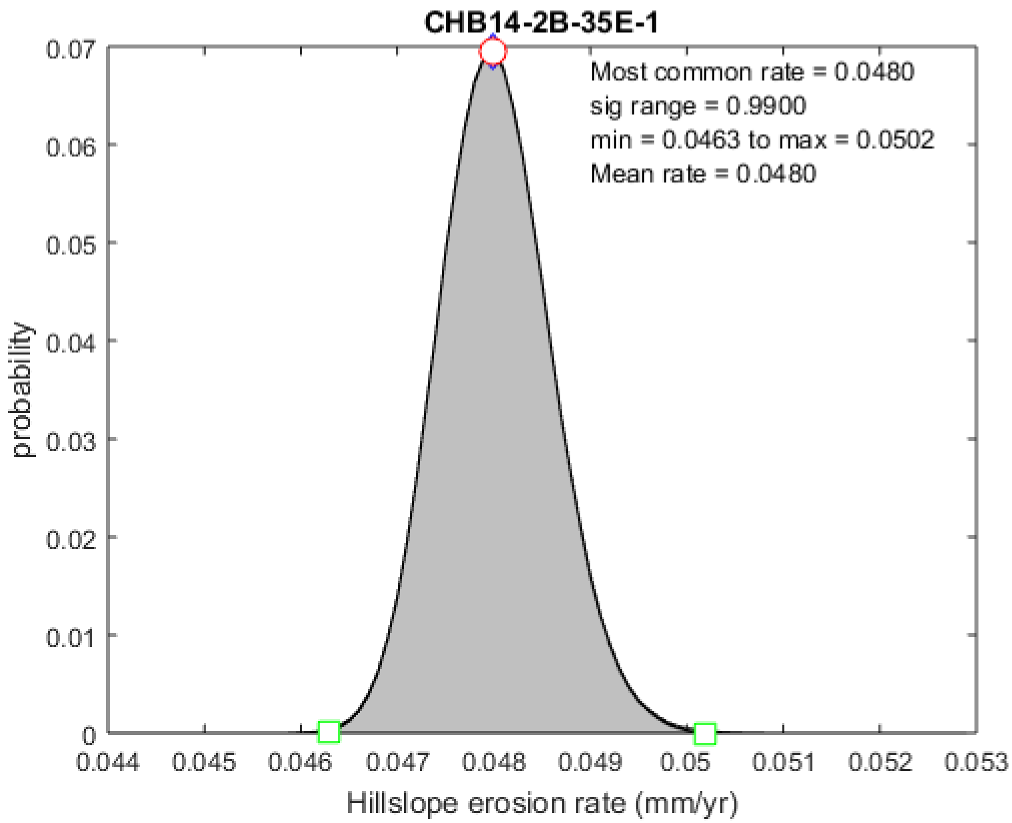

Figure D42. Normalized PDF of paleoerosion rate at 0.99 significance level with modal, mean, maximum, and minimum erosion rates for sample CHB14-2B-35E-1.

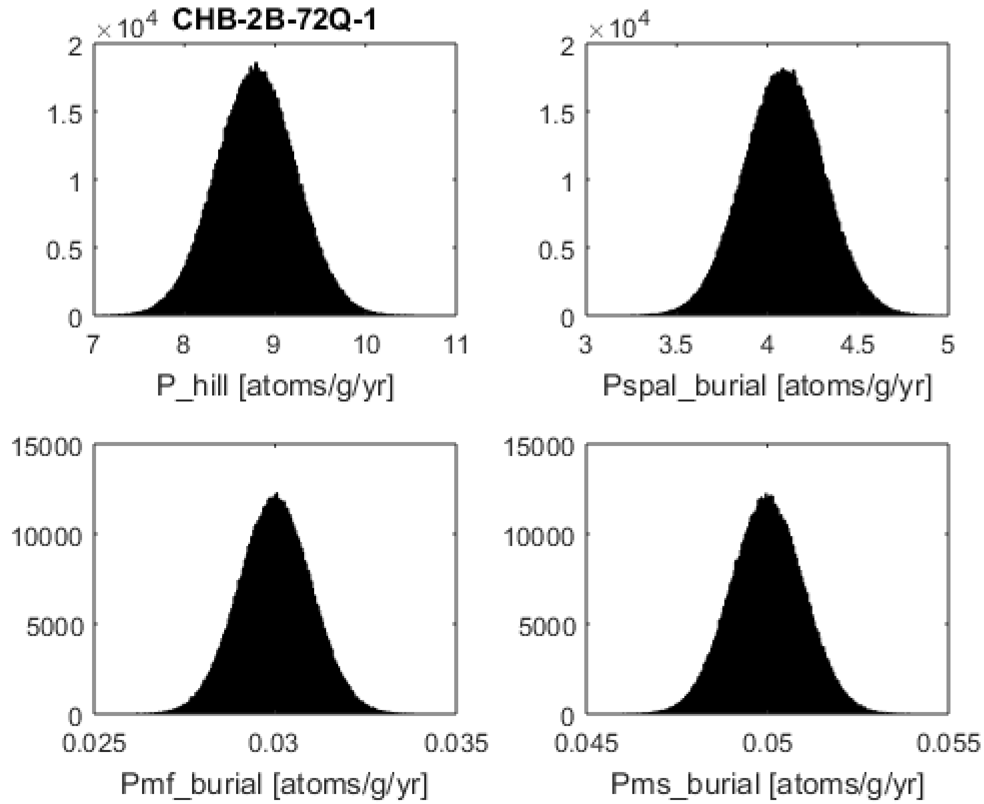

Figure D43. Normal distributions of production rate variables for sample CHB14-2B-72Q-1 P_hill = total hillslope production rate (atoms g^{-1} yr^{-1}), Pspal_burial = spallation production at burial site (atoms g^{-1} yr^{-1}), Pmf_burial = fast muons production at burial site (atoms g^{-1} yr^{-1}), and Pms_burial = slow muon capture production at burial site (atoms g^{-1} yr^{-1}).

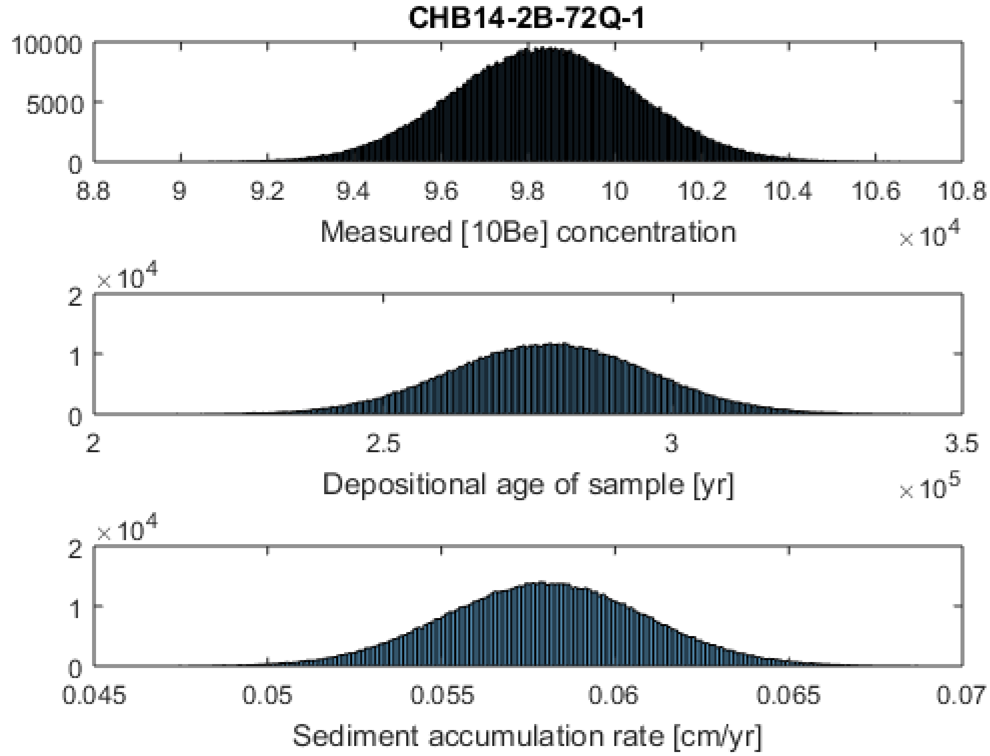

Figure D44. Normal histogram distribution of measured [^{10}Be] concentration, the depositional age of the sample, and sediment accumulation rate for sample CHB14-2B-72Q-1.

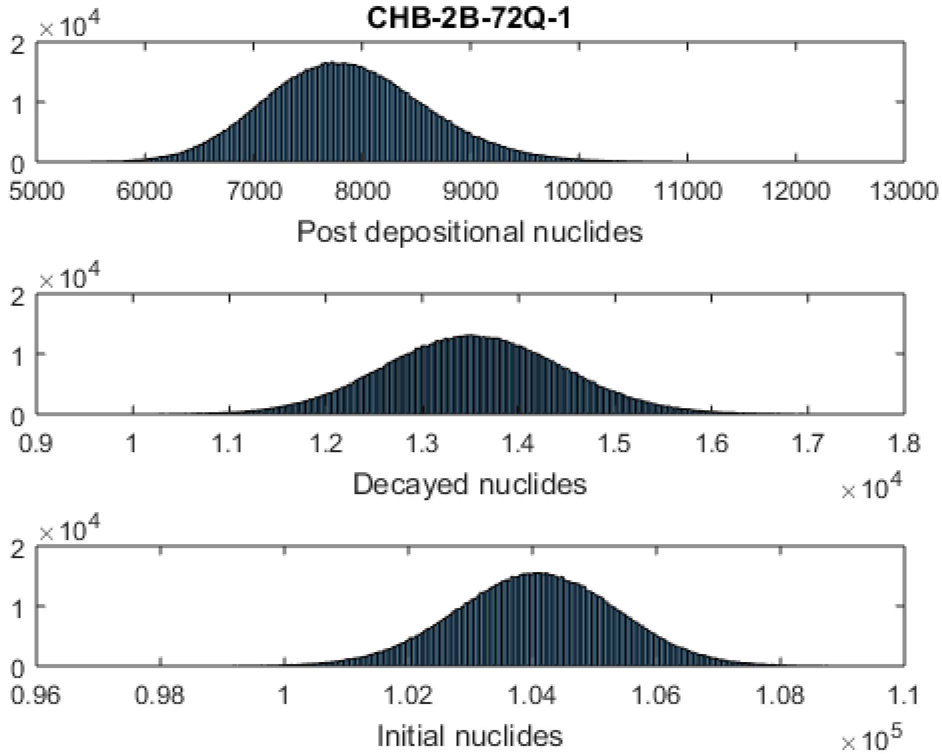

Figure D45. Calculated intermediate histogram distributions of total post-depositional nuclide accumulation, nuclide loss to radioactive decay, and the initial nuclide concentration for sample CHB14-2B-72Q-1.

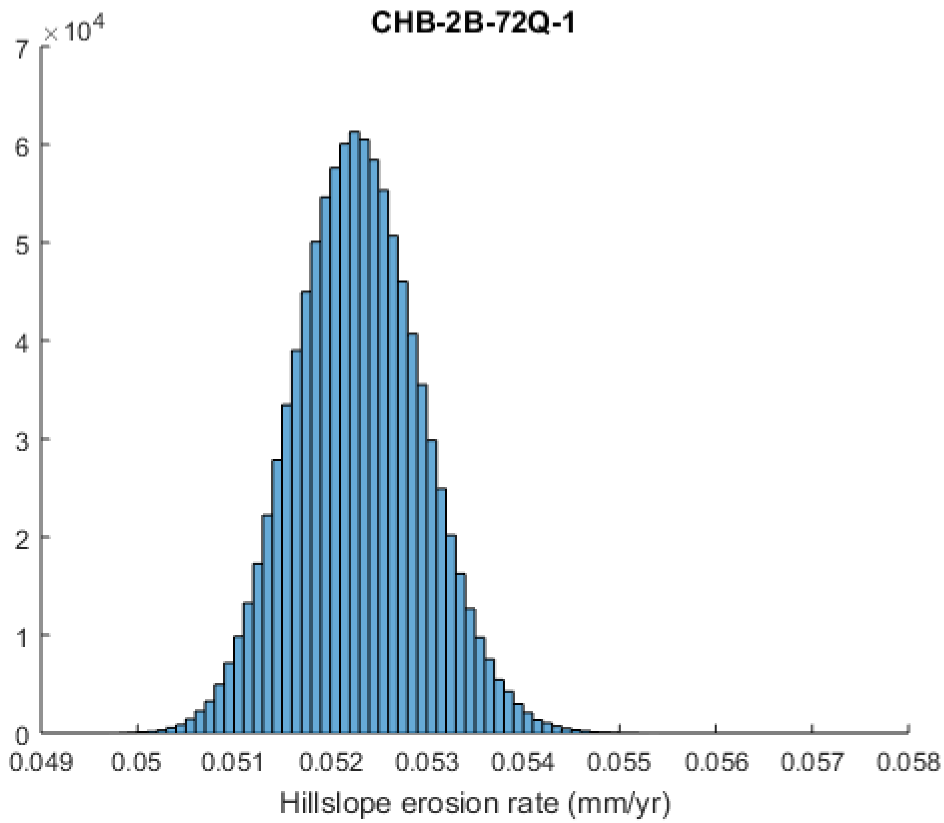

Figure D46. Calculated histogram distribution of paleoerosion rates for sample CHB14-2B-72Q-1.

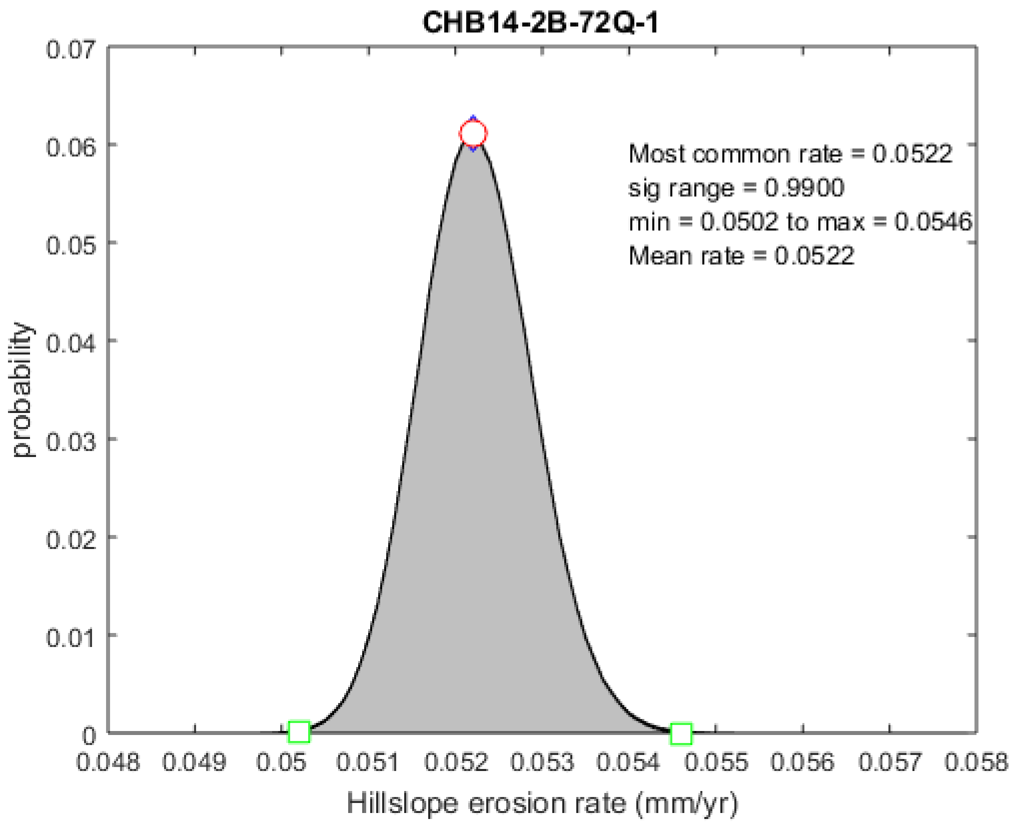

Figure D47. Normalized PDF of paleoerosion rate at 0.99 significance level with modal, mean, maximum, and minimum erosion rates for sample CHB14-2B-72Q-1.

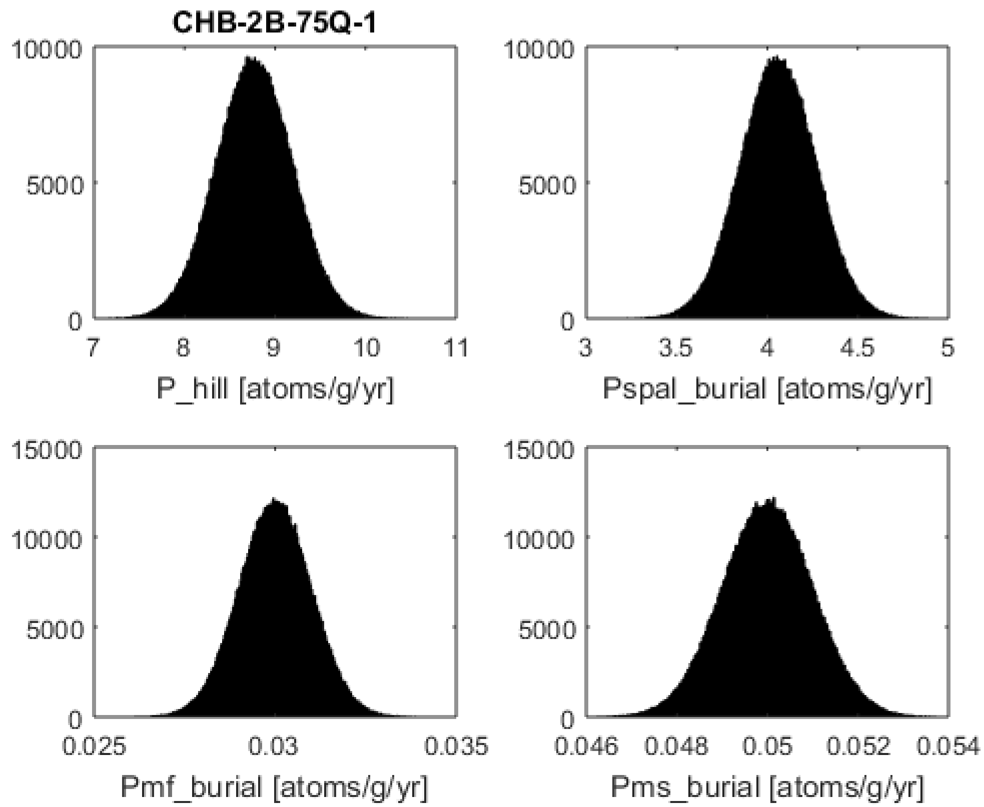

Figure D48. Normal distributions of production rate variables for sample CHB14-2B-75Q-1 P_hill = total hillslope production rate (atoms g^{-1} yr^{-1}), Pspal_burial = spallation production at burial site (atoms g^{-1} yr^{-1}), Pmf_burial = fast muons production at burial site (atoms g^{-1} yr^{-1}), and Pms_burial = slow muon capture production at burial site (atoms g^{-1} yr^{-1}).

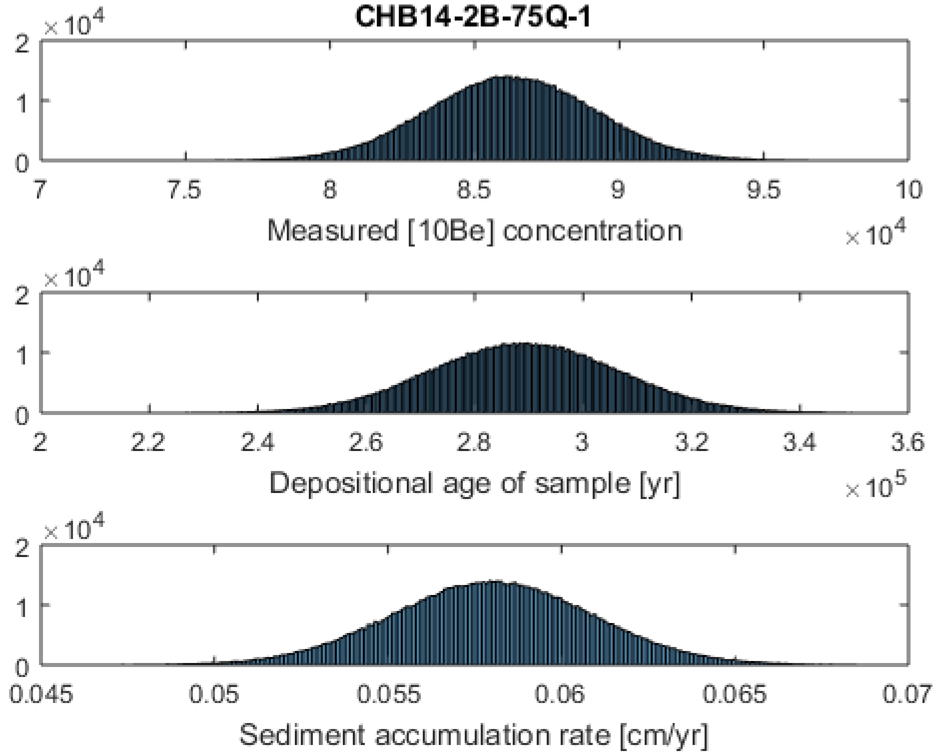

Figure D49. Normal histogram distribution of measured [^{10}Be] concentration, the depositional age of the sample, and sediment accumulation rate for sample CHB14-2B-75Q-1.

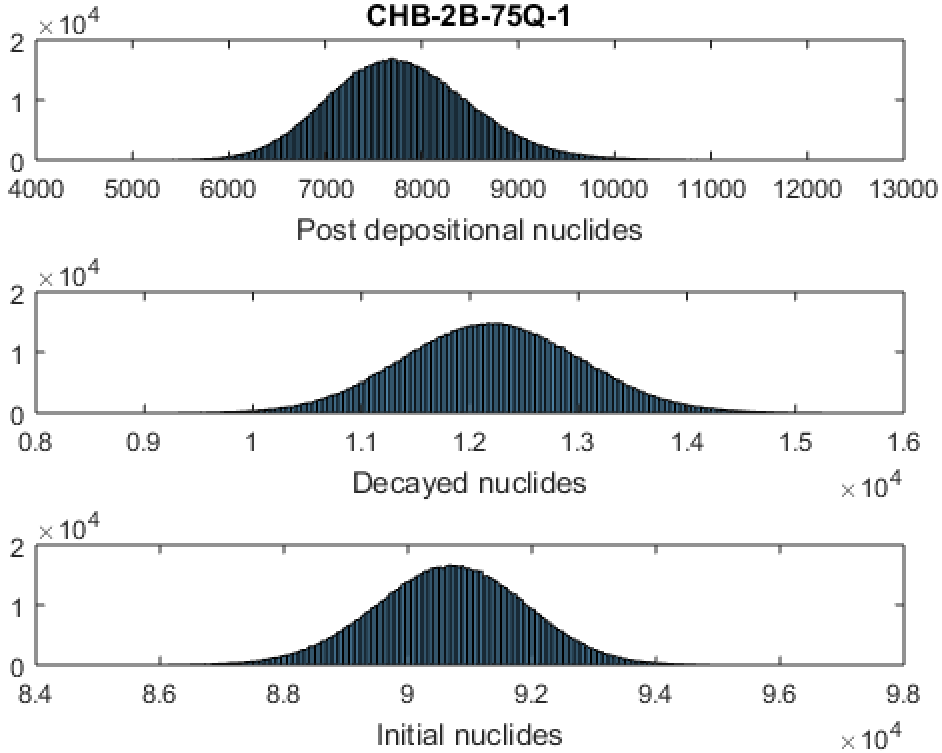

Figure D50. Calculated intermediate histogram distributions of total post-depositional nuclide accumulation, nuclide loss to radioactive decay, and the initial nuclide concentration for sample CHB14-2B-75Q-1.

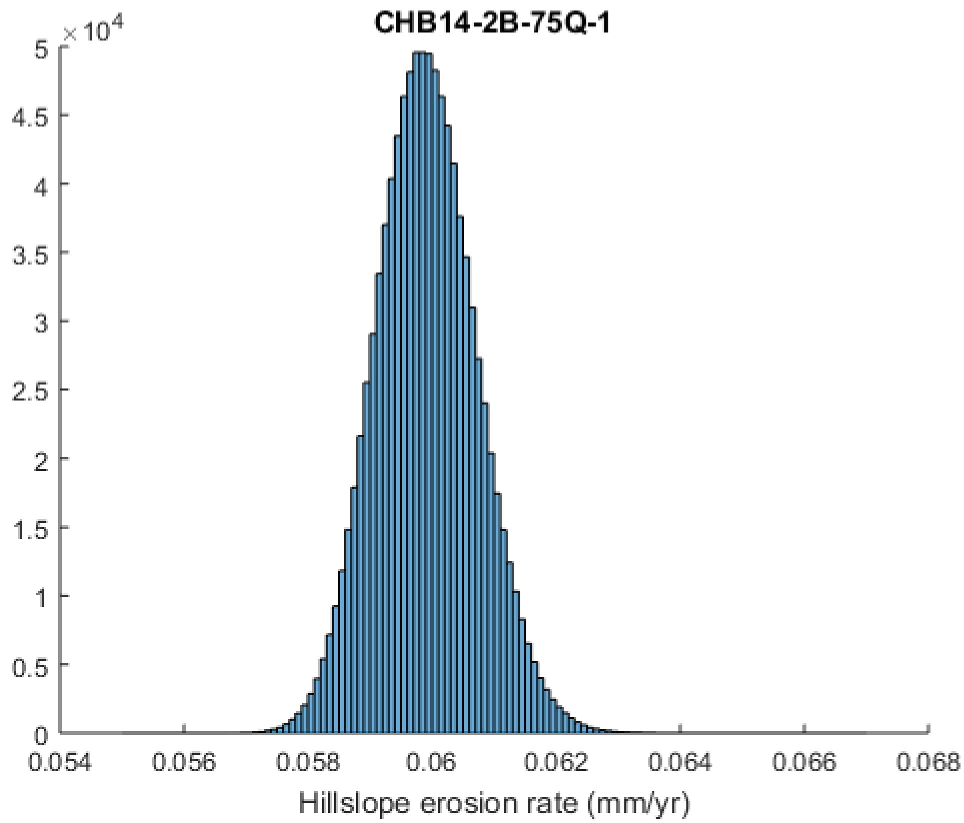

Figure D51. Calculated histogram distribution of paleoerosion rates for sample CHB14-2B-75Q-1.

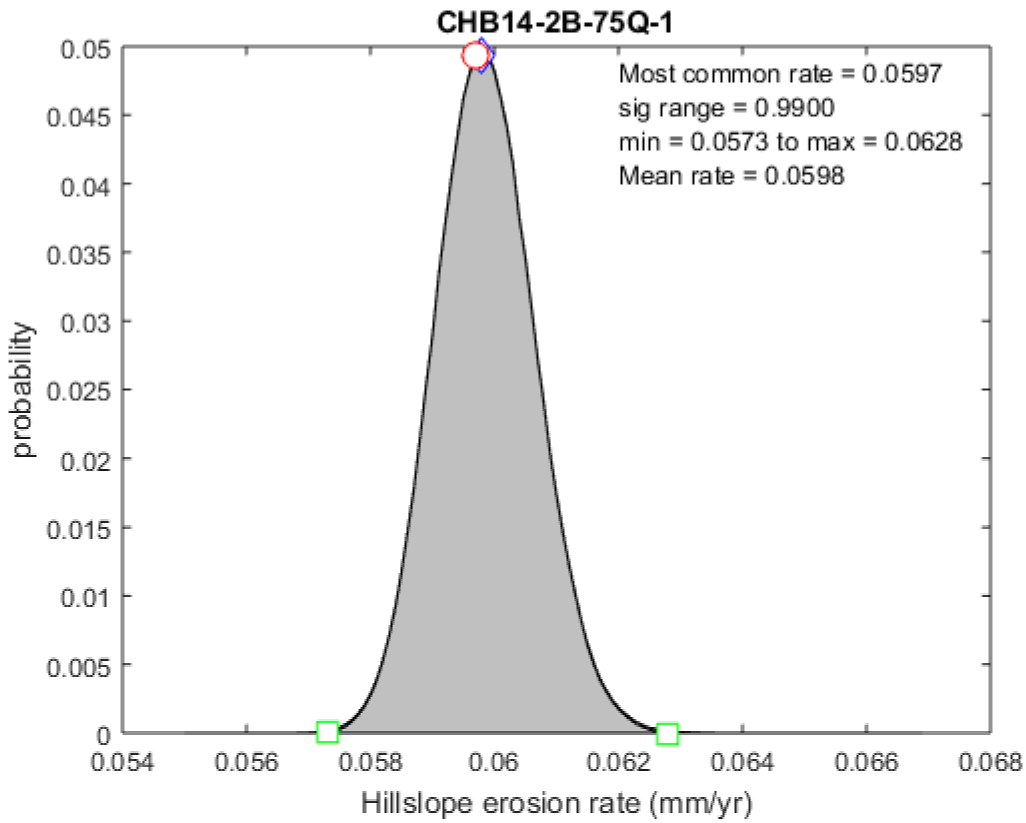

Figure D52. Normalized PDF of paleoerosion rate at 0.99 significance level with modal, mean, maximum, and minimum erosion rates for sample CHB14-2B-75Q-1.

APPENDIX E

CHAPTER 5 SUPPLEMENTARY MATERIALS

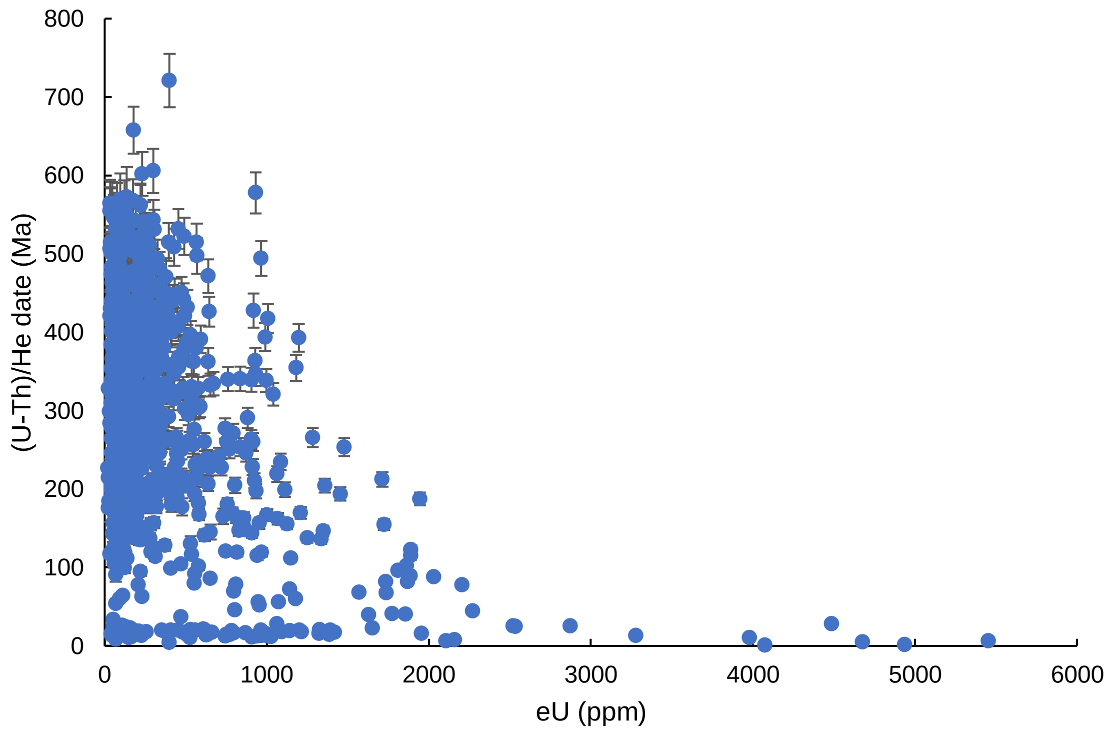

Figure E1. Effective uranium (eU) concentration vs. zircon (U-Th)/He date for all CHB zircons. There is no observed age-eU correlation or trend.

Explanation of variables for Supplementary Tables E1-10

- He pit vol. (μm^3) = The volume of the helium analysis determined by white light interferometry.
- err. (2σ) = Associated 2σ error for corresponding variable.
- U-Th Pit Vol. (μm^3) = The volume of the material ablated during U-Th-Pb LA-ICP-MS analysis, which is the measured void volume as determined by white light interferometry minus the pit.

- [^{4}He] (nmoles/g) = The ^{4}He concentration in nmoles/g calculated from the blank corrected measured He amount in moles and the helium laser pit volume converted to an ablated sample mass using a nominal zircon density of 4.65 g/cm^{3}.
- [^{238}U] (nmoles/g) = The U concentration in nmoles/g.
- [^{232}Th] (nmoles/g) = The Th concentration in nmoles/g.
- ^{232}Th/^{238}U = ^{232}Th/^{238}U ratio
- eU (ppm) = The effective uranium concentration calculated as follows:
  U + 0.235 x Th.
- (U-Th)/He date (Ma) = The (U-Th/He) date calculated using the He, U, and Th concentrations in the table using the iterative approach.
- ^{207}Pb/^{235}U date (Ma) and err. (2σ) = The ^{207}Pb/^{235}U date and 2σ error, which includes all analytical errors including those in the U/Pb standard and downhole fractionation correction, but not errors in the decay constants.
- ^{206}Pb/^{238}U = The ^{206}Pb/^{238}U ratio as exported from the Iolite Data Reduction software.
- ^{206}Pb/^{238}U date (Ma) and err. (2σ) = The ^{206}Pb/^{238}U date and 2σ error, which includes all analytical errors including those in the U/Pb standard and downhole fractionation correction, but not errors in the decay constants.

Supplementary Table E1

(U-Th)/He and U/Pb dates by LADD of detrital zircon for sample CHB14-2A-28A-1

Grain	He Pit Vol. (µm^3)	err. (2σ)	U-Th Pit Vol. (µm^3)	err. (2σ)	[^{4}He] (nmol/g)	err. (2σ)	[^{238}U] (nmol/g)	err. (2σ)	[^{232}Th] (nmol/g)	err. (2σ)	^{232}Th/^{238}U	eU (ppm)	(U-Th)/He date (Ma)	err. (2σ)	^{207}Pb/^{235}U date (Ma)	err. (2σ)	^{206}Pb/^{238}U	err. (2σ)	^{206}Pb/^{238}U date (Ma)	err. (2σ)
1	8716	87	67741	762	9.6	0.5	170.9	6.5	212.5	19.0	1.20	53	33.8	2.2	588.0	13.0	0.0950	0.0013	18.8	7.7
2	1801.3	18	71002	811	166.3	6.3	304.2	11.3	256.4	22.9	0.82	87	344.5	18.2	557.0	13.0	0.0895	0.0012	552.3	7.1
3	1865.7	19	74614	834	747.5	20.7	910.8	33.7	682.0	60.9	0.72	256	518.6	23.9	521.0	11.0	0.0836	0.0009	517.2	5.6
4	1776.6	20	71756	786	181.5	6.0	312.0	11.5	151.4	13.5	0.47	83	391.4	19.3	550.6	11.0	0.0887	0.0010	547.5	6.2
5	2030	20	71749	802	402.0	12.7	589.5	21.9	410.8	36.7	0.67	164	438.3	21.2	543.4	8.5	0.0865	0.0009	535.0	5.2
6	2014	20	68657	773	54.1	2.2	2706.3	100.2	1802.2	160.9	0.64	747	13.4	0.7	23.1	4.5	0.0031	0.0001	19.7	0.4
7	1924.1	19	73591	802	8.2	1.1	562.8	20.8	245.4	21.9	0.42	148	10.2	1.4	19.9	1.9	0.0030	0.0001	19.0	0.5
8	2040	20	68600	772	180.1	6.7	230.4	8.6	243.2	21.7	1.02	68	468.6	24.8	534.2	10.0	0.0868	0.0011	536.7	6.7
9	2235	22	71031	788	474.9	13.1	843.1	31.2	691.6	61.8	0.79	240	356.2	16.1	499.8	7.5	0.0795	0.0010	493.3	6.1
10	2215	22	72049	789	84.2	3.0	157.3	5.8	90.7	8.1	0.56	43	354.6	18.0	531.0	16.0	0.0853	0.0013	527.8	7.5
11	1533.2	15	71862	825	243.1	9.1	386.8	14.3	260.3	23.2	0.65	107	407.0	21.4	511.0	24.0	0.0803	0.0011	497.8	6.5
12	1626.7	16	70200	790	271.1	11.2	665.2	25.1	319.6	28.5	0.46	177	277.4	15.4	670.0	15.0	0.1072	0.0015	656.5	8.6
13	1756.8	18	70930	836	251.6	11.1	413.5	15.4	514.7	46.0	1.20	127	356.1	20.7	529.0	21.0	0.0848	0.0011	524.8	6.5
14	1955.9	20	72800	819	68.1	2.3	2257.0	83.9	1357.9	121.3	0.58	615	20.5	1.0	12.3	8.3	0.0030	0.0001	19.6	0.5
15	1924.2	19	70696	771	187.5	9.8	368.2	13.7	239.8	21.5	0.63	101	333.3	21.4	539.2	9.4	0.0870	0.0010	537.6	6.1
16	2014	20	68881	797	937.1	24.9	1657.8	61.8	1091.9	97.6	0.64	457	368.3	16.5	497.8	6.5	0.0793	0.0009	491.7	5.2
17	2147	22	74462	912	845.6	22.8	1172.9	43.9	957.8	85.7	0.79	333	452.4	20.6	524.6	6.9	0.0840	0.0010	520.1	5.9
18	2067	21	80096	835	95.5	3.7	208.9	7.7	141.3	12.6	0.65	58	298.6	15.8	607.0	12.0	0.0977	0.0013	601.0	7.7
19	2343	23	68206	776	416.6	13.3	1066.3	39.7	566.9	50.7	0.51	287	263.5	12.7	757.9	15.0	0.1221	0.0029	742.9	17.0
20	1609.0	17	61482	694	756.9	21.3	1337.6	52.1	350.9	31.5	0.25	340	398.5	19.2	528.0	17.0	0.0832	0.0016	515.0	9.4
21	1582.0	17	69514	784	146.2	4.7	269.8	10.0	169.4	15.1	0.61	74	355.7	17.3	524.5	10.0	0.0853	0.0011	527.5	6.4
22	1791.4	18	71297	808	72.4	2.7	2726.5	100.8	2609.5	233.0	0.93	796	16.8	0.8	21.4	0.9	0.0030	0.0000	19.3	0.3
23	1374.8	14	72300	814	320.8	14.7	518.1	19.3	546.1	48.8	1.02	154	374.3	22.2	525.0	31.0	0.0864	0.0010	534.0	5.9
25	1829.9	19	70322	814	190.3	8.4	432.8	16.1	250.3	22.4	0.56	117	293.0	16.9	566.0	18.0	0.0926	0.0013	570.9	7.7
26	1931.1	19	74902	827	513.9	15.7	773.3	28.6	1027.3	91.7	1.29	241	382.5	18.3	544.0	11.0	0.0868	0.0010	536.5	6.2
27	1950	20	68740	756	201.7	9.4	658.2	24.4	559.4	50.0	0.82	188	195.3	11.5	560.9	8.3	0.0901	0.0011	556.1	6.2
28	2114	21	62557	739	14.3	1.3	603.2	22.5	385.1	34.4	0.62	166	16.0	1.5	16.0	24.0	0.0029	0.0002	18.9	1.4
29	2106	21	71277	795	191.9	7.7	353.7	13.1	273.2	24.4	0.75	100	346.4	18.8	529.0	21.0	0.0848	0.0013	524.9	7.7
30	2077	21	72679	866	272.7	13.7	563.4	21.0	554.1	49.5	0.95	165	298.3	18.7	496.0	7.9	0.0792	0.0010	491.2	5.7
31	1516.2	17	69100	778	970.3	26.6	1403.3	52.4	1535.6	137.6	1.06	420	413.6	19.0	597.1	7.1	0.0963	0.0012	592.8	6.9
32	1318.8	15	74685	831	9.6	1.7	298.1	11.1	219.4	19.6	0.71	83	21.3	3.8	22.9	4.5	0.0029	0.0001	18.8	0.8
33	4248	44	107868	1138	22.3	1.0	125.6	4.7	87.7	7.8	0.68	35	117.5	6.5	571.0	12.0	0.0921	0.0012	567.8	7.1
34	1799.0	19	71853	819	160.4	6.6	370.6	13.7	283.1	25.3	0.74	104	278.5	15.2	535.0	20.0	0.0866	0.0010	535.3	6.0
35	1516.2	16	71420	806	105.4	4.0	114.5	4.2	112.3	10.0	0.95	34	555.2	29.7	599.0	95.0	0.0857	0.0021	530.0	13.0

Supplementary Table E1 Continued

Grain	He Pit Vol. (μm^3)	err. (2σ)	U-Th Pit Vol. (μm^3)	err. (2σ)	[^{4}He] (nmol/g)	err. (2σ)	[^{238}U] (nmol/g)	err. (2σ)	[^{232}Th] (nmol/g)	err. (2σ)	^{232}Th/^{238}U	eU (ppm)	(U-Th)/He date (Ma)	err. (2σ)	^{207}Pb/^{235}U date (Ma)	err. (2σ)	^{206}Pb/^{238}U	err. (2σ)	^{206}Pb/^{238}U date (Ma)	err. (2σ)
36	1384.1	15	69266	817	772.0	22.4	1611.5	59.8	783.7	70.0	0.47	429	324.3	15.1	500.8	8.8	0.0801	0.0009	496.9	5.3
37	1764.4	18	74309	837	76.5	2.7	151.6	5.7	97.8	8.8	0.62	42	330.7	16.8	499.0	84.0	0.0853	0.0019	528.0	11.0
38	1141.8	12	60800	684	1013.8	31.2	3603.3	133.2	1323.0	120.6	0.36	936	197.5	9.3	499.0	7.8	0.0804	0.0011	498.0	6.6
39	1904.2	19	75400	849	152.6	5.2	392.1	14.6	224.7	20.1	0.55	106	260.4	12.9	553.9	9.6	0.0901	0.0012	555.9	7.0
40	1949.0	20	70940	817	172.8	6.5	366.5	13.6	240.4	21.5	0.63	101	308.9	16.1	527.8	9.5	0.0847	0.0010	524.1	5.9
41	878.0	9	67675	767	1694.1	45.3	2382.1	88.4	1236.9	110.5	0.50	638	471.9	21.5	537.4	14.0	0.0869	0.0017	536.9	9.9
42	3042	31	72880	835	187.4	7.6	1005.3	37.9	825.3	73.9	0.79	286	120.2	6.5	537.1	7.1	0.0861	0.0010	532.1	5.9
43	1898.6	20	75723	816	3.3	1.2	147.2	5.4	74.9	6.7	0.49	39	15.5	5.5	19.0	1.6	0.0030	0.0003	19.2	1.6
44	2225	27	73004	818	71.9	2.7	269.8	10.1	172.7	15.5	0.62	74	177.2	9.2	576.0	11.0	0.0924	0.0013	569.5	7.6
45	1578.4	17	68479	743	191.1	7.1	352.7	13.1	220.5	19.7	0.61	97	355.7	18.6	562.0	9.5	0.0904	0.0010	558.8	6.2
46	1873.5	19	70500	794	1451.4	38.3	1806.2	67.2	1080.9	96.6	0.58	492	522.4	23.7	544.4	6.3	0.0877	0.0010	541.8	5.7
47	1736.7	18	72881	822	153.7	5.9	303.7	11.3	240.5	21.5	0.77	86	322.6	17.1	539.8	10.0	0.0867	0.0012	535.9	7.0
48	1840.6	19	71408	833	201.3	8.9	472.5	17.6	368.7	32.9	0.76	133	273.3	15.7	547.0	19.0	0.0877	0.0017	541.8	10.0
49	1833.4	18	71134	880	241.7	12.5	376.7	14.3	200.8	18.0	0.52	101	426.4	27.7	544.6	9.9	0.0875	0.0010	540.5	6.2
50	1703.0	19	72000	810	88.3	3.5	187.9	7.0	191.0	17.1	0.98	55	288.1	15.5	510.0	45.0	0.0836	0.0015	517.2	9.1
51	942.4	10	71200	801	579.1	22.0	806.3	29.9	529.1	47.2	0.64	222	464.2	24.7	500.0	13.0	0.0804	0.0010	498.6	6.0
52	1474.8	16	71115	795	383.4	20.5	466.6	17.4	177.5	15.9	0.37	122	556.2	37.4	515.0	24.0	0.0863	0.0010	533.5	6.2
54	1323.6	15	68472	782	486.1	22.7	1765.3	66.1	310.6	27.8	0.17	440	201.3	12.1	587.0	13.0	0.0948	0.0015	583.7	9.0
57	1515.8	17	72378	864	616.9	18.2	844.6	32.3	515.3	46.1	0.59	231	475.8	22.9	552.4	8.1	0.0884	0.0011	546.3	6.6
58	1698.8	17	70953	844	92.8	3.3	303.0	11.3	128.8	11.5	0.41	80	212.1	10.9	720.0	13.0	0.1185	0.0020	722.0	12.0
59	3109	33	74725	814	113.9	4.9	371.3	13.8	235.3	21.0	0.61	102	203.7	11.4	541.0	9.2	0.0874	0.0011	539.9	6.3
60	1824.1	20	71587	801	345.2	17.0	683.7	25.4	518.6	46.3	0.73	192	323.9	20.0	547.9	8.7	0.0876	0.0010	541.2	5.8
62	1619.8	17	70131	819	370.3	15.9	611.8	22.7	453.8	40.5	0.72	171	387.4	22.0	540.1	8.1	0.0869	0.0009	537.3	5.4
63	2048	27	66600	750	81.4	3.0	241.2	8.9	180.8	16.2	0.73	68	218.9	11.2	551.0	30.0	0.0889	0.0011	548.9	6.5
64	2104	22	71116	828	64.1	2.7	277.1	10.4	161.2	14.4	0.56	75	155.9	8.5	557.0	36.0	0.0910	0.0013	561.5	7.6
65	1774.6	18	68237	760	579.6	16.2	1104.2	40.8	1061.0	94.7	0.93	323	324.2	14.8	510.0	7.6	0.0814	0.0009	504.7	5.5
66	5989	60	79294	892	30.5	1.0	312.8	12.0	345.1	31.3	1.07	94	59.9	2.9	537.0	29.0	0.0858	0.0011	530.9	6.6
67	687.4	7	69164	813	271.0	9.1	368.7	13.7	155.6	13.9	0.41	97	496.2	25.0	561.0	23.0	0.0927	0.0012	572.1	7.1
68	1567.9	17	70300	791	576.9	17.5	818.6	30.4	613.0	54.8	0.72	230	448.1	21.3	562.0	14.0	0.0918	0.0010	565.9	6.2
69	1597.5	17	71600	806	208.2	7.0	693.3	25.7	319.1	28.5	0.45	184	206.5	10.2	797.3	9.0	0.1314	0.0014	795.8	8.2
70	1725.0	18	67254	744	544.2	15.5	931.7	34.5	948.8	84.8	0.99	275	356.0	16.4	537.0	12.0	0.0864	0.0010	534.3	6.0
71	1860.3	19	72952	818	308.1	15.0	427.5	16.0	224.7	20.1	0.51	115	477.3	29.8	554.1	11.0	0.0895	0.0011	552.6	6.4
72	2128	22	70420	789	716.4	19.6	1409.2	52.6	1135.2	101.5	0.78	400	323.3	14.6	537.7	12.0	0.0872	0.0010	539.0	5.8
73	1671.1	17	71271	837	397.3	19.4	946.0	35.4	714.5	63.9	0.73	266	270.9	16.6	563.2	7.1	0.0900	0.0010	555.2	5.7
74	1788.3	18	68973	754	145.1	5.4	381.2	14.2	345.3	30.9	0.88	110	239.2	12.4	541.5	29.0	0.0855	0.0010	528.6	6.1

Supplementary Table E1 Continued

Grain	He Pit Vol. (µm^3)	err. (2σ)	U-Th Pit Vol. (µm^3)	err. (2σ)	[^{4}He] (nmol/g)	err. (2σ)	[^{238}U] (nmol/g)	err. (2σ)	[^{232}Th] (nmol/g)	err. (2σ)	^{232}Th/^{238}U	eU (ppm)	(U-Th)/He date (Ma)	err. (2σ)	^{207}Pb/^{235}U date (Ma)	err. (2σ)	^{206}Pb/^{238}U	err. (2σ)	^{206}Pb/^{238}U date (Ma)	err. (2σ)
75	1178.0	12	78675	932	212.8	6.9	237.7	9.0	208.5	18.7	0.85	68	550.8	27.5	526.0	40.0	0.0867	0.0015	536.0	9.2
76	1912.6	19	72306	819	135.5	5.2	233.8	8.8	143.4	12.9	0.59	64	380.5	20.3	535.0	11.0	0.0866	0.0011	535.3	6.6
77	1831.3	19	71400	804	101.2	3.5	211.2	7.9	84.9	7.6	0.39	55	329.7	16.7	521.0	11.0	0.0818	0.0011	506.8	6.5
78	1970	21	86400	973	849.5	23.0	2476.0	92.5	1049.1	93.9	0.41	651	237.1	10.7	701.2	15.0	0.1128	0.0024	689.2	14.0
79	1224.5	14	72700	818	1042.6	29.0	1573.1	58.5	833.1	74.4	0.51	423	440.1	20.3	648.6	7.7	0.1050	0.0011	643.3	6.2
80	1811.7	18	71138	777	180.8	6.9	418.9	15.5	408.8	36.6	0.94	123	267.1	14.0	529.0	23.0	0.0850	0.0011	525.5	6.7
81	1467.4	16	73600	828	146.5	5.4	261.4	9.7	170.8	15.3	0.63	72	365.6	19.0	547.0	11.0	0.0885	0.0011	546.7	6.4
82	1212.8	13	73726	871	585.2	26.5	749.5	27.8	520.9	46.5	0.67	208	499.3	29.6	559.0	27.0	0.0925	0.0009	570.5	5.3
83	1508.1	15	73800	831	937.3	25.3	1474.6	54.6	1009.4	90.1	0.66	409	410.6	18.5	504.4	6.3	0.0807	0.0009	500.2	5.4
84	1244.0	13	71297	879	191.6	7.6	301.6	11.3	223.7	20.0	0.72	84	406.0	22.1	549.0	26.0	0.0863	0.0011	533.6	6.6
85	1696.8	18	73752	805	81.4	3.3	160.4	5.9	142.4	12.7	0.86	46	317.8	17.2	545.0	30.0	0.0861	0.0013	532.6	7.7
87	1732.0	18	72867	797	165.1	5.9	386.4	14.3	255.4	22.8	0.64	107	280.4	14.2	505.4	9.0	0.0814	0.0010	504.2	6.0
88	1809.7	18	71118	808	521.6	15.7	850.4	31.7	581.7	52.0	0.66	236	396.7	18.8	507.9	7.2	0.0813	0.0009	504.0	5.4
89	1984.3	20	71778	900	108.2	4.2	215.1	8.1	163.6	14.6	0.74	60	322.7	17.1	537.0	11.0	0.0848	0.0012	524.7	7.1
90	1941.2	20	67783	773	1205.2	31.8	2307.3	85.5	1829.2	163.4	0.77	653	332.7	14.8	494.5	8.9	0.0795	0.0009	493.0	5.4
91	1514.6	16	71577	886	159.7	5.3	265.9	9.9	150.9	13.5	0.55	72	397.3	19.8	565.0	18.0	0.0913	0.0012	563.2	6.8
92	1339.0	14	70903	870	161.2	6.2	265.8	9.9	248.4	22.2	0.90	77	374.7	20.1	515.8	10.0	0.0813	0.0010	503.8	6.2
93	1716.8	17	79509	948	414.3	17.9	640.9	24.4	344.1	30.9	0.52	172	429.2	24.8	573.4	8.6	0.0928	0.0012	572.2	7.2
94	1313.9	14	71168	795	601.3	18.8	798.0	29.6	739.4	66.1	0.90	232	462.8	22.4	744.0	18.0	0.1198	0.0023	729.5	13.0
95	1636.0	17	71759	790	149.0	5.1	353.0	13.2	267.4	23.9	0.73	99	272.1	13.6	511.0	9.4	0.0817	0.0011	506.4	6.5
96	1525.3	16	75500	850	163.0	5.8	428.4	16.0	498.3	44.7	1.13	130	228.3	11.7	516.0	24.0	0.0847	0.0010	524.0	5.9
100	1545.3	16	73248	791	73.5	2.8	334.2	12.5	415.2	37.3	1.20	103	131.1	6.9	634.0	22.0	0.1025	0.0014	629.2	8.1
101	1793.1	18	75229	820	578.6	16.6	698.1	26.2	548.2	49.0	0.76	197	520.0	24.4	556.9	9.1	0.0895	0.0010	552.5	5.7
102	1564.9	16	68895	777	249.6	10.3	613.8	22.8	464.4	41.5	0.73	172	262.4	14.4	570.0	7.9	0.0918	0.0010	566.4	6.2
104	1668.5	17	71552	792	128.9	4.1	256.4	9.5	174.2	15.6	0.66	71	327.6	15.8	551.0	10.0	0.0901	0.0013	556.0	7.6
106	1506.7	16	73100	823	651.7	19.6	902.1	33.5	574.5	51.3	0.62	248	468.5	22.3	558.9	7.9	0.0898	0.0011	554.6	6.7
108	1716.8	18	69989	862	184.9	6.6	412.9	15.5	319.6	28.6	0.75	116	287.4	14.6	542.9	8.6	0.0876	0.0010	541.1	6.1
109	2230	22	73760	814	190.7	7.7	411.0	15.8	312.5	28.3	0.74	116	298.3	16.4	548.3	9.6	0.0887	0.0012	547.9	7.1
110	1070.0	11	68600	772	512.4	25.3	768.7	28.6	867.8	77.6	1.09	232	396.9	24.8	530.7	7.4	0.0850	0.0010	526.0	5.7

Supplementary Table E2
(U-Th)/He and U/Pb dates by LADD of detrital zircon for sample CHB14-2A-29A-1

Grain	He Pit Vol. (μm^3)	err. (2σ)	U-Th Pit Vol. (μm^3)	err. (2σ)	[^{4}He] (nmol/g)	err. (2σ)	[^{238}U] (nmol/g)	err. (2σ)	[^{232}Th] (nmol/g)	err. (2σ)	^{232}Th/^{238}U	eU (ppm)	(U-Th)/He date (Ma)	err. (2σ)	^{207}Pb/^{235}U date (Ma)	err. (2σ)	^{206}Pb/^{238}U	err. (2σ)	^{206}Pb/^{238}U date (Ma)	err. (2σ)
1	1461.4	15.3	67872	777	376.8	24.8	1965.7	75.1	1094.8	98.6	0.54	531	130.2	9.8	529.8	9.1	0.0852	0.0009	527.1	5.0
2	1431.1	15.3	68151	740	463.5	22.7	1819.4	67.4	756.2	67.5	0.40	477	177.3	10.8	761.1	6.3	0.1242	0.0013	754.5	7.7
4	1389.0	14.7	68715	730	110.2	3.8	4985.3	183.3	3493.1	311.5	0.68	1386	14.7	0.7	32.0	23.6	0.0039	0.0002	24.8	1.4
5	1374.2	15.3	69769	790	189.0	7.2	671.9	24.9	573.1	51.3	0.83	192	179.5	9.3	558.9	6.5	0.0898	0.0009	554.5	5.1
6	1338.9	14.9	71079	839	485.3	24.7	1089.5	40.6	1169.3	104.7	1.04	325	270.7	17.1	580.3	17.2	0.0924	0.0012	569.6	6.8
7	1322.5	14.0	70183	783	104.8	4.3	271.5	10.1	188.2	16.8	0.67	75	252.4	13.7	568.2	9.9	0.0917	0.0011	565.0	6.4
8	1011.0	10.7	60760	693	1316.8	36.4	3100.1	114.7	2987.6	266.8	0.93	906	263.5	11.9	481.7	8.9	0.0776	0.0012	482.0	7.4
9	1074.0	11.3	73138	875	80.6	3.4	2850.8	106.3	1867.9	167.2	0.63	785	19.0	1.0	21.4	1.1	0.0030	0.0000	19.6	0.3
10	1070.0	11.3	53038	659	24.7	2.8	930.5	34.8	630.5	56.5	0.66	257	17.7	2.1	22.1	6.8	0.0030	0.0001	19.3	0.6
12	1661.6	16.6	74528	818	106.6	3.2	211.1	7.8	176.4	15.7	0.81	60	319.3	14.9	559.5	10.0	0.0871	0.0010	539.0	6.1
13	1268.7	13.7	65681	750	662.6	22.1	818.1	31.0	658.3	59.1	0.78	232	506.9	25.5	564.7	7.6	0.0909	0.0010	560.9	5.9
14	1311.3	15.0	81550	888	208.8	7.8	230.2	8.6	270.2	24.2	1.14	70	529.7	28.2	544.2	11.3	0.0873	0.0012	539.0	7.1
16	964.2	10.2	71138	829	3056.0	80.7	3314.4	123.3	2527.1	225.8	0.74	932	578.0	26.3	565.3	8.8	0.0910	0.0010	561.6	6.0
17	1402.0	14.8	68206	779	114.9	5.3	822.9	30.6	466.6	41.7	0.55	223	94.9	5.5	595.1	11.9	0.0979	0.0010	602.0	5.8
18	1254.0	13.2	71516	782	393.9	22.0	671.5	24.8	371.5	33.2	0.54	181	389.5	26.4	565.3	7.6	0.0919	0.0011	566.6	6.5
19	905.2	9.6	73409	836	434.1	19.7	488.8	18.3	490.6	43.9	0.97	144	534.5	31.9	553.0	8.3	0.0887	0.0011	547.5	6.6
21	1550.5	16.3	76447	850	918.9	24.9	1524.1	56.4	800.0	71.4	0.51	409	402.2	18.3	537.6	4.9	0.0866	0.0009	535.4	5.2
22	1139.1	11.9	72263	789	997.9	28.8	1071.3	39.5	2237.1	199.7	2.02	379	470.8	23.4	516.5	12.8	0.0839	0.0010	519.0	5.8
23	1042.0	11.4	73885	850	38.7	2.6	178.7	6.6	122.7	11.0	0.66	50	143.2	10.8	538.8	13.2	0.0875	0.0012	540.8	7.0
24	1435.8	15.1	71500	860	173.5	5.7	292.3	10.9	332.7	29.7	1.10	88	354.0	17.5	546.5	10.7	0.0867	0.0009	535.8	5.4
25	1358.4	14.7	68999	756	91.8	3.4	191.3	7.1	147.0	13.1	0.74	54	307.5	16.0	551.9	11.8	0.0887	0.0012	547.8	6.9
28	1769.5	18.4	75100	808	70.5	2.6	2145.9	79.4	1772.1	158.2	0.80	611	21.4	1.1	24.2	9.5	0.0031	0.0001	20.0	0.9
29	1774.5	17.9	73419	826	329.5	13.1	546.6	20.3	486.1	43.5	0.86	158	375.7	20.3	545.3	7.2	0.0866	0.0010	535.5	5.6
30	1649.8	16.7	72730	817	330.2	12.1	494.5	18.3	376.0	33.6	0.74	139	424.5	22.0	570.0	18.0	0.0934	0.0013	575.6	7.7
32	1620.0	17.1	61291	699	79.7	3.2	298.1	11.1	392.9	35.1	1.28	93	156.9	8.4	553.0	38.2	0.0935	0.0013	576.3	7.6
34	1493.2	15.7	76466	857	466.6	18.9	754.6	28.0	338.6	30.2	0.43	199	418.2	23.1	572.3	9.3	0.0927	0.0010	571.4	5.7
36	1752.5	17.6	74500	801	593.7	17.8	814.2	30.0	697.6	62.2	0.83	233	454.0	21.4	526.8	8.5	0.0851	0.0010	526.5	5.8
43	1598.3	16.1	72543	836	623.7	19.3	1115.1	41.6	943.1	84.5	0.82	319	352.1	16.8	708.4	9.1	0.1162	0.0014	708.8	7.8
44	1557.1	16.5	71034	812	136.2	4.7	282.1	10.5	214.4	19.2	0.74	79	310.0	15.5	525.6	37.6	0.0871	0.0013	538.5	7.6
48	1382.9	15.0	43398	617	286.4	10.1	865.0	33.0	417.2	37.5	0.47	230	226.3	11.6	564.2	18.7	0.0927	0.0013	571.3	7.7
49	1002.0	10.6	67110	783	922.4	29.8	1555.4	57.7	719.9	64.3	0.45	412	400.6	19.6	505.4	7.4	0.0821	0.0009	508.6	5.6
55	1692.2	17.4	77600	834	124.1	3.8	396.9	14.8	281.0	25.1	0.69	110	204.7	9.6	566.5	7.6	0.0910	0.0009	561.7	5.1
57	1691.8	17.0	66687	782	616.3	17.5	1216.0	45.3	782.4	70.0	0.62	334	332.3	15.3	587.8	6.3	0.0944	0.0011	581.5	6.6
58	1433.0	15.1	74143	880	115.8	4.4	236.3	8.9	195.0	17.5	0.80	67	310.8	16.4	515.2	41.0	0.0869	0.0011	537.0	6.8

Supplementary Table E2 Continued

Grain	He Pit Vol. (μm³)	err. (2σ)	U-Th Pit Vol. (μm³)	err. (2σ)	[⁴He] (nmol/g)	err. (2σ)	[²³⁸U] (nmol/g)	err. (2σ)	[²³²Th] (nmol/g)	err. (2σ)	²³²Th/²³⁸U	eU (ppm)	(U-Th)/He date (Ma)	err. (2σ)	²⁰⁷Pb/²³⁵U date (Ma)	err. (2σ)	²⁰⁶Pb/²³⁸U	err. (2σ)	²⁰⁶Pb/²³⁸U date (Ma)	err. (2σ)
59	1839.3	22.6	75800	815	6.1	1.1	230.9	8.6	163.8	14.6	0.69	64	17.4	3.2	18.9	7.8	0.0030	0.0004	19.0	2.3
60	1655.6	17.0	72700	782	57.6	2.9	224.8	8.4	166.6	15.1	0.72	63	167.2	10.4	522.5	12.8	0.0824	0.0011	510.3	6.7
65	1509.0	15.9	78671	982	1582.5	42.1	3326.3	124.9	703.7	62.9	0.20	836	340.5	15.7	679.4	4.6	0.1102	0.0011	673.7	6.3
67	1770.8	17.7	55081	634	145.7	5.1	455.7	17.0	512.2	45.9	1.09	137	193.7	9.7	511.6	21.4	0.0854	0.0009	528.1	5.5
68	1672.2	17.3	53400	684	731.2	20.0	2802.8	105.6	2165.4	193.9	0.75	790	169.2	7.6	716.4	7.1	0.1161	0.0014	708.2	7.9
73	1503.8	15.9	104749	1165	267.3	10.0	984.4	36.8	688.2	61.6	0.68	274	178.5	9.2	567.6	9.3	0.0927	0.0010	571.2	6.0
76	2266.0	23.9	89653	987	158.0	5.2	520.7	19.4	651.1	58.6	1.21	160	180.0	8.8	540.6	18.5	0.0893	0.0012	551.3	7.0
77	1394.0	14.7	91900	988	331.1	15.1	601.2	22.4	674.5	60.4	1.09	181	330.1	19.5	601.9	6.8	0.0972	0.0010	597.7	5.6
78	1725.5	17.3	73794	810	1082.0	29.5	2586.1	95.7	2463.1	220.0	0.92	754	260.2	11.7	543.1	4.4	0.0875	0.0010	540.8	5.7
82	2051.4	20.8	94736	1032	198.6	8.0	342.8	12.7	284.5	25.4	0.80	98	365.4	19.9	505.4	26.0	0.0855	0.0010	528.6	5.8
83	1821.1	18.7	107132	1111	20.0	1.3	221.0	8.2	283.0	25.3	1.24	68	53.9	3.9	607.5	23.0	0.0998	0.0009	613.0	5.3
91	1692.8	17.0	75800	815	61.8	2.2	2393.1	88.6	1594.5	142.5	0.64	661	17.3	0.9	21.4	4.0	0.0031	0.0001	20.2	0.4
93	1838.8	18.4	95442	1030	414.8	19.7	933.5	34.6	450.1	40.2	0.47	248	301.6	18.2	511.8	5.1	0.0821	0.0009	508.7	5.4
96	1207.9	13.0	75996	804	918.9	27.5	1072.8	40.0	905.2	81.0	0.82	307	531.0	25.4	529.2	5.7	0.0847	0.0008	524.2	4.8
101	884.3	9.3	72125	808	887.2	30.2	1267.7	47.5	904.2	81.2	0.69	353	448.0	22.6	652.8	12.8	0.1051	0.0016	644.4	9.2
103	1097.2	13.2	78873	827	549.9	30.3	1189.5	44.0	862.9	77.0	0.70	332	299.1	19.9	556.0	7.7	0.0894	0.0012	551.9	7.1
105	1403.8	15.3	89471	945	238.4	8.7	456.9	17.0	327.0	29.2	0.69	127	337.2	17.4	560.1	13.5	0.0927	0.0011	571.4	6.2
106	1347.4	13.9	91100	980	702.0	21.0	856.0	32.1	269.9	24.2	0.31	220	562.3	27.5	720.9	7.1	0.1174	0.0014	715.8	8.3
110	1106.0	13.6	91981	1176	179.9	6.4	260.5	10.0	134.8	12.1	0.50	70	458.9	24.1	516.5	9.2	0.0837	0.0012	517.9	7.1
2_1	1452.5	14.5	43555	440	957.6	25.8	3776.2	139.8	4064.0	363.3	1.04	1127	155.5	6.9	520.7	8.5	0.0808	0.0007	500.7	4.1
2_3	6375.7	64.2	81752	848	1880.3	50.0	3180.7	117.2	3075.2	274.6	0.94	930	363.5	16.2	553.0	11.2	0.0885	0.0009	546.5	5.2
2_4	6637.2	66.4	82613	855	670.8	18.0	642.8	23.7	446.5	39.8	0.67	178	657.8	30.2	763.9	12.9	0.1239	0.0012	753.0	6.9
2_5	6150.3	61.7	85498	920	166.1	4.8	284.4	10.5	198.8	17.7	0.68	79	377.2	17.3	564.2	24.4	0.0903	0.0013	557.3	7.7
2_6	6492.0	67.5	83044	881	507.1	14.3	665.8	24.6	351.2	31.4	0.51	179	503.0	23.4	770.1	12.8	0.1246	0.0010	757.0	5.7
2_7	6850.2	68.6	81181	830	787.7	21.7	1160.2	42.6	1483.3	132.4	1.24	359	393.8	18.0	776.3	10.9	0.1245	0.0015	756.4	8.6
2_8	7326.0	73.6	70093	734	1159.9	31.8	1824.6	67.5	1017.8	90.9	0.54	493	420.5	19.2	506.6	12.3	0.0812	0.0008	503.3	4.9
2_9	6352.1	63.7	80631	863	175.0	5.1	555.9	20.5	238.6	21.3	0.42	146	217.7	10.1	822.5	24.0	0.1323	0.0018	801.0	10.2
2_10	6698.8	67.7	81697	861	232.8	6.6	426.2	15.8	279.3	24.9	0.63	117	356.5	16.3	552.4	17.1	0.0873	0.0011	539.6	6.5
2_11	8052.0	80.5	85204	898	576.6	16.0	2229.1	82.7	813.7	72.7	0.35	579	181.9	8.3	516.5	7.9	0.0809	0.0007	501.2	4.4
2_12	7042.9	70.7	81198	869	667.1	17.6	1062.5	39.5	983.9	88.0	0.90	308	388.2	17.4	740.7	11.3	0.1157	0.0013	705.8	7.5
2_13	6013.9	60.6	81515	860	724.8	19.3	2420.4	89.2	1070.2	95.5	0.43	639	206.7	9.2	772.5	11.9	0.1231	0.0012	748.4	6.9
2_14	7205.0	72.3	79756	851	1139.6	29.6	3002.7	112.4	430.3	38.7	0.14	743	277.4	12.7	584.3	13.1	0.0903	0.0008	557.2	4.7
2_15	7273.1	73.0	77979	813	1106.3	28.9	2004.4	75.4	1257.3	112.9	0.61	549	362.1	16.2	604.1	9.5	0.0910	0.0009	561.7	5.6
2_17	1399.4	14.4	42647	437	1793.4	47.1	3130.0	115.4	3309.8	297.8	1.02	931	347.0	15.5	556.0	13.5	0.0813	0.0008	503.6	4.9
2_18	1143.7	11.5	52692	539	385.3	21.7	499.6	18.5	265.2	23.7	0.51	134	508.9	35.2	560.1	25.8	0.0859	0.0013	531.2	7.7

Supplementary Table E2 Continued

Grain	He Pit Vol. (μm³)	err. (2σ)	U-Th Pit Vol. (μm³)	err. (2σ)	[⁴He] (nmol/g)	err. (2σ)	[²³⁸U] (nmol/g)	err. (2σ)	[²³²Th] (nmol/g)	err. (2σ)	²³²Th/²³⁸U	eU (ppm)	(U-Th)/He date (Ma)	err. (2σ)	²⁰⁷Pb/²³⁵U date (Ma)	err. (2σ)	²⁰⁶Pb/²³⁸U	err. (2σ)	²⁰⁶Pb/²³⁸U date (Ma)	err. (2σ)
2_19	1201.8	12.3	50441	510	213.7	7.9	277.1	10.4	170.8	15.3	0.60	76	500.6	26.4	621.9	30.8	0.0900	0.0019	555.5	11.2
2_20	6715.9	67.9	82983	856	1245.5	32.6	2290.0	84.7	2250.1	201.3	0.95	672	334.3	14.9	515.8	12.8	0.0815	0.0010	505.1	6.0
2_21	6605.6	66.1	83502	863	461.2	12.3	1293.2	47.6	1397.3	124.7	1.05	386	217.4	9.6	756.3	19.8	0.1240	0.0017	753.6	9.7
2_22	6657.1	66.6	83972	920	187.0	5.2	866.1	32.3	490.6	43.8	0.55	234	146.1	6.6	718.9	16.0	0.1160	0.0014	707.5	8.1
2_23	6353.0	64.1	83513	858	762.6	19.9	933.5	34.3	459.6	41.0	0.48	249	541.5	24.5	538.8	9.6	0.0877	0.0008	541.8	4.9
2_24	8403.0	84.4	78910	836	347.5	9.1	4947.9	187.0	8122.0	730.3	1.59	1629	39.4	1.8	439.7	41.4	0.0698	0.0013	435.0	7.8
2_25	7125.1	71.3	81207	860	992.8	25.7	4524.9	167.7	4614.7	412.3	0.99	1336	136.2	5.9	483.6	18.9	0.0701	0.0010	436.8	6.0
2_26	6717.6	67.2	84383	886	645.4	17.2	1148.3	42.3	822.2	73.5	0.69	320	362.3	16.2	779.1	12.3	0.1237	0.0010	751.8	5.7
2_27	6758.0	67.8	83179	890	455.4	12.0	656.7	24.4	542.7	48.4	0.80	187	435.0	19.5	557.7	14.1	0.0892	0.0012	550.8	7.1
2_28	7149.7	72.0	82072	860	666.1	17.6	2368.1	90.1	21.6	1.9	0.01	569	213.1	10.1	585.5	10.8	0.0876	0.0008	541.4	4.9
2_29	7207.0	72.1	80740	836	350.7	9.2	505.5	19.0	192.6	17.3	0.37	132	473.3	21.8	709.9	20.2	0.1152	0.0020	702.9	11.6
2_30	5930.8	59.7	83857	897	461.8	12.1	816.6	30.2	592.5	53.0	0.70	228	363.9	16.2	709.9	15.6	0.1099	0.0013	672.2	7.6
2_31	6311.9	63.1	84120	885	517.5	13.6	709.9	26.3	579.4	51.7	0.79	202	457.2	20.5	560.1	12.9	0.0874	0.0009	540.3	5.1
2_32	6724.7	67.4	83633	883	330.5	8.8	474.5	17.7	567.9	50.7	1.16	145	409.4	18.6	544.2	29.8	0.0874	0.0018	540.1	10.7
2_33	6804.7	69.4	75927	795	447.4	11.8	4179.3	155.3	2577.6	230.8	0.60	1142	72.2	3.1	574.6	16.1	0.0907	0.0016	559.7	9.5
2_35	4500.0	45.3	80914	849	997.6	26.0	2335.5	86.2	554.6	49.5	0.23	590	305.1	13.8	538.2	44.8	0.0808	0.0020	500.9	11.9
2_36	3443.1	35.0	75297	794	873.1	23.0	1191.3	44.9	1036.6	92.7	0.84	342	455.2	20.6	649.6	18.2	0.0981	0.0019	603.3	11.2
2_38	1173.9	11.8	43801	447	361.0	18.1	807.8	30.0	418.7	37.4	0.50	216	301.2	18.8	692.1	18.0	0.1066	0.0014	653.0	8.2
2_39	3256.8	33.1	81672	881	273.6	8.6	407.7	15.0	258.6	23.2	0.61	112	436.7	21.1	548.3	17.2	0.0859	0.0011	531.2	6.5
2_40	1235.2	12.5	44234	449	140.8	5.9	271.8	10.1	154.2	13.8	0.55	74	344.4	19.2	552.4	33.0	0.0868	0.0018	536.6	10.7
2_41	4516.5	45.5	81676	880	248.5	6.6	431.5	15.9	312.0	27.8	0.70	120	370.5	16.6	558.3	22.2	0.0882	0.0011	544.9	6.5
2_42	5287.2	52.9	76772	865	777.5	20.8	1959.2	74.8	1461.9	131.9	0.72	549	256.7	11.6	548.9	10.6	0.0854	0.0008	528.2	4.7
2_43	4768.1	47.8	83557	899	539.1	14.2	1027.6	38.2	1848.4	165.1	1.74	347	281.4	13.1	617.5	13.8	0.0985	0.0012	605.6	7.0
2_44	4471.3	45.8	70732	748	87.8	3.3	7665.9	283.8	5912.9	528.2	0.75	2160	7.5	0.4	337.3	32.8	0.0525	0.0008	329.9	5.1
2_45	1451.4	14.5	45599	465	335.0	16.3	1010.9	37.7	974.6	87.3	0.93	295	206.5	12.5	551.9	19.5	0.0861	0.0014	532.4	8.3
2_46	5013.3	50.8	75029	813	1525.0	39.5	5093.3	188.2	2519.4	224.9	0.48	1358	204.5	9.0	642.6	18.3	0.0987	0.0017	606.8	10.0
2_47	4985.6	50.0	80153	842	1437.3	37.7	2618.9	97.3	2449.7	219.2	0.91	761	340.1	15.1	535.8	13.2	0.0852	0.0008	527.0	4.7
2_48	4925.2	49.3	81457	875	38.1	1.4	216.2	8.2	105.3	9.5	0.47	58	121.4	6.3	710.9	27.8	0.1153	0.0021	703.5	12.1
2_49	935.2	10.1	43665	448	798.9	23.9	1203.8	44.2	888.7	79.2	0.71	337	423.7	19.9	508.5	24.0	0.0808	0.0014	500.9	8.4
2_50	4725.7	47.8	77800	827	152.5	5.2	5085.7	188.1	3187.8	284.7	0.61	1393	20.3	1.0	25.6	2.7	0.0030	0.0001	19.4	0.4
2_51	5469.2	54.7	103762	1103	218.0	6.5	318.3	11.8	54.7	4.9	0.17	79	487.4	23.9	585.5	97.0	0.0883	0.0019	545.5	11.3
2_52	4866.0	48.7	81960	851	555.4	14.6	688.4	25.6	539.6	48.2	0.76	194	506.9	22.9	579.2	18.4	0.0897	0.0010	553.8	5.9
2_55	3801.6	38.4	74691	788	639.3	17.2	6524.4	243.0	3185.0	289.0	0.47	1738	67.8	3.0	565.9	8.7	0.0879	0.0012	543.1	7.1
2_57	5168.4	51.8	113335	1186	763.0	20.2	2266.8	89.9	1146.1	103.1	0.49	606	228.9	10.6	765.4	15.3	0.1158	0.0016	706.3	9.2
2_58	4755.7	47.7	81455	848	173.7	4.9	290.1	10.8	218.8	19.6	0.73	81	382.6	17.6	643.7	42.0	0.0949	0.0022	584.5	13.0

Supplementary Table E2 Continued

Grain	**He Pit Vol. (μm^3)**	**err. (2σ)**	**U-Th Pit Vol. (μm^3)**	**err. (2σ)**	**[^{4}He] (nmol/g)**	**err. (2σ)**	**[^{238}U] (nmol/g)**	**err. (2σ)**	**[^{232}Th] (nmol/g)**	**err. (2σ)**	**^{232}Th/^{238}U**	**eU (ppm)**	**(U-Th)/He date (Ma)**	**err. (2σ)**	**^{207}Pb/^{235}U date (Ma)**	**err. (2σ)**	**^{206}Pb/^{238}U**	**err. (2σ)**	**^{206}Pb/^{238}U date (Ma)**	**err. (2σ)**
2_59	4637.0	46.7	73498	769	136.8	6.1	183.1	6.8	124.0	11.1	0.66	51	480.3	28.2	588.9	26.8	0.0886	0.0017	547.3	10.1
2_60	3756.8	39.2	78880	814	1534.9	40.5	2237.6	82.1	1974.1	176.1	0.85	644	426.1	19.0	512.2	7.4	0.0829	0.0007	513.2	3.9
2_61	1275.8	12.8	45652	465	493.8	22.1	798.9	29.5	877.4	78.3	1.06	239	370.8	21.6	802.0	18.4	0.1282	0.0015	777.6	8.6
2_62	3881.6	39.5	76283	790	155.3	5.0	234.0	8.7	279.2	24.9	1.15	71	390.7	19.2	565.3	26.2	0.0875	0.0014	540.7	8.3

Supplementary Table E3

(U-Th)/He and U/Pb dates by LADD of detrital zircon for sample CHB14-2A-51Q-1

Grain	He Pit Vol. (μm^3)	err. (2σ)	U-Th Pit Vol. (μm^3)	err. (2σ)	[^{4}He] (nmol/g)	err. (2σ)	[^{238}U] (nmol/g)	err. (2σ)	[^{232}Th] (nmol/g)	err. (2σ)	^{232}Th/^{238}U	eU (ppm)	(U-Th)/He date (Ma)	err. (2σ)	^{207}Pb/^{235}U date (Ma)	err. (2σ)	^{206}Pb/^{238}U	err. (2σ)	^{206}Pb/^{238}U date (Ma)	err. (2σ)
4	867.4	10.5	69140	818	106.0	4.5	3847.3	143.8	3126.8	279.7	0.79	1093	18.0	1.0	19.3	7.9	0.0030	0.0001	19.5	0.6
5	838.2	9.6	68965	795	407.5	13.3	1491.8	55.6	1025.6	91.8	0.67	414	179.9	8.7	515.2	4.8	0.0830	0.0006	513.8	3.7
6	953.7	12.2	78800	891	209.3	7.9	451.9	16.9	493.6	44.2	1.06	135	280.3	14.7	578.0	8.7	0.0923	0.0010	569.1	5.6
9	1138.0	14.5	88251	1378	80.1	3.9	190.7	7.4	151.2	13.6	0.77	54	269.0	16.5	541.2	40.0	0.0878	0.0011	542.5	6.5
14	797.6	8.0	66974	763	404.1	13.5	753.3	28.4	478.1	42.8	0.61	207	351.7	17.5	558.9	6.5	0.0912	0.0007	562.6	4.4
19	1153.7	18.9	62425	679	91.0	4.2	346.3	12.9	304.4	27.2	0.85	100	167.0	9.7	557.7	33.4	0.0892	0.0008	550.9	4.6
20	1007.0	12.8	66464	823	99.3	4.5	194.3	7.3	163.5	14.6	0.81	55	322.8	18.9	570.0	24.4	0.0879	0.0013	543.1	7.7
22	950.7	12.1	59539	769	1458.1	40.6	5766.8	218.5	6255.9	561.0	1.05	1724	154.8	7.0	493.6	13.1	0.0792	0.0013	491.4	7.8
23	866.3	11.0	65316	781	130.9	5.7	230.6	8.7	134.8	12.1	0.57	63	375.0	21.5	554.8	12.4	0.0878	0.0009	542.2	5.1
26	1480.5	24.2	98072	1026	79.0	5.4	123.2	4.6	74.2	6.6	0.58	34	420.7	33.5	545.9	14.3	0.0872	0.0008	539.0	4.7
28	1047.0	13.3	62733	722	68.3	4.3	3633.0	137.2	2527.5	226.7	0.67	1009	12.5	0.9	24.6	2.4	0.0030	0.0001	19.3	0.6
29	691.0	7.4	63568	716	48.0	4.1	1618.5	60.4	1144.5	102.5	0.68	450	19.7	1.8	20.1	15.9	0.0030	0.0001	19.4	0.9
30	1054.6	17.4	74201	815	160.2	6.3	348.2	12.9	238.8	21.3	0.66	96	300.0	16.1	554.2	12.4	0.0860	0.0013	531.8	7.7
32	719.5	10.9	78484	898	716.7	33.4	1029.8	38.4	169.5	15.2	0.16	256	495.7	30.6	522.5	8.5	0.0832	0.0011	515.2	6.6
33	769.5	11.6	69191	795	961.4	36.2	1907.2	71.0	1963.4	175.5	1.00	564	307.9	16.2	520.7	4.7	0.0838	0.0006	518.9	3.6
34	1407.0	17.9	82666	897	196.7	7.0	726.8	27.0	612.2	54.7	0.82	208	173.1	8.7	540.6	6.6	0.0859	0.0011	531.2	6.6
37	953.6	9.7	66964	741	130.3	5.4	307.2	11.7	316.3	28.4	1.00	91	260.1	14.4	554.8	11.2	0.0884	0.0008	546.1	4.8
38	900.2	11.5	69230	815	199.7	7.0	448.3	16.8	311.1	27.8	0.67	124	290.2	14.7	550.7	8.3	0.0888	0.0009	548.6	5.1
41	938.5	12.0	72112	804	40.0	3.3	1819.6	68.0	1318.0	118.0	0.70	508	14.6	1.3	19.1	17.9	0.0030	0.0002	19.1	1.0
42	789.2	7.9	69395	798	431.2	16.2	586.3	22.0	422.2	37.8	0.70	164	469.3	24.9	567.1	7.6	0.0910	0.0008	561.5	4.5
45	1058.5	13.1	71523	885	371.7	14.4	917.2	34.3	1122.4	100.4	1.18	281	240.3	12.8	484.8	12.0	0.0784	0.0009	486.6	5.3
47	888.2	9.2	69759	768	69.7	4.4	2882.8	106.8	1814.4	162.3	0.61	790	16.3	1.2	23.0	1.7	0.0029	0.0001	19.0	0.4
48	915.7	9.2	68190	777	246.3	9.0	355.4	13.3	283.4	25.3	0.77	101	437.1	22.8	550.1	14.2	0.0866	0.0010	535.4	6.0
50	1538.0	19.6	62091	708	386.2	18.1	4155.9	155.4	3346.6	300.3	0.78	1179	60.4	3.5	512.2	17.8	0.0804	0.0009	498.5	5.3
51	761.1	7.8	59414	736	484.1	16.4	1032.9	38.7	506.2	45.3	0.47	275	317.2	15.8	533.4	7.2	0.0847	0.0009	524.0	5.1
52	1566.7	19.8	44670	555	345.6	16.4	2919.4	109.9	2032.2	182.1	0.67	811	78.5	4.6	499.8	14.9	0.0786	0.0008	487.8	4.9
53	925.7	11.8	73144	999	100.0	5.1	160.7	6.1	112.2	10.1	0.68	45	401.3	25.6	551.8	47.8	0.0894	0.0010	552.0	5.9
60	855.4	10.9	71471	815	174.4	7.1	522.1	19.6	654.2	58.5	1.21	161	197.8	10.9	596.3	8.5	0.0961	0.0009	591.3	5.4
65	757.9	8.3	37951	496	51.7	4.1	313.3	11.9	184.2	16.5	0.57	85	111.4	9.8	554.2	13.6	0.0884	0.0009	546.2	5.1
69	497.2	9.8	71778	825	2197.2	74.6	2944.8	109.7	3909.8	349.5	1.28	919	427.9	21.7	447.6	10.5	0.0709	0.0006	441.5	3.5
70	1612.0	20.5	73895	828	209.6	7.3	990.4	36.8	774.5	69.2	0.76	280	137.4	6.8	531.6	10.9	0.0870	0.0008	537.8	4.8
71	1541.0	19.6	76679	848	28.9	1.9	1870.6	69.6	1452.6	129.8	0.75	528	10.1	0.8	26.1	2.3	0.0031	0.0001	19.9	0.8
73	1755.9	22.7	61739	728	78.3	3.2	449.7	16.9	319.0	28.6	0.69	125	114.8	6.2	530.4	23.4	0.0879	0.0012	543.1	7.1
79	799.3	9.4	28838	467	260.0	10.3	1347.7	52.7	908.6	81.9	0.65	373	128.0	6.9	546.5	7.2	0.0876	0.0008	541.1	4.8

Supplementary Table E3 Continued

Grain	He Pit Vol. (μm^3)	err. (2σ)	U-Th Pit Vol. (μm^3)	err. (2σ)	[^{4}He] (nmol/g)	err. (2σ)	[^{238}U] (nmol/g)	err. (2σ)	[^{232}Th] (nmol/g)	err. (2σ)	^{232}Th/^{238}U	eU (ppm)	(U-Th)/He date (Ma)	err. (2σ)	^{207}Pb/^{235}U date (Ma)	err. (2σ)	^{206}Pb/^{238}U	err. (2σ)	^{206}Pb/^{238}U date (Ma)	err. (2σ)
81	800.3	8.4	56875	684	55.0	3.7	3288.1	123.1	2242.5	200.7	0.66	910	11.2	0.8	21.6	1.1	0.0030	0.0000	19.3	0.3
83	844.7	8.8	46738	564	225.6	8.9	687.1	26.0	792.5	71.0	1.12	208	197.8	10.6	539.4	8.4	0.0862	0.0008	533.3	4.6
86	1429.0	18.2	77792	927	832.9	24.5	2080.2	77.9	2467.7	220.9	1.15	633	239.1	11.2	509.7	7.4	0.0820	0.0012	508.1	7.2
87	1107.0	14.1	54951	632	519.1	28.4	2217.7	84.4	2236.9	201.2	0.98	654	145.4	9.6	511.6	8.6	0.0832	0.0010	515.4	5.7
88	817.6	8.3	43629	579	16.0	3.4	845.7	32.0	455.8	40.9	0.52	228	13.0	2.8	17.1	29.0	0.0031	0.0002	20.0	1.5
91	790.3	8.4	68638	789	17.5	3.5	488.3	18.2	292.7	26.2	0.58	133	24.3	4.9	33.7	9.3	0.0031	0.0002	20.2	1.3
92	852.3	8.9	68482	832	200.6	7.3	413.3	15.5	244.5	21.9	0.57	112	321.8	16.6	546.5	8.9	0.0877	0.0010	541.9	6.0
95	1174.0	15.0	82425	889	78.9	4.1	180.2	6.7	168.5	15.0	0.90	52	273.0	17.3	553.6	17.7	0.0870	0.0012	537.8	7.1
97	1161.0	14.8	76415	1077	178.5	6.4	710.5	27.1	483.0	43.4	0.66	197	165.9	8.5	514.0	6.8	0.0818	0.0009	507.1	5.4
99	1315.0	16.8	73334	855	99.8	4.5	387.6	14.5	297.0	26.6	0.74	109	167.3	9.6	548.3	8.3	0.0890	0.0008	549.5	4.5
100	1401.0	17.9	67920	795	476.2	19.4	2228.2	83.6	1530.6	137.0	0.66	618	141.2	7.7	518.4	4.6	0.0828	0.0008	512.9	5.0
101	865.4	11.0	33873	476	205.9	7.6	1066.8	41.3	828.2	74.6	0.75	301	125.5	6.5	493.6	18.7	0.0795	0.0009	493.2	5.4
2_1	6158.0	61.8	86906	926	566.6	14.8	1845.5	68.1	1132.2	101.1	0.59	504	204.8	9.0	529.2	8.4	0.0831	0.0006	514.6	3.7
2_2	4393.8	45.7	87614	902	265.4	7.3	640.9	23.9	888.4	79.5	1.34	202	238.7	10.9	613.1	20.6	0.0889	0.0010	549.0	5.9
2_5	3965.4	41.0	75140	765	586.6	15.6	801.7	30.0	467.8	41.8	0.56	218	479.0	21.8	782.9	16.0	0.1276	0.0016	774.2	9.1
2_7	1411.2	14.1	42388	428	236.4	8.8	622.2	22.9	381.7	34.1	0.59	170	252.3	13.0	542.4	21.4	0.0871	0.0011	538.4	6.5
2_8	4005.5	41.7	78100	797	545.8	14.6	1061.1	39.0	672.3	60.0	0.61	291	337.7	15.1	589.5	11.9	0.0907	0.0010	559.4	5.7
2_9	4070.0	41.2	84559	862	79.9	4.0	179.7	6.7	100.7	9.0	0.54	49	297.1	18.6	613.6	111.0	0.0871	0.0020	538.4	11.9
2_10	1273.4	12.8	46630	475	746.9	21.6	1976.2	72.8	1974.1	176.4	0.97	581	233.5	10.7	793.6	18.1	0.1277	0.0019	774.7	10.9
2_11	3933.4	39.7	77949	807	742.8	19.7	911.8	33.7	557.7	49.8	0.59	249	528.1	24.0	541.8	18.5	0.0882	0.0013	544.9	7.7
2_12	3951.6	39.8	56326	595	273.0	7.9	783.4	28.9	500.1	44.6	0.62	215	230.7	10.5	543.0	16.1	0.0865	0.0011	534.8	6.5
2_14	1391.6	14.1	37081	381	1871.1	49.9	3520.3	130.5	2793.6	250.9	0.77	996	338.3	15.1	594.6	16.4	0.0868	0.0015	536.6	8.9
2_15	4133.9	41.5	73925	779	67.6	2.6	3537.1	130.1	2223.2	198.3	0.61	969	12.9	0.7	22.7	2.0	0.0030	0.0001	19.4	0.4
2_16	3965.0	40.9	77772	810	131.6	5.8	300.3	11.1	197.5	17.6	0.64	83	287.5	16.4	535.8	20.4	0.0869	0.0013	537.2	7.7
2_17	1447.1	15.1	42327	438	1052.5	29.2	2128.0	78.1	1239.4	110.5	0.56	578	328.3	14.8	544.8	11.3	0.0870	0.0010	538.0	5.6
2_18	4077.9	42.8	78925	822	418.4	11.4	979.6	36.2	719.9	64.6	0.71	274	276.4	12.4	704.3	18.8	0.1071	0.0013	655.9	7.6
2_19	1416.3	14.2	80351	806	676.5	19.2	1008.0	40.1	710.4	64.4	0.68	280	431.0	20.7	776.8	14.2	0.1276	0.0024	774.2	13.7
2_20	4221.6	43.0	76896	805	104.2	4.4	239.9	8.9	229.2	20.5	0.92	70	269.7	15.1	613.6	166.4	0.0949	0.0026	584.5	15.3
2_21	4283.4	43.8	73624	744	320.1	8.8	2184.6	80.2	1045.4	93.3	0.46	581	101.4	4.5	597.4	29.4	0.0937	0.0011	577.4	6.5
2_22	1280.6	13.5	40009	413	246.5	9.2	563.3	20.8	366.8	32.7	0.63	155	287.6	14.9	557.1	19.9	0.0870	0.0015	537.8	8.9
2_23	1445.9	14.5	38903	394	140.2	5.1	346.7	12.8	217.1	19.4	0.61	95	267.5	13.7	558.3	41.0	0.0886	0.0021	547.3	12.4
2_25	5910.6	59.4	79140	811	602.2	15.9	1593.4	59.7	1175.2	105.2	0.71	446	245.1	10.9	561.8	9.9	0.0865	0.0006	534.5	3.7
2_26	5680.3	57.2	66095	677	392.8	10.5	10573.6	391.4	6203.8	554.5	0.57	2873	25.3	1.1	545.3	27.2	0.0804	0.0010	498.5	6.0
2_27	3972.1	40.4	79172	818	84.9	2.8	508.2	18.7	328.2	29.3	0.63	140	111.6	5.4	526.2	15.7	0.0825	0.0010	511.0	5.8
2_30	4451.9	47.1	77642	808	51.6	1.7	2712.4	100.6	1741.7	155.7	0.62	745	12.8	0.6	25.1	3.2	0.0031	0.0001	19.8	0.7

Supplementary Table E3 Continued

Grain	He Pit Vol. (μm^3)	err. (2σ)	U-Th Pit Vol. (μm^3)	err. (2σ)	[^{4}He] (nmol/g)	err. (2σ)	[^{238}U] (nmol/g)	err. (2σ)	[^{232}Th] (nmol/g)	err. (2σ)	$^{232}Th/^{238}U$	eU (ppm)	(U-Th)/He date (Ma)	err. (2σ)	$^{207}Pb/^{235}U$ date (Ma)	err. (2σ)	$^{206}Pb/^{238}U$	err. (2σ)	$^{206}Pb/^{238}U$ date (Ma)	err. (2σ)
2_31	5248.8	52.9	87469	891	69.8	3.5	6004.1	222.5	12262.8	1095.1	1.98	2108	6.1	0.4	518.9	20.8	0.0803	0.0009	498.2	5.3
2_33	4065.4	41.2	80940	825	978.4	25.6	2119.6	77.9	1356.1	120.9	0.62	582	303.6	13.4	538.2	11.4	0.0855	0.0009	528.8	5.4
2_35	4047.4	41.0	78777	823	288.7	8.2	452.9	16.7	459.2	41.0	0.98	134	387.8	17.9	565.9	16.3	0.0861	0.0013	532.4	7.7
2_36	4071.9	41.6	78675	801	62.6	2.3	3381.9	124.0	2331.0	207.9	0.67	938	12.4	0.6	21.6	2.3	0.0030	0.0001	19.2	0.5
2_37	4032.8	41.0	79087	832	206.2	5.9	459.7	17.0	165.1	14.7	0.35	119	312.0	14.4	542.4	17.3	0.0876	0.0011	541.3	6.5
2_38	3843.9	39.6	77699	804	48.3	1.8	152.4	5.6	144.2	12.9	0.92	44	198.3	10.2	618.6	34.8	0.0938	0.0019	578.0	11.2
2_40	1279.1	13.1	41748	428	244.8	9.9	651.4	24.0	358.0	31.9	0.53	176	252.8	13.6	549.5	20.0	0.0898	0.0013	554.4	7.7
2_41	4021.3	41.0	71450	730	67.3	2.4	3683.8	135.5	2643.6	235.8	0.69	1027	12.1	0.6	20.4	2.6	0.0030	0.0001	19.3	0.6
2_42	1366.3	14.1	42831	438	2066.8	56.1	6011.4	221.5	689.0	61.5	0.11	1479	253.4	11.7	652.3	18.2	0.1066	0.0012	653.0	7.0
2_43	3903.8	40.9	79243	800	97.8	4.7	252.3	9.3	84.0	7.5	0.32	65	272.1	16.6	550.1	20.0	0.0892	0.0014	550.8	8.3
2_44	1390.6	14.1	61284	621	165.2	5.9	598.9	22.6	715.3	64.4	1.16	183	165.4	8.4	499.2	16.8	0.0805	0.0012	499.1	7.2
2_45	3969.1	40.7	93231	942	261.7	7.3	404.4	15.0	225.5	20.1	0.54	109	427.7	19.6	554.2	18.2	0.0893	0.0012	551.4	7.1
2_46	4435.1	47.2	79967	825	98.4	4.2	234.4	8.6	227.3	20.3	0.94	69	260.2	14.5	639.4	23.2	0.1036	0.0018	635.5	10.5
2_47	4049.2	41.9	91743	962	1031.9	27.2	1618.9	59.8	1091.1	97.4	0.65	448	412.5	18.5	548.9	8.9	0.0881	0.0008	544.2	4.6
2_49	1585.4	16.0	32585	330	129.1	4.9	435.9	16.1	288.8	25.8	0.64	120	195.8	10.2	598.5	30.4	0.0911	0.0017	562.0	10.0
2_50	4003.4	41.4	78790	797	21.3	1.1	769.2	28.2	488.6	43.6	0.61	211	18.7	1.2	30.0	167.6	0.0030	0.0013	19.3	8.4
2_52	4184.5	42.0	78269	790	184.7	6.9	405.4	14.9	209.2	18.7	0.50	109	307.0	15.9	554.2	18.2	0.0864	0.0011	534.2	6.5
2_53	3996.0	41.1	82242	858	533.9	14.1	2243.7	82.8	826.9	73.9	0.36	583	167.4	7.4	507.9	9.9	0.0804	0.0007	498.5	4.4
2_54	1326.1	13.5	43665	441	9.7	2.4	568.6	21.0	463.5	41.4	0.79	162	11.1	2.8	24.1	10.9	0.0030	0.0003	19.4	2.0
2_56	4043.0	41.2	80194	822	52.8	1.8	219.2	8.1	259.4	23.2	1.15	67	145.1	7.1	622.5	23.6	0.1017	0.0016	624.4	9.4
2_57	1324.0	13.4	42774	435	170.8	6.3	478.3	17.6	295.6	26.4	0.60	131	237.2	12.1	576.9	38.0	0.0876	0.0022	541.3	13.0
2_58	3970.0	40.1	80303	816	135.6	6.1	254.7	9.4	213.9	19.1	0.81	73	336.0	19.5	526.2	24.2	0.0808	0.0013	500.9	7.8
2_59	3977.1	40.6	79324	802	166.9	7.1	373.0	13.7	350.3	31.2	0.91	109	278.5	15.5	595.1	26.0	0.0883	0.0011	545.5	6.5
2_60	4054.3	42.1	73482	761	938.9	24.8	4588.3	177.2	2765.9	247.3	0.58	1251	137.6	6.2	648.5	11.8	0.0971	0.0014	597.4	8.2
2_61	1351.1	13.9	46240	472	241.4	8.8	1032.4	38.4	694.9	62.2	0.65	285	154.8	7.8	615.8	19.9	0.1006	0.0015	617.9	8.8
2_62	3952.6	41.2	80249	811	190.8	6.8	446.0	16.3	258.6	23.1	0.56	121	285.2	14.4	650.7	18.2	0.1072	0.0013	656.5	7.6
2_63	1894.5	18.9	43419	449	91.5	3.4	331.8	12.3	406.2	36.3	1.18	102	164.6	8.5	600.2	37.2	0.0869	0.0019	537.2	11.3

Supplementary Table E4
(U-Th)/He and U/Pb dates by LADD of detrital zircon for sample CHB14-2A-90Q-1

Grain	He Pit Vol. (μm^3)	err. (2σ)	U-Th Pit Vol. (μm^3)	err. (2σ)	[^4He] (nmol/g)	err. (2σ)	[^{238}U] (nmol/g)	err. (2σ)	[^{232}Th] (nmol/g)	err. (2σ)	$^{232}Th/^{238}U$	eU (ppm)	(U-Th)/He date (Ma)	err. (2σ)	$^{207}Pb/^{235}U$ date (Ma)	err. (2σ)	$^{206}Pb/^{238}U$	err. (2σ)	$^{206}Pb/^{238}U$ date (Ma)	err. (2σ)
1	936.6	10.1	71460	839	118.8	4.6	249.3	9.3	166.9	14.9	0.65	69	311.6	16.7	572.9	15.0	0.0872	0.0010	538.8	5.9
4	1259.1	13.6	72000	782	307.8	11.5	544.9	20.6	477.3	42.8	0.85	157	353.5	18.6	546.5	9.5	0.0874	0.0007	540.0	4.2
5	1272.8	12.8	71863	784	152.4	5.8	321.2	11.9	206.3	18.4	0.62	88	311.7	16.5	556.0	12.3	0.0891	0.0009	550.2	5.4
6	1146.0	12.3	70190	766	1083.0	31.4	1653.8	61.6	642.3	57.5	0.38	431	447.2	21.2	515.0	5.8	0.0821	0.0006	508.9	3.7
7	967.5	12.9	72485	821	105.5	4.7	145.2	5.7	87.5	7.9	0.58	40	474.1	28.4	579.2	16.6	0.0943	0.0013	580.9	7.7
8	1352.5	14.6	69780	775	63.6	3.1	154.8	5.8	119.8	10.7	0.75	44	264.3	16.2	557.7	17.6	0.0884	0.0013	546.1	7.7
9	1395.6	15.0	70724	775	274.6	9.7	368.9	13.8	252.2	22.6	0.66	102	477.9	24.6	570.5	14.5	0.0874	0.0010	540.1	5.9
10	1434.0	15.5	72328	794	1033.7	27.8	1795.3	66.8	1083.0	96.8	0.58	489	378.9	17.1	509.8	5.7	0.0812	0.0004	503.2	2.6
11	2534.0	27.4	114000	1276	40.6	2.8	77.9	2.9	67.0	6.0	0.83	22	328.3	25.8	545.9	25.0	0.0819	0.0012	507.5	7.2
12	1082.0	11.7	71616	781	259.8	9.0	542.3	20.1	524.0	46.8	0.94	159	296.3	14.8	534.6	8.4	0.0859	0.0006	531.2	3.7
13	1239.3	12.9	71649	734	14.4	1.7	672.3	24.9	423.6	37.8	0.61	184	14.4	1.7	22.1	18.9	0.0030	0.0002	19.3	1.2
14	1815.0	19.6	69033	751	675.9	18.8	17455.1	651.6	5552.1	496.5	0.31	4487	27.9	1.3	551.4	5.1	0.0881	0.0006	544.4	3.4
15	1527.0	16.5	66278	723	1850.8	48.9	3618.4	134.6	3178.7	284.1	0.85	1041	320.9	14.3	519.7	5.1	0.0812	0.0007	503.3	4.0
16	1170.7	12.5	69590	823	7.0	1.7	194.0	7.3	140.8	12.6	0.70	54	24.1	5.9	19.3	1.0	0.0030	0.0002	19.4	1.0
17	1369.7	14.6	68670	742	118.6	4.3	178.9	6.7	165.3	14.8	0.89	52	409.4	21.2	511.6	13.5	0.0829	0.0010	513.4	5.8
20	1141.8	12.4	70619	801	232.7	7.8	346.8	13.0	240.2	21.5	0.67	96	431.8	21.6	551.3	11.8	0.0874	0.0011	540.1	6.5
21	1385.1	15.1	72299	827	149.9	4.6	283.5	10.6	276.4	24.7	0.94	83	325.7	15.5	545.3	17.2	0.0875	0.0010	540.7	5.9
22	1431.6	14.8	70840	775	10.7	1.4	534.1	19.8	293.4	26.2	0.53	144	13.7	1.8	25.7	5.9	0.0030	0.0002	19.3	1.0
24	1262.6	14.1	75496	791	18.1	1.8	761.0	28.5	584.6	52.3	0.74	214	15.7	1.7	26.3	2.8	0.0030	0.0001	19.3	0.6
25	1485.0	16.0	59339	647	492.1	20.4	1087.3	40.6	1371.9	122.6	1.22	335	266.1	14.8	545.3	9.5	0.0864	0.0008	534.5	4.7
26	1151.9	14.2	73533	842	217.4	7.4	534.0	19.8	459.7	41.1	0.83	153	257.6	12.7	596.8	12.4	0.0932	0.0011	574.4	6.5
27	1374.4	15.2	68535	752	818.6	23.6	1172.7	43.5	639.5	57.2	0.53	316	461.2	21.6	521.3	8.5	0.0824	0.0009	510.2	5.3
28	1339.3	14.0	73203	854	559.0	22.6	1064.2	39.6	1281.5	114.6	1.17	325	310.8	17.0	550.1	7.1	0.0879	0.0007	543.3	4.0
33	1175.7	13.2	56487	679	236.2	9.2	508.4	20.1	449.1	40.6	0.85	146	291.9	15.9	607.5	11.7	0.0944	0.0009	581.7	5.5
35	1516.0	16.4	75540	845	90.8	3.8	3510.4	130.9	2275.8	203.5	0.63	966	17.4	0.9	24.8	2.0	0.0030	0.0001	19.6	0.6
36	1540.5	16.6	77680	869	435.7	18.1	1271.0	47.7	375.6	33.9	0.29	325	243.2	13.6	549.5	7.7	0.0879	0.0010	543.1	5.6
37	1312.7	14.0	70509	788	152.0	5.3	287.6	10.7	179.3	16.0	0.60	79	347.5	17.6	534.0	12.0	0.0878	0.0009	542.2	5.1
38	1299.6	13.7	72012	796	26.4	2.7	82.8	3.1	47.7	4.3	0.56	22	214.4	23.6	510.9	17.8	0.0806	0.0013	499.7	7.8
39	1508.8	16.3	71215	797	107.0	4.5	165.9	7.4	120.5	11.1	0.70	46	413.1	24.9	532.8	14.4	0.0810	0.0012	502.1	7.2
40	1541.0	16.6	66778	810	457.3	21.1	837.6	31.5	913.5	81.9	1.06	251	329.2	19.6	572.9	9.8	0.0884	0.0008	546.1	4.9
41	1003.5	11.4	71213	790	766.9	37.3	1907.8	70.7	1581.4	141.2	0.80	544	256.0	15.5	509.1	7.4	0.0814	0.0005	504.2	3.0
44	1002.2	12.1	63650	695	2177.5	60.4	3788.0	140.9	1496.1	133.7	0.38	990	393.9	18.2	579.2	6.9	0.0894	0.0007	551.9	4.0
45	1430.1	14.7	68958	789	404.2	18.7	685.3	25.5	460.1	41.1	0.65	189	382.8	22.8	535.2	7.2	0.0861	0.0006	532.6	3.3
46	1161.9	13.0	61562	661	37.2	2.8	20345.8	764.6	1106.9	99.3	0.05	4938	1.4	0.1	454.8	10.4	0.0704	0.0008	438.5	4.6

Supplementary Table E4 Continued

Grain	He Pit Vol. (μm^3)	err. (2σ)	U-Th Pit Vol. (μm^3)	err. (2σ)	[^4He] (nmol/g)	err. (2σ)	[^{238}U] (nmol/g)	err. (2σ)	[^{232}Th] (nmol/g)	err. (2σ)	$^{232}Th/^{238}U$	eU (ppm)	(U-Th)/He date (Ma)	err. (2σ)	$^{207}Pb/^{235}U$ date (Ma)	err. (2σ)	$^{206}Pb/^{238}U$	err. (2σ)	$^{206}Pb/^{238}U$ date (Ma)	err. (2σ)
47	2420.0	26.1	79450	889	78.6	3.9	837.5	31.2	544.3	48.7	0.63	230	62.9	3.8	551.9	9.4	0.0882	0.0012	544.9	7.1
51	1277.5	13.8	70623	753	268.0	9.6	1830.1	67.9	618.0	55.3	0.33	472	104.3	5.3	695.7	6.7	0.1107	0.0011	676.8	6.4
52	823.0	12.0	68099	769	359.4	13.2	775.9	29.0	602.4	53.9	0.75	219	296.8	15.4	525.0	7.3	0.0841	0.0006	520.5	3.8
54	1245.9	13.5	68565	769	159.9	6.3	351.6	13.1	157.2	14.1	0.43	93	310.6	16.7	780.5	10.4	0.1255	0.0012	762.1	6.9
57	1279.2	14.1	68125	747	151.7	4.9	211.7	7.9	139.9	12.5	0.64	58	462.8	22.8	541.8	11.3	0.0865	0.0009	534.6	5.1
58	1456.0	15.7	79300	887	167.6	6.5	223.4	8.5	228.3	20.5	0.99	66	453.2	24.6	560.7	14.0	0.0880	0.0008	543.4	4.9
59	1108.6	14.5	80640	902	258.9	10.0	412.5	16.0	198.4	17.9	0.47	110	421.6	23.1	556.0	8.2	0.0884	0.0009	545.9	5.3
60	1345.5	14.9	72377	893	1595.3	43.1	2045.8	77.1	1449.6	129.9	0.69	569	497.5	22.9	571.1	9.3	0.0873	0.0010	539.3	5.9
61	1412.6	15.3	54634	678	122.0	4.6	347.7	13.1	232.3	20.8	0.65	96	231.0	12.1	535.8	10.8	0.0873	0.0010	539.6	5.9
62	1566.9	17.1	81410	911	124.8	4.5	252.9	9.4	162.1	14.5	0.62	69	324.0	16.6	590.6	15.3	0.0876	0.0008	541.3	5.0
65	1338.6	14.9	70054	839	420.9	20.6	866.0	32.8	878.9	78.9	0.98	256	297.9	18.4	576.3	7.5	0.0938	0.0009	577.9	5.1
66	2159.5	22.3	86520	968	380.5	13.8	472.3	18.5	371.2	33.5	0.76	133	506.0	27.0	590.0	8.5	0.0936	0.0012	576.8	7.1
68	1390.6	16.0	72340	809	903.7	29.3	1108.8	41.4	1091.1	97.5	0.95	325	494.0	24.4	558.3	7.0	0.0877	0.0006	542.0	3.6
70	1444.9	15.4	71867	787	95.5	3.5	120.0	4.5	85.5	7.6	0.69	33	506.6	26.5	535.8	16.8	0.0877	0.0012	541.9	7.1
71	1954.6	22.6	79990	895	925.0	25.3	1084.9	41.1	751.4	67.3	0.67	301	543.3	25.3	553.6	10.6	0.0862	0.0015	533.0	8.9
72	1337.9	15.2	68296	829	260.6	10.6	941.1	35.5	567.0	50.8	0.58	257	185.4	10.1	511.6	6.7	0.0808	0.0007	501.1	4.4
73	1511.0	16.2	78253	842	155.6	4.9	269.3	10.1	187.0	16.7	0.67	75	373.6	18.1	555.4	12.3	0.0876	0.0009	541.2	5.2
74	1364.4	16.5	69002	789	54.7	3.1	164.0	6.1	77.5	6.9	0.46	44	228.3	15.4	572.9	15.0	0.0943	0.0015	580.9	8.8
75	1184.1	12.8	61746	734	661.1	31.7	2909.0	109.6	631.7	56.7	0.21	732	165.1	10.1	659.7	8.5	0.1009	0.0015	619.7	8.8
76	1708.0	18.4	73219	835	62.3	2.7	193.1	7.3	139.8	12.6	0.70	54	210.5	11.8	554.8	18.8	0.0870	0.0015	537.8	8.9
77	1277.8	13.8	68274	705	167.5	7.4	390.8	14.5	353.0	31.5	0.87	113	268.8	15.4	571.1	13.9	0.0866	0.0008	535.1	4.9
78	1417.2	15.1	69090	773	93.2	3.4	159.5	6.0	137.3	12.3	0.83	46	366.5	19.0	558.9	21.6	0.0872	0.0012	539.0	7.1
80	1253.7	13.1	77969	842	904.7	29.4	3050.2	114.5	1350.4	122.8	0.43	805	204.8	10.0	612.5	10.0	0.0942	0.0015	580.3	8.8
81	1787.0	19.3	75188	892	78.4	2.9	259.2	9.8	137.6	12.3	0.51	70	205.1	10.6	528.6	12.1	0.0861	0.0014	532.4	8.3
82	1382.0	15.7	70541	805	101.5	5.4	228.7	8.6	219.2	19.6	0.93	67	275.3	18.0	558.3	11.7	0.0901	0.0011	556.1	6.5
85	1559.8	17.0	72959	885	1182.0	33.8	2953.3	111.2	3010.4	269.6	0.99	872	246.1	11.3	513.9	5.7	0.0821	0.0008	508.5	4.7
86	1588.9	18.1	77821	892	1209.7	33.3	1800.5	67.5	1040.2	93.5	0.56	488	441.9	20.4	537.0	8.4	0.0865	0.0011	534.8	6.5
88	896.3	10.6	77980	841	946.3	32.1	4707.6	178.4	12520.9	1127.8	2.57	1811	96.0	5.2	575.7	6.9	0.0878	0.0011	542.5	6.5
89	1550.5	16.8	70661	780	51.6	3.1	110.1	4.1	88.1	7.9	0.77	31	299.2	21.3	596.3	16.9	0.0863	0.0011	533.6	6.5
91	1272.5	14.5	68479	773	549.3	23.4	924.8	34.6	927.0	82.9	0.97	272	362.8	20.6	501.1	11.8	0.0802	0.0011	497.3	6.6
94	1513.1	17.2	73080	776	180.5	6.5	338.1	12.5	266.4	23.8	0.76	96	340.2	17.4	540.6	14.3	0.0839	0.0008	519.3	4.9
95	1458.7	15.4	70738	766	91.8	3.9	170.2	6.3	106.4	9.5	0.61	47	354.2	20.0	579.2	15.5	0.0878	0.0011	542.5	6.5
96	1373.3	15.1	67573	734	1996.8	53.5	5844.9	216.3	5713.9	511.6	0.95	1713	212.3	9.4	519.8	5.4	0.0810	0.0009	501.9	5.2
99	1602.0	17.3	79790	893	154.6	5.6	335.3	13.2	277.0	25.1	0.80	95	292.9	15.3	545.9	10.1	0.0864	0.0008	534.1	4.9
101	1012.6	10.9	60905	681	335.0	13.2	10334.1	384.1	1033.5	92.3	0.10	2534	24.5	1.3	479.8	8.9	0.0700	0.0014	436.2	8.4

Supplementary Table E4 Continued

Grain	He Pit Vol. (μm³)	err. (2σ)	U-Th Pit Vol. (μm³)	err. (2σ)	[⁴He] (nmol/g)	err. (2σ)	[²³⁸U] (nmol/g)	err. (2σ)	[²³²Th] (nmol/g)	err. (2σ)	²³²Th/²³⁸U	eU (ppm)	(U-Th)/He date (Ma)	err. (2σ)	²⁰⁷Pb/²³⁵U date (Ma)	err. (2σ)	²⁰⁶Pb/²³⁸U	err. (2σ)	²⁰⁶Pb/²³⁸U date (Ma)	err. (2σ)
102	1057.5	11.6	67044	741	67.1	3.9	410.9	15.2	459.1	41.0	1.08	124	99.8	6.8	510.3	10.4	0.0809	0.0009	501.7	5.6
103	1203.8	12.9	71353	816	259.5	9.0	534.5	19.9	630.2	57.2	1.14	163	289.0	14.6	512.8	8.6	0.0808	0.0011	500.9	6.6
104	1277.4	13.6	70062	812	163.9	5.7	576.8	21.6	356.4	32.2	0.60	158	189.6	9.5	609.7	8.9	0.0975	0.0011	599.7	6.5
105	1401.2	15.9	72953	808	335.9	12.3	654.7	24.4	574.5	51.4	0.85	188	321.9	16.6	629.0	7.7	0.1015	0.0009	623.3	5.2
106	1178.0	12.7	72638	819	104.3	4.1	210.9	7.9	161.7	14.5	0.74	59	316.9	16.9	541.8	19.1	0.0867	0.0012	536.0	7.1
108	1576.5	17.3	70514	772	161.1	6.3	301.4	11.2	158.9	14.2	0.51	81	357.7	19.3	575.7	15.0	0.0869	0.0011	537.2	6.5
109	1376.2	15.7	67836	726	8.1	1.4	321.5	12.0	208.5	18.6	0.63	88	17.0	3.0	29.0	61.2	0.0031	0.0006	19.9	3.6
110	1474.6	16.8	68655	738	156.5	6.1	275.2	10.3	278.9	24.9	0.98	81	347.1	18.6	540.0	10.7	0.0862	0.0008	533.0	4.5

Supplementary Table E5
(U-Th)/He and U/Pb dates by LADD of detrital zircon for sample CHB14-2A-117Q-2

Grain	He Pit Vol. (μm^3)	err. (2σ)	U-Th Pit Vol. (μm^3)	err. (2σ)	[^{4}He] (nmol/g)	err. (2σ)	[^{238}U] (nmol/g)	err. (2σ)	[^{232}Th] (nmol/g)	err. (2σ)	$^{232}Th/^{238}U$	eU (ppm)	(U-Th)/He date (Ma)	err. (2σ)	$^{207}Pb/^{235}U$ date (Ma)	err. (2σ)	$^{206}Pb/^{238}U$	err. (2σ)	$^{206}Pb/^{238}U$ date (Ma)	err. (2σ)
2	1439.5	16.1	67445	767	341.6	11.6	9406.6	353.4	4853.8	434.6	0.50	2520	25.1	1.2	392.5	7.6	0.0547	0.0005	343.3	3.3
3	1555.6	16.8	67760	758	840.9	23.6	1583.2	58.9	765.4	68.4	0.47	421	358.6	16.5	504.2	7.4	0.0804	0.0007	498.6	4.2
5	1500.4	16.3	67060	750	122.0	5.1	178.3	6.7	75.1	6.7	0.41	47	463.3	26.3	520.7	13.4	0.0863	0.0010	533.5	5.8
6	1459.0	16.0	66540	745	83.6	2.9	413.7	15.5	281.1	25.2	0.66	114	133.8	6.6	561.2	9.9	0.0905	0.0011	558.5	6.5
7	1286.0	13.9	60115	766	704.0	25.5	3202.5	120.9	1706.6	152.9	0.52	861	149.7	7.6	507.4	6.8	0.0798	0.0015	494.9	9.0
8	1478.6	15.9	66256	751	136.6	4.3	276.4	10.4	244.7	22.0	0.86	80	309.8	14.8	648.0	11.3	0.1063	0.0011	651.2	6.4
9	1373.9	15.2	65210	730	119.2	4.7	265.8	9.9	115.7	10.3	0.42	70	307.3	16.6	504.2	11.1	0.0809	0.0009	501.4	5.4
10	1366.4	15.9	63930	715	111.1	3.8	182.1	6.8	98.0	8.8	0.52	49	405.9	20.4	534.0	13.2	0.0859	0.0009	531.4	5.6
11	1595.4	17.7	78930	883	237.9	8.7	341.2	13.5	211.7	19.1	0.60	93	454.3	24.3	579.8	28.2	0.0867	0.0009	536.1	5.2
12	1364.0	15.4	59121	719	432.1	20.7	863.8	32.5	591.4	53.0	0.66	239	325.5	19.8	655.5	7.5	0.1071	0.0009	655.7	5.0
13	1409.9	15.3	63550	711	58.5	3.4	255.1	9.5	99.9	8.9	0.38	67	160.7	11.1	552.4	12.4	0.0893	0.0009	551.1	5.3
14	1274.8	14.1	63083	684	140.5	5.2	231.0	8.6	153.5	13.7	0.64	64	394.8	20.6	538.8	12.5	0.0870	0.0010	537.8	5.9
15	1540.2	17.1	55432	616	151.2	7.0	295.7	11.0	224.9	20.1	0.74	83	327.7	19.5	588.9	19.3	0.0880	0.0014	543.7	8.3
16	1520.2	17.9	65985	827	659.0	19.9	1063.1	40.1	343.8	30.8	0.31	274	429.7	20.9	655.5	8.5	0.1062	0.0010	650.6	5.8
17	1446.5	16.4	60900	681	144.4	4.6	321.7	12.1	148.5	13.3	0.45	85	305.9	14.9	726.4	13.4	0.1178	0.0015	717.9	8.7
18	1341.0	15.3	62202	722	831.9	24.0	1132.2	43.0	1502.3	134.9	1.28	353	421.6	20.1	653.3	6.9	0.1064	0.0009	652.0	5.5
19	1298.0	14.5	61885	712	137.7	4.8	359.3	13.4	398.7	35.7	1.07	108	232.1	11.6	653.9	14.4	0.1063	0.0020	651.2	11.7
20	1332.5	15.1	62400	698	170.9	5.6	498.9	19.1	532.7	48.8	1.03	149	209.4	10.3	489.8	33.8	0.0798	0.0014	494.9	8.4
21	1561.9	17.6	64080	717	204.2	7.5	305.5	11.5	345.5	31.0	1.09	92	397.9	20.9	526.8	10.9	0.0856	0.0009	529.6	5.6
22	1554.6	17.7	66140	740	519.5	21.5	919.2	34.1	492.5	44.0	0.52	247	377.0	21.0	536.8	7.2	0.0874	0.0007	540.4	4.2
23	1542.5	17.7	61096	720	902.2	25.1	2699.5	100.7	1338.2	119.8	0.48	720	227.8	10.3	711.4	8.6	0.1141	0.0011	696.5	6.4
24	1521.6	16.9	66480	755	233.8	9.3	781.9	29.0	306.8	27.4	0.38	204	208.5	11.3	717.4	9.0	0.1182	0.0012	720.2	6.9
25	1568.0	17.8	67167	756	586.1	22.7	1820.4	67.7	274.2	24.5	0.15	451	235.8	12.7	604.1	6.2	0.0980	0.0006	602.9	3.5
26	1599.8	16.7	67920	760	247.9	9.5	498.1	18.6	363.1	32.5	0.71	139	321.3	17.0	538.8	10.2	0.0868	0.0009	536.4	5.5
27	1496.0	15.7	70280	786	666.5	23.1	2029.2	75.3	1480.6	132.3	0.71	567	214.0	10.6	650.8	5.9	0.1058	0.0008	648.1	4.4
28	1536.0	16.6	64259	748	1183.9	31.6	6152.5	229.7	7581.2	680.9	1.19	1888	115.1	5.1	627.4	12.6	0.0967	0.0019	595.0	11.2
29	1512.3	16.6	69460	777	164.0	5.8	830.1	30.7	424.8	38.0	0.50	222	135.3	6.8	779.1	9.0	0.1277	0.0013	774.7	7.4
30	1501.8	16.0	69150	774	530.0	22.2	653.1	24.4	804.6	72.0	1.19	200	471.5	26.8	656.5	9.0	0.1068	0.0010	654.2	5.6
31	1529.3	16.3	69345	773	39.3	3.1	124.8	4.6	70.0	6.3	0.54	34	211.9	18.8	509.1	14.8	0.0807	0.0011	500.3	6.6
32	1430.2	15.0	66990	750	150.4	5.4	311.9	11.7	165.2	14.8	0.51	84	323.5	16.7	583.2	22.8	0.0878	0.0008	542.6	4.4
33	1467.3	15.5	68151	741	104.9	3.7	179.8	6.7	102.6	9.2	0.55	49	386.0	19.8	580.9	36.6	0.0861	0.0028	532.4	16.6
34	1525.3	17.5	72360	810	157.2	5.5	277.6	10.4	186.3	16.7	0.65	77	368.2	18.7	538.8	12.5	0.0864	0.0011	534.2	6.5
35	1551.9	17.5	70061	789	619.3	19.0	967.2	36.1	450.3	40.3	0.45	256	431.0	20.8	507.9	7.4	0.0811	0.0008	502.6	4.8
36	1563.4	16.6	70755	835	219.6	7.3	415.3	15.6	394.6	35.3	0.92	121	327.1	16.2	561.2	8.8	0.0857	0.0007	530.1	4.4

Supplementary Table E5 Continued

Grain	He Pit Vol. (μm³)	err. (2σ)	U-Th Pit Vol. (μm³)	err. (2σ)	[^{4}He] (nmol/g)	err. (2σ)	[^{238}U] (nmol/g)	err. (2σ)	[^{232}Th] (nmol/g)	err. (2σ)	^{232}Th/^{238}U	eU (ppm)	(U-Th)/He date (Ma)	err. (2σ)	^{207}Pb/^{235}U date (Ma)	err. (2σ)	^{206}Pb/^{238}U	err. (2σ)	^{206}Pb/^{238}U date (Ma)	err. (2σ)
37	1575.2	16.4	70678	795	126.5	4.7	248.2	9.3	162.6	14.5	0.63	68	333.4	17.4	536.4	10.2	0.0866	0.0009	535.6	5.3
38	1403.1	16.9	69388	808	23.8	2.3	96.7	3.6	27.6	2.5	0.28	25	176.0	18.1	662.4	18.0	0.1059	0.0014	648.9	8.2
39	1429.4	15.2	69599	772	365.1	19.8	817.3	30.4	1147.7	102.7	1.36	258	256.4	17.0	514.6	8.6	0.0815	0.0008	504.8	4.5
40	1306.2	16.0	71059	799	778.0	25.8	1329.9	49.5	883.2	78.9	0.64	367	380.3	18.8	521.3	6.7	0.0820	0.0007	508.1	4.3
41	816.9	8.8	61679	662	200.0	6.9	3012.5	112.0	1497.2	134.0	0.48	804	46.0	2.3	659.7	10.6	0.1058	0.0008	648.3	4.6
42	1477.5	15.7	69500	778	559.1	18.5	939.2	34.9	267.8	23.9	0.28	240	416.5	21.0	563.0	7.6	0.0895	0.0008	552.6	4.9
43	1386.5	15.7	68250	764	180.7	6.4	371.5	13.9	232.1	20.8	0.60	102	320.5	16.3	520.1	11.6	0.0811	0.0010	502.7	6.0
45	1525.7	17.6	68352	764	203.9	7.7	476.1	17.7	323.8	28.9	0.66	132	280.0	14.6	542.4	8.9	0.0874	0.0008	539.9	4.5
46	1432.4	15.9	68850	770	114.6	3.8	196.0	7.3	144.1	12.9	0.71	55	375.2	18.5	501.7	11.8	0.0807	0.0010	500.3	6.0
47	1358.2	15.1	67430	755	253.2	8.4	321.1	12.0	232.4	20.8	0.70	90	501.4	25.0	568.2	15.7	0.0877	0.0014	541.9	8.3
48	1339.7	15.3	68710	769	713.5	24.2	1335.3	49.9	662.7	59.3	0.48	356	359.8	18.0	778.3	6.6	0.1278	0.0009	775.4	5.3
49	1267.0	13.7	65290	731	173.1	6.3	199.3	8.0	151.6	13.7	0.74	56	546.1	29.6	596.8	15.8	0.0874	0.0011	540.1	6.5
50	1323.1	16.1	66374	716	81.0	3.4	436.2	16.2	380.5	34.0	0.84	125	118.6	6.5	625.8	12.1	0.1015	0.0014	623.2	8.2
51	1314.5	16.3	68635	795	85.5	3.9	180.8	6.8	116.0	10.4	0.62	50	310.8	18.2	556.6	88.0	0.0897	0.0017	553.8	10.1
52	1355.6	15.8	66860	748	291.1	13.3	578.7	21.6	319.7	28.6	0.53	156	335.7	19.8	550.7	8.3	0.0894	0.0006	551.7	3.6
53	1321.4	14.6	65470	733	183.8	6.0	364.6	13.9	260.9	23.4	0.69	102	326.0	16.1	529.2	10.3	0.0815	0.0010	505.1	6.0
55	1479.9	17.3	69661	781	185.2	6.2	326.4	12.2	195.0	17.4	0.58	89	374.0	18.6	532.2	9.0	0.0862	0.0008	532.8	4.9
56	1430.8	16.6	72090	807	176.1	6.8	344.3	12.9	226.8	20.3	0.64	95	334.3	17.9	570.0	13.3	0.0890	0.0008	549.5	4.7
58	1551.6	18.7	66883	770	146.2	5.1	301.2	11.5	251.3	22.7	0.81	86	307.3	15.6	563.0	13.4	0.0920	0.0011	567.4	6.5
59	1174.3	14.9	63650	711	1997.8	55.2	7520.5	278.3	2605.6	232.7	0.34	1945	187.4	8.5	753.3	6.8	0.1181	0.0010	719.6	5.8
60	1277.8	15.3	68679	774	33.7	3.0	257.9	9.8	122.1	10.9	0.46	68	90.6	8.7	653.9	12.8	0.1073	0.0017	657.1	9.9
61	1434.5	16.8	68810	826	995.5	27.7	1457.3	54.5	848.6	75.9	0.56	396	448.6	20.7	555.8	6.5	0.0892	0.0005	550.5	3.2
62	560.7	6.1	56974	623	1037.4	44.9	7288.3	269.3	2129.7	190.1	0.28	1863	102.4	5.8	590.6	31.2	0.0873	0.0008	539.4	4.6
63	1300.3	14.6	69350	776	103.3	4.3	159.8	5.9	79.8	7.1	0.48	43	432.2	24.2	551.3	14.2	0.0878	0.0010	542.2	5.6
64	1297.6	14.8	67353	733	350.1	14.9	1221.7	45.2	481.2	43.0	0.38	319	200.0	11.2	647.8	7.0	0.1050	0.0007	643.8	4.3
65	1468.1	15.7	67438	762	653.0	20.0	1939.7	71.9	147.6	13.2	0.07	473	250.3	12.2	660.2	7.4	0.1062	0.0009	650.5	5.1
66	1468.5	16.2	69405	818	125.8	4.7	508.0	19.0	142.3	12.7	0.27	130	177.3	9.3	720.9	9.5	0.1174	0.0017	715.6	9.8
67	1560.0	17.9	70633	882	1100.4	30.2	1851.4	69.5	1195.4	107.0	0.62	509	387.6	17.7	569.4	5.8	0.0888	0.0006	548.5	3.3
68	1440.2	15.7	69480	777	24.7	2.3	74.3	2.8	37.1	3.3	0.48	20	226.6	22.6	519.5	23.2	0.0811	0.0013	502.7	7.8
69	1447.6	15.9	68637	744	209.5	7.2	441.0	16.3	286.4	25.6	0.63	121	311.7	15.5	548.3	8.3	0.0880	0.0007	543.8	3.9
70	1528.1	15.6	67066	749	77.3	3.5	3162.1	117.0	2020.1	180.4	0.62	868	16.5	0.9	26.1	12.9	0.0032	0.0001	20.6	0.7
71	1304.5	15.8	67900	764	204.3	7.7	490.0	18.3	562.8	50.4	1.11	148	250.4	13.2	552.4	8.8	0.0877	0.0008	541.9	4.6
72	1449.4	16.2	68444	791	265.6	10.9	560.0	20.9	482.3	43.1	0.83	161	299.0	16.4	590.0	18.7	0.0872	0.0007	539.2	4.1
73	1481.0	15.7	70220	786	181.4	5.4	371.3	13.8	238.6	21.3	0.62	102	320.7	15.0	554.8	10.6	0.0873	0.0007	539.4	4.3
74	1082.9	12.1	66880	748	1884.2	50.0	5344.7	198.4	53.3	4.8	0.01	1284	265.6	12.4	623.0	7.1	0.1010	0.0010	620.3	5.7

Supplementary Table E5 Continued

Grain	He Pit Vol. (μm^3)	err. (2σ)	U-Th Pit Vol. (μm^3)	err. (2σ)	[^{4}He] (nmol/g)	err. (2σ)	[^{238}U] (nmol/g)	err. (2σ)	[^{232}Th] (nmol/g)	err. (2σ)	^{232}Th/^{238}U	eU (ppm)	(U-Th)/He date (Ma)	err. (2σ)	^{207}Pb/^{235}U date (Ma)	err. (2σ)	^{206}Pb/^{238}U	err. (2σ)	^{206}Pb/^{238}U date (Ma)	err. (2σ)
75	1449.4	16.6	66900	749	138.5	5.4	206.0	7.6	98.6	8.8	0.46	55	450.7	24.4	549.5	12.4	0.0878	0.0010	542.5	5.9
76	1910.4	19.1	70760	792	737.9	20.2	1449.7	53.7	406.8	36.6	0.27	370	358.4	16.5	659.7	8.0	0.1071	0.0012	655.9	7.0
77	1506.8	17.6	69110	773	108.3	3.6	171.5	6.4	88.4	7.9	0.50	46	421.4	21.0	558.3	12.9	0.0890	0.0010	549.3	5.6
78	1594.3	17.9	67736	783	280.7	13.0	419.0	15.6	318.2	28.4	0.73	118	425.9	25.5	596.3	18.6	0.0883	0.0013	545.5	7.7
79	1826	20.2	68019	740	415.7	15.6	1100.4	40.7	531.0	47.4	0.47	293	257.5	13.4	760.1	12.0	0.1241	0.0018	754.1	10.3
80	1648.1	19.5	68593	756	147.4	5.3	782.8	29.1	168.6	15.1	0.21	197	137.3	7.0	701.8	8.1	0.1146	0.0011	699.4	6.4
81	1420.8	15.9	66720	747	928.6	25.1	1419.1	52.6	914.2	82.0	0.62	390	425.4	19.3	555.4	7.6	0.0864	0.0008	534.3	4.7
82	1683.7	18.8	66864	760	540.7	18.7	957.6	35.8	887.5	79.7	0.90	278	350.1	17.6	700.8	28.6	0.1152	0.0011	702.9	6.4
83	1565.7	17.4	69315	826	268.9	11.4	560.6	20.9	587.9	52.6	1.02	166	292.3	16.4	545.3	8.3	0.0861	0.0009	532.2	5.2
84	1341.4	15.2	62415	738	845.3	24.3	1892.8	71.1	1174.3	105.3	0.60	518	295.1	13.6	679.1	7.3	0.1073	0.0013	657.1	7.6
85	1588.6	17.4	66395	754	132.0	4.3	259.6	9.7	173.3	15.5	0.65	72	331.9	16.2	531.6	10.8	0.0863	0.0009	533.7	5.3
86	1519.6	16.8	69510	778	69.3	2.7	164.9	6.1	102.8	9.2	0.60	45	277.8	14.9	592.9	21.6	0.0864	0.0012	534.2	7.1
87	1639.0	18.3	67960	748	842.9	24.1	2041.5	76.2	1162.0	103.9	0.55	553	276.1	12.7	760.6	6.7	0.1246	0.0011	757.0	6.3
88	1382.9	14.8	67820	801	592.7	19.8	719.4	26.9	379.7	34.0	0.51	193	542.2	27.4	539.4	8.4	0.0866	0.0008	535.5	4.7
90	1465.8	17.4	66070	739	184.8	5.7	381.2	14.2	285.8	25.5	0.73	107	311.9	14.8	545.9	58.8	0.0869	0.0017	537.2	10.1
91	1495.1	17.6	66943	784	411.9	18.6	1249.2	47.0	786.6	70.5	0.61	342	218.9	12.7	763.9	7.2	0.1255	0.0010	762.1	5.4
92	1452.1	16.9	69185	824	1147.6	31.1	1539.8	57.7	460.6	41.2	0.29	394	515.0	24.1	820.7	7.2	0.1367	0.0011	826.0	6.2
93	1526.7	15.8	68631	740	124.5	4.2	300.1	11.2	150.4	13.5	0.49	80	281.0	13.9	648.0	10.7	0.1064	0.0009	651.8	5.1
94	1398.9	16.0	66262	751	1650.5	44.6	2043.2	76.8	1436.0	128.5	0.68	568	515.1	23.7	555.3	6.5	0.0900	0.0006	555.5	3.7
95	1421.6	15.0	68378	760	257.4	9.0	477.5	17.9	246.0	22.0	0.50	128	361.6	18.4	543.6	8.3	0.0879	0.0008	543.2	4.6
96	1443.1	19.0	67485	802	218.5	6.9	1368.5	51.6	1450.5	129.9	1.03	407	98.6	4.7	620.2	30.4	0.1019	0.0016	625.5	9.4
97	565.3	6.1	56888	624	545.7	20.6	9103.5	342.4	1659.2	148.9	0.18	2273	44.4	2.3	557.7	8.8	0.0870	0.0006	537.6	3.7
98	1431.6	15.3	67248	753	168.6	6.6	532.4	20.1	217.7	19.5	0.40	140	219.8	11.8	663.4	13.2	0.1067	0.0016	653.6	9.3
99	1430.6	15.3	64740	724	165.6	5.3	356.1	13.4	172.8	15.5	0.47	95	315.2	15.3	507.9	10.5	0.0812	0.0011	503.3	6.6
100	1334.9	14.7	65750	736	109.8	4.1	143.2	5.4	82.6	7.4	0.56	39	501.3	27.0	498.0	16.2	0.0806	0.0011	499.7	6.6
101	1451.9	15.9	68120	762	167.0	6.3	556.4	20.7	391.0	34.9	0.68	155	196.8	10.2	760.1	10.6	0.1247	0.0015	757.6	8.6
102	947.0	10.2	63312	743	261.9	11.8	438.8	16.4	178.9	16.0	0.39	115	407.5	24.1	545.9	11.9	0.0877	0.0011	541.9	6.5
103	1439.5	16.1	66220	741	215.9	8.5	500.2	18.6	526.6	47.1	1.02	149	263.5	14.1	504.8	8.0	0.0815	0.0006	505.1	3.7
104	1465.5	16.0	70030	784	160.0	5.0	441.5	16.4	137.3	12.3	0.30	113	255.9	12.3	652.8	11.7	0.1068	0.0009	654.3	5.1
105	1283.3	14.3	67130	751	92.6	3.8	394.9	15.1	327.7	29.3	0.80	113	150.5	8.2	600.8	9.0	0.0966	0.0009	594.2	5.1
106	1421.5	15.8	65480	733	110.0	6.1	167.8	6.2	80.3	7.2	0.46	45	439.8	29.9	551.9	19.5	0.0876	0.0013	541.3	7.7
107	1420.3	15.2	67790	759	35.8	2.4	201.8	7.5	96.6	8.6	0.46	54	122.5	9.3	532.8	16.2	0.0813	0.0013	503.9	7.8
108	1389.8	14.7	69260	775	144.4	5.2	333.4	12.4	259.7	23.2	0.75	94	277.8	14.2	570.0	40.0	0.0881	0.0016	544.3	9.5
109	1395.3	15.5	67200	752	301.8	11.4	748.6	27.9	361.0	32.3	0.47	199	274.4	14.4	537.6	7.8	0.0869	0.0009	537.4	5.2
110	1277.2	14.3	63140	707	166.7	6.0	728.3	27.2	542.5	48.6	0.72	204	149.4	7.6	561.2	13.4	0.0815	0.0014	505.1	8.3

Supplementary Table E6

(U-Th)/He and U/Pb dates by LADD of detrital zircon for sample CHB14-2B-20H-1

Grain	He Pit Vol. (μm^3)	err. (2σ)	U-Th Pit Vol. (μm^3)	err. (2σ)	[^4He] (nmol/g)	err. (2σ)	[^{238}U] (nmol/g)	err. (2σ)	[^{232}Th] (nmol/g)	err. (2σ)	$^{232}Th/^{238}U$	eU (ppm)	(U-Th)/He date (Ma)	err. (2σ)	$^{207}Pb/^{235}U$ date (Ma)	err. (2σ)	$^{206}Pb/^{238}U$	err. (2σ)	$^{206}Pb/^{238}U$ date (Ma)	err. (2σ)
4	5502.0	55.1	79080	918	256.1	6.9	366.5	14.1	228.0	20.6	0.60	100	455.1	21.1	578.6	24.2	0.0871	0.0012	538.4	7.1
5	5254.4	52.5	78468	895	112.8	4.3	217.7	8.1	122.8	11.0	0.55	59	344.6	18.2	553.0	24.8	0.0882	0.0015	544.9	8.9
6	5482.1	54.9	75430	875	346.0	9.2	451.5	17.5	188.6	17.0	0.40	119	516.7	24.4	668.7	16.3	0.1062	0.0014	650.6	8.2
7	6444.7	64.6	75134	899	162.1	4.7	416.1	15.7	253.7	22.8	0.59	114	258.8	12.0	545.3	11.9	0.0867	0.0011	535.8	6.6
8	5597.3	56.0	75515	755	158.8	4.7	290.1	10.8	209.0	18.7	0.70	81	352.9	16.4	586.1	19.4	0.0861	0.0012	532.4	7.1
9	6301.0	63.4	83550	965	590.0	15.4	2145.5	80.4	759.8	68.0	0.34	556	193.6	8.7	538.2	20.4	0.0809	0.0014	501.5	8.4
10	5275.0	52.9	79590	924	1230.5	32.1	1443.2	54.7	1540.2	138.4	1.03	430	508.4	23.2	532.2	12.0	0.0853	0.0013	527.7	7.7
11	5411.7	54.5	75497	882	416.2	11.0	497.4	19.3	252.7	22.7	0.49	133	552.2	25.9	571.7	26.0	0.0917	0.0015	565.6	8.9
12	14060.0	140.9	80337	940	88.2	2.4	758.2	39.0	478.9	46.0	0.61	208	78.2	4.2	630.1	65.6	0.0981	0.0034	603.3	20.0
14	5496.5	55.0	76843	885	82.0	3.7	167.3	6.3	100.5	9.0	0.58	46	324.3	19.0	598.0	32.2	0.0876	0.0020	541.3	11.9
15	5246.1	52.5	78963	857	199.9	6.1	333.3	12.5	260.9	23.3	0.76	94	381.2	18.2	547.7	15.4	0.0869	0.0011	537.3	6.5
16	8442.3	84.4	83610	970	109.3	3.1	119.2	5.6	103.5	9.7	0.84	34	564.2	30.2	570.5	37.0	0.0891	0.0025	550.2	14.8
17	5522.2	55.2	79146	876	193.2	5.5	1057.4	39.7	1072.1	96.3	0.98	312	113.7	5.2	778.7	9.0	0.1310	0.0013	793.6	7.5
18	6034.7	60.4	80080	929	102.3	4.0	264.3	10.0	160.7	14.4	0.59	72	257.3	13.8	550.1	19.5	0.0879	0.0012	543.1	7.1
19	5586.2	56.1	71399	812	939.4	24.4	2495.8	94.6	1959.8	175.7	0.76	705	242.0	10.8	686.4	11.9	0.1023	0.0014	627.9	8.2
20	5808.9	58.2	78328	929	277.5	7.4	399.2	15.2	276.5	24.8	0.67	111	446.8	20.5	538.8	15.0	0.0875	0.0010	540.6	5.8
21	5199.9	52.0	79410	998	240.7	6.5	424.3	16.2	241.9	21.7	0.55	115	375.8	17.3	529.2	11.5	0.0853	0.0010	527.6	5.7
22	6831.5	68.3	81090	911	257.6	6.9	422.6	16.0	292.9	26.3	0.67	117	393.6	18.0	534.0	10.8	0.0854	0.0011	528.2	6.6
23	5997.9	60.0	91840	1066	145.6	4.4	166.6	6.4	102.6	9.2	0.60	46	563.9	27.8	558.9	19.9	0.0879	0.0016	543.1	9.5
24	5064.1	50.6	78320	884	370.5	10.0	514.7	19.3	320.3	28.7	0.60	141	468.2	21.5	529.2	12.7	0.0859	0.0010	531.4	5.7
25	6293.4	62.9	81020	930	135.4	4.3	266.5	10.1	204.9	18.4	0.74	75	325.3	15.7	534.0	17.4	0.0864	0.0012	534.2	7.1
26	6554.0	65.7	86039	951	23.7	0.9	16836.8	637.8	703.3	63.1	0.04	4075	1.1	0.1	518.9	21.4	0.0802	0.0012	497.3	7.2
27	5473.3	54.8	75240	873	87.0	3.6	165.3	6.3	86.6	7.8	0.51	44	352.5	19.7	560.1	22.2	0.0887	0.0017	547.8	10.1
28	5767.1	58.2	81120	941	124.4	4.4	144.9	5.9	90.1	8.2	0.60	40	553.9	29.9	540.6	26.2	0.0873	0.0018	539.6	10.7
29	5924.2	60.0	76956	944	179.5	5.4	335.1	12.8	308.7	27.7	0.89	97	332.9	15.9	569.4	16.2	0.0864	0.0012	534.2	7.1
30	5683.2	56.8	81323	968	137.7	4.4	276.3	10.5	164.1	14.7	0.57	75	330.1	16.1	546.5	16.6	0.0852	0.0012	527.1	7.2
31	6239.6	62.4	81602	926	139.8	4.5	425.8	16.1	383.4	34.4	0.87	123	207.1	10.0	545.3	15.4	0.0859	0.0011	531.1	6.6
32	5496.7	55.0	78566	944	138.5	4.3	215.7	8.2	115.4	10.4	0.52	58	426.4	20.8	547.7	18.4	0.0859	0.0013	531.2	7.7
33	5586.5	56.0	82072	931	201.5	5.6	393.9	14.9	245.9	23.4	0.60	108	336.5	15.5	531.0	14.5	0.0850	0.0011	525.9	6.6
34	5247.0	52.5	79958	923	146.9	4.9	219.6	8.3	123.8	11.1	0.55	59	441.1	22.1	545.9	19.6	0.0864	0.0013	534.2	7.7
35	5735.8	57.4	79412	918	407.8	11.0	724.9	27.7	567.3	51.0	0.76	205	358.2	16.4	597.4	15.8	0.0939	0.0012	578.6	7.1
36	5547.6	55.5	77202	898	653.7	17.2	1001.7	38.6	619.0	55.7	0.60	274	426.4	19.6	517.7	10.4	0.0812	0.0010	503.0	5.9
37	5470.7	54.7	78383	920	276.9	7.5	613.9	23.2	226.6	20.3	0.36	160	313.1	14.4	757.2	11.6	0.1218	0.0014	740.9	8.1

Supplementary Table E6 Continued

Grain	He Pit Vol. (μm^3)	err. (2σ)	U-Th Pit Vol. (μm^3)	err. (2σ)	[^4He] (nmol/g)	err. (2σ)	[^{238}U] (nmol/g)	err. (2σ)	[^{232}Th] (nmol/g)	err. (2σ)	$^{232}Th/^{238}U$	eU (ppm)	(U-Th)/He date (Ma)	err. (2σ)	$^{207}Pb/^{235}U$ date (Ma)	err. (2σ)	$^{206}Pb/^{238}U$	err. (2σ)	$^{206}Pb/^{238}U$ date (Ma)	err. (2σ)
38	5581.5	55.8	74910	827	2621.7	68.0	3889.4	145.2	4858.4	434.7	1.21	1197	393.0	17.7	492.4	12.5	0.0801	0.0008	496.7	4.9
39	5543.4	55.4	80246	925	44.0	1.6	1471.5	55.2	1021.2	91.5	0.67	408	19.9	1.0	21.2	2.8	0.0030	0.0001	19.6	0.6
40	7150.9	71.5	79130	918	817.4	21.3	3228.0	125.8	3322.6	301.1	1.00	955	156.6	7.0	465.1	17.4	0.0731	0.0008	455.0	4.9
41	5061.8	50.9	77471	920	158.1	4.9	262.3	9.9	154.5	13.8	0.57	71	397.1	19.2	543.6	17.3	0.0871	0.0012	538.4	7.1
42	7463.8	74.6	82607	892	100.4	3.4	258.7	9.7	182.9	16.4	0.68	72	253.0	12.4	566.5	17.5	0.0862	0.0012	533.0	7.1
43	5668.4	56.8	80111	906	798.6	20.9	972.2	36.3	813.2	72.7	0.81	277	510.8	23.1	565.3	7.6	0.0876	0.0011	541.5	6.5
44	5993.9	60.0	84361	1015	165.8	4.7	290.5	10.9	219.6	19.7	0.73	82	365.0	16.8	559.5	27.6	0.0879	0.0013	543.1	7.7
45	5533.3	55.4	79804	949	93.1	5.7	251.8	9.5	179.2	16.1	0.69	70	241.0	17.3	532.8	66.0	0.0877	0.0016	541.9	9.5
46	5500.8	55.0	77988	899	201.0	5.7	495.8	18.6	180.7	16.2	0.35	129	282.5	13.1	501.1	11.8	0.0801	0.0010	496.5	6.0
47	6934.1	69.3	81912	965	240.6	6.4	2240.9	84.6	293.1	26.3	0.13	553	80.2	3.7	580.3	6.9	0.0904	0.0010	557.8	5.9
48	5868.9	58.8	76124	871	506.0	13.4	922.1	34.8	685.6	61.5	0.72	258	352.2	15.8	519.5	11.0	0.0801	0.0015	496.7	9.0
50	6584.0	66.0	77450	899	287.7	7.7	3271.3	126.9	2987.3	269.8	0.88	947	56.0	2.5	349.6	15.8	0.0511	0.0011	321.3	6.8
51	5271.0	53.2	77075	962	190.0	5.5	259.0	9.9	202.1	18.2	0.76	73	463.0	22.0	597.4	22.0	0.0891	0.0019	550.2	11.3
52	5172.5	51.8	79590	924	3.5	0.6	179.0	6.8	94.7	8.5	0.51	48	13.4	2.4	30.0	118.2	0.0031	0.0010	19.7	6.4
53	5521.6	55.2	76960	893	295.6	7.9	666.9	25.9	355.8	31.9	0.52	179	297.9	13.7	762.5	14.4	0.1246	0.0016	757.0	9.2
54	5731.9	57.3	82157	891	877.9	23.0	1416.2	52.7	646.2	57.8	0.44	375	418.6	18.9	504.8	6.8	0.0812	0.0008	503.1	4.8
55	6148.6	61.5	58896	640	931.6	24.3	7646.0	287.6	6830.0	614.2	0.86	2205	77.8	3.4	577.9	5.7	0.0868	0.0012	536.6	7.1
56	5405.5	54.1	79909	910	240.2	6.5	286.4	10.8	226.2	20.2	0.76	81	525.5	24.2	580.3	19.5	0.0885	0.0012	546.7	7.1
57	5750.6	57.8	78638	888	297.1	8.0	494.9	18.6	389.1	34.8	0.76	140	381.2	17.3	574.0	14.4	0.0871	0.0011	538.3	6.5
58	5592.3	56.0	81829	986	244.1	6.6	434.1	16.4	338.9	30.4	0.76	123	358.3	16.3	539.4	19.7	0.0878	0.0016	542.5	9.5
59	7988.2	79.9	74610	866	883.9	22.8	1695.6	66.3	1446.5	131.0	0.83	485	328.4	14.9	544.8	15.5	0.0811	0.0011	502.4	6.6
60	5606.9	56.1	72536	869	224.6	6.3	475.6	18.0	336.8	30.2	0.69	132	306.4	14.1	550.7	17.7	0.0924	0.0013	569.7	7.7
61	5726.2	57.5	64627	797	179.6	5.0	385.8	14.7	277.2	24.9	0.70	108	301.6	13.9	563.0	20.4	0.0871	0.0014	538.4	8.3
62	5633.5	56.7	73818	829	359.6	9.5	670.2	25.4	548.7	49.4	0.79	191	339.9	15.3	559.5	12.3	0.0878	0.0010	542.8	5.9
63	6381.5	64.1	76937	878	122.2	3.7	272.0	10.3	181.8	16.3	0.65	75	294.0	14.0	586.1	24.0	0.0891	0.0012	550.2	7.1
65	7568.9	75.7	86700	1006	304.7	8.2	2388.1	92.8	1434.3	129.8	0.58	651	86.2	3.9	359.6	24.2	0.0517	0.0010	325.1	6.0
66	5488.9	55.4	78846	964	111.9	5.3	138.1	5.3	99.6	8.9	0.70	39	515.0	32.0	757.7	46.2	0.1243	0.0027	755.3	15.5
67	5904.0	59.1	83100	964	290.2	7.7	569.0	21.7	446.8	40.2	0.76	161	325.5	14.8	569.4	15.7	0.0863	0.0012	533.6	7.1
68	5858.9	58.6	76663	892	1030.0	26.7	1412.7	53.1	2105.1	188.5	1.44	453	407.5	18.7	545.3	11.9	0.0809	0.0013	501.5	7.8
69	5955.3	59.6	67282	780	883.5	22.9	2277.0	86.3	1284.0	115.0	0.55	616	260.1	11.6	592.3	15.9	0.0936	0.0014	576.8	8.3
70	5471.1	55.1	76501	917	182.7	5.1	349.8	13.2	352.3	31.6	0.97	103	319.9	14.6	658.7	17.0	0.1062	0.0014	650.6	8.2
71	6117.8	61.2	79359	891	228.3	6.1	476.7	17.9	313.4	28.1	0.64	131	313.6	14.1	525.0	18.8	0.0850	0.0012	525.9	7.2
72	5460.5	54.6	76690	890	205.2	5.8	241.0	9.1	164.5	14.7	0.66	67	543.5	25.4	582.1	22.4	0.0873	0.0015	539.6	8.9
75	5776.7	57.8	76250	887	205.8	5.7	375.0	14.1	244.2	21.9	0.63	103	358.4	16.4	546.5	17.2	0.0869	0.0014	537.2	8.3
76	5749.3	57.5	77430	899	129.2	4.4	236.5	8.9	144.8	13.0	0.59	65	359.5	18.0	595.1	23.8	0.0872	0.0017	539.0	10.1

Supplementary Table E6 Continued

Grain	He Pit Vol. (μm³)	err. (2σ)	U-Th Pit Vol. (μm³)	err. (2σ)	[⁴He] (nmol/g)	err. (2σ)	[²³⁸U] (nmol/g)	err. (2σ)	[²³²Th] (nmol/g)	err. (2σ)	²³²Th/²³⁸U	eU (ppm)	(U-Th)/He date (Ma)	err. (2σ)	²⁰⁷Pb/²³⁵U date (Ma)	err. (2σ)	²⁰⁶Pb/²³⁸U	err. (2σ)	²⁰⁶Pb/²³⁸U date (Ma)	err. (2σ)
77	5536.3	55.4	75170	829	175.3	5.2	360.0	13.5	294.2	26.3	0.79	102	309.3	14.5	601.3	43.2	0.0850	0.0014	525.9	8.3
78	5583.2	55.8	79450	922	212.5	5.9	1006.6	38.0	280.8	25.3	0.27	257	151.6	7.0	650.1	13.9	0.1026	0.0013	629.6	7.6
79	6272.0	62.9	82570	946	45.4	1.6	1671.9	62.8	1518.4	136.1	0.88	484	17.4	0.9	31.0	19.7	0.0031	0.0002	19.6	1.2
80	5839.0	58.6	80396	1036	120.0	4.6	413.7	15.8	496.3	44.6	1.16	126	173.7	9.2	608.6	13.4	0.0951	0.0012	585.6	7.1
81	5612.5	56.2	78710	913	104.4	4.4	186.5	7.0	117.4	10.5	0.61	51	366.8	20.7	531.6	20.4	0.0875	0.0015	540.7	8.9
83	5482.1	54.9	78389	883	404.6	10.6	870.0	32.8	745.7	66.9	0.83	249	293.6	13.1	495.5	21.8	0.0800	0.0014	496.1	8.4
84	6112.2	61.1	74518	945	130.7	4.1	292.9	11.2	203.7	18.3	0.67	81	290.6	14.0	553.0	18.3	0.0875	0.0013	540.7	7.7
85	5779.2	58.0	78713	869	191.8	5.8	369.7	13.8	288.1	25.8	0.75	104	331.4	15.7	600.2	26.4	0.0876	0.0013	541.3	7.7
86	5871.3	58.7	81260	943	192.7	5.4	364.8	13.8	296.5	26.6	0.79	104	335.2	15.4	546.5	15.4	0.0881	0.0011	544.1	6.5
87	5654.6	56.7	75337	845	116.9	4.1	221.8	8.3	120.8	10.8	0.53	60	351.7	17.9	545.3	20.8	0.0863	0.0014	533.6	8.3
90	5960.5	59.6	80609	967	65.5	2.4	203.1	7.7	219.9	19.7	1.05	61	196.9	10.2	610.8	25.6	0.0974	0.0017	599.2	10.0
91	5848.4	58.5	82370	956	1283.8	33.3	4210.2	160.0	1023.5	91.8	0.24	1065	219.3	10.0	570.0	22.0	0.0878	0.0018	542.5	10.7
92	9699.8	97.2	89825	942	203.1	5.4	5787.9	218.1	4870.4	436.3	0.81	1653	22.7	1.0	413.7	12.8	0.0613	0.0006	383.7	3.8
95	5789.5	57.9	84651	942	309.1	8.2	458.8	17.3	330.3	29.6	0.70	128	431.4	19.6	636.1	26.0	0.1060	0.0019	649.5	11.1
96	6374.0	63.9	84397	998	41.9	1.6	223.5	8.5	140.1	12.6	0.61	61	125.5	6.7	502.3	130.0	0.0807	0.0024	500.3	14.3
97	5866.7	58.9	77780	903	435.3	11.5	1238.3	46.7	405.8	36.4	0.32	319	247.6	11.2	711.4	13.6	0.1166	0.0012	711.0	7.0
98	6013.2	60.4	79120	918	8.3	0.5	254.7	9.8	160.2	14.4	0.61	70	22.1	1.6	58.2	84.4	0.0030	0.0008	19.4	4.9
99	5910.6	59.3	76789	937	187.8	5.4	356.8	13.5	279.4	25.1	0.76	101	335.8	15.6	569.4	16.2	0.0923	0.0013	569.1	7.7
100	5863.9	58.9	75230	873	647.3	17.0	1319.9	49.9	2405.7	218.8	1.76	448	262.5	12.3	723.4	9.0	0.1168	0.0012	712.3	7.0
101	5490.7	54.9	80731	937	561.3	14.8	1524.6	57.8	1968.3	176.6	1.25	473	216.2	9.8	564.7	7.0	0.0950	0.0013	585.0	7.7
102	5676.5	57.5	81780	949	810.7	21.5	962.6	36.6	1279.8	114.9	1.29	301	480.8	22.3	563.0	14.0	0.0881	0.0011	544.4	6.5
103	5559.6	55.7	76135	902	116.0	5.5	158.8	6.0	83.4	7.5	0.51	43	483.5	29.6	511.6	31.2	0.0811	0.0018	502.7	10.7
104	6400.6	64.1	81563	1009	203.6	5.6	316.1	11.9	274.5	24.6	0.84	91	402.0	18.4	529.8	21.2	0.0852	0.0014	527.1	8.3
105	6205.7	62.4	81840	950	254.9	7.0	321.2	12.3	243.8	21.9	0.73	90	501.3	23.4	535.8	17.4	0.0854	0.0012	528.3	7.1
106	5704.0	57.1	80420	933	161.0	4.6	352.3	13.4	339.0	30.5	0.93	103	283.1	13.1	601.9	18.0	0.0970	0.0013	596.8	7.7
107	6427.0	64.4	76578	803	829.5	21.7	7216.1	271.1	2540.1	227.7	0.34	1868	81.8	3.6	525.6	10.3	0.0807	0.0013	500.3	7.8
108	6570.7	65.7	80357	881	3.1	0.5	252.6	9.4	167.3	15.0	0.64	70	8.2	1.4	49.5	106.4	0.0031	0.0012	20.0	7.7
110	5933.9	59.4	77244	938	628.4	16.6	707.9	26.9	843.1	75.8	1.15	216	517.5	23.9	537.6	13.8	0.0849	0.0011	525.3	6.6

Supplementary Table E7

(U-Th)/He and U/Pb dates by LADD of detrital zircon for sample CHB14-2B-23E-1

Grain	He Pit Vol. (μm^3)	err. (2σ)	U-Th Pit Vol. (μm^3)	err. (2σ)	[^{4}He] (nmol/g)	err. (2σ)	[^{238}U] (nmol/g)	err. (2σ)	[^{232}Th] (nmol/g)	err. (2σ)	^{232}Th/^{238}U	eU (ppm)	(U-Th)/He date (Ma)	err. (2σ)	^{207}Pb/^{235}U date (Ma)	err. (2σ)	^{206}Pb/^{238}U	err. (2σ)	^{206}Pb/^{238}U date (Ma)	err. (2σ)
2	6034.8	60.3	80430	937	618.3	16.2	1333.9	51.7	596.6	54.0	0.43	352	316.5	14.5	579.8	8.6	0.0905	0.0009	558.3	5.3
3	5627.3	56.8	75489	867	14.9	0.8	672.4	25.3	498.5	44.7	0.72	188	14.6	0.9	25.0	5.2	0.0029	0.0002	18.9	1.2
4	6161.0	61.8	75168	869	119.4	3.8	16744.6	633.7	12127.6	1087.2	0.70	4675	4.7	0.2	275.0	9.3	0.0389	0.0004	246.3	2.7
5	5242.3	52.4	81906	986	11.2	0.7	328.4	12.4	206.5	18.5	0.61	90	23.1	1.6	30.0	118.2	0.0045	0.0012	28.9	7.7
7	5943.8	59.7	72729	894	1402.9	36.6	4233.4	161.4	1315.1	118.1	0.30	1087	234.6	10.7	470.9	12.8	0.0725	0.0007	451.4	4.0
8	5547.0	55.7	76433	849	55.0	2.1	282.2	10.7	129.8	11.6	0.44	75	134.8	7.1	794.1	24.2	0.1220	0.0025	742.1	14.4
9	5225.8	52.3	75872	849	46.1	1.7	205.3	7.7	83.2	7.4	0.39	54	157.0	8.1	665.5	24.8	0.1042	0.0016	639.0	9.3
10	6058.0	60.8	71057	783	181.8	5.1	22574.8	848.8	735.1	65.8	0.03	5452	6.2	0.3	427.8	14.0	0.0641	0.0009	400.6	5.3
11	5512.6	55.3	78853	875	463.5	12.3	542.7	20.5	501.3	45.1	0.89	157	522.1	23.9	595.7	20.8	0.0858	0.0010	530.7	5.9
13	5878.3	58.8	77067	896	811.2	21.6	2192.0	82.5	2244.7	201.1	0.99	648	227.7	10.2	518.9	13.4	0.0811	0.0008	502.7	4.5
14	5451.1	54.5	80980	944	11.9	0.7	313.1	11.8	182.4	16.4	0.56	85	26.0	1.8	30.0	216.8	0.0031	0.0020	20.0	12.9
15	5708.5	57.2	74340	866	429.5	11.4	1544.5	58.2	553.1	49.5	0.35	400	195.6	8.8	818.9	7.7	0.1333	0.0008	806.4	4.4
16	5638.8	56.4	80010	933	280.7	7.8	513.2	19.3	411.2	36.8	0.78	145	347.4	15.9	572.3	12.1	0.0918	0.0008	566.1	4.8
17	5596.9	56.0	85298	957	207.6	5.9	269.7	10.2	198.8	17.8	0.71	75	488.7	22.9	546.5	15.4	0.0885	0.0011	546.7	6.5
18	5573.8	55.9	78579	881	224.8	6.3	354.8	13.4	398.7	35.7	1.09	107	378.1	17.6	563.0	13.4	0.0852	0.0009	527.0	5.0
19	5511.2	55.2	77565	910	442.2	11.7	638.8	24.3	786.5	70.7	1.19	196	404.5	18.6	574.6	16.1	0.0849	0.0010	525.3	5.9
20	5550.4	55.5	75217	872	521.7	14.0	1200.7	45.6	590.8	53.0	0.48	320	294.6	13.4	747.5	8.3	0.1212	0.0008	737.7	4.4
21	5606.1	56.1	78859	878	303.7	8.3	402.0	15.2	376.7	33.8	0.91	117	463.0	21.3	565.3	16.9	0.0852	0.0010	527.1	5.8
22	5514.6	55.2	77670	905	220.8	6.3	350.7	13.3	217.6	19.5	0.60	96	411.6	19.3	544.2	14.9	0.0883	0.0010	545.5	5.9
23	5499.3	55.0	76993	835	107.1	4.2	247.5	9.3	138.6	12.4	0.54	67	289.4	15.7	563.6	18.7	0.0892	0.0012	550.8	7.1
24	5484.1	54.8	77050	866	19.2	0.9	635.4	24.0	361.1	32.4	0.55	172	20.7	1.2	24.1	31.8	0.0030	0.0003	19.2	1.8
25	5468.9	54.7	74860	873	201.0	5.4	375.4	14.2	224.9	20.2	0.58	102	353.4	16.2	545.3	14.2	0.0873	0.0010	539.6	5.9
26	5453.6	54.5	76910	896	191.9	5.7	301.1	11.4	190.6	17.1	0.61	83	415.7	19.9	535.2	15.6	0.0857	0.0009	530.2	5.6
27	5438.4	54.3	78770	918	318.8	8.4	485.9	18.4	413.9	37.1	0.82	139	410.5	18.6	557.1	12.9	0.0852	0.0009	527.0	5.6
28	5423.2	54.2	80919	907	131.2	6.7	242.2	9.1	154.2	13.8	0.62	66	354.9	22.6	576.9	17.8	0.0889	0.0012	549.0	7.1
29	5407.9	54.0	75317	839	136.4	5.3	216.8	8.2	124.7	11.2	0.56	59	414.9	22.5	558.3	20.6	0.0865	0.0014	534.8	8.3
30	5392.7	53.9	77937	898	286.2	7.6	402.5	15.2	296.3	26.6	0.71	113	453.0	20.6	543.0	13.1	0.0851	0.0009	526.6	5.3
31	5377.5	53.7	83380	972	235.1	6.3	383.2	14.5	287.8	26.1	0.73	108	391.8	17.8	543.6	13.7	0.0870	0.0011	537.8	6.5
32	5362.2	53.5	86573	1057	134.2	3.7	231.8	8.9	154.7	13.9	0.65	64	376.4	17.5	739.7	18.1	0.1220	0.0016	742.1	9.2
33	5347.0	53.4	81080	945	244.9	6.6	344.1	13.0	265.7	23.8	0.75	97	450.5	20.7	540.6	15.5	0.0857	0.0010	530.3	5.6
35	5331.8	53.2	80900	943	531.2	13.9	3145.9	120.7	1164.2	104.7	0.36	818	119.3	5.4	544.8	7.1	0.0814	0.0012	504.5	7.2
36	5316.5	53.0	81960	955	272.5	7.4	411.1	15.4	267.6	24.0	0.63	113	430.1	19.6	556.0	16.4	0.0884	0.0011	546.1	6.5
38	5301.3	52.9	79230	923	175.3	5.7	303.2	11.5	237.0	21.3	0.76	86	367.9	18.0	561.8	14.6	0.0878	0.0011	542.5	6.5
39	5286.0	52.7	78040	910	229.0	6.2	392.3	14.7	272.7	24.4	0.67	109	377.3	17.1	549.5	12.4	0.0853	0.0009	527.8	5.5

Supplementary Table E7 Continued

Grain	He Pit Vol. (μm³)	err. (2σ)	U-Th Pit Vol. (μm³)	err. (2σ)	[⁴He] (nmol/g)	err. (2σ)	[²³⁸U] (nmol/g)	err. (2σ)	[²³²Th] (nmol/g)	err. (2σ)	²³²Th/²³⁸U	eU (ppm)	(U-Th)/He date (Ma)	err. (2σ)	²⁰⁷Pb/²³⁵U date (Ma)	err. (2σ)	²⁰⁶Pb/²³⁸U	err. (2σ)	²⁰⁶Pb/²³⁸U date (Ma)	err. (2σ)
40	5270.8	52.5	82880	966	176.0	5.1	357.2	13.6	261.3	23.4	0.71	100	318.0	14.9	569.4	15.1	0.0909	0.0011	560.9	6.5
43	5255.6	52.4	65311	796	326.6	8.8	4288.8	162.6	853.3	77.1	0.19	1075	56.1	2.6	603.0	19.6	0.0981	0.0013	603.3	7.6
45	5240.3	52.2	81190	946	183.7	5.3	281.2	10.7	276.5	24.8	0.95	82	399.2	18.8	575.2	15.6	0.0866	0.0010	535.4	5.9
47	5225.1	52.1	78912	858	60.4	2.5	165.7	6.2	90.7	8.1	0.53	45	245.7	13.7	514.6	32.4	0.0808	0.0026	500.9	15.5
48	5209.9	51.9	67038	713	1261.8	32.8	7137.9	270.9	3292.0	295.5	0.45	1891	122.5	5.4	450.2	7.8	0.0641	0.0008	400.5	4.8
50	5194.6	51.7	80565	924	279.1	7.5	2035.2	76.9	1279.7	115.1	0.61	558	92.1	4.1	694.6	10.2	0.1076	0.0020	658.8	11.6
51	5179.4	51.6	82430	961	699.7	18.3	2770.0	107.1	3684.3	331.6	1.29	865	148.1	6.7	466.4	15.4	0.0719	0.0010	447.7	5.8
52	5164.2	51.4	77585	933	61.2	1.9	194.4	7.4	131.5	11.8	0.65	54	207.4	9.9	551.3	24.8	0.0874	0.0017	540.1	10.1
53	5148.9	51.2	89371	1011	415.2	11.0	935.5	35.3	445.4	40.0	0.46	249	301.7	13.6	629.6	9.8	0.0988	0.0008	607.6	4.4
55	5133.7	51.1	78227	904	277.9	7.4	501.2	18.9	258.4	23.1	0.50	134	371.6	16.9	654.4	11.7	0.1076	0.0014	658.8	8.1
57	5118.5	50.9	78180	911	155.1	4.3	265.4	10.4	165.1	14.9	0.60	73	382.9	17.9	605.3	21.8	0.0903	0.0015	557.3	8.9
58	5103.2	50.8	80890	943	154.4	4.6	405.2	15.5	304.9	27.5	0.73	114	246.4	11.6	560.7	20.4	0.0862	0.0011	533.0	6.5
59	5088.0	50.6	79260	924	252.2	6.7	339.1	12.8	236.1	21.1	0.67	94	476.3	21.7	551.9	14.7	0.0850	0.0010	525.9	5.9
61	5072.7	50.4	79547	1123	135.8	4.2	238.9	9.2	145.6	13.1	0.59	65	373.8	18.2	592.9	28.8	0.0897	0.0012	553.8	7.1
62	5057.5	50.3	72704	838	700.8	18.4	4493.3	169.5	1310.5	117.5	0.28	1149	112.1	5.0	579.8	8.6	0.0854	0.0010	528.3	5.9
64	5042.3	50.1	71192	826	1147.3	29.6	3069.3	115.9	3263.9	292.9	1.03	914	228.4	10.1	513.4	18.4	0.0799	0.0009	495.4	5.5
66	5027.0	49.9	84340	983	1083.7	28.0	1872.4	72.2	1603.0	144.1	0.83	536	363.3	16.4	491.7	8.1	0.0727	0.0010	452.4	6.0
68	5011.8	49.8	79697	901	135.4	4.4	209.1	7.9	154.3	13.8	0.71	59	413.9	20.5	521.3	16.4	0.0852	0.0013	527.1	7.7
69	4996.6	49.6	79700	929	903.7	23.7	1611.8	61.7	1298.8	116.8	0.78	457	355.5	16.1	513.4	9.8	0.0807	0.0008	500.4	4.7
70	4981.3	49.4	68906	808	302.6	8.1	3120.6	119.1	920.3	82.6	0.29	798	69.9	3.2	545.3	26.2	0.0810	0.0019	502.1	11.3
71	4966.1	49.3	81758	919	396.5	10.6	7282.3	273.9	543.4	48.7	0.07	1775	41.3	1.9	477.2	19.7	0.0724	0.0014	450.6	8.4
72	4950.9	49.1	82210	1039	946.3	24.4	4156.5	166.6	1307.9	118.4	0.30	1068	162.1	7.5	604.1	12.3	0.0954	0.0007	587.3	4.1
76	4935.6	49.0	82805	899	191.9	5.2	386.5	14.5	286.8	25.7	0.72	108	319.7	14.4	582.6	21.8	0.0877	0.0011	541.9	6.5
77	4920.4	48.8	82564	982	11.7	0.7	399.1	15.1	249.7	22.4	0.61	109	19.8	1.4	20.1	85.6	0.0031	0.0007	20.2	4.6
80	4905.2	48.6	82112	954	168.6	4.9	360.4	13.6	285.0	25.5	0.77	102	298.9	13.8	548.3	18.3	0.0860	0.0015	531.8	8.9
81	4889.9	48.5	77495	866	261.4	7.1	432.5	16.3	394.5	35.5	0.88	125	375.0	17.1	538.8	12.5	0.0875	0.0009	540.6	5.3
82	4874.7	48.3	78879	899	166.6	4.8	5828.5	219.2	10237.5	917.3	1.70	1955	15.8	0.7	279.6	9.3	0.0386	0.0006	243.8	3.4
83	4859.4	48.1	84760	1074	198.2	5.5	304.8	11.6	220.8	19.8	0.70	85	416.5	19.3	551.3	17.1	0.0877	0.0011	541.9	6.5
84	4844.2	48.0	81803	1023	229.6	6.3	493.8	18.7	577.0	51.7	1.13	150	277.6	12.7	646.9	12.9	0.1039	0.0016	637.2	9.3
85	4829.0	47.8	85898	979	142.7	4.4	220.6	8.3	163.3	14.6	0.72	62	413.2	19.8	587.2	23.4	0.0887	0.0019	547.8	11.3
89	4813.7	47.7	81521	951	86.7	3.8	145.3	5.5	103.8	9.3	0.69	40	383.9	22.3	551.8	22.4	0.0873	0.0016	539.6	9.5
90	4798.5	47.5	80230	935	2333.2	60.1	4909.1	185.4	68.7	6.2	0.01	1181	354.7	16.7	615.3	7.8	0.0976	0.0008	600.6	4.8
91	4783.3	47.3	78119	851	100.6	4.0	180.6	6.7	156.2	14.0	0.84	52	349.5	18.8	574.0	86.6	0.0854	0.0055	528.3	32.6
92	4768.0	47.2	82444	979	183.5	5.1	276.6	10.4	189.5	17.0	0.66	77	427.7	19.6	543.0	17.3	0.0871	0.0013	538.4	7.7
93	4752.8	47.0	78852	951	187.8	5.5	323.1	12.2	228.8	20.5	0.69	90	374.9	17.6	541.2	17.9	0.0853	0.0014	527.7	8.3

Supplementary Table E7 Continued

Grain	He Pit Vol. (μm^3)	err. (2σ)	U-Th Pit Vol. (μm^3)	err. (2σ)	[^{4}He] (nmol/g)	err. (2σ)	[^{238}U] (nmol/g)	err. (2σ)	[^{232}Th] (nmol/g)	err. (2σ)	^{232}Th/^{238}U	eU (ppm)	(U-Th)/He date (Ma)	err. (2σ)	^{207}Pb/^{235}U date (Ma)	err. (2σ)	^{206}Pb/^{238}U	err. (2σ)	^{206}Pb/^{238}U date (Ma)	err. (2σ)
94	4737.6	46.8	74780	872	265.5	7.1	429.4	16.1	266.5	23.9	0.60	117	404.5	18.3	529.2	14.5	0.0868	0.0013	536.6	7.7
95	4722.3	46.7	81745	941	71.5	2.7	357.2	13.4	343.5	30.7	0.93	104	125.7	6.6	571.7	22.6	0.0882	0.0018	544.9	10.7
96	4707.1	46.5	80445	946	494.6	13.0	1155.2	43.2	1087.9	97.3	0.91	336	266.7	11.9	579.8	9.8	0.0932	0.0010	574.4	5.8
97	4691.9	46.3	82445	996	153.5	4.8	287.7	10.8	151.8	13.6	0.51	77	357.2	17.3	535.2	18.0	0.0854	0.0011	528.3	6.5
98	4676.6	46.2	89949	1173	75.7	4.1	197.1	7.5	147.3	13.2	0.72	55	248.7	16.4	568.2	81.2	0.0815	0.0021	505.1	12.5
99	4661.4	46.0	79161	906	112.1	4.7	219.8	8.2	209.6	18.8	0.92	64	315.6	17.7	609.2	21.2	0.0886	0.0013	547.3	7.7
100	4646.2	45.9	79333	892	330.6	8.8	546.9	20.4	370.7	33.2	0.66	151	391.6	17.7	532.8	11.4	0.0863	0.0009	533.6	5.5
101	4630.9	45.7	87465	996	89.1	4.0	308.2	11.6	198.5	17.8	0.62	85	191.8	11.0	645.8	22.0	0.1040	0.0014	637.8	8.2
102	4615.7	45.5	78556	904	135.3	4.0	274.6	10.3	137.0	12.3	0.48	73	332.5	15.7	546.5	18.4	0.0866	0.0012	535.4	7.1
103	4600.4	45.4	82028	933	161.5	5.1	252.4	9.5	139.1	12.5	0.53	68	423.7	20.7	545.9	17.8	0.0870	0.0012	537.8	7.1
104	4585.2	45.2	83820	977	1285.4	33.2	1726.1	65.0	4145.0	371.2	2.32	640	362.2	17.7	660.8	7.4	0.1073	0.0008	657.1	4.8
105	4570.0	45.0	88170	1028	78.2	3.2	359.5	13.6	281.2	25.2	0.76	102	141.1	7.7	522.5	30.4	0.0836	0.0018	517.6	10.7
106	4554.7	44.9	83210	970	718.1	18.7	1199.1	45.2	626.3	56.1	0.51	322	399.7	18.1	502.9	8.0	0.0806	0.0009	499.8	5.3
107	4539.5	44.7	80740	941	210.7	5.9	311.8	11.7	175.4	15.7	0.54	84	445.6	20.7	527.4	19.3	0.0854	0.0012	528.3	7.1
108	4524.3	44.5	80303	921	405.0	10.6	679.2	26.0	352.2	32.0	0.50	182	398.4	18.2	759.6	12.5	0.1221	0.0012	742.6	6.9
109	4509.0	44.4	74823	834	1188.5	30.8	2988.3	112.3	1428.1	127.9	0.46	794	271.0	12.1	601.9	10.1	0.0896	0.0014	553.2	8.3
110	4493.8	44.2	81200	1022	154.6	5.2	798.2	30.7	276.7	25.1	0.34	206	137.2	6.8	681.2	13.5	0.1082	0.0017	662.3	9.9

Supplementary Table E8

(U-Th)/He and U/Pb dates by LADD of detrital zircon for sample CHB14-2B-35E-1

Grain	He Pit Vol. (μm^3)	err. (2σ)	U-Th Pit Vol. (μm^3)	err. (2σ)	[^4He] (nmol/g)	err. (2σ)	[^{238}U] (nmol/g)	err. (2σ)	[^{232}Th] (nmol/g)	err. (2σ)	$^{232}Th/^{238}U$	eU (ppm)	(U-Th)/He date (Ma)	err. (2σ)	$^{207}Pb/^{235}U$ date (Ma)	err. (2σ)	$^{206}Pb/^{238}U$	err. (2σ)	$^{206}Pb/^{238}U$ date (Ma)	err. (2σ)
1	5611.1	56.1	83302	958	401.4	10.7	685.7	25.7	444.9	39.8	0.63	189	381.7	17.2	593.0	18.0	0.0935	0.0017	576.4	9.9
2	1818.3	18.1	43013	440	443.0	15.5	610.5	22.6	347.3	31.0	0.55	165	476.6	24.3	533.0	16.0	0.0860	0.0014	531.6	8.6
3	6501.3	65.1	78890	962	232.1	6.3	477.7	18.1	348.5	31.2	0.71	134	313.7	14.2	542.0	20.0	0.0869	0.0018	537.0	11.0
4	6554.2	65.5	72696	836	1063.7	28.2	2581.7	97.7	2792.0	250.6	1.05	771	250.4	11.3	527.0	24.0	0.0825	0.0021	511.0	12.0
5	5866.8	58.7	72310	849	793.1	21.3	1115.1	42.2	1123.7	100.7	0.98	329	431.5	19.7	532.0	16.0	0.0845	0.0013	522.8	7.9
6	5900.4	59.0	84740	1052	407.5	11.0	1060.5	40.3	766.9	68.8	0.70	296	249.8	11.3	512.0	14.0	0.0826	0.0012	511.4	7.2
7	5673.3	56.8	82006	931	287.7	7.8	503.0	19.0	276.4	24.8	0.53	136	380.4	17.4	525.0	63.0	0.0879	0.0018	543.2	11.0
8	5740.5	57.4	80724	910	153.2	5.3	255.4	9.6	142.5	12.8	0.54	69	397.8	20.3	536.0	25.0	0.0877	0.0017	542.0	10.0
9	5701.3	57.0	77897	940	75.2	3.1	231.1	8.8	88.8	8.0	0.37	60	227.0	12.5	696.0	28.0	0.1076	0.0020	658.9	12.0
10	5768.2	57.7	80464	997	202.4	5.8	367.8	14.1	338.1	30.5	0.89	107	342.0	16.0	563.0	26.0	0.0889	0.0016	549.2	9.7
11	6795.8	68.0	84395	1052	755.9	19.5	1880.0	71.4	1343.0	120.5	0.69	524	261.6	11.6	458.0	32.0	0.0754	0.0012	468.8	6.9
12	6067.1	60.7	79052	944	286.1	7.6	789.1	29.9	474.3	42.5	0.58	215	241.7	10.8	533.0	17.0	0.0791	0.0016	491.0	9.3
13	5862.3	58.6	83210	946	537.8	14.0	740.1	27.8	486.0	43.5	0.64	204	469.4	21.2	770.0	17.0	0.1256	0.0021	762.3	12.0
14	5867.0	58.7	79270	913	232.6	6.3	439.4	16.5	303.9	27.2	0.67	122	343.5	15.5	583.0	60.0	0.0886	0.0019	547.0	11.0
15	5844.8	58.5	81452	935	187.9	5.1	341.3	12.8	214.4	19.2	0.61	94	361.0	16.4	569.0	20.0	0.0908	0.0015	560.1	9.1
17	5729.8	57.4	80410	940	280.6	7.3	801.1	30.1	1129.4	101.1	1.36	254	201.7	9.1	770.0	14.0	0.1260	0.0022	764.6	12.0
18	7020.5	70.2	75899	877	490.8	12.9	2755.5	103.5	1609.6	144.1	0.57	748	120.4	5.3	683.0	26.0	0.1122	0.0021	685.0	12.0
19	5859.0	58.6	78117	1009	208.5	5.7	415.8	15.8	303.3	27.2	0.71	116	323.5	14.8	576.0	21.0	0.0878	0.0018	542.1	10.0
20	6827.1	68.3	78843	903	748.3	20.0	2435.5	91.4	3176.6	284.4	1.26	757	180.5	8.1	521.0	23.0	0.0820	0.0014	507.8	8.3
21	5875.8	58.8	80703	920	80.7	3.8	344.8	13.0	196.1	17.6	0.55	93	158.2	9.4	571.0	27.0	0.0869	0.0019	537.0	11.0
22	5865.5	58.7	73233	832	304.8	8.1	671.8	25.3	617.3	55.3	0.89	195	283.4	12.7	561.0	20.0	0.0885	0.0017	546.2	10.0
23	5377.2	53.8	81617	951	398.9	10.4	735.7	28.1	392.2	35.1	0.52	198	362.4	16.5	631.0	18.0	0.1022	0.0018	627.4	11.0
24	5821.3	58.2	75277	860	429.5	11.2	596.6	22.4	387.3	34.7	0.63	164	465.9	21.1	584.0	18.0	0.0953	0.0017	586.5	9.8
25	5767.2	57.7	81205	928	115.9	3.9	208.0	7.8	141.3	12.7	0.66	58	361.7	18.1	581.0	29.0	0.0877	0.0019	541.8	11.0
26	5699.7	57.1	80800	966	157.2	4.4	274.6	10.5	234.2	21.1	0.83	79	359.8	16.6	556.0	25.0	0.0897	0.0017	553.5	10.0
27	5748.8	57.5	79160	937	315.1	8.3	571.0	21.5	385.2	34.5	0.65	158	358.7	16.1	539.0	19.0	0.0878	0.0017	542.2	10.0
28	5718.8	57.2	81520	935	361.1	9.5	554.0	20.8	411.6	36.8	0.72	155	416.1	18.7	555.0	20.0	0.0890	0.0015	549.3	8.9
29	5841.4	58.4	78219	928	28.7	1.0	104.1	3.9	63.9	5.7	0.59	28	184.5	9.2	489.0	34.0	0.0802	0.0023	497.0	14.0
30	5986.0	59.9	79722	881	725.6	18.9	1291.6	48.2	821.2	73.4	0.62	354	367.7	16.4	559.4	14.0	0.0890	0.0014	549.8	8.6
31	5996.9	60.0	81177	904	940.9	24.5	1880.4	70.8	1544.2	138.5	0.79	535	317.4	14.1	780.0	15.0	0.1259	0.0024	764.0	14.0
32	5709.3	57.1	79407	875	223.2	6.1	505.3	18.9	289.6	25.9	0.55	137	294.6	13.3	548.0	20.0	0.0881	0.0018	544.3	11.0
33	5581.6	55.8	78448	1011	240.1	6.5	569.8	21.7	489.1	43.9	0.83	163	266.6	12.1	545.0	19.0	0.0881	0.0018	544.3	11.0
34	6077.3	60.8	80808	933	76.1	3.6	155.8	5.8	93.3	8.3	0.58	42	323.4	19.4	560.0	35.0	0.0890	0.0020	550.0	12.0
35	1916.7	19.2	41670	429	163.4	5.8	243.0	8.9	205.5	18.4	0.82	69	420.9	21.5	490.0	140.0	0.0859	0.0029	531.0	17.0

Grain	He Pit Vol. (μm^3)	err. (2σ)	U-Th Pit Vol. (μm^3)	err. (2σ)	[^4He] (nmol/g)	err. (2σ)	[^{238}U] (nmol/g)	err. (2σ)	[^{232}Th] (nmol/g)	err. (2σ)	$^{232}Th/^{238}U$	eU (ppm)	(U-Th)/He date (Ma)	err. (2σ)	$^{207}Pb/^{235}U$ date (Ma)	err. (2σ)	$^{206}Pb/^{238}U$	err. (2σ)	$^{206}Pb/^{238}U$ date (Ma)	err. (2σ)
36	5704.2	57.0	83540	979	264.6	7.1	340.9	12.8	287.7	25.8	0.82	97	483.2	22.1	566.0	21.0	0.0876	0.0017	541.4	10.0
37	5899.8	59.0	79806	888	255.7	6.8	405.6	15.2	267.4	23.9	0.64	112	409.3	18.5	557.0	20.0	0.0885	0.0017	546.3	9.9
39	7806.5	78.1	80895	918	769.2	19.8	6454.3	245.3	3452.0	310.3	0.52	1735	81.6	3.6	420.0	37.0	0.0630	0.0016	393.9	9.7
40	5920.1	59.2	77813	932	234.7	6.4	386.9	14.6	175.1	15.7	0.44	102	410.2	19.0	534.0	21.0	0.0827	0.0015	512.0	9.1
41	6120.1	61.2	76494	970	405.5	10.6	1258.1	49.1	1262.5	114.1	0.97	370	199.6	9.0	519.5	13.0	0.0843	0.0014	521.5	8.6
42	6335.9	63.4	79515	920	70.4	2.5	199.8	7.5	128.9	11.5	0.62	55	232.9	11.9	540.0	27.0	0.0886	0.0019	547.2	11.0
43	5933.8	59.3	80326	949	308.6	8.4	1202.2	45.5	551.8	49.4	0.44	318	177.1	8.0	763.0	16.0	0.1247	0.0020	757.6	11.0
44	6407.1	64.1	81971	1078	501.6	13.1	725.2	28.0	1083.1	97.6	1.45	233	387.0	18.0	555.0	18.0	0.0836	0.0013	517.2	7.9
45	5682.1	56.8	82674	936	198.1	5.3	503.2	18.9	283.8	25.4	0.55	136	263.8	11.8	644.0	20.0	0.1026	0.0021	629.0	12.0
47	6014.0	60.2	78303	949	248.2	6.7	817.9	30.9	979.3	87.8	1.16	249	181.7	8.2	604.0	37.0	0.0951	0.0018	585.0	10.0
48	2072.7	20.8	42581	442	86.8	2.8	130.9	4.8	85.7	7.7	0.63	36	430.2	21.1	582.0	38.0	0.0906	0.0022	559.0	13.0
49	5772.9	57.7	78560	923	169.9	4.7	241.3	9.4	146.5	13.1	0.59	66	459.7	21.8	526.0	30.0	0.0847	0.0020	524.0	12.0
50	6469.3	64.7	82040	958	187.2	5.1	393.0	14.8	255.1	22.8	0.63	108	312.4	14.2	521.0	26.0	0.0835	0.0017	517.0	9.9
52	6471.6	65.1	86628	914	79.6	3.4	447.5	16.7	199.3	18.0	0.43	118	123.6	6.9	554.0	19.0	0.0890	0.0017	549.2	9.9
53	6069.5	60.7	78000	916	152.8	4.4	325.7	12.2	279.3	25.0	0.83	93	296.1	13.7	589.0	21.0	0.0875	0.0017	540.5	10.0
54	6475.9	64.8	76840	902	243.3	6.5	283.9	10.7	147.0	13.2	0.50	76	564.0	26.1	591.0	24.0	0.0942	0.0020	580.4	12.0
55	7732.7	77.3	74626	882	1081.4	27.9	4661.5	177.6	4269.0	383.4	0.89	1350	146.7	6.5	418.0	25.0	0.0654	0.0011	408.6	6.9
56	5801.3	58.0	79617	945	317.8	8.4	713.4	27.0	503.1	45.1	0.68	198	289.7	13.0	563.0	15.0	0.0892	0.0015	551.5	8.9
57	6054.3	60.8	82649	1028	172.0	5.0	287.3	12.2	160.7	14.4	0.54	78	396.9	19.9	574.0	29.0	0.0873	0.0020	539.0	12.0
58	6128.6	61.3	81576	937	161.8	4.6	3607.2	136.0	3630.5	325.2	0.97	1063	28.1	1.3	27.0	15.0	0.0043	0.0002	27.7	1.0
59	1885.1	18.8	43387	446	147.3	5.1	285.2	10.5	256.9	22.9	0.87	82	322.5	16.1	555.0	20.0	0.0900	0.0016	555.3	9.7
60	6370.0	63.7	80350	944	39.2	1.3	402.1	15.2	287.4	25.8	0.69	112	64.5	3.1	479.0	90.0	0.0856	0.0020	529.6	12.0
61	5668.4	56.7	79096	920	99.8	3.9	428.3	16.3	227.9	20.4	0.51	115	158.6	8.4	568.0	24.0	0.0936	0.0018	576.9	10.0
62	6220.4	62.2	68745	901	501.0	13.3	1289.5	49.5	764.2	68.7	0.57	351	259.0	11.7	581.0	16.0	0.0920	0.0014	567.1	8.3
63	7603.0	76.1	82930	974	229.3	6.1	11459.7	441.8	9707.7	874.0	0.82	3276	13.0	0.6	263.0	30.0	0.0382	0.0008	241.6	4.8
64	5855.5	58.6	81490	919	238.5	6.4	604.5	23.0	381.3	34.3	0.61	166	261.0	11.8	692.0	21.0	0.1097	0.0018	671.1	11.0
66	5946.3	59.5	78052	966	141.2	4.4	183.9	7.0	223.9	20.1	1.18	56	448.2	21.9	592.0	54.0	0.0882	0.0035	545.0	21.0
67	5973.1	59.8	79260	931	359.3	9.5	657.9	24.9	377.7	33.9	0.56	178	362.0	16.4	586.0	18.0	0.0931	0.0015	573.6	8.8
68	5829.8	58.3	76850	903	134.1	4.5	194.1	7.3	109.4	9.8	0.55	52	455.2	22.8	581.0	41.0	0.0869	0.0023	537.0	14.0
69	5991.2	59.9	80334	913	1663.0	42.8	1574.5	59.1	408.7	36.6	0.25	400	721.3	34.1	782.0	17.0	0.1263	0.0018	766.7	10.0
71	6107.8	61.1	77966	914	15.3	0.6	370.4	14.0	355.4	31.9	0.93	108	26.2	1.3	564.0	22.0	0.0891	0.0016	549.9	9.5
72	1806.9	18.1	43559	444	189.7	7.3	421.4	15.6	448.2	40.2	1.03	125	274.0	14.5	566.0	34.0	0.0862	0.0023	533.0	14.0
73	5680.2	56.9	78521	949	179.9	5.4	688.2	26.4	443.8	39.8	0.62	189	173.7	8.2	765.0	18.0	0.1243	0.0021	754.9	12.0
74	5718.6	57.2	77072	859	189.7	5.2	299.1	11.3	263.0	23.6	0.85	86	395.3	18.1	572.0	23.0	0.0893	0.0018	551.3	10.0
75	5897.4	59.0	80420	944	200.2	5.5	510.0	19.2	406.9	36.5	0.77	144	251.5	11.4	530.0	110.0	0.0887	0.0022	548.0	13.0

Supplementary Table E8 Continued

Grain	He Pit Vol. (μm^3)	err. (2σ)	U-Th Pit Vol. (μm^3)	err. (2σ)	[^{4}He] (nmol/g)	err. (2σ)	[^{238}U] (nmol/g)	err. (2σ)	[^{232}Th] (nmol/g)	err. (2σ)	$^{232}Th/^{238}U$	eU (ppm)	(U-Th)/He date (Ma)	err. (2σ)	$^{207}Pb/^{235}U$ date (Ma)	err. (2σ)	$^{206}Pb/^{238}U$	err. (2σ)	$^{206}Pb/^{238}U$ date (Ma)	err. (2σ)
77	6995.0	70.0	77940	915	1311.1	33.8	3145.2	121.9	2940.3	266.1	0.90	914	260.1	11.7	493.0	15.0	0.0743	0.0012	461.9	7.1
78	6248.4	62.5	82433	980	833.1	21.5	1685.3	64.3	1101.4	99.0	0.63	464	323.7	14.5	725.0	16.0	0.1083	0.0018	663.0	11.0
80	2198.5	21.9	43209	446	157.4	6.1	755.4	27.9	579.6	51.8	0.74	213	135.7	7.1	575.0	17.0	0.0930	0.0014	573.4	8.5
81	5801.7	58.0	78910	927	83.9	4.1	156.4	5.9	129.3	11.6	0.80	45	339.2	20.8	550.0	34.0	0.0911	0.0024	562.0	14.0
82	5887.0	58.9	77790	914	382.3	10.0	904.9	34.2	639.0	57.3	0.68	252	275.0	12.3	529.0	16.0	0.0833	0.0014	515.5	8.0
83	5775.7	57.9	82399	942	175.8	5.2	420.5	15.9	243.1	21.8	0.56	114	279.0	13.0	565.0	26.0	0.0915	0.0016	564.1	9.4
84	4792.8	48.4	81873	857	138.4	5.4	263.0	9.8	148.2	13.3	0.55	71	349.9	18.8	621.0	24.0	0.1022	0.0023	627.0	13.0
85	6350.0	63.5	77520	910	523.7	13.8	651.4	25.5	449.6	40.8	0.67	181	513.9	24.0	531.0	24.0	0.0850	0.0015	525.6	8.8
86	6027.0	60.3	83650	1040	172.4	5.0	344.2	13.1	332.3	29.8	0.93	101	309.4	14.4	504.0	22.0	0.0808	0.0015	500.8	9.1
87	6005.9	60.1	79707	978	404.6	10.8	917.7	34.9	636.9	57.1	0.67	255	287.3	13.0	526.0	13.0	0.0843	0.0013	521.4	7.8
88	5725.5	57.3	81088	902	221.3	6.1	297.9	12.4	205.9	18.5	0.67	83	476.5	23.4	553.0	25.0	0.0890	0.0017	549.3	9.8
90	6356.0	63.6	70902	826	970.1	25.2	7719.8	292.3	3325.0	298.1	0.42	2032	87.9	3.9	456.0	21.0	0.0704	0.0013	438.3	7.6
91	1987.9	19.9	41220	422	148.0	5.6	584.3	22.5	488.1	44.0	0.81	167	162.4	8.6	504.0	16.0	0.0799	0.0015	495.2	8.9
92	5830.7	58.3	78072	997	275.7	7.3	487.0	18.6	437.8	39.3	0.87	141	352.8	16.0	558.0	20.0	0.0891	0.0016	549.9	9.4
93	5882.2	58.8	75859	895	1420.8	36.6	3238.9	123.7	1960.5	176.0	0.59	883	290.8	13.0	526.5	12.0	0.0813	0.0011	503.9	6.5
94	1958.3	19.7	40022	414	591.1	16.5	3887.8	143.2	209.5	18.8	0.05	943	115.1	5.3	644.8	8.7	0.1017	0.0015	624.3	8.7
95	6061.3	60.6	78894	907	176.0	4.8	384.7	14.5	378.9	33.9	0.95	113	282.4	12.8	574.0	21.0	0.0943	0.0017	581.0	9.8
96	1916.7	19.2	41276	430	422.4	12.2	843.6	31.3	678.9	60.7	0.78	239	318.6	14.7	541.0	43.0	0.0905	0.0016	558.2	9.4
97	6029.9	60.3	78667	924	309.4	8.1	655.2	24.8	614.6	55.1	0.91	191	293.6	13.1	587.0	20.0	0.0904	0.0015	558.0	8.8
98	6169.3	61.7	77181	909	177.9	4.9	374.8	14.2	248.4	22.3	0.64	103	310.5	14.2	581.0	19.0	0.0934	0.0017	575.7	10.0
99	2115.5	21.2	42799	436	173.2	6.1	285.3	10.6	177.1	15.8	0.60	78	397.4	20.3	586.0	23.0	0.0945	0.0018	581.9	11.0
100	2058.5	20.5	43932	448	19.4	1.1	566.8	20.9	415.5	37.1	0.71	159	22.6	1.5	40.0	120.0	0.0033	0.0012	21.4	7.8
101	5938.4	59.4	78691	862	167.3	5.1	528.5	19.8	303.3	27.2	0.56	143	212.6	10.0	690.0	26.0	0.1088	0.0019	665.8	11.0
102	2124.9	21.2	42328	440	65.8	2.3	182.6	6.7	115.8	10.3	0.61	50	238.6	11.9	596.0	42.0	0.0904	0.0035	558.0	20.0
103	6113.4	61.2	76914	899	291.6	7.8	390.5	14.7	305.6	27.4	0.76	110	470.8	21.5	619.0	24.0	0.0914	0.0017	563.9	9.9
104	6200.0	62.0	71190	836	579.4	15.2	6338.0	239.6	927.8	83.1	0.14	1570	68.1	3.1	528.0	19.0	0.0814	0.0012	504.7	7.2
105	5718.1	57.2	78922	945	541.8	14.2	1545.6	58.4	1141.6	102.5	0.71	433	227.7	10.1	511.0	40.0	0.0811	0.0015	502.4	9.0
106	1842.3	18.3	40779	414	293.3	14.3	637.3	23.7	453.8	40.5	0.69	178	298.6	18.2	532.0	13.0	0.0865	0.0013	534.8	8.0
107	5746.8	57.5	76895	911	158.2	4.8	309.8	11.7	194.1	17.4	0.61	85	335.8	16.0	568.0	23.0	0.0918	0.0020	566.0	12.0
108	5992.8	59.9	76060	945	242.6	6.4	425.9	16.4	392.2	35.2	0.89	123	353.5	16.1	601.0	23.0	0.0905	0.0018	558.0	10.0
109	6213.1	62.1	78410	958	229.5	6.4	609.6	23.5	741.0	66.9	1.18	187	223.9	10.4	604.0	60.0	0.0914	0.0022	564.0	13.0
110	2025.5	20.3	42342	436	1025.4	27.6	961.3	35.4	1249.2	111.6	1.26	299	605.7	28.1	753.0	16.0	0.1217	0.0020	740.0	12.0

Supplementary Table E9
(U-Th)/He and U/Pb dates by LADD of detrital zircon for sample CHB14-2B-72Q-1

Grain	He Pit Vol. (μm^3)	err. (2σ)	U-Th Pit Vol. (μm^3)	err. (2σ)	[^{4}He] (nmol/g)	err. (2σ)	[^{238}U] (nmol/g)	err. (2σ)	[^{232}Th] (nmol/g)	err. (2σ)	$^{232}Th/^{238}U$	eU (ppm)	(U-Th)/He date (Ma)	err. (2σ)	$^{207}Pb/^{235}U$ date (Ma)	err. (2σ)	$^{206}Pb/^{238}U$	err. (2σ)	$^{206}Pb/^{238}U$ date (Ma)	err. (2σ)
1	5176.2	51.8	76809	825	666.4	17.4	3342.6	124.7	501.5	45.4	0.15	829	147.3	6.7	659.2	8.0	0.1056	0.0011	647.1	6.4
2	7425.0	74.3	83500	969	105.8	3.5	166.6	6.8	110.2	10.0	0.64	46	411.8	21.3	536.4	22.2	0.0847	0.0016	524.1	9.5
3	5865.0	58.7	76109	904	403.5	10.5	6782.6	256.0	4207.9	376.9	0.60	1855	40.2	1.8	465.1	15.4	0.0664	0.0009	414.7	5.4
4	5739.1	57.4	83324	989	1201.2	31.1	1730.4	65.2	1108.5	99.3	0.62	475	450.6	20.3	541.8	7.1	0.0842	0.0010	521.3	5.8
5	5301.9	53.0	80290	896	197.1	5.7	314.2	11.8	224.3	20.1	0.69	88	403.1	18.8	550.1	14.2	0.0882	0.0013	544.9	7.7
6	5479.5	54.8	79133	873	2684.9	69.5	3274.6	122.5	3326.8	297.6	0.98	966	494.1	22.3	507.9	16.0	0.0797	0.0011	494.5	6.6
7	5299.9	53.0	83590	936	269.3	7.5	359.9	13.5	241.8	21.6	0.65	99	481.4	22.3	530.4	13.2	0.0855	0.0013	528.9	7.7
8	5649.0	56.5	79941	909	218.5	6.0	272.5	10.3	226.6	20.3	0.80	78	499.6	23.0	550.7	20.6	0.0879	0.0015	543.1	8.9
9	1749.1	17.5	44226	452	665.7	17.8	940.2	34.6	735.2	65.6	0.76	265	447.4	20.1	551.0	12.0	0.0872	0.0014	538.6	8.3
10	5461.0	54.6	80428	930	15.4	0.7	515.0	19.5	313.5	28.1	0.59	141	20.3	1.2	16.1	73.0	0.0031	0.0006	20.2	4.0
11	5352.4	53.5	82160	935	707.0	18.6	829.9	31.6	423.1	38.0	0.49	222	561.6	26.0	766.3	11.9	0.1233	0.0014	749.5	8.0
12	5145.0	51.5	79897	892	52.3	1.9	1855.9	70.0	1407.0	126.1	0.73	522	18.6	0.9	23.1	17.9	0.0031	0.0002	19.7	1.2
13	5509.9	55.1	79710	925	150.8	5.6	229.6	8.7	243.8	21.9	1.03	68	395.9	20.8	555.4	17.6	0.0904	0.0017	557.9	10.1
14	1669.1	16.8	46687	478	196.8	8.2	323.7	12.2	198.2	17.7	0.59	88	398.8	22.4	521.0	22.0	0.0807	0.0020	500.0	12.0
15	5529.2	55.3	81864	968	1224.6	31.7	1243.4	47.1	3872.8	347.2	3.01	509	431.9	22.5	620.8	8.8	0.1010	0.0011	620.2	6.4
17	5447.4	54.5	81010	940	160.7	4.7	269.3	10.2	147.9	13.3	0.53	73	396.2	18.7	510.3	25.2	0.0811	0.0015	502.7	8.9
18	5971.4	59.7	81564	937	211.9	5.8	626.6	23.8	693.7	62.2	1.07	188	205.4	9.3	591.7	10.8	0.0954	0.0013	587.4	7.7
19	5675.0	56.8	81234	927	69.4	2.5	145.7	5.5	100.3	9.0	0.67	40	309.9	16.0	560.7	21.6	0.0854	0.0015	528.3	8.9
20	5205.7	52.1	82380	939	36.6	1.3	1391.5	52.2	801.5	71.8	0.56	377	18.0	0.9	31.0	11.8	0.0031	0.0002	20.2	1.3
21	5816.6	58.2	79146	880	1216.7	31.8	4435.1	166.6	909.4	81.5	0.20	1113	199.3	9.0	612.5	21.6	0.0967	0.0015	595.0	8.8
22	5498.3	55.0	78513	863	613.7	16.2	960.2	36.0	713.5	63.8	0.72	269	408.3	18.4	541.8	28.0	0.0843	0.0012	521.7	7.1
23	5699.1	57.0	80860	938	906.5	23.9	1381.1	52.5	840.3	75.6	0.59	377	429.5	19.6	570.5	8.7	0.0916	0.0010	564.7	5.9
24	5627.0	56.3	81059	943	713.4	18.7	2168.1	81.7	768.2	68.8	0.34	562	230.8	10.4	634.5	7.6	0.1011	0.0012	621.0	7.0
25	6184.9	61.9	84544	948	1292.0	33.8	2095.5	78.8	1652.0	148.0	0.76	592	391.0	17.6	475.3	29.2	0.0777	0.0011	482.3	6.6
27	5742.4	57.4	78907	948	46.3	1.5	2204.8	83.4	1803.2	161.7	0.79	627	13.7	0.6	24.8	3.7	0.0032	0.0002	20.5	1.0
28	5503.2	55.0	83230	1020	78.3	3.8	149.1	5.6	197.4	17.7	1.28	46	304.4	18.9	539.4	29.2	0.0860	0.0017	531.8	10.1
29	5478.0	54.8	79810	926	522.9	13.9	622.8	23.4	390.5	35.0	0.61	171	541.9	24.9	570.0	11.6	0.0897	0.0011	553.8	6.5
30	5366.1	53.7	80653	884	386.2	10.2	652.6	24.4	792.4	71.0	1.18	200	348.4	15.7	564.7	11.6	0.0907	0.0013	559.7	7.7
31	5482.3	54.9	77362	878	214.9	5.8	332.1	12.6	250.8	22.5	0.73	93	412.2	18.9	518.3	19.5	0.0832	0.0017	515.2	10.1
32	5547.0	55.5	81250	943	17.9	0.6	738.7	29.2	364.6	33.1	0.48	197	16.8	0.9	23.9	5.0	0.0033	0.0002	20.9	1.4
33	6477.9	64.8	76640	862	59.9	2.3	1922.6	72.8	1272.0	114.1	0.64	530	20.9	1.1	22.9	2.2	0.0031	0.0001	19.8	0.6
34	5893.4	58.9	77320	897	914.8	23.8	1155.9	43.4	1132.6	101.4	0.95	339	480.6	21.8	507.9	9.2	0.0793	0.0012	491.9	7.2
35	5761.3	57.6	79479	903	579.2	15.1	2009.1	75.8	226.9	20.4	0.11	494	213.4	9.8	607.5	10.0	0.0904	0.0015	557.9	8.9
37	5321.6	53.2	81785	942	185.1	5.3	594.1	22.4	288.9	25.9	0.47	158	213.1	9.8	643.7	12.4	0.1053	0.0016	645.4	9.3

Supplementary Table E9 Continued

Grain	He Pit Vol. (μm^3)	err. (2σ)	U-Th Pit Vol. (μm^3)	err. (2σ)	[^4He] (nmol/g)	err. (2σ)	[^{238}U] (nmol/g)	err. (2σ)	[^{232}Th] (nmol/g)	err. (2σ)	$^{232}Th/^{238}U$	eU (ppm)	(U-Th)/He date (Ma)	err. (2σ)	$^{207}Pb/^{235}U$ date (Ma)	err. (2σ)	$^{206}Pb/^{238}U$	err. (2σ)	$^{206}Pb/^{238}U$ date (Ma)	err. (2σ)
38	6971.3	70.3	80906	902	431.8	11.3	972.7	36.9	1188.4	106.6	1.18	298	262.9	11.8	504.8	12.4	0.0807	0.0013	500.3	7.8
39	1867.3	18.8	40084	408	298.8	14.1	801.9	29.7	448.0	40.1	0.54	217	250.2	14.9	622.0	14.0	0.1013	0.0016	622.2	9.2
40	6114.9	61.2	74460	864	128.3	4.7	4335.1	164.1	2994.1	268.4	0.67	1202	19.8	1.0	19.1	1.3	0.0029	0.0001	18.7	0.4
41	5503.7	55.0	72054	890	1069.5	27.8	3605.2	137.0	1092.0	98.0	0.29	924	210.8	9.5	425.2	13.4	0.0669	0.0011	417.2	6.6
42	5709.6	57.1	79370	921	102.4	4.5	386.3	15.0	630.1	56.8	1.58	127	147.7	8.7	575.7	23.0	0.0916	0.0013	565.0	7.7
43	5919.1	59.2	79600	923	103.4	4.6	3436.1	129.6	2616.5	234.4	0.74	966	19.8	1.1	21.5	1.2	0.0029	0.0001	18.5	0.8
44	5947.7	59.5	77990	905	207.0	5.6	279.6	10.8	197.1	17.8	0.68	78	473.6	22.0	534.0	18.6	0.0849	0.0014	525.3	8.3
45	10094.0	101.0	85235	961	482.7	12.5	966.3	36.5	630.9	56.5	0.63	266	327.0	14.6	510.9	27.6	0.0806	0.0012	499.9	7.2
46	5306.4	53.1	78620	912	502.1	13.2	699.6	26.4	504.9	45.2	0.70	195	458.3	20.8	501.7	29.2	0.0808	0.0013	500.9	7.8
47	5388.6	53.9	81626	900	749.4	19.5	1075.9	40.1	564.3	50.4	0.51	289	462.1	20.9	732.8	11.8	0.1193	0.0019	726.5	10.9
48	5265.7	52.7	81870	968	419.2	11.0	1265.4	47.6	925.6	82.9	0.71	354	215.7	9.5	652.8	9.6	0.1055	0.0013	646.6	7.6
49	5367.2	53.7	81570	946	488.4	12.7	1072.8	40.2	948.8	84.9	0.86	309	286.1	12.7	687.4	10.3	0.1105	0.0013	675.7	7.5
50	1798.8	18.0	40140	413	562.9	16.4	650.1	24.0	346.6	30.9	0.52	175	567.9	26.9	549.0	16.0	0.0885	0.0018	546.3	10.0
51	2033.1	20.3	43233	440	402.7	14.1	673.6	24.8	351.7	31.4	0.51	181	399.1	20.2	555.0	37.0	0.0876	0.0019	541.3	11.0
52	5665.3	56.7	81225	1068	206.7	5.8	258.2	9.9	124.4	11.2	0.47	69	532.2	25.2	776.3	23.2	0.1230	0.0026	747.8	14.9
53	5702.0	57.0	81280	943	344.2	9.1	434.6	16.3	213.5	19.1	0.48	116	525.8	24.1	552.4	15.9	0.0855	0.0013	528.9	7.7
54	5666.4	56.7	77429	909	203.4	5.5	373.9	14.1	234.6	21.0	0.61	102	357.0	16.3	538.2	26.2	0.0847	0.0017	524.1	10.1
55	5388.3	53.9	79734	927	166.7	5.4	327.4	12.3	156.5	14.0	0.46	87	344.7	16.9	500.5	17.4	0.0805	0.0014	499.1	8.4
56	5511.0	55.1	81323	909	135.5	5.5	420.4	15.7	223.2	20.0	0.51	113	218.2	11.8	634.5	17.4	0.1027	0.0022	630.2	12.9
57	5823.0	58.2	76270	885	232.1	6.3	305.8	11.4	250.4	22.4	0.79	87	475.2	21.7	586.6	16.5	0.0862	0.0015	533.0	8.9
58	5562.0	55.6	78416	928	81.1	4.1	163.4	6.1	100.1	9.0	0.59	45	327.4	20.6	543.0	29.8	0.0854	0.0016	528.3	9.5
59	5290.8	52.9	85631	984	334.7	9.0	403.7	15.1	576.6	51.6	1.38	128	466.0	21.7	567.6	22.6	0.0908	0.0016	560.3	9.5
60	1754.6	17.4	43468	446	114.0	4.4	184.8	6.8	113.0	10.1	0.59	50	404.4	21.5	555.0	24.0	0.0880	0.0020	543.0	12.0
61	1808.3	18.1	46490	479	857.2	23.4	1348.6	51.7	822.9	74.0	0.59	368	416.3	19.3	565.0	11.0	0.0888	0.0015	548.3	8.7
63	5884.2	58.9	78885	902	248.7	6.7	513.6	19.2	567.5	50.8	1.07	154	292.1	13.2	546.5	14.8	0.0838	0.0013	518.8	7.7
64	5733.5	57.3	83577	955	271.7	7.4	329.6	12.3	290.3	26.0	0.85	95	508.6	23.4	544.2	15.4	0.0857	0.0013	530.1	7.7
65	5797.7	58.0	84946	979	74.6	3.0	216.2	8.1	179.1	16.0	0.80	62	220.4	11.9	561.8	18.1	0.0854	0.0015	528.3	8.9
67	5465.0	54.7	81206	959	238.0	6.8	373.5	14.0	239.7	21.4	0.62	103	414.9	19.3	529.8	14.5	0.0838	0.0013	518.8	7.7
68	1826.6	18.3	42447	436	700.1	19.1	1341.3	49.3	1026.9	91.6	0.74	378	334.1	15.0	565.0	11.0	0.0915	0.0014	564.3	8.1
69	5621.5	56.2	80976	954	470.4	12.5	950.2	35.6	657.4	58.8	0.67	264	321.8	14.4	512.2	11.6	0.0812	0.0010	503.2	5.7
70	1897.1	19.0	43113	440	103.1	3.6	400.4	14.7	402.8	35.9	0.97	118	159.8	7.9	540.0	110.0	0.0948	0.0029	584.0	17.0
71	1800.2	18.1	43479	442	501.3	14.3	844.6	31.1	685.6	61.6	0.79	240	375.3	17.3	522.0	30.0	0.0841	0.0014	520.7	8.1
72	5515.8	55.2	76645	848	287.6	7.7	448.3	16.9	277.5	24.9	0.60	123	419.4	19.1	763.5	26.4	0.1196	0.0022	728.3	12.7
73	5363.9	53.6	77980	889	349.8	9.4	789.8	30.3	493.4	44.2	0.60	216	292.5	13.3	774.9	24.6	0.1197	0.0019	728.8	10.9
74	7225.6	72.3	76264	875	715.1	18.9	3280.8	126.0	2253.6	202.5	0.66	909	144.0	6.4	460.6	10.3	0.0713	0.0011	443.7	6.6

Supplementary Table E9 Continued

Grain	He Pit Vol. (μm^3)	err. (2σ)	U-Th Pit Vol. (μm^3)	err. (2σ)	[^4He] (nmol/g)	err. (2σ)	[^{238}U] (nmol/g)	err. (2σ)	[^{232}Th] (nmol/g)	err. (2σ)	$^{232}Th/^{238}U$	eU (ppm)	(U-Th)/He date (Ma)	err. (2σ)	$^{207}Pb/^{235}U$ date (Ma)	err. (2σ)	$^{206}Pb/^{238}U$	err. (2σ)	$^{206}Pb/^{238}U$ date (Ma)	err. (2σ)
75	6451.2	64.5	77330	897	119.6	4.7	4107.1	156.4	2908.3	260.9	0.69	1143	19.4	1.0	20.0	1.3	0.0028	0.0001	18.3	0.4
76	5768.0	57.7	81653	943	60.1	2.1	2713.1	102.9	2251.5	202.0	0.80	773	14.4	0.7	22.0	2.3	0.0029	0.0001	18.8	0.8
77	5752.2	57.5	81219	959	190.6	5.2	310.3	11.8	197.2	17.7	0.61	85	401.0	18.5	513.4	15.3	0.0810	0.0014	502.1	8.3
78	5615.3	56.2	78273	922	465.3	12.2	1429.5	54.3	1948.4	174.8	1.32	449	189.2	8.5	773.5	10.0	0.1227	0.0017	746.1	9.8
79	5359.8	53.6	79312	999	750.2	19.5	1076.9	41.2	1164.3	104.6	1.05	322	417.6	19.0	572.9	18.5	0.0851	0.0011	526.5	6.5
80	5314.4	53.2	79777	972	303.6	8.1	455.1	17.3	443.9	39.8	0.94	133	408.0	18.6	502.3	13.0	0.0798	0.0013	494.9	7.8
81	5415.0	54.2	81372	1019	339.8	9.2	404.8	15.3	378.7	34.0	0.91	118	512.4	23.6	544.2	13.1	0.0850	0.0012	525.9	7.1
82	5800.8	58.0	80246	1012	830.1	21.5	2003.1	75.8	283.2	25.4	0.14	496	302.2	14.0	576.3	8.1	0.0915	0.0010	564.4	5.9
83	6124.0	61.3	78800	914	117.9	3.7	4305.0	161.7	3354.5	300.3	0.75	1215	18.0	0.8	18.6	1.0	0.0028	0.0000	18.3	0.3
84	1850.1	18.6	43641	452	183.9	6.7	437.3	16.1	181.9	16.2	0.40	115	289.7	14.9	527.0	26.0	0.0874	0.0020	540.0	12.0
85	5369.3	53.7	82196	1025	50.0	2.0	2321.9	87.9	1444.9	129.5	0.60	635	14.6	0.8	23.3	2.3	0.0028	0.0001	18.3	0.4
86	5431.1	54.4	79610	923	317.1	8.4	382.4	14.3	304.2	27.2	0.77	108	519.4	23.7	528.6	13.9	0.0846	0.0012	523.5	7.1
88	5576.0	55.8	79270	920	592.9	15.4	735.3	27.6	742.9	66.5	0.98	217	486.7	22.0	525.0	13.3	0.0809	0.0012	501.5	7.2
89	5555.0	55.6	81473	888	521.9	13.6	759.5	28.3	793.7	71.0	1.01	225	414.7	18.6	534.6	9.6	0.0855	0.0010	529.1	5.8
90	5443.3	54.4	81309	1020	163.8	4.8	257.5	9.8	257.8	23.1	0.97	76	387.9	18.3	557.1	19.9	0.0854	0.0014	528.3	8.3
91	5496.9	55.0	79570	901	407.0	10.8	1217.3	45.8	581.5	52.1	0.46	324	228.7	10.3	694.1	20.0	0.1104	0.0017	675.1	9.9
92	1909.6	19.0	43306	454	85.0	2.9	3475.7	128.2	2887.5	257.7	0.80	991	15.9	0.8	22.7	2.3	0.0030	0.0001	19.3	0.5
93	1901.5	19.0	41977	438	1123.7	29.8	5012.3	184.6	150.3	13.4	0.03	1210	169.7	7.8	598.6	8.8	0.0972	0.0016	597.8	9.5
94	1840.7	18.3	44126	472	451.7	14.6	726.6	26.9	439.3	39.2	0.59	198	408.0	19.9	541.0	15.0	0.0879	0.0015	543.2	8.6
96	5861.0	58.6	80144	981	333.7	8.8	475.3	18.1	735.6	66.1	1.50	154	389.2	18.1	704.3	15.2	0.1056	0.0018	647.1	10.5
97	6075.3	60.8	79960	967	1365.8	35.9	1684.5	65.9	926.0	83.9	0.53	454	531.8	25.0	673.9	9.9	0.1098	0.0015	671.6	8.7
99	6106.9	61.1	76790	891	8.9	0.8	1384.2	52.4	1209.3	108.4	0.85	398	4.1	0.4	4.5	0.9	0.0005	0.0001	3.5	0.6
100	5867.9	58.7	78306	890	519.6	13.8	1427.7	53.8	1664.3	149.1	1.13	433	218.5	9.8	766.3	9.5	0.1229	0.0014	747.2	8.0
101	5772.4	57.7	80776	933	670.6	17.7	989.8	37.5	707.4	63.4	0.69	276	434.2	19.7	573.4	15.6	0.0858	0.0011	530.7	6.5
102	2158.8	21.6	43190	444	202.3	8.4	686.4	25.3	565.3	50.5	0.80	195	188.9	10.3	574.0	20.0	0.0867	0.0016	535.8	9.7
103	6256.4	62.6	77971	877	750.2	19.6	1162.9	43.8	926.6	83.2	0.77	329	407.9	18.4	486.7	27.6	0.0753	0.0014	468.0	8.4
104	5462.8	54.6	79936	913	350.6	9.5	713.7	26.9	219.0	19.7	0.30	183	344.4	15.9	625.8	12.6	0.1003	0.0013	616.2	7.6
105	5297.0	53.0	79400	921	272.2	7.4	460.3	17.3	303.6	27.2	0.64	127	384.7	17.5	531.6	13.8	0.0851	0.0012	526.5	7.1
106	5689.9	56.9	78842	893	233.0	6.2	405.9	15.3	389.0	34.9	0.93	119	353.7	15.9	556.6	111.6	0.0855	0.0020	528.9	11.9
107	5980.2	59.8	79241	879	1170.8	30.6	3213.5	120.2	1241.7	111.1	0.37	838	253.4	11.3	654.4	8.0	0.1058	0.0011	648.0	6.4
108	5897.7	59.0	79839	944	1196.8	31.3	2009.9	76.0	1531.2	137.3	0.74	565	380.0	17.1	489.2	8.2	0.0786	0.0011	487.8	6.6
109	5633.1	56.4	80290	965	53.9	2.1	126.6	4.8	73.1	6.6	0.56	34	284.1	15.1	536.4	25.2	0.0859	0.0018	531.2	10.7
110	5607.1	56.1	78004	931	510.1	13.5	664.2	25.1	876.6	78.7	1.28	207	440.6	20.3	493.6	41.2	0.0798	0.0012	494.8	7.2

Supplementary Table E10

(U-Th)/He and U/Pb dates by LADD of detrital zircon for sample CHB14-2B-75Q-1

Grain	He Pit Vol. (μm^3)	err. (2σ)	U-Th Pit Vol. (μm^3)	err. (2σ)	[^{4}He] (nmol/g)	err. (2σ)	[^{238}U] (nmol/g)	err. (2σ)	[^{232}Th] (nmol/g)	err. (2σ)	^{232}Th/^{238}U	eU (ppm)	(U-Th)/He date (Ma)	err. (2σ)	^{207}Pb/^{235}U date (Ma)	err. (2σ)	^{206}Pb/^{238}U	err. (2σ)	^{206}Pb/^{238}U date (Ma)	err. (2σ)
1	3356.0	34.1	76646	822	94.4	4.2	1761.3	65.0	905.8	81.1	0.50	472	37.0	2.1	714.9	10.5	0.1156	0.0011	705.2	6.4
2	3728.8	38.1	69428	720	219.6	6.5	16557.5	615.8	170.1	15.2	0.01	3979	10.2	0.5	530.4	12.0	0.0802	0.0013	497.3	7.8
3	3718.4	37.2	80252	827	650.3	17.4	1636.7	60.1	922.5	82.3	0.55	443	266.2	11.8	777.7	9.0	0.1281	0.0008	777.1	4.6
4	3863.5	38.9	79789	813	171.2	6.3	278.1	10.2	196.3	17.5	0.68	77	396.4	20.6	559.5	34.6	0.0871	0.0017	538.4	10.1
5	4064.3	40.6	82545	857	59.2	2.3	2707.8	100.1	1863.6	166.5	0.67	751	14.6	0.8	27.1	3.9	0.0031	0.0001	20.1	0.8
6	4887.1	49.0	82576	880	823.7	21.7	1487.0	55.0	1313.7	117.3	0.85	428	346.4	15.4	772.0	10.0	0.1242	0.0013	754.7	7.5
7	5069.5	50.7	80131	816	135.2	4.9	237.3	8.7	176.7	15.8	0.72	67	365.3	18.7	569.4	21.4	0.0903	0.0015	557.3	8.9
8	5025.6	50.3	80434	811	294.5	8.0	479.1	17.6	278.5	24.8	0.56	130	405.3	18.3	525.0	18.8	0.0874	0.0011	540.1	6.5
9	3997.5	40.2	79858	854	222.3	6.4	636.3	23.8	399.7	35.8	0.61	174	231.8	10.6	574.6	15.6	0.0912	0.0011	562.6	6.5
11	3596.8	36.0	74749	768	6.8	0.9	276.5	10.2	136.2	12.2	0.48	74	17.1	2.3	24.2	9.0	0.0030	0.0003	19.4	1.7
12	3353.5	33.7	77446	798	1046.1	27.4	1882.1	69.4	775.7	69.2	0.40	493	380.1	17.0	768.7	8.6	0.1246	0.0008	757.2	4.8
13	3761.8	37.6	78400	842	462.3	12.4	1301.3	48.0	529.0	47.3	0.39	341	246.2	11.0	750.5	12.6	0.1233	0.0012	749.5	6.9
14	1168.1	11.7	48121	491	218.8	9.1	345.5	12.9	218.0	19.6	0.61	95	413.2	23.2	548.3	25.4	0.0872	0.0018	539.0	10.7
15	3657.7	36.6	81733	888	529.1	13.9	1308.3	48.4	909.2	81.2	0.67	363	264.1	11.6	518.3	10.4	0.0821	0.0006	508.4	3.6
16	4030.4	40.5	80168	823	239.8	6.8	456.7	16.8	412.1	36.8	0.87	132	327.7	15.0	556.6	82.2	0.0912	0.0014	562.6	8.3
17	1325.0	13.3	41594	430	73.4	3.4	3620.1	133.3	2629.6	234.7	0.70	1011	13.4	0.8	19.5	2.3	0.0029	0.0001	18.4	0.6
18	3672.2	36.8	77807	830	131.5	5.6	241.0	8.9	179.2	16.0	0.72	68	350.3	19.6	557.7	22.2	0.0889	0.0014	549.0	8.3
19	3672.8	37.1	80763	815	123.0	6.4	323.3	12.0	110.7	9.9	0.33	84	266.7	17.1	506.0	19.1	0.0816	0.0011	505.7	6.6
20	3897.4	39.0	77733	817	267.1	7.8	3871.6	144.9	478.4	42.7	0.12	954	51.7	2.4	647.4	9.7	0.1028	0.0007	630.5	4.1
21	1018.2	10.4	42340	437	629.0	20.1	1110.7	41.2	742.2	66.4	0.65	307	368.3	17.8	653.3	16.5	0.1076	0.0013	658.8	7.6
22	3839.3	38.4	80184	826	264.8	7.4	556.1	20.5	267.0	23.8	0.46	148	322.8	14.7	657.1	19.1	0.1054	0.0011	646.0	6.4
23	3455.7	35.3	76355	789	37.6	1.4	1315.1	49.0	709.9	63.6	0.52	354	19.7	1.0	24.4	9.1	0.0031	0.0004	19.8	2.3
24	1285.0	12.8	42348	430	729.4	21.7	3147.6	115.4	1054.1	94.0	0.32	812	164.2	7.6	589.5	10.8	0.0916	0.0010	565.2	5.7
25	3601.8	36.0	81911	849	573.8	15.2	1281.2	47.3	1643.7	146.8	1.24	397	262.4	11.8	792.7	11.6	0.1289	0.0010	781.4	5.5
26	1264.0	12.6	44987	470	764.9	21.0	3014.9	110.6	2490.0	222.1	0.80	858	162.9	7.2	502.9	9.3	0.0808	0.0008	501.0	4.7
27	3811.4	38.2	79689	816	168.5	5.9	376.0	13.8	239.5	21.4	0.62	103	295.2	14.8	600.8	28.6	0.0886	0.0012	547.3	7.1
28	4249.7	42.8	80119	862	916.1	23.9	3961.6	145.9	966.2	86.2	0.24	1002	167.1	7.4	532.2	25.2	0.0806	0.0009	499.6	5.2
29	1244.5	12.4	41960	430	112.6	4.4	4702.2	173.7	3624.0	323.8	0.75	1325	15.7	0.8	24.4	3.1	0.0030	0.0001	19.4	0.5
30	1149.9	11.5	44157	452	147.6	6.0	4765.2	175.7	3376.2	301.3	0.69	1326	20.6	1.1	27.5	5.4	0.0031	0.0002	19.6	1.3
31	3787.1	38.0	79937	816	425.8	11.5	788.8	29.0	375.4	33.5	0.46	210	364.9	16.5	685.4	21.8	0.1064	0.0012	651.8	7.0
32	3579.2	35.8	79410	812	245.4	7.4	507.2	18.6	312.5	27.9	0.60	139	319.2	14.9	574.0	14.4	0.0936	0.0010	576.8	5.9
33	3725.6	37.3	85433	871	260.9	7.6	1051.2	38.8	960.6	86.0	0.88	304	156.8	7.1	771.1	13.8	0.1228	0.0014	746.7	8.0
34	1292.0	12.9	46030	468	443.4	23.4	470.5	18.3	438.4	39.7	0.90	137	572.6	38.3	590.6	28.4	0.0893	0.0019	551.4	11.2
35	3765.3	38.2	82623	840	473.7	12.7	767.1	28.1	790.7	70.5	1.00	227	374.9	16.8	793.6	13.5	0.1284	0.0010	778.7	5.7

Supplementary Table E10 Continued

Grain	He Pit Vol. (μm³)	err. (2σ)	U-Th Pit Vol. (μm³)	err. (2σ)	[^{4}He] (nmol/g)	err. (2σ)	[^{238}U] (nmol/g)	err. (2σ)	[^{232}Th] (nmol/g)	err. (2σ)	^{232}Th/^{238}U	eU (ppm)	(U-Th)/He date (Ma)	err. (2σ)	^{207}Pb/^{235}U date (Ma)	err. (2σ)	^{206}Pb/^{238}U	err. (2σ)	^{206}Pb/^{238}U date (Ma)	err. (2σ)
36	3788.4	38.2	79438	830	484.1	13.4	741.3	27.4	384.1	34.3	0.50	199	434.9	19.9	581.5	15.5	0.0882	0.0011	544.9	6.5
37	3744.9	37.8	82988	877	393.5	10.8	782.1	28.8	501.7	44.7	0.62	215	330.0	14.8	525.0	12.1	0.0825	0.0008	511.0	4.7
38	1275.5	12.8	43794	447	345.6	18.1	650.6	24.5	252.3	22.5	0.38	170	365.5	23.9	780.5	20.8	0.1288	0.0018	781.0	10.3
39	4032.0	40.6	81482	863	340.9	9.2	1141.1	41.9	873.7	77.9	0.74	321	193.6	8.5	521.9	10.3	0.0825	0.0008	511.3	4.9
40	3810.3	38.3	79657	834	335.4	9.2	1087.1	40.0	533.6	47.6	0.48	290	210.8	9.4	786.2	11.7	0.1283	0.0010	778.2	5.7
41	3739.5	37.7	81617	829	218.4	7.0	340.2	12.6	216.6	19.3	0.62	93	418.2	20.3	571.7	19.7	0.0893	0.0015	551.4	8.9
42	3448.2	34.5	72918	780	76.2	2.6	150.8	5.6	95.0	8.5	0.61	41	332.0	16.6	570.0	31.2	0.0893	0.0019	551.4	11.2
43	1072.0	10.7	39816	403	12.3	2.6	450.4	16.5	196.6	17.5	0.42	119	19.2	4.1	25.1	21.8	0.0030	0.0007	19.5	4.5
44	3805.0	38.7	83052	870	74.8	2.5	205.9	7.6	209.2	18.7	0.98	61	223.9	11.0	667.1	22.6	0.1068	0.0016	654.1	9.3
45	1165.1	11.9	41529	421	234.1	9.0	468.2	17.1	294.9	26.3	0.61	128	328.8	17.3	558.3	25.2	0.0877	0.0014	541.9	8.3
46	3559.6	36.5	82976	902	185.7	6.0	244.0	9.0	181.0	16.1	0.72	68	483.0	23.7	552.4	23.0	0.0876	0.0015	541.3	8.9
47	3785.6	39.0	78030	834	207.5	6.6	273.4	10.5	247.9	22.4	0.88	79	467.6	23.2	582.6	34.8	0.0933	0.0020	575.0	11.8
48	1286.9	12.9	41541	421	174.4	6.6	248.7	9.2	142.8	12.8	0.56	67	460.8	24.5	591.2	62.4	0.0980	0.0028	602.7	16.4
49	3876.9	39.3	80871	852	273.8	7.5	502.3	18.6	311.9	27.8	0.60	137	358.2	16.2	542.4	16.1	0.0877	0.0009	542.0	5.3
50	3705.5	37.6	78746	800	197.9	6.5	271.9	10.0	209.2	18.7	0.74	77	460.5	22.7	554.8	23.6	0.0896	0.0015	553.2	8.9
51	1306.0	13.3	44953	462	202.8	7.0	683.8	25.3	251.8	22.5	0.36	178	207.9	10.4	810.7	19.2	0.1344	0.0019	812.9	10.8
52	3668.3	37.5	79092	810	273.8	7.8	1018.6	37.6	106.9	9.5	0.10	250	199.5	9.3	600.2	13.5	0.0977	0.0011	600.9	6.5
53	3753.1	38.0	78586	823	288.7	7.9	838.5	30.9	295.8	26.4	0.34	217	241.4	10.9	653.9	12.8	0.1063	0.0010	650.9	5.7
54	3570.1	36.3	77812	790	7.3	0.9	209.7	7.7	133.6	11.9	0.62	58	23.5	3.0	26.1	13.9	0.0032	0.0005	20.9	3.0
55	3824.6	39.0	79830	823	488.5	13.4	799.7	29.4	637.3	56.9	0.77	226	386.9	17.5	818.0	15.4	0.1286	0.0013	779.9	7.4
57	1312.2	13.2	44257	454	315.9	16.2	764.3	28.5	631.7	56.7	0.80	218	263.2	16.7	656.0	26.6	0.1010	0.0014	620.3	8.2
58	1376.5	14.2	63546	638	1176.2	31.3	1955.6	74.5	1154.8	105.5	0.57	532	396.2	18.1	548.3	14.2	0.0858	0.0012	530.7	7.1
59	3759.1	38.5	94134	997	144.4	5.6	252.4	9.4	175.7	15.7	0.67	70	370.1	19.8	564.7	26.8	0.0900	0.0017	555.5	10.1
60	3657.1	36.7	78063	840	99.6	4.5	358.5	13.5	300.2	26.9	0.81	102	177.7	10.3	501.1	19.8	0.0811	0.0012	502.7	7.2
61	3542.2	35.5	78404	808	146.7	5.4	621.6	23.1	2.0	0.2	0.00	149	179.5	9.5	659.7	17.0	0.1054	0.0013	646.0	7.6
63	3659.4	36.7	77142	823	289.9	8.2	488.1	18.2	402.6	36.0	0.80	139	374.6	17.2	543.0	17.3	0.0891	0.0013	550.2	7.7
64	1203.8	12.0	42847	436	134.0	4.6	4968.2	181.6	4155.8	370.3	0.81	1418	17.5	0.8	24.7	2.2	0.0030	0.0001	19.3	0.5
65	3731.5	38.4	80511	824	111.7	5.8	291.0	10.7	207.5	18.5	0.69	81	250.1	15.8	541.8	19.7	0.0871	0.0013	538.4	7.7
66	3839.8	39.6	80702	834	529.5	14.2	886.9	32.6	158.0	14.1	0.17	221	426.9	19.7	694.6	12.8	0.1127	0.0012	688.4	7.0
67	3644.1	38.5	80353	811	51.9	2.0	193.5	7.1	107.0	9.5	0.54	52	181.4	9.3	824.3	37.4	0.1356	0.0032	819.7	18.2
68	3687.2	37.6	80950	851	986.9	25.8	1849.1	68.0	1748.2	156.1	0.91	539	330.4	14.6	512.2	9.2	0.0814	0.0007	504.2	4.4
69	3682.8	38.1	96264	1008	225.8	6.9	375.7	13.8	144.8	12.9	0.37	98	412.0	19.7	534.6	16.8	0.0865	0.0011	534.8	6.5
70	3719.0	37.3	80604	827	255.0	7.4	606.6	22.3	376.7	33.6	0.60	166	278.1	12.7	760.6	43.6	0.1241	0.0018	754.1	10.3
71	1191.5	11.9	42674	434	259.4	10.2	500.0	18.3	251.5	22.4	0.49	134	349.3	18.8	557.1	23.4	0.0904	0.0017	557.9	10.1
72	1168.4	11.7	47986	486	134.5	5.6	377.5	13.8	124.2	11.1	0.32	97	250.8	13.9	675.0	23.0	0.1083	0.0017	662.9	9.9

Supplementary Table E10 Continued

Grain	He Pit Vol. (μm^3)	err. (2σ)	U-Th Pit Vol. (μm^3)	err. (2σ)	[^4He] (nmol/g)	err. (2σ)	[^{238}U] (nmol/g)	err. (2σ)	[^{232}Th] (nmol/g)	err. (2σ)	$^{232}Th/^{238}U$	eU (ppm)	(U-Th)/He date (Ma)	err. (2σ)	$^{207}Pb/^{235}U$ date (Ma)	err. (2σ)	$^{206}Pb/^{238}U$	err. (2σ)	$^{206}Pb/^{238}U$ date (Ma)	err. (2σ)
73	1299.6	13.1	44057	453	2351.2	61.9	3480.3	127.8	3184.7	284.1	0.89	1008	417.4	18.6	545.9	10.7	0.0862	0.0008	533.0	4.9
74	3584.3	36.5	76829	795	95.2	3.9	362.8	13.3	158.2	14.1	0.42	96	181.7	9.8	784.8	33.8	0.1284	0.0018	778.7	10.3
75	1248.4	12.6	63341	638	415.7	20.3	772.2	29.4	315.6	28.3	0.40	202	368.8	23.1	830.6	17.5	0.1354	0.0018	818.6	10.2
76	4303.8	43.7	80625	857	631.4	17.0	3736.0	139.0	1351.7	120.8	0.35	969	119.6	5.3	772.0	12.3	0.1284	0.0017	778.7	9.7
77	1189.9	12.0	45300	480	347.0	16.1	643.3	23.7	407.3	36.4	0.61	176	353.6	21.0	528.0	19.9	0.0864	0.0014	534.2	8.3
78	3684.9	38.0	87537	927	434.5	11.8	872.6	32.3	549.4	49.1	0.61	239	327.5	14.7	615.3	19.9	0.0911	0.0012	562.0	7.1
79	3751.1	37.8	81278	827	496.1	13.5	901.6	33.1	473.0	42.2	0.51	242	368.1	16.6	651.7	12.3	0.1060	0.0010	649.2	5.8
80	3861.0	41.4	81541	825	243.0	7.3	415.1	15.3	289.9	25.9	0.68	115	378.1	17.8	544.8	19.0	0.0878	0.0013	542.5	7.7
81	3753.8	39.0	75969	799	341.1	9.3	2107.5	77.9	583.6	52.1	0.27	537	116.6	5.2	644.2	10.2	0.0981	0.0010	603.4	5.6
83	3786.0	38.6	78174	817	35.0	1.5	219.5	8.3	155.7	14.0	0.69	61	105.3	5.8	537.6	34.6	0.0891	0.0020	550.2	11.8
84	3690.7	38.9	80019	809	227.3	7.2	370.0	13.5	332.8	29.7	0.87	107	381.9	18.3	550.7	18.9	0.0893	0.0011	551.4	6.5
85	3883.6	40.2	77864	824	637.0	17.0	1394.4	51.8	1102.5	98.7	0.77	394	292.1	13.0	762.5	11.5	0.1236	0.0013	751.3	7.5
86	4156.6	44.4	75444	768	741.0	19.6	1578.5	58.0	858.8	76.6	0.53	425	314.4	14.0	590.6	9.1	0.0940	0.0006	578.9	3.8
87	1268.0	13.3	44342	449	312.3	14.0	357.2	13.1	203.6	18.2	0.55	97	569.0	33.6	955.7	35.2	0.1578	0.0039	944.5	21.8
88	3677.7	38.7	78904	799	242.2	7.4	411.9	15.1	300.4	26.8	0.71	115	377.6	17.8	563.0	21.6	0.0879	0.0013	543.1	7.7
89	4408.0	44.3	83215	862	918.8	24.2	6809.1	250.3	4679.3	417.4	0.67	1887	89.6	3.9	239.5	21.6	0.0330	0.0006	209.1	3.6
90	4004.1	42.1	78526	797	48.0	1.8	160.3	5.9	87.9	7.8	0.53	43	202.4	10.4	518.3	26.8	0.0829	0.0017	513.4	10.1
91	4095.9	45.3	78546	798	303.0	8.3	734.9	27.0	554.2	49.4	0.73	206	266.1	11.9	655.5	12.8	0.1063	0.0013	651.2	7.6
92	3693.5	37.9	79680	808	220.9	7.8	628.0	23.1	111.9	10.0	0.17	157	255.7	13.1	702.8	16.3	0.1126	0.0013	687.8	7.5
93	1251.1	12.5	45458	461	60.4	3.0	2052.3	75.4	1226.3	109.4	0.58	559	20.0	1.2	23.5	5.0	0.0030	0.0002	19.4	1.2
94	3969.5	41.8	79994	822	320.4	8.9	600.6	22.0	667.7	59.5	1.08	180	320.6	14.5	541.2	14.9	0.0870	0.0009	537.5	5.3
97	3837.7	39.1	80244	838	260.0	7.5	447.7	16.4	294.9	26.3	0.64	123	378.1	17.4	543.6	16.1	0.0873	0.0011	539.6	6.5
98	1273.0	12.9	59078	602	158.1	5.0	225.0	8.4	150.0	13.5	0.65	62	453.7	22.0	568.2	49.4	0.0864	0.0021	534.2	12.5
99	3772.5	38.0	84168	901	152.6	7.3	264.8	9.8	232.9	20.8	0.85	76	360.3	21.8	551.3	20.6	0.0870	0.0014	537.8	8.3
100	3930.9	42.0	78122	813	456.8	12.2	1462.1	53.7	756.7	67.5	0.50	392	212.3	9.4	793.2	10.2	0.1292	0.0011	783.3	6.3
101	3711.1	38.4	80666	829	256.1	7.8	426.1	15.6	285.5	25.5	0.65	118	390.1	18.4	538.8	17.3	0.0873	0.0012	539.6	7.1
102	1287.3	13.3	45179	460	725.1	20.6	1462.4	53.6	900.2	80.3	0.60	400	327.0	14.9	540.6	13.7	0.0868	0.0009	536.4	5.5
103	1332.9	13.4	45101	461	584.3	20.1	1104.5	40.6	880.5	78.6	0.77	313	336.6	16.8	549.5	19.5	0.0856	0.0009	529.6	5.2
104	1359.3	13.7	45448	463	293.2	14.1	959.2	35.1	880.2	78.5	0.89	278	192.5	11.5	703.8	55.8	0.1081	0.0019	661.7	11.1
105	1224.9	12.5	39807	417	469.6	17.8	830.4	30.6	476.3	42.5	0.56	225	374.5	19.8	777.2	20.8	0.1280	0.0015	776.5	8.6
106	3687.8	37.9	80691	817	356.5	9.7	399.0	14.8	390.8	34.9	0.95	117	539.8	24.8	579.2	19.5	0.0929	0.0012	572.7	7.1
107	3796.0	38.1	79851	806	124.7	5.6	219.5	8.0	174.0	15.5	0.77	62	361.1	21.0	538.8	22.0	0.0886	0.0016	547.3	9.5
108	3821.9	38.4	79338	826	796.4	21.1	885.3	32.9	368.4	32.9	0.40	232	602.0	27.8	675.5	14.1	0.1068	0.0013	654.1	7.6
109	4098.0	41.2	75650	792	1545.1	40.1	5551.2	204.3	2261.9	202.0	0.39	1454	193.8	8.5	651.7	12.8	0.1026	0.0008	629.5	4.7
110	3989.9	41.1	77419	809	1704.9	44.5	3017.0	110.8	3336.0	297.5	1.07	905	339.5	15.1	554.8	7.6	0.0878	0.0007	542.3	4.3

Supplementary tables E11-18

- R = half-width (μm)
- L= length (μm)
- Apatite F_T correction following Farley, Kenneth A. (2002). "U-Th)/He dating: Techniques, calibrations, and applications. *Reviews in Mineralogy and Geochemistry*, 47, 1, p. 819–844.

Supplementary Table E11**.** (U-Th)/He detrital apatite data for sample CHB14-2A-28A-1.

Grain	**R (μm)**	**L (μm)**	**He (pmol)**	**[^{238}U] (ppm)**	**[^{232}Th] (ppm)**	**F_T**	**Raw Age (Ma)**	**Corr. Age (Ma)**	**err. (2σ)**
1	64.8	275.8	0.0032	1.52	3.87	0.781	24.76	31.71	4.51
2	63.0	226.9	0.0087	6.02	3.74	0.776	30.70	39.58	1.53
4	69.4	313.4	0.0024	2.36	5.78	0.797	9.62	12.08	1.62
5	53.1	239.8	0.0089	5.40	4.83	0.745	43.86	58.86	2.15
6	66.6	192.3	0.0029	2.44	0.69	0.780	28.67	36.78	5.27
7	69.7	318.4	0.0181	7.48	0.44	0.807	33.29	41.26	1.26
9	48.2	263.8	0.0010	1.26	2.74	0.723	17.42	24.09	1.51
10	55.7	226.8	0.0028	6.27	9.27	0.750	10.43	13.92	0.64

Supplementary Table E12. (U-Th)/He detrital apatite data for sample CHB14-2A-29A-1.

Grain	**R (μm)**	**L (μm)**	**He (pmol)**	**[^{238}U] (ppm)**	**[^{232}Th] (ppm)**	**F_T**	**Raw Age (Ma)**	**Corr. Age (Ma)**	**err. (2σ)**
1	68.7	460.1	0.0563	8.85	2.60	0.812	59.59	73.34	2.07
2	83.2	296.8	0.0027	1.89	3.92	0.823	10.44	12.69	0.66
3	64.8	228.9	0.0013	1.30	13.29	0.764	6.72	8.80	0.69
4	67.8	339.5	0.0638	13.26	16.58	0.799	52.53	65.77	1.73
5	49.5	222.0	0.0006	1.54	1.22	0.729	13.67	18.76	1.91
8	74.6	403.4	0.0267	3.30	7.03	0.816	52.80	64.74	1.90
9	60.4	298.6	0.0053	2.37	2.55	0.776	36.21	46.66	2.12
10	58.2	260.2	0.0031	1.27	2.45	0.761	39.63	52.05	2.74

Supplementary Table E13. (U-Th)/He detrital apatite data for sample CHB14-2A-51Q-1.

Grain	R (μm)	L (μm)	He (pmol)	[^{238}U] (ppm)	[^{232}Th] (ppm)	F_T	Raw Age (Ma)	Corr. Age (Ma)	err. (2σ)
1	52.5	199.7	0.0020	2.41	5.73	0.729	21.60	29.62	1.53
2	46.3	184.1	0.0209	21.53	8.52	0.709	49.49	69.85	1.88
3	52.8	255.1	0.0311	12.67	26.01	0.742	51.21	69.05	1.90
5	47.4	181.6	0.0030	4.12	6.24	0.706	28.99	41.05	1.67
6	60.5	241.7	0.0003	0.26	1.03	0.761	16.82	22.11	1.76
7	59.9	179.1	0.0218	11.75	4.40	0.758	58.19	76.78	2.03
8	79.0	210.5	0.0033	0.99	1.78	0.803	37.99	47.32	2.11
9	53.5	266.4	0.0058	3.41	6.44	0.746	33.99	45.54	1.33
10	52.9	234.4	0.0004	1.20	1.21	0.743	9.19	12.37	1.25

Supplementary Table E14. (U-Th)/He detrital apatite data for sample CHB14-2A-90Q-1.

Grain	R (μm)	L (μm)	He (pmol)	[^{238}U] (ppm)	[^{232}Th] (ppm)	F_T	Raw Age (Ma)	Corr. Age (Ma)	err. (2σ)
1	60.7	323.5	0.0038	2.15	2.18	0.780	26.23	33.65	1.14
3	59.1	263.3	0.0002	0.64	2.86	0.759	4.25	5.60	1.02
4	70.9	312.9	0.0155	16.77	6.53	0.807	11.89	14.73	0.39
5	87.4	249.7	0.0001	0.03	0.23	0.816	17.84	21.88	5.91
6	69.0	265.1	0.0052	3.95	10.51	0.790	14.22	18.01	0.55
7	55.8	316.4	0.0120	4.24	15.55	0.755	33.85	44.82	1.25
8	58.4	256.8	0.0027	1.20	0.97	0.766	46.74	60.99	2.94
9	67.5	293.5	0.0002	0.05	0.37	0.783	19.28	24.62	6.88
10	71.5	302.1	0.0040	1.45	5.35	0.798	21.01	26.34	1.02

Supplementary Table E15. (U-Th)/He detrital apatite data for sample CHB14-2A-117Q-2.

Grain	R (µm)	L (µm)	He (pmol)	[^{238}U] (ppm)	[^{232}Th] (ppm)	F_T	Raw Age (Ma)	Corr. Age (Ma)	err. (2σ)
1	48.7	222.1	0.0065	5.18	15.26	0.716	30.81	43.01	1.25
2	48.5	127.4	0.0011	3.12	3.35	0.693	21.56	31.11	2.22
3	55.7	241.3	0.0008	3.11	0.82	0.758	7.11	9.37	0.86
4	54.3	237.3	0.0010	3.46	4.68	0.747	6.75	9.04	0.84
5	51.1	220.9	0.0013	0.73	3.26	0.723	33.79	46.75	3.20
6	53.9	222.8	0.0007	3.54	2.20	0.747	6.10	8.17	0.55
7	45.0	314.6	0.0033	5.59	18.98	0.709	11.26	15.87	0.57
8	47.2	223.0	0.0014	8.92	6.95	0.719	5.69	7.92	0.47
9	53.0	202.5	0.0151	21.48	26.23	0.736	21.12	28.67	0.79
10	48.9	236.5	0.0004	2.47	8.87	0.718	3.29	4.58	0.50

Supplementary Table E16. (U-Th)/He detrital apatite data for sample CHB14-2B-20H-1.

Grain	R (µm)	L (µm)	He (pmol)	[^{238}U] (ppm)	[^{232}Th] (ppm)	F_T	Raw Age (Ma)	Corr. Age (Ma)	err. (2σ)
3	54.3	246.0	0.0025	1.17	5.47	0.739	30.37	41.07	1.74
4	71.0	194.0	0.0013	0.82	0.71	0.787	27.01	34.33	2.52
5	56.7	233.8	0.0013	2.93	1.63	0.759	11.25	14.83	0.82
6	69.9	230.0	0.0075	8.98	3.01	0.795	15.12	19.04	0.55
7	73.3	255.0	0.0107	6.50	22.83	0.796	14.48	18.20	0.48
8	60.8	276.4	0.0013	2.20	4.21	0.771	8.47	10.97	0.70
9	78.2	277.6	0.0003	0.43	0.12	0.818	9.58	11.71	1.69
10	60.2	221.4	0.0004	1.60	1.39	0.766	5.57	7.27	0.66

Supplementary Table E17. (U-Th)/He detrital apatite data for sample CHB14-2B-23E-1.

Grain	**R (μm)**	**L (μm)**	**He (pmol)**	**[^{238}U] (ppm)**	**[^{232}Th] (ppm)**	**F_T**	**Raw Age (Ma)**	**Corr. Age (Ma)**	**err. (2σ)**
1	79.3	212.6	0.0015	3.23	1.46	0.809	6.83	8.44	0.43
2	49.9	283.1	0.0075	8.39	18.31	0.733	18.54	25.30	0.68
3	82.4	357.5	0.0321	11.57	0.36	0.834	24.99	29.96	0.81
4	71.9	304.9	0.0036	4.13	0.81	0.810	11.63	14.37	0.46
8	62.3	62.1	0.0039	18.93	6.64	0.672	17.30	25.73	1.12
9	52.0	50.4	0.0009	11.08	9.72	0.606	10.52	17.35	1.56
10	71.2	74.6	0.0011	4.11	2.62	0.714	13.29	18.62	1.54

Supplementary Table E18. (U-Th)/He detrital apatite data for sample CHB14-2B-35E-1.

Grain	**R (μm)**	**L (μm)**	**He (pmol)**	**[^{238}U] (ppm)**	**[^{232}Th] (ppm)**	**F_T**	**Raw Age (Ma)**	**Corr. Age (Ma)**	**err. (2σ)**
1	67.0	301.2	0.1398	7.31	27.26	0.787	164.55	209.14	5.38
2	71.2	227.6	0.0307	4.52	7.92	0.791	91.30	115.42	3.20
3	59.0	228.9	0.0054	0.69	2.42	0.755	117.57	155.75	5.40
5	60.2	196.4	0.0182	8.32	11.62	0.758	49.89	65.81	1.93
6	69.3	232.2	0.0343	14.86	9.18	0.792	39.00	49.23	1.30
7	64.4	245.4	0.0586	18.08	25.33	0.779	52.75	67.70	1.71